SYNTHETIC STRATEGIES TO TAILOR ACTIVE AND DEFECT SITE STRUCTURES IN LEWIS ACID ZEOLITES FOR SUGAR ISOMERIZATION CATALYSIS

A Dissertation

Submitted to the Faculty

of

Purdue University

by

Juan Carlos Vega-Vila

In Partial Fulfillment of the

Requirements for the Degree

of

Doctor of Philosophy

December 2019

Purdue University

West Lafayette, Indiana

THE PURDUE UNIVERSITY GRADUATE SCHOOL
STATEMENT OF DISSERTATION APPROVAL

Dr. Rajamani Gounder, Chair

Davidson School of Chemical Engineering

Dr. Jeffrey Greeley

Davidson School of Chemical Engineering

Dr. Jeffrey T. Miller

Davidson School of Chemical Engineering

Dr. Christina Li

Department of Chemistry

Approved by:

Dr. John A. Morgan

Head of the Graduate Program

To my mother, Isabel Vila Martínez, for her unconditional love and support.

ACKNOWLEDGMENTS

I would like to first acknowledge the incredible mentorship of Professor Rajamani Gounder, my advisor. His pursuit to further our understanding of the nature of active sites and their consequences on catalytic systems, together with his interest in precise and concise communication of scientific results, helped me grow as a researcher. I hope I can share all the skills he helped me develop with other young researchers throughout the rest of my career. Thank you for helping me become the young scientist I am today.

I acknowledge my committee members: Prof. Jeffrey Greeley, Prof. Jeffrey Miller, and Prof. Christina Li for their willingness to participate in my qualifying exam, preliminary exam, and thesis defense. Thank you for the guidance and valuable advice through the last five years. I would also like to acknowledge insightful technical discussions with Prof. Fabio Ribeiro. I also thank Dr. Yury Zvinevich, Jeffrey Valley, and Nick S. Humphrey for experimental and instrumentation support.

I acknowledge helpful technical discussions and experimental help provided by the Gounder Research Group. The contributions of the group members to my work were an invaluable asset to the success of my studies. In particular, I would like to acknowledge the support through the years by Laura Wilcox and Claire Nimlos. I would also like to acknowledge the contributions of Dr. Michael J. Cordon and Dr. James W. Harris to my research and professional development. Michael and Jamie were an invaluable source of knowledge and encouragement during their time at Purdue.

Next, I acknowledge the staff of the Davidson School of Chemical Engineering for all the help in the last five years. I thank Beverly Johnson for academic guidance

during my time as a graduate student, as well as support by Robin Waling and Yvette Rosas.

I thank Kristin Soto Rosa, Andrew Pigman, Lyndsey Smith, Jayce Lane, Zachary Bates, Erin Lang, Kathleen Welling, Molly Sheetz Jones, Doddy McIntyre, and Shelly Pullins for their friendship and for giving me necessary distractions from research.

Finally, I am thankful to my family for their unparalleled love and support during my time at Purdue. I especially would like to thank Isabel Vila Martínez (mother), Juan Carlos Vega Morales (father), Karla Isabel Vega Vila (sister), Ruth Esther Martínez Sanabria (grandmother), and Billy Vila Ramírez (grandfather) for being a consistent source of support and encouragement. I thank them for reminding me of the reasons I do everything I do.

TABLE OF CONTENTS

Page

LIST OF TABLES xi

LIST OF FIGURES xiv

ABSTRACT xxxv

1 INTRODUCTION 1

2 TITRATION AND QUANTIFICATION OF OPEN AND CLOSED LEWIS ACID SITES IN SN-BETA ZEOLITES THAT CATALYZE GLUCOSE ISOMERIZATION 7

2.1 Abstract 7

2.2 Introduction 9

2.3 Experimental Methods 13

2.3.1 Catalyst Synthesis 13

2.3.2 Catalyst Characterization 15

2.3.3 Temperature Programmed Desorption 17

2.3.4 Infrared Spectroscopy and Determination of Integrated Molar Extinction Coefficients 18

2.3.5 Kinetic and Isotopic Tracer Studies of Glucose Reactions with Sn-Beta 20

2.4 Results and Discussion 23

2.4.1 Structural Characterization of Stannosilicates 23

2.4.2 Quantification of Lewis Acid Sites: IR Studies with Pyridine . 27

2.4.3 Quantification of Lewis Acid Sites: TPD Studies with n-Propylamine and Ammonia 32

2.4.4 Quantification of Open and Closed Lewis Acid Sites: IR Studies with Deuterated Acetonitrile 35

2.4.5 Glucose Isomerization Rate Constants on Hydrophobic and Hydrophilic Sn-Beta Zeolites 40

2.5 Conclusions 47

2.6 Acknowledgements 49

2.7 Supporting Information 50

2.7.1 X-ray Diffractograms of Stannosilicate Samples. 50

2.7.2 N_2 and H_2O Adsorption Isotherms of Zeolite Samples. 51

2.7.3 Diffuse-Reflectance UV-Visible Spectra of Zeolite Samples. . . . 55

Page

2.7.4 ^{1}H NMR Spectra of Sugars after Reaction of Glucose-D2 with Zeolite Samples in Water. 62
2.7.5 Determination of Integrated Molar Extinction Coefficients for Pyridine on H-Y Zeolite. 64
2.7.6 Pyridine Titration and Infrared Spectroscopy of Zeolite Samples. 68
2.7.7 n-Propylamine Temperature Programmed Desorption (TPD) Experiments on Zeolites. 72
2.7.8 Ammonia Temperature Programmed Desorption Experiments on Zeolite Samples. 79
2.7.9 Deuterated Acetonitrile Titration and Infrared Spectroscopy of Zeolites. 84
2.7.10 Kinetic Measurements of Glucose Isomerization on Zeolite Samples.96

3 CONTROLLED INSERTION OF TIN ATOMS INTO ZEOLITE FRAMEWORK VACANCIES AND CONSEQUENCES FOR GLUCOSE ISOMERIZATION CATALYSIS 103
3.1 Abstract 103
3.2 Introduction 105
3.3 Experimental Methods 109
3.3.1 Catalyst synthesis 109
3.3.2 Catalyst Characterization 111
3.3.3 Kinetic studies of glucose isomerization 114
3.4 Results and Discussion 116
3.4.1 Sn-Beta prepared post-synthetically by grafting in isopropanol 116
3.4.2 Sn-Beta prepared post-synthetically by grafting in dichloromethane 118
3.4.3 Controlling framework Sn content and speciation in post-synthetic Sn-Beta 125
3.4.4 Catalytic consequences for aqueous-phase glucose isomerization to fructose 129
3.5 Conclusions 141
3.6 Acknowledgements 143
3.7 Supporting Information 144
3.7.1 X-ray diffractograms of zeolite samples. 144
3.7.2 Scanning electron microscope images of stannosilicate samples. 150
3.7.3 Physicochemical properties of stannosilicates and synthesis specification. 151
3.7.4 Diffuse reflectance UV-Vis spectra of stannosilicate samples. . 154
3.7.5 Temperature programmed desorption with adsorbed isopropanol and dichloromethane. 175
3.7.6 Studies with Infrared spectroscopy: OH stretching region during isopropanol dosing. 176

Page

3.7.7 Studies with Infrared spectroscopy after titration with CD_3CN and pyridine. . . . 178
3.7.8 Derivation of Langmuir isotherm expression describing Sn grafting into framework vacancy defects. . . . 181
3.7.9 Kinetic studies of glucose isomerization to fructose with stannosilicates and assessment of intraparticle mass transfer limitations. . . . 182
3.7.10 Assessment of the hydrophobicity of Sn-Beta with vapor-phase adsorption of H_2O and CH_3OH. . . . 185

4 THE DOMINANT ROLE OF ENTROPY IN STABILIZING SUGAR ISOMERIZATION TRANSITION STATES WITHIN HYDROPHOBIC ZEOLITE PORES . . . 191
4.1 Abstract . . . 191
4.2 Introduction . . . 193
4.3 Materials and Methods . . . 197
4.3.1 Catalyst Synthesis . . . 197
4.3.2 Characterization of Bulk Catalyst Properties . . . 198
4.3.3 Transmission Infrared Spectroscopy . . . 200
4.3.4 Glucose Isomerization Kinetic Studies . . . 203
4.3.5 Computational Methods . . . 205
4.3.6 ATR-IR Spectroscopy with MES-PSD MCR-ALS . . . 207
4.3.7 X-Ray Absorption Spectroscopy (XAS) Measurements . . . 209
4.4 Results and Discussion . . . 210
4.4.1 Bulk Structural and Lewis Acid Site Characterization of Ti-Beta Zeolites . . . 210
4.4.2 Characterization of Hydrophobic Properties of Ti-Beta Zeolites 216
4.4.3 Aqueous-Phase Glucose Isomerization Mechanisms and Kinetic Measurements . . . 223
4.4.4 Characterization of Active Site Complexes in First-Order and Zero-Order Kinetic Regimes . . . 231
4.4.5 Enthalpic and Entropic Consequences of Hydrophobic Reaction Pockets for Aqueous-Phase Glucose Isomerization . . . 238
4.5 Conclusions . . . 252
4.6 Acknowledgements . . . 255
4.7 Supporting Information . . . 256
4.7.1 Bulk Structural and Lewis Acid Site Characterization of Ti-Beta Zeolites . . . 256
4.7.2 Characterization of the Hydrophobic Properties of Ti-Beta Zeolites . . . 270
4.7.3 Glucose Isomerization Mechanisms and Kinetic Measurements 278
4.7.4 Characterization and Kinetic Effects of Bound Surface Species in First-Order and Zero-Order Regimes . . . 285

Page

4.7.5 Thermodynamic Contributions of Hydrophobic Reaction Pockets for Aqueous-Phase Glucose Isomerization 297

5 QUANTIFICATION OF INTRAPOROUS HYDROPHILIC BINDING SITES IN LEWIS ACID ZEOLITES AND CONSEQUENCES FOR SUGAR ISOMERIZATION CATALYSIS 319
5.1 Abstract 319
5.2 Introduction 321
5.3 Experimental Methods 324
5.3.1 Catalyst synthesis 324
5.3.2 Catalyst Characterization 326
5.3.3 Kinetic studies of glucose isomerization 328
5.4 Results and Discussion 330
5.4.1 Preparation of solid Lewis acids with varying density of hydrophilic binding sites 330
5.4.2 Evaluation of micropore polarity using alcohol probe molecules 331
5.4.3 IR spectra of Sn-Beta in flowing CH_3OH 335
5.4.4 Quantification of silanol groups in Lewis acid zeolites via H/D isotopic exchanges 337
5.4.5 Quantification of silanol groups via IR spectroscopy in Lewis acid zeolites with CD_3CN 339
5.4.6 Influence of intrapore silanol density on sugar isomerization catalysis 342
5.5 Conclusions 346
5.6 Acknowledgements 348
5.7 Supporting Information 349
5.7.1 X-ray diffractograms patters of Sn-Beta zeolites and parent Al-Beta 349
5.7.2 Micropore volumes and physicochemical properties of zeolite samples 354
5.7.3 Diffuse reflectance UV-Vis spectra of stannosilicate samples . 354
5.7.4 Assessment of the hydrophobicity of Sn-Beta with vapor-phase adsorption of CH_3OH at 293 K 358
5.7.5 Isotopic H/D exchange experiments on stannosilicates 362
5.7.6 Assessment of intraparticle mass transfer limitations 363

6 TIGHTER CONFINEMENT INCREASES SELECTIVITY OF D-GLUCOSE ISOMERIZATION TOWARDS L-SORBOSE IN TI-ZEOLITES 365
6.1 Abstract 365
6.2 Introduction 366
6.3 Experimental Methods 368
6.3.1 Synthesis of titanosilicates with varying pore sizes 368
6.3.2 Characterization of materials 371

Page

6.3.3 Glucose isomerization kinetic studies 372
6.4 Results and Discussion 374
6.5 Conclusions 382
6.6 Acknowledgements 383
6.7 Supporting Information 384
6.7.1 Characterization of titanosilicate catalysts 384
6.7.2 Liquid NMR analysis for detection of products 391
6.7.3 Kinetic details of fructose and sorbose formation over titanosilicates 393

REFERENCES 396

VITA 414

LIST OF TABLES

Table Page

2.1 Site and structural characterization data for the samples in this study. . . 24

2.2 Integrated molar extinction coefficients ($\mathcal{E}$) for infrared peaks for pyridine and deuterated acetonitrile adsorbed to different sites on Sn-Beta and H-Y zeolites, determined assuming equimolar titrant binding to each type of site. 29

2.3 Fraction of Lewis acidic Sn sites (per mol Sn) on each sample counted with different base titrants. Binding stoichiometries of 1 per site for each titrant. 31

2.4 Edge energies for all samples determined from x-intercepts of linear portions of Tauc plots (Figs. 2.19 and 2.20) DRUV band centers at maximum F(R) intensity are reported for spectra collected after dehydration treatments (Figs. 2.17 and 2.18), and parenthetical values are for second band observed in some DRUV spectra. 56

2.5 Molecules of NPA desorbed per Sn after saturation with 1000 ppm NPA for 4 h at 323 K followed by purging for 4 h and 8 h. 73

2.6 Moles of NPA desorbed per g zeolite after saturation with 1000 ppm NPA for 4 h at 323 K followed by purging for 8 h. 75

2.7 Molecules of NH_3 desorbed (per Sn) after saturation with 500 ppm NH_3 for 5 h at 323 K, followed by purging for 8 h. 80

2.8 Moles of NH_3 desorbed (per g) after saturation with 500 ppm NH_3 for 5 h at 323 K followed by purging for 8 h. 82

2.9 Peak areas at saturation for the 2316 cm^{-1}, 2308 cm^{-1}, 2287 cm^{-1}, 2275 cm^{-1} and 2265 cm^{-1} peaks for all Sn samples in this study. 95

2.10 Site and structural characterization data for the samples in this study. . 102

3.1 Structural characterization of Sn-Beta samples prepared via post-synthetic grafting with isopropanol and dichloromethane as reflux solvents. 123

3.2 Number of open (2316 cm^{-1}) and closed (2308 cm^{-1}) Sn sites titrated by CD_3CN and quantified by IR spectral band deconvolution. 124

3.3 Number of open (2316 cm^{-1}) and closed (2308 cm^{-1}) Sn sites titrated by CD_3CN and quantified by IR spectral band deconvolution. 127

Table Page

3.4 Glucose conversion, monosaccharide yields and turnover numbers (TON) for aqueous-phase (1% (w/w)) glucose isomerization (373 K), and apparent first-order isomerization rate constants (per open Sn). 132

3.5 Elemental composition, and fraction of open (2316 cm^{-1}) and closed (2308 cm^{-1}) Sn sites, for post-synthetic Sn-Beta-F samples. 137

3.6 Synthesis conditions, elemental compositions, and pore volume for Sn-Beta samples. 152

3.6 Synthesis conditions, elemental compositions, and pore volume for Sn-Beta samples. 153

3.7 DRUV peak maximum and edge energy after thermal treatment at 523 K. 174

3.8 Moles of 2287 cm^{-1} (g zeolite)$^{-1}$ for stannosilicates prepared through post-synthetic grafting under dichloromethane reflux (333 K). 180

3.9 First-order rate constants (per open Sn) for hydrothermally-synthesized Sn-Beta samples [26] in Fig. 3.7. 185

3.10 H_2O uptake of Sn-Beta samples measured at a relative pressure (P/P_0) of 0.2. 190

4.1 Site and structural characterization data for Ti-Beta samples in this study. 214

4.2 Semi-quantitative measurements of the hydrophobic properties of microporous voids in Ti-Beta-F and Ti-Beta-OH materials. 215

4.3 Relative concentrations[a] of MARI and minor species during modulation of liquid-phase glucose concentration (42-50 wt%) at 373 K followed by processing by PSD and MCR-ALS. 233

4.4 Apparent enthalpies and entropies for first-order and zero-order rate constants describing fructose and sorbose formation on Ti-Beta-F-155 and Ti-Beta-OH-46. 247

4.5 Edge energies of Ti-Beta samples after exposure to ambient conditions, dehydrated, and rehydrated in wet Ar flow. Band maxima correspond to the primary UV-Vis F(R) peaks after dehydration shown in Figure 4.14 above. 261

4.6 E(1605 cm^{-1}) values determined for four separate Ti-Beta samples by sequentially dosing pyridine at 423 K. 267

4.7 Surface-area-to-volume (SA/V) ratios and silanol defect densities for selected Ti-Beta-F and Ti-Beta-OH samples normalized to Ti-Beta-F-155. 269

Table Page

4.8 Ti energies, coordination numbers, and bond distances determined from Ti XAS. 296

4.9 Apparent enthalpies and entropies for first-order and zero-order rate constants describing fructose and sorbose formation on Ti-Beta-F-155 and Ti-Beta-OH-46 derived from single rate measurements at 5 and 50 wt.% corresponding to first-order and zero-order rates. Differences in apparent activation enthalpies ($\Delta\Delta$ H_{app}) and entropies ($\Delta\Delta$ S_{app}) are listed as the difference between Ti-Beta-F-155 and Ti-Beta-OH-46. 317

5.1 Density of hydrophilic binding sites quantified via H/D isotopic exchange and IR spectra of samples saturated with CD_3CN (303 K), along with the methanol packing densities within solid Lewis acid zeolites. 334

5.2 Density of hydrophilic binding sites quantified via H/D isotopic exchange and IR spectra of samples saturated with CD_3CN (303 K), along with the methanol packing densities within solid Lewis acid zeolites. 355

5.3 Density of hydrophilic binding sites quantified via H/D isotopic exchange- and IR spectra of samples saturated with CD_3CN (303 K), along with the methanolpacking densities within solid Lewis acid zeolites. 357

6.1 Fructose and sorbose reaction rates (per Ti) and selectivities at 373 K for Ti-containing zeotype materials. 381

6.2 Physicochemical properties and topological details of titanosilicates of varied metal content and pore size. 388

6.4 Fructose and sorbose reaction rates (per Ti) and selectivities at 373 K for Ti-Beta molecular sieves of varied Ti content. 395

LIST OF FIGURES

Figure Page

2.1 Adsorption of CD_3CN on different sites in stannosilicates and corresponding $\nu(C{\equiv}N)$ infrared vibrational frequencies. 23

2.2 IR spectra measured at low pyridine coverage (0.09-0.20 pyridine/Sn) and saturated spectra (thick lines) for (a) Sn-Beta-F-100, (b) Sn-Beta-F-140, and (c) Sn-Beta-OH-170. Dashed reference lines shown for Lewis acid sites (1615 cm^{-1}, 1450 cm^{-1}), Lewis or Brønsted acid sites (1575 cm^{-1}, 1490 cm^{-1}), Brønsted acid sites (1550 cm^{-1}), and gas-phase pyridine (1595 cm^{-1}). 28

2.3 Determination of the integrated molar extinction coefficient for pyridine adsorbed on Lewis acid sites (1450 cm^{-1}) on Sn-Beta-OH-170 (squares), Sn-Beta-F-140 (triangles), Sn-Beta-F-100 (circles), from IR peak areas corresponding to pyridine/Sn coverages between 0.04 and 0.66. 30

2.4 Titrant molar uptakes (per Sn) compared to pyridine molar uptakes (per Sn) at saturation of Sn-Beta samples with (a) n-propylamine (NPA, squares), (b) ammonia (NH_3, triangles), and (c) CD_3CN (closed circles were included and open circles were not included in fitting of $\mathcal{E}$ values). Parity lines shown as dashed lines. NPA titration data not shown for samples denoted with an asterisk in Table 32.3, for which TPD quantification includes binding to residual defect sites. 33

2.5 FTIR difference spectra of Sn-Beta-F-105 (relative to the vacant surface) (a) with increasing CD_3CN increasing coverage and (b) at a coverage of 0.65 CD_3CN/Sn with deconvolution into component peaks. Dashed reference lines shown for open Sn sites (2316 cm^{-1}), closed Sn sites (2308 cm^{-1}), $(SiO)_2Sn(OH)_2$ sites (*speculative assignment*, 2287 cm^{-1}), silanol groups (2275 cm^{-1}), and gas-phase CD_3CN (2265 cm^{-1}). 36

2.6 Evolution of IR peak areas for 2316 cm^{-1} (closed diamonds), 2308 cm^{-1} (open diamonds), 2287 cm^{-1} (closed circles), and 2275 cm^{-1} (open circles) peaks with increasing CD_3CN coverage on Sn-Beta-F-105. 37

2.7 Moles of CD_3CN adsorbed on open Sn sites (open diamonds) and closed Sn sites (closed diamonds) on Sn-Beta-F-105, together with the ratio of open-to-closed Sn sites titrated (closed circles), as a function of CD_3CN coverage. 38

Figure Page

2.8 Dependence of initial glucose-fructose isomerization turnover rate (per total Sn, 373 K) for Sn-Beta-F-220 on the initial aqueous-phase glucose concentration (1-10% (w/w)). 40

2.9 Plausible reaction mechanism for glucose-fructose isomerization on open Sn sites in Sn-Beta involving kinetically-relevant 1,2-intramolecular hydride shift (Step 2). For clarity, kinetically-irrelevant steps are lumped as quasi-equilibrated reactions (Steps 1, 3-5). 42

2.10 Dependence of initial glucose-fructose isomerization turnover rates (per total Sn, 373 K, 1% (w/w) glucose) on pyridine coverage from titration before reaction on (a) Sn-Beta-F-110 and (b) Sn-Beta-F-170. The fraction of Sn open sites counted *ex situ* by CD_3CN are shown as open diamonds along the x-axes. 44

2.11 First-order glucose-fructose isomerization rate constant (per open Sn site, 373 K) in water for hydrophobic Sn-Beta-F (closed circle) and hydrophilic Sn-Beta-OH (open circle) samples as a function of Sn/Si ratio. Dashed lines indicate the averaged turnover rate within each series. 46

2.12 Powder XRD patterns of the stannosilicate samples in this study. Patterns for Sn-Beta-OH-170 and Sn-Beta-OH-200 multiplied by 10×, and Sn-xerogel multiplied by 5×, for clarity. 50

2.13 N_2 adsorption isotherms (77 K) for all samples used in this study. Isotherms offset by 200 cm^3 g^{-1} for clarity. 52

2.14 H_2O adsorption isotherms (293 K) for Sn-Beta-F samples used in this study. Isotherms offset by 100 cm^3 g^{-1} for clarity. 53

2.15 H_2O adsorption isotherms (293 K) for Sn-Beta-OH samples, SnO_2/Si-Beta-F, and Sn-xerogel used in this study. Isotherms offset by 300 cm^3 g^{-1} for clarity. 54

2.16 Diffuse reflectance UV-Vis spectra in Kubelka-Munk units (normalized to the maximum F(R) intensity within each series) for (a) Sn-Beta-F-170, (b) Sn-Beta-OH-200, and (c) SnO_2/Si-Beta collected under ambient conditions (thin solid line), after dehydration at 523 K (thick solid line), and after rehydration at 303 K (dashed line). 57

2.17 DRUV spectra for Sn-zeolite samples collected after dehydration treatments (523 K). Spectra normalized to F(R) at the peak maximum and artificially offset for clarity. 58

2.18 DRUV spectra for Sn-zeolite samples collected after dehydration treatments (523 K). Spectra normalized to F(R) at the peak maximum and artificially offset for clarity. 59

Figure Page

2.19 Tauc plots for Sn-zeolite samples from DRUV spectra collected after dehydration treatments (523 K). 60

2.20 Tauc plots for Sn-zeolite samples from DRUV spectra collected after dehydration treatments (523 K). Inset shows low-energy region for Sn-Beta-OH-200 that gives rise to the edge energy reported in Table 2.1. 61

2.21 ^{1}H NMR spectra for glucose recovered after glucose isomerization catalysis with the Sn-Beta samples tested in this study. The resonating multiplet centered around δ = 4.7 ppm corresponds to residual water present after freeze drying the monosaccharide products 62

2.22 ^{1}H NMR spectra for the fructose recovered after glucose isomerization catalysis with the Sn-Beta samples tested in this study. A small resonance at δ=3.47 ppm (denoted with an asterisk) is present in fructose products on Sn-Beta-OH-170 and Sn-Beta-OH-200, indicating a small contribution of the enolate mechanism by hydroxyl ions that becomes detectable at the longer reaction times (>4 h) used to attain higher glucose conversion on these samples. 63

2.23 IR spectra after progressive titration of pyridine on H-Y (Si/Al=2.6, Zeolyst) at 423 K (pyridine/Al = 0.005-0.040). Dashed lines at 1630 cm^{-1} (protonated pyridine), 1545 cm^{-1} (protonated pyridine), and 1490 cm^{-1} (protonated pyridine or pyridine bound to Lewis acidic Al sites). 65

2.24 Integrated area of 1545 cm^{-1} IR peak multiplied by wafer cross-sectional area plotted against the amount of pyridine adsorbed on H-Y (Si/Al=2.6, Zeolyst) at 423 K. 66

2.25 IR spectra after progressive titration of pyridine on high temperature-treated H-Y (Si/Al=2.6, Zeolyst) at 423 K (pyridine/Al = 0.012-0.13). Dashed lines shown at 1630 cm^{-1} (protonated pyridine), 1615 cm^{-1} (pyridine bound to Lewis acidic Al sites), 1545 cm^{-1} (protonated pyridine), 1490 cm^{-1} (protonated pyridine or pyridine bound to Lewis acidic Al sites), and 1455 cm^{-1} (pyridine bound to Lewis acidic Al sites). 67

Figure Page

2.26 IR difference spectra for pyridine saturated Sn-Beta samples after evacuation at 423 K for 900 s for (a) Sn-Beta-F-100, (b) Sn-Beta-F-105, (c) Sn-Beta-F-110, (d) Sn-Beta-F-140, (e) Sn-Beta-F-170, (f) Sn-Beta-F-220, (g) Sn-Beta-OH-170, (h) Sn-Beta-OH-200, (i) SnO_2/Si-Beta, and (j) Sn-xerogel. All spectra normalized to the overtone and combination modes of Si-O-Si stretches (1750-2100 cm^{-1}) and to the maximum peak intensity for clarity. Dashed lines shown at 1610 cm^{-1} (pyridine bound to Lewis acidic Sn sites), 1540 cm^{-1} (protonated pyridine), 1490 cm^{-1} (protonated pyridine or pyridine bound to Lewis acidic Sn sites), and 1450 cm^{-1} (pyridine bound to Lewis acidic Sn sites). 69

2.27 IR spectra for pyridine-saturated Sn-Beta-F-100 during exposure to dynamic vacuum at 423 K for 0 s, 300 s, and 900 s (thin to thick traces) after saturation with pyridine. Dashed lines shown at 1610 cm^{-1} (pyridine bound to Lewis acidic Sn sites), 1545 cm^{-1} (protonated pyridine), 1490 cm^{-1} (protonated pyridine or pyridine bound to Lewis acidic Sn sites), and 1450 cm^{-1} (pyridine bound to Lewis acidic Sn sites). 70

2.28 Integrated area of the IR peak at 1450 cm^{-1} as a function of time exposed to dynamic vacuum at 423 K for pyridine-saturated Sn-Beta-F-100. Dashed line at 900 seconds added for reference. 71

2.29 NPA (m/z = 59) response factor calibration curve of the mass spectrometer area ratio of NPA/Ar as a function of the molar ratio of NPA/Ar. . . 73

2.30 NPA TPD profiles after saturation with 1000 ppm NPA for 4 h at 323 K followed by purging for 4 h (grey trace) and 8 h (black trace) at 338 K in 25 cm^3 s^{-1} g^{-1} UHP He on (a) Sn-Beta-F-100, (b) Sn-Beta-F-105, (c) Sn-Beta-F-110, (d) Sn-Beta-F-140, (e) Sn-Beta-F-170, (f) Sn-Beta-F-220, and (g) Sn-Beta-OH-170 and (h) Sn-Beta-OH-200. 74

2.31 NPA TPD profiles on (a) Sn-Beta-F-140 and (b) Sn-Beta-F-170 after saturation in 1000 ppm NPA for 4 h followed by purging at 338 K in 25 cm^3 s^{-1} g^{-1} He for 4 h (dark grey trace), 8 h (grey trace), 12 h (light grey trace), and 16 h (faint grey trace). A purge performed at 323 K for 8 h in 25 cm^3 s^{-1} g^{-1} He is used to represent a 0 h purge at 338 K (black trace). 76

2.32 Molecules of NPA desorbed per molecule of Sn as a function of the purge length on (a) Sn-Beta-F-140 and (b) Sn-Beta-F-170 after saturation in 1000 ppm NPA for 4 h followed by purging at 338 K in 25 cm^3 s^{-1} g^{-1} He. A purge performed at 323 K for 8 h in 25 cm^3 s^{-1} g^{-1} He is used as a representation for a 0 h purge at 338 K. 77

Figure Page

2.33 NPA desorption rate on (a) Sn-Beta-F-140 and(b) Sn-Beta-OH-170 after saturation in 1000 ppm NPA for 4 h (grey trace) and 16 h (black trace) followed by an 8 h purge at 338 K in 25 cm^3 s^{-1} g^{-1} He. 78

2.34 NH_3 (m/z = 17) calibration curve of the mass spectrometer area ratio of NH_3/Ar as a function of the molar ratio of NH_3/Ar. 80

2.35 NH_3 TPD profiles after saturation in 75 cm^3 s^{-1} g^{-1} 500 ppm NH_3/He at 323 K for 5 h followed by purging in dry He (25 cm^3 s^{-1} g^{-1}) at 331 K for 8 h on (a) Sn-Beta-F-100, (b) Sn-Beta-F-105, (c) Sn-Beta-F-110 (d) Sn-Beta-F-140, (e) Sn-Beta-F-170, (f) Sn-Beta-F-200, (g) Sn-BEA-OH-170, (h) Sn-Beta-OH-200. 81

2.36 NH_3 TPD profiles after saturation of Sn-Beta-F-100 for 5 h in 75 cm^3 s^{-1} g^{-1} 500 ppm NH_3/He at 323 K followed by purging in dry He (25 cm^3 s^{-1} g^{-1}) at 331 K for 0 h (black trace), 4 h (dark grey trace), 8 h (grey trace), and 12 h (light grey trace). 82

2.37 NH_3 TPD profiles after saturation of Sn-Beta-F-100 for 5 h (black trace) or 16 h (grey trace) in 75 cm^3 s^{-1} g^{-1} 500 ppm NH_3/He at 323 K followed by purging in dry He (25 cm^3 s^{-1} g^{-1}) at 331 K for 8 h. 83

2.38 IR peak areas for Sn-BEA-F-100 after saturation and exposure to dynamic vacuum for open Sn sites (squares) and closed Sn sites (diamonds) as a function of time exposed to dynamic vacuum. 85

2.39 IR peak areas for Sn-BEA-F-140 after saturation for open Sn sites (squares) and closed Sn sites (diamonds) as a function of moles adsorbed at saturation 85

2.40 2275 cm^{-1} peak area versus perturbed OH peak area (3000-3600 cm^{-1}. . . 89

2.41 2275 cm^{-1} band area versus negative SiOH band area (∼3740 cm^{-1}). . . . 90

2.42 FTIR spectra of a dealuminated Beta zeolite after sequential doses of CD_3CN. Dashed lines shown at 2316 cm^{-1}, 2308 cm^{-1}, 2287 cm^{-1}, 2275 cm^{-1}, and 2265 cm^{-1}. 91

2.43 IR band area for the 2275 cm^{-1} peak on dealuminated Beta as a function of moles CD_3CN adsorbed. The slope of this line is the $\mathcal{E}$ value estimated for the 2275 cm^{-1} site. 92

2.44 IR spectra of CD_3CN three sequential doses (0.05 mol CD_3CN/Sn per dose) on Sn-xerogel. Dashed lines shown at 2316 cm^{-1}, 2308 cm^{-1}, 2287 cm^{-1}, and 2275 cm^{-1}. 93

2.45 IR spectra of CD_3CN dosed on Sn-xerogel to saturation. Dashed lines shown at 2316 cm^{-1}, 2308 cm^{-1}, 2287 cm^{-1}, and 2275 cm^{-1}. 93

Figure Page

2.46 IR difference spectra at CD_3CN saturation coverages (relative to the CD_3CN-free wafers and normalized to the maximum intensity of each spectra for clarity). (a) Spectra for (i) Sn-Beta-F-100, (ii) Sn-Beta-F-105, (iii) Sn-Beta-F-110, (iv) Sn-Beta-F-140, (v) Sn-Beta-F-170, (vi) Sn-Beta-F-220. (b) Spectra for (i) Sn-Beta-OH-170, (ii) Sn-Beta-OH-200, (iii) SnO_2/Si-Beta, (iv) Sn-xerogel. Dashed lines shown at 2316 cm^{-1}, 2308 cm^{-1}, 2287 cm^{-1}, 2275 cm^{-1} and 2265 cm^{-1}. 94

2.47 Initial glucose isomerization rates (373 K, normalized to untitrated samples) as a function of pre-adsorbed pyridine (a) per gram, (b) per micropore volume, and (c) per external surface area for Sn-Beta-F-110 (closed circles) and Sn-Beta-F-170 (open circles). 99

2.48 Scanning electron microscope images of Sn-Beta-F-110 and Sn-Beta-F-170. 100

2.49 Molar water uptake measured at P/P_0=0.2, after subtracting the contribution from (a) total Sn (estimated by AAS) or (b) Lewis acidic Sn assuming 2:1 H_2O:Sn binding stoichiometry, plotted as a function of the silanol content. 101

2.50 Rate constants per open Sn sites for all Sn-Beta-F samples as a function of the silanol content measured using the E value for the peak for CD_3CN bound to silanol sites centered at 2275 cm^{-1}. Trendlines show correlation of rate constant with 1/(mol SiOH g^{-1}) (dashed line) and 1/(mol SiOH g^{-1})^2 (solid line) determined by linear regression. 102

3.1 IR spectra (303 K) collected for (a) Al-Beta-OH-54, (b) dealuminated Beta, and (c) Sn-Beta-OH-47 grafted in dichloromethane as the reflux solvent. The spectrum of dealuminated Beta (dashed line) is superimposed on (c) for comparison. 121

3.2 IR spectra of (a) Al-Beta-OH-54, (b) dealuminated Beta, and (c) Sn-Beta-OH-47 after saturation with CD_3CN (303 K). 122

3.3 Fraction of vacancies grafted as a function of the equilibrium Sn concentration in the reflux solution (per vacancy defects) for Sn-Beta-OH samples grafted in dichloromethane reflux from parent Al-Beta-OH-54 (diamonds), Al-Beta-OH-29 (squares), and Al-Beta-OH-19 (circles), and Sn-Beta samples grafted using isopropanol reflux reported by Dijkmans et al. (open triangles) [22]. Dashed lines represent the best-fit Langmuir isotherms (Eq. 3.2) for each Sn-Beta-OH series. 126

3.4 Sn content and Al content (in the parent Al-Beta) with starting Al-Beta-OH-54 (diamonds), Al-Beta-OH-29 (squares), and Al-Beta-OH-19 (circles). Dashed line denotes the parity line. 128

Figure Page

3.5 Fraction of open Sn sites as a function of bulk Sn content in Sn-Beta-OH samples grafted under dichloromethane reflux starting from Al-Beta-OH-54 (diamonds), Al-Beta-OH-29 (squares), and Al-Beta-OH-19 (circles). . 129

3.6 Glucose isomerization rate constant (per total Sn, 373 K) and the Sn content in samples grafted using dichloromethane as the reflux solvent starting from Al-Beta-OH-54 (diamonds), Al-Beta-OH-29 (squares), and Al-Beta-OH-19 (circles). 131

3.7 Isomerization rate constant (per open Sn, 373 K) and Sn content for samples grafted in isopropanol reflux (open triangles), in dichloromethane reflux starting from Al-Beta-OH-54 (open diamonds), Al-Beta-F-45 (square with plus), Al-Beta-OH-29 (open squares), Al-Beta-OH-22 (square with cross) , Al-Beta-OH-19 (open circles), and hydrothermally-synthesized Sn-Beta-F (triangles) [26]. Dashed lines represent the average rate constant (per open Sn, 373 K) for Sn-Beta-F samples prepared hydrothermally and Sn-Beta-OH samples. 134

3.8 Vapor-phase H_2O adsorption isotherms (293 K) of Sn-Beta-OH-80 (circles), Sn-Beta-F-93 (squares), and Sn-Beta-F-220 prepared hydrothermally (triangles) [26]. 139

3.9 Vapor-phase CH_3OH adsorption isotherms (293 K) of Sn-Beta-OH-80 (circles), Sn-Beta-F-93 (squares), and Sn-Beta-F-220 prepared hydrothermally (triangles). 140

3.10 Powder XRD patterns of (a) Al-Beta-OH-54, (b) dealuminated Beta, (c) Sn-Beta-OH-170, (d) Sn-Beta-OH-200, and (e) Sn-Beta-OH-457. 144

3.11 XRD patterns of (a) Sn-Beta-OH-47 and (b) Sn-Beta-OH-84. The XRD patterns for the parent Al-Beta-OH-54 and its dealuminated Beta are given in Fig. 3.11. *Denotes a feature that is an artifact from the sample holder used. 145

3.12 XRD patterns of (a) Al-Beta-OH-19, (b) dealuminated Beta, and (c) Sn-Beta-OH-95, (d) Sn-Beta-OH-46, (e) Sn-Beta-OH-41, and (f) Sn-Beta-OH-30. *Denotes a feature that is an artifact from the sample holder used. 146

3.13 XRD patterns of (a) Al-Beta-OH-29, (b) Sn-Beta-OH-32, (c) Sn-Beta-OH-40, and (d) Sn-Beta-OH-80. *Denotes a feature that is an artifact from the sample holder used. 147

3.14 XRD patterns of (a) Al-Beta-OH-22, (b) dealuminated Beta, and (c) Sn-Beta-OH-144. *Denotes a feature that is an artifact from the sample holder used. 148

Figure Page

3.15 XRD patterns of (a) Al-Beta-F-45, (b) dealuminated Beta, (c) Sn-Beta-F-93, and (d) Sn-Beta-F-50. 149

3.16 SEM image of Al-Beta-OH-54. 150

3.17 SEM image of dealuminated Beta (starting Al-Beta-OH-54). 150

3.18 SEM image of Sn-Beta-OH-47. 151

3.19 DRUV spectra of Sn-Beta-OH-200 at ambient conditions (thin solid line), after dehydration at 523 K for 900 s (thick solid line) and after rehydration in flowing water vapor (thin dotted line). 154

3.20 DRUV spectra of Sn-Beta-OH-170 at ambient conditions (thin solid line), after dehydration at 523 K for 900 s (thick solid line) and after rehydration in flowing water vapor (thin dotted line). 155

3.21 DRUV spectra of Sn-Beta-OH-457 at ambient conditions (thin solid line), after dehydration at 523 K for 900 s (thick solid line) and after rehydration in flowing water vapor (thin dotted line). 156

3.22 DRUV spectra of Sn-Beta-OH-47 at ambient conditions (thin solid line), after dehydration at 523 K for 900 s (thick solid line) and after rehydration in flowing water vapor (thin dotted line). 157

3.23 DRUV spectra of Sn-Beta-OH-32 at ambient conditions (thin solid line), after dehydration at 523 K for 900 s (thick solid line) and after rehydration in flowing water vapor (thin dotted line). 158

3.24 DRUV spectra of Sn-Beta-OH-84 at ambient conditions (thin solid line), after dehydration at 523 K for 900 s (thick solid line) and after rehydration in flowing water vapor (thin dotted line). 159

3.25 DRUV spectra of Sn-Beta-OH-40 at ambient conditions (thin solid line), after dehydration at 523 K for 900 s (thick solid line) and after rehydration in flowing water vapor (thin dotted line). 160

3.26 DRUV spectra of Sn-Beta-OH-80 at ambient conditions (thin solid line), after dehydration at 523 K for 900 s (thick solid line) and after rehydration in flowing water vapor (thin dotted line). 161

3.27 DRUV spectra of Sn-Beta-OH-95 at ambient conditions (thin solid line), after dehydration at 523 K for 900 s (thick solid line) and after rehydration in flowing water vapor (thin dotted line). 162

3.28 DRUV spectra of Sn-Beta-OH-46 at ambient conditions (thin solid line), after dehydration at 523 K for 900 s (thick solid line) and after rehydration in flowing water vapor (thin dotted line). 163

Figure Page

3.29 DRUV spectra of Sn-Beta-OH-41 at ambient conditions (thin solid line), after dehydration at 523 K for 900 s (thick solid line) and after rehydration in flowing water vapor (thin dotted line). 164

3.30 DRUV spectra of Sn-Beta-OH-30 at ambient conditions (thin solid line), after dehydration at 523 K for 900 s (thick solid line) and after rehydration in flowing water vapor (thin dotted line). 165

3.31 DRUV spectra of Sn-Beta-OH-144 at ambient conditions (thin solid line), after dehydration at 523 K for 900 s (thick solid line) and after rehydration in flowing water vapor (thin dotted line). 166

3.32 DRUV spectra of Sn-Beta-F-93 at ambient conditions (thin solid line), after dehydration at 523 K for 900 s (thick solid line) and after rehydration in flowing water vapor (thin dotted line). 167

3.33 DRUV spectra of Sn-Beta-F-50 at ambient conditions (thin solid line), after dehydration at 523 K for 900 s (thick solid line) and after rehydration in flowing water vapor (thin dotted line). 168

3.34 Tauc plots of (a) Sn-Beta-OH-95, (b) Sn-Beta-OH-46, (c) Sn-Beta-OH-41, and (d) Sn-Beta-OH-30. Data collected at 523 K. 169

3.35 Tauc plots of (a) Sn-Beta-OH-80, (b) Sn-Beta-OH-41, and (c) Sn-Beta-OH-32. Data collected at 523 K. 170

3.36 Tauc plots of (a) Sn-Beta-OH-84 and (b) Sn-Beta-OH-47. Data collected at 523 K. 171

3.37 Tauc plots of (a) Sn-Beta-OH-200 and (b) Sn-Beta-OH-170. Data originally reported in Harris et al. [26]. 172

3.38 Tauc plots of (a) Sn-Beta-OH-144, (b) Sn-Beta-F-93, and (c) Sn-Beta-F-50. Data collected at 523 K. 173

3.39 Temperature programmed desorption profiles of dealuminated Beta after saturation at ambient temperature with isopropanol (solid line) and dichloromethane (dashed line). 175

3.40 IR spectra of dealuminated Beta before dosing isopropanol (thin line), after saturation (thick line), and at steady-state under vacuum (dashed line) at 383 K. 176

3.41 IR spectra (383 K) of dealuminated Beta after dosing isopropanol until saturation and subsequent evacuation. 177

Figure Page

3.42 IR spectrum of Sn-Beta-OH-47 (solid line) after CD_3CN saturation and its deconvolution components (dashed lines) at 2265 cm^{-1}, 2275 cm^{-1}, 2285 cm^{-1}, 2308 cm^{-1}, and 2316 cm^{-1} for CD_3CN in the gas-phase or physisorbed, bound to silanol groups, bound to a defective Sn site (e.g., $Sn(OSi)_2(OH)_2$), closed Sn sites, and open Sn sites, respectively [26]. . . 178

3.43 IR spectrum of Sn-Beta-OH-47 (solid line) after saturation with pyridine. The spectrum was convoluted with contributions for Lewis acid sites at 1450 cm^{-1} and 1615 cm^{-1}, Brønsted or Lewis acid sites at 1490 cm^{-1} and 1575 cm^{-1}, Brønsted acid sites at 1550 cm^{-1}, and gas-phase pyridine at 1595 cm^{-1}. The moles of Lewis acidic Sn were obtained by deconvolution of the band at 1450 cm^{-1} and integrated molar extinction coefficients reported in Harris et al. [26]. 179

3.44 First-order dependence of initial rate of fructose (per g) formation on the initial glucose concentration for Sn-Beta-OH-47. 184

3.45 H_2O isotherms (293 K) of (a) Sn-Beta-OH-84 and (b) Sn-Beta-OH-47. Sn-Beta-OH samples were synthesized from Al-Beta-OH-54. 186

3.46 H_2O isotherms (293 K) of (a) Sn-Beta-OH-41, (b) Sn-Beta-OH-95, (c) Sn-Beta-OH-30, and (d) Sn-Beta-OH-46. All the Sn-Beta-OH samples were synthesized from Al-Beta-OH-19. 187

3.47 H_2O isotherms (293 K) of (a) Sn-Beta-OH-80 and (b) Al-Beta-OH (Si/Al = 29). Sn-Beta-OH samples synthesized from parent Al-Beta-OH-29. . . 187

3.48 H_2O isotherms (293 K) of (a) Sn-Beta-F-93 and (b) Al-Beta-F-45. Sn-Beta-F was synthesized with parent Al-Beta-F-45. 188

3.49 H_2O isotherms (293 K) of (a) Sn-Beta-F-220 prepared hydrothermally, (b) Sn-Beta-OH-170, and (c) Sn-Beta-OH-200. Isotherms originally reported in Harris et al. [26]. 189

4.1 CD_3CN IR spectra of the $\nu(C{\equiv}N)$ stretching region with increasing coverage of CD_3CN on Ti-Beta-F-155 (0.013, 0.026, 0.065, 0.170, and 0.235 CD_3CN/Ti, light to dark). Dashed vertical lines correspond to 2308 and 2275 cm^{-1} for $\nu(C{\equiv}N)$ stretching vibrations of CD_3CN bound to Lewis acidic Ti sites and silanol groups, respectively. The inset shows the integrated area of the 2308 cm^{-1} peak multiplied by the cross-sectional area of the IR wafer, plotted against the moles of CD_3CN adsorbed at Lewis acidic Ti sites for Ti-Beta-F-155 (circles), Ti-Beta-F-135 (squares), and Ti-Beta-OH-38 (triangles). The dashed line in the inset is the best fit line through all data, with the slope representing the integrated molar extinction coefficient for CD_3CN adsorbed onto Lewis acidic Ti sites. . . 211

Figure Page

4.2 Baseline-corrected difference IR spectra of adsorbed water on Ti-Beta-F-155 (top, magnified for clarity) and Ti-Beta-OH-46 (bottom) at 298 K for (a) δ(HOH) scissoring modes in the water bending region and (b) the ν(O-H) water stretching region. Difference spectra reflect the subtraction of spectrum measured on the sample under vacuum prior to water flow and corrected for background water adsorption onto the IR cell. Spectra for each sample displayed from bottom-to-top correspond to P/P_0=0.1, 0.2, 0.5, and 0.75. The insets display the change in (a) the water bending peak area and (b) the water stretching peak maximum with increasing water concentration for Ti-Beta-F-155 (circles) and Ti-Beta-OH-46 (triangles). 219

4.3 Free energy (373 K, 1 bar) reaction coordinate diagram for the formation of fructose from glucose on closed-form Ti Lewis acid sites. Reaction arrows with overlaid circles indicate quasi-equilibrated events or the formation of transition states from relevant precursors. Relative enthalpies are given near inset images. 223

4.4 Initial first-order (a) fructose and (b) sorbose formation rates (373 K, pH 4) normalized per total Ti content as a function of Ti/Si ratio, for Ti-Beta-F (circles) and Ti-Beta-OH samples (triangles). Data on Ti-Beta-F (X) and Ti-Beta-OH (squares) samples reported previously in Ref. [35] are plotted for comparison. Dashed lines correspond to average values within the series of Ti-Beta-F and Ti-Beta-OH samples. 227

4.5 Dependence of initial glucose isomerization rates (373 K, pH 4) for fructose (filled) and sorbose (open) formation on Ti-Beta-F-155 (closed circles,open circles) and Ti-Beta-OH-46 (closed triangles, open triangles) as a function of initial glucose thermodynamic activity (corresponding to 1-50 wt% initial glucose concentration). Solid lines represent fits of the experimental data to the rate equation (Eq. 4.9) using activation enthalpies and entropies given in Table 4.4. The inset shows initial glucose isomerization rates at low glucose thermodynamic activities, highlighting the first-order kinetic regime. 229

Figure Page

4.6 (a) ATR-IR spectra of MARI (top, water derived) and minor (bottom, glucose derived) intermediates on Ti-Beta-F-155 (black) and Ti-Beta-OH-46 (gray) that oscillate with aqueous-phase glucose activity (0-700 mol m^{-3}) at 373 K. Glucose spectra are normalized by the peak at ∼1030 cm^{-1} and water spectra are normalized by the peak at ∼1630 cm^{-1}. Spectra reflecting aqueous-phase glucose (330 mol m^{-3}) flowing over the ZnSe crystal is overlaid on the glucose spectra (dashed). Dashed vertical lines at 1630 and 3400 cm^{-1} indicate water bending and stretching vibrational modes, respectively. (b) ATR-IR spectra of the MARI (bottom four) and minor (top four) species that oscillate with aqueous-phase glucose activity (∼3000-3750 mol glucose m^{-3}, 373 K, normalized by the maximum feature at ∼1030 cm^{-1}) over Ti-Beta-F-155, Ti-Beta-OH-46, Si-Beta-F, and blank ZnSe crystal from top to bottom, respectively. The inset depicts difference spectra between aqueous-phase glucose flowing over the ZnSe crystal and the MARI (black) or minor species (gray) species observed on Ti-Beta-OH-46 (top) and Ti-Beta-F-155 (bottom) spectra from modulating aqueous-phase glucose activity (∼3000-3750 mol glucose m^{-3}) at 373 K after normalization by the peak centered at ∼1030 cm^{-1}; dashed lines (- - -) indicate the baseline. All spectra are obtained during MES experiments and isolated by processing through PSD and MCR-ALS. . . 232

4.7 Plausible glucose isomerization mechanism for fructose and sorbose formation on Lewis acidic Ti sites 238

4.8 Dependence of initial fructose formation rates (pH 3) on Ti-Beta-F-155 on initial glucose thermodynamic activity (corresponding to 1-50 wt% glucose concentration) at 368 (squares), 373 (X), 378 (triangles), and 383 K (circles). Solid lines represent regression of the data to the rate equation (Eq. 4.9) using activation enthalpies and entropies given in Table 4.4. The inset shows initial glucose isomerization rates at low glucose thermodynamic activities, highlighting the first-order kinetic regime. 242

4.9 Powder XRD patterns of (a) Ti-Beta-F and (b) Ti-Beta-OH samples studied in this work. Weak signals around 9-10^o reflect an artifact from the sample holders used to collect XRD patterns. 256

4.10 N_2 adsorption isotherms (77 K) of (a) Ti-Beta-F and (b) Ti-Beta-OH samples studied in this work. Isotherms are offset by 200 cm^3 g^{-1} for clarity.257

4.11 SEM images of selected Ti-Beta-F samples: (a) Ti-Beta-F-135, (b) Ti-Beta-F-155, and (c) Ti-Beta-F-180. Bulk sample uniformity is assumed based on images for (d) Ti-Beta-F-135, (e) Ti-Beta-F-155, and (f) Ti-Beta-F-180. Larger crystal aggregates reflect Si-Beta-F seeds used to nucleate the formation of Ti-Beta-F. 257

Figure Page

4.12 SEM images of selected Ti-Beta-OH samples: (a) Ti-Beta-OH-46, (b) Ti-Beta-OH-34, and (c) Ti-Beta-OH-71. Bulk sample uniformity is assumed based on images for (d) Ti-Beta-OH-46, (e) Ti-Beta-OH-34, and (f) Ti-Beta-OH-71 which show larger agglomerates of small crystals. 258

4.13 SEM images of Ti-Beta-OH-34 at various steps of the synthesis procedure: (a) Al-Beta parent material, (b) after nitric acid treatment for dealumination, and (c) after $TiCl_4$ grafting to form Ti-Beta-OH-34. Bulk sample uniformity is assumed based on images for (d) Al-Beta parent material, (e) after nitric acid treatment for dealumination, and (f) after TiCl4 grafting to form Ti-Beta-OH-34. All show larger agglomerates of small crystals. . 258

4.14 Hydrated UV-Vis spectra of (A) Ti-Beta-F and (B) Ti-Beta-OH samples studied in this work collected prior to dehydration at 523 K. 259

4.15 Dehydrated UV-Vis spectra (523 K, 1800 s) of (A) Ti-Beta-F and (B) Ti-Beta-OH samples studied in this work. 259

4.16 Tauc plots of (A) Ti-Beta-F and (B) Ti-Beta-OH samples studied in this work prior to heating and sample dehydration ("hydrated" samples). Edge energies are summarized in Table 4.5 260

4.17 Tauc plots of (A) Ti-Beta-F and (B) Ti-Beta-OH samples studied in this work after treatment in flowing He at 523 K for 1800 s. Edge energies are summarized in Table 4.5 260

4.18 IR spectra on Ti-Beta-OH-46 after progressive titration of CD_3CN at 303 K (CD_3CN/Ti = 0.002-2.34). Dashed lines are drawn at 2308 cm^{-1} (CD_3CN bound to Lewis acidic Ti) and 2275 cm^{-1} (CD_3CN hydrogen bound to silanols). Note that the peak center shifts slightly to lower wavenumbers with increasing adsorbed CD_3CN concentrations. 262

4.19 CD_3CN-saturated IR spectra for Ti-Beta-F-155. The thickest solid line reflects the measured spectra upon saturation with CD_3CN while thinner lines indicate constitute peaks associated with CD_3CN bound to Lewis acidic Ti sites (2308 cm^{-1}), CD_3CN bound to silanols (2275 cm^{-1}), and gas phase physisorbed CD_3CN (2265 cm^{-1}). The dashed line represents the modeled spectra from combining deconvoluted peaks. 263

4.20 IR spectra collected on (A) CD_3CN-saturated Ti-Beta-F and (B) CD_3CN-saturated Ti-Beta-OH samples studied in this work. Dashed lines are drawn at 2308 cm^{-1} (CD_3CN bound to Lewis acidic Ti) and 2275 cm^{-1} (CD_3CN bound to silanols). 264

Figure Page

4.21 IR spectra measured (a) after the first four doses of pyridine on Ti-Beta-F-135 (0.015-0.058 mol pyridine (mol Ti)$^{-1}$ and (b) after saturation of Ti-Beta-F-135 with pyridine (1.05 mol pyridine (mol Ti)$^{-1}$). The components included in the deconvolution are shown (thin solid lines) with the resulting fit envelope (dotted line) and the measured spectra (thick solid line). . . 265

4.22 (A) Integrated peak area normalized by wafer cross-sectional areas for the IR feature centered at 1605 cm^{-1} as a function of moles pyridine adsorbed onto Ti-Beta-F-155 (diamonds), Ti-Beta-F-135 (circles), Ti-Beta-F-170 (triangles), and Ti-Beta-OH-46 (squares). Dashed lines indicate best fit lines through the origin for each sample with slopes equal to integrated molar extinction coefficients as listed in Table 4.7 (B) Integrated peak area normalized by wafer cross-sectional areas for the IR feature centered at 1605 cm^{-1} as a function of moles pyridine adsorbed onto Ti-Beta-F-155, Ti-Beta-F-135, Ti-Beta-F-170, and Ti-Beta-OH-46 as a single data set. The dashed line indicates the best fit line through the origin for the combined data set with the slope equal to the average integrated molar extinction coefficient. 266

4.23 Lewis acid site densities determined from pyridine-saturation IR experiments plotted against Lewis acid site densities determined from CD_3CN-saturation IR experiments. The dashed line is a parity line drawn to guide the eye. 267

4.24 Vapor-phase water adsorption isotherms at 293 K on Ti-Beta-F samples studied in this work. Isotherms are offset by 100 cm^3 g^{-1} for clarity. . . . 270

4.25 Vapor-phase water adsorption isotherms at 293 K on Ti-Beta-OH samples studied in this work. Isotherms are offset by 100 cm^3 g^{-1} for clarity. . . . 271

4.26 Water uptakes at $P/P_0 = 0.2$ (373 K) after subtracting two moles of water molecules per mol Ti Lewis acid site (quantified by CD_3CN IR) as a function of the bulk silanol defect density (quantified by CD_3CN IR). The solid line is a best fit line drawn through the origin to guide the eye. 272

4.27 Vapor-phase methanol adsorption isotherms at 293 K on Ti-Beta-F samples studied in this work. Isotherms are offset by 100 cm^3 g^{-1} for clarity. 273

4.28 Vapor-phase methanol adsorption isotherms at 293 K on Ti-Beta-OH samples studied in this work. Isotherms are offset by 100 cm^3 g^{-1} for clarity. 274

Figure Page

4.29 Differential, subtracted, normalized, cell-corrected IR spectra of adsorbed H2O at P/P_0=0.1, 0.2, 0.5, and 0.75 (lightest to darkest, 298 K) on (A) Ti-Beta-F-155 and (B) Ti-Beta-OH-46. Differential spectra are spectral changes between a given P/P_0 value and the previous relative pressure spectra, isolating changes in spectral features due only to increasing water partial pressure. 275

4.30 Vapor-phase water adsorption isotherms at 298 K on Ti-Beta-F-155 (closed circles) and Ti-Beta-OH-46 (open squares) 276

4.31 Subtracted IR spectra of the OH stretching region as a function of increased relative pressure of water on (A) Ti-Beta-F-155 and (B) Ti-Beta-OH-46. 277

4.32 Solution phase ^{13}C NMR of monosaccharide solutions after contacting 5 wt% glucose solutions with Ti-Beta-F-133, Ti-Beta-F-155, and Ti-Beta-OH-46. Glucose, fructose and sorbose standards are given for direct comparison. 278

4.33 Free energy (373 K, 1 bar) reaction coordinate diagram for the formation of sorbose from glucose on closed-form Ti Lewis acid sites. Reaction arrows with overlaid circles indicate quasi-equilibrated events or the formation of transition states from relevant precursors. Relative enthalpies are given near inset images. 279

4.34 First-order fructose (closed circles, closed triangles) and sorbose (open circles, open triangles) formation rate constants (373 K, pH 4) normalized per total Lewis acidic Ti content (measured from CD_3CN IR) as a function of Lewis acidic Ti density for (A) Ti-Beta-F and (B) Ti-Beta-OH samples. 282

4.35 Dependence of initial glucose isomerization rates (373 K, pH 4) for fructose (filled) and sorbose (open) formation on Ti-Beta-F-155 (closed circles, open circles) and Ti-Beta-OH-46 (closed triangles, open triangles) as a function of initial glucose concentration (1-50 wt.%). Solid lines represent fits of the experimental data to the rate equation (Eq. 4.9 of the main text) using activation enthalpies and entropies given in Table 4.4. 284

4.36 a) Time-resolved infrared spectra obtained *in situ* during reactions of glucose and water over Ti-Beta-F-155 while modulating glucose concentrations (42-50 wt%) with a period length of 250 s at 373 K. b) Phase resolved spectra that result from phase sensitive detection of the time resolved spectra in (a). Coloring indicates absorbance intensity. 287

Figure Page

4.37 Dependence of fructose-to-sorbose selectivity (373 K, pH 4) on Ti-Beta-F-155 (circles) and Ti-Beta-OH-46 (triangles) as a function of initial glucose thermodynamic activity. Relatively constant product selectivities support the identification of the secondary bound glucose species being a bound intermediate which is not directly responsible for sorbose formation as relative coverages of MARI and secondary bound species observed from ATR-IR are affected by changes in initial glucose activity. 288

4.38 Ti K edge XANES of water exchanged Ti-Beta-OH-46 zeolite after dehydration at 523 K in He (solid) and under ambient conditions (dashed). The increase in intensity of the pre-edge peak is consistent with a decrease in coordination number from 6 to 4 upon dehydration. 291

4.39 Magnitude of the Fourier transform of the k_2-weighted Ti K edge EXAFS of water exchanged Ti-Beta-OH-46 zeolite under ambient conditions (solid) and after dehydration at 523 K in He (dashed). 292

4.40 Magnitude of the Fourier transform of the k_2-weighted Ti K edge EXAFS of water exchanged Ti-Beta-OH-46 zeolite after dehydration at 523 K in He (solid) and Δ EXAFS of the hydrated and dehydrated water exchanged catalyst (dashed). The Δ EXAFS spectrum was obtained by subtracting the k_0-weighted EXAFS of the sample after dehydration from the k_0-weighted EXAFS of the sample under ambient conditions and is representative of the water adsorbed on Ti under ambient conditions. . . 293

4.41 Ti K edge XANES of water (dashed) and glucose (solid) exchanged Ti-Beta-OH-46 zeolite under ambient conditions. The spectra are identical within experimental error indicating Ti has equivalent coordination environments in the two samples. The intensity of the pre-edge peak is consistent with a coordination number of 6. 294

4.42 Ti K edge XANES of Ti-Beta-OH-46 zeolite: solid – glucose exchanged under ambient conditions, long dashes – glucose exchanged after treatment at 523 K in He, and short dashes – water exchanged after treatment at 523 K in He. The intensity of the pre-edge peak in the glucose exchanged sample after treatment in He at 523 K is consistent with a coordination number of 5 and suggests glucose adsorbed through a single oxygen. . . . 295

Figure Page

4.43 Plausible glucose isomerization mechanism for fructose and sorbose formation on Lewis acidic Ti sites. Quasi-equilibrated glucose adsorption (Steps 1a, 1b) forms bound glucose intermediates which form bound fructose (Step 2a) or sorbose (Step 2b) isomers through kinetically relevant hydride shifts. Quasi-equilibrated fructose (Step 3a) and sorbose (Step 3b) desorption phenomena release the product into the liquid phase. Quasi-equilibrated water adsorption onto Lewis acidic active sites (Steps 4 and 5) inhibits isomerization rates at low glucose coverages. 298

4.44 Dependence of initial sorbose formation rates (pH 3) on Ti-Beta-F-155 on initial glucose thermodynamic activity (corresponding to 1-50 wt.% initial glucose concentration) at 368 (squares), 373 (cross), 378 (triangles), and 383 K (circles). Solid lines for all data represent modeled regressions of the experimental data to the overall rate equation given in Eq. 4.16 in the main text using activation enthalpies and entropies given in Table 4.4. . 305

4.45 Dependence of initial fructose formation rates (pH 3) on Ti-Beta-OH-46 on initial glucose thermodynamic activity (corresponding to 1-50 wt.% initial glucose concentration) at 368 (squares), 373 (cross), 378 (triangles), and 383 K (circles). Solid lines for all data represent modeled regressions of the experimental data to the overall rate equation given in Eq. 4.16 in the main text using activation enthalpies and entropies given in Table 4.4. . 306

4.46 Dependence of initial sorbose formation rates (pH 3) on Ti-Beta-OH-46 on initial glucose thermodynamic activity (corresponding to 1-50 wt.% initial glucose concentration) at 368 (squares), 373 (cross), 378 (triangles), and 383 K (circles). Solid lines for all data represent modeled regressions of the experimental data to the overall rate equation given in Eq. 4.16 in the main text using activation enthalpies and entropies given in Table 4.4. . 307

4.47 Dependence of initial fructose formation rates (pH 3) on Ti-Beta-F-155 on initial glucose and osmotic thermodynamic activity ratio (corresponding to 1-50 wt.% initial glucose concentration) at 368 (squares), 373 (cross), 378 (triangles), and 383 K (circles). Solid lines for all data represent modeled regressions of the experimental data to the overall rate equation given in Eq. 4.16 in the main text using activation enthalpies and entropies given in Table 4.4. 308

Figure Page

4.48 Dependence of initial sorbose formation rates (pH 3) on Ti-Beta-F-155 on initial glucose and osmotic thermodynamic activity ratio (corresponding to 1-50 wt.% initial glucose concentration) at 368 (squares), 373 (cross), 378 (triangles), and 383 K (circles). Solid lines for all data represent modeled regressions of the experimental data to the overall rate equation given in Eq. 4.16 in the main text using activation enthalpies and entropies given in Table 4.4. 309

4.49 Percent residual plot of fructose formation rates on Ti-Beta-F-155 as a function of initial glucose thermodynamic activity (corresponding to 1-50 wt.% initial glucose concentration) at 368 (squares), 373 (cross), 378 (triangles), and 383 K (circles) comparing experimental rate measurements with modeled rate behavior from Eq. 4.16 from the main text. Percent residuals were obtained from Eq. 4.72. 311

4.50 Percent residual plot of sorbose formation rates on Ti-Beta-F-155 as a function of initial glucose thermodynamic activity (corresponding to 1-50 wt.% initial glucose concentration) at 368 (squares), 373 (cross), 378 (triangles), and 383 K (circles) comparing experimental rate measurements with modeled rate behavior from Eq. 4.16 from the main text. Percent residuals were obtained from Eq. 4.72. 312

4.51 Percent residual plot of fructose formation rates on Ti-Beta-OH-46 as a function of initial glucose thermodynamic activity (corresponding to 1-50 wt.% initial glucose concentration) at 368 (squares), 373 (cross), 378 (triangles), and 383 K (circles) comparing experimental rate measurements with modeled rate behavior from Eq. 4.16 from the main text. Percent residuals were obtained from Eq. 4.72. 313

4.52 Percent residual plot of sorbose formation rates on Ti-Beta-OH-46 as a function of initial glucose thermodynamic activity (corresponding to 1-50 wt.% initial glucose concentration) at 368 (squares), 373 (cross), 378 (triangles), and 383 K (circles) comparing experimental rate measurements with modeled rate behavior from Eq. 4.16 from the main text. Percent residuals were obtained from Eq. 4.72. 314

4.53 Arrhenius plot for apparent first-order fructose (A) and sorbose (B) formation rate constants (368-383 K, 5 wt.%) on Ti-Beta-F-155 (closed circles) and Ti-Beta-OH-46 (open circles). Solid lines represent the results of the regression of Eq. 4.16 and dashed lines represent regressions using rate measurements at 5 wt.% on Ti-Beta-F-155 (black) and Ti-Beta-OH-46 (gray). Both regression lines follow the Eyring equation with activation enthalpies and entropies given in Table 4.4 of the main text and Table 4.9, respectively. 315

Figure Page

4.54 Arrhenius plot for apparent zero-order fructose (A) and sorbose (B) formation rate constants (368-383 K, 50 wt.%) on Ti-Beta-F-155 (closed circles) and Ti-Beta-OH-46 (open circles). Solid lines represent the results of the regression of Eq. 4.16 and dashed lines represent regressions using rate measurements at 50 wt.% on Ti-Beta-F-155 (black) and Ti-Beta-OH-46 (gray). Both regressions follow the Eyring equation with activation enthalpies and entropies given in Table 4.4 of the main text and Table 4.9, respectively. 316

4.55 DFT-calculated glucose adsorption energies (a) and effective first-order (b) and zero-order (c) energy barriers for glucose-fructose isomerization. Enthalpies (squares) and free energies (circles) are shown in kJ mol^1 and entropies (diamonds) in J mol^1 K^1 (373 K). The intrapore water molecule density was assumed to remain constant during glucose adsorption and reaction for first-order analyses yet water molecules were allowed to reorient into lowest energy configurations in all cases. 318

5.1 Methanol adsorption isotherms (293 K) of Sn-Beta-HT-F-220 (circles), Sn-Beta-PS-OH-80 (squares), Sn-Beta-PS-F-50 (plus), and Sn-Beta-PS-F-284 (diamonds). 332

5.2 IR spectra of Sn-Beta-PS-OH-OH-80 (a) and Sn-Beta-PS-F-284 (b) collected after high temperature oxidative treatments (823 K, black) and in flowing methanol (303 K) at $P/P_0 = 0.02$, 0.05, and 0.20 (increasing shade of gray). 336

5.3 Difference spectra of Sn-Beta-PS-OH-80 (a) and Sn-Beta-PS-F-284 (b) after subtraction of the contributions from the dehydrated spectrum. . . 337

5.4 Band maxima of the OH stretching vibration of Sn-Beta-PS-OH-80 (squares) and Sn-Beta-PS-F-284 (diamonds) as a function of the methanol partial pressure. 338

5.5 Methanol packing density (293 K) with respect to the density of hydrophilic binding sites quantified through H/D isotopic exchanges of Sn-Beta-PS-OH (squares) and Sn-Beta-PS-F-284 (diamonds). Dashed line represents the value associated with Sn-Beta-HT-F. 340

5.6 Density of hydrophilic binding sites quantified through H/D isotopic exchanges (y-axis) and by deconvolution of the 2275 cm^{-1} contribution in IR spectra after saturation with CD_3CN (303 K, x-axis) of Sn-Beta-PS-OH samples (squares) and Sn-Beta-PS-F-284 (diamonds). Dashed line represents parity. 342

Figure Page

5.7 Isomerization rate constants (per open Sn, 373 K) of Sn-Beta-HT-F (circles) [26], Sn-Beta-PS-OH (squares) [25], Sn-Beta-PS-F with starting Si/Al = 50 (plus), Sn-Beta-PS-F with starting Si/Al = 180 (diamond), and Sn-Beta-PS-F with a starting Si/Al = 110 (triangle). Dashed lines represent the average isomerization rate constants (per open Sn, 373 K) of Sn-Beta-HT-F and Sn-Beta-PS-OH. 344

5.8 Powder XRD patterns of (a) Al-Beta-HT-OH-19, (b) dealuminated Beta from Al-Beta-HT-OH-19, (c) Sn-Beta-PS-OH-95, (d) Sn-Beta-PS-OH-46, (e) Sn-Beta-PS-OH-41, and (f) Sn-Beta-PS-OH-30. 350

5.9 Powder XRD patterns of (a) Al-Beta-HT-OH-29, (b) Sn-Beta-PS-OH-32, (c) Sn-Beta-PS-OH-40, and (d) Sn-Beta-PS-OH-80. 351

5.10 Powder XRD patterns of (a) Al-Beta-HT-OH-54, (b) dealuminated Beta from Al-Beta-HT-OH-54, (c) Sn-Beta-PS-OH-47, and (d) Sn-Beta-PS-OH-84. 352

5.11 Powder XRD patterns of (a) Al-Beta-HT-F-45, (b) dealuminated Beta from Al-Beta-HT-F-45, (c) Sn-Beta-PS-F-93, and (d) Sn-Beta-PS-F-50. . 353

5.12 DRUV spectra of (a) Sn-Beta-PS-OH-95, (b) Sn-Beta-PS-OH-46, (c) Sn-Beta-PS-OH-41, (d) Sn-Beta-PS-OH-30, (e) Sn-Beta-PS-OH-32, (f) Sn-Beta-PS-OH-40, (g) Sn-Beta-PS-OH-80, (h) Sn-Beta-PS-OH-47, (i) Sn-Beta-PS-OH-84, (j) Sn-Beta-PS-F-93, and (k) Sn-Beta-PS-F-50 after dehydration treatments (523 K, 0.5 h). 356

5.13 CH_3OH adsorption isotherms (293 K) of (a) Sn-Beta-PS-OH-95, (b) Sn-Beta-PS-OH-46, (c) Sn-Beta-PS-OH-41, and (d) Sn-Beta-PS-OH-30. Isotherms are offset by 120 $cm^3\ g^{-1}$ for clarity. 358

5.14 CH_3OH adsorption isotherms (293 K) of (a) Sn-Beta-PS-OH-32, (b) Sn-Beta-PS-OH-40, and (c) Sn-Beta-PS-OH-80. Isotherms are offset by 120 $cm^3\ g^{-1}$ for clarity. 359

5.15 CH_3OH adsorption isotherms (293 K) of (a) Sn-Beta-PS-OH-47 and (b) Sn-Beta-PS-OH-84. Isotherms are offset by 120 $cm^3\ g^{-1}$ for clarity. . . . 360

5.16 CH_3OH adsorption isotherms (293 K) of (a) Sn-Beta-PS-F-93, and (b) Sn-Beta-PS-F-50, (c) Sn-Beta-PS-F-284, and (d) Sn-Beta-HT-F-220. Isotherms are offset by 120 $cm^3\ g^{-1}$ for clarity. 361

5.17 HD formation rate of (a) Sn-Beta-PS-OH-46, (b) Sn-Beta-PS-OH-41, (c) Sn-Beta-PS-OH-95, and (d) Sn-Beta-PS-OH-30. Formation rates are offset between samples for clarity. 362

Figure Page

5.18 HD formation rate of (a) Sn-Beta-PS-OH-80 and (b) Sn-Beta-PS-F-284. Formation rates are offset between samples for clarity. 363

5.19 HD formation rate of (a) Sn-Beta-PS-OH-84 and (b) Sn-Beta-PS-OH-47. Formation rates are offset between samples for clarity. 364

6.1 Reaction scheme for fructose and sorbose formation over tetrahedrally-coordinated Ti sites. 367

6.2 Hydrothermal and post-synthetic strategies for the preparation of titanosilicates with varied pore diameters and confining environments. 374

6.3 Sorbose selectivity, over fructose, of Ti-containing zeotype materials of varied pore diameter and confining environment. 378

6.4 Plausible sequence of elementary steps for the catalytic turnover of glucose isomerization to fructose and sorbose over Ti-containing zeotypes. 380

6.5 Powder XRD patterns of (a) Ti-Beta-133, (b) Ti-Beta-282, and (c) Ti-Beta-155. 384

6.6 Powder XRD patterns of (a) Ti-CHA, (b) Ti-MCM-41, (C) Ti-CON, (d) Ti-MFI-NS, (e) Ti-MFI. 385

6.7 N_2 adsorption isotherms (77 K) of (a) Ti-Beta-133, (b) Ti-Beta-282, and (c) Ti-Beta-155. Isotherms are offset by 200 cm^3 g^{-1} for clarity. 386

6.8 N_2 adsorption isotherms (77 K) of (a) Ti-MFI-NS and Ar adsorption isotherm (87 K) of (b) Ti-CHA. Isotherms are offset by 300 cm^3 g^{-1} for clarity. 387

6.9 Dehydrated DRUV spectra of Ti-MFI-NS. 389

6.10 IR spectra collected at saturation coverages of CD_3CN (303 K) on (a) Ti-Beta-133, (b) Ti-Beta-282, and (c) Ti-Beta-155. 390

6.11 ^{13}C NMR spectra of (a) glucose, (b) fructose, and (c) sorbose standards, together with product solutions of reactions performed over (d) Ti-CON, (e) Ti-MFI-NS, and (f) Ti-MFI. 391

6.12 ^{13}C NMR spectra of (a) glucose, (b) fructose, and (c) sorbose standards, together with product solutions of reactions performed over (d) Ti-Beta. 392

ABSTRACT

Vega-Vila, Juan Carlos Ph.D., Purdue University, December 2019. Synthetic Strategies to Tailor Active and Defect Site Structures in Lewis Acid Zeolites for Sugar Isomerization Catalysis. Major Professor: Rajamani Gounder.

Lewis acid zeolites contain framework metal heteroatoms that catalyze sugar isomerization reactions at different turnover rates depending on the local coordination around metal centers and the polarity of their confining secondary environments. Post-synthetic modification routes that react metal precursors with framework vacancy defects in dealuminated Beta zeolites (Sn-Beta-PS-OH) are developed as an alternative synthetic strategy to the hydrothermal crystallization of Sn-Beta zeolites (Sn-Beta-HT-F). Post-synthetic routes provide the ability to systematically tailor the structural features of active and defect sites in Sn-zeolites, especially in composition ranges inaccessible to materials crystallized by hydrothermal routes (Si/Sn $<$ 100; $>$ 2 wt.% Sn), yet often result in incomplete or unselective Sn grafting within framework vacancy defects and form extraframework metal oxide domains and residual defect sites. The development of robust post-synthetic routes to prepare Sn-zeolites with intended active and defect structures has been limited by the dearth of characterization techniques to unambiguously detect and quantify such structures present in stannosilicate materials, and of mechanistic links between such structures and the turnover rates of catalytic reactions.

The presence of framework Sn centers that can expand its coordination shell from four- to six-coordinate structures, and small extraframework tin oxide domains that cannot, were unambiguously detected from diffuse reflectance UV-Visible spectra of stannosilicate materials measured after dehydration treatments (523 K, 0.5 h) to discern ligand-to-metal charge transfer bands for tetrahedrally-coordinated Sn het-

eroatoms (< 220 nm, > 4.1 eV) and those for tin oxide domains (> 230 nm, < 4.1 eV). Liquid-phase grafting of stannic chloride in dichloromethane reflux (333 K) enables preparing Sn-Beta zeolites with higher framework Sn content (Si/Sn = 30–144; 1.4–6.1 wt.% Sn) than grafting performed in isopropanol reflux (423 K, Si/Sn > 120; 1.6 wt.% Sn). This reflects competitive adsorption of isopropanol solvents with stannic chloride at framework vacancy defects during grafting procedures, consistent with infrared spectroscopy (IR) and temperature-programmed desorption (TPD) of dealuminated Beta samples after saturation with isopropanol at reflux temperatures (423 K), and not any limitations inherent to the structure of vacancy defects within dealuminated zeolite supports that would prevent reaction with metal precursors as often proposed.

This insight enabled preparing Sn-Beta zeolites with varying densities of residual defects, via dichloromethane-assisted grafting of stannic chloride to different extents, into dealuminated Beta supports of different initial Al content (Si/Al = 19–180) and mineralizing agent used for hydrothermal crystallization of the parent Al-Beta sample (e.g., fluoride or hydroxide). Preparation of low-defect Sn-Beta zeolites using post-synthetic routes (Sn-Beta-PS-F) first required the synthesis of parent Al-Beta zeolites in fluoride media to minimize residual siloxy defects (OSi^-) formed during crystallization, and dilute Al content (Si/Al > 100, < 0.6 Al (unit cell)$^{-1}$), to minimize the density of intrapore silanol groups formed after dealumination and high temperature oxidative treatment. The methanol packing density within microporous voids of Sn-Beta zeolites was assessed from relative volumetric uptakes at the point of micropore filling from single-component methanol (293 K) and nitrogen (77 K) adsorption isotherms, and decreased systematically among samples with increasing density of silanol groups. The total density of silanol groups within micropores and at external crystallite surface in Sn-Beta zeolites was quantified by H/D isotopic exchange during temperature-programmed surface reactions (500–873 K), and within microporous voids from IR spectra measured after saturation of microporous binding sites with CD_3CN (2275 cm^{-1}, 303 K). *In situ* IR spectra collected at low methanol

pressures (P/P0 < 0.2, 303 K) provide further evidence that methanol molecules arrange in localized clusters within Sn-Beta-PS-F, but form extended hydrogen-bonded networks within Sn-Beta-PS-OH.

Glucose-fructose isomerization rate constants (373 K) were used to probe the local coordination of Sn heteroatoms and the polarity of the secondary environment as influenced by silanol defects within microporous cavities. *Ex situ* pyridine titration of Sn-Beta-HT-F samples suppressed isomerization rates (per total Sn, 373 K) after only a subset of Sn sites were poisoned, which correspond to the number of open Sn sites quantified *ex situ* via CD_3CN IR (303 K), providing further evidence that open Sn sites are dominant active sites for glucose isomerization. First-order isomerization rate constants (373 K) decrease with increasing Sn content when normalized by total Sn density, and are invariant when normalized by the number of open Sn sites, because open Sn sites are grafted preferentially within Sn-Beta-PS-OH (Si/Sn = 30–144; 1.4–6.1 wt.% Sn) at low Sn densities. Isomerization rate constants (per open Sn, 373 K), however, are lower by ∼4x and ∼15x on Sn-Beta-PS-F (Si/Sn = 284; 0.7 wt.% Sn) and Sn-Beta-PS-OH, respectively, than on Sn-Beta-HT-F. Open Sn sites catalyze aqueous-phase glucose isomerization at higher turnover rates (373 K) when their microporous surroundings contain silanol defects present in low (hydrophobic) densities than high (hydrophilic) densities, which are characteristic of Sn-Beta-HT-F and Sn-Beta-PS-OH samples, respectively. This reflects reorganization of extended water networks, which are stabilized in high-defect, hydrophilic micropore environments, at kinetically relevant 1,2-hydride shift transition states that incurs entropic penalties that lower turnover rates. This thesis highlights the development of synthesis-structure-function relationships to guide the preparation of catalytic materials with intended active and defect site structures within confining reaction environments, the development of characterization techniques for the identification and quantification of such structures, and the influence of such structures on turnover rates of liquid-phase sugar isomerization.

1. INTRODUCTION

The isomorphous substitution of silicon in pure-silica zeolitic frameworks with tetravalent metal heteroatoms can be used to prepare molecular sieves with isolated Lewis acid centers. The confinement of Lewis acid centers within zeolitic micropores of varying pore diameter (0.5–0.7 nm) generates reaction environments that are reported to perform stereoselective reactions of oxygenated molecules containing carbonyl groups through the concerted Meerwein-Ponndorf-Verley (MPV) reduction of ketones [1–3], the Oppenauer oxidation of alcohols [4], and the Baeyer-Villiger oxidation of ketones [5–10]. The rates at which these chemical reactions are catalyzed by Lewis acid zeolites, however, depends on their synthesis and treatment history because they lead to differences in framework metal density, metal speciation and coordination, and confining environment polarity.

Beta molecular sieves with framework tetravalent cations (Si/Sn $>$ 100, $<$2 wt.% Sn) can be crystallized hydrothermally in the presence of cationic tetraethylammonium (TEA^+) organic structure directing agents (SDAs) and fluoride anions (20 days, 413 K) [5,11]. The addition of Beta zeolite seeds to fluoride-based synthesis gels used in hydrothermal preparations of Sn-Beta can shorten crystallization times (2 days, 413 K) [12]. The incorporation of Sn heteroatoms in the framework of Beta molecular sieves (Si/Sn $>$ 100, $<$2 wt.% Sn) can also occur via steam-assisted crystallization of stannosilicate gels in the presence of TEA^+ cations in fluoride (5 days, 413 K) [13,14] or hydroxide media (6 h, 453 K) [15]. Crystallization of Beta frameworks in fluoride media results in the preferential stabilization of occluded TEA^+ cations with F^- anions and the selective formation of non-polar siloxane bonds, which disfavors formation of extended solvent (e.g., water) structures within microporous environments under relevant conditions for aqueous-phase sugar isomerization reactions [16].

In hydroxide media, however, charge compensation of the structure-directing agent (TEA^+) during crystallization processes results in the formation of siloxy defects (SiO^-) that become silanol groups after high temperature oxidative treatments. More recently, preparations of solid Lewis acids have been focused on the post-synthetic grafting of stannic chloride precursors into vacancy defects within dealuminated Beta supports via vapor-phase deposition [17], solid-state exchange [18–21], or liquid-phase grafting in solvent reflux [22–25]. Post-synthetic grafting of Sn heteroatoms into a subset of the total number of vacancy defects, however, results in hydrophilic solid Lewis acids because of residual silanol groups that are detected in methanol and water adsorption isotherms (293 K) and IR spectra (303 K) of dehydrated samples (823 K, 2 h) [25–28]. Altogether, differences in mineralizing agents used to prepare parent zeolite supports, and the extent of metal grafting within framework vacancy defects of dealuminated zeolites, determine the density of framework metal sites and of hydrophilic binding sites (e.g., silanol groups) present in post-synthetically prepared Lewis acid zeolites.

Selective incorporation of metal heteroatoms into the framework of Beta molecular sieves is also limited because extraframework metal oxide phases tend to form preferentially with increasing Sn density. Hydrothermal crystallization of Beta zeolites with Sn heteroatoms within their frameworks are reported to accommodate Sn densities up to ∼2 wt.% (Si/Sn > ∼100) [13, 14]. Incorporation of high Sn densities (Si/Sn = 100–400), however, results in longer crystallization times (4 days to 60 days, 413 K) [29]. Although the addition of dealuminated Beta seeds has been reported to decrease the crystallization time to 2 days, Sn incorporation into framework and extraframework positions was limited to Si/Sn = 126 (1.6 wt.% Sn) [12]. Post-synthetic grafting of stannic chloride precursors into vacancy defects formed by dealumination can accommodate higher Sn densities in framework positions by varying the Al density in the parent Al-Beta zeolite [22, 25]. For instance, Sn grafting via vapor-phase deposition [17], solid-state exchange [19], and impregnation methods [24] incorporated up to 5 wt.% Sn (Si/Sn = 37) in the framework, after which extraframework tin oxide

species are observed. Preparation of Sn-Beta molecular sieves with high Sn densities (Si/Sn < 100) becomes limited when post-synthetic grafting procedures incorporate Sn within only a subset of the total vacancy defects present. Solely varying the metal content, in turn, provides insufficient control of the active site features that are relevant for reactions whose turnover rates are sensitive to local metal coordination.

Sn heteroatoms coordinate with four framework bonds to form closed Sn sites ($Sn(OSi)_4$) or three framework bonds and a hydroxyl ligand to form open Sn sites ($Sn(OSi)_3(OH)$). Recent studies on the structure of open Sn sites combined IR spectra of various Sn-containing zeolites after saturation with CD_3CN (303 K) and post-synthetic treatments to conclude that persistent open Sn sites have a neighboring vacancy defect [28,30] in configurations that do not permit condensation to form closed sites, and that such defective open sites tend to form at grain boundaries located within Beta crystallites [31]. The presence of these framework Sn species, proposed to be stable species based on ONIOM and DFT calculations [30], are observed after deconvolution of the ν(C≡N) stretching region of IR spectra of Sn-Beta saturated with CD_3CN (303 K) [26, 32, 33]. Variations in the conditions of high temperature oxidative treatment (e.g., humidity and bed depth) results in modifications on the density of open and closed Sn sites in Sn-Beta [30]. Initial rates of Baeyer-Villiger oxidation of adamantanone with hydrogen peroxide (per g, 363 K) correlated linearly with the peak area of open Sn sites (2316 cm^{-1}), but not the peak area of closed Sn sites (2308 cm^{-1}) [5, 6]. Sn-Beta samples pre-poisoned with ammonia resulted in a selective decrease in the 2316 cm^{-1} CD_3CN IR peak (303 K), along with a decrease in the intensity of the resonance at -424 ppm in ^{119}Sn NMR, which have been assigned to partially-hydrolyzed Sn sites (open Sn sites) [32]. Ex situ pyridine titrations fully suppressed aqueous-phase glucose isomerization rates (per total Sn, 373 K), measured in the absence of intrazeolite mass transport limitations [26, 34, 35], when present at coverages equivalent to the number of open Sn sites (2316 cm^{-1}) quantified ex situ from CD_3CN IR spectra (303 K) on various hydrothermally-synthesized Sn-Beta zeolites [26]. These kinetic and spectroscopic experiments suggest that open Sn sites,

characterized by IR ν(C≡N) stretches at 2316 cm^{-1} after saturation with CD_3CN (303 K), are the dominant active sites for oxidation and sugar isomerization reactions on Sn-Beta.

Open Sn sites within the micropores of Sn-Beta are surrounded by the secondary environment provided by the zeolitic walls and other defect sites (e.g., silanol groups) that interact with water molecules [36,37], influencing the free energies of relevant reactive intermediates and transition states [38]. Systematic variations in the density of metal heteroatoms incorporated into the same dealuminated Beta supports [20,22,25], or of the density of vacancy defects present initially while keeping metal incorporation constant [27,39], provides metallosilicates of varying density of residual vacancy defects. Differences in the density of silanol groups upon incorporation of tetravalent heteroatoms are probed by the disappearance of IR bands associated with the OH stretching vibrations of perturbed silanol groups found in vacancy defects (∼3500–3600 cm^{-1}) [20, 24, 40–42]. Recently, systematic decreases in the peak intensity of perturbed silanol groups (3300–3700 cm^{-1}) upon Ti grafting within different parent dealuminated Beta supports were estimated by normalization to an ν(Si-O-Si) overtone peak intensity (1865 cm^{-1}) [27]. Consumption of silanol groups upon grafting of metal heteroatoms has also been observed in the selective decrease of ^{29}Si MAS NMR resonances at -102 ppm [17,24] corresponding to Si atoms with three –OSi neighbors and one non-silica neighbor or Q_3 sites (e.g., $(OSi)_3OH$) [43,44]. Internal and external silanol defects are also detected through ^{1}H MAS NMR of dehydrated zeolites with resonances located at 2.0 and 1.8 ppm, respectively [45–48]. Quantification of NMR spectra, however, has focused on the deconvolution of ^{29}Si NMR contributions at -102 ppm, corresponding to silanol groups located within various zeolitic environments (e.g., external crystallite surface and within micropores) [49]. Although NMR and IR experiments can be used to monitor the extent of metal incorporation, quantification of the density of hydrophilic binding sites located within different void environments of solid Lewis acids is required to interrogate reactivity trends specific to zeolitic micropores [26, 35, 38].

Glucose-fructose isomerization rates (per open Sn, 373 K) are sensitive to the speciation of Sn heteroatoms as well as the density of hydrophilic binding sites [32, 50]. First-order glucose-fructose isomerization rate constants (373 K), which reflect Gibbs free energy differences between water-covered open Sn sites and the 1,2 hydride shift transition state [35,51], decrease with increasing Sn content in post-synthetically prepared Sn-Beta samples when normalized by the total Sn density [19,22–24,52], because of the preferential formation of open Sn sites at low Sn densities [25]. Isomerization rate constants (373 K) are invariant among post-synthetically prepared Sn-Beta zeolites, but 15x lower than those measured on hydrothermally-synthesized Sn-Beta zeolites after rigorous normalization by the number of open Sn sites. These differences in isomerization rate constants (per open Sn, 373 K) between post-synthetically prepared and hydrothermally-synthesized Sn-Beta are the consequence of entropic penalties in the hydride shift transition state formation because of reorganization of extended networks of water molecules present within post-synthetically prepared Sn-Beta [38]. Taken together, aqueous-phase sugar isomerization rate constants (373 K) provide a sensitive probe of the active site structures within solid Lewis acid that consist of the local coordination of Sn heteroatoms and the secondary environment in the form of silanol groups.

Here, we interrogate the nature of synthetic procedures in order to develop techniques to tailor and characterize the metal density, metal coordination, and the framework polarity of solid Lewis acids. In Chapter 2, we first develop methods to quantify Sn heteroatoms in open and closed configuration through the use of IR spectroscopy of adsorbed CD_3CN (303 K). In Chapter 3, we evaluate how the identity of the reflux solvent in liquid-phase grafting preparations of Sn-Beta zeolites influence framework Sn density and coordination, and resulting consequences for sugar isomerization rate constants (per total Sn, 303 K). The techniques developed in Chapter 3 allowed for the preparation of Ti-containing Beta zeolites of varied density of silanol groups (and metal heteroatoms) to interrogate their consequences for first-order and zero-order glucose-fructose rate constants (per Lewis acid site, 303 K), as discussed in Chapter 4.

These mechanistic findings guided the post-synthetic preparation of Sn-Beta zeolites with confining micropore environments of polarity characteristic of hydrophobic Sn-Beta catalysts prepared hydrothermally in fluoride media, as summarized in Chapter 5. We also discuss in Chapter 5 the development of methods to quantify the density of hydrophilic binding sites located within intraporous voids. Lastly, Chapter 6 summarizes the preparation of solid Lewis acids within varying confining environments and its influence on the selectivity of glucose isomerization towards sorbose over fructose (373 K). Altogether, this thesis establishes guiding synthesis-structure-function principles for the preparation of Lewis acid zeolites with tailored structural features and with intended and predictable consequences for sugar isomerization catalysis in aqueous media.

2. TITRATION AND QUANTIFICATION OF OPEN AND CLOSED LEWIS ACID SITES IN SN-BETA ZEOLITES THAT CATALYZE GLUCOSE ISOMERIZATION

2.1 Abstract

Methods to quantify framework Lewis acidic Sn^{4+} sites in zeolite Beta (Sn-Beta) with four Lewis base titrants (pyridine, deuterated acetonitrile, n-propylamine, ammonia) were developed using infrared (IR) spectroscopy or temperature programmed desorption (TPD). Integrated molar extinction coefficients (E, cm mol^{-1}) were measured for IR bands of pyridine adsorbed to Lewis acidic Sn sites (E(1450 cm^{-1}) = 1.42 ± 0.30) and of CD_3CN adsorbed to open (E(2316 cm^{-1}) = 1.04 ± 0.22) and closed (E(2308 cm^{-1}) = 2.04 ± 0.43) Sn sites, and differ from analogous E values for Lewis acidic Al sites by up to 3.6. TPD of Sn-Beta samples after saturation with NH_3 or n-propylamine (NPA) and purging to remove physisorbed species also enabled quantification of Lewis acid sites, which is seldom performed despite analogous methods that use such titrants to quantify Brønsted sites in solid acids. These four Lewis bases titrated Lewis acidic Sn sites with equimolar stoichiometry and counted similar numbers of Sn sites on low-defect Sn-Beta samples synthesized in fluoride media (Sn-Beta-F) with high Sn content (Si/Sn < 150). NPA binding on residual silanol defect sites, however, caused overestimation of Sn sites by TPD on Sn-Beta-F samples with low Sn content (Si/Sn > 175) or high defect Sn-Beta samples prepared via post-synthetic insertion of Sn atoms into framework vacancy defects of dealuminated Beta zeolites (Sn-Beta-OH). Molar ratios of open-to-closed Sn sites varied widely (0.29–1.64) among the eight Sn-Beta samples studied here. Open Sn sites have been proposed as the dominant active sites for aqueous-phase glucose–fructose isomerization via intramolecular 1,2-hydride shift, consistent with successive poisoning

of Sn-Beta samples with pyridine prior to measurement of initial glucose isomerization rates that suppressed reactivity at pyridine uptakes similar to the number of open Sn sites counted *ex situ* by CD_3CN. Measured first-order glucose isomerization rate constants in water (per open Sn, 373 K), which reflect free energy differences between isomerization transition states and two coordinated water molecules at Sn sites, were 50x higher on hydrophobic Sn-Beta-F than on hydrophilic Sn-Beta-OH zeolites. The characterization methods reported herein enable normalization of initial glucose isomerization turnover rates on Sn-Beta zeolites by their number of open Sn sites, as required prior to interpreting the catalytic consequences of structural heterogeneities introduced by differences in sample preparation or treatment history.

2.2 Introduction

Pure-silica molecular sieve frameworks containing Lewis acidic tetravalent heteroatoms (e.g., Sn^{4+}, Ti^{4+}) catalyze a range of oxidation reactions [1, 2, 5, 6, 53], including the concerted Meerwein-Ponndorf-Verley carbonyl reduction (aldehyde, ketone) and Oppenauer alcohol oxidation via intramolecular or intermolecular cycles (MPVO), with recent attention focused on MPVO reactions of biomass-derived oxygenates containing carbonyl moieties [37, 54–58]. Lewis acidic heteroatoms (M) can be tetrahedrally coordinated (M-$(OSi)_4$, "closed" site) or tri-coordinated ((HO)-M-$(OSi)_3$; "open" site) to the zeolite framework [59], each with its own strength and reactivity. Lewis acidic Sn-Beta zeolites have been prepared by direct hydrothermal crystallization (fluoride-assisted [5, 11], hydroxide-assisted [15] and by several indirect post-synthetic modifications, which first involve removing framework silicon atoms [9, 60] or heteroatoms (e.g., Zn, Al) [61] to form vacancy defects, followed by insertion of Lewis acidic heteroatoms (e.g., Sn, Ti) via vapor-phase deposition [17], via liquid-phase reflux or exchange [22–24, 62], or via solid-state ion exchange [19–21]. Sn-Beta zeolites prepared by such diverse methods and treatments differ in their distribution of open and closed sites [30] and their density of other structures (e.g., Si-OH defects), requiring methods to quantify the number of open and closed sites in order to interpret turnover rate differences among samples of varying origin or treatment history.

Experimental and theoretical assessments of the strength of Lewis acid sites, inferred from their interactions with Lewis base probes, indicate that open sites are stronger than closed sites in Sn-Beta. Deuterated acetonitrile (CD_3CN) binding to framework Sn sites involves donation of electron density from the HOMO of CD_3CN (localized at the nitrogen atom) to the LUMO of the Sn site (a combination of the four antibonding σ^*(Sn-O) orbitals) and concomitant lengthening of the four Sn-O bonds, which occurs to a greater extent in open Sn sites than in less flexible closed Sn sites according to theory (ONIOM and DFT) [30]. These findings are consis-

tent with experiment, which has noted that infrared ν(C≡N) stretches for gas-phase CD_3CN (2265 cm^{-1}) are more strongly perturbed when bound to open (2316 cm^{-1}) than to closed Sn sites (2308 cm^{-1}), and that IR peaks for CD_3CN bound to closed sites disappear preferentially upon evacuation of CD_3CN-saturated surfaces (298-433 K) [30, 32, 33]. Sn-Beta zeolites saturated with ammonia at 298 K and then evacuated at 393 K give rise to ^{119}Sn NMR resonances for tetrahedrally-coordinated closed sites (ca. -443 ppm) but not for tetrahedrally-coordinated open sites (ca. -420 ppm), which instead appear as broad resonances characteristic of penta-coordinated Sn (-500 to -600 ppm; e.g., $(NH_3)(HO)$-Sn-$(OSi)_3$) [32], indicating that NH_3 binds more strongly at open Sn sites. Furthermore, NH_3-saturated Sn-Beta zeolites that are subsequently exposed to CD_3CN (308 K) show IR peaks at 2308 cm^{-1} but not at 2316 cm^{-1} [32], indicating that NH_3 binds more strongly than CD_3CN to open Sn sites, as also predicted by DFT [63]. Taken together, these spectroscopic data and theoretical calculations provide evidence that open Sn sites bind Lewis bases more strongly than closed Sn sites in Sn-Beta.

Experimental and theoretical assessments of catalytic oxidation reactivity also provide evidence that open sites are more reactive Lewis acid sites than closed sites in Sn-zeolites. Boronat et al. varied the distribution of open and closed sites in Sn-Beta by varying calcination conditions (e.g., humidity, bed depth) and observed that the initial rate of Baeyer-Villiger oxidation of adamantanone with aqueous H_2O_2 (per g, 363 K, dioxane solvent) correlated linearly with IR peak areas for CD_3CN bound to open Sn sites, but not for CD_3CN bound to closed Sn sites [30]. Bermejo-Deval et al. exchanged sodium cations onto silanol groups proximal to open Sn sites in Sn-Beta and observed suppression of glucose-fructose isomerization rates (per g, 353 K), concluding that open Sn sites were the dominant active site for this intramolecular MPVO reaction [32]. These experimental findings are consistent with activation enthalpies for intramolecular 1,2-hydride shift steps in glucose-fructose isomerization sequences that theory has predicted to be 5–10 kcal mol^{-1} lower on open than on closed Sn sites [34, 64, 65]. Both theory and experiment indicate that open Sn sites

are stronger Lewis acids and more reactive in oxidation reactions than closed sites, but these two types of sites have yet to be quantified precisely in Sn-zeolites, as required for rigorous normalization of catalytic turnover rates.

Pyridine is used as a base titrant of Lewis acid sites because it gives rise to IR peaks at 1455 cm^{-1} and 1623 cm^{-1} for perturbed gas-phase ring deformation modes (1439 cm^{-1} and 1580 cm^{-1}, respectively) when present in Lewis-bound adducts [66–69], but it does not distinguish between open and closed Lewis acid sites. As a result, pyridine titration of Sn-Beta zeolites has been used only to detect the presence of Lewis acidic Sn [12,70], to infer the density of Lewis acidic Sn sites from integrated IR peak areas [17,71], or to quantify the number of Lewis acidic Sn sites using integrated molar extinction coefficients ($\mathcal{E}$) for Lewis acidic Al sites [24,72–74]. Carbon monoxide has also been used as a base titrant to identify open (2185 cm^{-1}) and closed (2176 cm^{-1}) Lewis acidic Zr sites in Zr-Beta zeolites and to infer their density from integrated IR peak areas [75]. Deuterated acetonitrile, which is used to avoid Fermi resonance between the ν(C≡N) stretching mode and a combination of the symmetric ν(C-C) and deformation $\nu(CH_3)$ modes in CH_3CN [76, 77], can distinguish between open (2316 cm^{-1}) and closed (2308 cm^{-1}) Lewis acid sites in Sn-Beta zeolites [20, 30, 32, 33]. These different IR vibrational stretching frequencies have been proposed to reflect supra-stoichiometric CD_3CN binding to Sn sites or the presence of additional CD_3CN within the immediate vicinity, based on temperature programmed desorption-thermogravimetric analysis (TPD-TGA) of CD_3CN-saturated Sn-Beta samples that evolved 1.6 mol CD_3CN per mol Sn [78] and reports of solvent-induced shifts in CD_3CN IR vibrations [79]. Yet, the distinct assignments of IR peaks to one CD_3CN bound at open (2316 cm^{-1}) or closed (2308 cm^{-1}) Sn sites are consistent with ν(C≡N) stretches predicted by density functional theory [30] and with their correlations to ^{119}Sn NMR resonances for tetrahedral open (ca. -420 ppm) and closed Sn sites (ca. -443 ppm) in dehydrated Sn-Beta zeolites [34]. CD_3CN has been used to infer the relative density of open and closed sites in Sn-Beta from integrated IR peak areas [30], and to quantify Lewis acidic Zn sites in Zn-exchanged Al-Beta using E values for

CD_3CN bound to Lewis acidic Al sites [80, 81], but to our knowledge, it has not yet been used to quantify the number of open and closed Sn sites in Sn-zeolites.

Here, for the first time, integrated molar extinction coefficients ($\mathcal{E}$; cm μmol^{-1}) are measured and reported for IR peaks of pyridine adsorbed on Lewis acidic Sn sites and of CD_3CN adsorbed on open and closed Sn sites in Sn-zeolites. We use these $\mathcal{E}$ values to quantify open and closed Sn sites on stannosilicates, focusing on Sn-Beta as a representative zeolite topology for which several different preparation strategies have been reported [9, 15, 17, 19, 20, 22–24, 60–62]. We demonstrate that the total number of Lewis acidic Sn sites on a given sample, taken as the number of open and closed Sn sites titrated by CD_3CN (1:1 CD_3CN:Sn) in IR experiments, agrees quantitatively with the number of Sn sites titrated by pyridine (1:1 pyridine:Sn) in IR experiments and by ammonia (1:1 NH_3:Sn) and n-propylamine (1:1 NPA:Sn) in TPD experiments. We also show that the number of active Sn sites in Sn-Beta can be estimated by partial poisoning with pyridine titrants prior to aqueous-phase glucose isomerization catalysis, which provides further evidence that the open Sn site is the predominant active site for glucose-fructose isomerization [32]. We use the number of open Sn sites to normalize initial turnover rates of glucose-fructose isomerization, chosen as a model intramolecular MPVO reaction for which mechanistic interpretation of rate data is tractable, prior to interpreting the catalytic consequences of structural heterogeneities prevalent among Sn-Beta zeolites prepared by different synthetic or post-synthetic methods.

2.3 Experimental Methods

2.3.1 Catalyst Synthesis

Sn-Beta samples were synthesized directly in fluoride media (Sn-Beta-F) at different Si/Sn ratios (Sn-Beta-F-X, X = Si/Sn) by adapting the method reported by Chang et al. [12], who prepared a seed solution comprising dealuminated Beta zeolites (filtered to retain particles <200 nm in diameter) dispersed in water via sonication. Here, dealuminated Beta zeolites (unfiltered) were used as seed material, and were prepared by adding 5 g of H-form Al-Beta (Zeolyst, CP814C, Si/Al=19) to 125 cm^3 of concentrated nitric acid (HNO_3, Avantor, 69 wt.%) and stirring for 16 h at 353 K. Dealuminated Beta solids were collected via centrifugation, washed thoroughly with deionized water (18.2 MΩ,6 washes, 25 cm^3 (g zeolite)$^{-1}$ per wash), and then dried for 16 h at 373 K. The Sn-Beta synthesis gel was prepared by mixing 6.98 g of tetraethylorthosilicate (TEOS, Sigma Aldrich, >98 wt.%) and 7.67 g of tetraethylammonium hydroxide (TEAOH, Sachem, 35 wt.%) in a perfluoroalkoxy alkane (PFA) container (Savillex Corp.) and stirring for 1 h, followed by dropwise addition of a solution of 0.04-0.12 g of tin (IV) chloride pentahydrate ($SnCl_4$-$5H_2O$, Sigma-Aldrich, 98 wt.%) in 0.64 g of deionized water. The resulting gel was stirred in a closed PFA container for 12 h, and then ethanol (6.04 g) and excess water (1.95 g) were allowed to evaporate. Next, 0.74 g of hydrofluoric acid (HF, Alfa Aesar, 48%) were added into the solution in a fume hood and stirred manually with a Teflon spatula for 300 s and residual HF allowed to evaporate for an additional 900 s. After homogenization, 0.579 cm^3 of water and 0.085 g of dealuminated Beta seeds (∼4.1 wt.% of SiO_2) were added and the gel was stirred manually with a Teflon spatula. The final molar composition of the gel was 1 SiO_2/x $SnCl_4$/0.56 TEAOH/0.54 HF/8.38 H_2O, where x ranged between 0.003 and 0.01. This gel was transferred into a Teflon-lined stainless steel autoclave (45 cm^3, Parr Instruments) and heated at 413 K in an isothermal oven (Yamato DKN-402C) with rotation (∼60 rpm) for either 6 days (Sn-Beta-F-105 and Sn-Beta-F-140) or 14 days (Sn-Beta-F-100, Sn-Beta-F-110, Sn-Beta-F-170, Sn-Beta-

F-220). The products were removed from the Teflon liner, washed thoroughly with water and acetone (Sigma Aldrich, >99.5 wt.%, 5 washes each, ∼25 cm^3 (g zeolite)$^{-1}$ per wash)), isolated by centrifugation, and dried for 16 h at 373 K. The dry zeolite powders were then treated in dry air (Ultra Zero Grade, Indiana Oxygen, 1.67 cm^3 s^{-1} (g zeolite)$^{-1}$) to 853 K (0.0167 K s^{-1}) and held for 10 h in a muffle furnace (Nabertherm LE 6/11 equipped with a P300 controller).

Two Sn-Beta samples were prepared via the post-synthetic reflux method reported by Dijkmans et al. (samples denoted Sn-Beta-OH) [23]. First, H-form Al-Beta zeolites (gel Si/Al molar ratios of 30 or 100) were synthesized by adapting the method reported by Chang et al. [12] without the aluminosilicate gel filtration step, followed by washing the crystalline solids thoroughly with water and acetone, recovering the solids by centrifugation, drying overnight at 373 K, and then treating in air (Ultra Zero Grade, Indiana Oxygen, 1.67 cm^3 s^{-1} (g zeolite)$^{-1}$) to 853 K (0.0167 K s^{-1}) for 10 h in a muffle furnace. H-Beta zeolites with solid Si/Al ratios of 25 and 80 were dealuminated using the HNO_3 treatment described above (residual Si/Al >680 measured by AAS), and then used as the starting material to prepare Sn-Beta-OH-170 and Sn-Beta-OH-200, respectively. For Sn-Beta-OH-170, 2 g of dealuminated Beta was treated in air (Ultra Zero Grade, Indiana Oxygen, 1.67 cm^3 s^{-1} g zeolite^{-1}) to 853 K (0.0167 K s^{-1}) for 10 h, and then 2 g were placed in a round bottom flask (500 cm^3) and dried overnight at 423 K under rough vacuum (∼0.04 Torr, Oerlikon Trivac 140002E2) on a Schlenk line. For Sn-Beta-OH-200, the dealuminated Beta was not treated in air prior to the drying step under rough vacuum at 423 K. Next, isopropanol (Avantor, ChromAR HPLC Grade, >99.5 wt.%) was dried over 3A molecular sieves (W. R. Grace, Type 3A, Grade 562, 4-8 mesh) for 72 h, and then transferred into the flask containing the dried dealuminated zeolite via air- and moisture-free cannula transfer. Separately, $SnCl_4$-$5H_2O$ (0.027 or 0.081 mol Sn (g zeolite)$^{-1}$) was added to a 50 cm^3 flask sealed with a septum (white rubber, Ace Glass), and dissolved in dry isopropanol transferred into the flask via gas-tight syringe. The isopropanolic $SnCl_4$-$5H_2O$ solution was then transferred to the round bottom flask containing the dealuminated Beta, and the

contents were refluxed in argon (Indiana Oxygen, 99.999%) for 7 h. The solids were collected by centrifugation, washed 6 times (∼60 cm^3) with isopropanol to prepare Sn-Beta-OH-170, or with methanol (Sigma Aldrich, >99.9%) to prepare Sn-Beta-OH-200, and then dried 16 h at 373 K. Washing the solids with methanol after the reflux procedure has been reported to remove residual $SnCl_4$ that leads to extraframework Sn upon air treatment at 823 K [24]. The dried solids were treated in air (Ultra Zero Grade, Indiana Oxygen, 1.67 cm^3 s^{-1} (g zeolite)$^{-1}$) at 473 K (0.05 K s^{-1}) for 6 h, and then at 823 K (0.05 K s^{-1}) for 6 h in a muffle furnace. Sn-xerogel was synthesized according to the procedure from van Grieken et al. [82]. 5.74 g of a 0.1 M HCl solution (Macron, 37%) were stirred with 52.0 g of TEOS and 67.6 g of deionized water for 2 h at ambient temperature. Then, 0.77 g of $SnCl_4$-$5H_2O$ were added and the mixture stirred for 1 h. Finally, a 1 M NH_4OH solution (Sigma Aldrich, 28%-30 wt.% NH_3 basis) was added dropwise until the gel point was reached (∼12 cm^3). The resulting clear gel was dried at 433 K for 12 h. The dried solids were then thoroughly washed with deionized water (5-10x, ∼60 cm^3 per wash) until a stable pH was reached, dried at 433 K for 12 h, and then treated in air (Ultra Zero Grade, Indiana Oxygen, 1.67 cm^3 s^{-1} (g zeolite)$^{-1}$) to 853 K (0.0167 K s^{-1}) for 10 h in a muffle furnace. A sample containing predominantly extraframework SnO_2 was prepared via incipient wetness impregnation of 1.12 g of a $SnCl_4$-$5H_2O$ solution (0.60 M) on 1.82 g of as-made Si-Beta crystallized in fluoride medium [11] (sample denoted SnO_2/Si-Beta). The impregnated solids were dried under rough vacuum at ambient temperature for 16 h, then treated in air (Ultra Zero Grade, Indiana Oxygen, 1.67 cm^3 s^{-1} (g zeolite)$^{-1}$) at 853 K (0.0167 K s^{-1}) for 10 h in a muffle furnace.

2.3.2 Catalyst Characterization

Bulk elemental compositions of samples were determined using atomic absorption spectroscopy (AAS) performed with a Perkin Elmer AAnalyst 300 Atomic Absorption Spectrometer. 1000 ppm AAS standards (Alfa Aesar, TraceCERT, +/- 4 ppm) for each metal were diluted to create calibration standards, and the instrument was cal-

ibrated for each element prior to collecting measurements. Zeolite samples (typically 0.02 g) were dissolved in 2 g of HF (48 wt.%, Alfa Aesar) overnight and then further diluted with 30 g of deionized water. Absorbance values were measured at 396.2 nm and 284.0 nm in an acetylene/nitrous oxide flame for Al and Sn, respectively. Al and Sn weight fractions were used together with the unit cell formula for zeolite Beta to estimate Si/Al and Si/Sn ratios, respectively. Powder X-ray diffraction (XRD) patterns were collected on a Rigaku Smartlab X-ray diffractometer equipped with an ASC-6 automated sample changer and a Cu K x-ray source (1.76 kW). Typically, 0.01 g of sample were packed within zero background, low dead volume sample holders (Rigaku) and diffraction patterns were measured from 4-40° at a scan rate of 0.00417° s^{-1} with a step size of 0.02°.

Scanning electron microscopy (SEM) and electron dispersive X-ray spectroscopy (EDS) were performed on a FEI Quanta 3D FEG Dual-beam SEM with an Everhart-Thornlev detector for high vacuum imaging. SEM micrographs were collected using the focused beam operating mode with a voltage of 5 kV and spot size of 4 μm. EDS was performed using an Oxford INCA Xstrem-2 silicon drift detector with an Xmax80 window for supplemental elemental analysis. All analyses were performed at 20 kV at a spot size of 6 μm at a magnification of 3000-6000x.

N_2 (77 K) and H_2O (293 K) adsorption isotherms were measured on samples (˜0.03 g, pelleted and sieved to retain 180-250 μm diameter particles) using a Micromeritics ASAP2020 Surface Area and Porosity Analyzer. Prior to measurement of isotherms, samples were degassed by heating to 393 K (0.0167 K s^{-1}) under vacuum (<0.005 Torr) for 2 h, then heating to 623 K (0.0167 K s^{-1}) under vacuum for 8 h. Micropore volumes were determined from a semi-log derivative analysis of N2 isotherms ($\delta(V_{ads}/g)/\delta(\log(P/P_0)$ vs. $\log(P/P_0)$) to identify the completion of micropore filling (additional details in Section 2.7.2). The hydrophobicity of each sample was assessed from the amount of water adsorbed at a relative pressure of 0.2, chosen elsewhere as a reference pressure corresponding to cyclohexane (298 K) filling of micropores in hydrophobic zeolites [83].

Diffuse reflectance UV-Vis (DRUV) spectra were collected on a Varian Cary 5000 UV-VIS-NIR equipped with a Harrick Praying Mantis itin situ diffuse reflectance cell. Spectra were collected on samples: (i) first exposed to ambient conditions and held in flowing dry He (4.17 cm^3 s^{-1} (g zeolite)$^{-1}$) ("ambient" treatment); (ii) after subsequent treatment to 523 K (˜0.5 K s^{-1}) for 1800 s in flowing dry He (4.17 cm^3 s^{-1} (g zeolite)$^{-1}$) ("dehydration" treatment); and (iii) after subsequent exposure to a flowing wet He stream (4.17 cm^3 s^{-1} (g zeolite)$^{-1}$, ∼3% H2O, bubbled through a water saturator at ambient temperature) while cooling from 523 K to 303 K and holding for 300 s ("rehydration" treatment). Diffuse reflectance spectra were collected at a rate of 10 nm s^{-1}, using poly(tetraflouroethylene) (PTFE, 1 μm powder, Sigma-Aldrich) as the 100% reflectance standard, and then converted to an absorption spectrum using the Kubelka-Munk (F(R)) function. Absorption edge energies were calculated from Tauc plots of $[F(R)h\nu]^2$ vs. $h\nu$ (additional details in Section 2.7.3).

2.3.3 Temperature Programmed Desorption

Temperature programmed desorption (TPD) experiments were performed using a Micromeritics Autochem II 2920 Chemisorption Analyzer interfaced with an Agilent 5793N mass selective detector (MSD) to quantify gaseous titrants evolved from the catalysts. Zeolite samples (0.03-0.05 g, sieved to 180-250 μm) were supported in a U-tube reactor between two quartz wool plugs inside of a clam-shell furnace. Zeolite samples were treated in air (25 cm^3 s^{-1} (g zeolite)$^{-1}$, Indiana Oxygen, Ultra Zero Grade) to 673 K (0.167 K s^{-1}) for 4 h and then cooled to ambient temperature. For n-propylamine (NPA) titration experiments, samples were saturated in a flowing stream comprising NPA (1000 ppm certified concentration), 1% Ar and balance He (75 cm^3 s^{-1} (g zeolite)$^{-1}$, Airgas, Certified Standard Grade) at 323 K for 4 h, and then purged in flowing He (25 cm^3 s^{-1} (g zeolite)$^{-1}$) at 338 K for 4 h to remove weakly-bound NPA (additional details in Section 2.7.7). For NH_3 titration experiments, samples were saturated in flowing gaseous NH_3 (456 ppm certified concentration) in balance N_2 (25 cm^3 s^{-1} (g zeolite)$^{-1}$, Indiana Oxygen, Certified Standard Grade) for 12 h, and then

purged in flowing He (25 cm^3 s^{-1} (g zeolite)$^{-1}$, Indiana Oxygen, 99.999%) for 8 h at 331 K to remove gaseous and physisorbed NH_3 (additional details in Section 2.7.8). After titrant saturation and purge treatments, TPD was performed in flowing He (25 cm^3 s^{-1} (g zeolite)$^{-1}$) to 873 K (at 0.167 K s^{-1}), during which the U-tube reactor effluent was sent to the MSD via heated transfer lines held at 383 K. After each TPD experiment, a 0.5 cm^3 sample loop was filled with argon (99.999% Indiana Oxygen) and injected by flowing He (25 cm^3 s^{-1}) that was sent to the MSD in order to quantify the amount of NH_3 or NPA desorbed from the integrated MSD signals and a calibrated response factor for NH_3 or NPA relative to Ar.

2.3.4 Infrared Spectroscopy and Determination of Integrated Molar Extinction Coefficients

IR spectra were collected on a Nicolet 4700 spectrometer with a Hg-Cd-Te (MCT, cooled to 77 K by liquid N_2) detector by averaging 64 scans at 2 cm^{-1} resolution in the 4000 to 400 cm^{-1} range and were taken relative to an empty cell background reference collected under dynamic vacuum (rotary vane rough pump, Alcatel 2008A, <0.1 Torr) at either 303 K (CD_3CN) or 423 K (pyridine). Self-supporting wafers (0.01-0.03 g cm^{-1}) were sealed within a custom-built quartz IR cell with CaF_2 windows, equipped with a mineral-insulated resistive heating coil (ARi Industries) and encased in an alumina silicate ceramic chamber (Purdue Research Machining Services). Wafer temperatures were measured within 2 mm of each side of the wafer by K-type thermocouples (Omega). The quartz IR cell interfaced with a custom glass vacuum manifold that was used for sample pretreatment and exposure to controlled amounts of gaseous titrants. Prior to each IR experiment, wafers were treated in flowing dry air (6.66 cm^3 s^{-1} (g zeolite)$^{-1}$) purified by an FTIR purge gas generator (Parker Balston, <1 ppm CO_2, 200 K H_2O dew point) to 823 K (0.083 K s^{-1}) for 1 h, and then held under dynamic vacuum (rotary vane rough pump, Alcatel 2008A, <0.1 Torr) at 823 K for 1 h. The wafer was then cooled under dynamic vacuum to 303 K for adsorption experiments with CD_3CN, or to 423 K for adsorption experiments

with pyridine. Titrants were purified via freeze-pump-thaw (3 cycles) and admitted to the cell in sequential doses ($\sim$2.5 x 10^{-7} mol). Equilibration of the sample with each dose was assumed when the final pressure in the cell and transfer line did not change for 180 s. For doses in which the final pressure was recorded as 0.0 Torr, as occurred during sub-saturation coverages, all of the titrant introduced to the cell was assumed to adsorb on the sample wafer. After dosing was complete, which occurred when samples reached equilibrium with a detectable gaseous titrant pressure (0.4-2.0 Torr), samples were exposed to dynamic vacuum (at 303 K for CD_3CN or at 423 K for pyridine) in order to remove gas-phase and weakly-bound species, which occurred when the pressure was recorded as 0.0 Torr. IR peaks for bound titrants did not change between spectra recorded after evacuation or after saturation, regardless of the titrant pressure used for saturation (Fig. 2.39). Each wafer was also heated to 523 K (0.167 K s^{-1}) in dynamic vacuum to monitor the disappearance of IR peaks for bound titrant species.

IR spectra reported here were baseline-corrected and normalized to combination and overtone modes of zeolite Si-O-Si stretches (1750-2100 cm^{-1}). Integrated molar extinction coefficients ($\mathcal{E}$, cm μmol^{-1}) for pyridine adsorbed onto Lewis acid sites on three different Sn-Beta samples (Sn-Beta-F-100, Sn-Beta-F-140, and Sn-Beta-OH-170) were determined from the increase in integrated area for the IR peak at 1450 cm^{-1} with sequential doses of pyridine to the wafer, and multiplying by the cross-sectional area of the wafer (2.54 cm^2). This analysis assumed that pyridine selectively adsorbed on Lewis acid sites during titration, consistent with the absence of IR peaks for pyridine adsorbed to non-Lewis acidic sites and with the method proposed by Emeis [84] (details in Section 2.7.6). IR peaks for CD_3CN species bound to open (2316 cm^{-1}) and closed (2308 cm^{-1}) Lewis acid sites, bound to Sn sites in highly-defective oxide surfaces (2287 cm^{-1}), hydrogen-bound to Si-OH sites (2275 cm^{-1}), and physisorbed or gas phase CD_3CN (2265 cm^{-1}) overlapped and required deconvolution into individual components (details in Section 2.7.9). Integrated molar extinction coefficients for CD_3CN were determined for open Lewis acid sites (2316 cm^{-1}) and

closed Lewis acid sites (2308 cm^{-1}) on Sn-Beta by using a non-linear least squares regression of saturation peak areas on three Sn-Beta samples (Sn-Beta-F-100, Sn-Beta-F-105, Sn-Beta-OH-170), with the number of Lewis acid sites determined from pyridine chemisorption IR experiments. The number of sites titrated by pyridine or CD_3CN on self-supporting sample wafers was estimated from integrated IR peak areas and values using the following equation:

$$Site\,density\,(\mu mol\,g^{-1}) = \frac{Integrated\,Peak\,Area\,(cm^{-1})}{\mathcal{E}(cm\,\mu mol^{-1})} * \frac{a_{CS}(cm^2)}{m(g)} \qquad (2.1)$$

where a_{CS} and m are the cross-sectional area and mass of the wafer, respectively.

2.3.5 Kinetic and Isotopic Tracer Studies of Glucose Reactions with Sn-Beta

Catalytic studies were performed in batch reactors using 1-10% (w/w) aqueous D-glucose (Sigma Aldrich, 99.5%) solutions with Sn-Beta samples. Reactant solutions were made with water (18.2 MΩ) adjusted to pH 5 (measured by Mettler Toledo Seven Compact pH Ion S220 probe) by addition of hydrochloric acid (Macron, 37% (w/w)) prior to glucose addition and filtration through 0.2 μm PTFE filters (VWR). Catalytic solids (∼0.01 g) were added to thick-walled glass reactors (10 cm^3, VWR) sealed with crimp tops (PTFE/silicone septum, Agilent). Reactors and reactant solutions were heated separately for 600 s to 373 K atop a digital stirred hot plate (IKA RCT basic) prior to injecting the reactant solution (∼1 cm^3) into the capped reactors. Reactors remained at 373 K while stirring at 750 rpm under autogenous pressure for various time intervals (300-14440 s) prior to quenching in an ice bath. Resulting product solutions were filtered through 0.2 μm PTFE filters, diluted to 1% (w/w) sugar concentration if necessary, and mixed with a 1% (w/w) aqueous D-mannitol (Sigma Aldrich, ≥98 wt.%) solution as an internal standard. Component separation was performed using an Agilent 1260 high performance liquid chromatograph (HPLC) equipped with a Hi-Plex Ca column (7.7 x 300 mm, 8 μm particle size, Agilent) and

an aqueous mobile phase (0.01 cm^3 s^{-1}, 353 K), and quantification was performed using an evaporative light scattering detector (Agilent 1260 Infinity ELSD).

Initial rates of fructose formation were determined using a batch reactor model for a reversible first-order glucose-fructose isomerization reaction, which has been derived and discussed elsewhere [35]. Experimental batch reactor data were accurately described by this model and initial isomerization rates were determined by extrapolation of fructose product formation rates to zero reaction time. This extrapolation provides an estimate of initial reaction rates that are identical, within experimental error (15%), to reaction rates estimated using a differential (well-mixed) reactor model and data collected below 5% conversion (details in Section 2.7.10).

Kinetic evaluation of pyridine-titrated Sn-Beta samples was performed by treating zeolite wafers in the IR cell in air to 723 K, as described in Section 2.3.2. Samples were then exposed to controlled doses of pyridine at 423 K, typically between 0.03-0.40 moles of pyridine per Sn. An IR spectrum was collected to determine the moles of pyridine adsorbed on the sample, and then the titrated wafer was cooled to 333 K under dynamic vacuum, exposed to ambient conditions, removed from the cell, and crushed with a mortar and pestle. Powdered pyridine-titrated Sn-Beta samples were then transferred into a batch reactor and studied as described above.

Isotopic tracer studies were conducted using 1 cm^3 of a 5% (w/w) aqueous solution of D-glucose-D2 (Cambridge Isotope Laboratories, 2-D, 98%) adjusted to pH 5 and catalyst powders ($\sim$0.01 g) at 373 K for 1-4 hours prior to quenching the reactors and filtering the product solutions with 0.2 μm PTFE filters. Sugar separation was performed as described above, and the effluent was sent to an Agilent Infinity series fraction collector for solution collection. Liquid samples were frozen in liquid N_2 (77 K) prior to removal of water via a Labconco FreeZone lyophilizer. The recovered sugars were then dissolved in D2O (Cambridge Isotope Laboratories, 99.9%) and placed in a NMR tube (Wilmad LabGlass, 5 mm thin wall, 7 in., 400MHz) for NMR analysis. Solution ^{1}H NMR spectra were measured on a Bruker ARX400 spectrometer

equipped with a 5 mm QNP probe at ambient temperature and were the average of 64 scans acquired at a rate of ∼0.3 scans per second.

2.4 Results and Discussion

2.4.1 Structural Characterization of Stannosilicates

Characterization data for the Sn-Beta samples used in this study are shown in Table 2.1. Samples are denoted as Sn-Beta-X-Y, where X refers to the preparation method used (F = fluoride-assisted hydrothermal synthesis [12]; OH = post-synthetic Sn insertion into dealuminated Beta [23]) and Y is the Si/Sn ratio determined by atomic absorption spectroscopy. Powder XRD patterns for all zeolite samples(Fig. 2.12) were consistent with the Beta topology and did not show diffraction peaks for bulk SnO_2 at 26.7° or 34° 2θ. Diffraction peaks for bulk SnO_2 were also absent on a control sample prepared to contain SnO_2 supported on Si-Beta (SnO_2/Si-Beta), indicating that any SnO_2 domains on this sample were small enough to be X-ray amorphous (<3 nm in diam.) [85]. N_2 adsorption isotherms measured at 77 K (Fig. 2.13) indicated that micropore volumes were 0.21-0.24 cm^3 g^{-1} for all Sn-Beta-F samples and 0.19-0.22 cm^3 g^{-1} for all Sn-Beta-OH samples (Table 2.1), also consistent with the Beta topology. H_2O adsorption isotherms measured at 293 K (Fig. 2.14 and 2.15) showed H_2O uptakes (at $P/P_0 = 0.2$) of 0.005-0.017 cm^3 g^{-1} for Sn-Beta-F samples (Table 2.1), consistent with the hydrophobic nature of low-defect zeolites crystallized in fluoride media [16], but showed higher H_2O uptakes of 0.036-0.092 cm^3 g^{-1} for Sn-Beta-OH samples (Table 2.1), reflecting the more hydrophilic and defective nature of samples prepared via Sn insertion into framework vacancy defects of dealuminated zeolites.

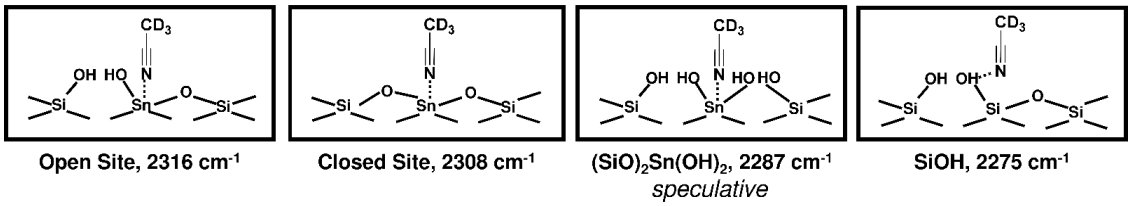

Figure 2.1: Adsorption of CD_3CN on different sites in stannosilicates and corresponding $\nu(C{\equiv}N)$ infrared vibrational frequencies.

Table 2.1: Site and structural characterization data for the samples in this study.

Sample	Crystallization Time (d)	Si/Sn Ratio (AAS)[a]	Si/Sn Ratio (EDS)[b]	V_{ads} (N_2, 77 K) ($cm^3\ g^{-1}$)[c]	V_{ads} (H_2O, 293 K) ($cm^3\ g^{-1}$)[d]	DRUV Band Center (nm)[e]	DRUV Edge Energy (eV)[e]	Glucose-D2 Isotopic Tracer Studies[f]
Sn-Beta-F-100	14	100	120	0.24	0.0069	244	4.09	Fructose-D1
Sn-Beta-F-105	6	105	140	0.22	0.015	216	4.17	n. m.*
Sn-Beta-F-110	14	110	130	0.23	0.0095	223	4.26	Fructose-D1
Sn-Beta-F-140	6	140	105	0.22	0.017	238	4.19	n. m.*
Sn-Beta-F-170	14	170	200	0.21	0.0073	207	4.20	Fructose-D1
Sn-Beta-F-220	14	220	300	0.22	0.0050	197	4.29	Fructose-D1
Sn-Beta-OH-170	-	170	245	0.22	0.036	193	4.25	Fructose-D1
Sn-Beta-OH-200	-	200	280	0.19	0.092	195	4.69	Fructose-D1
SnO_2/Si-Beta	-	66	63	0.22	0.0052	250	4.09	No products**
Sn-xerogel	-	110	130	0.02	0.024	245	4.37	No products**

[a] Bulk composition determined by atomic absorption spectroscopy (AAS).
[b] Composition determined by energy dispersive X-ray spectroscopy (EDS).
[c] Micropore volume determined from total N_2 uptake at the end of micropore filling in adsorption isotherms (77 K).
[d] H_2O uptake at $P/P_0 = 0.2$ (293 K) taken as a descriptor of hydrophobicity (P/P_0=0.2 corresponds to full micropore filling with cyclohexane [50]).
[e] Diffuse reflectance UV-Vis spectra (band center at maximum F(R) intensity) and Tauc plots for samples after dehydration at 523 K (Section S.3, Supporting Information).
[f] Fructose product formed from glucose-D2 reactants in water (373 K), ^{1}H NMR spectra shown in Figure S.6 (Section S.4, Supporting Information).
*n. m., not measured
**No products observed for SnO_2/Si-Beta (0.01 g catalyst, 4 h) and Sn-xerogel (0.10 g catalyst, 5 h) in aqueous glucose (1% (w/w), 1 cm^3 solution, 373 K, pH = 5).

Diffuse reflectance UV-visible (DRUV) spectroscopy has been used to probe Sn coordination and detect tetrahedrally-coordinated framework Sn centers, which have been assigned to bands centered at ∼205 nm [37, 86], yet such sites can coordinate water ligands to become penta- or hexa-coordinated [34] and give rise to bands centered at ∼220 nm and ∼255 nm, respectively [86]. DRUV bands for hexa-coordinated framework Sn centers at ∼255 nm, however, also fall within a range characteristic of small SnO_2 domains, which give rise to DRUV bands centered at lower wavelengths (∼240 nm) [50, 78] than for bulk SnO_2 (∼280 nm) because of quantum confinement effects [87–90], precluding unambiguous characterization of Sn structure from DRUV spectra of Sn-zeolites exposed to ambient conditions. Thus, DRUV spectra were collected on each sample under ambient conditions, after dehydration treatments in flowing dry helium at 523 K, and after rehydration treatments while cooling to 303 K in flowing wet (3% H_2O) helium (dehydrated spectra in Fig. 2.17 and 2.18). The positions of DRUV absorption (F(R)) bands of maximum intensity, together with absorption edge energies (Tauc plots of $[F(R)*h\nu]^2$ vs. $h\nu$ Fig. 2.19 and 2.20) are listed for each sample after dehydration treatments in Table 2.1.

DRUV spectra of Sn-Beta-F-170 (Fig. 2.16a) exposed to ambient conditions showed a broad band centered at ∼250 nm, while spectra collected after dehydration showed a new band centered at ∼207 nm with a shoulder centered at ∼250 nm, which

reverted to a band centered at ∼250 nm after rehydration treatments. These spectral features are consistent with framework Sn centers that are octahedrally-coordinated under ambient conditions or upon exposure to water, but become tetrahedrally-coordinated in the absence of water [34]. DRUV spectra of Sn-Beta-OH-200 (Fig. 2.16b) exposed to ambient conditions showed a band centered at ∼230 nm, which shifted to ∼190 nm upon dehydration and returned to ∼230 nm after rehydration, similar to the spectral changes observed on Sn-Beta-F-170 (Fig. 2.16a) and as expected from the reversible coordination of water ligands to framework Sn sites. These changes in DRUV spectra upon dehydration were observed to different extents among the different Sn-Beta samples in this study, for which bands did not always shift completely to ∼210 nm upon dehydration, but did revert to a single band centered between ∼230-250 nm upon rehydration. In sharp contrast, DRUV spectra of SnO_2/Si-Beta (Fig. 2.16c) did not change after dehydration or rehydration treatments and remained centered at ∼250 nm, indicating that Sn atoms within SnO_2 domains did not change coordination in the presence of water. Absorption edge energies (Table 2.1) on Sn-Beta-OH-170 (4.3 eV) and on Sn-xerogel (4.4 eV) are characteristic of isolated Sn sites in silica [78] and higher than the edge energy on SnO_2/Si-Beta (4.1 eV), which is characteristic of SnO_2 domains <3 nm in diameter (details in Section 2.7.3) [89]. Absorption edge energies for nearly all Sn-Beta-F samples (4.2-4.3 eV; Table 1) fall within a range higher than reported for SnO_2 domains [87–90] and reflect the predominance of isolated framework Sn sites in these samples, while the lower absorption edge energy of 4.1 eV on Sn-Beta-F-100 (Table 2.1) appears to reflect detectable amounts of small SnO_2 domains ($\leq$3 nm) on this sample.

We conclude that DRUV spectra collected on stannosilicates exposed to ambient conditions cannot unambiguously discern penta- or hexa-coordinated Sn atoms isolated within silica or stannic oxide domains [50, 78] , but changes to spectral features and absorption edge energies on dehydrated samples can distinguish between them because Sn centers isolated in silica (but not in stannic oxide) surfaces become tetrahedrally-coordinated [23, 86]. The subtle, yet measurable, differences in DRUV

absorption band maxima and edge energies among Sn-Beta-F and Sn-Beta-OH samples (Table 2.1) may reflect different densities of framework Sn and extraframework SnO_2 sites, which catalyze glucose-fructose isomerization by Lewis acid-mediated and base-mediated mechanisms, respectively [50]. Isotopic tracer studies with glucose reactants deuterated at the second carbon (glucose-D_2), performed in the aqueous phase under acidic conditions (pH=5) selectively formed fructose products that retained the deuterium label at the first carbon (fructose-D1) on all Sn-Beta samples in this study (additional details and NMR spectra in Section 2.7.4), as expected from Lewis acid-mediated isomerization via intramolecular 1,2-hydride shift [51]. Therefore, the aqueous-phase glucose isomerization rates measured here reflect reactions catalyzed solely by Lewis acid sites on Sn-Beta samples prepared by different routes and that contain structural heterogeneities. Their effects on isomerization turnover rates can be interpreted only after normalization by numbers of active Lewis acidic sites, which require methods to quantify them.

2.4.2 Quantification of Lewis Acid Sites: IR Studies with Pyridine

Infrared spectra were collected with increasing pyridine coverage on three Sn-Beta samples (Sn-Beta-F-100, Sn-Beta-F-140, Sn-Beta-OH-170) and are shown in Figure 2.2. IR spectra showed two peaks centered at 1450 cm^{-1} and 1610 cm^{-1}, reflecting perturbed deformation modes of pyridine bound to Lewis acid sites [68], and a third peak centered at 1490 cm^{-1} that reflects either ring stretches of pyridine coordinated to Lewis acid sites or pyridine protonated at Brønsted acid sites [68]. IR peaks centered at 1550 cm^{-1} and 1637 cm^{-1} characteristic only of protonated pyridine [67, 68, 91]were absent in all spectra (Fig. 2.2), however, indicating that only Lewis acid sites were present on these Sn-Beta samples. Integrated areas of IR peaks for Lewis acid-bound pyridine (1450 cm^{-1}) increased linearly with pyridine coverage on these three Sn-Beta samples with a slope of 1.42 $\pm$ 0.30 cm μmol^{-1} (Fig. 2.3), which is the integrated molar extinction coefficient ($\mathcal{E}$) for this IR peak. This $\mathcal{E}$(1450 cm^{-1}, Sn) value, which is listed in Table 2.2 together with literature values for reference, has not been reported previously and is $\sim$1.5$\times$ lower than the widely-used $\mathcal{E}$(1455 cm^{-1}, Al) value reported by Emeis for pyridine bound to Lewis acidic Al sites in crystalline and amorphous aluminosilicates (2.2 $\pm$ 0.3 cm μmol^{-1}) [84]. This single $\mathcal{E}$(1455 cm^{-1}, Al) value was determined by simultaneously fitting data collected on different zeolite topologies (H-MOR, H-FAU, H-MFI), yet $\mathcal{E}$ values among these different zeolites vary widely in the literature (>10x) [84, 92]. The $\mathcal{E}$(1455 cm^{-1}, Al) value measured in our experimental apparatus on H-Y zeolite was 1.45 $\pm$ 0.10 cm μmol^{-1} (Section 2.7.5) and within the range of values reported by Emeis and by Nesterenko et al. for dealuminated H-MOR zeolites (0.89 cm μmol^{-1}) [93], suggesting that our apparatus provides reasonable estimates of $\mathcal{E}$ values. Thus, we conclude that the generally-accepted literature $\mathcal{E}$(1455 cm^{-1}, Al) value [84] does not accurately predict the number of Lewis acidic Sn sites in zeolites of the Beta topology, and use instead the $\mathcal{E}$(1450 cm^{-1}, Sn) value of 1.42 $\pm$ 0.30 cm μmol^{-1} consistently measured here among Sn-Beta zeolites prepared by different routes.

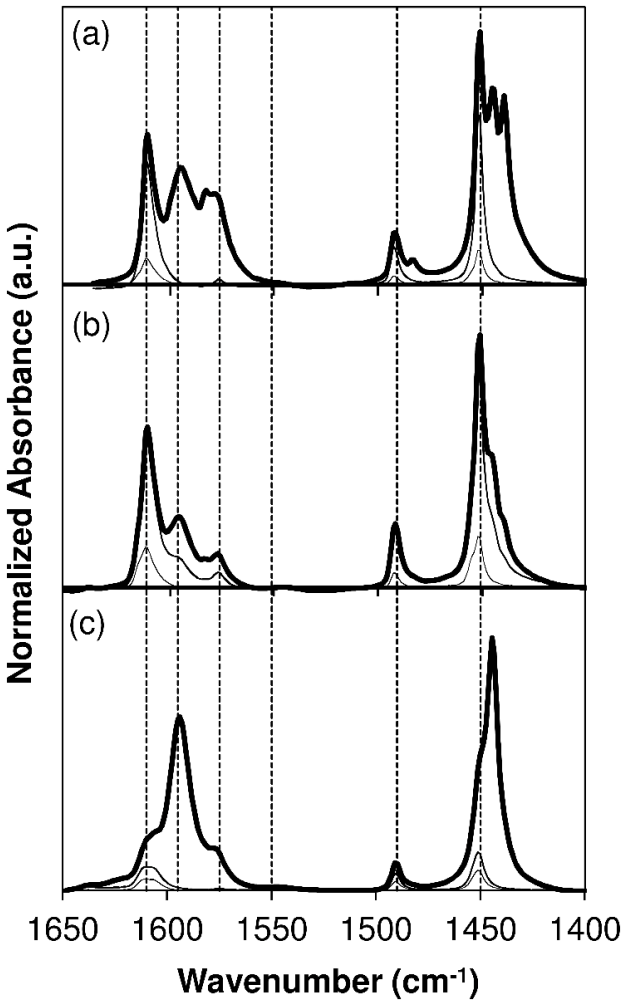

Figure 2.2: IR spectra measured at low pyridine coverage (0.09-0.20 pyridine/Sn) and saturated spectra (thick lines) for (a) Sn-Beta-F-100, (b) Sn-Beta-F-140, and (c) Sn-Beta-OH-170. Dashed reference lines shown for Lewis acid sites (1615 cm^{-1}, 1450 cm^{-1}), Lewis or Brønsted acid sites (1575 cm^{-1}, 1490 cm^{-1}), Brønsted acid sites (1550 cm^{-1}), and gas-phase pyridine (1595 cm^{-1}).

Infrared spectra were collected after saturation of all Sn-Beta samples with pyridine and subsequent evacuation at 423 K to remove gaseous and weakly-bound species (additional details and spectra in Section 2.7.6). Integrated IR peak (1450 cm^{-1}) areas, together with the $\mathcal{E}$(1450 cm^{-1}, Sn) value (Table 2.2) determined from spectra collected at sub-saturation coverages (0.04-0.66 pyridine/Sn; Fig. 2.3) that corre-

Table 2.2: Integrated molar extinction coefficients ($\mathcal{E}$) for infrared peaks for pyridine and deuterated acetonitrile adsorbed to different sites on Sn-Beta and H-Y zeolites, determined assuming equimolar titrant binding to each type of site.

Type of Site	Peak Center (cm^{-1})	$\mathcal{E}$, literature (cm μmol^{-1})	$\mathcal{E}$, this study (cm μmol^{-1})
		Pyridine	
Lewis acid, Al	1455	2.20 ± 0.30 [84]	1.45 ± 0.10
Brønsted acid, Al	1545	1.67 ± 0.25 [84]	1.95 ± 0.13
Lewis Acid, Sn	1450	n.a.*	1.42 ± 0.30
		Deuterated acetonitrile	
Open Lewis acid, Sn	2316	n.a.*	1.04 ± 0.22
Closed Lewis acid, Sn	2308	n.a.*	2.04 ± 0.43
$Sn(OH)_2$[a]	2287	n.a.*	2.13 ± 0.45
Silanol, SiOH	2275	n.a.*	0.74 ± 0.16
Lewis acid, Al	2325, 2310	3.6 ± 0.2 [81]	n.m.**
Brønsted acid, Al	2297	2.5 ± 0.1 [81]	n.m.**

[a] speculative assignment.
*n.a., not available
**n.m., not measured

spond to equimolar pyridine binding to Sn, were used to quantify the number of Lewis acidic Sn sites on each sample using Eq. 2.1 and are reported in Table 2.3. The fraction of Lewis acidic Sn sites (per total Sn) varied between 0.73-0.90 on seven of the eight Sn-Beta samples in this study (Table 2.3), but was markedly lower on Sn-Beta-F-100 (0.49, Table 2.3) that contained SnO_2 detectable in DRUV spectral band centers and edge energies (Table 2.1). The fraction of Lewis acidic Sn sites (per total Sn) was much lower, but measurable, on the SnO_2/Si-Beta control sample and Sn-xerogel (0.25 and 0.23, respectively Table 2.3), suggesting that some tetrahedrally-coordinated Sn atoms (analogous to open and closed Sn sites in Sn-Beta) at their defective and undercoordinated surfaces are able to bind pyridine. On every Sn-Beta sample, pyridine titrates only a fraction of Sn sites at saturation coverages (Table 2.3), either because of incomplete Sn incorporation within framework locations or

incomplete accessibility of pyridine to framework Sn sites. Therefore, we next obtain independent estimates of the number of Lewis acid sites in these Sn-Beta samples using smaller base titrants that coordinate with Lewis acid sites and that can be quantified in temperature-programmed desorption (TPD) experiments.

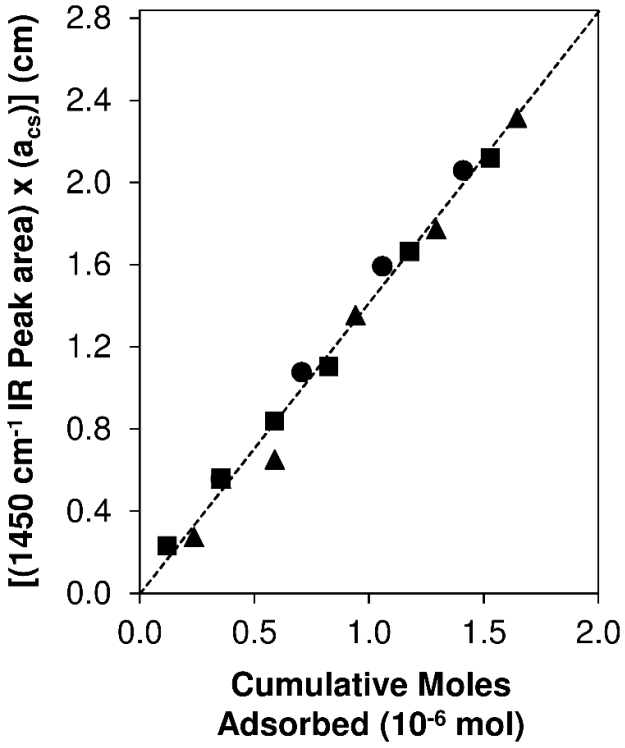

Figure 2.3: Determination of the integrated molar extinction coefficient for pyridine adsorbed on Lewis acid sites (1450 cm^{-1}) on Sn-Beta-OH-170 (squares), Sn-Beta-F-140 (triangles), Sn-Beta-F-100 (circles), from IR peak areas corresponding to pyridine/Sn coverages between 0.04 and 0.66.

Table 2.3: Fraction of Lewis acidic Sn sites (per mol Sn) on each sample counted with different base titrants. Binding stoichiometries of 1 per site for each titrant.

Sample	Pyridine[a]	NH_3[b]	NPA[c]	CD_3CN[d]	CD_3CN[d]	CD_3CN[d]	CD_3CN[d]
	Total	*Total*	*Total*	*Total*	*Open*	*Closed*	*Open/Closed*
Sn-Beta-F-100	0.49	0.42	0.44	0.49	0.13	0.36	0.35
Sn-Beta-F-105	0.88	0.61	0.62	0.88	0.35	0.54	0.64
Sn-Beta-F-110	0.81	0.73	0.99	1.00	0.35	0.65	0.53
Sn-Beta-F-140	0.90	1.06	1.04	0.78	0.21	0.58	0.35
Sn-Beta-F-170	0.75	0.69	1.24*	0.86	0.20	0.67	0.29
Sn-Beta-F-220	0.82	0.89	2.07*	0.94	0.33	0.61	0.54
Sn-Beta-OH-170	0.73	1.12	1.14*	0.73	0.46	0.28	1.64
Sn-Beta-OH-200	0.83	0.93	1.71*	0.69	0.15	0.54	0.29
SnO_2/Si-Beta	0.23	n.m.**	n.m.**	0.14	0.03	0.11	0.26
Sn-xerogel	0.25	n.m.**	n.m.**	0.10	0.04	0.06	0.58

[a]Errors are ± 20%.
[b]Errors are ± 5%.
[c]Errors are ± 10%.
[d]Errors are ± 15%.
*NPA binding on Sn-Beta-OH and Sn-Beta-F (with Si/Sn >150) overestimates Sn Lewis acid sites (Section 2.7.5).
**n.m., not measured.

2.4.3 Quantification of Lewis Acid Sites: TPD Studies with n-Propylamine and Ammonia

Reactive alkylamine titrants (e.g. n-propylamine, NPA) can distinguish between Lewis and Brønsted acid sites on a given surface because they coordinate to Lewis acid sites and desorb intact, but become protonated by Brønsted acid sites and decompose via Hoffman-type elimination reactions to form ammonia and the corresponding alkene (e.g., propene) [94–97]. The saturation of Sn-Beta samples with NPA and subsequent purging in flowing helium (338 K) led only to the desorption of NPA (TPD profiles in Section 2.7.7) and not to any ammonia or propene, consistent with the undetectable levels of Brønsted acid sites in infrared spectra collected after pyridine saturation (Section 2.4.2). The number of moles of NPA desorbed (per mol Sn) on each sample is listed in Table 2.3, and is plotted against the number of moles of pyridine adsorbed at saturation in IR experiments (per mol Sn) in Figure 2.4a for four Sn-Beta-F samples with high Sn content (Si/Sn <150). On these Sn-Beta samples, a similar number of NPA and pyridine molecules (within 1.25×) were adsorbed at saturation coverages (Table 2.3, Fig. 2.4a), suggesting that NPA also binds to Sn with equimolar stoichiometry. On Sn-Beta samples with low Sn content (Sn-Beta-F-170, Sn-Beta-F-220) or with high defect density (Sn-Beta-OH-170, Sn-Beta-OH-200), however, a larger number (by 1.6-2.5x, Table 2.3) of NPA desorbed during TPD than the number of pyridine adsorbed at saturation (Table 2.3), reflecting the retention of NPA at residual defect silanol sites under the conditions studied here (control experiments performed on dealuminated Beta zeolites in Section 2.7.7).

In contrast with reactive alkylamines, ammonia titrants desorb intact from both Lewis and Brønsted acid sites present on a given surface. The treatment of NH_3-saturated samples in flowing dry helium removes physisorbed NH_3 species and enables the concurrent measurement of NH_3 bound to Lewis and Brønsted sites during a TPD experiment, while treatment of NH_3-saturated samples in flowing wet helium has been shown to also desorb NH_3 bound to Lewis acid sites (Al [98]; Cu [99, 100]) to enable quantifying NH_4^+ species at Brønsted sites. The number of NH_3 bound to Lewis

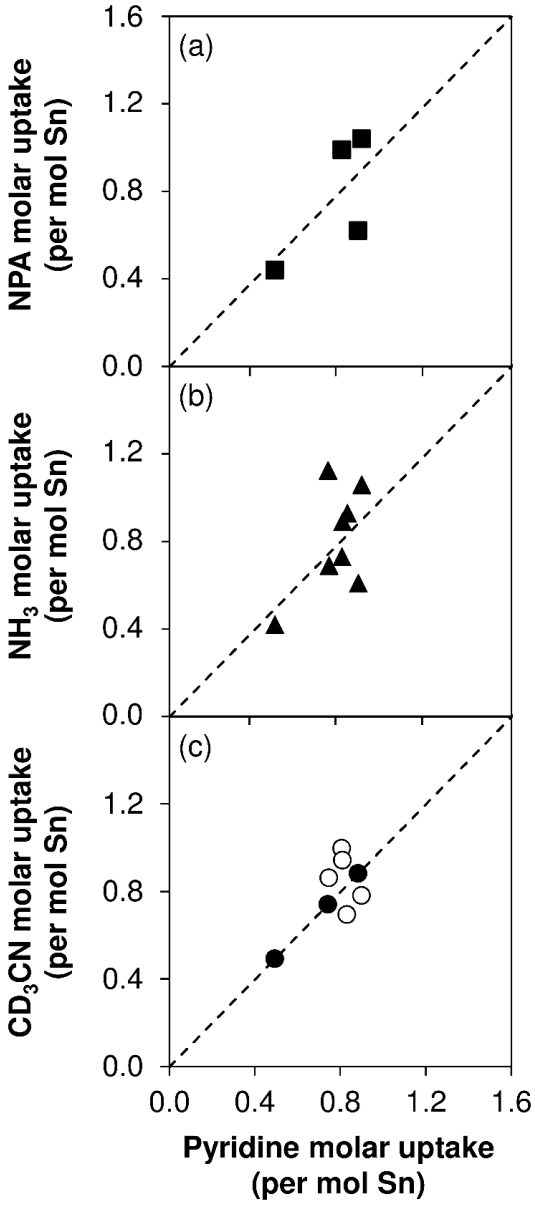

Figure 2.4: Titrant molar uptakes (per Sn) compared to pyridine molar uptakes (per Sn) at saturation of Sn-Beta samples with (a) n-propylamine (NPA, squares), (b) ammonia (NH_3, triangles), and (c) CD_3CN (closed circles were included and open circles were not included in fitting of $\mathcal{E}$ values). Parity lines shown as dashed lines. NPA titration data not shown for samples denoted with an asterisk in Table 32.3, for which TPD quantification includes binding to residual defect sites.

acid sites on solid acids can be estimated from the difference between these two TPD methods, but on Sn-Beta zeolites devoid of protons were estimated after purging NH_3-saturated samples only in dry helium at 331 K (NH_3 TPD profiles in Section 2.7.8). The number of moles of NH_3 desorbed (per mol Sn) in a subsequent TPD is listed in Table 2.3 for each sample and was identical, within experimental error, to the number of Lewis acidic Sn sites titrated by pyridine on all samples except for Sn-Beta-F-105 and Sn-Beta-OH-170 (Table 2.3, Fig. 2.4b). These data suggest that NH_3 binds to both open and closed Sn sites with equimolar stoichiometry, consistent with ^{119}Sn MAS NMR spectra of NH_3 -saturated Sn-Beta samples that show resonances attributed to penta-coordinated Sn (between -500 and -600 ppm) [32, 101]. Control experiments performed to saturate dealuminated Beta zeolites with NH_3 and purge in dry helium did not evolve any NHs_3 in a subsequent TPD (details in Section 2.7.8), in contrast to analogous control experiments performed with NPA. Thus, we conclude that the NPA and NH_3 TPD techniques developed here can be used to accurately quantify the number of Lewis acidic Sn sites on Sn-Beta-F samples with high Sn contents (Si/Sn <150), but that NPA TPD overestimates the number of Lewis acid sites on samples containing dilute amounts of Sn (Si/Sn >170) or high defect densities (Sn-Beta-OH).

2.4.4 Quantification of Open and Closed Lewis Acid Sites: IR Studies with Deuterated Acetonitrile

Infrared spectra were collected with increasing CD_3CN coverage (303 K) and are shown for one representative Sn-Beta sample (Sn-Beta-F-105) in Figure 2.5a. Each IR spectrum was deconvoluted into principal component peaks (Fig. 2.1, Fig. 2.5b) centered at 2316 cm^{-1}, 2308 cm^{-1}, 2287 cm^{-1}, 2275 cm^{-1} and 2265 cm^{-1} (additional details in Section 2.7.9), and the evolution of IR peak areas with increasing CD_3CN coverage is shown in Figure 2.6. Initial CD_3CN doses led to the appearance of the 2316 cm^{-1} peak, with a shoulder at 2308 cm^{-1} and even smaller and broader peaks at 2287 cm^{-1} and 2275 cm^{-1}. Increasing CD_3CN coverages caused the 2316 cm^{-1} peak to saturate, while the 2308 cm^{-1}, 2287 cm^{-1}, and 2275 cm^{-1} peaks continued to increase in area. At a coverage corresponding to $CD_3CN/Sn = 1$, the 2316 cm^{-1} and 2308 cm^{-1} peaks had already reached saturation, while the 2287 cm^{-1} and 2275 cm^{-1} peaks continued to increase in area. Finally, the 2265 cm^{-1} peak for gas-phase CD_3CN appeared after saturation of all adsorption sites on the sample [81].

The IR peaks at ~2316 cm^{-1} and ~2308 cm^{-1} reflect CD_3CN bound to open and closed Lewis acidic Sn sites, respectively [30, 32], and have been correlated to ^{119}Sn MAS NMR resonances at -423 ppm (open sites) and -443 ppm (closed sites) in dehydrated Sn-Beta (vacuum, 393 K) [32]. The ratio of open-to-closed site peak areas systematically decreases with increasing CD_3CN coverage (Fig. 2.7), indicating that CD_3CN binds preferentially to open Sn sites, as also reported previously [30,32,33,63]. Open and closed Sn sites become saturated at a sub-stoichiometric CD_3CN/Sn coverage of 0.80 ($4.14*10^{-6}$ mol CD_3CN, Fig. 2.6), which is similar to the number of total Sn sites titrated by pyridine (0.87, Table 2.3) and provides evidence that CD_3CN also binds to Lewis acidic Sn sites with equimolar stoichiometry. We *speculate* that the IR peak at ~2287 cm^{-1}, which appears prominently in IR spectra of Sn-xerogel samples at low CD_3CN coverages but is not prominent at any CD_3CN coverage for Si-xerogel or SnO_2/Si-Beta samples (spectra in Section 2.7.9), reflects CD_3CN interacting with Sn of highly-defective coordination (e.g., $(SiO)_2Sn(OH)_2$). The existence

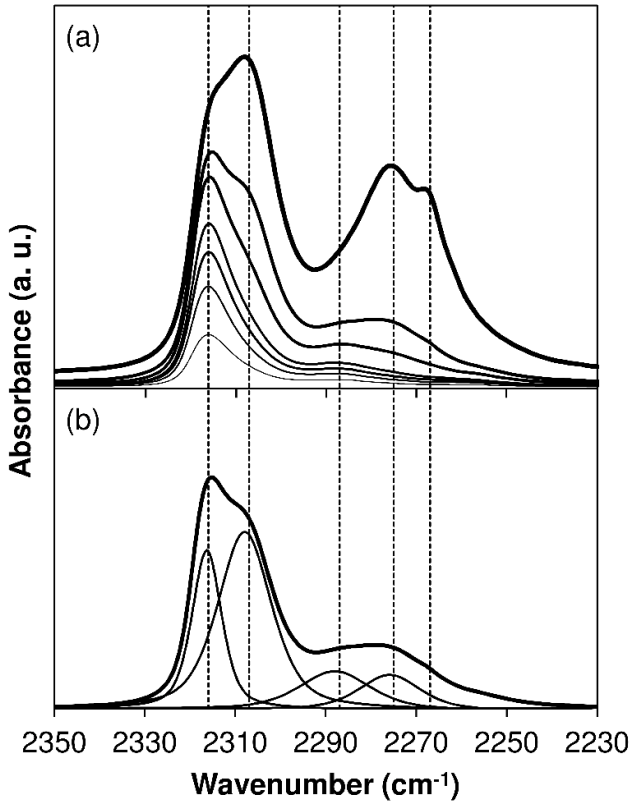

Figure 2.5: FTIR difference spectra of Sn-Beta-F-105 (relative to the vacant surface) (a) with increasing CD_3CN increasing coverage and (b) at a coverage of 0.65 CD_3CN/Sn with deconvolution into component peaks. Dashed reference lines shown for open Sn sites (2316 cm^{-1}), closed Sn sites (2308 cm^{-1}), $(SiO)_2Sn(OH)_2$ sites (*speculative assignment*, 2287 cm^{-1}), silanol groups (2275 cm^{-1}), and gas-phase CD_3CN (2265 cm^{-1}).

of doubly-hydroxylated Sn sites has been proposed on Sn-Beta using ^{119}Sn CPMAS NMR [58], and on grafted Sn-SiO_2 using *in situ* DRIFTS [102]. The IR peak centered at ∼2275 cm^{-1} reflects CD_3CN bound to silanol groups [80,81], and increases linearly in area with concomitant decreases in silanol OH stretching peak areas (∼3740 cm^{-1}) and concomitant increases in perturbed OH stretching peak areas (∼3300-3600 cm^{-1}) (Section 2.7.9) [103].

Infrared spectra of Sn-Beta samples after saturation with CD_3CN and subsequent evacuation at 303 K retained four peaks in the C≡N stretching region (2316, 2308,

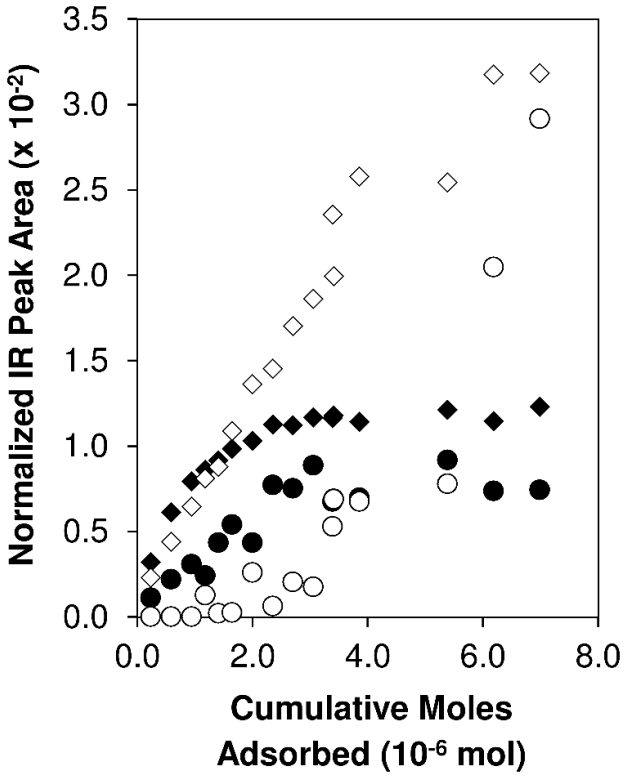

Figure 2.6: Evolution of IR peak areas for 2316 cm^{-1} (closed diamonds), 2308 cm^{-1} (open diamonds), 2287 cm^{-1} (closed circles), and 2275 cm^{-1} (open circles) peaks with increasing CD_3CN coverage on Sn-Beta-F-105.

2287, 2275 cm^{-1}, Fig. 2.5b), whose areas were determined by deconvolution and were present in different proportions for each sample (Table 2.9).

Integrated molar extinction coefficients were first determined for the 2316 cm^{-1} and 2308 cm^{-1} IR peaks from spectra of three Sn-Beta samples (Sn-Beta-F-100, Sn-Beta-F-105, Sn-Beta-OH-170), by non-linear least squares regression to minimize the error between the total number of Lewis acid sites counted by CD_3CN and pyridine (additional details in Section 2.7.9). These $\mathcal{E}$(2316 cm^{-1}, Sn) and $\mathcal{E}$(2308 cm^{-1}, Sn) values were determined to be 1.04±0.22 and 2.04±0.43 cm μmol^{-1} (Table 2.2), respectively. Both CD_3CN and pyridine estimated the same number of Lewis acid sites (to within 1.25×) on five other Sn-Beta samples that were not used in estimating $\mathcal{E}$ values for CD_3CN (Sn-Beta-F-110, Sn-Beta-F-140, Sn-Beta-F-170, Sn-Beta-F-220,

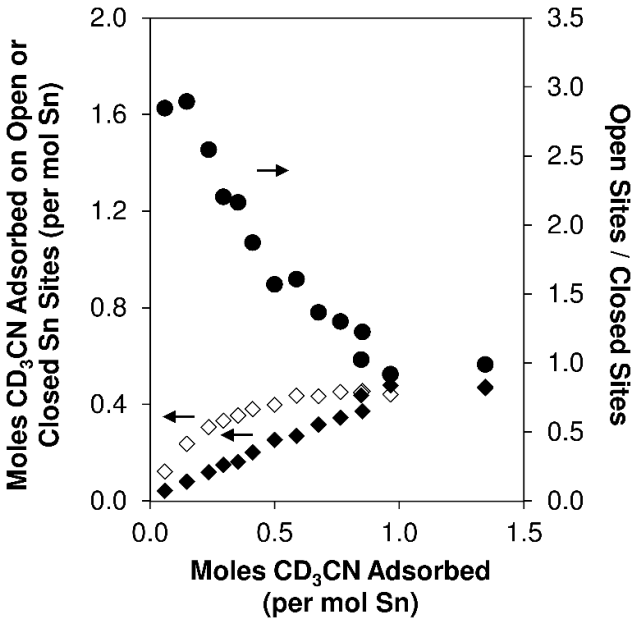

Figure 2.7: Moles of CD_3CN adsorbed on open Sn sites (open diamonds) and closed Sn sites (closed diamonds) on Sn-Beta-F-105, together with the ratio of open-to-closed Sn sites titrated (closed circles), as a function of CD_3CN coverage.

and Sn-Beta-OH-200), demonstrating that these $\mathcal{E}$ values can accurately quantify Lewis acid sites on Sn-Beta zeolites. Next, $\mathcal{E}$ values for the 2287 cm^{-1} and 2275 cm^{-1} peaks were estimated from non-linear least squares regression of IR peak areas with increasing CD_3CN coverage on Sn-Beta-OH-170 (additional details in Section 2.7.9), which was chosen because it showed the largest 2275 cm^{-1} peak area of any Sn-Beta sample. These $\mathcal{E}$(2287 cm^{-1}, Sn) and $\mathcal{E}$(2275 cm^{-1}) values were determined to be 2.13±0.45 and 0.74±0.16 cm μmol^{-1} (Table 2.2), respectively. Increasing CD_3CN coverage on dealuminated Beta led only to the appearance the 2275 cm^{-1} peak, whose integrated areas were used to independently estimate an $\mathcal{E}$(2275 cm^{-1}) value of 0.89±0.09 cm μmol^{-1} (details in Section 2.7.9), similar to the $\mathcal{E}$(2275 cm^{-1}) value determined from least-squares regression of IR data collected on Sn-Beta-OH-170.

The numbers of open and closed Lewis acidic Sn sites on each Sn-Beta sample, determined from IR spectra collected after CD_3CN saturation (303 K) and integrated molar extinction coefficients (Table 2.2), are listed in Table 2.3 and were calculated

using Eq. 2.1. The total number of Lewis acid sites quantified by CD_3CN (per mol Sn) is plotted against the number of sites quantified by pyridine (per mol Sn) in Figure 2.4c for each of the Sn-Beta-F and Sn-Beta-OH samples studied here. The total number of Lewis acid sites (open and closed) counted by CD_3CN was identical, within experimental error, to the number of Lewis acid sites counted by pyridine titration in IR experiments on each of the Sn-Beta samples (Table 2.3, Fig. 2.4c), providing evidence that CD_3CN also binds with equimolar stoichiometry to each Sn site and that either pyridine or CD_3CN can accurately quantify the total number of Lewis acid sites in IR experiments. Among the Sn-Beta samples in this study, the fraction of Sn present as Lewis acid sites was almost always below unity (0.49-1.00, Table 2.3), and the ratio of open-to-closed Lewis acid sites varied over a wide range (0.29-1.64, Table 2.3). The consistent estimates of Lewis acidic Sn sites determined by mfore than one base titrant provides further evidence that the integrated molar extinction coefficients in Table 2 apply generally to Sn-Beta zeolites prepared via different methods, in turn, enabling quantification of open (and closed) Sn sites to normalize turnover rates for glucose-fructose isomerization, as we discuss next.

2.4.5 Glucose Isomerization Rate Constants on Hydrophobic and Hydrophilic Sn-Beta Zeolites

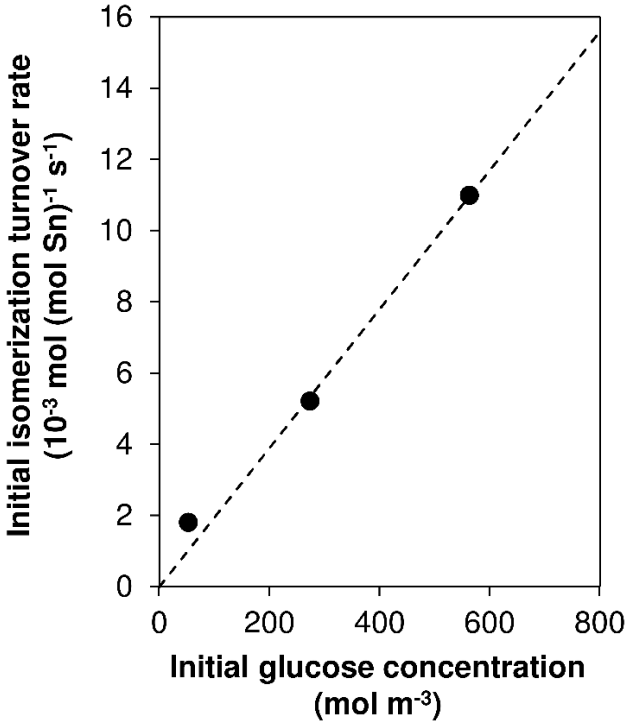

Figure 2.8: Dependence of initial glucose-fructose isomerization turnover rate (per total Sn, 373 K) for Sn-Beta-F-220 on the initial aqueous-phase glucose concentration (1-10% (w/w)).

Aqueous-phase glucose-fructose isomerization on Lewis acid sites proceeds via quasi-equilibrated adsorption and ring-opening of glucose to form intermediates that coordinate to Sn sites through oxygen atoms at the C1 (aldehyde) and C2 (deprotonated OH) positions [34], subsequent kinetically-relevant intramolecular 1,2-hydride shift to form ring-opened fructose intermediates [51], and quasi-equilibrated ring-closing and desorption of fructose (Fig. 2.9). Initial isomerization turnover rates are first-order in glucose concentration (0-10% (w/w), 373 K, Figure 2.8) with measured H/D kinetic isotope values of 2.0-2.4 (373 K) for glucose deuterated at the second carbon, as expected for kinetically-relevant intramolecular 1,2-hydride shift in the

absence of internal mass transfer limitations (details in Section 2.7.10) [35]. The first-order dependence of isomerization rates on glucose concentration is consistent with dilute glucose coverages and with two coordinated water molecules as the most abundant surface intermediate (MASI) during reaction in liquid water, as expected from the saturation of framework Sn sites with water even in ambient atmosphere to give ^{119}Sn MAS NMR resonances [34] and UV-Vis spectral features for octahedrally-coordinated Sn (Section 2.4.1). These quasi-equilibrated reactions, elementary steps and mechanistic assumptions give a turnover rate equation that accurately describes aqueous-phase glucose-fructose isomerization on Sn-Beta zeolites (mechanistic details and derivation of rate expression in Section 2.7.10) [35]:

$$r_{isom} = \alpha \frac{K_1 k_2}{K_4 K_5} C_G = k_{isom} C_G \tag{2.2}$$

In this turnover rate equation, K_1 is the adsorption equilibrium constant relating aqueous-phase glucose and ring-opened glucose intermediates bound to Sn sites, k_2 is the rate constant for the intramolecular 1,2-hydride shift to form fructose, K_4 and K_5 are adsorption equilibrium constants for the sequential adsorption of two water molecules at Sn sites, C_G is the aqueous-phase glucose concentration, α is a constant that contains the product of activity coefficients for reactants and intermediates in the mechanism (details in Section 2.7.10), and k_{isom} is the effective first-order isomerization rate constant. The rate and equilibrium constants that comprise k_{isom} can be decomposed to show that measured first-order isomerization rate constants reflect the difference in free energy between the kinetically-relevant transition state (bound glucose-fructose isomerization transition states ($\Delta G_{\ddagger,2*}{}^o$) and two aqueous-phase water molecules ($2\Delta G_W{}^o$)) and the most abundant surface intermediate (two bound water molecules ($\Delta G_{2W*}{}^o$) and aqueous-phase glucose ($\Delta G_G{}^o$); details in Section 2.7.10) [35]:

$$k_{isom} = \alpha \frac{K_1 k_2}{K_4 K_5} = \alpha \frac{k_B T}{h} e^{(-(\Delta G^o_{\ddagger,2*} + 2\Delta G^o_W) - (\Delta G^o_G + \Delta G^o_{2W*}))/RT)} \tag{2.3}$$

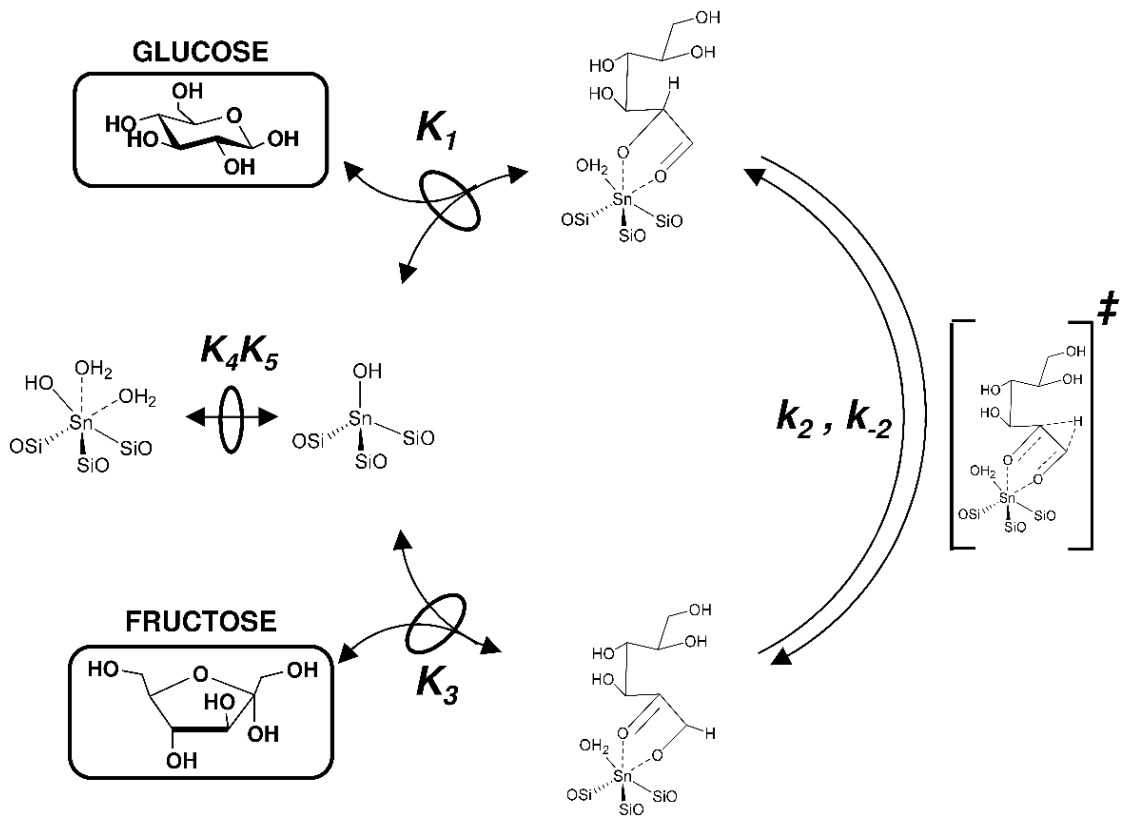

Figure 2.9: Plausible reaction mechanism for glucose-fructose isomerization on open Sn sites in Sn-Beta involving kinetically-relevant 1,2-intramolecular hydride shift (Step 2). For clarity, kinetically-irrelevant steps are lumped as quasi-equilibrated reactions (Steps 1, 3-5).

Isomerization turnover rates (Eq. 2.2) are rigorously normalized by the number of active Sn sites, demonstrated elsewhere to be open Sn sites based on selective NH_3 pre-poisoning of open sites in Sn-Beta before glucose isomerization catalysis [32]. The number of Sn sites active for glucose isomerization was independently estimated here on two different Sn-Beta-F samples (Sn-Beta-F-110, Sn-Beta-F-170) from pyridine pre-poisoning studies, in which samples were pressed into self-supporting wafers and sealed in the IR cell, titrated with different amounts of pyridine (quantified from IR spectra and the $\mathcal{E}$ values in Table 2.2), removed from the IR cell, and ground into a powder prior to measurement of isomerization rates. Initial isomerization

turnover rates (per total Sn, 373 K) decreased with increasing pyridine coverage (per total Sn) for Sn-Beta-F-110 and Sn-Beta-F-170 (Fig. 2.10), but not because of occlusion of intracrystalline void spaces or of pore openings at external crystallite surfaces, or because of restricted diffusion of glucose reactants within intracrystalline voids (details in Section 2.7.10). Linear extrapolation of initial isomerization rates with increasing pyridine coverage (Fig. 2.10) predicts full suppression of reactivity at pyridine uptakes of 0.49±0.10 and 0.15±0.03 (per total Sn) for Sn-Beta-F-110 and Sn-Beta-F-170, respectively, which are similar to their fractions of open Sn sites counted *ex situ* by CD_3CN (0.35±0.07 and 0.20±0.04, respectively). In contrast, pyridine uptakes required to fully suppress rates on Sn-Beta-F-110 and Sn-Beta-F-170 are not equivalent to their fractions of closed Sn sites (0.63±0.13 and 0.67±0.14, respectively), although closed Sn sites may be responsible for the residual isomerization reactivity observed at pyridine uptakes higher than predicted to fully suppress reactivity (Fig. 2.10). The pyridine uptakes required to completely suppress the rates were also not equal to the value of unity expected if residual Sn sites on pyridine-titrated samples were equally reactive or undergo quasi-equilibrated structural changes during initial reaction times. These findings also suggest that pyridine preferentially titrates open Sn sites either in vacuum (423 K) or upon exposure to liquid water (373 K) and that pyridine desorption from Sn sites in Sn-Beta-F appears irreversible on the timescale of initial glucose isomerization rate measurements (373 K). Thus, we conclude that *initial* isomerization turnover rates are rigorously normalized by the number of open Sn sites present *initially* on Sn-Beta zeolites, which can be quantified from *ex situ* CD_3CN IR experiments (Table 2.3). Turnover rates estimated at longer batch reaction times, or at steady-state in a flow reactor, may require different normalization to the extent that framework Sn sites change structure or coordination during exposure to liquid water at elevated temperatures (373 K) [104, 105].

Values of $k_i som$ (per open Sn, 373 K) are listed in Table 2.10 for each Sn-Beta sample in this study, and are plotted against Sn content in Figure 2.11. Values of $k_i som$ were higher by ∼50x (on average) on the six low-defect Sn-Beta-F samples

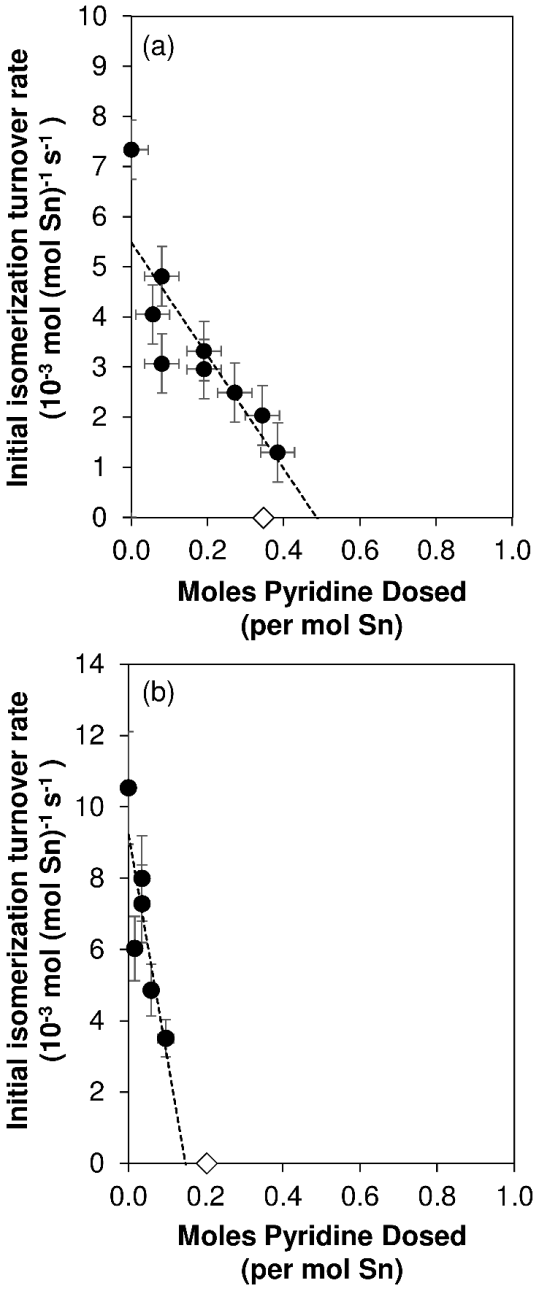

Figure 2.10: Dependence of initial glucose-fructose isomerization turnover rates (per total Sn, 373 K, 1% (w/w) glucose) on pyridine coverage from titration before reaction on (a) Sn-Beta-F-110 and (b) Sn-Beta-F-170. The fraction of Sn open sites counted *ex situ* by CD_3CN are shown as open diamonds along the x-axes.

synthesized in fluoride media than on the two highly-defective Sn-Beta-OH samples prepared by grafting of Sn atoms in dealuminated Beta zeolites (Fig. 2.11). Values of $k_i som$ reflect free energy differences between glucose isomerization transition states and two water molecules coordinated to active sites (Eq. 2.3), and would decrease as adsorption equilibrium constants for coordinated water molecules (K_4, K_5) become larger (Eq. 2.2), as proposed for hydrophilic zeolites with higher densities of defect silanol groups that hydrogen bond with water bound at framework metal sites [106]. This mechanistic interpretation suggests that $k_i som$ values are larger on hydrophobic Sn-Beta-F zeolites, *in part*, because of weaker kinetic inhibition of Sn sites by coordinated water molecules when such sites are confined within low-defect voids. These findings extend previous reports of $k_i som$ values (per *total* Ti, 373 K) that were 10-30× higher on hydrophobic than on hydrophilic Ti-Beta zeolites [35], and demonstrate that such differences persist after precise normalization by the number of active sites (open Sn) in Sn-Beta zeolites. We also note that the form of the kinetic rate equation in Eq. 2.2, which is derived with the assumption of sequential, quasi-equilibrated adsorption of two water molecules, can instead be treated as one quasi-equilibrated step ($K'=K_4*K_5$) [35] and is functionally equivalent to an equation derived for the case of only one water molecule as the MASI, as expected if framework Sn centers were penta-coordinated instead of tetrahedrally-coordinated [107].

Values of $k_i som$ (373 K), after normalization by open Sn sites, varied among Sn-Beta-F samples of different crystallization time and Sn content by ∼3x (Table 2.10), reflecting residual heterogeneities in Sn active site structure or coordination or in the surrounding environments that influence free energy differences between glucose-fructose isomerization transition states and two water molecules bound at Sn centers (Eq. 2.3). Total water uptakes measured from H_2O adsorption isotherms (293 K) at a reduced pressure of 0.2, which corresponds to complete micropore filling with cyclohexane and has been used elsewhere as a descriptor of the hydrophobic properties of zeolites [83], differed by 3.5× among these Sn-Beta-F samples (Table 2.1). Although this water uptake reflects an integrated adsorption measurement on multiple binding

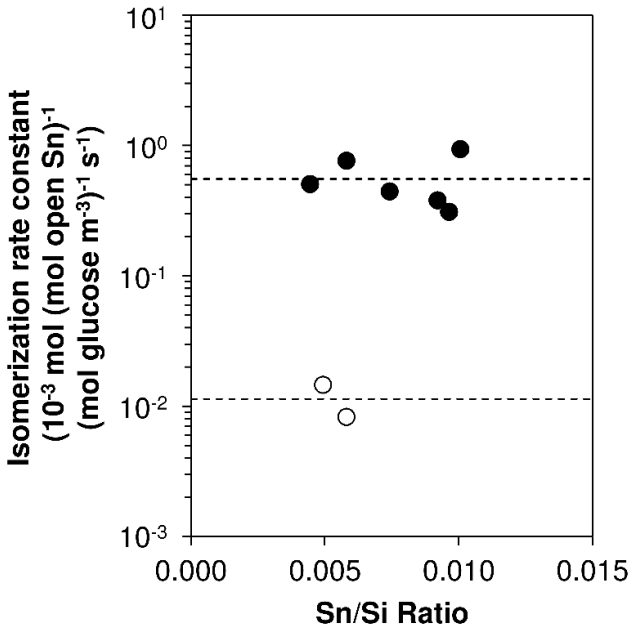

Figure 2.11: First-order glucose-fructose isomerization rate constant (per open Sn site, 373 K) in water for hydrophobic Sn-Beta-F (closed circle) and hydrophilic Sn-Beta-OH (open circle) samples as a function of Sn/Si ratio. Dashed lines indicate the averaged turnover rate within each series.

sites, including framework Sn centers and defect silanol groups at intracrystalline and extracrystalline locations, the residual water uptake after accounting for binding on Sn (2 H_2O/Sn) was directly proportional to the number of silanol groups titrated by CD_3CN on the Sn-Beta-F samples studied here (Fig. 2.49, Section 2.7.10). Values of k_{isom} (per open Sn, 373 K) on Sn-Beta-F samples generally decreased with increasing silanol content (Fig. 2.50, Section 2.7.10), albeit with residual scatter in the correlation that seems reasonable because k_{isom} values may only sense differences in the strength of water binding in the vicinity of active Sn sites. These findings and interpretations suggest that methods to insert Sn atoms into vacancy defects of Beta zeolites may benefit from further treatments to remove residual silanol defects to increase their hydrophobicity and, in turn, turnover rates for aqueous-phase glucose isomerization.

2.5 Conclusions

Titration and quantification procedures were developed for four different Lewis bases, two involving concurrent collection of infrared spectra (pyridine, deuterated acetonitrile) and two involving subsequent temperature programmed desorption (ammonia, n-propylamine), to quantify the number of Lewis acid sites in Sn-Beta zeolites prepared by hydrothermal and post-synthetic routes. On crystalline zeolites, integrated molar extinction coefficients ($\mathcal{E}$) for IR peaks reflecting pyridine bound to Lewis acidic Sn sites (1450 cm^{-1}) and CD_3CN bound to open (2316 cm^{-1}) and closed (2308 cm^{-1}) Sn sites were different from $\mathcal{E}$ values for Lewis acidic Al sites. $\mathcal{E}$ values for Al sites are available in the literature, but quantify Sn sites imprecisely from IR spectra of Sn-Beta samples at saturation pyridine or CD_3CN coverages, while the $\mathcal{E}$ values on Sn sites reported here estimate similar numbers of Lewis acid sites on the eight Sn-Beta samples in this study. Two additional TPD methods were also developed to selectively titrate and quantify Lewis acid sites in Sn-Beta zeolites with ammonia or n-propylamine, which are titrants used often to quantify Brønsted acid sites but seldom to quantify Lewis acid sites in solid acids.

Open Sn sites, which are partially hydrolyzed framework Sn centers with an OH ligand (Sn-OH) proximal to a silanol group (Si-OH), have been implicated as the dominant active site in Sn-Beta for glucose-fructose isomerization via intramolecular 1,2-hydride shift [32]. On two Sn-Beta samples, initial aqueous-phase glucose-fructose isomerization turnover rates (per total Sn, 373 K) decreased linearly with the number of pyridine titrants adsorbed prior to reaction, and become suppressed at pyridine uptakes similar to the number of open Sn sites counted *ex situ* by CD_3CN (303 K). These findings provide further evidence that open Sn sites are the dominant active site for glucose-fructose isomerization in Sn-Beta, and suggest that initial isomerization turnover rates should be normalized by the number of open Sn sites counted via CD_3CN titration, prior to interpretation of turnover rate differences among Sn-Beta zeolites of different preparation or treatment history.

Apparent first-order aqueous-phase isomerization rate constants (per open Sn site, 373 K) are ∼50x higher, on average, on hydrophobic Sn-Beta zeolites crystallized in fluoride media (Sn-Beta-F) than on hydrophilic Sn-Beta zeolites (Sn-Beta-OH) prepared by post-synthetic insertion of Sn atoms into framework vacancy defects. These data are consistent with the stronger kinetic inhibition of Lewis acidic Sn sites confined within hydrophilic than within hydrophobic voids by coordinated water molecules, which are most abundant surface intermediates during isomerization in liquid water [35]. We expect that the titration methods developed here can be adapted to quantify Lewis sites on silicates containing other tetravalent Lewis acidic heteroatoms (e.g., Ti^{4+}, Zr^{4+}, Hf^{4+}). The approach described herein, which quantifies active Lewis acid sites *ex situ* to normalize initial glucose-fructose isomerization turnover rates, provides the conceptual basis to rigorously assess how different synthetic and post-synthetic treatments of Sn-zeolites influence their density of open and closed Sn sites and, in turn, their catalytic behavior at initial reaction times. We expect that these methods can also be adapted to probe structural changes to framework Sn sites that occur during reaction or treatment in liquid media to cause different transient and steady-state catalytic behavior [58].

2.6 Acknowledgements

We acknowledge the financial support provided by the Purdue Process Safety and Assurance Center (P2SAC), a 3M Non-Tenured Faculty Grant, and a Kirk Endowment Exploratory Research Recharge Grant. We thank Jason Bates for helpful discussions and comments on this manuscript and Viktor Cybulskis for developing the IR cell design. We also thank Dr. Yury Zvinevich for assistance in constructing a custom-built active site titration unit, Cindy Tavera for experimental assistance with sample preparation, Jacklyn Hall for experimental assistance with isotopic tracer and liquid NMR experiments, and John Degenstein and Dr. Mike Detwiler for assistance with parameter estimation and spectral peak deconvolution. Finally, we thank Profs. John Morgan and Julie Liu for access to the lyophilizer, and Dr. John Harwood (Purdue Interdepartmental NMR Facility) for assistance with NMR.

This chapter was published in the Journal of Catalysis and is reproduced in this thesis with permission.

2.7 Supporting Information

2.7.1 X-ray Diffractograms of Stannosilicate Samples.

See Figure 2.12.

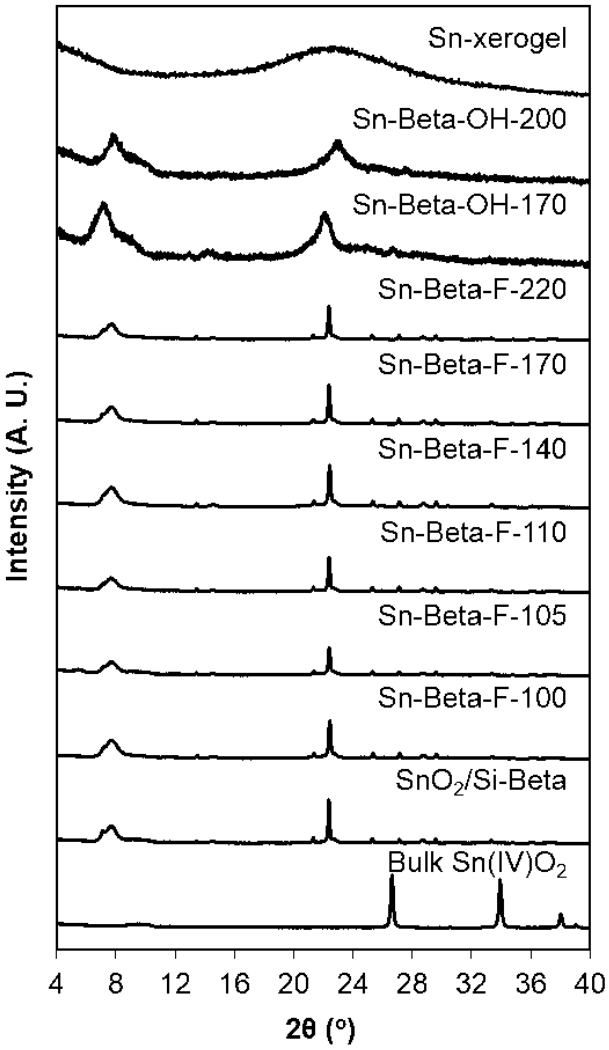

Figure 2.12: Powder XRD patterns of the stannosilicate samples in this study. Patterns for Sn-Beta-OH-170 and Sn-Beta-OH-200 multiplied by 10×, and Sn-xerogel multiplied by 5×, for clarity.

2.7.2 N_2 and H_2O Adsorption Isotherms of Zeolite Samples.

N2 adsorption isotherms (77 K) are shown for all Sn-Beta samples, SnO_2/Si-Beta, and Sn-xerogel in Figure S.2. On each sample, the micropore volume was determined from a semi-log derivative analysis of the N_2 isotherms, by plotting $\delta(V_{ads}/g)/\delta(\log(P/P_0)$ vs. log (P/P_0) to identify the micropore filling transition (first maximum) and then the end of micropore filling (subsequent minimum) [108, 109]. The volume of adsorbed N_2 (at STP) at the end of micropore filling was converted to the volume of adsorbed liquid using the liquid N_2 molar density (0.029 mol cm^{-3}). This method gave the micropore volumes listed in Table 2.1.

H_2O adsorption isotherms (293 K) are shown for Sn-Beta-F samples (Fig. 2.14) and for Sn-Beta-OH, SnO_2/Si-Beta, and Sn-xerogel samples (Fig. 2.15). On each sample, the amount of water adsorbed at a relative pressure (P/P_0) of 0.2 was used to assess hydrophobicity, as chosen originally by Chen [83] because cyclohexane (298 K) fills the pores of hydrophobic zeolites at $P/P_0 = 0.2$. The volume of adsorbed H_2O (at STP) at $P/P_0 = 0.2$ was converted to the volume of adsorbed liquid using the liquid H_2O molar density (0.055 mol cm^{-3}). This method gave the H_2O uptake values listed in Table 2.1.

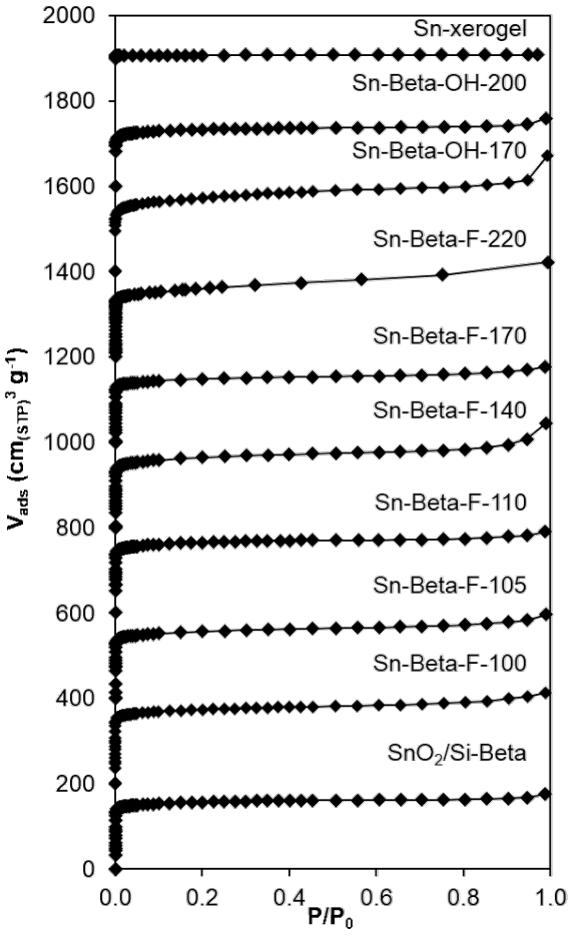

Figure 2.13: N_2 adsorption isotherms (77 K) for all samples used in this study. Isotherms offset by 200 cm^3 g^{-1} for clarity.

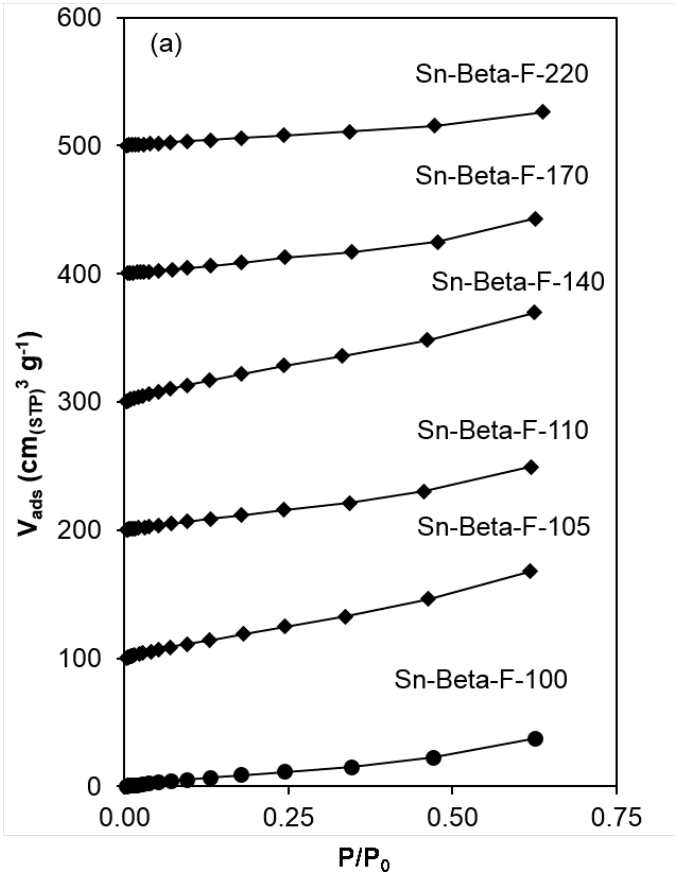

Figure 2.14: H_2O adsorption isotherms (293 K) for Sn-Beta-F samples used in this study. Isotherms offset by 100 cm^3 g^{-1} for clarity.

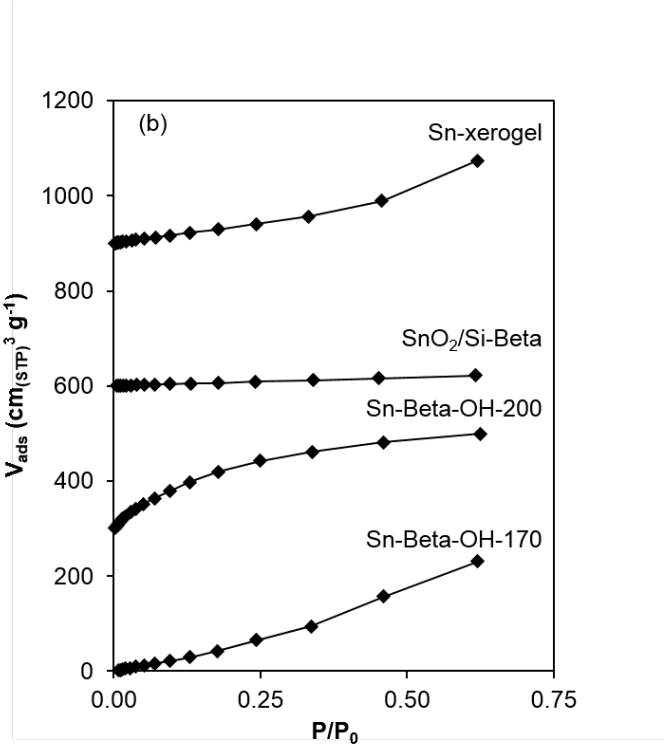

Figure 2.15: H_2O adsorption isotherms (293 K) for Sn-Beta-OH samples, SnO_2/Si-Beta-F, and Sn-xerogel used in this study. Isotherms offset by 300 cm^3 g^{-1} for clarity.

2.7.3 Diffuse-Reflectance UV-Visible Spectra of Zeolite Samples.

DRUV spectra under ambient conditions, dehydrated conditions and rehydrated conditions (see Section 2.3.2) are shown for SnO_2/Si-Beta, Sn-Beta-OH-200, and Sn-Beta-F-170 in Fig. 2.16. All samples contain DRUV bands with maxima at ∼240 nm under ambient conditions, characteristic of Sn in octahedral coordination [50, 78]. After dehydration treatments, DRUV bands for Sn-Beta-OH-200 and Sn-Beta-F-170 shift to ∼210 nm characteristic of tetrahedral Sn [37, 86], while DRUV bands for the SnO_2/Si-Beta do not change because octahedrally-coordinated Sn atoms in SnO_2 do not change coordination upon heating. Although under-coordinated Sn atoms near SnO_2 surfaces may lose coordinated water upon dehydration, the fraction of such Sn atoms appears small and noticeable changes to DRUV spectra after dehydration of SnO_2/Si-Beta are not observed.

DRUV spectra of all Sn-Beta-F samples, and for Sn-Beta-OH, SnO_2/Si-Beta, and Sn-xerogel after dehydration treatments at 523 K are shown in Figures 2.17 and 2.18, respectively. DRUV bands for Sn-Beta-F-100, Sn-Beta-F-105, and Sn-xerogel were centered at ∼240 nm upon dehydration. DRUV bands for Sn-Beta-F-110, Sn-Beta-F-140, and Sn-Beta-F-170 were centered at ∼210 nm, with a noticeable shoulder at ∼255 nm. For each of these samples, the lack of a complete shift or remaining shoulder in DRUV spectra upon dehydration likely reflects some non-framework Sn species on these samples. DRUV bands for Sn-Beta-OH-170 at ∼210 nm (ambient) may shift below 190 nm upon dehydration, while the shoulder present at ∼250 nm remains after the thermal treatment, likely reflecting SnO_2 nanoparticles larger than those that give rise to bands at ∼230 nm due to quantum confinement effects [87–90].

Tauc plots are shown for all Sn-Beta-F samples, and for Sn-Beta-OH, SnO_2/Si-Beta, and Sn-xerogel in Figures 2.19 and 2.20, respectively. Linear regions in the low energy regime (<∼5 eV) of Tauc plots were extrapolated to determine the x-intercept values, which correspond to the band gap energies for the Sn species [110–112], which

can be correlated to SnO_2 particle size [87–90]. These values are summarized in Table 2.4.

Table 2.4: Edge energies for all samples determined from x-intercepts of linear portions of Tauc plots (Figs. 2.19 and 2.20) DRUV band centers at maximum F(R) intensity are reported for spectra collected after dehydration treatments (Figs. 2.17 and 2.18), and parenthetical values are for second band observed in some DRUV spectra.

Sample	Ambient (eV)	Dehydrated (eV)	Rehydrated (eV)	Band Maximum (nm)
Sn-Beta-F-100	4.20	4.09	4.19	244
Sn-Beta-F-110	4.34	4.26	4.34	223
Sn-Beta-F-170	4.27	4.20	4.20	207
Sn-Beta-F-220	4.09	4.29	4.25	197 (260)
Sn-Beta-F-105	4.17	4.17	4.24	216
Sn-Beta-F-140	4.29	4.19	4.25	238
Sn-Beta-OH-170	4.02	4.25	4.10	267
Sn-Beta-OH-200	4.59	4.69	5.13	195
SnO_2/Si-Beta	4.06	4.09	4.16	250
Sn-xerogel	4.45	4.37	4.46	245

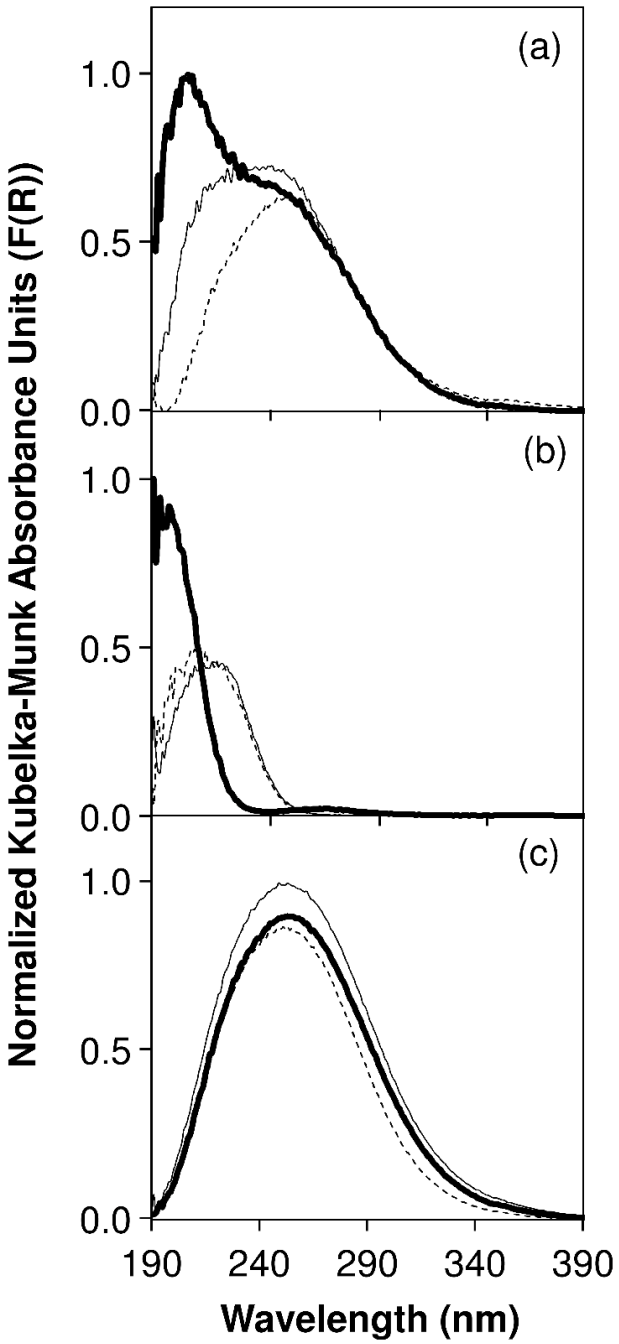

Figure 2.16: Diffuse reflectance UV-Vis spectra in Kubelka-Munk units (normalized to the maximum F(R) intensity within each series) for (a) Sn-Beta-F-170, (b) Sn-Beta-OH-200, and (c) SnO_2/Si-Beta collected under ambient conditions (thin solid line), after dehydration at 523 K (thick solid line), and after rehydration at 303 K (dashed line).

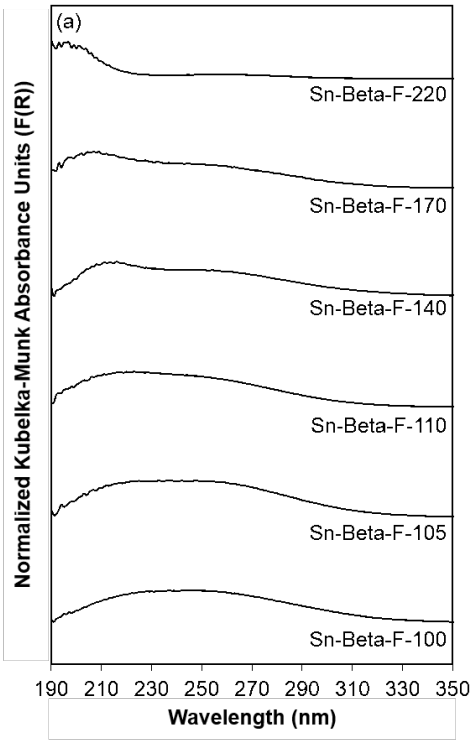

Figure 2.17: DRUV spectra for Sn-zeolite samples collected after dehydration treatments (523 K). Spectra normalized to F(R) at the peak maximum and artificially offset for clarity.

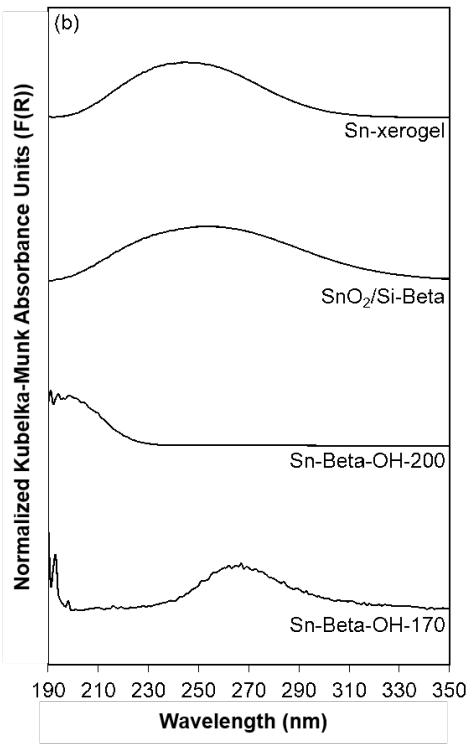

Figure 2.18: DRUV spectra for Sn-zeolite samples collected after dehydration treatments (523 K). Spectra normalized to F(R) at the peak maximum and artificially offset for clarity.

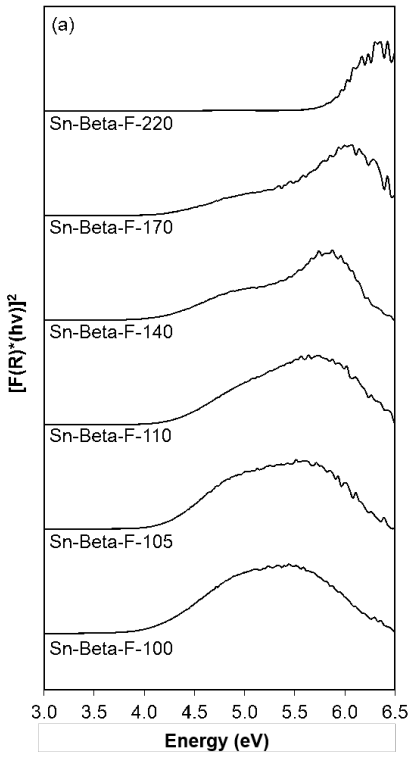

Figure 2.19: Tauc plots for Sn-zeolite samples from DRUV spectra collected after dehydration treatments (523 K).

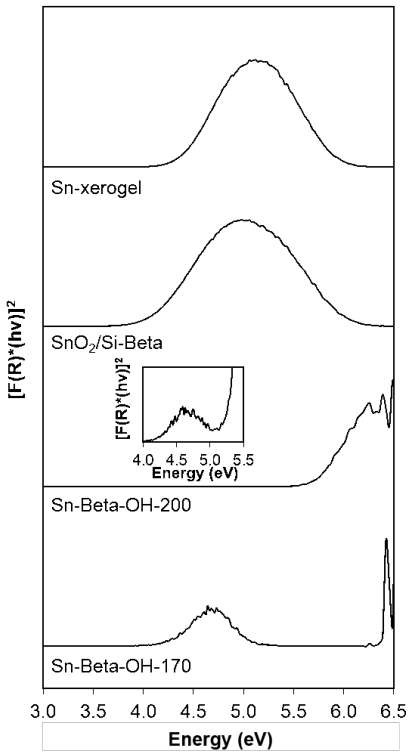

Figure 2.20: Tauc plots for Sn-zeolite samples from DRUV spectra collected after dehydration treatments (523 K). Inset shows low-energy region for Sn-Beta-OH-200 that gives rise to the edge energy reported in Table 2.1.

2.7.4 ^{1}H NMR Spectra of Sugars after Reaction of Glucose-D2 with Zeolite Samples in Water.

^{1}H NMR spectra of glucose fractions recovered after reaction show no change when compared to that of the labeled glucose-D2 reactant, which do not contain a resonance at $\delta = 3.1$ ppm (Fig. 2.21. The absence of this resonance corresponds to a deuterium atom bound to the α-carbonyl carbon (C2 position) of glucose and indicates negligible H/D scrambling of glucose-D2 under the reaction conditions studied here [50]. ^{1}H NMR spectra of fructose fractions collected after reaction do not show a resonance at $\delta = 3.45$ ppm, which indicates that deuterium rather than hydrogen is present at the fructose C1 position (Fig. 2.22). This reflects fructose formation only via the Lewis acid-mediated intramolecular 1,2-hydride shift mechanism instead of the enolate-mediated mechanism catalyzed by bases [51]. Fructose formation was not observed with aqueous glucose solutions adjusted to pH=5 (with HCl) on SnO_2/Si-Beta or in reactors without catalyst present, further demonstrating that the fructose products formed with Sn-Beta samples solely reflect catalytic contributions of Lewis acidic Sn sites.

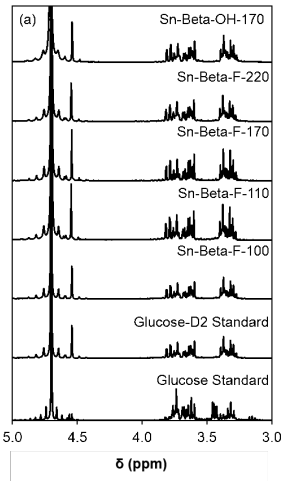

Figure 2.21: ^{1}H NMR spectra for glucose recovered after glucose isomerization catalysis with the Sn-Beta samples tested in this study. The resonating multiplet centered around $\delta = 4.7$ ppm corresponds to residual water present after freeze drying the monosaccharide products

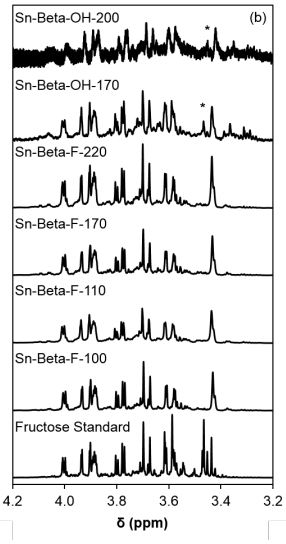

Figure 2.22: ^{1}H NMR spectra for the fructose recovered after glucose isomerization catalysis with the Sn-Beta samples tested in this study. A small resonance at δ=3.47 ppm (denoted with an asterisk) is present in fructose products on Sn-Beta-OH-170 and Sn-Beta-OH-200, indicating a small contribution of the enolate mechanism by hydroxyl ions that becomes detectable at the longer reaction times (>4 h) used to attain higher glucose conversion on these samples.

2.7.5 Determination of Integrated Molar Extinction Coefficients for Pyridine on H-Y Zeolite.

NH_4-Y (Zeolyst CBV300, Si/Al = 2.6) was treated at 823 K in flowing dry air (6.66 cm^3 s^{-1} (g zeolite)$^{-1}$) for 4 h to convert to the H-Y form. H-Y was pressed into a self-supporting wafer and treated under vacuum at 823 K in the IR cell for 1 h, before cooling to 423 K to perform pyridine titration experiments. As pyridine was successively dosed onto the wafer, IR spectra (Fig. 2.23) showed bands for protonated pyridine (1630 cm^{-1}, 1545 cm^{-1}) and for either protonated pyridine or pyridine bound to Lewis acidic Al sites (1490 cm^{-1}). Yet, no bands for pyridine bound to Lewis acidic Al sites (1610 cm^{-1}, 1455 cm^{-1}) were observed (Fig. 2.23). Deconvolution of IR spectra using the procedure described in Section S.9 was used to determine areas of individual IR peaks after each pyridine dose of known quantity. The $\mathcal{E}$ value for the IR band at 1540 cm^{-1} (protonated pyridine), which was determined from the linear relationship between [integrated IR band area (cm^{-1})*wafer cross sectional area (cm^2)] and the total moles dosed (μmol, Fig. 2.24), was 1.95 $\pm$ 0.13 cm μmol^{-1}. This value is similar, within error, to the value reported by Emeis (1.67 $\pm$ 0.25 cm μmol^{-1}) for pyridine adsorbed on Brønsted acid sites in Al-zeolites [84]. The error in the E value was estimated by propagation of error in the moles of titrant adsorbed within each dose ($\pm$0.05 Torr).

The H-Y wafer was then treated in flowing air at 953 K for 4 h, in dynamic vacuum (0.1 Torr) at 953 K for 1 h, and then cooled to 423 K for pyridine titration experiments. As pyridine was successively dosed onto the wafer, new IR bands at 1610 cm^{-1} and 1455 cm^{-1} characteristic of pyridine bound to Lewis acidic Al sites appeared (Fig 2.23) [68]. Deconvolution of IR spectra using the same procedure as above was used to determine IR peak areas for each dose of known quantity. The $\mathcal{E}$ value for the IR band at 1455 cm^{-1} (pyridine bound to Lewis acidic Al sites) was determined by first calculating the squared error between the number of moles dosed to the wafer and the estimated number of moles adsorbed for each dose, using the $\mathcal{E}$ value of 1.95 cm $\pm mol^{-1}$ for protonated pyridine at 1540 cm^{-1} and an initial guess

for the $\mathcal{E}$ value for pyridine bound to Lewis acidic Al. The sum of squared errors was minimized in order to determine the best fit of E values for pyridine bound to Lewis acidic Al sites, which was 1.45 ± 0.10 cm μmol^{-1}. This value is outside of the error of the E value for pyridine bound to Lewis acidic Al determined by Emeis on H-MOR, H-Y, and H-ZSM-5 zeolites and amorphous silica-alumina (2.20 ± 0.33 cm μmol^{-1} [84]), but falls within the range reported in the literature for pyridine bound to Lewis acidic Al sites in aluminosilicates (0.89-3.9 cm μmol^{-1} [93, 113, 114]).

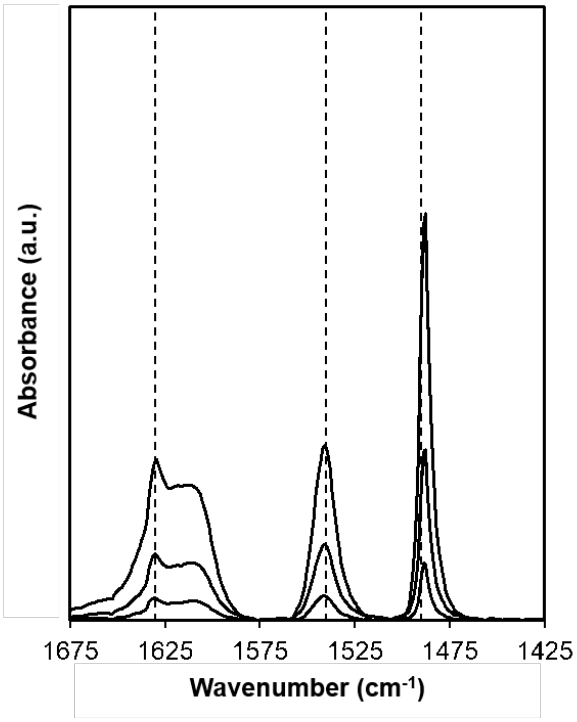

Figure 2.23: IR spectra after progressive titration of pyridine on H-Y (Si/Al=2.6, Zeolyst) at 423 K (pyridine/Al = 0.005-0.040). Dashed lines at 1630 cm^{-1} (protonated pyridine), 1545 cm^{-1} (protonated pyridine), and 1490 cm^{-1} (protonated pyridine or pyridine bound to Lewis acidic Al sites).

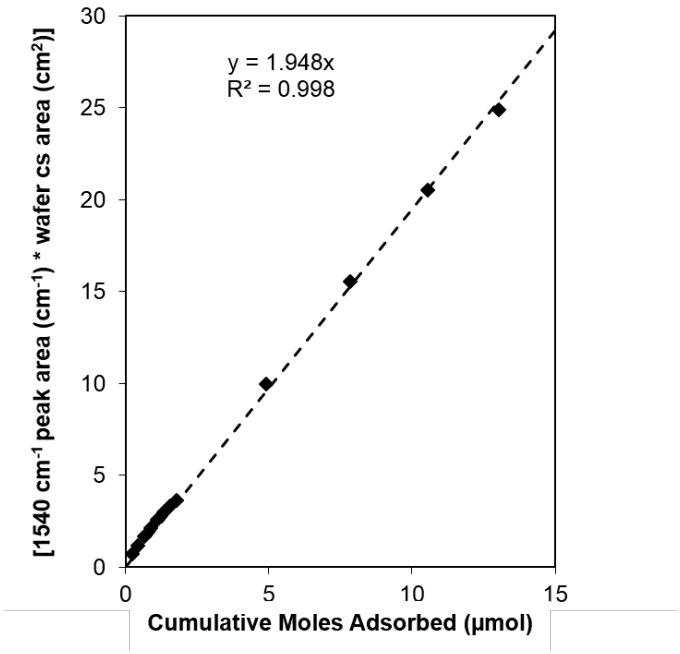

Figure 2.24: Integrated area of 1545 cm^{-1} IR peak multiplied by wafer cross-sectional area plotted against the amount of pyridine adsorbed on H-Y (Si/Al=2.6, Zeolyst) at 423 K.

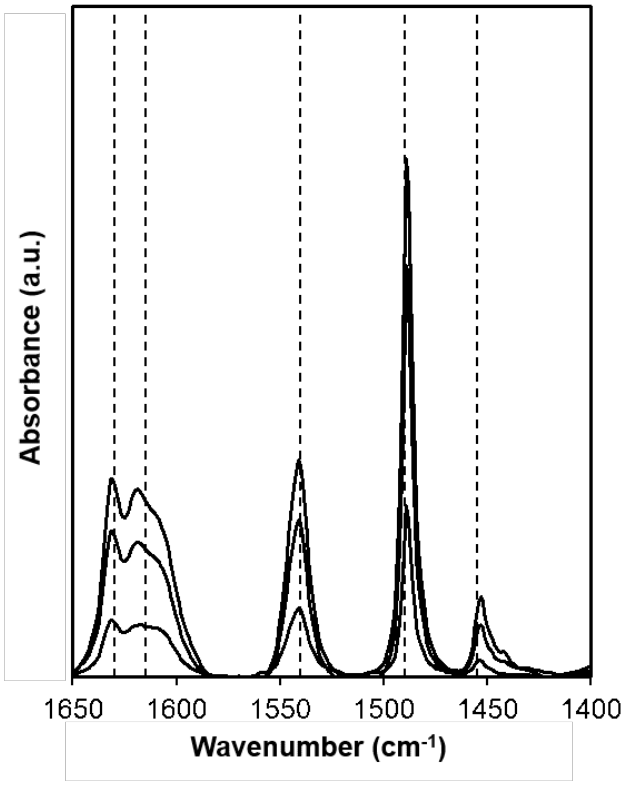

Figure 2.25: IR spectra after progressive titration of pyridine on high temperature-treated H-Y (Si/Al=2.6, Zeolyst) at 423 K (pyridine/Al = 0.012-0.13). Dashed lines shown at 1630 cm^{-1} (protonated pyridine), 1615 cm^{-1} (pyridine bound to Lewis acidic Al sites), 1545 cm^{-1} (protonated pyridine), 1490 cm^{-1} (protonated pyridine or pyridine bound to Lewis acidic Al sites), and 1455 cm^{-1} (pyridine bound to Lewis acidic Al sites).

2.7.6 Pyridine Titration and Infrared Spectroscopy of Zeolite Samples.

IR spectra for each Sn-Beta sample after pyridine saturation and evacuation for 900 seconds under vacuum (0.1 Torr) at 423 K are shown in Figure 2.26. This evacuation procedure was sufficient to remove gaseous pyridine and the majority of the weakly-bound physisorbed pyridine that convolutes the peak at 1450 cm^{-1} (Fig 2.27). IR spectra were baseline-corrected between 1400 cm^{-1} to 1650 cm^{-1} and deconvoluted in CasaXPS to determine the areas of IR peaks at 1610 cm^{-1} and 1450 cm^{-1}, which reflects pyridine bound to Lewis acidic Sn sites [68], using a combined Gauss-Lorentzian (SGL) lineshape with an 80% Lorentzian contribution. Additional bands at 1439 cm^{-1}, 1445 cm^{-1}, and 1490 cm^{-1} were included in the deconvolution and are representative of gas phase pyridine, physisorbed pyridine, and pyridine bound to Lewis acidic Sn sites or protonated pyridine [68]. Peak centers were allowed to vary within ± 3 cm^{-1} and full widths at half maximum peak height were constrained between 5 cm^{-1} and 20 cm^{-1}. The peak at 1450 cm^{-1} was virtually unchanged after exposure to dynamic vacuum at 423 K for 900 seconds (Fig 2.28), and these IR spectra (Fig 2.26) were used to determine the number of moles of Lewis acidic Sn sites present on each sample using Eq. 2.1. The error in the $\mathcal{E}$ value for pyridine bound to Lewis acidic Sn sites was estimated using the same procedure described in Section 2.7.5 . For Sn-Beta-OH-200, the peak area at 1445 cm^{-1} was $\sim 4\times$ that of the peak at 1450 cm^{-1} after saturation and exposure to dynamic vacuum for 900 s (while this was $\leq \sim$1x on all other samples), leading to inaccurate deconvolution of the 1450 and 1445 cm^{-1} peaks. In order to determine the saturation coverage of pyridine on Lewis acid sites in Sn-Beta-OH-200, the integrated absorbance at 1450 cm$\sim$ was estimated from the spectrum of a dose after the saturation of the peak for pyridine to Sn Lewis acid sites, but before complete saturation of the surface defect sites.

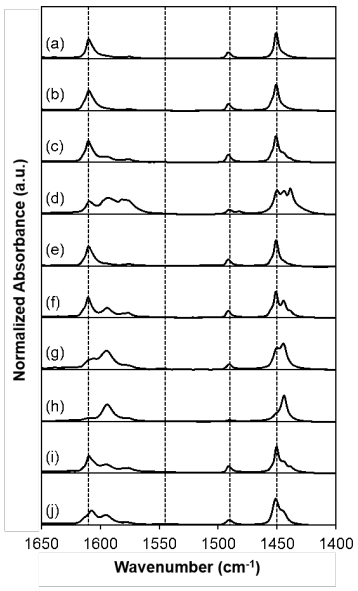

Figure 2.26: IR difference spectra for pyridine saturated Sn-Beta samples after evacuation at 423 K for 900 s for (a) Sn-Beta-F-100, (b) Sn-Beta-F-105, (c) Sn-Beta-F-110, (d) Sn-Beta-F-140, (e) Sn-Beta-F-170, (f) Sn-Beta-F-220, (g) Sn-Beta-OH-170, (h) Sn-Beta-OH-200, (i) SnO_2/Si-Beta, and (j) Sn-xerogel. All spectra normalized to the overtone and combination modes of Si-O-Si stretches (1750-2100 cm^{-1}) and to the maximum peak intensity for clarity. Dashed lines shown at 1610 cm^{-1} (pyridine bound to Lewis acidic Sn sites), 1540 cm^{-1} (protonated pyridine), 1490 cm^{-1} (protonated pyridine or pyridine bound to Lewis acidic Sn sites), and 1450 cm^{-1} (pyridine bound to Lewis acidic Sn sites).

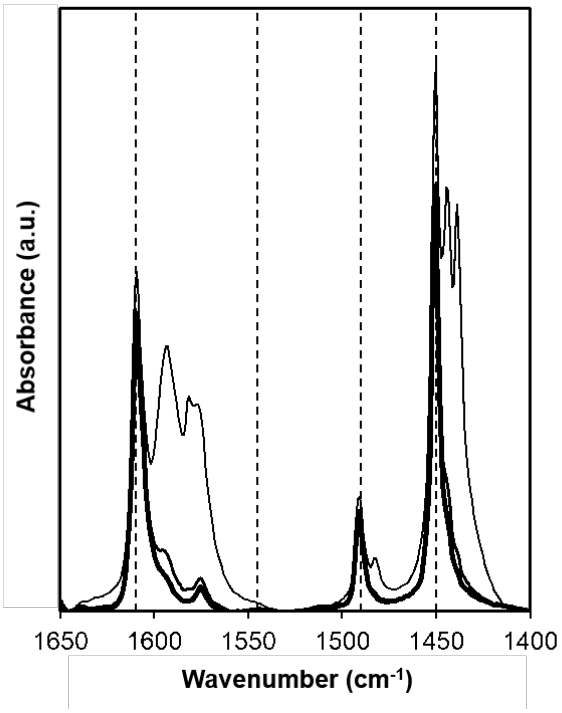

Figure 2.27: IR spectra for pyridine-saturated Sn-Beta-F-100 during exposure to dynamic vacuum at 423 K for 0 s, 300 s, and 900 s (thin to thick traces) after saturation with pyridine. Dashed lines shown at 1610 cm^{-1} (pyridine bound to Lewis acidic Sn sites), 1545 cm^{-1} (protonated pyridine), 1490 cm^{-1} (protonated pyridine or pyridine bound to Lewis acidic Sn sites), and 1450 cm^{-1} (pyridine bound to Lewis acidic Sn sites).

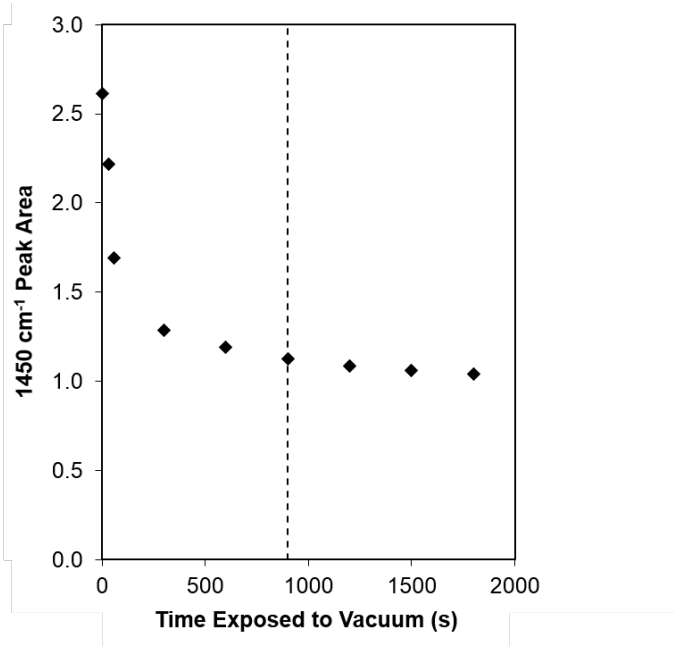

Figure 2.28: Integrated area of the IR peak at 1450 cm^{-1} as a function of time exposed to dynamic vacuum at 423 K for pyridine-saturated Sn-Beta-F-100. Dashed line at 900 seconds added for reference.

2.7.7 n-Propylamine Temperature Programmed Desorption (TPD) Experiments on Zeolites.

A response factor for n-propylamine (NPA, m/z = 59) was developed by filling a sample loop (1 or 5 cm^3) with a mixture of 1000 ppm NPA and 1% Ar in balance He (certified gas mixture, Airgas), and then injecting the loop contents into flowing He (1.66 cm^3 s^{-1}). This stream was transferred via heated gas lines (383 K) to an expansion volume (150 cm^3) and then into a mass selective detector (MSD). An additional data point was collected by flowing 20 cm^3 min^{-1} of 1000 ppm NPA to the MSD for 20 s. Afterwards, a 0.5 cm^3 sample loop was filled with Ar (99.999%, Indiana Oxygen) and injected into flowing He (1.66 cm^3 s^{-1}) and sent to the MSD. Integrated area ratios for NPA and Ar MSD traces and the molar ratios of each component are plotted in Figure 2.29 to obtain the response factor of NPA (relative to Ar), enabling quantification of NPA MSD traces when using an Ar standard to account for signal drift.

NPA TPD profiles are shown for all Sn-Beta samples in Figure S.14. Each sample was saturated with NPA for 4 h at 323 K (75 cm^3 s^{-1} g^{-1}), purged in flowing dry He for 4 or 8 h at 338 K (25 cm^3 s^{-1} g^{-1}), and then held in flowing He (25 cm^3 s^{-1} g^{-1}) from 338 to 773 K (0.167 K s^{-1}). After each TPD experiment, a 0.5 cm^3 sample loop was filled with Ar and pulsed into flowing He and sent to the MSD to quantify the NPA evolved in the TPD (Tables 2.5 and 2.6).

The appropriate saturation and purge length were determined by varying the purge duration (4 h, 8 h, 12 h, 16 h) at a given saturation condition (4 h at 323 K in 25 cm^3 s^{-1} g^{-1}, Figs. 2.31 and 2.32). A purge performed at 323 K after the same saturation conditions was taken as the 0 h purge length reference for the higher temperature (338 K) purge treatments. The low temperature purge (323 K) resulted in an NPA signal that is a convolution of two separate features, but purging at 338 K removed the low temperature feature and resulted in a symmetric and single TPD feature. For purges 4 h or longer, the number of NPA molecules evolved during TPD was constant, within experimental error, at 1.03 NPA/Sn for Sn-Beta-F-140 and 1.30

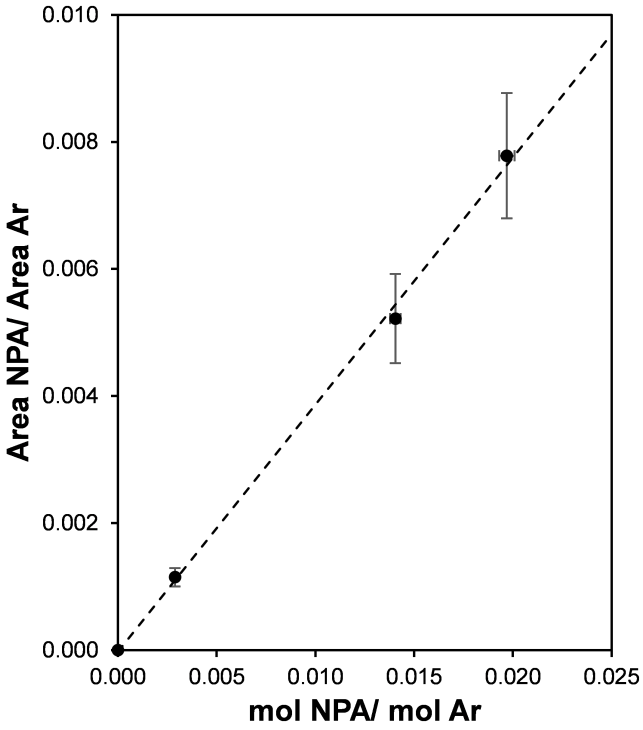

Figure 2.29: NPA (m/z = 59) response factor calibration curve of the mass spectrometer area ratio of NPA/Ar as a function of the molar ratio of NPA/Ar.

Table 2.5: Molecules of NPA desorbed per Sn after saturation with 1000 ppm NPA for 4 h at 323 K followed by purging for 4 h and 8 h.

Sample	NPA/Sn (4 hr purge)	NPA/Sn (4 hr purge)
Sn-Beta-F-100	0.48±0.07	0.44 ±0.06
Sn-Beta-F-105	0.59± 0.09	0.62 ±0.09
Sn-Beta-F-110	1.07± 0.15	0.99 ±0.13
Sn-Beta-F-140	1.18± 0.16	1.04 ±0.1
Sn-Beta-F-170	1.30± 0.17	1.24 ±0.17
Sn-Beta-F-220	2.02± 0.27	2.07 ±0.28
Sn-Beta-OH-170	1.37± 0.16	1.14 ±0.14
Sn-Beta-OH-200	n.d.*	1.71 ±0.21

*n.d.: data not collected

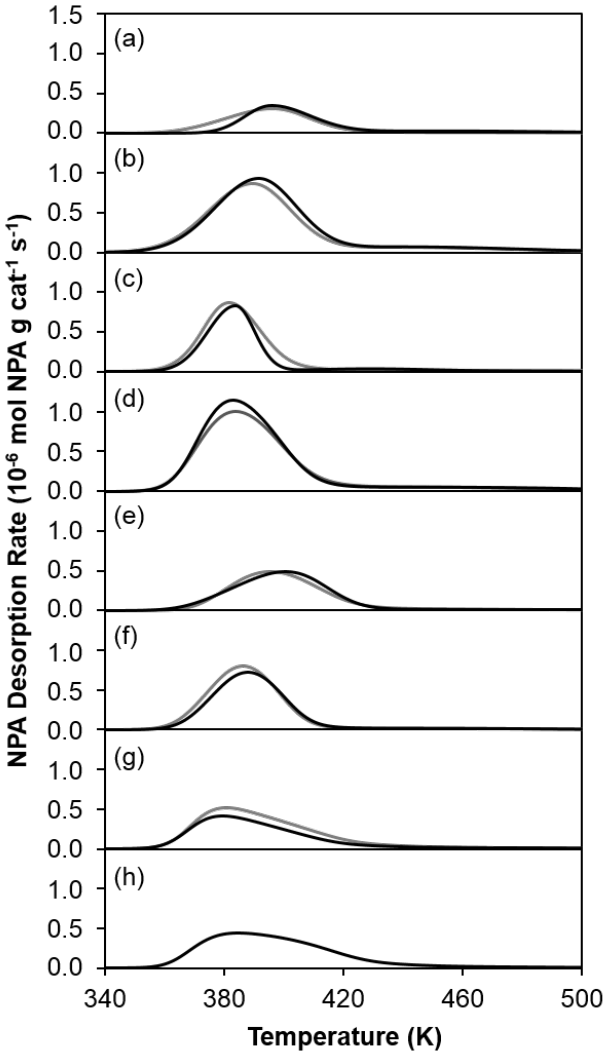

Figure 2.30: NPA TPD profiles after saturation with 1000 ppm NPA for 4 h at 323 K followed by purging for 4 h (grey trace) and 8 h (black trace) at 338 K in 25 cm^3 s^{-1} g^{-1} UHP He on (a) Sn-Beta-F-100, (b) Sn-Beta-F-105, (c) Sn-Beta-F-110, (d) Sn-Beta-F-140, (e) Sn-Beta-F-170, (f) Sn-Beta-F-220, and (g) Sn-Beta-OH-170 and (h) Sn-Beta-OH-200.

NPA/Sn for Sn-Beta-F-170 (Fig. 2.32). In order to verify that increased saturation time did not influence the quantification, the saturation time was varied as the purge conditions were kept constant (8 h, 338 K, He flow = 0.83 cm^3 g zeolite^{-1} s^{-1}). The number of NPA molecules evolved during the TPD was constant, within experimental error, at 1.02 NPA/Sn for Sn-Beta-F-140 (Fig. 2.33).

Table 2.6: Moles of NPA desorbed per g zeolite after saturation with 1000 ppm NPA for 4 h at 323 K followed by purging for 8 h.

Sample	NPA/g ($x10^4$)
Sn-Beta-F-100	.719
Sn-Beta-F-105	.971
Sn-Beta-F-110	1.48
Sn-Beta-F-140	1.26
Sn-Beta-F-170	1.18
Sn-Beta-F-220	1.52
Sn-Beta-OH-170	1.09
Sn-Beta-OH-200	1.39
Si-Beta-F	0.031
Dealuminated Beta	1.59

The number of NPA molecules (per Sn) evolved on Sn-Beta-F samples with low Sn content (Sn-Beta-F-170, Sn-Beta-F-220) and on highly-defective Sn-Beta-OH samples (Sn-Beta-OH-170, Sn-Beta-OH-200) were much larger than unity (Table 2.5). These findings suggest that the saturation and purge treatments used here may not be sufficient to remove NPA at other binding sites on zeolite samples. Control experiments performed on purely-siliceous Beta zeolites (Si-Beta-F) did not evolve a significant amount of NPA in TPD experiments (Table2.6), but those performed on dealuminated Beta zeolites (parent Si/Al = 15) evolved as much or more NPA (per g) as the low Sn content Sn-Beta-F and the highly-defective Sn-Beta-OH samples (Table 2.6). These findings suggest that the saturation and purge conditions used in this study causes NPA retention on residual defect sites in zeolite samples, which may lead to inaccurate quantification of Lewis acidic Sn sites by NPA TPD for samples with low Sn content and high defect densities.

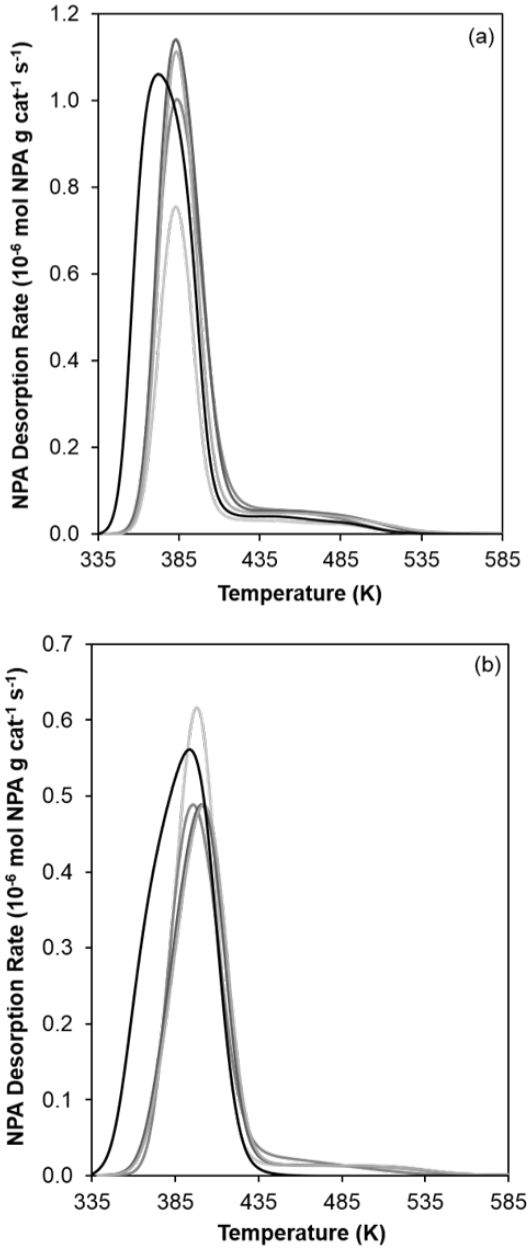

Figure 2.31: NPA TPD profiles on (a) Sn-Beta-F-140 and (b) Sn-Beta-F-170 after saturation in 1000 ppm NPA for 4 h followed by purging at 338 K in 25 cm^3 s^{-1} g^{-1} He for 4 h (dark grey trace), 8 h (grey trace), 12 h (light grey trace), and 16 h (faint grey trace). A purge performed at 323 K for 8 h in 25 cm^3 s^{-1} g^{-1} He is used to represent a 0 h purge at 338 K (black trace).

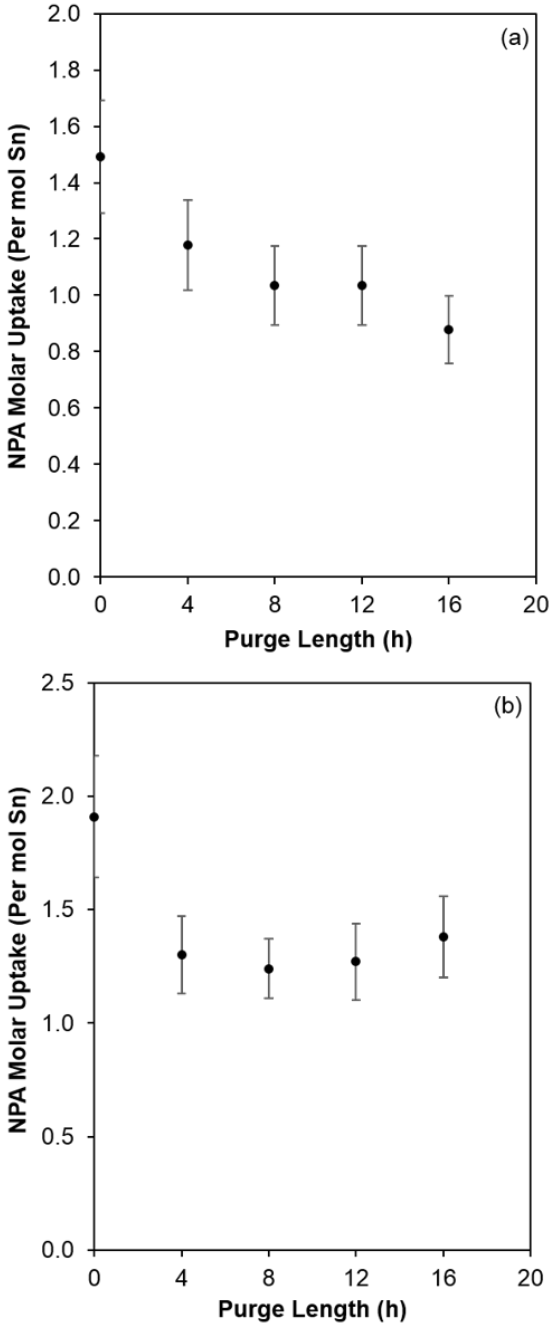

Figure 2.32: Molecules of NPA desorbed per molecule of Sn as a function of the purge length on (a) Sn-Beta-F-140 and (b) Sn-Beta-F-170 after saturation in 1000 ppm NPA for 4 h followed by purging at 338 K in 25 cm^3 s^{-1} g^{-1} He. A purge performed at 323 K for 8 h in 25 cm^3 s^{-1} g^{-1} He is used as a representation for a 0 h purge at 338 K.

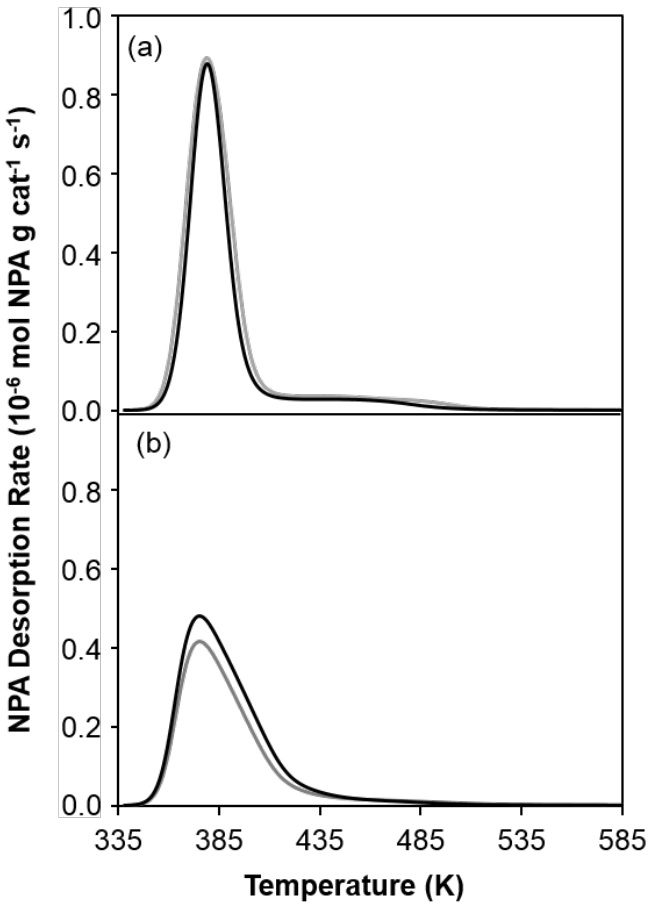

Figure 2.33: NPA desorption rate on (a) Sn-Beta-F-140 and(b) Sn-Beta-OH-170 after saturation in 1000 ppm NPA for 4 h (grey trace) and 16 h (black trace) followed by an 8 h purge at 338 K in 25 cm^3 s^{-1} g^{-1} He.

2.7.8 Ammonia Temperature Programmed Desorption Experiments on Zeolite Samples.

A response factor for ammonia (NH_3, m/z = 17) was developed by performing NH_3 TPD experiments on four NH_4-ZSM-5 zeolites (Si/Al = 17–89, Zeolyst). The moles of NH_3 desorbed from each material was measured in independent TPD experiments performed in a gas-phase plug-flow reactor connected to a MKS Multigas 2030 gas-phase FTIR spectrometer with an on-board NH_3 calibration as described elsewhere [100]. After each NH_3 TPD experiment, a 0.5 cm^3 loop was filled with Ar and injected into flowing He (0.83 cm^3 s^{-1}). The total NH_3 desorbed was quantified from the m/z = 17 MSD trace after subtracting the contributing fractionation products of water (m/z = 17), which appears in constant proportion to the m/z = 18 signal for its parent ion. The ratio of integrated areas for NH_3 and Ar are plotted as a function of their molar ratio (Figure 2.34) to give a response factor of NH_3 (relative to Ar) in the MSD, which enables the quantification of NH_3 MSD traces when using an Ar standard to account for signal drift.

NH_3 TPD profiles are shown for all Sn-Beta samples in Fig. 2.35. Each sample was saturated with NH_3 for 5 h at 323 K (75 cm^3 s^{-1} g^{-1}), purged in flowing dry He for 8 h at 331 K (25 cm^3 s^{-1} g^{-1}) to remove any physisorbed NH_3, then kept in flowing He (25 cm^3 s^{-1} g^{-1}) as the temperature increased to 773 K (0.167 K s^{-1}). After each TPD experiment, a 0.5 cm^3 loop (383 K) was filled with Ar and pulsed into flowing He sent to the MSD to correct for instrument drift. The number of molecules of NH_3 desorbed (per Sn) are given in Tables 2.7 and 2.8.

Appropriate saturation and purge durations were determined by varying the purge length (0, 4, 8, 12 h) at a fixed saturation conditions (5 h, 323 K, flowing 500 ppm NH_3 at 75 cm^3 s^{-1} g^{-1}). For purges of 4 h and longer, the number of NH_3 molecules evolved per Sn during the TPD was constant, within experimental error, at 0.43 NH_3/Sn for Sn-Beta-F-100 (Fig. 2.36). In order to verify that saturation times did not influence the quantification, the saturation time was varied at fixed purge conditions (8 h, 331

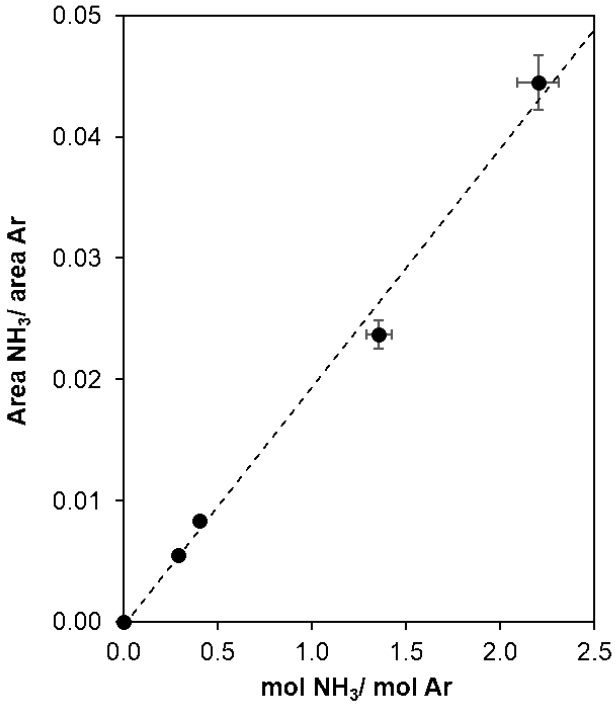

Figure 2.34: NH_3 (m/z = 17) calibration curve of the mass spectrometer area ratio of NH_3/Ar as a function of the molar ratio of NH_3/Ar.

Table 2.7: Molecules of NH_3 desorbed (per Sn) after saturation with 500 ppm NH_3 for 5 h at 323 K, followed by purging for 8 h.

Sample	NH_3/Sn (8 hr purge)
Sn-Beta-F-100	0.42±0.02
Sn-Beta-F-105	0.61± 0.04
Sn-Beta-F-110	0.73± 0.04
Sn-Beta-F-140	1.06± 0.05
Sn-Beta-F-170	0.69± 0.03
Sn-Beta-F-220	0.89± 0.04
Sn-Beta-OH-170	1.12± 0.06
Sn-Beta-OH-200	0.93±0.05

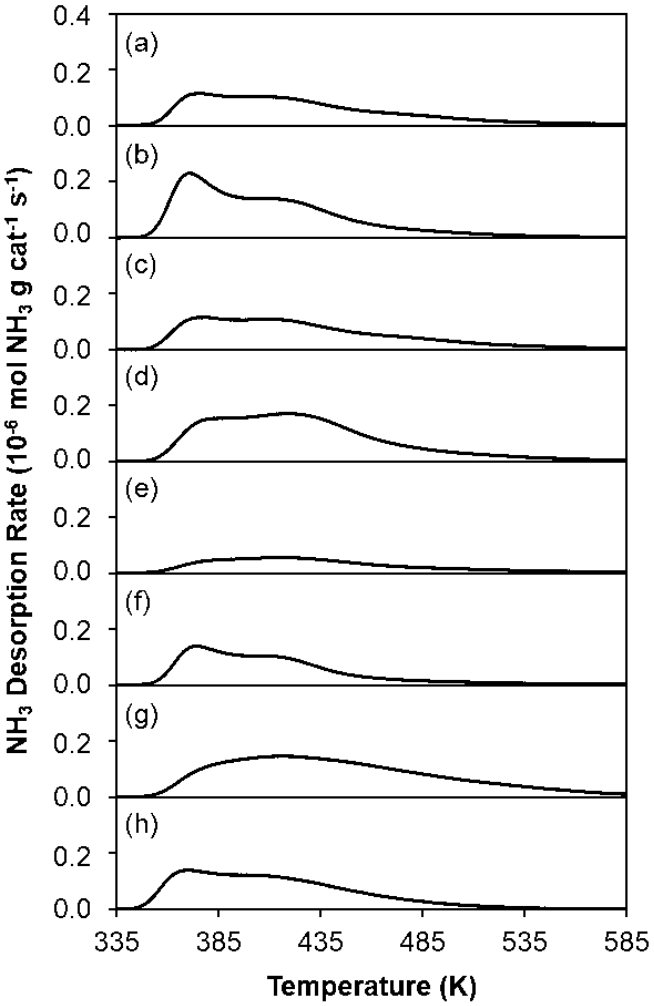

Figure 2.35: NH_3 TPD profiles after saturation in 75 cm^3 s^{-1} g^{-1} 500 ppm NH_3/He at 323 K for 5 h followed by purging in dry He (25 cm^3 s^{-1} g^{-1}) at 331 K for 8 h on (a) Sn-Beta-F-100, (b) Sn-Beta-F-105, (c) Sn-Beta-F-110 (d) Sn-Beta-F-140, (e) Sn-Beta-F-170, (f) Sn-Beta-F-200, (g) Sn-BEA-OH-170, (h) Sn-Beta-OH-200.

K, flowing He at 25 cm^3 s^{-1} g^{-1}) and the moles of NH_3 evolved during TPD was constant, within experimental error, at 0.44 NH_3/Sn for Sn-Beta-F-100 (Fig. 2.37).

Table 2.8: Moles of NH_3 desorbed (per g) after saturation with 500 ppm NH_3 for 5 h at 323 K followed by purging for 8 h.

Sample	NH_3/g (x10^4)
Sn-Beta-F-100	0.686
Sn-Beta-F-105	0.956
Sn-Beta-F-110	1.09
Sn-Beta-F-140	1.29
Sn-Beta-F-170	0.657
Sn-Beta-F-220	0.652
Sn-Beta-OH-170	1.08
Sn-Beta-OH-200	0.754
Si-Beta-F	0.003
Dealuminated Beta	0.157

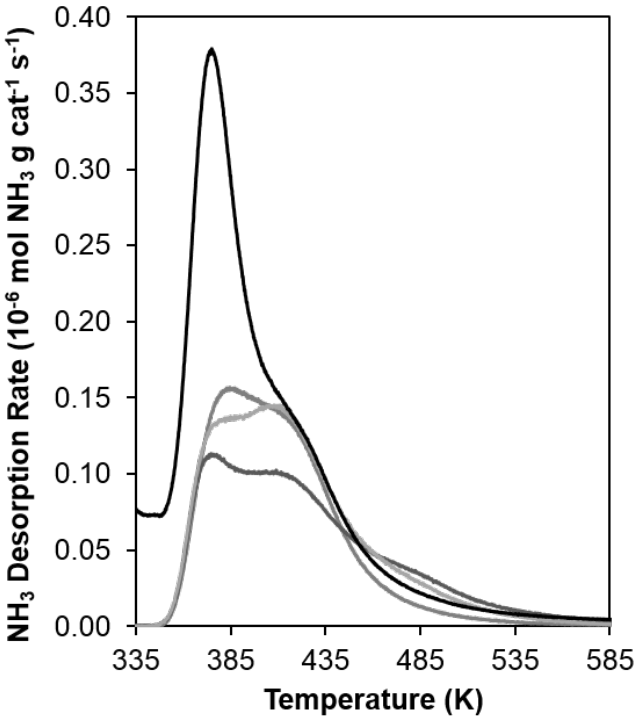

Figure 2.36: NH_3 TPD profiles after saturation of Sn-Beta-F-100 for 5 h in 75 cm^3 s^{-1} g^{-1} 500 ppm NH_3/He at 323 K followed by purging in dry He (25 cm^3 s^{-1} g^{-1}) at 331 K for 0 h (black trace), 4 h (dark grey trace), 8 h (grey trace), and 12 h (light grey trace).

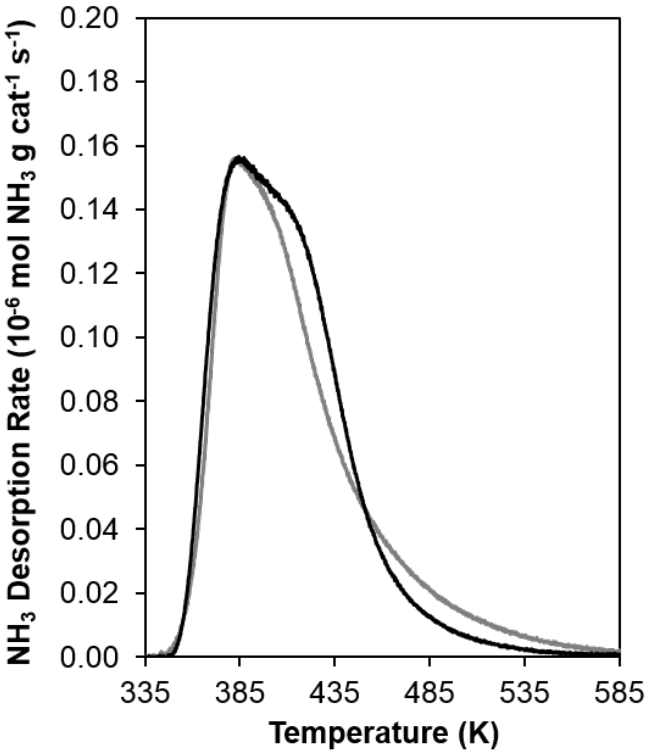

Figure 2.37: NH_3 TPD profiles after saturation of Sn-Beta-F-100 for 5 h (black trace) or 16 h (grey trace) in 75 $cm^3\ s^{-1}\ g^{-1}$ 500 ppm NH_3/He at 323 K followed by purging in dry He (25 $cm^3\ s^{-1}\ g^{-1}$) at 331 K for 8 h.

2.7.9 Deuterated Acetonitrile Titration and Infrared Spectroscopy of Zeolites.

Sn-Beta samples were saturated with CD_3CN by exposure to a gaseous pressure sufficient to give rise to an IR peak at 2265 cm^{-1} for gaseous CD_3CN. IR spectra corresponding to samples saturated with CD_3CN were collected after subsequent exposure to ∼30 seconds of dynamic vacuum (∼0.1 Torr) at 303 K, which did not noticeably decrease the IR peaks for closed Sn sites at 2308 cm^{-1} but did remove gaseous CD_3CN present in the cell (Fig. 2.38). The IR peak areas for CD_3CN-saturated samples after evacuation at 303 K were not a function of the initial saturation pressure (and number of moles) of CD_3CN used (Fig. 2.39)

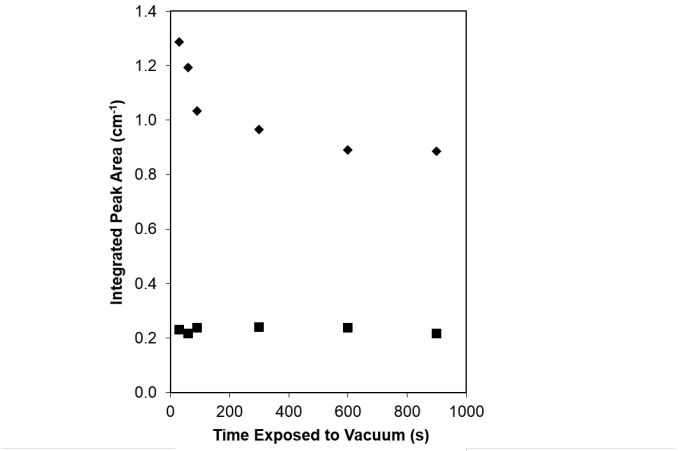

Figure 2.38: IR peak areas for Sn-BEA-F-100 after saturation and exposure to dynamic vacuum for open Sn sites (squares) and closed Sn sites (diamonds) as a function of time exposed to dynamic vacuum.

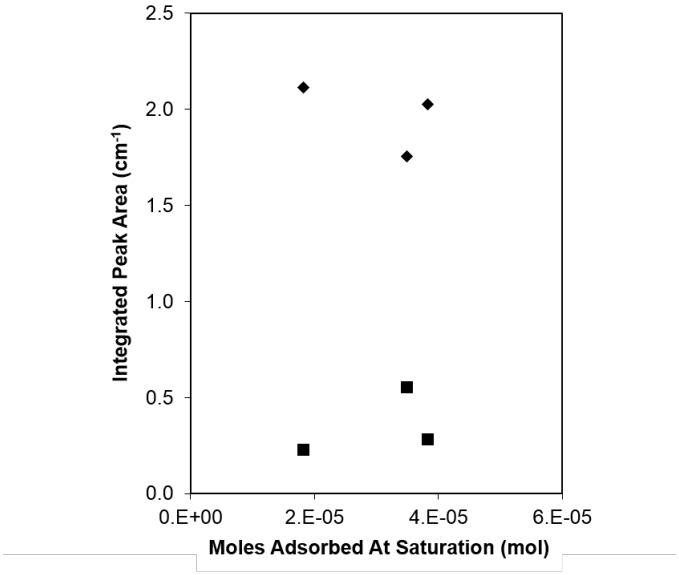

Figure 2.39: IR peak areas for Sn-BEA-F-140 after saturation for open Sn sites (squares) and closed Sn sites (diamonds) as a function of moles adsorbed at saturation

Deconvolution of IR spectral features, after subtraction of IR spectra for CD_3CN-free wafers, was performed in CasaXPS. Individual components for IR peaks at 2316

cm^{-1}, 2308 cm^{-1}, 2287 cm^{-1}, 2275 cm^{-1}, and 2265 cm^{-1} were used to determine areas within each CD_3CN dose that correspond to open Sn sites, closed Sn sites, $(SiO)_2Sn(SiOH)_2$ sites (speculative assignment), SiOH sites, and gas phase CD_3CN, respectively (Table 2.9). IR peak centers were fixed within ± 5 cm^{-1}, and the full widths at half maxima were constrained to be between 5 cm^{-1} and 20 cm^{-1}. The sum of Gauss-Lorentzian (SGL) line shapes were used for each component, with a 50% Lorentzian correction to a normally distributed Gaussian line shape (SGL(50)), as was used previously for deconvolution of IR spectra obtained after CD_3CN adsorption to Zn exchanged Al-Beta [80].

The relationship between the number of moles of CD_3CN dosed, the number of moles adsorbed to each type of site (resulting in a band area, BA, for each site), and the value of the integrated molar extinction coefficient (IMEC, or $\mathcal{E}$ for short) is given by:

$$Cumulative\,Moles\,Adsorbed = \frac{2316\,cm^{-1}\,BA}{2316\,cm^{-1}\,IMEC} + \frac{2308\,cm^{-1}\,BA}{2308\,cm^{-1}\,IMEC} + \frac{2287\,cm^{-1}\,BA}{2287\,cm^{-1}\,IMEC} + \frac{(2275\,cm^{-1}\,BA}{2275\,cm^{-1}\,IMEC} \quad (2.4)$$

$\mathcal{E}$ values were determined for CD_3CN bound to Lewis acidic Sn sites in Sn-Beta by minimizing the squared error between the moles of pyridine bound to Lewis acidic Sn sites (using the $\mathcal{E}$ value measured for Sn-Beta: 1.42 ± 0.30 cm μmol^{-1}, Section 2.7.6). This was achieved by varying the $\mathcal{E}$ values for CD_3CN bound to open and closed Sn sites using the Excel Solver function with multistart, in order to avoid finding initial guess-dependent local minima. This procedure led to values of $\mathcal{E}$(2316 cm^{-1}) and $\mathcal{E}$(2308 cm^{-1}) of 1.04 ± 0.22 cm μmol^{-1} and 2.04 ± 0.43 cm μmol^{-1}, and agreement with the total number of moles of Lewis acidic Sn sites counted by pyridine (Fig. 2.4). Then, $\mathcal{E}$ values for the 2287 cm^{-1} and 2275 cm^{-1} peaks were determined from a series of spectra collected with increasing CD_3CN coverage on Sn-Beta-OH-170,

which showed an intense 2275 cm^{-1} peak for all CD_3CN doses and an IR peak at 2287 cm^{-1} of similar intensity to the rest of the samples in this study. The $\mathcal{E}$ values for 2316 cm^{-1} and 2308 cm^{-1} were fixed from the previous fitting, and only the initial doses were used for which there was no detectable IR peak at 2265 cm^{-1} for gas phase or physisorbed CD_3CN. The $\mathcal{E}$ values that minimized the sum of squared errors for all CD_3CN doses on Sn-Beta-OH-170 were 2.13 ± 0.45 cm μmol^{-1} and 0.74 ± 0.16 cm μmol^{-1} for the IR peaks at 2287 cm^{-1} and 2275 cm^{-1}, respectively. The four $\mathcal{E}$ values can be used to quantify the numbers of each type of site using integrated peak areas determined after saturation of Sn-Beta samples using Eq. 2.1. The error in the $\mathcal{E}$ value for CD_3CN bound to each of the sites (open Sn sites, closed Sn sites, $(SiO)_2Sn(SiOH)_2$ sites, and SiOH sites) was estimated using the same procedure described in Section 2.7.5. The assignment of the 2275 cm^{-1} peak to CD_3CN bound to SiOH groups is supported by the correlation between the integrated areas for perturbed SiOH groups (Fig. 2.40), which give rise to a broad absorption between 3000-3600 cm^{-1}, that increased linearly with 2275 cm^{-1} peak areas. Furthermore, the integrated areas for terminal SiOH groups (Fig. 2.41), which give rise to IR peaks at 3740 cm^{-1}, decreased linearly with an increase in 2275 cm^{-1} peak areas. CD_3CN adsorption experiments performed on a dealuminated Beta sample gave rise to IR spectra that showed a small peak at 2300 cm^{-1} that saturated quickly, while the IR 2275 cm^{-1} peak grew continuously with increasing CD_3CN coverage (Fig. 2.42). These IR data were used to independently estimate the $\mathcal{E}$ value for the 2275 cm^{-1} peak to be 0.89 ± 0.09 cm μmol^{-1} (Fig. 2.43). A sample prepared to have framework Sn in an amorphous silica network (Sn-xerogel), gave rise primarily to a peak at 2287 cm^{-1} at low CD_3CN coverages (Fig. 2.44, $CD_3CN/Sn < 0.2$), prior to the appearance of the peak at 2275 cm^{-1} for CD_3CN hydrogen bound to SiOH groups (Fig. 2.45). The peak at 2287 cm^{-1} was also observed at low CD_3CN coverages for all Sn-Beta samples. This peak was not observed to a significant degree for SnO_2/Si-Beta, a sample with small extraframework octahedral SnO_2 domains (Fig. 2.46), nor on bulk SnO_2 or a metal-free silica sample (Si-xerogel). Thus, we speculate this peak may be a highly

defective framework Sn site, such as an $(SiO_2)Sn(OH)_2$ site. No clear correlation with any band in the ν(OH) region is observed for this 2287 cm^{-1} peak, as in the case of the 2275 cm^{-1} peak. The peak at 2287 cm^{-1} was included in deconvolution of the spectra for the Sn-Beta samples, which may contain these defective framework Sn sites.

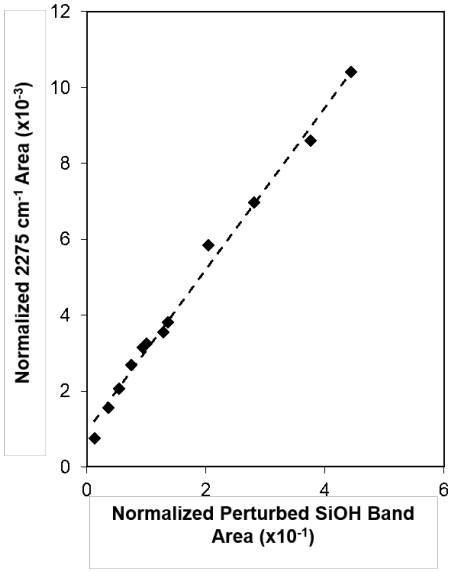

Figure 2.40: 2275 cm^{-1} peak area versus perturbed OH peak area (3000-3600 cm^{-1}.

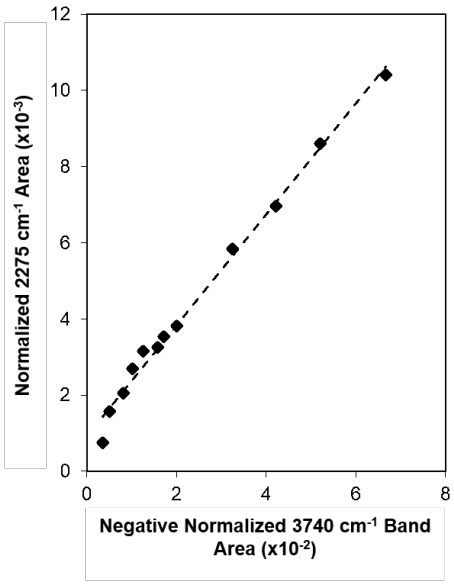

Figure 2.41: 2275 cm^{-1} band area versus negative SiOH band area ($\sim$3740 cm^{-1}).

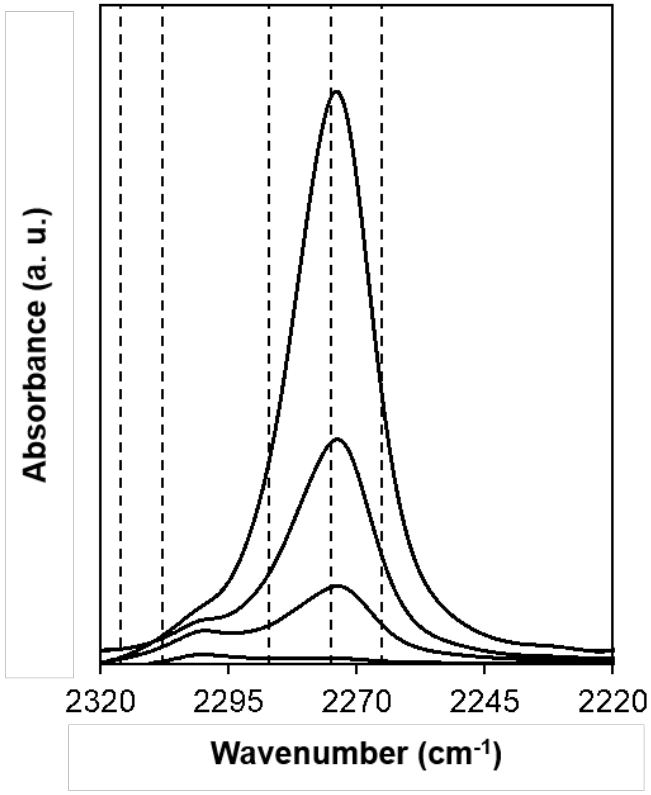

Figure 2.42: FTIR spectra of a dealuminated Beta zeolite after sequential doses of CD_3CN. Dashed lines shown at 2316 cm^{-1}, 2308 cm^{-1}, 2287 cm^{-1}, 2275 cm^{-1}, and 2265 cm^{-1}.

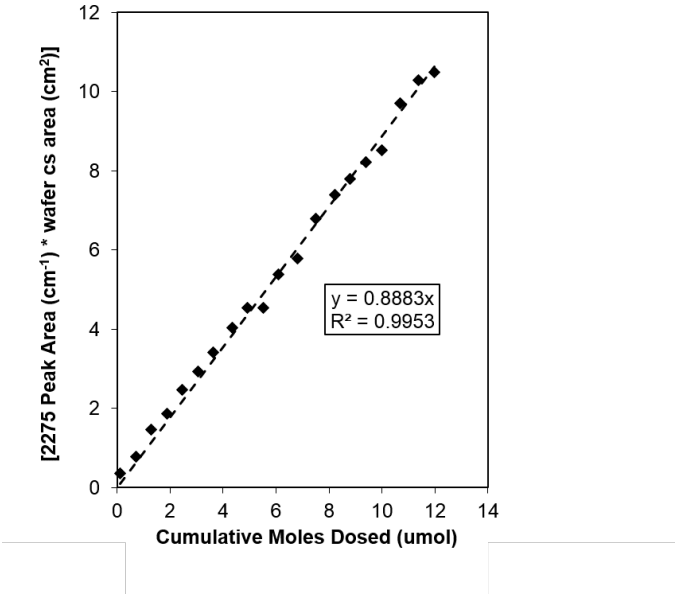

Figure 2.43: IR band area for the 2275 cm^{-1} peak on dealuminated Beta as a function of moles CD_3CN adsorbed. The slope of this line is the $\mathcal{E}$ value estimated for the 2275 cm^{-1} site.

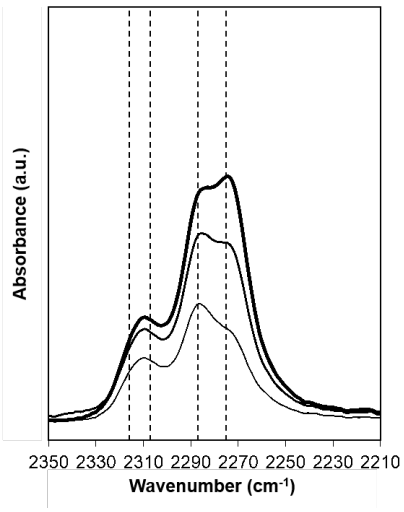

Figure 2.44: IR spectra of CD_3CN three sequential doses (0.05 mol CD_3CN/Sn per dose) on Sn-xerogel. Dashed lines shown at 2316 cm^{-1}, 2308 cm^{-1}, 2287 cm^{-1}, and 2275 cm^{-1}.

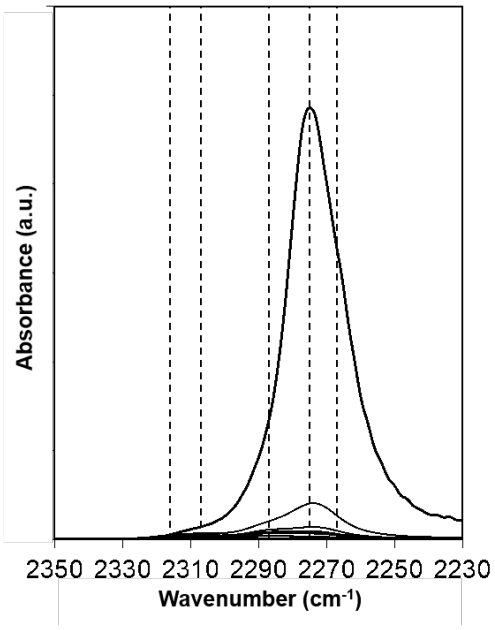

Figure 2.45: IR spectra of CD_3CN dosed on Sn-xerogel to saturation. Dashed lines shown at 2316 cm^{-1}, 2308 cm^{-1}, 2287 cm^{-1}, and 2275 cm^{-1}.

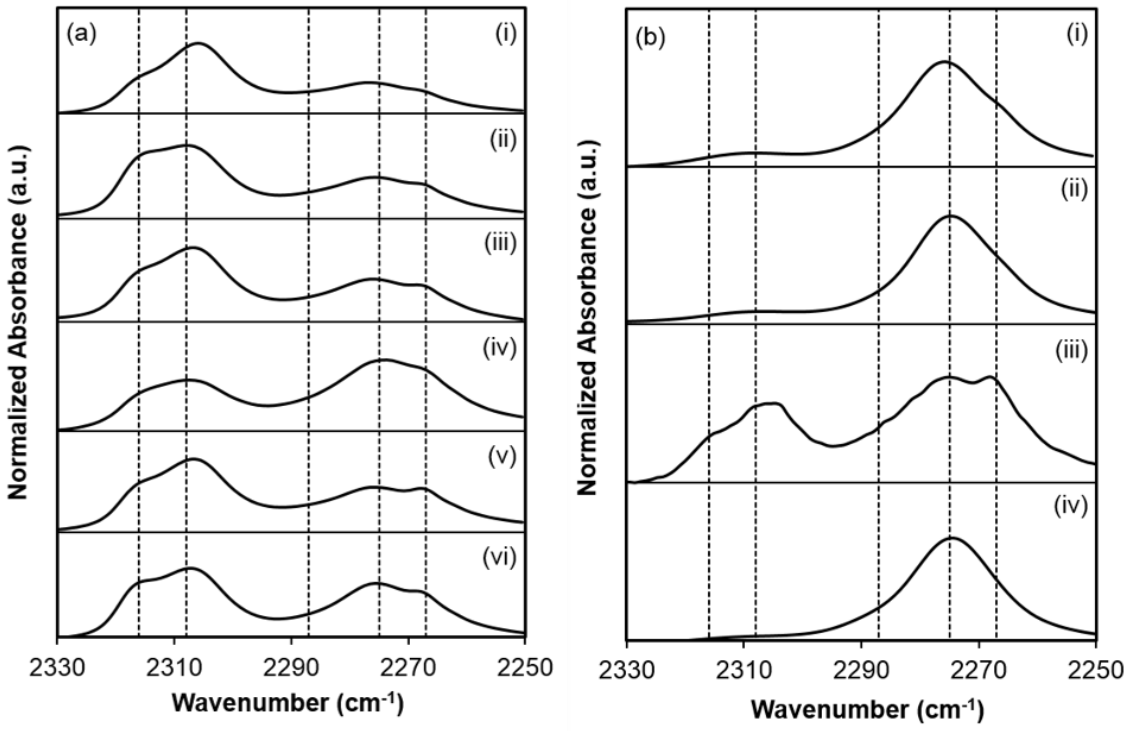

Figure 2.46: IR difference spectra at CD_3CN saturation coverages (relative to the CD_3CN-free wafers and normalized to the maximum intensity of each spectra for clarity). (a) Spectra for (i) Sn-Beta-F-100, (ii) Sn-Beta-F-105, (iii) Sn-Beta-F-110, (iv) Sn-Beta-F-140, (v) Sn-Beta-F-170, (vi) Sn-Beta-F-220. (b) Spectra for (i) Sn-Beta-OH-170, (ii) Sn-Beta-OH-200, (iii) SnO_2/Si-Beta, (iv) Sn-xerogel. Dashed lines shown at 2316 cm^{-1}, 2308 cm^{-1}, 2287 cm^{-1}, 2275 cm^{-1} and 2265 cm^{-1}.

Table 2.9: Peak areas at saturation for the 2316 cm^{-1}, 2308 cm^{-1}, 2287 cm^{-1}, 2275 cm^{-1} and 2265 cm^{-1} peaks for all Sn samples in this study.

Sample	2316 cm^{-1} [Area cm^{-1}]	2308 cm^{-1} [Area cm^{-1}]	2287 cm^{-1} [Area cm^{-1}]	2275 cm^{-1} [Area cm^{-1}]	Moles 2287 cm^{-1} sites [per Sn]
Sn-Beta-F-100	0.22	1.19	0.27	043	0.078
Sn-Beta-F-105	0.36	1.96	0.33	2.24	0.079
Sn-Beta-F-110	0.92	3.36	1.26	1.17	0.23
Sn-Beta-F-140	0.73	2.22	0.34	3.24	0.094
Sn-Beta-F-170	0.37	2.47	0.37	1.39	0.096
Sn-Beta-F-220	0.50	1.81	1.26	1.17	0.41
Sn-Beta-OH-170	0.74	0.88	0.17	12.4	0.052
Sn-Beta-OH-200	0.30	2.03	0.07	24.5	0.019
SnO_2/Si-Beta	0.20	1.49	0.08	1.95	0.0059
Sn-xerogel	0.066	0.223	1..66	4.12	0.42

2.7.10 Kinetic Measurements of Glucose Isomerization on Zeolite Samples.

A more detailed kinetic and mechanistic study of glucose-fructose isomerization on Lewis acids has been previously reported [35]; here, we include an abridged discussion to supplement the data and analysis in this manuscript. Aqueous-phase glucose (G) adsorbs onto vacant Sn sites (*) and forms ring-opened intermediates on Sn sites (G*) in a quasi-equilibrated step (Step 1, Fig. 2.9), followed by kinetically-relevant intramolecular 1,2-hydride shift to form ring-opened fructose intermediates (F*) (Step 2, Fig. 2.9) that undergo quasi-equilibrated ring-closing and desorption into the aqueous phase (Step 3, Fig. 2.9). Two water molecules sequentially adsorb onto Sn sites (W*, 2W*) in quasi-equilibrated steps (Steps 4-5, Fig. 2.9), and 2W* is assumed to be the most abundant surface intermediate (MASI) during catalysis in liquid water [35]. These mechanistic assumptions lead to glucose-fructose isomerization turnover rates ($\eta << 1$) per total number of active Sn sites ([L]) given by [35]:

$$\frac{r_{isom}}{[L]} = \frac{\gamma_{2W*}\gamma_G\gamma_*}{\gamma_W^2 c_W^2 \gamma_*}\frac{k_2 K_1}{K_4 K_5} c_G = k_{isom} c_G \tag{2.5}$$

In this equation, γ_j are activity coefficients for species j, c_W is the water concentration, c_G is the glucose concentration, K_j is the equilibrium coefficient for a given step, and k_2 is the isomerization rate constant for the kinetically-relevant hydride shift step. This turnover rate equation gives a first-order dependence in aqueous glucose concentration, and an effective first order isomerization rate constant that can be decomposed to give the following dependence on Gibbs free energies of reactive intermediates and transition states in the mechanism, where α is a constant that contains the product of the activity coefficients for reactants and intermediates as shown in equation 2.5 [35]:

$$k_{isom} = \alpha\frac{K_1 k_2}{K_4 K_5} = \alpha\frac{k_B T}{h} e^{-((\Delta G^o_{\ddagger,2*} + 2\Delta G^o_W) - (\Delta G^o_G + \Delta G^o_{2W*})/RT)} \tag{2.6}$$

Initial glucose isomerization turnover rates (per mol Sn, 373 K) were measured on Sn-Beta samples in batch reactors under autogenous pressure according to methods

reported previously and described in the main text [35]. Initial rates were measured by fitting a reversible, first-order rate expression integrated in a batch reactor model to the temporal evolution of measured monosaccharide concentrations, and extrapolated to initial times using the model derived previously [35]. Initial rates calculated from data collected under differential conditions (<5% conversion) and a differential reactor model (with corrections for approach-to-equilibrium) give the same value, within experimental error, as the initial rates calculated by extrapolating batch reactor data to initial time using the batch reactor model.

Here, we focus on measurements of initial rates of glucose-fructose isomerization. At initial times, high fructose to mannose (F/M) selectivities are expected for Sn-Beta samples containing predominantly framework Sn sites, as mannose is formed only as a series product via reverse hydride shift from fructose, instead of via direct 1,2-carbon shift from glucose in parallel [32]. After 600 s of reaction time, mannose formation was undetectable on all samples in this study, indicating that initial mannose formation rates are negligible and can be neglected from initial rate calculations. Therefore, initial rates of fructose formation are indistinguishable (within 10%) from initial rates of glucose consumption for all samples in this study.

The H/D kinetic isotope effect (KIE) was measured with glucose-D2 reactants, and is predicted to be 2.1 (at 373 K) if the intramolecular 1,2-hydride shift is kinetically-relevant (C-H scissoring frequency of 1500 cm-1) [34]. In the presence of strong internal reactant mass transfer limitations, the observed H/D KIE value would be equivalent to the square root of the kinetically-relevant value (∼1.4 at 373 K) [35]. Measured H/D KIE values were between 2.0-2.4 for all Sn-Beta samples tested in this study, consistent with the absence of internal mass transfer limitations [35].

The H/D KIE value was also measured on a Sn-Beta-F-170 pre-poisoned with pyridine to be 2.3 ± 0.2, as expected for kinetically-limited isomerization rates, suggesting the decrease in observed isomerization rates with increasing amounts of pyridine pre-titration (Fig. 2.10) does not reflect the introduction of diffusion limitations for glucose reactants. Initial isomerization turnover rates (373 K, normalized to rates

on untitrated samples) are plotted in Figure 2.47 against the moles of pyridine adsorbed per gram, per micropore volume, and per surface area of Sn-Beta-F-110 and Sn-Beta-F-170. If occlusion of micropore volume were the mechanism by which pyridine titration suppressed catalytic reactivity, then the amount of pyridine titrants adsorbed onto Sn-Beta-F-110 and Sn-Beta-F-170 (nearly identical N_2 micropore volumes of 0.22 and 0.21 $cm^3\ g^{-1}$, respectively) should be similar on a per gram or per micropore volume basis. Analogously, if occlusion of pore mouths at external crystallite surfaces by adsorbed pyridine were responsible for the decrease in isomerization rates, then the amount of pyridine required to fully suppress rates would be similar on an external surface area basis, which can be estimated from crystallite sizes (approximating the Beta crystallites as spheres) derived from SEM images (Fig. 2.48). The amount of pyridine required to fully suppress rates on both Sn-Beta samples does not agree with any of these properties, suggesting that occlusion of external pore mouths or internal void spaces cannot account for the decrease in reactivity with increasing pyridine coverage.

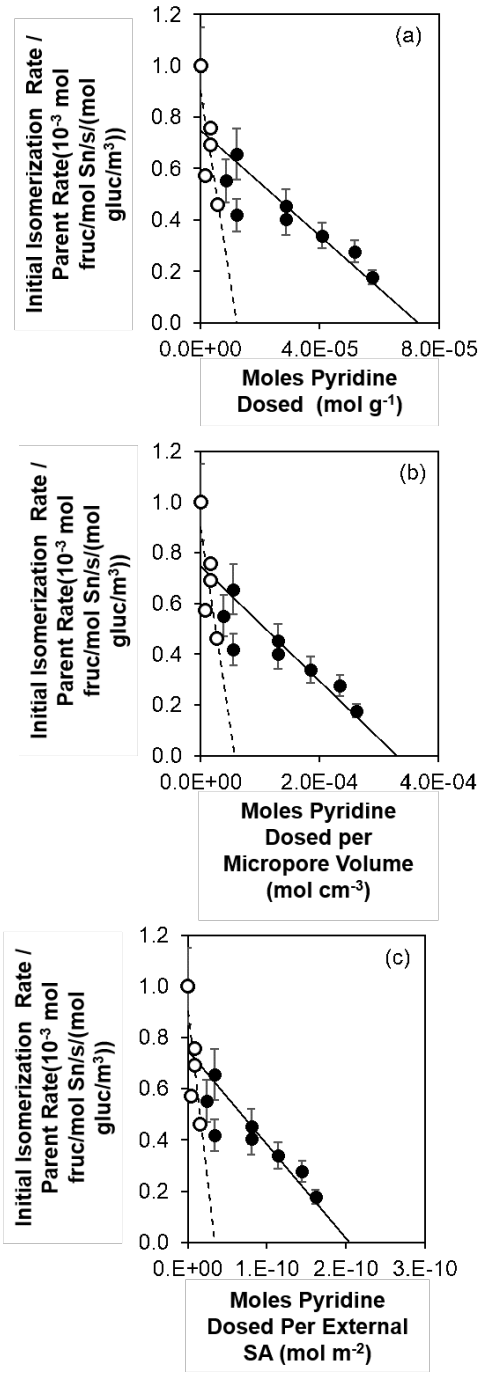

Figure 2.47: Initial glucose isomerization rates (373 K, normalized to untitrated samples) as a function of pre-adsorbed pyridine (a) per gram, (b) per micropore volume, and (c) per external surface area for Sn-Beta-F-110 (closed circles) and Sn-Beta-F-170 (open circles).

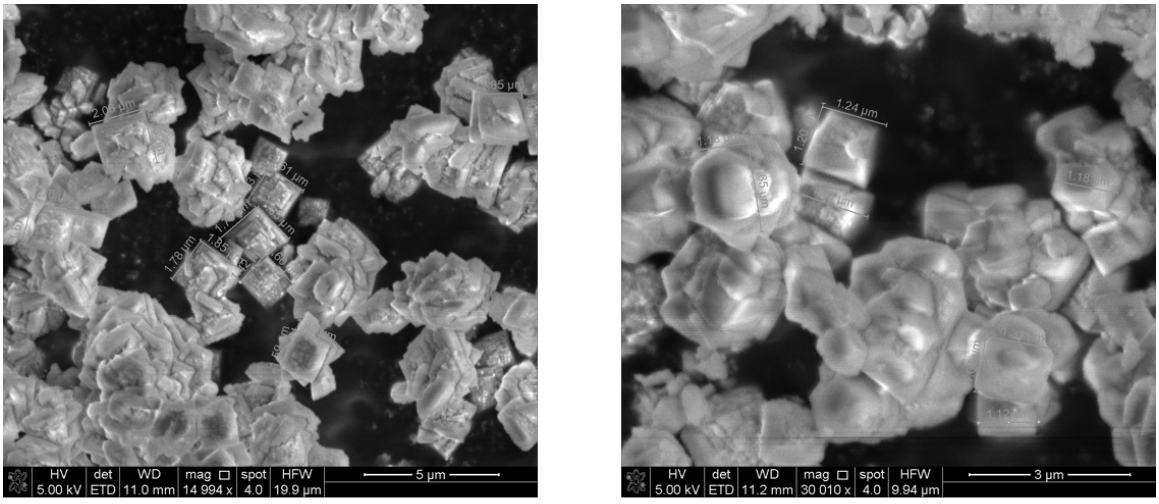

Sn-Beta-F-110 **Sn-Beta-F-170**

Figure 2.48: Scanning electron microscope images of Sn-Beta-F-110 and Sn-Beta-F-170.

Measurements of water adsorption isotherms on Sn-Beta zeolites and subsequent calculations of the volume of water adsorbed at a relative pressure of 0.2, a reference pressure reflecting complete micropore filling of hydrophobic zeolites with cyclohexane, were used to estimate the hydrophobicity of the zeolites in this study. The volume of water adsorbed within low-defect, Sn-Beta-F samples was ∼6x smaller, on average, than that adsorbed within post-synthetically prepared Sn-Beta-OH samples. The volume of water adsorbed among Sn-Beta-F samples, however, varied by 3.4× (0.005-0.017 $cm^3\ g^{-1}$). Glucose isomerization rate constants (per open Sn site, 373 K) generally decreased with increasing silanol content among Sn-Beta-F samples (Fig. 2.50), although significant scatter is observed in the correlations shown in Fig. 2.50 suggesting other structural heterogeneities among the Sn-Beta-F samples may influence isomerization rates. The silanol densities (mol g^{-1}) measured from IR peaks at 2275 cm^{-1} in spectra of CD_3CN-saturated samples and their E value (0.74 cm μmol^{-1}, Section 2.7.9) was directly proportional to the molar water uptake at P/P_0 = 0.2 after accounting for water bound to all Sn sites (Fig. 2.49(a)) or to Lewis

acidic Sn sites (Fig. 2.49(b)), assuming 2:1 H_2O:Sn binding stoichiometry (^{119}Sn NMR evidence [34]).

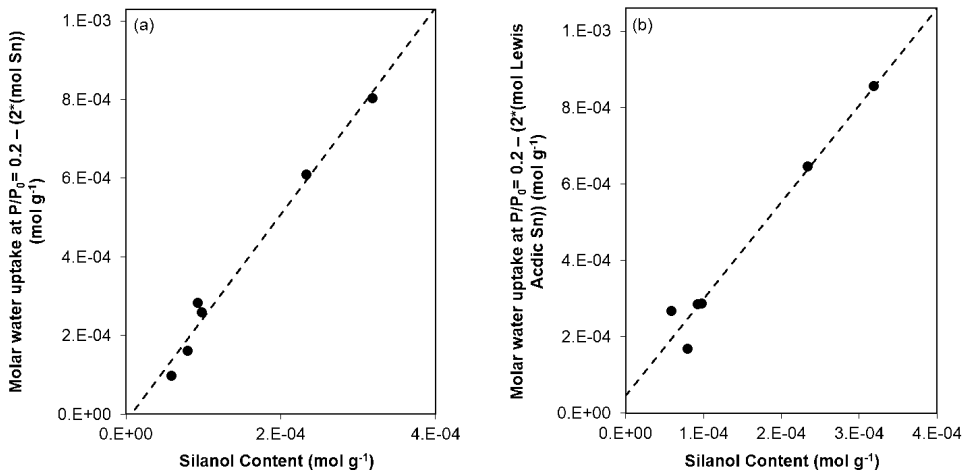

Figure 2.49: Molar water uptake measured at P/P_0=0.2, after subtracting the contribution from (a) total Sn (estimated by AAS) or (b) Lewis acidic Sn assuming 2:1 H_2O:Sn binding stoichiometry, plotted as a function of the silanol content.

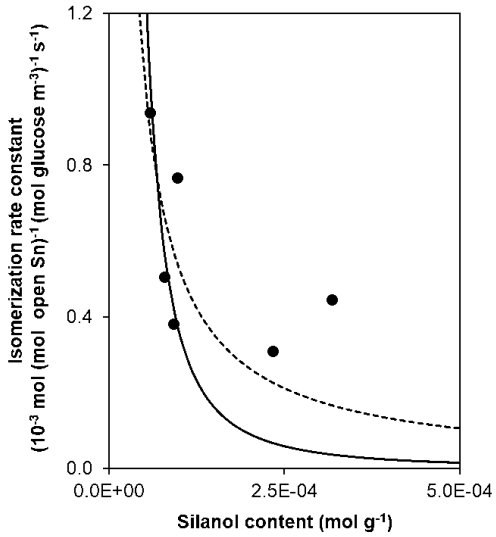

Figure 2.50: Rate constants per open Sn sites for all Sn-Beta-F samples as a function of the silanol content measured using the E value for the peak for CD_3CN bound to silanol sites centered at 2275 cm^{-1}. Trendlines show correlation of rate constant with 1/(mol SiOH g^{-1}) (dashed line) and 1/(mol SiOH g^{-1})^2 (solid line) determined by linear regression.

Table 2.10: Site and structural characterization data for the samples in this study.

Sample	V_{ads} at P/P_0 = 0.2[a]	Rate Constant Per Open Sn Sites 10^3 mol fructose (mol open Sn^{-1} (mol glucose $m^{-3})^{-1}$ s^{-1}[b]
Sn-Beta-F-100	0.0069	0.94
Sn-Beta-F-105	0.015	0.31
Sn-Beta-F-110	0.0095	0.38
Sn-Beta-F-140	0.017	0.44
Sn-Beta-F-170	0.0073	0.77
Sn-Beta-F-220	0.0048	0.50
Sn-Beta-OH-170	0.036	0.0083
Sn-Beta-OH-200	0.092	0.015

[a]Errors are ± 5%.
[b]Errors are ± 15%.

3. CONTROLLED INSERTION OF TIN ATOMS INTO ZEOLITE FRAMEWORK VACANCIES AND CONSEQUENCES FOR GLUCOSE ISOMERIZATION CATALYSIS

3.1 Abstract

The incorporation of tin heteroatoms within framework vacancy defects of dealuminated Beta zeolites via stannic chloride reflux in dichloromethane solvent (333 K) enables preparing Sn-Beta zeolites comprising a wide range of Sn content (Si/Sn = 30–144; 1.4–6.1 wt.% Sn) and >4x higher framework Sn densities than reported (Si/Sn > 120) for reflux in isopropanol solvent (383 K). Silanol defects form hydrogen bonds with isopropanol but not with dichloromethane under reflux conditions, evident in the evolution of adsorbed isopropanol (∼5x per vacancy) but not dichloromethane during temperature programmed desorption of dealuminated zeolites saturated with either solvent at ambient, and in IR features for perturbed hydroxyl stretches (∼3350 cm^{-1}) and C-H stretches (∼2700–3000 cm^{-1}) that were retained after dealuminated zeolites were saturated with isopropanol and evacuated at 383 K. Dichloromethane-assisted tin grafting provides a route to precisely control the density of framework Sn sites and residual vacancy defects in Sn-Beta, up to the point of grafting virtually every framework vacancy with Sn. Open Sn sites ($(OSi)_3$-Sn-(OH), $\nu(CD_3C{\equiv}N)$: 2316 cm^{-1}), quantified from IR spectra collected after CD_3CN titration (303 K), are preferentially incorporated over closed Sn sites ($Sn(OSi)_4$, $\nu(CD_3C{\equiv}N)$: 2308 cm^{-1}) at low Sn densities via grafting in dichloromethane solvent, suggesting that this preparation method can tune the open-to-closed framework Sn site ratio more systematically than hydrothermal synthesis methods. Open Sn sites are dominant active sites for aqueous-phase glucose-fructose isomerization; consequently, isomerization turnover rates (per total Sn) decrease systematically with increasing Sn content. Initial isomerization

rates (per open Sn) are invariant (within ∼2x, 373 K) among twelve Sn-Beta samples of varying Sn content (Si/Sn = 30–144), the behavior expected of a single-site catalyst in which open framework Sn sites are the loci of catalytic reactivity. First-order isomerization rate constants are 15–50x lower (373 K) when open Sn sites are confined within high-defect than within low-defect Beta micropores, consistent with previous reports that aqueous-phase sugar isomerization cycles turn over at faster rates within hydrophobic, low-defect micropores. These findings clarify the consequences of liquid-phase reflux procedures on the coordination of tin heteroatoms incorporated within zeolite framework vacancies, and underscore the requirement to quantify putative active site structures in order to rigorously normalize measured rate data prior to kinetic or mechanistic interpretation.

3.2 Introduction

Large-pore molecular sieves (>0.7 nm diameter) containing Lewis acidic heteroatoms, such as pure-silica Beta zeolites with framework Sn^{4+} centers (Sn-Beta), catalyze stereoselective isomerization reactions of monosaccharides [37] and disaccharides [35], among other reactions of oxygenated molecules containing carbonyl moieties [5, 7, 55, 115]. Sn-Beta zeolites crystallize hydrothermally in fluoride media containing tetraethylammonium cations (TEA^+) over the course of 20 days or longer (413 K) [5, 11], or in less than 2 days upon judicious addition of seed material [12], and typically contain framework Sn atoms that are present in low densities (Si/Sn > 100; <2 wt.% Sn) and that concentrate toward external crystallite surfaces when crystallized in the absence of seeds [29]. Sn-Beta zeolites (Si/Sn > 100; <2 wt.% Sn) also crystallize via steam-assisted conversion of stannosilicate gels containing TEA^+ cations using either fluoride (413 K, 5 days) [13, 14] or hydroxide (453 K, 6 hours) [15] anions as mineralizers. During hydrothermal crystallization, fluoride anions are occluded together with TEA^+ cations to form low-defect frameworks with predominantly siloxane (Si-O-Si) connectivities that are non-polar and preclude the formation of extended water structures within micropores under conditions typically used for aqueous-phase catalysis [16]. In contrast, hydroxide mineralizers form framework siloxy defects (SiO^-) to compensate TEA^+ cations that, after treatments to remove occluded organic compounds, become silanol defect (SiOH) sites that stabilize intrapore networks of hydrogen-bonded water [16, 116, 117].

Alternative procedures to hydrothermal crystallization of Sn-Beta have focused on post-synthetic insertion of Sn atoms into framework vacancy defects via vapor-phase deposition [17], liquid-phase grafting [22–24], or solid-state exchange [18–21], each with different consequences for the coordination and density of framework Sn atoms and of residual silanol defects. Sn-Beta containing tetrahedral Sn sites, which give rise to an absorption band centered at ∼200 nm in UV-Visible spectra of dehydrated samples, can be prepared at low Sn densities (Si/Sn > 120, <1.6 wt.% Sn)

via reflux of stannic chloride in isopropanol solvent with dealuminated Beta zeolites (initial Si/Al = 12.5) [22, 23]. The incorporation of higher densities of Sn within dealuminated Beta zeolites via liquid-phase reflux procedures, either by increasing the Sn precursor concentration in isopropanol or by addition of water to the reflux solution, have been reported to form extraframework octahedral SnO_2 domains that give rise to a band centered at ∼255 nm in UV-Visible spectra [22]. The preferential incorporation of Sn precursors within only a fraction of available framework vacancy defects (Sn/vacancy = 0.11), beyond which non-specific Sn deposition led to the formation of extraframework SnO_2, was proposed to reflect Sn grafting within specific framework tetrahedral site (T-site) locations by Dijkmans et al. [22]. Sn-Beta with higher framework Sn content (Si/Sn = 35, 5 wt.% Sn) can be prepared from dealuminated Beta zeolites of the same composition (initial Si/Al = 12.5), however, by grafting anhydrous $SnCl_4$ in inert atmosphere and subsequently removing (by methanol washing) extraneous Sn species that form SnO_2 [24], or by solid-state exchange of $Sn(CH_3CO_2)_2$ precursors [18,20]. Collectively, these findings suggest that reported liquid-phase reflux methods to incorporate Sn precursors within framework vacancy defects provide limited control over the framework Sn density in Sn-Beta zeolites.

Framework Sn sites within Sn-Beta zeolites catalyze the isomerization of glucose to fructose via intramolecular 1,2-hydride shift [51]: yet, ammonia [32] and pyridine [26] pre-poisoning experiments of hydrothermally-crystallized samples have shown that catalytic reactivity becomes suppressed after only a fraction of framework Sn sites are titrated. Characterization of Sn-Beta samples with suppressed isomerization reactivity (353 K) upon ammonia pre-poisoning indicates that ammonia selectively titrates tetrahedral Sn sites that perturb infrared C≡N stretches in adsorbed CD_3CN to 2316 cm^{-1} and that appear as ^{119}Sn NMR resonances at -424 ppm, which have been assigned to Sn sites in open coordination ($(SiO)_3$-Sn-(OH)) [32]. Pyridine titration suppressed aqueous-phase glucose isomerization rates (373 K), measured at initial reaction times and in the absence of intrazeolite transport artifacts, when present at

coverages equivalent to the number of open Sn sites quantified *ex situ* from CD_3CN IR spectra (2316 cm^{-1}) on two different Sn-Beta zeolites [26]. These titration experiments provide evidence that open framework Sn sites are the dominant active site for glucose-fructose isomerization in Sn-Beta, consistent with theory predictions of 20-40 kJ mol^{-1} lower activation enthalpies for intramolecular 1,2-hydride shift steps on open than on closed framework Sn sites (Sn-$(OSi)_4$) [34, 64, 65]. Moreover, homogeneous analogs of open framework Sn sites with a proximal silanol group isomerize glucose selectively via intramolecular 1,2-hydride shift to form fructose, in contrast to homogeneous methyl-ligated tin silsesquioxane complexes that mimic closed framework Sn structures and instead isomerize glucose selectively via intramolecular 1,2-carbon shift routes to form mannose [118, 119].

Among post-synthetically prepared Sn-Beta zeolites, aqueous-phase glucose-fructose isomerization rates (per total Sn) measured under differential (373 K, 5% (w/w) glucose, initial time) [120] and integral (383 K, 10% (w/w) glucose, 15 minutes) [22] reaction conditions, have been reported to decrease systematically with increasing framework Sn content. This behavior has been rationalized by invoking intrazeolite mass transfer limitations [22, 23] or heterogeneities in framework Sn site reactivity conferred by different T-site locations [22, 52, 120], as studied recently using ^{119}Sn dynamic nuclear polarization (DNP) NMR to identify probable Sn substitution among different T-sites of Beta zeolites [28]. An analogous decrease in turnover rates (per total Sn) for 1,3-dihydroxyacetone isomerization to methyl lactate with increasing Sn content, among Sn-Beta samples prepared via reflux with anhydrous $SnCl_4$, was speculated to reflect differences in open and closed Sn site densities [24]. The incomplete incorporation of Sn atoms within vacancy defects of zeolite Beta using isopropanol-assisted grafting (Sn/vacancy = 0.11) [22], together with structural models fitted to Sn extended X-ray absorption fine structure (EXAFS) spectra, has been taken as evidence to support alternate proposals that Sn incorporation occurs at specific vacancy locations that form frustrated Lewis pairs between Sn centers with three framework bonds and a distant siloxy (-OSi-) group [52]. Precise knowledge about the densities

and coordination of Sn sites formed by liquid-phase grafting procedures, together with glucose isomerization turnover rate measurements uncorrupted by transport artifacts and normalized rigorously by the number of reactive Sn sites, are thus required to clarify the structural and catalytic differences prevalent among Sn-Beta zeolites prepared hydrothermally and via post-synthetic routes.

Here, we report methods to prepare Sn-Beta zeolites post-synthetically via grafting of Sn precursors under dichloromethane reflux (333 K), which enables incorporating Sn heteroatoms within virtually all framework vacancies in a given dealuminated Beta zeolite. We provide evidence that the incorporation of framework Sn via grafting under isopropanol reflux is inhibited because of competitive adsorption between Sn precursors and isopropanol at framework vacancy defects. Such inhibition does not occur with dichloromethane reflux, which enables precisely controlling the framework Sn content and the residual vacancy defect density in post-synthetically prepared Sn-Beta zeolites, and provides a facile route to prepare Sn-Beta zeolites with high framework Sn densities (Si/Sn = 30, 6.1 wt.% Sn). IR spectra of samples titrated with CD_3CN are used to quantify open (2316 cm^{-1}) and closed (2308 cm^{-1}) Sn sites [26], providing evidence that liquid-phase grafting procedures preferentially form open Sn sites at low framework Sn densities, with the consequence that increasing framework Sn content leads to systematic decreases in glucose isomerization turnover rates (373 K) when normalized by total Sn content. We show that glucose isomerization turnover rates (per open Sn, 373 K) are essentially invariant (within $\sim$2x) among twelve Sn-Beta zeolites prepared post-synthetically via dichloromethane reflux, and are consistently lower by 15-50$\times$ (373 K) than turnover rates among hydrothermally-synthesized Sn-Beta zeolites for the 21 samples studied here, providing further evidence for the dominant effects of open Sn sites and intrazeolite silanol defect density on aqueous-phase sugar isomerization catalysis [26].

3.3 Experimental Methods

3.3.1 Catalyst synthesis

Al-Beta zeolites were synthesized in hydroxide media (Al-Beta-OH) with different Si/Al ratios by adapting the procedure reported by Chang et al. [12]. In a typical synthesis, tetraethylammonium hydroxide (TEAOH, Sigma Aldrich, 35%) and Ludox HS-30 colloidal silica (Sigma Aldrich, 30%) were added to a perfluoroalkoxy alkane (PFA) container (Savillex Corp.) that was covered and stirred for 1 h at ambient conditions. Then, sodium hydroxide (NaOH, Avantor, 98%) was added to deionized water (18.2 MΩ and stirred until completely dissolved, followed by the addition of aluminum isopropoxide (Sigma Aldrich, 98%) to the synthesis gel. The resulting gel solution was covered and stirred for 24 h at ambient conditions and the target H2O/SiO2 ratio was obtained by complete evaporation of ethanol and partial evaporation of water. The final gel composition was 1 SiO_2: x Al_2O_3: 13.24 H_2O: 0.18 TEAOH: 0.014 Na_2O (where x was 0.00165, 0.01, and 0.005 for target solid Si/Al ratios of 30, 50, and 100, respectively). The gel was placed into a Teflon-lined stainless steel autoclave and heated to 413 K for 7 days under static conditions. The recovered solids were washed thoroughly with water and acetone, isolated by centrifugation, and dried overnight at 373 K. Afterward, the solids were treated at 853 K (0.0167 K s^{-1}) for 10 h in air (Ultra Zero Grade, Indiana Oxygen, 1.67 cm^3 s^{-1} (g zeolite)$^{-1}$) in a muffle furnace (Nabertherm P300).

Al-Beta zeolites were also synthesized in fluoride media (Al-Beta-F) with a target Si/Al = 50. Using a similar procedure, tetraethylammonium hydroxide was mixed with tetraorthosilicate (TEOS, Sigma Aldrich, >98 wt.%) and stirred for 1 h in a covered PFA container, followed by addition of deionized water and aluminum isopropoxide. The synthesis gel was stirred for 24 h in the covered PFA container. After reaching the desired H_2O/SiO_2 by evaporation of ethanol and water, hydrofluoric acid (HF, Sigma Aldrich, 48 wt.%) was added to the synthesis gel and stirred manually with a Teflon spatula for ∼300 s. Dealuminated Beta zeolites (initial Si/Al = 54)

were used as seeds for this synthesis (4 wt.% of SiO_2). The final gel molar ratio was 1 SiO_2: 0.02 Al_2O_3: 7.52 H_2O: 0.54 TEAOH: 0.54 HF. As in the case of Al-Beta-OH syntheses, the gel was placed into a Teflon-lined stainless steel autoclave and heated to 413 K for 7 days under static conditions. The recovered solids were washed thoroughly with water and acetone, isolated by centrifugation, and dried overnight at 373 K. Afterward, the solids were treated at 853 K (0.0167 K s^{-1}) for 10 h in air (1.67 cm^3 s^{-1} (g zeolite)$^{-1}$) in a muffle furnace.

Dealumination treatments of Al-Beta zeolites were performed using nitric acid. 25 cm^3 of concentrated nitric acid (HNO_3, Avantor, 69%) were added to 1 g of Al-Beta and stirred in a covered PFA jar for 16 h at 353 K. The recovered solids were washed thoroughly with water until the pH of the supernatant was constant, isolated by centrifugation, and dried overnight at 373 K.

Dealuminated Beta zeolites were used for post-synthetic grafting of tin precursors via isopropanol reflux. In a typical procedure, a dealuminated zeolite sample was placed into a three-neck round-bottom flask (500 cm^3) with a septum stopper (white rubber, Ace Glass) on one of the openings, connected to a Schlenk line, and dried overnight at 423 K under vacuum conditions (∼0.005 kPa, Oerlikon Trivac 140002E2). Separately, isopropanol (Sigma Aldrich, 99.5%) was dried using molecular sieves (W. R. Grace, Type 3A, Grade 562, 4-8 mesh) for 72 h in inert atmosphere (Argon, Indiana Oxygen, 99.999%). Solutions of tin (IV) chloride (0.027–0.081 mol Sn (g zeolite)$^{-1}$) were prepared by adding tin (IV) chloride pentahydrate ($SnCl_4 \cdot 5H_2O$, Sigma Aldrich, 98%) in a pear-shaped vial, sealed with a septum, and subsequent addition of dry isopropanol via cannula transfer (76 cm, 15 gauge, Ace Glass). Then, dry isopropanol (100 cm^3 (g zeolite)$^{-1}$) and the tin (IV) chloride solution were added to the round-bottom flask through a moisture-free cannula transfer and heated to 383 K for 7 h under reflux conditions in argon.

Dealuminated Beta was also used to perform post-synthetic grafting procedures using dichloromethane (Sigma Aldrich, 99.8%) and tin (IV) chloride ($SnCl_4$, Sigma Aldrich, 1 M in dichloromethane). As in the case of isopropanol, the dichloromethane

solvent was dried using molecular sieves in argon for 72 h prior to grafting procedures. The addition of dichloromethane to the round-bottom flask was performed through moisture-free cannula transfer, followed by Sn precursor addition (0.001–0.040 mol Sn (g zeolite)$^{-1}$) with 1 or 10 cm^3 syringes (Becton, Dickinson, and Company) with attached precision needles (Becton, Dickinson, and Company). Then, the solution was heated to 333 K for 7 h under reflux conditions in argon.

After reflux procedures were completed, solids were recovered by centrifugation, washed thoroughly with ∼120 cm^3 (g zeolite)$^{-1}$ of methanol (Sigma Aldrich, 99.9%) or isopropanol, and dried overnight at 373 K. The recovered solids were treated at 473 K (0.05 K s^{-1}) for 6 h and 823 K (0.05 K s^{-1}) for 6 h in air (1.67 cm3 s^{-1} (g zeolite)$^{-1}$) in a muffle furnace.

3.3.2 Catalyst Characterization

Powder X-ray diffraction (XRD) patterns were collected in the range 4–40° of 2θ (scan rate of 0.0044° s^{-1} and a step size of 0.02°) using a Rigaku Smartlab X-ray diffractometer with a Cu Kα X-ray source (1.76 kW) and an ASC-6 automated sample changer.

Vapor-phase N_2 (77 K), H_2O (293 K), and CH_3OH (293 K) adsorption isotherms were collected with a Micromeritics ASAP2020 instrument. Typically, ∼0.04 g of zeolite sample, pelleted and sieved to retain particles between 180–250 μm in diameter, were degassed by heating under vacuum (<0.0007 kPa) to 393 K for 2 h and 623 K for 8 h prior to adsorption measurements. The micropore volume was determined from semi-log derivative analysis of the isotherm ($\delta(V_{ads}/g)/\delta(\log(P/P_0)$ vs. $\log(P/P_0)$), where the first maximum represents the micropore filling transition and the subsequent minimum represents the end of micropore filling.

Scanning electron microscopy (SEM) images were taken in a FEI Quanta 3D FEG Dual-beam SEM with an Everhart-Thornlev attachment for high vacuum imaging. Images were taken using the focused beam mode at 5 kV with a 4 μm spot size.

Atomic absorption spectroscopy (AAS) was performed with a Perkin Elmer AAnalyst 300 to determine bulk elemental compositions. The instrument was calibrated prior to measurements with standards for each metal (Alfa Aesar, TraceCERT, ±4ppm). Samples (∼0.02 g) were dissolved overnight in 2 g of HF (48 wt.%, Alfa Aesar) and diluted with ∼50 g of deionized water. The measured values of absorbance were collected at 284.0 nm and 396.2 nm in an acetylene/nitrous oxide flame for Al and Sn, respectively. The Si/M ratios were calculated using the unit cell formula for the Beta framework topology. The fraction of vacancies grafted (Sn/vacancy) were calculated from the molar ratio of Sn to the Al present initially, assuming that every Al atom was removed from the framework and formed a vacancy available for grafting.

Diffuse reflectance UV-Vis spectra were collected using a Varian Cary 5000 spectrometer with an *in situ* Harrick Praying Mantis cell. Spectra were collected at ambient temperatures under dry helium flow (4.17 cm^3 s^{-1} (g zeolite)$^{-1}$), after dehydration at 523 K (∼0.5 K s^{-1}) under dry helium flow (4.17 cm^3 s^{-1} (g zeolite)$^{-1}$) for 0.5 h, and after rehydration by cooling (∼-0.4 K s^{-1}) the system under wet (saturator at ambient conditions) helium (4.17 cm^3 s^{-1} (g zeolite)$^{-1}$, 3% H_2O) [26]. All spectra were corrected with poly(tetrafluoroethylene) (PTFE, 1 μm, Sigma Aldrich) as the 100% reflectance standard at all conditions (ambient, dehydrated, rehydrated) and converted to absorption spectra using the Kubelka-Munk function (F(R)).

Interactions between silanol groups and different solvents were studied by stirring dealuminated Beta in isopropanol and dichloromethane for 7 h at ambient conditions, recovering the solids by centrifugation, and then drying in air at ambient conditions. Dried samples were used to perform temperature programmed desorption (TPD) experiments with a Micromeritics Autochem II 2920 Analyzer equipped with an Agilent 5973N mass selective detector (MSD) to identify gaseous species desorbed from catalyst samples. Solvent-treated dealuminated zeolites (∼0.03 g, sieved to 180–250 μm) were placed in a U-tube reactor and supported between two quartz wool plugs. The samples were held for 1 h in helium (0.83 cm^3 s^{-1}, Indiana Oxygen, 99.999%) at ambient conditions to desorb weakly bound and physisorbed molecules prior to TPD

(heated to 873 K, 0.167 K s^{-1}) and data collection. The isopropanol that desorbed from the dealuminated Beta was sent to the MSD through heated gas lines (>383 K) and quantified by integration of the TPD peak centered at ∼400 K. A response factor for isopropanol was generated by bubbling helium through a saturator containing isopropanol at various temperatures (303 K, 308 K, or 313 K) to generate known partial pressures, followed by dosing into a sample loop (0.5 cm^3) and injection into a helium (0.83 cm^3 s^{-1}) stream that was sent to the MSD for quantification of the signal at m/z = 45. After every TPD or isopropanol pulse, the sample loop (0.5 cm^3) was filled with argon (Indiana Oxygen, 99.999%) and injected into a helium stream (0.83 cm^3 s^{-1}) for correction of any drift in the instrument.

Infrared (IR) spectra were collected using a Nicolet 4700 spectrometer with a Hg-Cd-Te (MCT, maintained at 77 K by liquid N_2) detector by averaging 64 scans at 2 cm^{-1} resolution from 4000 to 400 cm^{-1} and were taken relative to an empty cell background reference collected under dynamic vacuum (rotary vane rough pump, Alcatel 2008A, <0.01 kPa) at 303 K. Self-supporting wafers of zeolite samples (0.02–0.04 g cm^{-2}) were sealed within a custom-built quartz IR cell with CaF_2 windows, which was inserted into a mineral-insulated resistive heating coil (ARi Industries) encased in an alumina silicate ceramic chamber (Purdue Research Machining Services). The quartz IR cell was connected to a custom glass vacuum manifold that was used for sample pretreatment and exposure to controlled amounts of CD_3CN (Sigma-Aldrich, 99.96% D-atom). Prior to measurement of spectra at 303 K, wafers were treated in flowing dry air (6.66 cm^3 s^{-1} (g zeolite)$^{-1}$) purified by an FTIR purge gas generator (Parker Balston, <1 ppm CO_2, 200 K H_2O dew point) to 723 K (0.083 K s^{-1}) for 1 h, and then held under dynamic vacuum (rotary vane rough pump, Alcatel 2008A, <0.01 kPa) at 723 K for 1 h before cooling under dynamic vacuum to 303 K. Spectra for the ν(OH) region were collected prior to CD_3CN adsorption under static vacuum (∼0.01 kPa) at 303 K. After sufficient dosing to saturate the samples until equilibrium with a residual gas phase pressure of CD_3CN (0.07–0.67 kPa), samples were exposed to dynamic vacuum (at 303 K for CD_3CN) in order to remove gas-phase and weakly-bound species,

which occurred when the pressure was recorded as 0.0 kPa. IR spectra reported here were baseline-corrected and normalized to combination and overtone modes of zeolite Si-O-Si stretches (1750–2100 cm^{-1}). IR peaks for CD_3CN bound to open (2316 cm^{-1}) and closed (2308 cm^{-1}) Sn sites, bound to Sn sites in highly-defective oxide surfaces (2287 cm^{-1}), hydrogen-bound to Si-OH sites (2275 cm^{-1}), and physisorbed or gas phase CD_3CN (2265 cm^{-1}) overlapped with each other and required deconvolution into individual components (Fig. 3.42). Integrated molar extinction coefficients ($\mathcal{E}$) for CD_3CN bound to open Lewis acid sites ($\mathcal{E}$ = 1.04 cm μmol^{-1}, 2316 cm^{-1}) and to closed Lewis acid sites ($\mathcal{E}$ = 2.04 cm μmol^{-1}, 2308 cm^{-1}) on Sn-Beta determined in Harris et al. [26] were used to quantify the number of Lewis acid sites titrated by CD_3CN using integrated IR peak areas and the following equation:

$$Sitedensity(\mu molg^{-1}) = \frac{IntegratedPeakArea(cm^{-1})}{\mathcal{E}(cm\mu mol^{-1})} * \frac{a_{CS}(cm^2)}{m(g)} \tag{3.1}$$

where a_{CS} and m are the cross-sectional area (2.54 cm^2) and mass of the wafer, respectively.

3.3.3 Kinetic studies of glucose isomerization

Glucose isomerization (373 K) studies were performed in batch reactors with 1% (w/w) glucose (Sigma Aldrich, ≥99.5%) solutions in water (18.2 MΩ), controlled to a pH of 4 (Mettler Toledo Seven Compact pH Ion S220 probe) by addition of hydrochloric acid (Macron, 37%) and then filtered with 0.2 μm PTFE filters (VWR). In a typical experiment, ∼0.01 g of catalyst were added to 10 cm^3 glass batch reactors (VWR) and sealed with crimp tops (PTFE/silicone septum, Agilent). The reactor containing the catalyst was heated to 373 K for 600 s. In a separate 2 cm^3 vial, the reactant solution was heated to 373 K for 600 s. The reaction was started by injecting the preheated reactant solution through the septum into the reactor containing the preheated catalyst. The reactor remained at 373 K with stirring at 750 RPM in an oil

bath for reaction times chosen to maintain differential conditions (<6% conversion). The reactors were quenched after the specified reaction time in an ice bath and the product solutions were filtered through 0.2 μm PTFE filters. Products were analyzed using high-performance liquid chromatography (HPLC, Agilent 1260 with a Hi-Plex Ca column) with an evaporative light scattering detector (Agilent 1260 Infinity ELSD). An aqueous mannitol (1% (w/w), Sigma Aldrich, $\geq$99.8%) solution was used as an internal standard for product quantification. Isotopic tracer studies were performed with 1% (w/w) glucose-D_2 (Cambridge Isotope Laboratories, 2-D, 98%) solutions in pH-controlled water (pH = 4) to obtain the kinetic isotope effects (details in Section 3.7.9).

3.4 Results and Discussion

3.4.1 Sn-Beta prepared post-synthetically by grafting in isopropanol

The synthetic protocols used to prepare all Sn-Beta samples, together with their elemental composition and fraction of vacancies grafted by Sn, are listed in Table 3.1. Each sample is denoted as M-Beta-X-Y, where M represents the heteroatom in the framework, X represents the mineralizing agent used to synthesize the parent Al-Beta zeolite (OH^- or F^-), and Y reflects the Si/M ratio measured by atomic absorption spectroscopy (AAS) in the final Beta zeolites. Sn-Beta-OH-170, Sn-Beta-OH-200, and Sn-Beta-OH-457 were prepared by dealumination of Al-Beta-OH zeolites via treatment in nitric acid (residual Si/Al $>$ 1500) and subsequent grafting of Sn atoms via reflux of $SnCl_4$-$5H_2O$ in isopropanol according to reported methods [22, 23]. The solids recovered after isopropanol reflux treatments to prepare Sn-Beta-OH-200 were first washed in methanol, a procedure reported to remove extraneous Sn species that are precursors to SnO_2 formation [24], prior to high temperature oxidative treatment. Similarly, the solids recovered after isopropanol reflux treatments to prepare Sn-Beta-OH-170 and Sn-Beta-OH-457 were washed with isopropanol prior to high temperature oxidative treatment. XRD patterns of the parent Al-Beta-OH, dealuminated Beta, and Sn-Beta-OH zeolites (Fig. 3.10) were consistent with the Beta topology, with broad diffraction peaks that reflect small primary crystallites. N_2 adsorption isotherms (77 K) were used to determine micropore volumes of 0.19–0.22 $cm^3\ g^{-1}$ (Table 3.6), also consistent with the Beta topology. These characterization data indicate that zeolitic framework structural integrity was maintained throughout the reflux and high temperature oxidative treatment procedures used to prepare Sn-Beta-OH samples via isopropanol-assisted grafting.

Diffuse reflectance UV-Visible (DRUV) spectra of Sn-Beta-OH-170, Sn-Beta-OH-200, and Sn-Beta-OH-457 were collected at ambient conditions, after dehydration treatments (523 K), and after rehydration treatments in flowing "wet" helium (303 K, $\sim$3% H_2O). These samples showed DRUV bands centered at $\sim$220–230 nm under

ambient conditions, bands centered at ∼190–200 nm after dehydration treatments with corresponding adsorption edge energies (>4.2 eV) characteristic of tetrahedral Sn sites isolated in silica [50], and bands that reverted to their initial positions (∼220–230 nm) and edge energies after rehydration (Figs. 3.19-3.21, Table 3.7). Such spectral changes are consistent with ligand-to-metal charge transfer bands for tetrahedral framework Sn centers (∼205 nm) that shift to those for octahedral Sn (∼260 nm) upon coordination with Lewis bases (e.g, H_2O, CH_3OH) [86]. A feature centered at ∼260 nm for SnO_2 [87–90] remains after dehydration of Sn-Beta-OH-170 and Sn-Beta-OH-457, but not of the Sn-Beta-OH-200 sample that was washed with methanol prior to high temperature oxidative treatment, consistent with reports that such methanol washing treatments mitigate the formation of extraframework SnO_2 [24].

These characterization data indicate that Sn-Beta-OH samples were successfully synthesized by isopropanol-assisted grafting of Sn within framework vacancies of dealuminated Beta at different Sn contents (Si/Sn = 170–457, 0.4–1.2 wt.% Sn) and fractions of vacancies grafted (Sn/vacancy = 0.03–0.27). Previous studies of isopropanol-assisted Sn grafting have concluded that Sn can incorporate within only a subset of available framework vacancies (Sn/vacancy = 0.11, Si/Sn = 121), beyond which additional Sn incorporation forms extraframework SnO_2 domains that lead to increases in the intensity of DRUV bands centered at ∼255 nm [22]. At first glance, the higher fraction of framework vacancies grafted here (Sn/vacancy = 0.27) than reported by Dijkmans et al. (Sn/vacancy = 0.11) [22] via isopropanol-assisted reflux, together with higher fractions of vacancies grafted via reflux with anhydrous $SnCl_4$ (Sn/vacancy = 0.34) [24] and via solid-state ion exchange (Sn/vacancy = 0.74) [19], suggest that limitations to Sn incorporation are not inherently conferred by the structure or coordination of framework vacancy defects. Yet, even the Sn-Beta-OH-200 sample (Sn/vacancy = 0.27) contains nearly three times more vacant than grafted defects, suggesting that using isopropanol as the reflux solvent may inhibit reactions between Sn precursors and vacancy defects during reflux procedures (383 K).

The interactions of isopropanol with dealuminated Beta surfaces and microporous voids were probed with temperature programmed desorption (TPD) and infrared (IR) spectroscopy. TPD performed on dealuminated Beta saturated with isopropanol at ambient conditions (7 h) resulted in a desorption profile centered at ∼400 K (Fig. 3.39) and evolved ∼5× more isopropanol than the number of vacancies present, an amount equivalent to a volume of ∼0.30 cm^3 g^{-1}. These findings suggest that isopropanol adsorbs within available micropore volume (∼0.22 cm^3 g^{-1}) and also at hydroxyl groups at external crystallite surfaces at ambient conditions, and that it will saturate such voids and surfaces when present in excess (relative to Sn precursors) at reflux temperatures (383 K). IR spectra collected after saturation of dealuminated Beta with isopropanol at 383 K were dominated by broad features for perturbed OH stretches (∼3000–3600 cm^{-1}) and contained a feature centered at 3350 cm^{-1}, which has been assigned to silanol groups perturbed by hydrogen bonding (Fig. 3.40) [121]. The incomplete disappearance of perturbed hydroxyl groups (3350 cm^{-1}) in IR spectra after evacuation at 383 K (Fig. 3.40), together with isopropanol C-H stretches at 2700–3000 cm^{-1} (Fig. 3.41) [122], reflects isopropanol that remains hydrogen bound to a fraction of silanol groups. Taken together, these TPD and IR experiments suggest that isopropanol can competitively adsorb with Sn precursors at framework vacancy defects (383 K) and limit the incorporation of framework Sn centers. In contrast, TPD experiments performed on dealuminated Beta after saturation with dichloromethane at ambient conditions did not evolve any detectable amount of dichloromethane (Fig. 3.39), suggesting that the reactions of Sn precursors with framework vacancy defects should not be inhibited during dichloromethane-assisted reflux procedures (333 K).

3.4.2 Sn-Beta prepared post-synthetically by grafting in dichloromethane

Sn grafting via dichloromethane reflux was performed onto the same dealuminated Beta sample used to prepare Sn-Beta-OH-200, which was grafted in isopropanol, but using an ∼8× lower Sn concentration (0.010 mol Sn (g zeolite)$^{-1}$) than was present during isopropanol reflux (0.081 mol Sn (g zeolite)$^{-1}$)). The resulting Sn-Beta-OH-47

sample retained structural properties of the Beta topology, assessed by XRD (Fig. 3.11) and N_2 micropore volume (Table 3.6), and contained predominantly framework Sn centers, reflected in DRUV spectra collected after dehydration treatments that showed only an absorption band (∼214 nm, Fig. 3.22) and an edge energy (>4.2 eV, Table 3.7) characteristic of isolated, tetrahedral Sn [26, 50]. The amount of Sn grafted in Sn-Beta-OH-47 was >4× larger than in Sn-Beta-OH-200, in spite of the ∼8× lower Sn concentration present in the reflux solution with the same dealuminated Beta zeolite (initial Si/Al = 54). Furthermore, the number of Sn atoms grafted into Sn-Beta-OH-47 (0.00034 mol Sn (g zeolite)$^{-1}$)) was equivalent, within experimental accuracy, to the number of Al vacancies present in the dealuminated Beta support (0.0003 mol (g zeolite)$^{-1}$)). These findings indicate that dichloromethane does not inhibit the reaction of Sn precursors with framework vacancy defects, as occurs in the case of isopropanol, and that Sn grafting can occur within all framework vacancies present in a given dealuminated Beta zeolite.

The incorporation of Sn centers within the framework of Sn-Beta-OH-47 was assessed using IR spectroscopy to monitor the ν(OH) and ν(C≡N) stretching regions before and after saturation with CD_3CN (303 K). IR spectra of the parent Al-Beta-OH-54, the dealuminated Beta formed via nitric acid treatment, and the final Sn-Beta-OH-47 prepared via dichloromethane-assisted reflux are shown in Fig. 3.1 and 3.2. The spectrum of Al-Beta-OH-54 shows peaks at 3610 cm^{-1}) for Brønsted acidic Si-OH-Al groups [123] and at 3660 cm^{-1}) for perturbed Al-OH groups [124]. These peaks disappear upon dealumination, with the concomitant appearance of peaks at 3500–3600 cm^{-1}) for silanol nests [24] and at 3740 cm^{-1} for isolated silanol groups [103]. The incorporation of Sn in Sn-Beta-OH-47 causes disappearance of features in the 3500–3600 cm^{-1}) range and restoration of the peak at 3740 cm^{-1}), also observed with post-synthetic treatments of dealuminated Beta through solid-state ion exchange [18] and grafting with anhydrous $SnCl_4$ [24], reflecting the preferential consumption of silanol nests during Sn grafting (Fig. 3.1). The spectrum of Al-Beta-OH-54 at saturation coverages with CD_3CN (Fig. 3.1) shows peaks at 2265

cm^{-1}) for physisorbed CD_3CN, at 2275 cm^{-1}) for CD_3CN hydrogen bound to silanol groups, at 2290 cm^{-1}) for CD_3CN bound to Brønsted acidic Si-OH-Al groups, and at 2325 cm^{-1}) for CD_3CN bound to Lewis acidic Al sites [79]. The spectrum of dealuminated Beta (Fig. 3.2) only contains peaks for CD_3CN hydrogen bound to silanol groups (2275 cm^{-1})) and in the gas-phase or physisorbed within microporous voids (2265 cm^{-1})), but not for any CD3CN at Brønsted or Lewis acid sites. The spectrum for Sn-Beta-OH-47 contains peaks at 2287 cm^{-1}), 2308 cm^{-1}), and 2316 cm^{-1}) that have been assigned to CD_3CN bound to highly-defective Sn sites (e.g., $(SiO)_2Sn(OH)_2$), closed Sn sites, and open Sn sites in Sn-Beta [26], respectively (Fig. 3.2). Taken together, these IR spectra provide evidence for complete dealumination to form silanol nest defects, which are preferentially grafted with Sn precursors via dicholoromethane-assisted reflux to form predominantly open and closed Lewis acidic Sn sites in the framework.

The numbers of open and closed Lewis acidic Sn sites in Sn-Beta-OH-47 were quantified from integrated molar extinction coefficients for their respective IR peaks centered at 2316 cm^{-1}) and 2308 cm^{-1}), which were deconvoluted from IR spectra after CD_3CN saturation at 303 K (Fig. 3.42) according to procedures we have reported elsewhere [26]. The numbers of open and closed Sn sites present in each sample in this study are summarized in Table 3.2, while the number of sites quantified by the IR peak at 2287 cm^{-1}) is summarized in Table 3.8. On Sn-Beta-OH-47, the number of Lewis acidic Sn sites (per mol Sn) was 0.80, within unity considering the error of the deconvolution procedure (±20%). The number of Lewis acidic Sn sites (per mol Sn) in Sn-Beta-OH-47 was also quantified from IR spectra collected after saturation with pyridine at 423 K (Fig. 3.43), which shows a peak at 1450 cm^{-1}) for Lewis acidic-bound pyridine [69], and from integrated molar extinction coefficients reported in Harris et al. [26]. Pyridine titrated 1.15 Lewis acidic Sn sites (per mol Sn) on Sn-Beta-OH-47, also within experimental accuracy of unity (±20%), suggesting that Sn atoms are preferentially incorporated within tetrahedral framework positions and consistent with DRUV spectra collected after dehydration

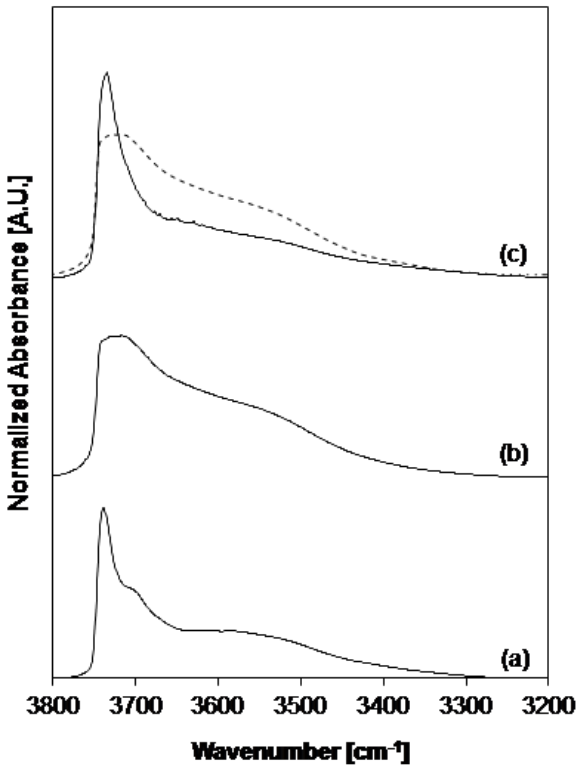

Figure 3.1: IR spectra (303 K) collected for (a) Al-Beta-OH-54, (b) dealuminated Beta, and (c) Sn-Beta-OH-47 grafted in dichloromethane as the reflux solvent. The spectrum of dealuminated Beta (dashed line) is superimposed on (c) for comparison.

(Fig. 3.22). These data provide quantitative evidence that Sn can be grafted indiscriminately within all framework vacancies in a given dealuminated Beta zeolite via dichloromethane-assisted reflux, while avoiding the formation of extraframework SnO_2, providing access to routes that enable precisely controlling the framework Sn content and residual silanol defect density, as we explore next.

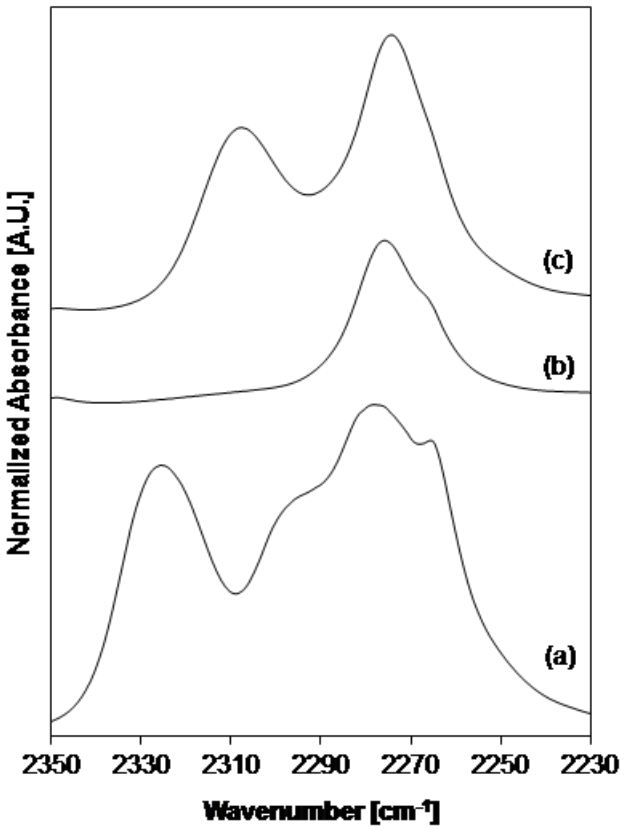

Figure 3.2: IR spectra of (a) Al-Beta-OH-54, (b) dealuminated Beta, and (c) Sn-Beta-OH-47 after saturation with CD_3CN (303 K).

Table 3.1: Structural characterization of Sn-Beta samples prepared via post-synthetic grafting with isopropanol and dichloromethane as reflux solvents.

Catalyst	Solvent[a]	Sn concentration[b] (10^{-3} mol Sn $(g_{zeolite})^{-1}$)	Initial Si/Al[c,d]	Si/Sn (Sn wt.%)[d]	Sn/vacancy[e,f]
Sn-Beta-OH-95	DCM	1	19	95 (2.0)	0.20
Sn-Beta-OH-46	DCM	10	19	46 (4.1)	0.41
Sn-Beta-OH-41	DCM	27	19	41 (4.6)	0.46
Sn-Beta-OH-30	DCM	40	19	30 (6.1)	0.64
Sn-Beta-OH-80	DCM	1	29	80 (2.4)	0.36
Sn-Beta-OH-40	DCM	10	29	40 (4.7)	0.73
Sn-Beta-OH-32	DCM	27	29	32 (5.8)	0.90
Sn-Beta-OH-84	DCM	1	54	84 (2.3)	0.64
Sn-Beta-OH-47	DCM	10	54	47 (4.0)	1.15
Sn-Beta-OH-144	DCM	0.5	22	144 (1.4)	0.15
Sn-Beta-OH-457	IPA	27	15	457 (0.4)	0.03
Sn-Beta-OH-200[g]	IPA	81	54	200 (1.0)	0.27
Sn-Beta-OH-170[g]	IPA	27	25	170 (1.2)	0.13

[a]DCM = dichloromethane; IPA = isopropanol.
[b]Sn concentration in reflux solution.
[c]Si/Al ratio of parent Al-Beta zeolite.
[d]Errors are ±15%.
[e]Number of vacancies assumed to be equal to the Al content in the parent Al-Beta zeolite.
[f]Errors are ±21%.
[g]Originally reported in Harris et al. [26].

Table 3.2: Number of open (2316 cm^{-1}) and closed (2308 cm^{-1}) Sn sites titrated by CD_3CN and quantified by IR spectral band deconvolution.

Catalyst	Lewis Acidic Sn (per total Sn)[a]	Open Sn Sites (per total Sn)[a]	Closed Sn Sites (per total Sn)[a]
Sn-Beta-OH-95	1.22	0.49	0.73
Sn-Beta-OH-46	0.92	0.22	0.70
Sn-Beta-OH-41	1.32	0.50	0.82
Sn-Beta-OH-30	0.72	0.18	0.54
Sn-Beta-OH-80	1.01	0.42	0.59
Sn-Beta-OH-40	1.21	0.36	0.85
Sn-Beta-OH-32	0.81	0.29	0.53
Sn-Beta-OH-84	1.21	0.24	0.96
Sn-Beta-OH-47	0.80	0.19	0.61
Sn-Beta-OH-144	1.17	0.43	0.73
Sn-Beta-OH-457	0.52	0.26	0.26
Sn-Beta-OH-200[b]	0.69	0.15	0.54
Sn-Beta-OH-170[b]	0.73	0.46	0.28

[a]Errors are ±20%.

[bg]Originally reported in Harris et al. [26].

3.4.3 Controlling framework Sn content and speciation in post-synthetic Sn-Beta

The ability to graft Sn atoms within virtually every silanol nest defect present in a dealuminated zeolite suggests that dichloromethane-assisted reflux procedures can be adjusted precisely to prepare Sn-Beta zeolites with a desired Si/Sn ratio, by varying the Al content in the parent zeolite or the fraction of vacancies grafted within a given dealuminated zeolite support. Therefore, dichloromethane-assisted grafting of $SnCl_4$ was studied with dealuminated Al-Beta-OH zeolites of varying initial Al content (Si/Al = 19, 29, 54) and with different Sn concentrations in the reflux solution (0.0005–0.040 mol Sn (g zeolite)$^{-1}$). DRUV spectra of each Sn-Beta-OH sample grafted in dichloromethane, collected after dehydration treatments, showed absorption bands centered at <220 nm without detectable absorbance at>250 nm for SnO_2 (Figs. 3.22 to 3.31). The fraction of Sn present as Lewis acidic Sn sites detected by CD_3CN titration varied about unity (0.72–1.32, Table 3.2) among the twelve Sn-Beta samples prepared via dichloromethane reflux studied here, providing evidence for the preferential incorporation of Sn within framework vacancies. The deviations from unity, however, indicate that some structural heterogeneities persist among Sn sites, underscoring the importance of quantifying framework Sn sites even for samples prepared via similar protocols and without extraframework SnO_2 domains detectable by spectroscopic or diffraction measurements.

The number of Sn atoms (per vacancy) incorporated into the final Sn-Beta-OH solids is plotted in Fig. 3.3 as a function of the Sn concentration in the reflux solution for samples prepared via dichloromethane grafting, together with Sn-Beta samples that contained predominantly framework Sn prepared by Dijkmans et al. [22] via isopropanol grafting. Among Sn-Beta-OH samples grafted under dichloromethane reflux, Sn atoms were incorporated into framework positions at more than twice the densities than reported for samples prepared by grafting in isopropanol reflux [22], at the same or even at lower Sn concentrations in the reflux solution (Fig. 3.3), reflecting the inhibition of grafting caused by competitive adsorption of isopropanol at frame-

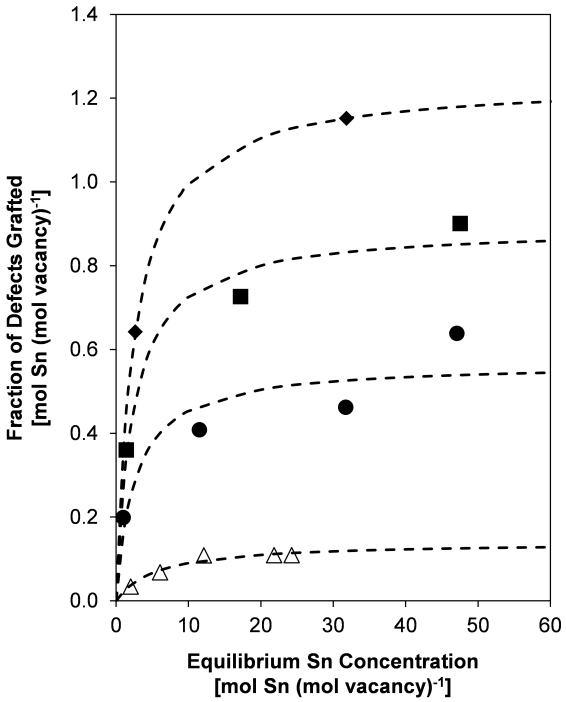

Figure 3.3: Fraction of vacancies grafted as a function of the equilibrium Sn concentration in the reflux solution (per vacancy defects) for Sn-Beta-OH samples grafted in dichloromethane reflux from parent Al-Beta-OH-54 (diamonds), Al-Beta-OH-29 (squares), and Al-Beta-OH-19 (circles), and Sn-Beta samples grafted using isopropanol reflux reported by Dijkmans et al. (open triangles) [22]. Dashed lines represent the best-fit Langmuir isotherms (Eq. 3.2) for each Sn-Beta-OH series.

work vacancy defects. The amount of Sn incorporated within each of the starting dealuminated Beta samples increased with Sn concentration in the dichloromethane reflux solution according to Langmuirian behavior and the following expression (detailed derivation in Section 3.7.8):

$$\theta_{Sn} = \frac{([Sn*])}{[*]_0} = (\theta_{max})\frac{(K[Sn])}{(1+K[Sn])} \tag{3.2}$$

In Eq. 3.2, [Sn*] is the concentration of vacancy defects incorporated with Sn atoms, $[*]_0$ is the concentration of vacancy defects present initially on the dealuminated Beta support, K is the equilibrium constant relating Sn incorporated within a vacancy defect to the Sn present in the reflux solution, [Sn] is the equilibrium Sn con-

centration in the reflux solution (per vacancy), and θ_{max} is the fraction of vacancies that can be grafted in a given dealuminated Beta support. The fraction of vacancies grafted (θ_{Sn}) for each Sn-Beta-OH series as a function of the Sn concentration in the reflux solution (per vacancy) were regressed to Eq. 3.2 and plotted as dashed lines in Fig. 3.3, with corresponding numerical values for K and θ_{max} given in Table 3.3. Values of K were invariant among the three different Sn-Beta-OH series prepared via grafting in dichloromethane (333 K), yet were lower by 2× for Sn-Beta-OH grafted in isopropanol (383 K), reflecting both the different temperatures used and the different Gibbs free energy differences between adsorption of Sn precursors and the solvent at vacancy defect sites. Values of θ_{max} (Table 3.3) were >5× higher for Sn-Beta-OH samples grafted using dichloromethane than those grafted using isopropanol as the reflux solvent [22], approaching values of ∼1 for two different dealuminated Beta supports (Table 3.3). Using dichloromethane-assisted reflux procedures, framework vacancies present in dealuminated Al-Beta-OH-29 and Al-Beta-OH-54 zeolites were nearly completely grafted ($\theta_{Sn} > 0.90$, Fig. 3.3) at sufficiently high Sn concentrations in the reflux solution, while only a fraction of those present ($\theta_{max} = 0.58$, Table 3.3) in dealuminated Al-Beta-OH-19 zeolites were apparently able to be grafted with Sn (Fig. 3.4), perhaps reflecting the higher density of vacancy defects present initially, some fraction of which may change structure after high temperature oxidative treatments so as to be incompatible hosts for Sn heteroatoms.

Table 3.3: Number of open (2316 cm^{-1}) and closed (2308 cm^{-1}) Sn sites titrated by CD_3CN and quantified by IR spectral band deconvolution.

Parent sample	Solvent	K	θ_{max}
Al-Beta-OH-19	Dichloromethane	0.40	0.57
Al-Beta-OH-29	Dichloromethane	0.43	0.89
Al-Beta-OH-54	Dichloromethane	0.40	1.24
Al-Beta-OH-13[a]	Isopropanol	0.18	0.14

[a]Data reported by Dijkmans et al. [22].

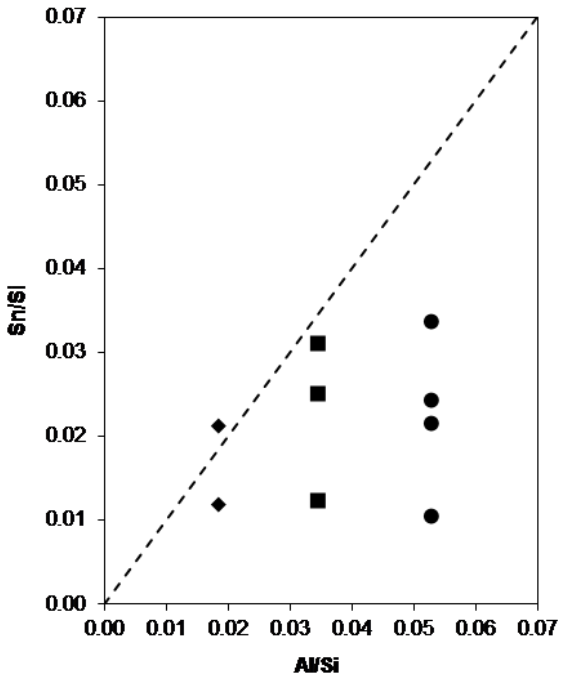

Figure 3.4: Sn content and Al content (in the parent Al-Beta) with starting Al-Beta-OH-54 (diamonds), Al-Beta-OH-29 (squares), and Al-Beta-OH-19 (circles). Dashed line denotes the parity line.

The fraction of open Sn sites quantified by CD_3CN IR (Table 3.2) is plotted as a function of total Sn content in Fig. 3.5 for Sn-Beta-OH samples prepared via dichloromethane-assisted reflux starting from dealuminated versions of Al-Beta-OH-19, Al-Beta-OH-29, and Al-Beta-OH-54. Within each Sn-Beta-OH series, the fraction of open Sn sites decreased systematically with increasing Sn content (Fig. 3.5), except for Sn-Beta-OH-41, which appears to be the sole outlier among these nine samples. These site quantification data indicate that dichloromethane-assisted grafting procedures preferentially incorporates open Sn sites at low framework Sn densities. Although the underlying origin for this phenomenon remains a topic of ongoing research, the data in Fig. 3.5 describe one of the rare instances in which the open-to-closed Sn site ratio can be systematically varied using a given synthesis or treatment procedure. Systematic changes in open and closed Sn site fractions with Sn content will, in turn, cause systematic turnover rate dependences for catalytic reactions that preferentially

turnover on one of the two sites, as we explore next in the context of glucose-fructose isomerization cycles that turn over predominantly on framework open Sn sites [26,32].

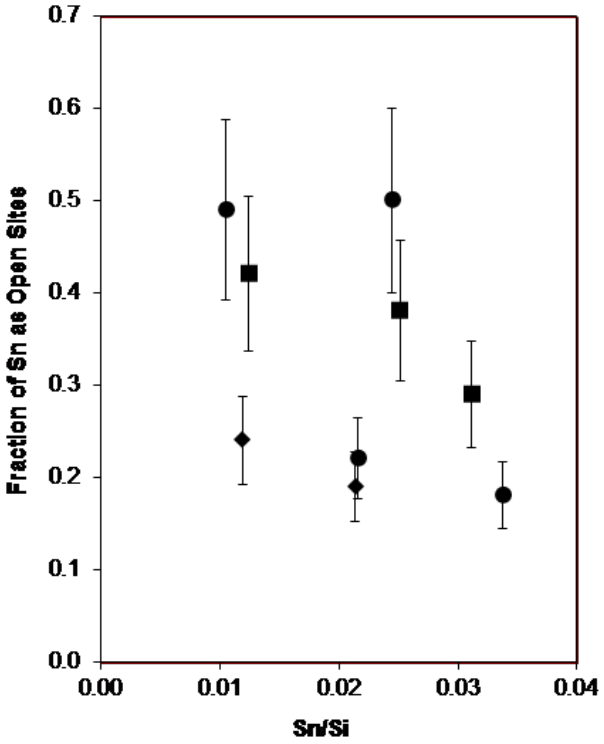

Figure 3.5: Fraction of open Sn sites as a function of bulk Sn content in Sn-Beta-OH samples grafted under dichloromethane reflux starting from Al-Beta-OH-54 (diamonds), Al-Beta-OH-29 (squares), and Al-Beta-OH-19 (circles).

3.4.4 Catalytic consequences for aqueous-phase glucose isomerization to fructose

Glucose-to-fructose isomerization proceeds via quasi-equilibrated adsorption and ring opening of glucose onto an open Sn site, kinetically-relevant intramolecular 1,2-hydride shift, and quasi-equilibrated ring closing and desorption of fructose [34, 51]. Aqueous-phase isomerization turnover rates (per open Sn, 373 K) on Sn-Beta-OH samples are first-order in glucose concentration under dilute conditions (1–10% (w/w) glucose, Fig. 3.44), in which two water molecules coordinated at Sn sites are most

abundant surface intermediates (MASI) [34]. These mechanistic assumptions result in a glucose-to-fructose isomerization rate expression given by:

$$r_{isom} = \alpha \frac{K_1 k_2}{K_4 K_5} C_G = k_{isom} C_G \tag{3.3}$$

where α represents a product of activity coefficients of reactants and intermediate species, k_2 is the intrinsic rate constant for intramolecular 1,2-hydride shift, K_1 is the equilibrium constant for glucose adsorption from the aqueous phase to ring-opened glucose intermediates at Sn sites, K_4 and K_5 are equilibrium constants for the sequential adsorption of two water molecules at Sn sites, C_G is the glucose concentration in water, and k_{isom} is the measured first-order isomerization rate constant (full derivation of this rate expression in Section 3.7.9).

The glucose conversions, turnover numbers, and monosaccharide yields in the batch reactor experiments used to measure kinetic data on each Sn-Beta sample are shown in Table 3.4, confirming both their differential and catalytic nature. Measured first-order isomerization rate constants (373 K), normalized by the total number of Sn sites, are shown in Fig. 3.6 for Sn-Beta-OH samples grafted using dichloromethane as the reflux solvent. Rate constants (per total Sn, 373 K) varied by ∼2.5× among samples of widely varying Sn content (Si/Sn = 30–95), and decreased systematically with increasing Sn content within each Sn-Beta-OH series, as observed previously for Sn-Beta samples prepared via post-synthetic grafting using isopropanol [22] and via solid-state ion exchange [19]. Decreases in isomerization rates (per total Sn, 383 K) with increasing Sn content have been ascribed to intracrystalline mass transfer limitations [22, 23], yet the isomerization rates reported in Fig. 3.6 are uncorrupted by transport limitations, reflected in the kinetic isotope effect value of ∼2.1 (at 373 K) measured when using glucose reactants deuterated at their α-carbonyl position (details in Section 3.7.9) [26, 34, 35]]. Decreases in glucose isomerization rates (per total Sn, 383 K) with increasing Sn content have also been speculated to reflect differences in Sn siting at different T-site locations [22, 52]. The CD_3CN titration

data shown in Fig. 3.5, however, indicate that the fraction of open Sn sites decreases systematically with increasing Sn content within each series of Sn-Beta-OH samples.

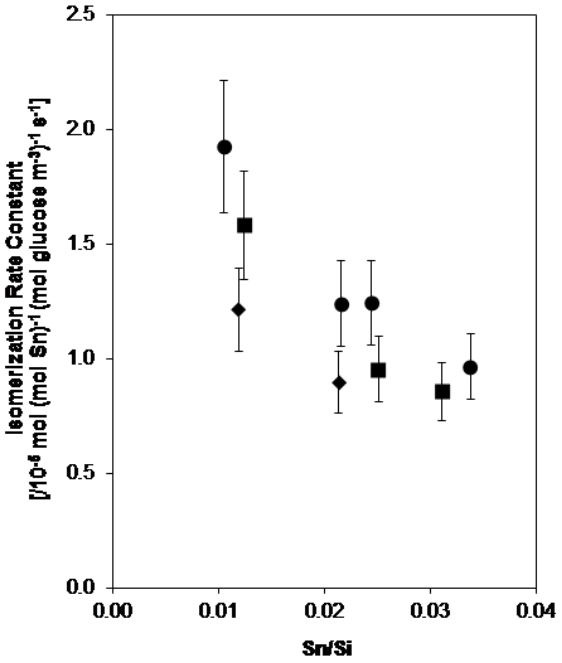

Figure 3.6: Glucose isomerization rate constant (per total Sn, 373 K) and the Sn content in samples grafted using dichloromethane as the reflux solvent starting from Al-Beta-OH-54 (diamonds), Al-Beta-OH-29 (squares), and Al-Beta-OH-19 (circles).

Table 3.4: Glucose conversion, monosaccharide yields and turnover numbers (TON) for aqueous-phase (1% (w/w)) glucose isomerization (373 K), and apparent first-order isomerization rate constants (per open Sn).

Catalyst	Conversion (%)	Monosaccharide Yield (w/w %)			TON[a]	k_{isom} (per open Sn)[b,c]
		Glucose	*Fructose*	*Mannose*		
Sn-Beta-OH-95	4.5	96	4	n.d.*	2.5	3.9
Sn-Beta-OH-46	5.2	94	5	0.3	3.8	5.6
Sn-Beta-OH-41	5.9	93	6	0.3	1.7	2.5
Sn-Beta-OH-30	6.1	93	6	1	4.1	5.4
Sn-Beta-OH-80	4.6	95	5	n.d.*	2.4	3.8
Sn-Beta-OH-40	3.2	97	3	n.d.*	1.2	2.5
Sn-Beta-OH-32	3.4	97	3	n.d.*	1.4	3.0
Sn-Beta-OH-84	2.0	98	2	n.d.*	2.4	5.1
Sn-Beta-OH-47	2.6	97	3	n.d.*	2.3	4.7
Sn-Beta-OH-144	1.8	98	2	n.d.*	2.1	4.3
Sn-Beta-F-93	5.3	94	5	1	3.3	5.7
Sn-Beta-F-50	6.0	93	6	1	2.9	4.9
Sn-Beta-OH-457	2.1	98	2	n.d.*	11.0	1.4
Sn-Beta-OH-200[d]	2.4	98	2	n.d.*	4.5	1.5
Sn-Beta-OH-170[d]	3.1	97	3	n.d.*	7.9	0.8

[a]Total moles of product per mole of open Sn sites.
[b]Units are 10^{-5} mol (mol open Sn)$^{-1}$ (mol glucose m^{-3})$^{-1}$ s^{-1}.
[c]Errors are ±15%.
[d]Originally reported in Harris et al. [26].
*n.d., not detected.

First-order isomerization rate constants (373 K), normalized by the number of open Sn sites (Table 3.2), for all post-synthetically prepared Sn-Beta samples are given in Table 3.4 and are plotted in Fig. 3.7 as a function of Sn content, together with rate constants on hydrothermally-synthesized Sn-Beta samples reported in Harris et al. [26] (data in Table 3.10). Among the different Sn-Beta-OH samples prepared by dichloromethane-assisted reflux, isomerization rate constants (per open Sn, 373 K) are similar (within ∼2×) and do not depend systematically on Sn content, which is the single-site kinetic behavior expected upon accurate normalization of turnover rates by the number of reactive Sn sites. Interestingly, values of k_{isom} (per open Sn, 373 K, Fig. 3.7) were consistently ∼3× higher among Sn-Beta-OH samples prepared via grafting in dichloromethane reflux than those in isopropanol reflux. The underlying reasons for the rate constant differences among these two sample sets remain unclear, although unlikely to reflect differences in framework Sn site distribution considering that Sn-Beta-OH-170 and Sn-Beta-OH-144 samples respectively grafted in isopropanol and dichloromethane contain similar framework Sn and residual vacancy content (Table 3.1). The small variations in k_{isom} values (within ∼2×, 373 K) among the ten post-synthetic Sn-Beta-OH samples prepared via dichloromethane reflux (Fig. 3.7) can be accounted for by differences of only 2.5 kJ mol^{-1} in apparent Gibbs free energies of activation, and resemble the similar variation (within ∼3×, 373 K) reported previously among six hydrothermally-synthesized Sn-Beta-F samples (Fig. 3.7) [26]. We conclude that isomerization rates (per total Sn) among post-synthetically prepared Sn-Beta zeolites decrease systematically with increasing Sn content (Fig. 3.6) [22, 120] because open Sn sites are the dominant active site for glucose-fructose isomerization [26, 32, 34] and are incorporated preferentially at low Sn content when Sn-Beta samples are prepared via grafting procedures (Fig. 3.5).

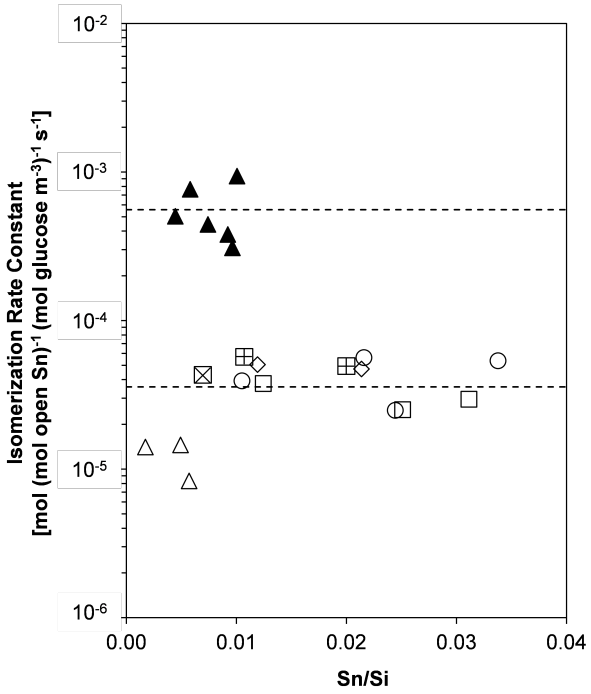

Figure 3.7: Isomerization rate constant (per open Sn, 373 K) and Sn content for samples grafted in isopropanol reflux (open triangles), in dichloromethane reflux starting from Al-Beta-OH-54 (open diamonds), Al-Beta-F-45 (square with plus), Al-Beta-OH-29 (open squares), Al-Beta-OH-22 (square with cross) , Al-Beta-OH-19 (open circles), and hydrothermally-synthesized Sn-Beta-F (triangles) [26]. Dashed lines represent the average rate constant (per open Sn, 373 K) for Sn-Beta-F samples prepared hydrothermally and Sn-Beta-OH samples.

In contrast to the small variations (∼3–5×) in kisom values among post-synthetically prepared, high-defect Sn-Beta-OH zeolites, higher k_{isom} values (by ∼15–50×) were measured on hydrothermally-synthesized, low-defect Sn-Beta-F samples (Fig. 3.7), as reported previously [26]. Such kinetic behavior suggests that Gibbs free energy differences between intramolecular 1,2-hydride shift transition states and two coordinated water ligands, which are the most abundant surface intermediates on open Sn sites under these reaction conditions [26,35], are larger in the presence of co-adsorbed hydrogen-bonded water networks that exist within high-defect Sn-Beta-OH zeolite pores, but not within low-defect Sn-Beta-F pores, during conditions of aqueous-phase catalysis (373 K). The similar k_{isom} values (per open Sn, 373 K) among the ten Sn-Beta-OH samples grafted in dichloromethane, which contain a wide range of residual vacancy defect densities (Sn/vacancy = 0.15–1.15), indicate that glucose isomerization turnover rates in this kinetic regime are insensitive to the residual silanol density. We speculate that this insensitivity reflects a critical density of hydrophilic binding sites, including both Sn heteroatoms and silanol defects (of at most $3*10^{-4}$ mol (g zeolite)$^{-1}$) required to stabilize hydrogen-bonded water networks throughout zeolitic micropores during conditions of aqueous-phase catalysis (373 K).

Therefore, we hypothesized that preparing an Al-Beta zeolite in fluoride media, which should form low-defect frameworks containing predominantly hydrophobic siloxane (Si-O-Si) connectivities, could be subject to dealumination treatments and subsequent dichloromethane-assisted grafting of tin precursors in order to prepare a post-synthetic Sn-Beta-F sample with low residual defect density. Sn-Beta-F-93 and Sn-Beta-F-50 samples were prepared in this manner (characterization data in Table 3.6, Fig. 3.15, 3.32, and 3.33) and indeed showed H_2O uptakes ($P/P_0 = 0.2$ at 293 K, used elsewhere as a descriptor of hydrophobicity [16,26]) that were ∼3.5× lower than the H_2O uptakes averaged among the Sn-Beta-OH sample series (Table 3.10, Figs. 3.45–3.48). When normalized on a total Sn basis, the first-order glucose isomerization rate constant (373 K) on Sn-Beta-F-93 was ∼3× larger than for the Sn-Beta-OH samples and only ∼3.5× lower than for the hydrothermally-synthesized Sn-Beta-F

samples, similar to previous observations reported for Sn-Beta-F samples prepared via solid-state ion exchange of Sn onto dealuminated Beta-F supports [28]. Surprisingly, CD_3CN IR spectra of Sn-Beta-F-93 at saturation coverages showed the highest fraction of Lewis acidic Sn present in open configuration (0.62, Table 3.5) that we have observed among >20 samples prepared hydrothermally [26] or by post-synthetic grafting under isopropanol and dichloromethane reflux (Table 3.2). The underlying reasons why this sample showed an unprecedentedly high open-to-closed Sn site ratio ($\sim$1.2) remains under investigation, but another Sn-Beta-F sample prepared from the same support with higher Sn content (Sn-Beta-F-50) also showed a high open-to-closed Sn site ratio ($\sim$1; Table 3.5). The Sn-Beta-F-50 sample also showed a smaller fraction of open sites than on Sn-Beta-F-93, consistent with the dependence of open-to-closed Sn ratio on bulk Sn content observed for the Sn-Beta-OH series (Fig. 3.5). First-order glucose isomerization rate constants (373 K), when normalized to the number of open Sn sites, were identical on the post-synthetically prepared Sn-Beta-F samples and on the post-synthetically prepared Sn-Beta-OH samples (Fig. 3.7), in spite of the H_2O uptake ($P/P_0 = 0.2$, 293 K) on Sn-Beta-F-93 that more closely resembled that on hydrothermally-synthesized Sn-Beta-F samples (Table 3.10). These catalytic data suggest that the intrapore environments in post-synthetically prepared Sn-Beta-F samples, within which framework Sn sites are sequestered and glucose isomerization reaction coordinates are confined, resemble structurally those in post-synthetically prepared Sn-Beta-OH samples rather than hydrothermally-synthesized Sn-Beta-F samples.

Table 3.5: Elemental composition, and fraction of open (2316 cm^{-1}) and closed (2308 cm^{-1}) Sn sites, for post-synthetic Sn-Beta-F samples.

Catalyst	Si/Sn (Sn wt.%)[a]	Lewis Acidic Sn[b]	Open Sn Sites[b]	Closed Sn Sites[b]	Sn/vacancy[b,c]
Sn-Beta-F-93	93 (2.1)	1.15	0.62	0.52	0.48
Sn-Beta-F-50	50 (3.8)	0.85	0.44	0.41	0.90

[a]Errors are ±15%.

[b]Per total Sn, errors are ±20%.

[c]Number of vacancies assumed to be equal to the Al content in the parent Al-Beta zeolite.

Water uptakes ($P/P_0 = 0.2$, 293 K) have been used previously as a proxy to describe the hydrophobic character of zeolites, given the ability of organic molecules to fill hydrophobic micropores at equivalent reduced pressures [83], yet such uptakes represent an integral measurement of adsorption at heteroatom sites, silanol defects within pores and at external crystal surfaces, and any other hydrophilic binding sites that may be present [26]. In contrast, alcohols adsorb preferentially within low-defect, organophilic micropores until condensation occurs and before adsorption begins within mesopores or at external crystallite surfaces [16, 125–128], providing a means to distinguish hydrophilic sites located within micropores and at external surfaces. H_2O and CH_3OH adsorption isotherms (293 K) measured on Sn-Beta-F-93, Sn-Beta-OH-80 (chosen as a representative Sn-Beta-OH sample), and a Sn-Beta-F sample prepared hydrothermally [26] are shown in Fig. 3.8 and 3.9. For the Sn-Beta-F-93 sample, the H_2O adsorption isotherm (Fig. 3.8) more closely resembled that of the hydrothermally-synthesized Sn-Beta-F sample, as reported by Wolf et al. for Sn-Beta-F samples prepared post-synthetically by solid-state ion exchange [28]. In contrast, the CH_3OH adsorption isotherm (293 K) on Sn-Beta-F-93 resembled a type I isotherm (Fig. 3.9), reflecting micropore condensation driven by adsorbate-adsorbent interactions as observed on high-defect micropores such as those present in Sn-Beta-OH-80. These CH_3OH adsorption isotherms (293 K) were distinctly different than the type V adsorption isotherm measured on the low-defect hydrothermally-synthesized Sn-Beta-F sample (Fig. 3.9), reflecting micropore condensation driven by strong adsorbate-adsorbate interactions [16]. As a result, the similar k_{isom} values (per open Sn, 373 K) for the two post-synthetically grafted Sn-Beta-F samples (Sn-Beta-F-93, Sn-Beta-F-50) and the ten post-synthetically grafted Sn-Beta-OH samples via dichloromethane-assisted reflux appear to reflect similarities in the residual silanol defect density within their microporous voids and the kinetic consequences of such defect groups and the hydrogen-bonded water networks they stabilize during catalysis in liquid water. This interpretation suggests that subsequent treatments to further

decrease the density of internal defects may increase glucose-fructose isomerization rate constants for Sn-Beta samples prepared via post-synthetic routes.

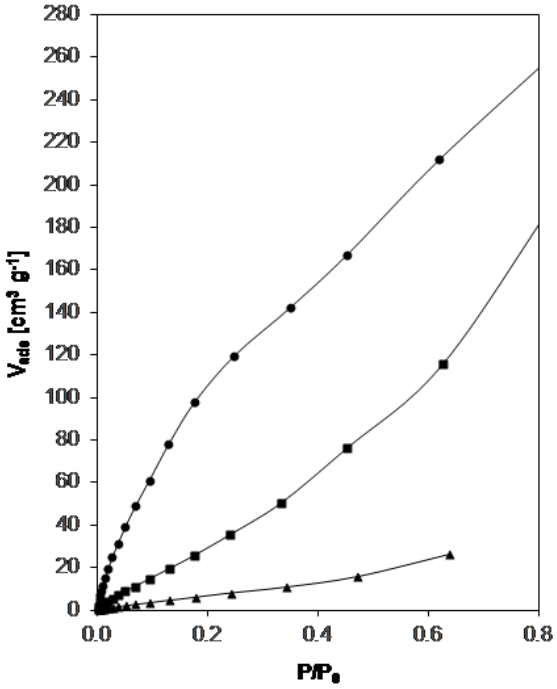

Figure 3.8: Vapor-phase H_2O adsorption isotherms (293 K) of Sn-Beta-OH-80 (circles), Sn-Beta-F-93 (squares), and Sn-Beta-F-220 prepared hydrothermally (triangles) [26].

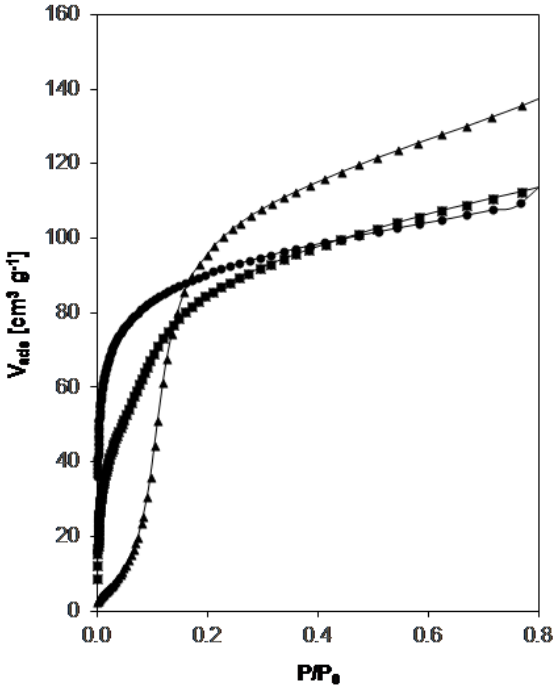

Figure 3.9: Vapor-phase CH_3OH adsorption isotherms (293 K) of Sn-Beta-OH-80 (circles), Sn-Beta-F-93 (squares), and Sn-Beta-F-220 prepared hydrothermally (triangles).

3.5 Conclusions

Protocols for the selective grafting of stannic precursors within virtually every framework vacancy defect present in dealuminated Beta zeolites were developed using dichloromethane reflux (333 K), which avoids the competitive adsorption of isopropanol, a commonly used reflux solvent (383 K), at vacancy defects that inhibits the incorporation of Sn precursors. Dichloromethane-assisted reflux allows preferential grafting of Lewis acidic Sn sites in framework locations at Sn densities higher (Si/Sn = 30, 6.1 wt.% Sn) than accessible via isopropanol-assisted reflux (Si/Sn >120, <1.6 wt.% Sn) [22]. Additionally, the fraction of open Sn sites decreased systematically with increasing Sn content among Sn-Beta samples prepared via dichloromethane-assisted reflux, indicating that open Sn sites are preferentially grafted at low framework Sn densities. The ability to incorporate Sn atoms within virtually all vacancies (Sn/vacancy >0.9) present in different dealuminated Beta supports demonstrates that Sn grafting can occur indiscriminately within all silanol nests and not only at a subset of vacancies with special coordination or geometry conferred by T-site location. By extension, methods to graft Sn precursors within each available framework vacancy open routes to prepare stannosilicates with tailored framework Sn site distribution among different intrazeolite locations and T-sites by controlling the placement of Al atoms in the parent zeolite framework before dealumination. The dichloromethane-assisted reflux methods to prepare Sn-Beta reported herein enable tailoring the ratio of open-to-closed framework Sn sites more systematically than hydrothermal synthesis methods, and controlling the densities of framework Sn and residual vacancy defects, by varying the initial Si/Al ratio of the parent zeolite and the Sn concentrations present in the reflux solutions. We expect that these synthesis protocols can be easily adapted to incorporate other heteroatoms into framework vacancy defects, and for those located in zeolite topologies other than Beta.

Aqueous-phase glucose-fructose isomerization rates (per total Sn, 373 K), measured in a kinetic regime that is first-order in extrazeolite glucose concentration,

were consistently lower (∼15–50×) among post-synthetically prepared Sn-Beta samples than among hydrothermally-synthesized Sn-Beta samples. The former contain high-defect micropore environments while the latter contain low-defect micropore environments, assessed from vapor-phase CH_3OH adsorption behavior, providing guidance that removing residual intrapore hydrophilic defect sites in post-synthetically prepared Sn-Beta samples should increase glucose isomerization turnover rates. Measured first-order isomerization rate constants (per total Sn, 373 K) decreased systematically with increasing Sn content for Sn-Beta-OH samples prepared post-synthetically via dichloromethane-assisted grafting. Similar observations have previously been interpreted as resistance to intrazeolite mass transfer [22,23] or reactive heterogeneities among Sn sites at crystallographically unique framework locations [22, 52, 120] , yet here reflect differences in the fraction of framework Sn sites present in "open" coordination ($(SiO)_3Sn(OH)$), which give rise to peaks at 2316 cm^{-1} in CD_3CN IR spectra and are the dominant active sites for glucose isomerization. First-order isomerization rate constants (373 K), when normalized to the number of open Sn sites, were similar (within ∼2×) and did not vary systematically with Sn content among twelve Sn-Beta samples prepared via dichloromethane reflux. The invariance in rate constant (per open Sn site, 373 K) for samples with widely varying Sn content (Si/Sn = 30–457; 0.4–6.1 wt.% Sn) and residual silanol density reflect the single-site behavior of open Sn sites confined in a high-defect microporous environment, as expected when turnover rates are normalized accurately by the number of reactive centers. These findings underscore the importance of quantifying active sites in order to rigorously normalize measured rate data prior to kinetic or mechanistic interpretation.

3.6 Acknowledgements

We acknowledge the financial support provided by the Purdue Process Safety and Assurance Center (P2SAC), a 3M Non-Tenured Faculty Grant, and a Purdue Showalter Trust Research Grant. We thank John Di Iorio for assistance with the TPD experiments and Michael Cordon for acquisition of SEM images. Finally, we thank Jason Bates and Michael Cordon for careful review of this manuscript and helpful technical discussions.

Further, we acknowledge Elsevier for granting permission to reproduce this chapter as the paper was originally published in Journal of Catalysis (344 (2016) 108-120. The article is available here: http://dx.doi.org/10.1016/j.jcat.2016.09.011.

3.7 Supporting Information

3.7.1 X-ray diffractograms of zeolite samples.

XRD patterns collected for Sn-Beta-(OH, F) samples as well as their parent Al-Beta-(OH, F) and their dealuminated Beta samples show prominent diffraction peaks at 6-8° and 22.5°, consistent with the Beta topology. Broad diffraction peaks were detected for all Al-Beta-OH samples that are consistent with small primary crystallite sizes as observed in Section 3.7.2. Samples are denoted as M-Beta-X-Y, where M represents the heteroatom in the framework (e.g., Al or Sn), X represents the mineralizing agent used to synthesize the starting Al-Beta zeolite (OH- or F-), and Y reflects the Si/M ratio measured by atomic absorption spectroscopy (AAS) in the recovered solids.

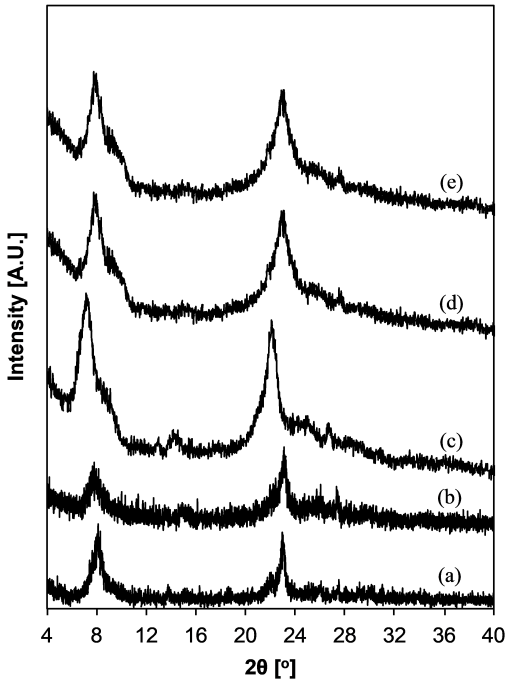

Figure 3.10: Powder XRD patterns of (a) Al-Beta-OH-54, (b) dealuminated Beta, (c) Sn-Beta-OH-170, (d) Sn-Beta-OH-200, and (e) Sn-Beta-OH-457.

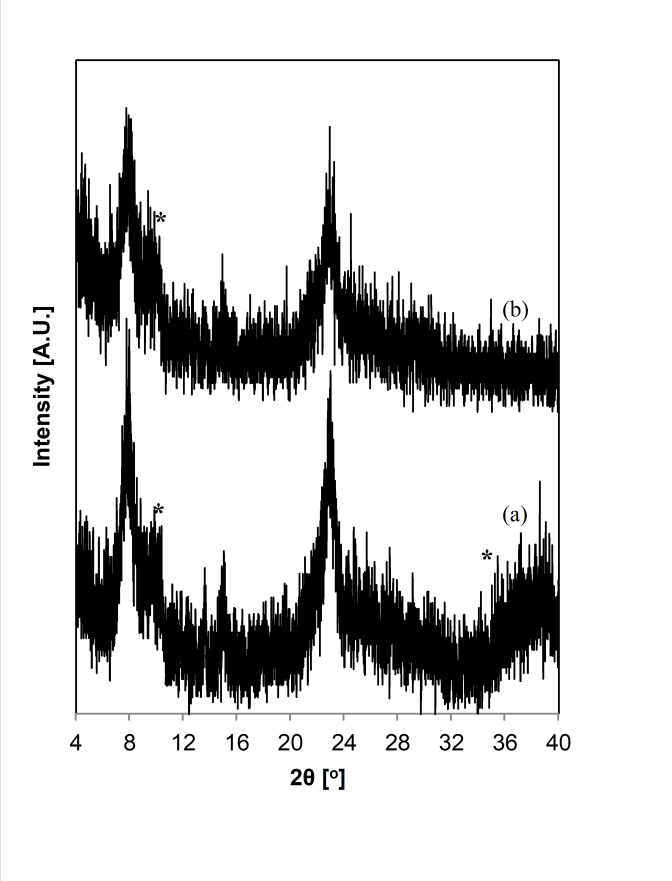

Figure 3.11: XRD patterns of (a) Sn-Beta-OH-47 and (b) Sn-Beta-OH-84. The XRD patterns for the parent Al-Beta-OH-54 and its dealuminated Beta are given in Fig. 3.11. *Denotes a feature that is an artifact from the sample holder used.

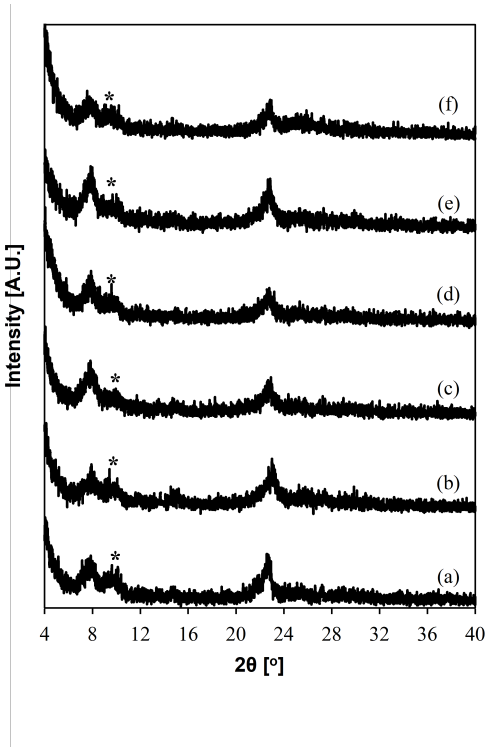

Figure 3.12: XRD patterns of (a) Al-Beta-OH-19, (b) dealuminated Beta, and (c) Sn-Beta-OH-95, (d) Sn-Beta-OH-46, (e) Sn-Beta-OH-41, and (f) Sn-Beta-OH-30. *Denotes a feature that is an artifact from the sample holder used.

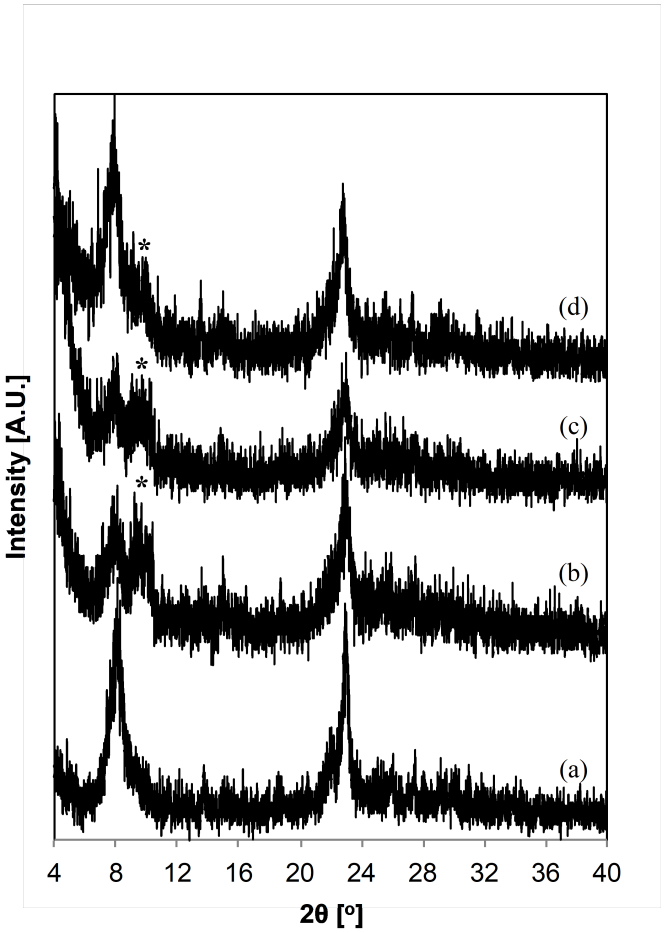

Figure 3.13: XRD patterns of (a) Al-Beta-OH-29, (b) Sn-Beta-OH-32, (c) Sn-Beta-OH-40, and (d) Sn-Beta-OH-80. *Denotes a feature that is an artifact from the sample holder used.

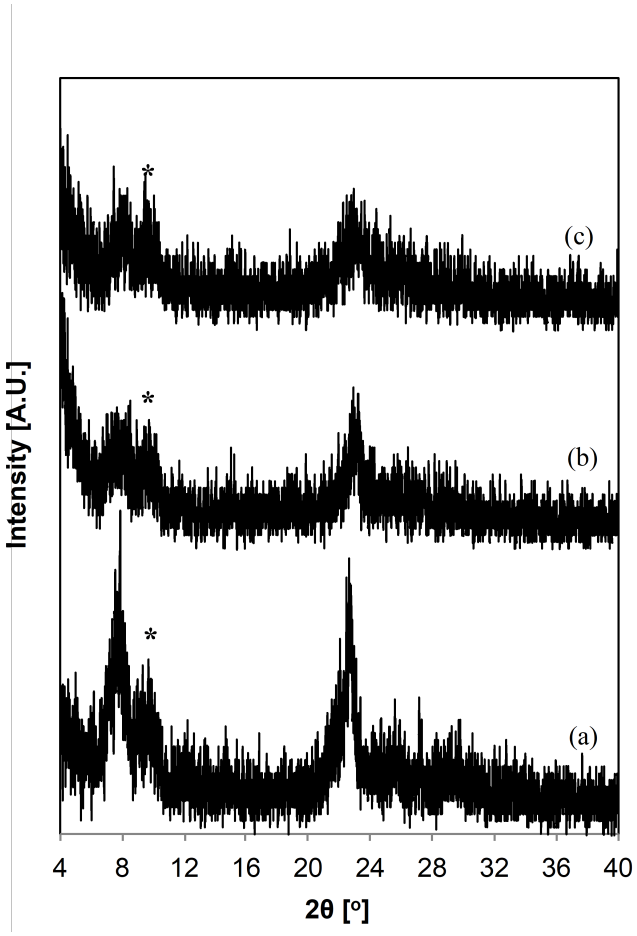

Figure 3.14: XRD patterns of (a) Al-Beta-OH-22, (b) dealuminated Beta, and (c) Sn-Beta-OH-144. *Denotes a feature that is an artifact from the sample holder used.

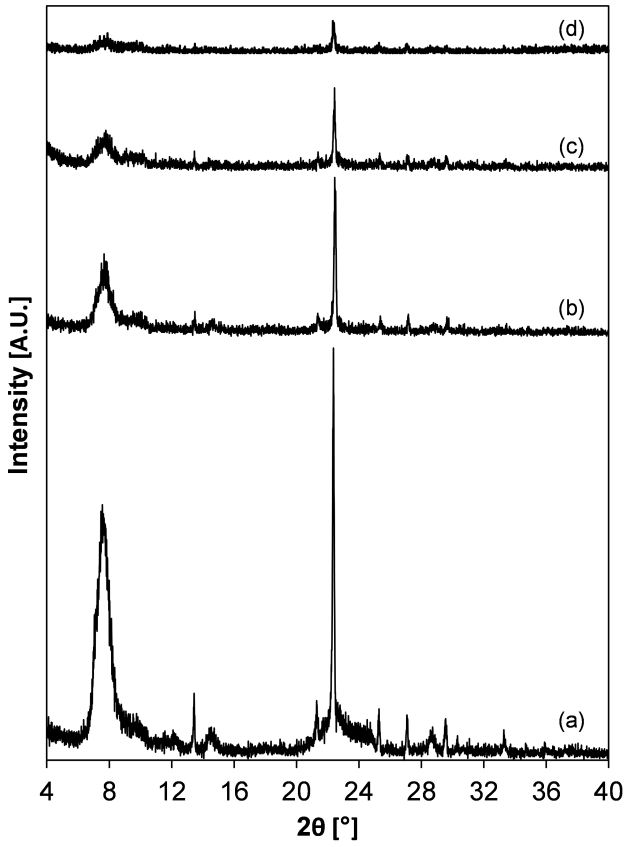

Figure 3.15: XRD patterns of (a) Al-Beta-F-45, (b) dealuminated Beta, (c) Sn-Beta-F-93, and (d) Sn-Beta-F-50.

3.7.2 Scanning electron microscope images of stannosilicate samples.

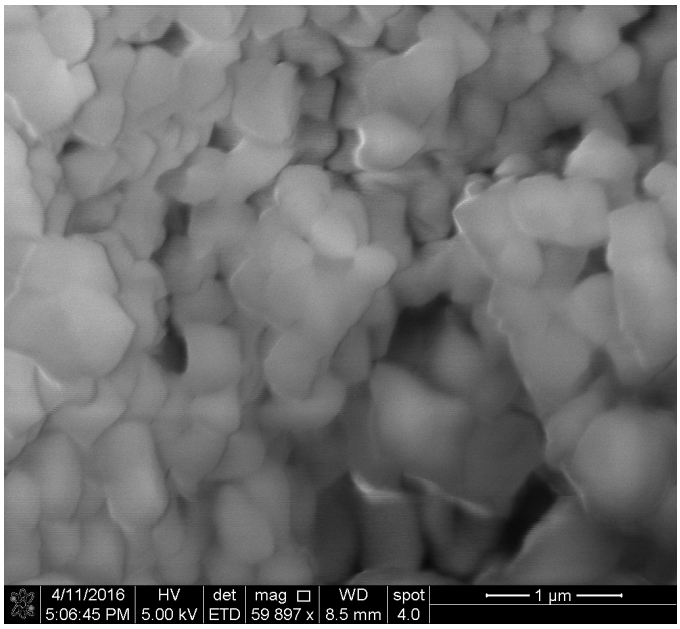

Figure 3.16: SEM image of Al-Beta-OH-54.

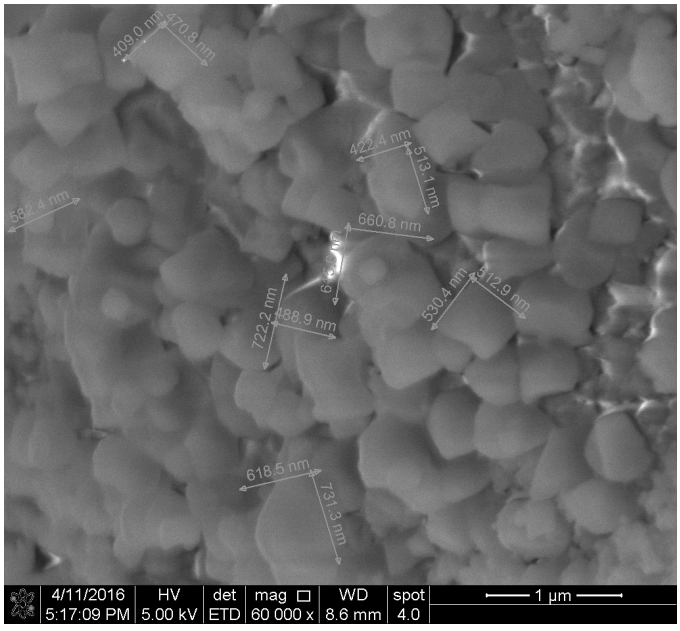

Figure 3.17: SEM image of dealuminated Beta (starting Al-Beta-OH-54).

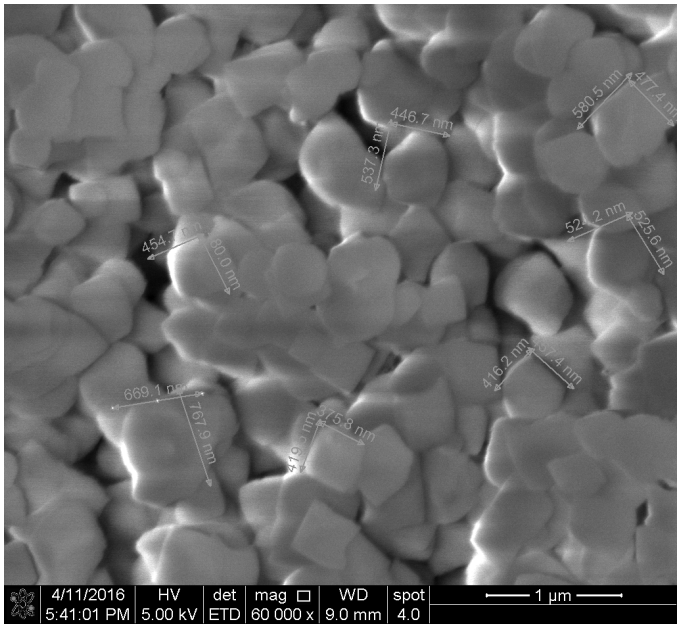

Figure 3.18: SEM image of Sn-Beta-OH-47.

3.7.3 Physicochemical properties of stannosilicates and synthesis specification.

Table 3.6 contains the elemental compositions and reflux concentration used to synthesize each Sn-Beta sample described in the main text. Also, micropore volumes were regularly between 0.19-0.22 cm^3 (per g), consistent with the Beta topology. Decreases in the V_{pore} (cm^3 g^{-1}) were observed for each Sn-Beta series that may reflect partial occlusion of micropore volume from incomplete Sn incorporation, or some framework degradation, that becomes more pronounced with higher amounts of Sn incorporated into the final material.

Table 3.6: Synthesis conditions, elemental compositions, and pore volume for Sn-Beta samples.

Catalyst	Solvent[a]	Initial Si/Al[b,c]	Si/Sn[b,c]	V_{pore} $cm^3\ g^{-1}$
Al-Beta-OH-19	-	19	-	0.22
Dealuminated Beta	-	>1500	-	-
Sn-Beta-OH-95	DCM	19	95	0.22
Sn-Beta-OH-46	DCM	19	46	0.19
Sn-Beta-OH-41	DCM	19	41	0.19
Sn-Beta-OH-30	DCM	19	30	0.16
Al-Beta-OH-29	-	29	-	0.24
Dealuminated Beta	-	>1500	-	-
Sn-Beta-OH-80	DCM	29	80	0.22
Sn-Beta-OH-40	DCM	29	40	0.19
Sn-Beta-OH-32	DCM	29	32	0.19
Al-Beta-OH-54	-	54	-	0.22
Dealuminated Beta	-	>1500	-	-
Sn-Beta-OH-84	DCM	54	84	0.20
Sn-Beta-OH-47	DCM	54	47	0.21
Al-Beta-OH-22	-	22	-	0.22
Dealuminated Beta	-	>1500	-	-
Sn-Beta-OH-144	DCM	22	144	0.23
Al-Beta-F-45	-	45	-	0.22
Dealuminated Beta	-	>1500	-	0.23
Sn-Beta-F-93	DCM	45	93	0.22
Sn-Beta-F-50	DCM	45	50	0.22
Sn-Beta-OH-170[d]	IPA	25	170	0.22
Sn-Beta-OH-457	IPA	15	457	0.22

Table 3.6: Synthesis conditions, elemental compositions, and pore volume for Sn-Beta samples.

Catalyst	Solvent[a]	Initial Si/Al[b,c]	Si/Sn[b,c]	V_{pore} $cm^3\ g^{-1}$
Sn-Beta-OH-200[d]	IPA	54	200	0.19

[a]DCM = dichloromethane; IPA = isopropanol.

[b]Measured by AAS.

[c]Errors are ±15%.

[d]Originally reported in Harris et al. [26].

3.7.4 Diffuse reflectance UV-Vis spectra of stannosilicate samples.

Diffuse reflectance UV-Visible (DRUV) spectra were collected for all the Sn-Beta samples grafted using isopropanol and dichloromethane as reflux solvents, and are shown in Figs. 3.19-3.33. Spectra were collected at ambient conditions with a dry Helium flow (thin line), after a heat treatment at 523 K for 0.5 h under inert flow (thick line), and after rehydration under "wet" He flow to 303 K (dashed line). Spectra and edge energies for Sn-Beta-OH-170 and Sn-Beta-200 were first published in Harris et al. [26]. The edge energies (Table 3.7) were calculated from the linear regime x-intercept of the low energy from Tauc plots (Figs. 3.34-3.38).

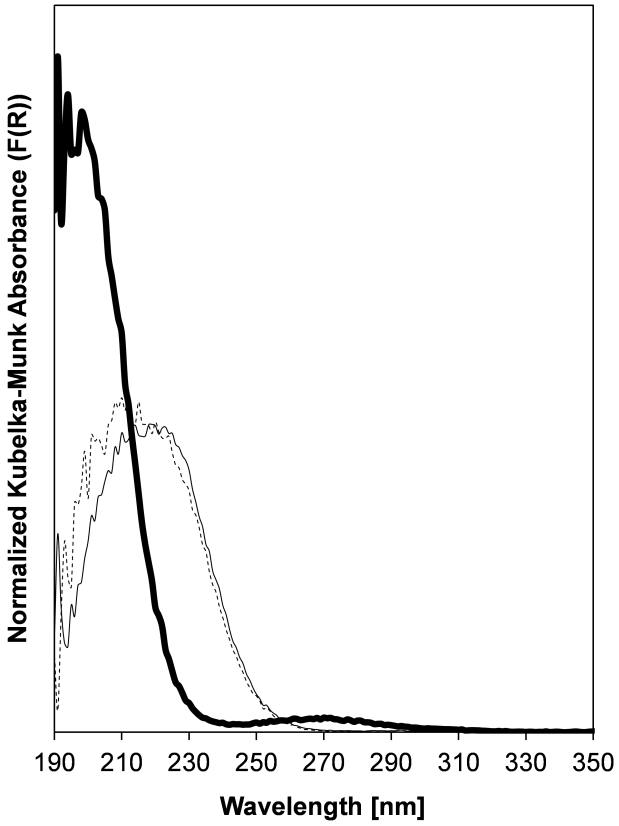

Figure 3.19: DRUV spectra of Sn-Beta-OH-200 at ambient conditions (thin solid line), after dehydration at 523 K for 900 s (thick solid line) and after rehydration in flowing water vapor (thin dotted line).

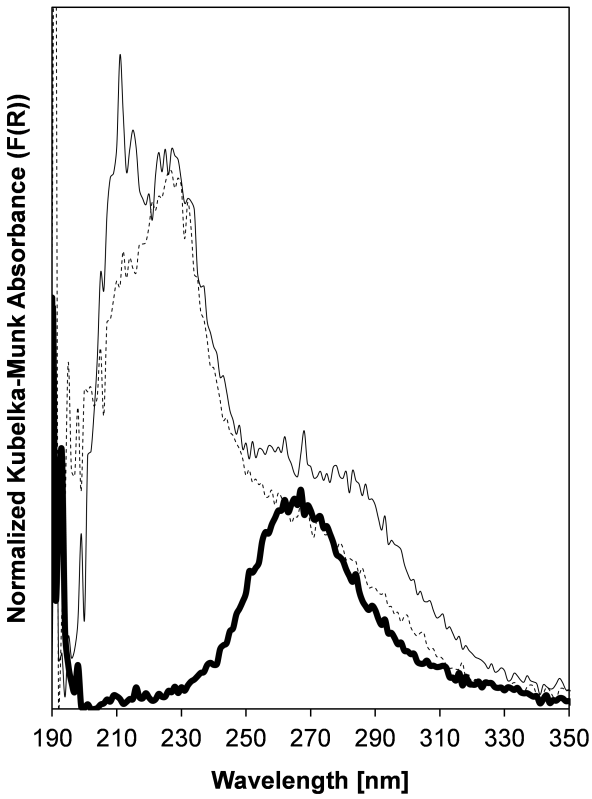

Figure 3.20: DRUV spectra of Sn-Beta-OH-170 at ambient conditions (thin solid line), after dehydration at 523 K for 900 s (thick solid line) and after rehydration in flowing water vapor (thin dotted line).

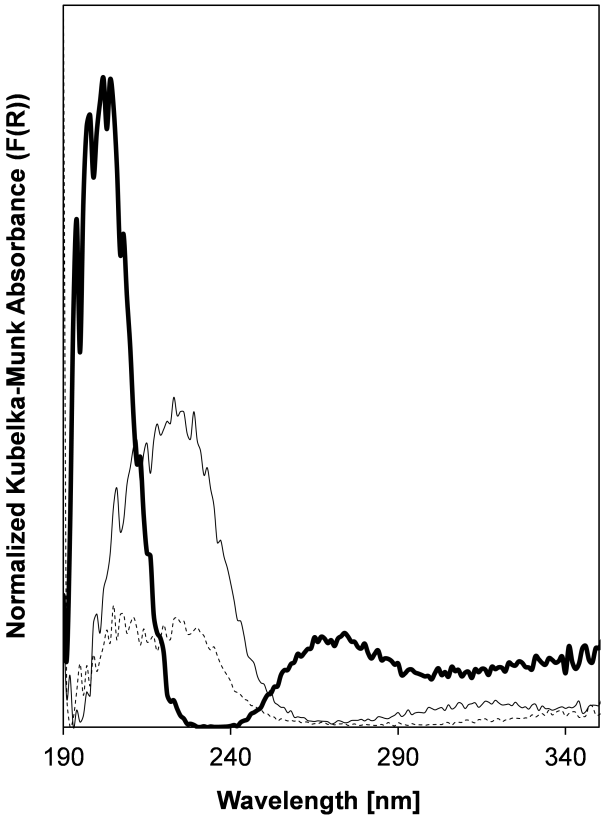

Figure 3.21: DRUV spectra of Sn-Beta-OH-457 at ambient conditions (thin solid line), after dehydration at 523 K for 900 s (thick solid line) and after rehydration in flowing water vapor (thin dotted line).

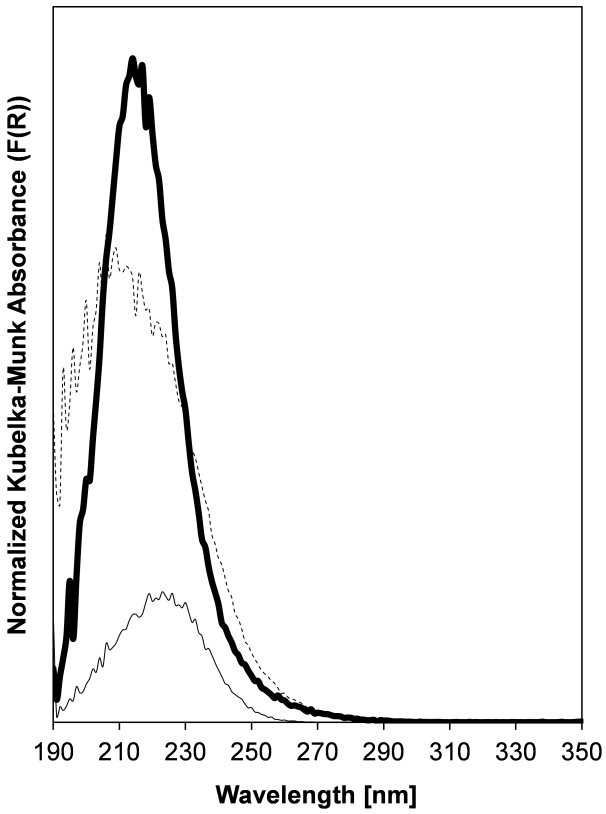

Figure 3.22: DRUV spectra of Sn-Beta-OH-47 at ambient conditions (thin solid line), after dehydration at 523 K for 900 s (thick solid line) and after rehydration in flowing water vapor (thin dotted line).

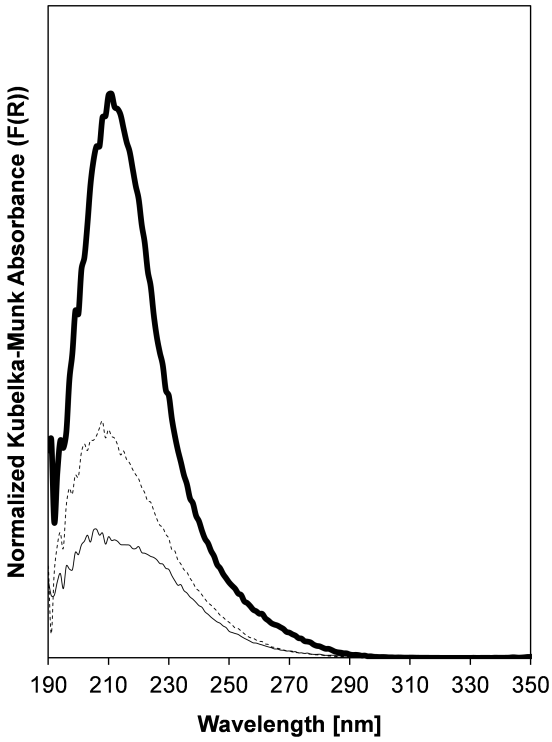

Figure 3.23: DRUV spectra of Sn-Beta-OH-32 at ambient conditions (thin solid line), after dehydration at 523 K for 900 s (thick solid line) and after rehydration in flowing water vapor (thin dotted line).

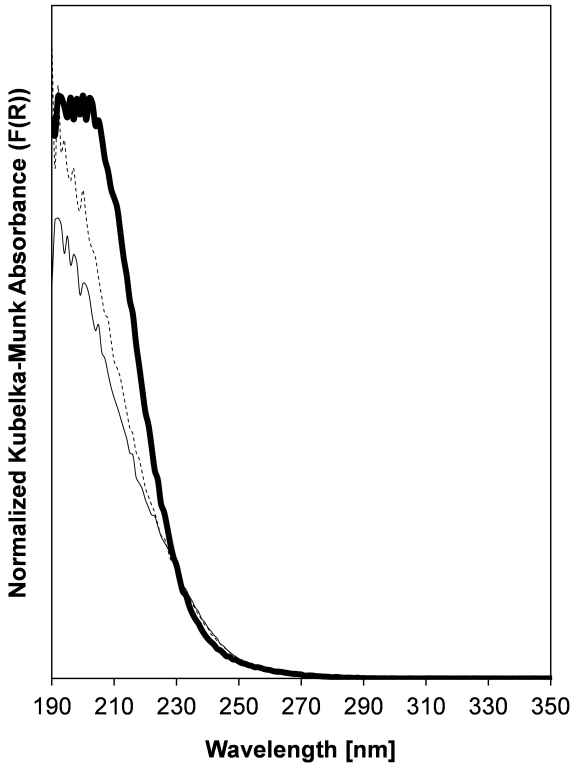

Figure 3.24: DRUV spectra of Sn-Beta-OH-84 at ambient conditions (thin solid line), after dehydration at 523 K for 900 s (thick solid line) and after rehydration in flowing water vapor (thin dotted line).

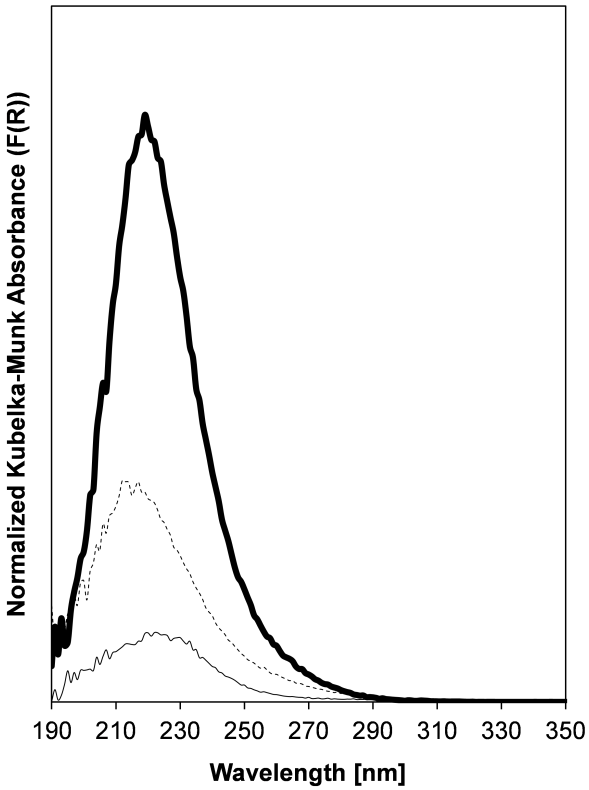

Figure 3.25: DRUV spectra of Sn-Beta-OH-40 at ambient conditions (thin solid line), after dehydration at 523 K for 900 s (thick solid line) and after rehydration in flowing water vapor (thin dotted line).

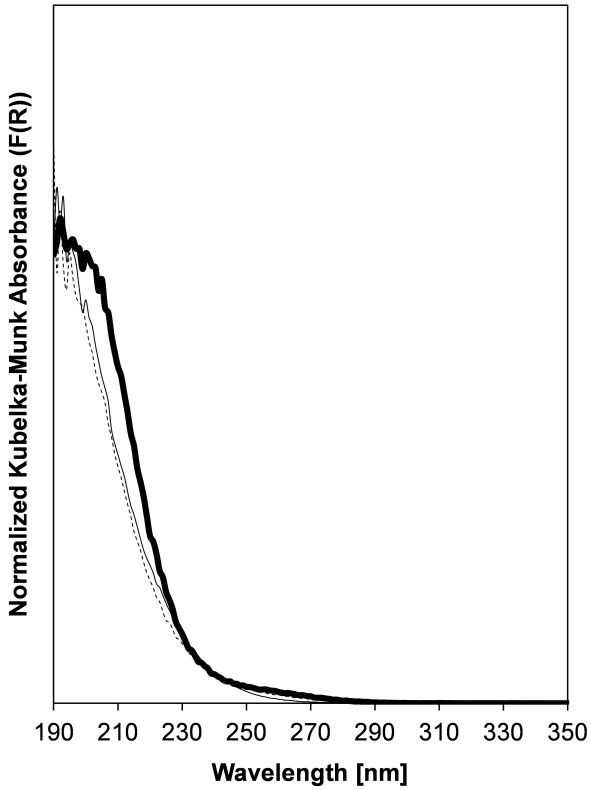

Figure 3.26: DRUV spectra of Sn-Beta-OH-80 at ambient conditions (thin solid line), after dehydration at 523 K for 900 s (thick solid line) and after rehydration in flowing water vapor (thin dotted line).

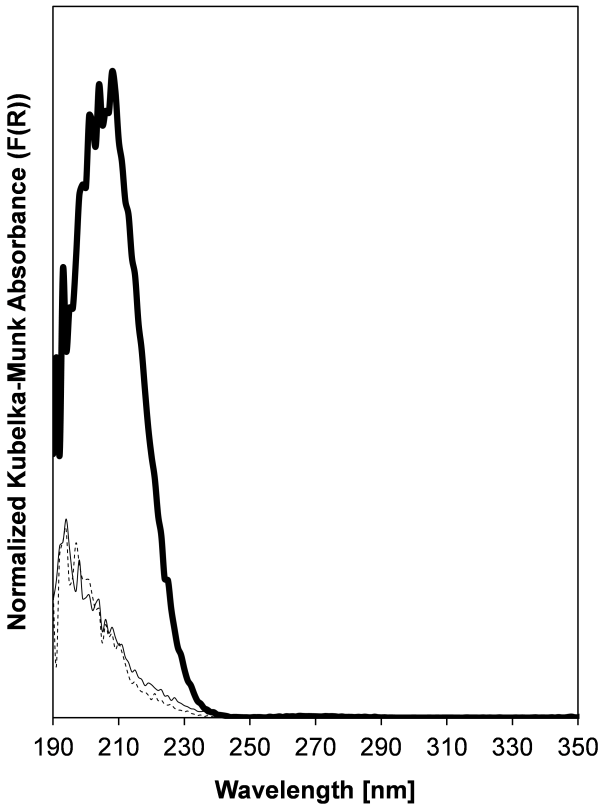

Figure 3.27: DRUV spectra of Sn-Beta-OH-95 at ambient conditions (thin solid line), after dehydration at 523 K for 900 s (thick solid line) and after rehydration in flowing water vapor (thin dotted line).

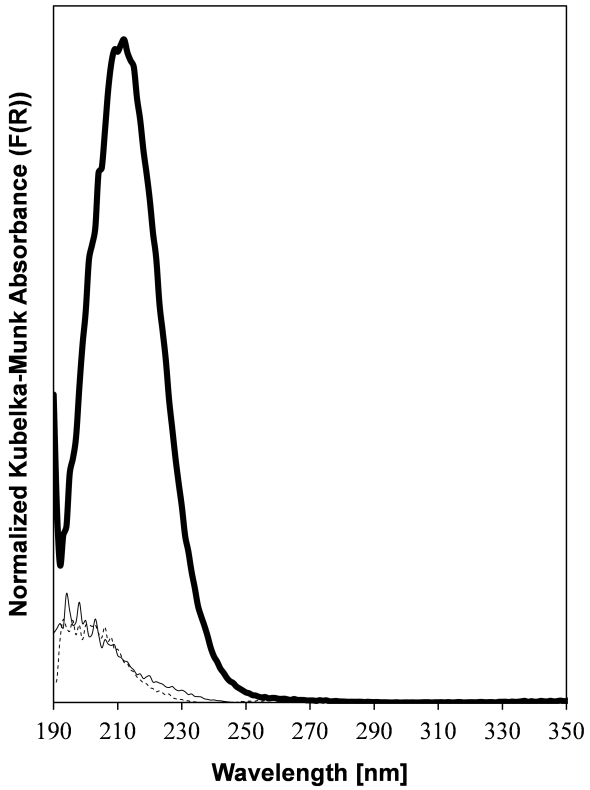

Figure 3.28: DRUV spectra of Sn-Beta-OH-46 at ambient conditions (thin solid line), after dehydration at 523 K for 900 s (thick solid line) and after rehydration in flowing water vapor (thin dotted line).

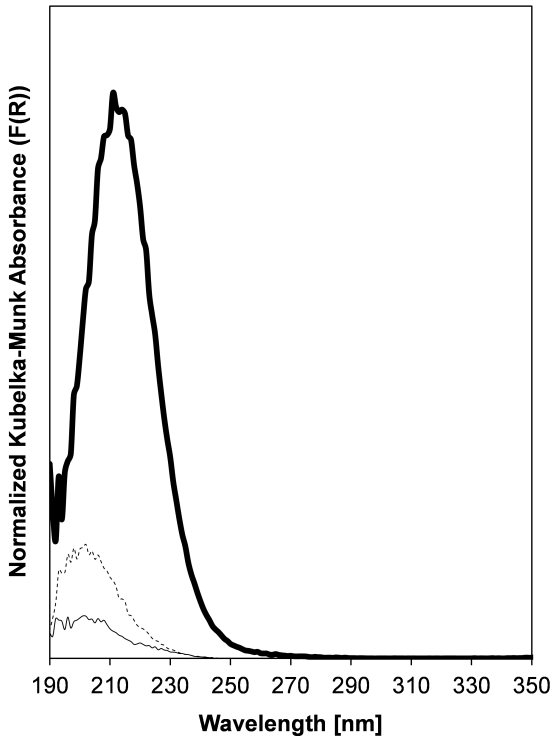

Figure 3.29: DRUV spectra of Sn-Beta-OH-41 at ambient conditions (thin solid line), after dehydration at 523 K for 900 s (thick solid line) and after rehydration in flowing water vapor (thin dotted line).

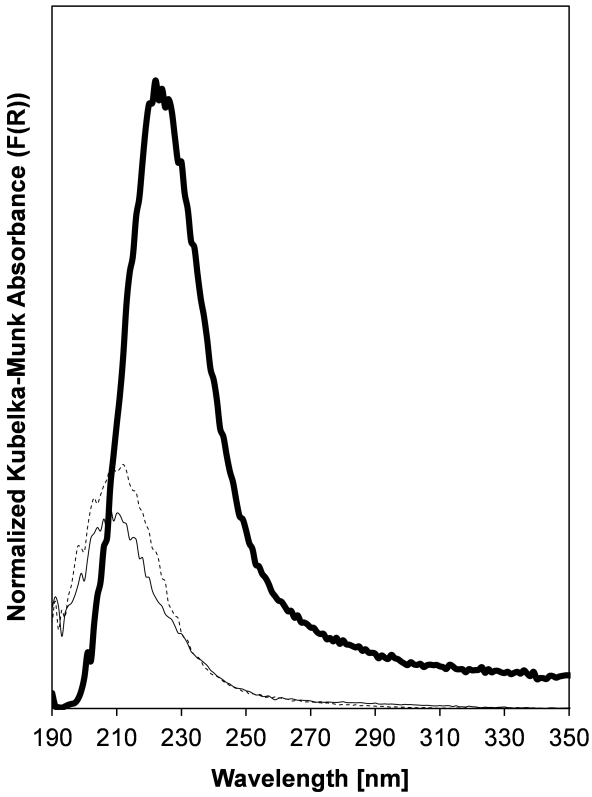

Figure 3.30: DRUV spectra of Sn-Beta-OH-30 at ambient conditions (thin solid line), after dehydration at 523 K for 900 s (thick solid line) and after rehydration in flowing water vapor (thin dotted line).

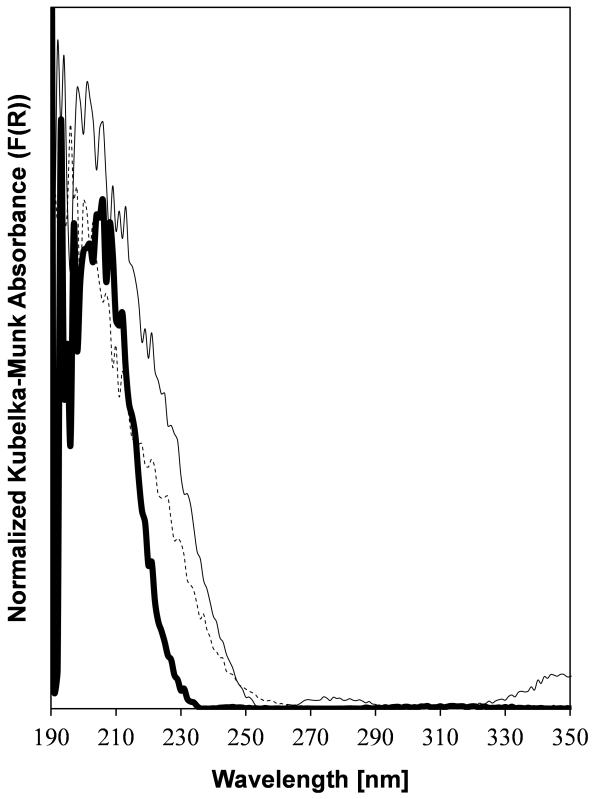

Figure 3.31: DRUV spectra of Sn-Beta-OH-144 at ambient conditions (thin solid line), after dehydration at 523 K for 900 s (thick solid line) and after rehydration in flowing water vapor (thin dotted line).

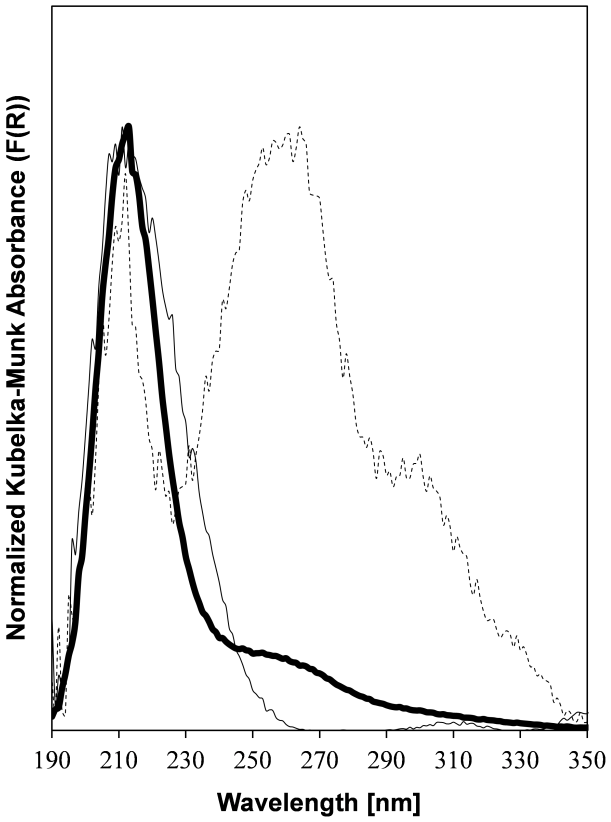

Figure 3.32: DRUV spectra of Sn-Beta-F-93 at ambient conditions (thin solid line), after dehydration at 523 K for 900 s (thick solid line) and after rehydration in flowing water vapor (thin dotted line).

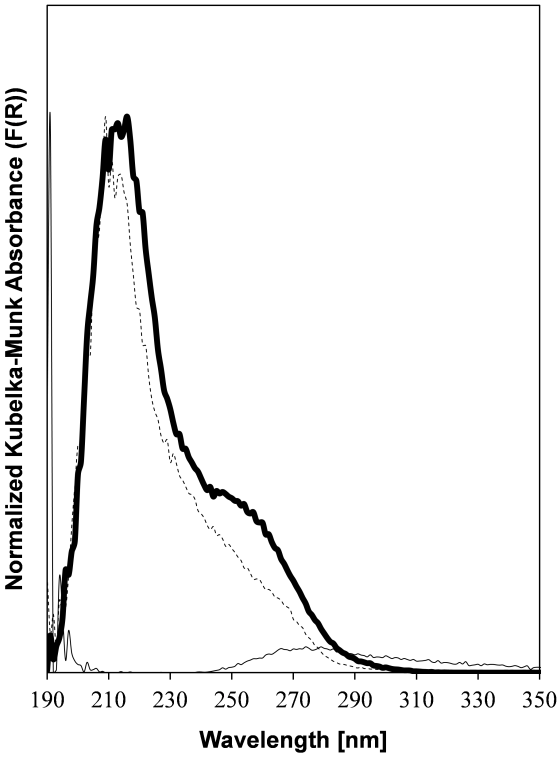

Figure 3.33: DRUV spectra of Sn-Beta-F-50 at ambient conditions (thin solid line), after dehydration at 523 K for 900 s (thick solid line) and after rehydration in flowing water vapor (thin dotted line).

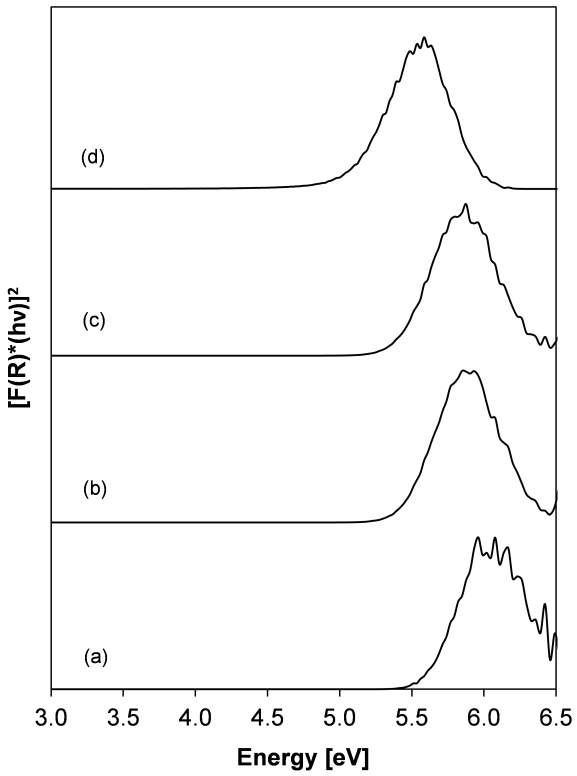

Figure 3.34: Tauc plots of (a) Sn-Beta-OH-95, (b) Sn-Beta-OH-46, (c) Sn-Beta-OH-41, and (d) Sn-Beta-OH-30. Data collected at 523 K.

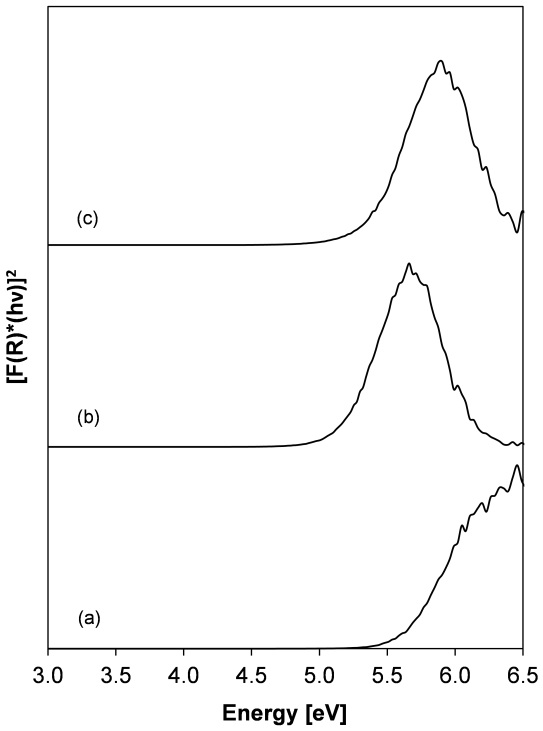

Figure 3.35: Tauc plots of (a) Sn-Beta-OH-80, (b) Sn-Beta-OH-41, and (c) Sn-Beta-OH-32. Data collected at 523 K.

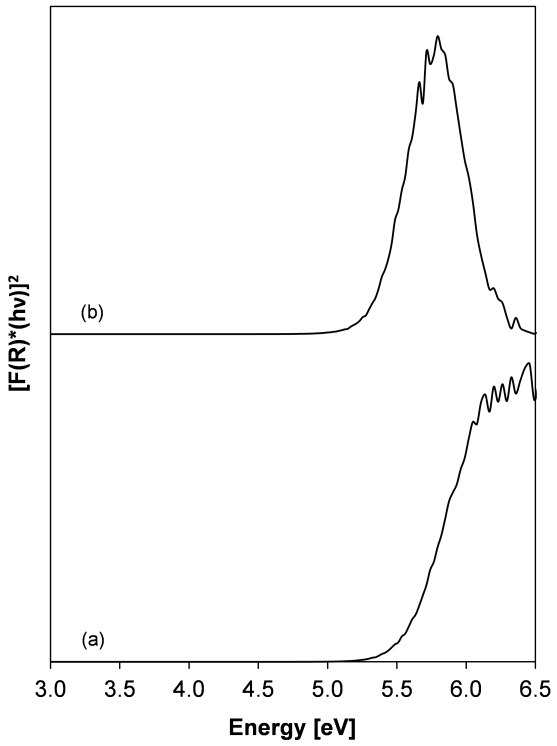

Figure 3.36: Tauc plots of (a) Sn-Beta-OH-84 and (b) Sn-Beta-OH-47. Data collected at 523 K.

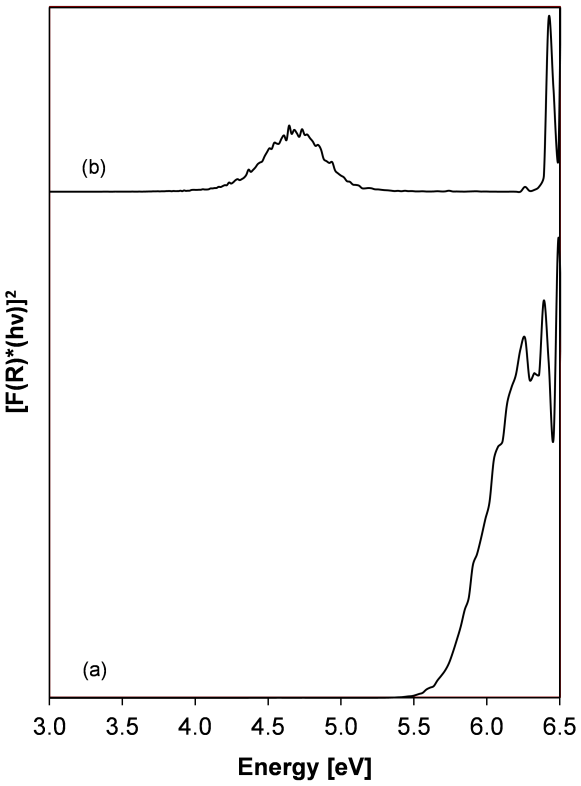

Figure 3.37: Tauc plots of (a) Sn-Beta-OH-200 and (b) Sn-Beta-OH-170. Data originally reported in Harris et al. [26].

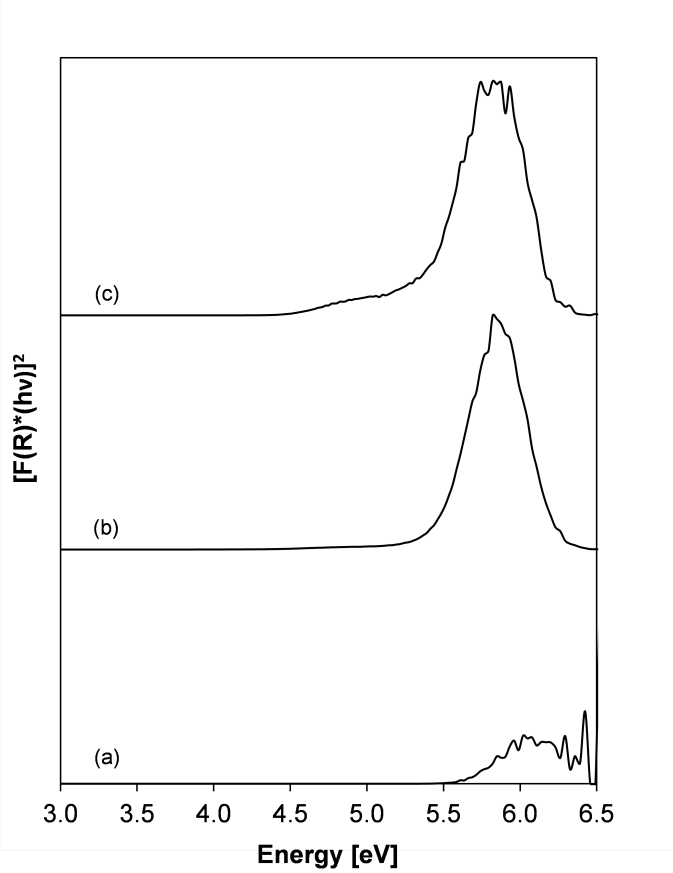

Figure 3.38: Tauc plots of (a) Sn-Beta-OH-144, (b) Sn-Beta-F-93, and (c) Sn-Beta-F-50. Data collected at 523 K.

Table 3.7: DRUV peak maximum and edge energy after thermal treatment at 523 K.

Sample	Solvent	Peak Maximum (nm)	Edge Energy (eV)
Sn-Beta-OH-95	Dichloromethane	208	5.60
Sn-Beta-OH-46	Dichloromethane	212	5.42
Sn-Beta-OH-41	Dichloromethane	211	5.40
Sn-Beta-OH-30	Dichloromethane	222	5.06
Sn-Beta-OH-32	Dichloromethane	211	5.32
Sn-Beta-OH-40	Dichloromethane	219	5.15
Sn-Beta-OH-80	Dichloromethane	192	5.61
Sn-Beta-OH-47	Dichloromethane	214	5.32
Sn-Beta-OH-84	Dichloromethane	200	5.54
Sn-Beta-OH-144	Dichloromethane	193	5.60
Sn-Beta-F-93	Dichloromethane	213	4.35 (5.45)[a]
Sn-Beta-F-50	Dichloromethane	216	4.47 (5.37)[a]
Sn-Beta-OH-457	Isopropanol	204	4.16 (5.85)[a]
Sn-Beta-OH-200[b]	Isopropanol	195	4.69
Sn-Beta-OH-170[b]	Isopropanol	193	4.25

[a]Edge energy in parenthesis represents an x-intercept of a distinctive linear regime at a higher energy.

[b]Originally reported in Harris et al. [26].

3.7.5 Temperature programmed desorption with adsorbed isopropanol and dichloromethane.

TPD profiles (Fig. 3.39) were obtained for dealuminated Beta (starting Si/Al = 54) after saturation with isopropanol and dichloromethane at ambient conditions discussed in details in Section 3.4.2. The total moles of isopropanol evolved (4.1 x 10^{-3} mol isopropanol (g zeolite)$^{-1}$) from the TPD, calculated by integration of the area under the obtained profile, were $\sim$5$\times$ the amount of vacancies (8.3 x 10^{-4} mol Al (g zeolite)$^{-1}$ in the starting Al-Beta-OH-54), suggesting adsorption to different binding sites (e.g., silanol nests and silanol defects in the external crystal surface).

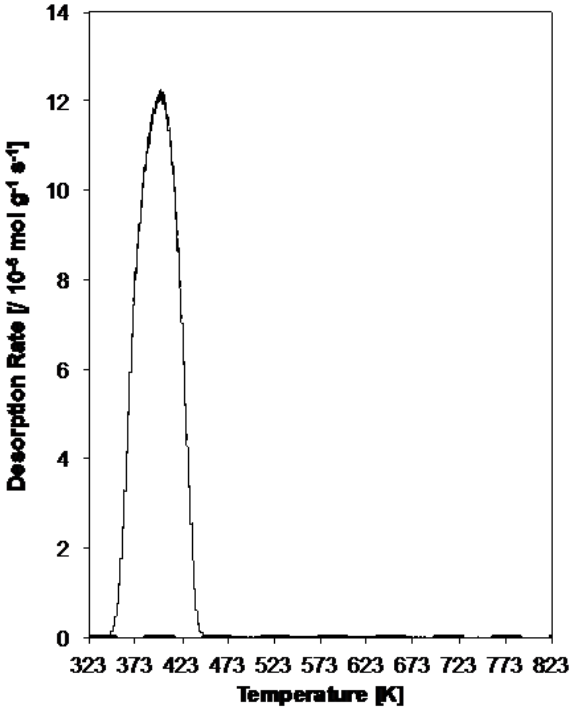

Figure 3.39: Temperature programmed desorption profiles of dealuminated Beta after saturation at ambient temperature with isopropanol (solid line) and dichloromethane (dashed line).

3.7.6 Studies with Infrared spectroscopy: OH stretching region during isopropanol dosing.

IR spectra collected after titration of dealuminated Beta with isopropanol (383 K) before dosing (solid, thin line), after saturation (solid, thick line), and after steady-state (2 h) was reached under static vacuum (dashed line).

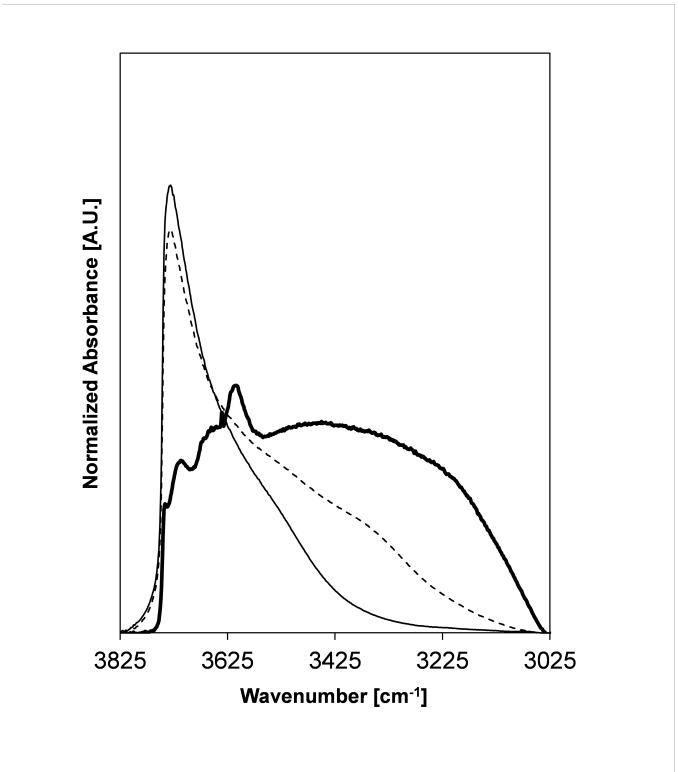

Figure 3.40: IR spectra of dealuminated Beta before dosing isopropanol (thin line), after saturation (thick line), and at steady-state under vacuum (dashed line) at 383 K.

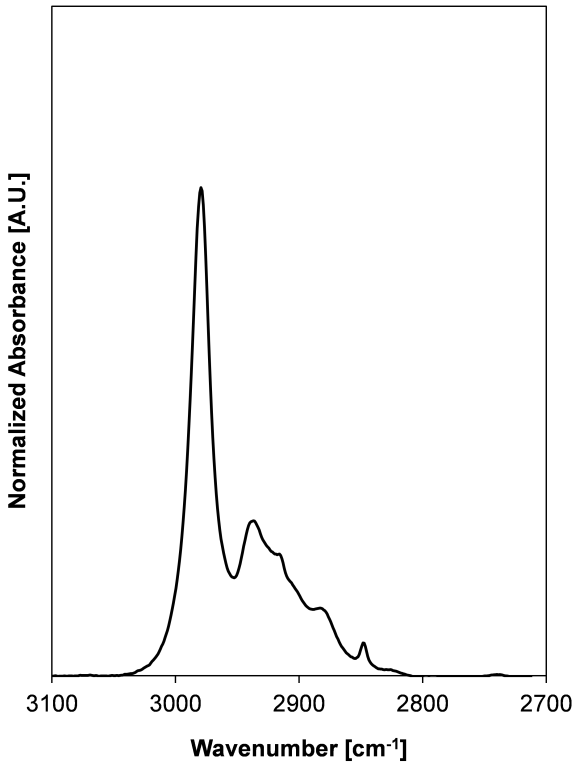

Figure 3.41: IR spectra (383 K) of dealuminated Beta after dosing isopropanol until saturation and subsequent evacuation.

3.7.7 Studies with Infrared spectroscopy after titration with CD_3CN and pyridine.

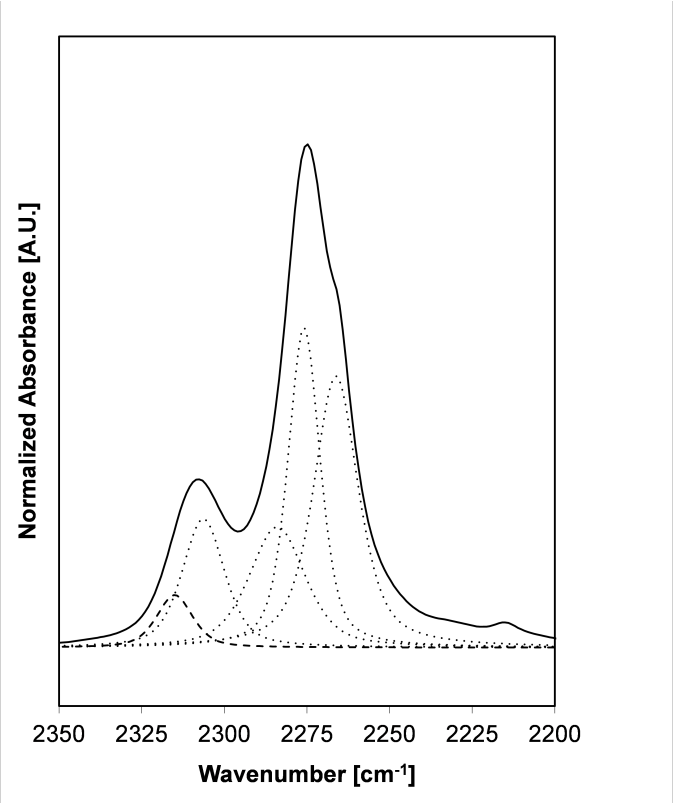

Figure 3.42: IR spectrum of Sn-Beta-OH-47 (solid line) after CD_3CN saturation and its deconvolution components (dashed lines) at 2265 cm^{-1}, 2275 cm^{-1}, 2285 cm^{-1}, 2308 cm^{-1}, and 2316 cm^{-1} for CD_3CN in the gas-phase or physisorbed, bound to silanol groups, bound to a defective Sn site (e.g., $Sn(OSi)_2(OH)_2$), closed Sn sites, and open Sn sites, respectively [26].

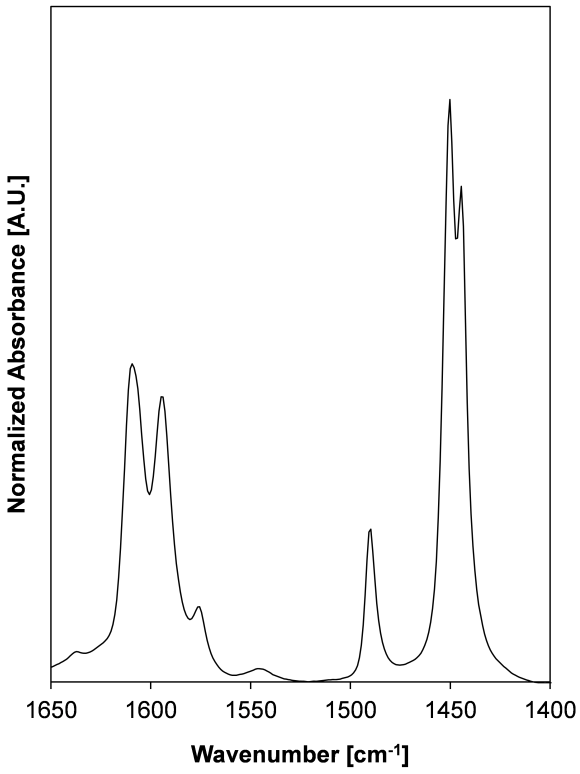

Figure 3.43: IR spectrum of Sn-Beta-OH-47 (solid line) after saturation with pyridine. The spectrum was convoluted with contributions for Lewis acid sites at 1450 cm^{-1} and 1615 cm^{-1}, Brønsted or Lewis acid sites at 1490 cm^{-1} and 1575 cm^{-1}, Brønsted acid sites at 1550 cm^{-1}, and gas-phase pyridine at 1595 cm^{-1}. The moles of Lewis acidic Sn were obtained by deconvolution of the band at 1450 cm^{-1} and integrated molar extinction coefficients reported in Harris et al. [26].

Table 3.8: Moles of 2287 cm^{-1} (g zeolite)$^{-1}$ for stannosilicates prepared through post-synthetic grafting under dichloromethane reflux (333 K).

Catalyst	Mol 2287 cm^{-1} $(g)^{-1}$ $(/10^{-5})^a$
Sn-Beta-OH-95	8.2
Sn-Beta-OH-46	17.0
Sn-Beta-OH-41	13.1
Sn-Beta-OH-30	18.6
Sn-Beta-OH-80	8.3
Sn-Beta-OH-40	21.6
Sn-Beta-OH-32	22.3
Sn-Beta-OH-84	13.6
Sn-Beta-OH-47	10.5
Sn-Beta-OH-144	11.4
Sn-Beta-F-93	5.6
Sn-Beta-F-50	8.3

[a]Molar extinction coefficient used to calculate the moles of 2287 cm^{-1} sites was obtained from Harris et al. [26].

3.7.8 Derivation of Langmuir isotherm expression describing Sn grafting into framework vacancy defects.

The grafting of Sn atoms into framework vacancy defects follows a Langmuir isotherm that can be described by Eq. 3.2. To form these vacancies, Al-Beta (initial aluminum content = total vacancy defects = $[*]_0$) samples were dealuminated to form graftable vacancies (Σ Vac$_{graft}$) and non-graftable vacancies (Vac$_{non-graft}$):

$$[*]_0 = [*]_{non-graft} + [*]_{graft} \tag{3.4}$$

Furthermore, the number of graftable vacancies can be expressed as the summation of the available graftable vacancies (*) and the vacancies that have been grafted with Sn atoms (Sn*) as follows:

$$[*]_{graft} = [*] + [Sn*] \tag{3.5}$$

Substitution of Eq. 3.5 into 3.4 then provides the total amount of starting aluminum as a function of the non-graftable vacancies, available vacancies for grafting, and vacancies grafted with Sn:

$$[*]_0 = [*]_{non-graft} + [*] + [Sn*] \tag{3.6}$$

Eq. 3.6 can be normalized to the total concentration of vacancy defects to provide:

$$1 = \frac{[*]_{non-graft}}{[*]_0} + \frac{[*]}{[*]_0} + \frac{[Sn*]}{[*]_0} \tag{3.7}$$

Which can also be expressed in terms of fractional coverages (θ_i) of each species (i):

$$1 = \theta_{non-graft} + \theta_* + \theta_{Sn} \tag{3.8}$$

This expression can be rearranged to obtained the fractional coverage of available defects for grafting:

$$\theta_* = (1 - \theta_{non-graft}) + \theta_{Sn} \ , = \frac{[*]_{graft}}{[*]_0} + \theta_{Sn} \tag{3.9}$$

The grafting of Sn into available vacancy defects, which takes place in solvent reflux (e.g., dichloromethane or isopropanol), is described by the following equilibrium reaction:

$$Sn_{eq.} + * \, K_0 \, Sn* \tag{3.10}$$

where K', the equilibrium constant, can be expressed as:

$$K_0 = \frac{[Sn*]}{C^0} = \frac{\theta_{Sn} C^0}{[Sn_{reflux}][\theta_*]} \tag{3.11}$$

where C^0 is the standard state reference concentration (1 M). Now, multiplying Eq. 3.11 by the total concentration of vacancies:

$$K = \frac{\theta_{Sn}}{[Sn_{eq.}][\theta_*]}[*]_0 = \frac{\theta_{Sn}}{[Sn][\theta_*]} \tag{3.12}$$

where K is defined as the multiplication of the equilibrium constant and the total concentration of vacancies in a given dealuminated Beta ($K_0[*]_0$) and [Sn] represents the equilibrium concentration of Sn in the reflux solution (per vacancy). Eq. 3.12 can be combined with Eq. 3.9 and rearranged to obtain an expression for the Langmuir isotherms described in Section 3.4.3:

$$\theta_S n = \frac{[Sn*]}{[*]_0} = (\frac{[*]_{graft}}{[*]_0}) \frac{K[Sn]}{1 + K[Sn]} = (\theta_{max}) \frac{K[Sn]}{1 + K[Sn]} \tag{3.13}$$

3.7.9 Kinetic studies of glucose isomerization to fructose with stannosilicates and assessment of intraparticle mass transfer limitations.

Though a detailed mechanistic study of glucose-to-fructose has been reported [2], we provide a supplementary derivation for the rate expression used in Section 3.4.4. Glucose-to-fructose isomerization reactions take place through quasi-equilibrated des-

orption of two water molecules (W*, 2W*) from Sn sites (*), followed by quasi-equilibrated glucose (G) adsorption and ring opening intermediates (G*), kinetically-limited hydride shift to produce fructose (F*), and quasi-equilibrated ring closing and desorption of fructose. At dilute concentrations of aqueous glucose concentration (1% (w/w)), the most likely most abundant surface intermediate is the two water molecules (2W*) [1,2]. Thus, turnover rates normalized per total number of active sites ([L]), under differential conditions (η <<1), can be written as [2]:

$$\frac{r_{isom}}{[L]} = \frac{\gamma_{2W*}\gamma_G\gamma_*}{\gamma_W^2 C_W^2 \gamma_*}\frac{k_2 K_1}{K_4 K_5} C_G = k_{isom} C_G \tag{3.14}$$

where γ_i represents the activity coefficients of reactants and intermediate species (i), k_2 is the rate constant of the intramolecular 1,2-hydride shift to form fructose, K_1 is the equilibrium constant for glucose adsorption and ring-opened glucose intermediates at Sn sites, K_4 and K_5 are equilibrium constants for adsorption of two water molecules at Sn sites, C_W is the water concentration, C_G is the extrazeolite glucose concentration in water, and kisom is the measured first-order isomerization rate constant.

Turnover rates (373 K) written in Eq. 3.14 reflect first-order dependence on the glucose concentration for kinetically-limited hydride shift steps, but also for reactions limited by glucose transport to intrazeolitic voids. First-order rate constants (373 K) measured with glucose-D2 will provide a kinetic isotope effect equal to ∼2.1 if the rates were kinetically-limited by C1-C2 hydride shift (C-H scissoring vibrational frequency of ∼1500 cm^{-1}) [3] and equal to ∼1.5 if rates were limited by intraparticle mass transfer [2]. Here, a KIE experiment on the Sn-Beta-OH with the highest isomerization rate constant (per total Sn, 373 K), most likely to present mass transfer limitations, provided a k_H/k_D of ∼2.1. By extension, the initial rates reported in the main text represent kinetically-limited processes, a requirement for rigorous interpretation of measured kinetic data.

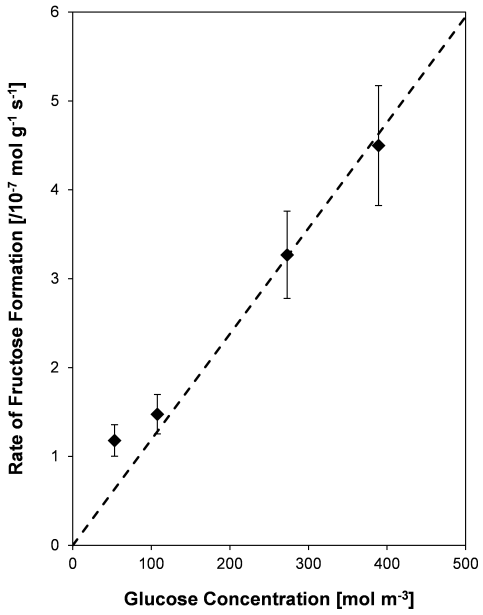

Figure 3.44: First-order dependence of initial rate of fructose (per g) formation on the initial glucose concentration for Sn-Beta-OH-47.

Table 3.9: First-order rate constants (per open Sn) for hydrothermally-synthesized Sn-Beta samples [26] in Fig. 3.7.

Catalyst	k_{isom} ($/10^{-3}$ mol fructose (mol open Sn)$^{-1}$ (mol glucose m^{-3})$^{-1}$ s^{-1})
Sn-Beta-F-100	0.94
Sn-Beta-F-105	0.31
Sn-Beta-F-110	0.38
Sn-Beta-F-140	0.44
Sn-Beta-F-170	0.77
Sn-Beta-F-220	0.50

3.7.10 Assessment of the hydrophobicity of Sn-Beta with vapor-phase adsorption of H_2O and CH_3OH.

H_2O adsorption isotherms (293 K) were collected for the Sn-Beta samples grafted under dichloromethane (Figs.3.45-3.48) and isopropanol (Fig. 3.49) reflux, and one representative sample prepared hydrothermally (Fig. 3.49) [26] to evaluate the hydrophobic character of these zeolites. The H_2O uptake at P/P_0=0.2 (Table 3.10) is consistently higher (>4x) for all Sn-Beta-(OH,F) samples than for the hydrothermal Sn-Beta-F, and within 2× of their parent Al-Beta-(OH,F) for the twelve samples studied here. The similar H_2O uptakes for Sn-Beta samples grafted from the same dealuminated Beta results from the binding of vapor-phase H_2O to a variety of binding sites such as Sn centers and silanol defects located in the external crystallite surface and in internal voids.

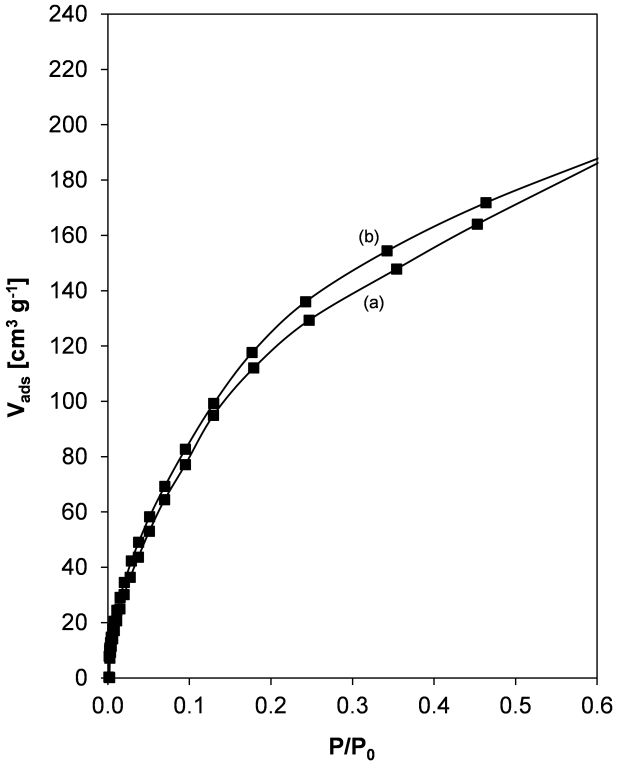

Figure 3.45: H_2O isotherms (293 K) of (a) Sn-Beta-OH-84 and (b) Sn-Beta-OH-47. Sn-Beta-OH samples were synthesized from Al-Beta-OH-54.

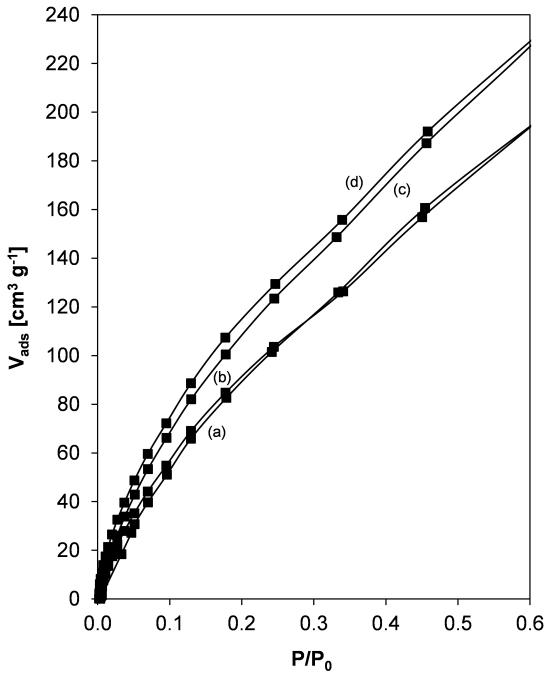

Figure 3.46: H_2O isotherms (293 K) of (a) Sn-Beta-OH-41, (b) Sn-Beta-OH-95, (c) Sn-Beta-OH-30, and (d) Sn-Beta-OH-46. All the Sn-Beta-OH samples were synthesized from Al-Beta-OH-19.

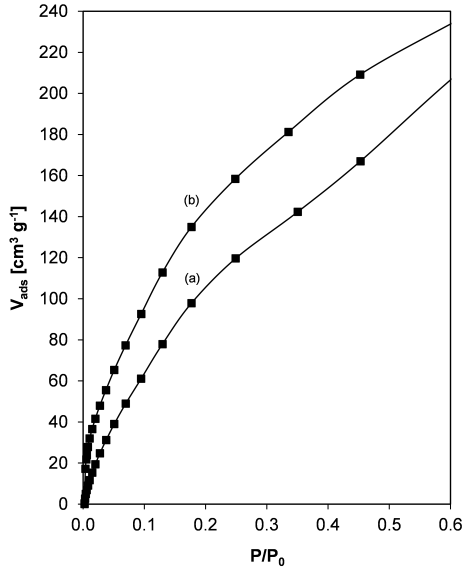

Figure 3.47: H_2O isotherms (293 K) of (a) Sn-Beta-OH-80 and (b) Al-Beta-OH (Si/Al = 29). Sn-Beta-OH samples synthesized from parent Al-Beta-OH-29.

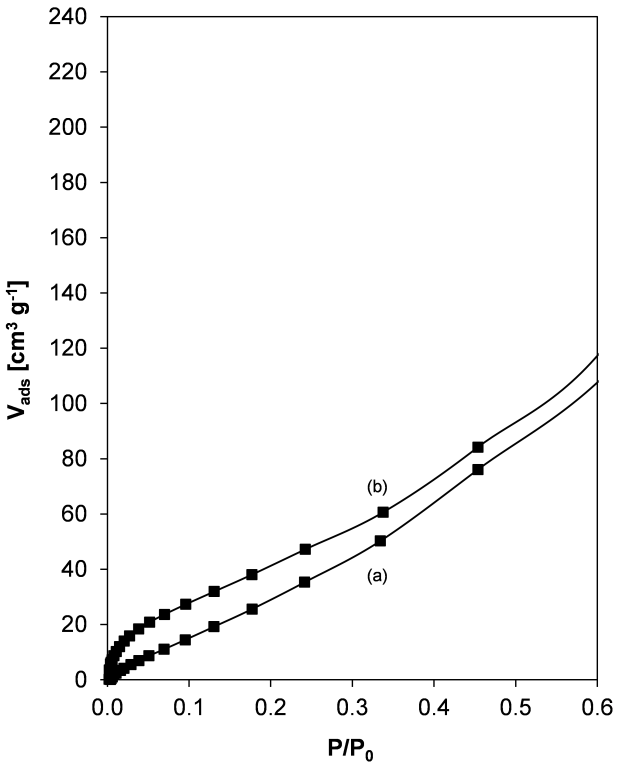

Figure 3.48: H_2O isotherms (293 K) of (a) Sn-Beta-F-93 and (b) Al-Beta-F-45. Sn-Beta-F was synthesized with parent Al-Beta-F-45.

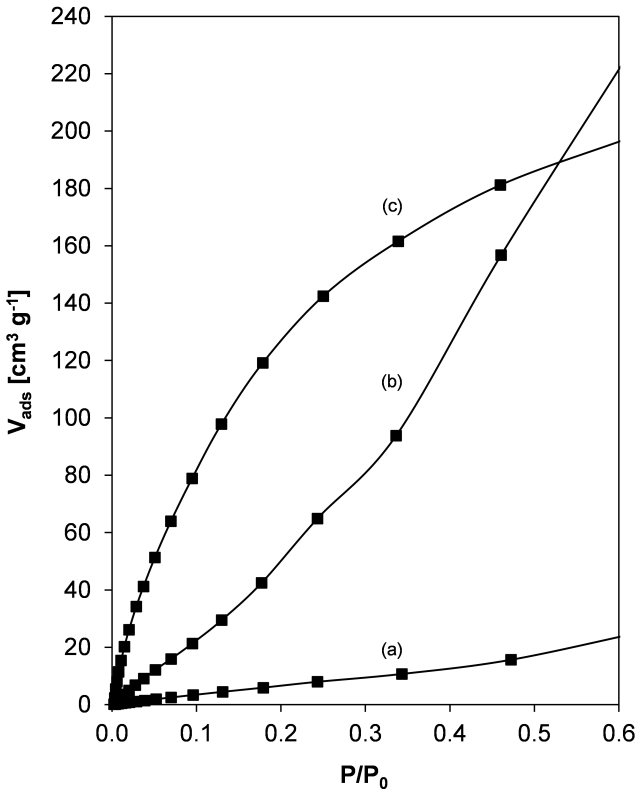

Figure 3.49: H_2O isotherms (293 K) of (a) Sn-Beta-F-220 prepared hydrothermally, (b) Sn-Beta-OH-170, and (c) Sn-Beta-OH-200. Isotherms originally reported in Harris et al. [26].

Table 3.10: H_2O uptake of Sn-Beta samples measured at a relative pressure (P/P_0) of 0.2.

Catalyst	H_2O uptake ($cm^3\ g^{-1}$)
Sn-Beta-OH-84	0.085
Al-Beta-OH-29	0.103
Sn-Beta-OH-47	0.090
Sn-Beta-OH-80	0.076
Sn-Beta-OH-95	0.066
Sn-Beta-OH-46	0.083
Sn-Beta-OH-41	0.065
Sn-Beta-OH-30	0.078
Al-Beta-F-45	0.030
Sn-Beta-F-93	0.021
Sn-Beta-OH-170[a]	0.036
Sn-Beta-OH-200[a]	0.092
Sn-Beta-F-220[a,b]	0.005

[a]Reported in Harris et al. [26].

[b]Hydrothermally-synthesized Sn-Beta-F.

4. THE DOMINANT ROLE OF ENTROPY IN STABILIZING SUGAR ISOMERIZATION TRANSITION STATES WITHIN HYDROPHOBIC ZEOLITE PORES

4.1 Abstract

Lewis acid sites in zeolites catalyze aqueous-phase sugar isomerization at higher turnover rates when confined within hydrophobic than within hydrophilic micropores; however, relative contributions of competitive water adsorption at active sites and preferential stabilization of isomerization transition states have remained unclear. Here, we employ a suite of experimental and theoretical techniques to elucidate the effects of co-adsorbed water on glucose isomerization reaction coordinate free energy landscapes. Transmission IR spectra provide evidence that water forms extended hydrogen-bonding networks within hydrophilic but not hydrophobic micropores of Beta zeolites. Aqueous-phase glucose isomerization turnover rates measured on Ti-Beta zeolites transition from a first-order to zero-order dependence on glucose thermodynamic activity, as Lewis acidic Ti sites transition from water-covered to glucose-covered, consistent with intermediates identified from modulation excitation spectroscopy during *in situ* attenuated total reflectance IR experiments. First-order and zero-order isomerization rate constants are systematically higher (by 3–12x, 368–383 K) when Ti sites are confined within hydrophobic micropores. Apparent activation enthalpies and entropies reveal that glucose and water competitive adsorption at Ti sites depends weakly on confining environment polarity, while Gibbs free energies of hydride-shift isomerization transition states are lower when confined within hydrophobic micropores. DFT calculations suggest that interactions between intraporous water and isomerization transition states increase effective transition state sizes through second-shell solvation spheres, reducing primary solvation sphere flex-

ibility. These findings clarify the effects of hydrophobic pockets on the stability of co-adsorbed water and isomerization transition states and suggest design strategies that modify micropore polarity to influence turnover rates in liquid water.

4.2 Introduction

Hydrophobic surfaces are characterized by weak hydrogen bonding interactions with water molecules, which cause structural changes to molecular ensembles and extended water networks near surfaces [129] that are referred to collectively as "hydrophobic effects" [130]. At least three distinct hydrophobic effects have been recognized during aqueous-phase reactions catalyzed within metalloenzymes, including hydrophobic side chains that provide contacts that increase free energies to drive water diffusion from binding pockets during protein folding [131], hydrophilic side chains that hydrogen bond with water molecules to preferentially position them within specific locations in binding pockets [132], and hydrophobic and hydrophilic groups that regulate water movement along reaction coordinates to facilitate enthalpy-entropy compromises that moderate reaction free energy landscapes [133–135]. Hydrophobic effects on water adsorption have also been observed at silica surfaces [136], as well as within defect-free carbon nanotubes of sub-nanometer pore diameter [137] and defect-free silica surfaces positioned less than one nanometer apart [138], which lack surface groups capable of hydrogen bonding and lead to the confinement of gas-like water rather than the "ice-like" structures confined within highly-defective and hydrophilic microporous voids. The influence of surrounding environment hydrophobicity on the structure and behavior of confined water has been noted generally in biomolecular recognition [130] and in reports of enhanced water transport in carbon nanotubes for separation and molecular sensing applications [139–142], in addition to applications in catalysis [143, 144].

Within the context of liquid-phase catalysis, hydrophobic pockets within inorganic microporous materials influence the free energies of reactive intermediates and transition states that result in differences in adsorption equilibrium constants and reaction rate constants. Several studies have focused on zeolites, which are crystalline silica-based materials whose microporous surfaces are composed of non-polar and hydrophobic siloxane bonds, but become increasingly hydrophilic with increas-

ing densities of framework heteroatom substituents or of silanol and other hydroxyl groups that donate and accept hydrogen bonds. Silanol groups originate from framework siloxy (i.e., SiO^-) defects that form during hydrothermal synthesis when cationic structure directing agents are not charge balanced either by aliovalent heteroatoms substituted in framework positions (e.g., Al^{3+}) [145, 146] or by counter-anions occluded within extraframework locations (i.e., F-) [116, 147, 148]. Silanol groups can also form after synthesis upon hydrolysis of framework siloxane linkages in neutral or basic aqueous media [60, 149], or upon removal of framework heteroatoms (e.g., Al, B) in acidic media [150, 151]. The adsorption of gaseous water on zeolites measured by gravimetry increases with silanol density [16, 106], consistent with higher intraporous water densities that are stabilized with increasing silanol density when zeolites are contacted or equilibrated with liquid water [26]. Higher intraporous water densities have been shown to influence the kinetics of catalytic reactions, such as to cause preferential stabilization of protonated water and propanol clusters during gas-phase propanol dehydration on Brønsted acidic Al-MFI zeolites that enhances rates of bimolecular or trimolecular dehydration pathways over those of monomolecular routes [152]. Hydrophobic channels in Lewis acidic Ti-MFI zeolites increase 1-hexene epoxidation rates relative to hydrophilic TiO_2-SiO_2 surfaces by mitigating the formation of bulk water structures near Ti sites [153], while silanol groups near Ti sites in UCB-4 zeotypes lead to increases cyclohexene epoxidation rates [154]. Hydrophobic channels also increase rates for a variety of monomolecular and bimolecular reactions, such as aqueous-phase and biphasic m-cresol alkylation with 2-propanol in Al-FAU zeolites [155, 156], aqueous-phase 1-hexene epoxidation on Ti-MWW zeolites [157], hydrogenation and etherification of hydroxymethylfurfural in alcohol solvents on metal-substituted Beta zeolites [58], gas-phase bimolecular ethanol dehydration at high water partial pressures on Sn-Beta zeolites [158, 159], and aqueous-phase Meerwein-Ponndorf-Verley reduction and Oppenauer oxidation (MPVO) reactions in Ti-Beta [35] and Sn-Beta zeolites [26].

Here, we study aqueous-phase glucose isomerization catalysis that proceeds via Lewis acid-mediated intramolecular hydride shift steps on a suite of materials synthesized with site-isolated framework Ti centers (Si/Ti = 30-300) and residual silanol defect densities that vary by two orders of magnitude (10^{-5}-10^{-3} mol g^{-1}) to isolate the kinetic effects of hydrophobic confining pockets around Ti centers. In prior reports, first-order aqueous-phase glucose isomerization rate constants were higher on hydrophobic Ti-Beta (∼7-10x, 373 K) [35] and Sn-Beta (∼50x, 373 K) [26] zeolites than their hydrophilic analogs, but rate data measured in first-order kinetic regimes are unable to resolve the kinetic contributions of glucose and water competitive adsorption from those of isomerization transition state stabilization. Co-adsorbed water within Sn-Beta micropores has been reported to decrease experimentally measured glucose and 1,3-dihydroxyacetone isomerization rates, which was attributed to the competitive adsorption of water and substrate molecules at Sn sites [160]. In contrast, density functional theory (DFT) studies report that silanol defects in Sn-Beta lower activation barriers to form 1,2-hydride shift transition states during glucose-fructose isomerization [64] and enthalpically stabilize adsorbed deprotonated glucose intermediates [161] via hydrogen bonding interactions, while *ab initio* molecular dynamics (AIMD) simulations indicate that explicit co-adsorbed water molecules lower activation free energies via solvent reorganization and charge redistribution throughout the reaction coordinate [162]. These studies emphasize that understanding the specific structure and density of co-adsorbed water molecules under reaction conditions, and their separate influence on the free energies of reactive intermediates and transition states involved in sugar isomerization, remains a relevant and active area of research.

The incomplete understanding of water density and structure within microporous environments of different polarity precludes more precise definitions of the kinetic and mechanistic effects of hydrophobic reaction pockets on sugar isomerization catalysts. Here, we report a detailed kinetic analysis of initial glucose isomerization turnover rates (normalized per Lewis acid site) on hydrophobic Ti-Beta-F and hydrophilic

Ti-Beta-OH zeolites in first-order and zero-order kinetic regimes as a function of temperature (368-383 K), which enables measuring rate constants, activation enthalpies and activation entropies that separate the effects of confining environment polarity on transition state stabilization and water competitive adsorption. The kinetic effects of co-adsorbed solvent molecules on relevant intermediates and transition states are determined from a suite of *ex situ* and *in situ* experimental characterizations and insights from DFT calculations. These combined experimental and computational results highlight the dominant role of hydrophobic pockets to prevent the formation of extended water structures. Such co-adsorbed water structures confer modest enthalpic stabilization, but more severe entropic destabilization, of isomerization transition states that ultimately lead to lower turnover rates.

4.3 Materials and Methods

4.3.1 Catalyst Synthesis

Ti-Beta-F zeolites were synthesized in fluoride media following a previously reported hydrothermal synthesis method [106]. A gel was prepared by first mixing 4.89 g of tetraethylammonium fluoride (TEAF, Alfa Aesar, 97 wt.%) with 7.25 g of deionized water (18.2 MΩ) in a perfluoroalkoxy alkane (PFA) container (Savillex Corp.) followed by the addition of 10.0 g of tetraethylorthosilicate (TEOS, Sigma Aldrich, >98 wt.%). The resulting gel was stirred for 1 h prior to adding 0.221 g of titanium(IV) isopropoxide (TIPO, Sigma Aldrich, 99.999%). The PFA container was sealed and the contents stirred for 16 h prior to removing the cover to allow ethanol, isopropanol, and excess water to evaporate. The final gel molar composition was 1 SiO_2 / x TIPO / 0.55 TEAF / 7.15 H_2O where x ranged between 0.005 and 0.0087. The gel was then loaded and sealed into a Teflon-lined stainless steel autoclave (45 cm^3, Parr Instruments) with 0.14 g of Si-Beta-F (∼5% of Si in the gel) and heated to 413 K while rotating (60 rpm) in an isothermal oven (Yamato DKN-402C) for 25 days. The products were removed from the liner and washed with water and acetone (Sigma Aldrich, >99.5 wt.%, 6 washes each, ∼20 cm^3 (g zeolite) $^{-1}$ per wash), centrifuged to recover the solid portion, and dried for 16 h at 373 K. The resulting solids were then heated in a muffle furnace (Nabertherm LE 6-11 with P300 controller) in flowing dry air (Indiana Oxygen, Ultra Zero Grade, 1.67 cm^3 s^{-1} (g solids) $^{-1}$) to 853 K (0.0167 K s^{-1}) for 10 h.

Ti-Beta-OH zeolites were prepared using a previously reported post-synthetic reflux technique [25]. Briefly, Al-Beta zeolites (Si/Al = 20-50) were synthesized using a method similar to that reported previously [12] without the aluminosilicate gel filtration step. The recovered solids were washed, centrifuged, dried, and treated in air, as described above for Ti-Beta-F preparation. The resulting Al-Beta samples were dealuminated by stirring with nitric acid (69 wt.% HNO_3, Avantor, 25 cm^3 of solution per 1 g H-form zeolite) in a covered PFA container for 16 h at 353 K. The solids were

then washed thoroughly with water until a constant supernatant pH was observed, isolated via centrifugation, and dried for 16 h at 373 K. Dealuminated Beta samples were then treated in flowing dry air (Indiana Oxygen, Ultra Zero Grade, 1.67 cm^3 s^{-1} (g solids) $^{-1}$) to 853 K (0.0167 K s^{-1}) for 10 h. On each dealuminated Beta sample, the resulting Si/Al ratio was greater than 1500 as measured by atomic absorption spectroscopy (AAS). Afterward, 2 g of dealuminated Beta were loaded into a 500 cm^3 round bottom flask and dried for 12 h on a Schlenk line under rough vacuum (Oerlikon Trivac 140002E2, ∼0.04 Torr). Dichloromethane (CH_2Cl_2, Sigma Aldrich, ¿99.8%) was dried over 3A molecular sieves (W. R. Grace, 4-8 mesh, Grade 562) prior to being transferred via moisture-free and air-free cannula to the flask containing the dealuminated Beta zeolites. A solution of titanium (IV) tetrachloride pre-dissolved in CH_2Cl_2 (Sigma Aldrich, 1.0 M $TiCl_4$ in CH_2Cl_2) was further diluted in dry CH_2Cl_2 to achieve a concentration of 1 mmol $TiCl_4$ per gram of dealuminated Beta prior to cannula transfer to the round-bottom flask containing the dealuminated zeolite sample. This mixture was heated for 7 h under reflux at 333 K. The solids were then collected via centrifugation, washed 6 times (∼60 cm^3 per wash) with methanol (Sigma Aldrich, >99.9%), dried for 16 h at 373 K, and then thermally treated in air (Indiana Oxygen, Ultra Zero Grade, 1.67 cm_3 s^{-1} (g solids) $^{-1}$) to 473 K (0.05 K s^{-1}) for 6 h and then at 823 K (0.05 K s^{-1}) for 6 h in a muffle furnace.

4.3.2 Characterization of Bulk Catalyst Properties

Bulk elemental compositions were determined using atomic absorption spectroscopy (AAS) on a Perkin Elmer AAnalyst 300 Atomic Absorption Spectrometer after calibration using standard solutions for each element generated by dilution of 1000 ppm AAS standards (Alfa Aesar, TraceCERT, ± 4 ppm). Typically, 0.02 g of zeolite samples were dissolved in 2.6 g of HF (48 wt.%, Alfa Aesar) and 50 g of deionized water prior to characterization. Extreme caution should be taken when working with hydrofluoric acid, and appropriate personal protective equipment, ventilation, and other engineering controls should be used. Absorbance values were measured in

an acetylene/nitrous oxide flame at 396.2, 399.9, and 251.6 nm for Al, Ti, and Si respectively. Samples are denoted as Ti-Beta-X-Y, where X refers to the synthetic history (F = fluoride-mediated hydrothermal synthesis; OH = post-synthetic grafting of dealuminated Al-Beta) and Y reflects the bulk Si/Ti ratio (by AAS).

Powder X-ray diffraction (XRD) patterns were collected using a Rigaku Smartlab X-ray diffractometer with a Cu Kα source (1.76 kW) and an ASC-6 automated sample changer. Zero background, low dead volume sample holders (Rigaku) were loaded with approximately 0.01 g of sample prior to collecting diffraction patterns from 4-40^o at a scan rate of 0.00417^o s^{-1} with a step size of 0.01^o. The presence of TiOx domains larger than 3 nm (25.4^o and 37.9^o for anatase, 27.4^o and 35.2^o for rutile) was not observable in the XRD pattern of any sample studied here.

Nitrogen (77 K), water (293 or 298 K), and methanol (293 K) adsorption isotherms were collected using a Micromeritics ASAP2020 Surface Area and Porosity Analyzer. Typically, $\sim$0.03 g of sample were pelleted and sieved to obtain particle diameters between 180 and 250 μm. Samples were degassed prior to analysis by heating to 393 K (0.0167 K s^{-1}) under vacuum (<0.005 Torr) for 2 h then heating to 623 K (0.0167 K s^{-1}) under vacuum for 8 h. A semi-log derivative analysis of N_2 isotherms ($\delta(V_{ads}/g)/\delta(\log(P/P_0)$ vs. log (P/ P_0)) was used to identify the end of the micropore filling regime, in order to quantify the micropore volume of each sample. Water uptakes are reported at a reduced pressure of 0.2, which has been used previously [83] as a reference pressure corresponding to micropore filling of cyclohexane (298 K) within hydrophobic zeolites.

Scanning electron microscopy (SEM) was performed on a FEI Quanta 3D FEG Dual-beam SEM equipped with an Everhart-Thornlev detector for high vacuum imaging. The focused beam operating mode was used to collect SEM micrographs with a spot size of 4 μm and a voltage of 5 kV.

Diffuse reflectance UV-Vis (DRUV) spectra were collected on a Varian Cary 5000 UV-VIS-NIR equipped with a Harrick Praying Mantis *in situ* diffuse reflectance cell. UV-Vis spectra were collected at ambient conditions prior to thermally treating sam-

ples to 523 K (1800 s, ∼0.5 K s^{-1}) in dry flowing He (4.17 cm^3 s^{-1} (g solids) $^{-1}$), at which point spectra of dehydrated samples were collected at 523 K. Spectra were collected at a resolution of 10 nm s^{-1} using poly(tetraflouroethylene) (PTFE, Sigma Aldrich, 1 Ωm powder) as the 100% reflectance standard. Diffuse reflectance spectra were converted into absorbance spectra using the Kubelka-Munk (F(R)) function. Band centers are reported as that corresponding to the highest F(R) intensity on dehydrated samples.

4.3.3 Transmission Infrared Spectroscopy

A Nicolet 4700 spectrometer with an Hg-Cd-Te detector (MCT, cooled to 77 K by liquid N_2) was used to collect IR spectra by averaging 64 scans at a resolution of 2 cm^{-1} in the 4000 to 400 cm^{-1} range. Spectra were taken relative to an empty cell background reference collected under dynamic vacuum (<0.1 Torr, rotary vane rough pump, Alcatel 2008A) at either 303 K for deuterated acetonitrile (CD_3CN) adsorption studies or 423 K for pyridine adsorption studies. Self-supporting wafers of 0.01-0.03 g cm^{-2} were sealed in a custom-built quartz IR cell [163] with CaF_2 windows positioned within an alumina silicate ceramic chamber (Purdue Research Machining Services) with a mineral-insulated resistive heating coil (ARi Industries). K-type thermocouples (Omega) were positioned within 2 mm of each side of the wafer. A custom glass vacuum manifold was used for sample pretreatment and for dosing controlled amounts of gaseous titrants into the cell. Wafers were first thermally treated to 823 K (0.083 K s^{-1}) for 1 h in flowing dry air (6.66 cm^3 s^{-1} (g solids) $^{-1}$), which was further purified by an FTIR purge gas generator (<1 ppm CO_2, 200 K water dew point, Parker Balston) prior to each experiment. Wafers were then exposed to dynamic vacuum for 1 h at 823 K (¡0.1 Torr, rotary vane rough pump, Alcatel 2008A).

For CD_3CN titration experiments, wafers were then cooled under dynamic vacuum to 303 K. CD_3CN (Sigma Aldrich, >99.9%, 99.96 atom% D) was purified through three freeze-pump-thaw cycles prior to dosing ∼1.5 x 10^{-7} mol into the cell (similar

procedures for pyridine titration given in Section 4.7.1.2, Supp. Info.). The cell was allowed to equilibrate for 180 s at a constant final pressure for each dose prior to collecting each IR spectrum. Subsequent doses were introduced until wafer saturation was achieved, which was determined when final pressures >0.4 Torr were observed due to residual gaseous titrant within the cell. Wafers were then exposed to dynamic vacuum at the dosing temperature to remove gas phase and weakly-adsorbed species until a final pressure of 0.0 Torr was measured in the cell. IR spectra were baseline-corrected and normalized to combination and overtone modes of zeolite Si-O-Si stretches (1750-2100 cm^{-1}) followed by subtraction of the parent spectrum and deconvolution of the CD_3CN IR peaks into their individual components (2308, 2275, and 2265 cm^{-1}) as reported elsewhere [26]. Peak areas were used in conjunction with integrated molar extinction coefficients (E) to determine site concentrations per gram of zeolite:

$$Site\,density\,(\mu mol\,g^{-1}) = \left(\frac{Integrated\,Peak\,Area\,(cm^{-1})}{E\,(cm\,\mu mol^{-1})}\right)\left(\frac{a_{CS}(cm^2)}{m(g)}\right) \quad (4.1)$$

In the case of CD_3CN adsorbed onto silanol groups (2275 cm^{-1}), an integrated molar extinction coefficient value (E (2275 cm^{-1}) = 0.74 cm μmol^{-1}) measured on dealuminated Beta was used [26]. In the case of Lewis acidic Ti sites that give rise to the CD_3CN IR peak at 2308 cm^{-1}, an integrated molar extinction coefficient was measured following previously reported methods [26]. Briefly, Ti-Beta wafers were pretreated as mentioned above and sequentially dosed with small amounts of CD_3CN in vacuum (0.1–0.3 μmol CD_3CN per dose) prior to equilibration for 180 s. For these initial doses, the final recorded pressure in the cell was measured to be 0.0 Torr, and all of the CD_3CN dosed into the cell was assumed to be adsorbed onto the sample wafer. IR spectra were collected after each dose, baseline-corrected and normalized, and then deconvoluted into constituent peaks associated with v(C≡N) stretching vibrations for CD_3CN adsorbed onto Lewis acidic Ti sites (2308 cm^{-1}) and

silanols (2275 cm^{-1}) and for gas-phase or physisorbed CD_3CN (2265 cm^{-1}) at higher doses. The number of CD_3CN adsorbed onto Lewis acidic Ti sites was determined by quantifying the total amount of adsorbed CD_3CN via equilibrated pressure differences before and after dosing and subtracting contributions from silanol-bound CD_3CN.

For water adsorption experiments, the cell was first assembled without a sample wafer to quantify the contributions of water in the gas phase and adsorbed on cell windows. The cell was treated in flowing He (UHP, Indiana Oxygen, 0.96 cm^3 s^{-1}) at 823 K (0.0833 K s^{-1}) for 1 h, then cooled to 298 K. The temperature was controlled at 298 K (±2 K, the gradient observed between the two thermocouples on either side of the wafer was <1.5 K) by flowing air free of carbon dioxide and moisture through the cooling channels of the insulated brass block and by resistive heating. A spectrum was collected at 298 K in flowing He (0.96 cm^3 s^{-1}) and used as the background for all subsequent spectra. Liquid water (18.2 MΩ cm) was vaporized into the flowing He stream (0.96 cm^3 s^{-1}) from a syringe pump (KD Scientific Legato 100) equipped with a 1 cm^3 syringe (Hamilton) and delivered to the cell in heated lines (>363 K). The liquid water flow rate was varied to achieve partial pressures of 0.32, 0.63, 1.58, and 2.37 kPa, corresponding to P/P_0=0.10, 0.20, 0.50, and 0.75, respectively, at 298 K. Spectra were averaged over 64 scans at 2 cm^{-1} resolution in the 4000–650 cm^{-1} range and were monitored over time at each condition until invariant (>30 min), indicating that equilibrium was reached. After equilibrium was verified, a 640-scan spectrum at 2 cm^{-1} resolution was collected to average out temporal variations in gas-phase pressures and temperature.

Next, self-supporting wafers (0.015–0.040 g) of Ti-Beta-F-155 and Ti-Beta-OH-46 were pressed and loaded into the cell, and subjected to treatments identical to those described above for the empty cell. Spectra were processed first to remove the contributions of water adsorbed in the cell and gas-phase water by subtracting the respective spectrum of the empty cell measured at the same P/P_0 value. Then, spectra were normalized by the combination and overtone modes of zeolite Si-O-Si stretches (1750–2100 cm^{-1}) of the wafer prior to water exposure followed by subtraction of the

normalized spectrum for the sample before water adsorption. The resulting difference spectra represent the vibrations of adsorbed water and any differences on the sample induced by this adsorption (e.g., perturbation of silanol groups). These spectra were further baseline-corrected with pivot points at 4000, 2400, and 1350 cm^{-1}, where no absorbance was detected.

4.3.4 Glucose Isomerization Kinetic Studies

Kinetic studies were performed in 10 cm^3 thick-walled glass batch reactors (VWR) with 1–50 wt% aqueous D-glucose (Sigma-Aldrich, ≥99.5%) solutions. The reactant solutions were first prepared by adjusting the pH of deionized water (18.2 MΩ cm) with hydrochloric acid (HCl, Macron, 37 wt%) to 4 for kinetic studies performed at ≤373 K, or 3 for kinetic studies performed at >373 K, in order to suppress contributions from background isomerization reactivity catalyzed by hydroxide anions. The pH-adjusted water was then mixed with D-glucose to the desired concentration, filtered (0.2 μm PTFE filters, VWR), and loaded into 2 mL glass vials capped with a PTFE/silicone septum (Waters) for pre-heating. Catalytic solids (∼0.01–0.06 g) were added to a batch reactor and sealed with a crimp top (PTFE/silicone septum, Agilent). The vials containing the reactant solution and the catalyst were heated separately for 600 s to the reaction temperature atop a digital stirred hotplate (IKA RCT basic) prior to injecting ∼1–4 cm^3 of the pre-heated reactant solution into the capped reactors.

Reactors were maintained at temperature (368–383 K, 750 rpm, autogenous pressure) for various time intervals (300–14400 s) before quenching in an ice bath. Product solutions were filtered (0.2 μm, PTFE), diluted to 1 wt% sugar concentration with deionized water, and then mixed with a 1 wt% aqueous D-mannitol (Sigma Aldrich, ≥98 wt%) solution as an internal quantification standard. Product separation was performed using an Agilent 1260 high performance liquid chromatograph (HPLC) with an aqueous mobile phase (0.01 cm^3 s^{-1}, 353 K) through a Hi-Plex Ca column (7.7 × 300 mm, 8 μm particle size, Agilent). Quantification was performed using

an Agilent 1260 Infinity evaporative light scattering detector (ELSD) using separate calibration curves for each sugar compound. Initial rates were determined by extrapolating transient product formation rates to zero reaction time, a procedure that gave values identical to rate measurements from batch reactors operated at differential conversions (<5%) upon correcting for approach to equilibrium. Reaction enthalpies and entropies were obtained from Bayesian nonlinear regression in Athena Visual Studio (Athena Visual Software, Inc., v 14.2) and reported errors represent 95% marginal highest posterior density intervals.

Isotopic labeling studies were performed using 1 cm^3 of a 5 wt% aqueous D-glucose-D_2 (Cambridge Isotope Laboratories, 98% 2-D) solution (pH = 4) and 0.01–0.04 g of catalytic solids for variable times (300–3600 s) at 373 K. Reactor contents were then quenched and products were filtered and separated as described above. Liquid samples containing products and unreacted glucose were collected using an Agilent 1260 Infinity series fraction collector, frozen in liquid N_2 to 77 K, and freeze-dried to remove water using a Labconco FreeZone lyophilizer (<0.01 Torr, 36 h). Afterward, 0.06 cm^3 D_2O (Cambridge Isotope Laboratories, 99.9%) was added to dissolve dried sugar products prior to loading into NMR tubes (Wilmad LabGlass, 5 mm thin wall, 7 in., 500MHz) for liquid NMR analysis. ^{13}C NMR spectra were collected on a Bruker ARX500 spectrometer equipped with a 5 mm BBFO Z-gradient probe at ambient temperature and represent the average of 1500 scans acquired at ∼0.3 scans per second.

Glucose adsorption experiments were performed using 10 cm^3 of 50 wt% aqueous D-glucose solution (pH = 4) and 0.1 g of catalytic solids for 1800 s at 373 K. Reactor contents were then quenched and centrifuged prior to decanting off the aqueous solution. Solids were dried in ambient flowing air overnight prior to removal from the reactor for XAS analysis.

4.3.5 Computational Methods

Periodic planewave-based DFT calculations were carried out using the Vienna ab initio simulation package (VASP) [164–166]. Planewaves were constructed using the projector augmented wave method (PAW) with an energy cutoff of 400 eV [167, 168]. Exchange and correlation energies were computed using the revised Perdew-Burke-Ernzerhof (RPBE) form of the generalized gradient approximation [169–171]. Dispersive interactions were accounted for using the DFT-D3 method with Becke-Johnson damping (D3BJ) [172, 173]. The Brillouin zone was sampled using the Γ-point [174].

Wavefunctions were converged to electronic energies within 10^{-6} eV; forces were determined using a fast Fourier transform (FFT) grid with a cutoff equal to twice the planewave cutoff and structures were optimized to forces less than 0.05 eV Å^{-1}. Transition state structures were obtained using a two-step method. First, the nudged elastic band (NEB) method [175, 176] was used to approximate the minimum energy pathway using 16 images along the reaction coordinate and converging forces normal to the pathway to less than 0.5 eV Å^{-1}, while calculating forces using an FFT grid with a cutoff of 1.5 times the planewave cutoff and converging wavefunctions to energies within 10^{-4} eV. The approximate pathway generated by this method was used to generate input transition state geometries and reaction trajectories for the dimer method [177], which was then used to determine transition state structures using the same electronic and structural convergence criteria described for optimizations above.

The Beta zeolite was modeled using a fully periodic structure obtained from the IZA-SC database of zeolite structures [178] (tetragonal, $a = b = 12.632$ Å, $c = 26.186$ Å) and is structurally similar to the polymorph A structure of Beta reported elsewhere [179]. Closed Lewis acid sites were created by replacing a framework Si atom (T6 site) with a Ti heteroatom, which are similar to models used in previous studies [161]. The amount of additional intraporous water (0–10 molecules) was varied

to determine the effects of intraporous water content on the reaction energetics for glucose isomerization to fructose.

Desorbed glucose was modeled in vacuum and within a crystalline water structure (hexagonal ice, Ih phase). Neither of these desorbed states accurately captures the enthalpy and entropy of glucose within liquid water, but they represent extremes of enthalpic stabilization (ice), entropic stabilization (vapor), and the upper bounds for the glucose free energy, which will be lower in the aqueous phase than in gaseous or ice-like phases at reaction conditions. Inaccuracies in modeling the thermodynamics of the desorbed glucose state may introduce systematic error into the free energy values calculated in this study but will not affect the conclusions regarding the effects of intraporous water, because all reactions modeled at various water contents involve the same number of glucose adsorption events.

Frequency calculations were performed on all states (including transition states) to determine zero-point vibrational energies (ZPVE), vibrational enthalpies (H_{vib}), and free energies (G_{vib}). The finite difference method was used with two displacements per unconstrained atom to calculate the Hessian matrix and vibrational frequencies of guest species (e.g., glucose, water) within the Beta zeolite in addition to the heteroatom and framework O bound to that heteroatom. Vibrational frequency values <60 cm^{-1} are inaccurate from fixed displacement DFT methods but are commonly observed weakly-bound species adsorbed within zeolite pores. In this work, low vibrational frequency modes (<60 cm^{-1}) were replaced with a value of 60 cm^{-1}, such that frustrated translations and rotations of weakly bound molecules contribute to entropy, while preventing exact values from being inaccurately used. These vibrational frequencies were used, together with VASP-derived electronic energies (E_0), to obtain enthalpies:

$$H = E_0 + E_d + ZPVE + H_{vib} + H_{trans} + H_{rot} \tag{4.2}$$

and free energies:

$$G = E_0 + E_d + ZPVE + G_{vib} + G_{trans} + G_{rot} \tag{4.3}$$

for all reactant, product, and transition state structures, where E_d is the dispersive energy estimated by DFT-D3BJ methods [172, 173]. For gaseous molecules, translational and rotational enthalpies and free energies were computed from statistical mechanics.

4.3.6 ATR-IR Spectroscopy with MES-PSD MCR-ALS

In situ attenuated total reflectance infrared (ATR-IR) spectroscopy was used to verify the identities of the most abundant reactive intermediates (MARI) and the structures of reactive intermediates that form on Ti-Beta surfaces during reactions with glucose. Untreated samples were ground to a fine powder (¡200 mesh), and 0.03 g were suspended in 5 cm^3 of methanol (Macron Chemicals, anhydrous). A ZnSe cylindrical internal reflection element (IRE, International Crystal Labs) was dipped into the methanol suspension and then dried at ambient temperature. The dip coating procedure was repeated through 10 cycles to evenly coat the IRE with a thin layer of catalyst material. The coated IRE was then loaded into a customized ATR flow cell (Axiom TNL-120) equipped with two liquid inlets and one outlet with a cell volume of 40 μL. The ATR cell was mounted within the sample compartment of a FTIR spectrometer (Bruker, Vertex 70 RapidScan) equipped with a liquid N_2 cooled HgCdTe detector. Liquid streams of pure water and 50 wt.% glucose in water were introduced at controlled flow rates using two high-pressure piston pumps (SSI Series 1), which were controlled using LabVIEW. The cell was heated by a resistive heating cartridge placed within the wall of the cell. A K-type thermocouple (Omega) placed adjacent to the IRE at the center of the z-axis measured the temperature, which was controlled by an electronic temperature controller (Watlow, EZ-Zone). Background scans were obtained under steady-state conditions flowing 1 cm^3 min^{-1} of pure deionized water at 373 K after loading the ATR cell. Spectra obtained during

transient cutoff experiments were collected at a resolution of 4 cm^{-1} and averaged over 4 scans. Spectra obtained during modulation experiments were collected at a resolution of 1 cm^{-1} and averaged over 64 scans. All spectra acquisition was performed using Bruker Corporation's OPUS Spectroscopy Software 7.0.129.

Modulation excitation spectroscopy (MES) is a powerful technique in which a periodic stimulation is applied to the system while acquiring spectra as a function of time. The time domain response is then converted to a phase domain response, and only spectral features that change in synchrony with the applied stimulation are extracted using a phase sensitive detection (PSD) method described by the following equation:

$$A_k(\varphi_k^{PSD}) = \frac{2}{T}\int_0^T A_{average}(\vartheta, t) sin(k\omega t + \varphi_k^{PSD}) dt \tag{4.4}$$

Here, A(t) and $A_k(\varphi_k^{PSD})$ are time-domain and phase-domain responses of the measured species, respectively, T is the period of the applied stimulus in seconds, ω is the demodulation index and φ_k^{PSD} is the user defined phase demodulation angle. The application of the MES-PSD technique to FTIR spectra of intermediates on catalytic surfaces reveals spectra that only contain contributions from intermediates that change as a result of the applied stimulus (e.g., changing reactant concentrations) under relevant conditions and, in doing so, simultaneously reduces contributions from random sources of spectral noise [180]. Here, concentrations of glucose and water were modulated sinusoidally by controlling the flow rate of liquid through the two piston pumps and set specifically such that the set points of the pumps were changed in a step-wise manner every 0.5 s to approximate a sine wave with the desired frequency. Recorded time domain spectra were resampled to a single period, and subsequently the spectra of the active species were extracted by PSD using Eq. 4.4. The resultant phase domain spectra reflect contributions from multiple species that oscillate at the same frequency as the applied stimulus, and these chemically distinct species may be separated using principle component analyses that recognize the different phase delays of kinetically distinct groups of species. Multicurve resolution-alternating least

squares (MCR-ALS) analysis was performed to extract the spectra and concentration profiles (or surface coverages) of independent species from the phase domain spectra (additional details in Section 4.7.4.1, Supp. Info.) using a recently published MATLAB code [181].

4.3.7 X-Ray Absorption Spectroscopy (XAS) Measurements

Ti K-edge (4.966 keV) XAS measurements were performed on the bending magnet beamline of the Materials Research Collaborative Access Team (MRCAT) at the Advanced Photon Source at Argonne National Laboratory. Measurements were taken in step-scan transmission mode with a Ti foil reference spectrum collected simultaneously using a third ion chamber in series for energy calibration. Samples were pressed into a stainless-steel sample holder containing six wells and placed in a quartz reactor tube with Kapton windows. The reactor was purged with He prior to collecting measurements on the hydrated samples to minimize photon absorption by the gas phase. Spectra were collected under ambient conditions prior to heating the samples in flowing He to 523 K for 30 min. Samples were then cooled to room temperature prior to collection of dehydrated spectra.

XAS data were analyzed using WinXAS 3.2 software [182] for spectra normalization and background subtraction. Coordination parameters were obtained via simultaneous R-space least-squares fits of the magnitude and imaginary component of the k^2-weighted EXAFS Fourier transform (Δk = 2.90-10.0 $\mathring{A}^{-1}$). Experimental phase shift and back scattering amplitude fitting functions for Ti-O scattering paths were obtained from the TiO_2 anatase phase (6 Ti-O bonds at 1.96 $\mathring{A}$).

4.4 Results and Discussion

4.4.1 Bulk Structural and Lewis Acid Site Characterization of Ti-Beta Zeolites

Ti-Beta zeolites were crystallized via direct hydrothermal synthesis in fluoride media (Ti-Beta-F) and via post-synthetic grafting of $TiCl_4$ into framework defect vacancies of dealuminated Beta supports (Ti-Beta-OH; residual Si/Al >1500). Relevant structural characterization data on these samples are summarized in Table 4.1. X-ray diffraction patterns and micropore volumes measured from N_2 adsorption isotherms (77 K) of all samples were consistent with the Beta topology (Figures 4.9 and 4.10, Supp. Info.). The higher signal-to-noise XRD patterns measured for Ti-Beta-F samples reflect crystallites that are larger (∼3-12 μm) than Ti-Beta-OH samples (∼0.6-1.2 μm), consistent with average crystallite sizes determined from SEM images (Figures 4.11 and 4.12, Supp. Info.) and as expected from prior reports [16, 183]. Crystallite sizes of all Ti-Beta-OH samples prepared post-synthetically resemble those of their dealuminated and parent Al-Beta samples, which vary with Al content and crystallization time (Figure 4.13, Supp. Info.) [183]. UV-Visible spectra on Ti-Beta-F and Ti-Beta-OH samples (Figure 4.14 and 4.15, Supp. Info.) collected after dehydration treatments (523 K) were used to estimate edge energies (4.2-5.3 eV, Table 4.1) from Tauc plots (Figures 4.16 and 4.17 and Table 4.5, Supp. Info.) that are characteristic of isolated Ti^{4+} centers within zeolite frameworks (≥4.1 eV) [184]. These bulk characterization data indicate that this suite of Ti-Beta samples contains framework Ti centers of widely varying content (Si/Ti = 34-297; 0.09-1.36 Ti per unit cell).

The fraction of Ti^{4+} sites that behave as Lewis acid centers was quantified from IR spectra collected after titration by CD_3CN at 303 K. Figure 4.1 shows IR spectra for ν(C≡N) stretching vibrations on Ti-Beta-F-155 with increasing CD_3CN coverage (spectra of Ti-Beta-OH-46 in Figure 4.18, Supp. Info.). At low CD_3CN coverages (CD_3CN /Ti = 0.2–0.6), a peak centered at 2308 cm^{-1} for CD_3CN adsorbed at Lewis acidic Ti sites appears first, followed by peaks for CD_3CN bound to silanol groups (2275 cm^{-1}) and for gas-phase or physisorbed CD_3CN (2265 cm^{-1}) [185], indicating

that CD_3CN preferentially adsorbs onto framework Lewis acidic Ti sites over silanol defects. The 2308 cm^{-1} peak increases in area with subsequent CD_3CN exposure until saturation coverages are reached. Integrated areas for the 2308 cm^{-1} peak were quantified from deconvoluting IR spectra into their 2308 cm^{-1}, 2275 cm^{-1} and 2265 cm^{-1} components (Figure 4.19, Supp. Info.), using a previously reported procedure to isolate component peaks for CD_3CN bound to hydrolyzed-open ($Sn(OH)(OSi)_3$, 2316 cm^{-1}) and closed ($Sn(OSi)_4$, 2308 cm^{-1}) Sn sites within Sn-zeolites [26].

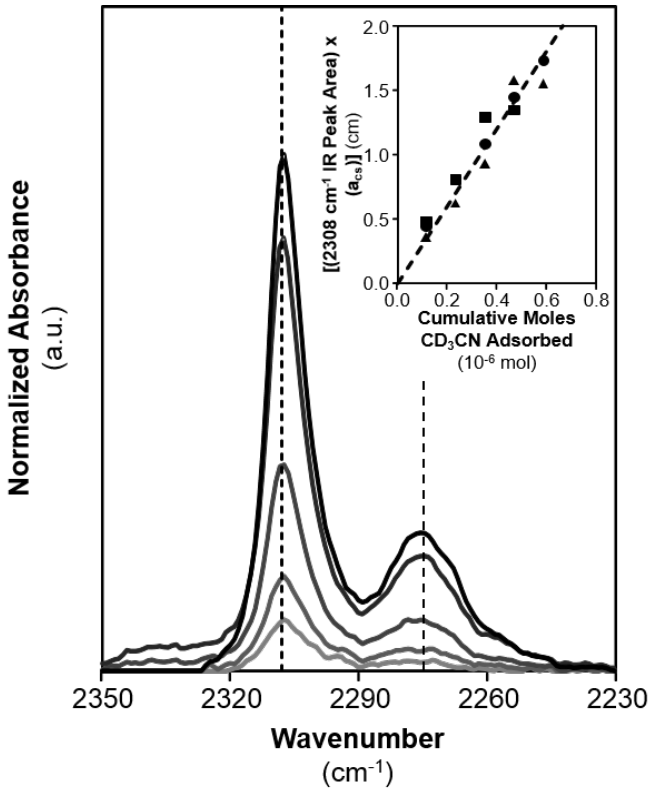

Figure 4.1: CD_3CN IR spectra of the $\nu(C{\equiv}N)$ stretching region with increasing coverage of CD_3CN on Ti-Beta-F-155 (0.013, 0.026, 0.065, 0.170, and 0.235 CD_3CN/Ti, light to dark). Dashed vertical lines correspond to 2308 and 2275 cm^{-1} for $\nu(C{\equiv}N)$ stretching vibrations of CD_3CN bound to Lewis acidic Ti sites and silanol groups, respectively. The inset shows the integrated area of the 2308 cm^{-1} peak multiplied by the cross-sectional area of the IR wafer, plotted against the moles of CD_3CN adsorbed at Lewis acidic Ti sites for Ti-Beta-F-155 (circles), Ti-Beta-F-135 (squares), and Ti-Beta-OH-38 (triangles). The dashed line in the inset is the best fit line through all data, with the slope representing the integrated molar extinction coefficient for CD_3CN adsorbed onto Lewis acidic Ti sites.

The inset of Figure 4.1 shows the integrated area for the 2308 cm^{-1} peak as a function of the number of CD_3CN molecules bound to Lewis acidic Ti sites (Ti_{LA}), determined in coverage ranges (CD_3CN /Ti = 0.2-0.6) that correspond to equimolar titrant-to-site binding stoichiometry. Integrated 2308 cm^{-1} peak areas increase linearly with the amount of CD_3CN adsorbed onto Lewis acidic Ti sites, and in an equivalent proportion for three Ti-Beta samples of different Ti content and synthetic origin (Ti-Beta-F-155, Ti-Beta-F-135, and Ti-Beta-OH-38). This proportion reflects the integrated molar extinction coefficient for this IR peak (E(2308 cm^{-1}) = 3.01 ± 0.60 cm μmol^{-1}) via Eq. 4.1. This E(2308 cm^{-1}) value was then used to quantify Lewis acidic Ti sites on each Ti-Beta sample after saturation with CD_3CN and deconvolution of IR spectra (Figure 4.20, Supp. Info.). Site quantification values are reported in Table 4.1 as the fraction of Lewis acidic Ti sites titrated by CD_3CN (per total Ti). Dichloromethane-assisted grafting of $TiCl_4$ within framework vacancies of dealuminated Beta zeolites formed Ti-Beta-OH samples that generally contained higher fractions of Lewis acidic Ti sites (0.40-1.00, Table 4.1) than fluoride-assisted, hydrothermally synthesized Ti-Beta-F samples (0.24–0.62, Table 4.1). The numbers of Lewis acid sites quantified by CD_3CN on these Ti-Beta samples are consistent with the numbers quantified by pyridine titration (0.38-1.03 Lewis acid sites per Ti, E(1605 cm^{-1}) = 1.16 ± 0.23 cm μmol^{-1}, details in Section 4.7.1.2, Supp. Info.). The fraction of Lewis acidic Ti species are below unity for most samples, necessitating such site quantification techniques to normalize catalytic rate measurements, since residual Ti species reflect small TiO_2 domains that do not contribute to measured glucose-fructose isomerization rates [35].

Exposure to higher CD_3CN pressures gives rise to IR peaks centered at 2275 cm^{-1} that reflect CD_3CN bound to silanol defects (Figure 4.18, Supp. Info.). Using an integrated molar extinction coefficient (E(2275 cm^{-1}) = 0.74 ± 0.16 cm μmol^{-1}) determined previously from CD_3CN IR spectra of a dealuminated Beta sample [26], the total number of silanol defects was estimated for each Ti-Beta sample and listed in Table 4.2. Silanol groups are present in significantly higher densities (∼4-100x) on

Ti-Beta-OH than on Ti-Beta-F samples, as expected for Ti-Beta-OH samples that contain silanol groups formed during the hydrothermal synthesis of the parent Al-Beta zeolite in hydroxide media and silanol nest defects that remain after partial grafting with Ti precursors. CD_3CN does not discriminate between silanol groups located within microporous voids from those located at extracrystalline surfaces, which may be present in higher concentrations on smaller Ti-Beta-OH crystallites than on larger Ti-Beta-F crystallites ($\sim$0.9 μm vs. 7.5 μm, Figures 4.11-4.13, Supp. Info.). These total silanol concentrations, however, do not correlate with external crystallite surface areas among the Ti-Beta-F and Ti-Beta-OH samples studied here (details in Section 4.7.1.3, Supp. Info.), implying that higher defect densities are present within the microporous channels of Ti-Beta-OH.

From these characterization data, we conclude that the synthesized Ti-Beta-F and Ti-Beta-OH samples are crystalline Beta zeolites that contain varying quantities of Ti atoms located within framework positions and that behave as Lewis acid centers. Furthermore, CD_3CN titration experiments indicate that Ti-Beta-OH samples contain significantly higher bulk silanol densities than Ti-Beta-F samples. We next use a suite of adsorption and spectroscopic probes that are sensitive to the location of silanol groups within microporous voids, to provide evidence that the density of silanol defects is higher within the microporous voids of Ti-Beta-OH than Ti-Beta-F.

Table 4.1: Site and structural characterization data for Ti-Beta samples in this study.

Sample	V_{ads} (N_2, 77 K) (cm^3 g^{-1})[a]	Edge Energy (eV)[b]	Lewis Acidic Ti Density (10^{-5} mol Ti_{LA} g^{-1}, CD_3CN)[c]	Lewis Acidic Ti Density (Ti_{LA} unit $cell^{-1}$, CD_3CN)[d]	Fraction of Lewis Acidic Ti[e]	Lewis Acidic Ti Density (10^{-5} mol Ti_{LA} g^{-1}, Pyridine)[f]
Ti-Beta-F-133	0.21	5.3	4.17	0.16	0.34	n.m.
Ti-Beta-F-135	0.19	4.5	3.93	0.15	0.32	6.35
Ti-Beta-F-142	0.20	4.3	6.70	0.26	0.58	8.40
Ti-Beta-F-143	0.21	4.2	4.63	0.18	0.40	6.51
Ti-Beta-F-155	0.20	5.3	6.64	0.26	0.62	4.64
Ti-Beta-F-170	0.20	5.3	2.36	0.09	0.24	4.87
Ti-Beta-F-180	0.22	4.4	2.99	0.12	0.33	n.m.
Ti-Beta-F-282	0.20	5.1	0.89	0.03	0.15	n.m.
Ti-Beta-OH-34	0.22	4.5	18.77	0.72	0.40	16.85
Ti-Beta-OH-38	0.19	4.7	14.80	0.57	0.35	n.m.
Ti-Beta-OH-46	0.23	4.4	35.20	1.36	1.00	36.29
Ti-Beta-OH-71	0.21	4.7	13.08	0.50	0.57	11.79
Ti-Beta-OH-297	0.18	4.5	26.88	1.03	0.32	32.70

[a]N_2 volumes at the end of micropore filling transition (77 K). [b]Determined from Tauc plots after dehydration (523 K).
[c]Lewis acidic Ti densities measured from CD_3CN titration IR experiments.
[d]Lewis acidic Ti densities measured from CD_3CN titration IR experiments normalized per unit cell.
[e]Fraction of total Ti concentration present as Lewis acidic Ti sites measured from CD_3CN titration IR experiments.
[f]Lewis acidic Ti densities measured from pyridine titration IR experiments. [g]n.m.: not measured.

Table 4.2: Semi-quantitative measurements of the hydrophobic properties of microporous voids in Ti-Beta-F and Ti-Beta-OH materials.

Sample	Silanol Density (10^{-4} mol SiOH g^{-1})[a]	Silanol Density (mol SiOH mol Ti_{LA}^{-1})[b]	V_{ads} (H_2O, 293 K) (10^{-3} cm^3 g^{-1}, P/P_0=0.2)[c]	Normalized V_{ads} (H_2O, 293 K) (cm^3 g^{-1})[d]	V_{ads} (H_2O) / V_{ads} (N_2)[e]	V_{ads} (CH_3OH) (cm^3 g^{-1})[f]
Ti-Beta-F-133	1.21	2.9	2.31	0.04	0.011	0.062
Ti-Beta-F-135	0.86	2.2	2.02	0.03	0.011	0.072
Ti-Beta-F-142	1.54	2.3	2.53	0.01	0.013	0.083
Ti-Beta-F-143	1.32	2.8	3.52	0.10	0.017	0.080
Ti-Beta-F-155	1.93	2.9	4.48	0.12	0.022	0.051
Ti-Beta-F-170	0.65	2.8	3.10	0.12	0.015	0.082
Ti-Beta-F-180	1.66	5.5	3.88	0.16	0.018	0.062
Ti-Beta-F-282	0.29	3.2	1.33	0.06	0.007	0.035
Ti-Beta-OH-34	6.72	3.6	46.39	2.20	0.211	1.04
Ti-Beta-OH-38	14.79	10.0	93.57	4.90	0.492	0.98
Ti-Beta-OH-46	7.02	2.0	37.93	1.40	0.165	0.33
Ti-Beta-OH-71	7.97	6.1	41.77	2.06	0.199	1.09
Ti-Beta-OH-297	6.28	2.3	53.03	2.41	0.295	1.19
Si-Beta-F	–	–	2.20	2.20	–	–

[a]Silanol densities measured from CD_3CN titration IR experiments. [b]Silanol densities normalized by Lewis acidic Ti densities measured from CD_3CN titration IR experiments. [c]Water volumes at $P/P_0 = 0.2$ (293 K). [d]Water volumes at $P/P_0 = 0.2$ (293 K) after normalization by two times the number of Lewis acidic Ti sites determined from CD_3CN titration IR experiments. [e]Fraction of total micropore volume filled by water at $P/P_0 = 0.2$ (293 K). [f]CH_3OH volumes taken at the end of the first adsorption regime (293 K), indicative of adsorbate-adsorbent interactions. This corresponds to low P/P_0 values (0.02–0.04) for Type V isotherms on Ti-Beta-F samples and the highest measured P/P_0 values (0.6–0.7) on Ti-Beta-OH samples.

4.4.2 Characterization of Hydrophobic Properties of Ti-Beta Zeolites

In this section, we compare the polarity of microporous voids in Ti-Beta-F and Ti-Beta-OH samples by combining semi-quantitative assessments of vapor-phase water and methanol adsorption isotherms with structural assessments of adsorbed water phases from IR spectra collected in the presence of water vapor. Taken together, these data reveal differences in the intraporous density of polar silanol groups within microporous voids of Ti-Beta-F and Ti-Beta-OH and in the structures of water stabilized within these voids.

4.4.2.1 Semi-Quantitative Assessments of Hydrophobicity using Vapor-Phase Adsorption Isotherms

Water adsorption isotherms provide an assessment of the hydrophobic properties of zeolitic surfaces, as bulk water uptakes increase with the density of polar defect sites (e.g., framework heteroatoms, hydroxyl groups) located in otherwise non-polar siloxane frameworks [25, 26]. Vapor-phase water adsorption isotherms of Ti-Beta-F samples (Figure 4.24, Supp. Info.) show water uptakes similar to Si-Beta-F (within 2.5x, 293 K, P/ P_0 = 0-0.6), suggesting that surfaces with low defect densities are also present within Ti-Beta-F micropores [16]. Table 4.2 summarizes the total water uptake per gram at P/ P_0 = 0.2, a parameter that allows for semi-quantitative comparison of hydrophobicity among samples and which corresponds to the reduced pressure required for micropore filling of cyclohexane within hydrophobic MOR zeolites [83]. Table 4.2 also summarizes the residual water uptakes after subtraction of two water molecules adsorbed per Lewis acid site, a stoichiometry that has been observed experimentally from gravimetric and microcalorimetric studies on Ti-Beta zeolites for water adsorption on isolated framework Ti sites [106]. Water uptakes (per g) at a given reduced pressure are systematically higher on Ti-Beta-F than on Si-Beta-F samples but are similar (within 1.5x) after accounting for two water molecules adsorbed onto Lewis acidic Ti site. These low water uptakes ($V_{ads}(H_2O)/V_{ads}(N_2)$

= 0.001-0.011, Table 4.2) reflect the hydrophobic nature of intraporous void environments, consistent with water intrusion studies in defect-free siliceous Beta zeolites that require significantly higher water pressures (57 MPa) for pore filling [186]. Hydrophobic channels in Beta zeolites (∼0.7 nm diameter) mitigate the formation of bulk water structures under ambient conditions because polar surface groups capable of hydrogen bonding are absent [16], consistent with findings from experimental studies of defect-free carbon nanotubes (¡1 nm diam.) [137] and from computational studies identifying the presence of only vapor-phase water between hydrophobic pure-silica surfaces positioned 0.7 nm apart [138].

Among the Ti-Beta-OH samples studied here, vapor-phase water adsorption isotherms (Figure 4.25, Supp. Info.) showed water uptakes that were 10-40x higher than on Ti-Beta-F samples (293 K, P/ P_0 = 0-0.6) after accounting for two water molecules adsorbed onto each Lewis acid site (Table 4.2). These order of magnitude higher water uptakes indicate the presence of additional water adsorption sites on Ti-Beta-OH samples, which have ∼4-100x higher silanol defect densities than Ti-Beta-F as measured by CD_3CN IR (Table 4.2). Indeed, a linear correlation between total silanol concentration (per g) and water uptake (per g, P/ P_0 = 0.2) is observed among all Ti-Beta-F and Ti-Beta-OH samples studied (Figure 4.26, Supp. Info.), which has previously been noted among Sn-Beta samples [26] and among H-form FAU, MFI and Beta samples [149]. These findings are qualitatively consistent with computational studies indicating that extended water structures (up to 27 molecules) can be stabilized when two adjacent silanol defects are present between hydrophobic SiO_2 plates positioned 0.7 nm apart [138]. These water adsorption uptakes and silanol density measurements reflect bulk properties of zeolite samples, however, and do not provide direct information about the density of silanol defects within microporous environments.

In contrast to water, methanol fills microporous voids in both low-defect and high-defect samples, but with distinct adsorption behavior. Methanol adsorption isotherms (293 K) on low-defect Ti-Beta-F samples show Type V isotherm behavior (Figure 4.27,

Supp. Info.), reflecting micropore condensation driven by adsorbate-adsorbate interactions that are stronger than adsorbate-adsorbent interactions of methanol with non-polar framework siloxane linkages [16, 25, 127, 159], as observed previously for ethanol within hydrophobic Ti-Beta-F [35] and Si-MFI [187]. In contrast, methanol adsorption isotherms on Ti-Beta-OH materials show Type I isotherm behavior (Figure 4.28, Supp. Info.), reflecting micropore condensation driven by strong adsorbate-adsorbent interactions through methanol hydrogen bonding interactions with specific binding sites located on micropore walls. These adsorption sites are not Lewis acidic Ti sites, evident from the direct comparison of Ti-Beta-F-155 and Ti-Beta-OH-71, which contain similar Lewis acid site densities (0.26 and 0.50 per unit cell, respectively, Table 4.1) but show significant differences in adsorption behavior. The Type I isotherms on Ti-Beta-OH therefore reflect the presence of silanol defects located within microporous channels that hydrogen bond with methanol, while the Type V isotherms on Ti-Beta-F reflect essentially undetectable amounts of silanol groups or other hydrogen bonding moieties located within the microporous channels of Ti-Beta-F [116].

4.4.2.2 Spectroscopic Characterization of Co-adsorbed Water Structures using Transmission IR

Transmission IR spectroscopy was used to probe differences in the vibrational signatures and extended structures of adsorbed water on Ti-Beta-F-155 and Ti-Beta-OH-46, which are representative Ti-Beta-F and Ti-Beta-OH samples from bulk characterization data, Lewis acid site densities, and glucose-fructose isomerization rate measurements (see Tables 4.1 and 4.2 and Section 4.4.3). Figures 4.2A and 4.2B show IR spectra collected on Ti-Beta-F-155 and Ti-Beta-OH-46 after removing background contributions for water vapor present in the cell and subtracting the spectrum of dehydrated zeolite samples (full spectra in Figure 4.29, Supp. Info.). Upon equilibration in flowing water, two prominent features appear as positive broad peaks in the 1500–1750 cm^{-1} range and the 2600–3700 cm^{-1} range, while a third negative peak appears centered around 3735–3745 cm^{-1}.

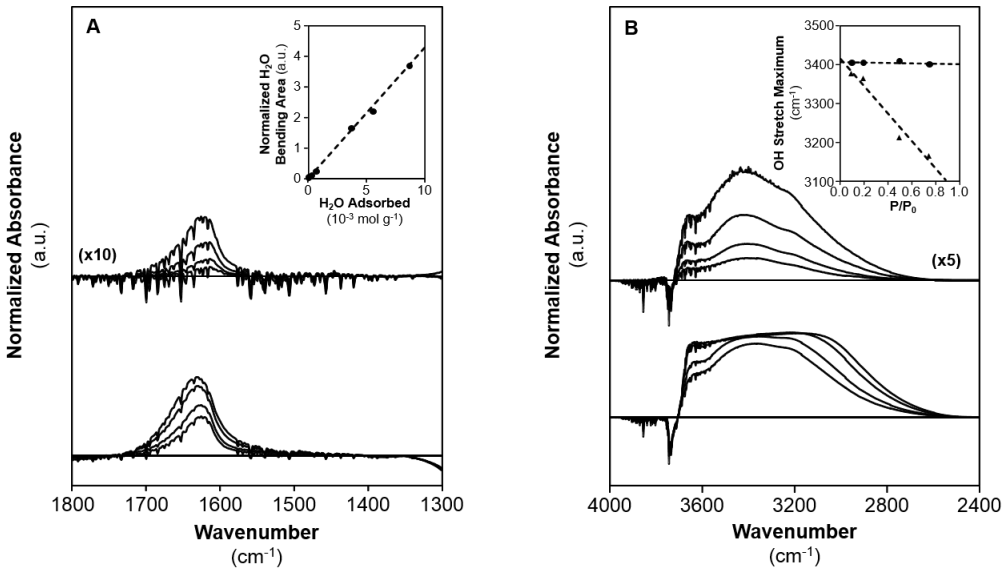

(a) (b)

Figure 4.2: Baseline-corrected difference IR spectra of adsorbed water on Ti-Beta-F-155 (top, magnified for clarity) and Ti-Beta-OH-46 (bottom) at 298 K for (a) δ(HOH) scissoring modes in the water bending region and (b) the ν(O-H) water stretching region. Difference spectra reflect the subtraction of spectrum measured on the sample under vacuum prior to water flow and corrected for background water adsorption onto the IR cell. Spectra for each sample displayed from bottom-to-top correspond to P/P_0=0.1, 0.2, 0.5, and 0.75. The insets display the change in (a) the water bending peak area and (b) the water stretching peak maximum with increasing water concentration for Ti-Beta-F-155 (circles) and Ti-Beta-OH-46 (triangles).

Figure 4.2A shows the IR peak centered between 1615–1630 cm^{-1}, which reflects the δ(H-O-H) scissoring mode of adsorbed water [188]. This peak does not significantly change shape or center with increasing water uptake. The integrated area of this peak is proportional to the total water uptake (at equivalent reduced pressures) estimated from vapor-phase adsorption experiments (298 K, Figure 4.30, Supp. Info.), as shown in the inset of Figure 4.2A. The linear relation in the inset of Figure 4.2A establishes a direct connection between the total water uptake and each IR spectrum as quantified through the integrated area of the 1615–1630 cm^{-1} peak.

Figure 4.2B shows a negative peak (3735-3745 cm^{-1}) on both samples reflecting a convolution of two peaks centered at 3745 cm^{-1} and 3735 cm^{-1} for OH stretch-

ing modes of external and internal silanol groups, respectively [189]. These features appear as negative peaks because hydrogen bonding interactions between adsorbed water and hydroxyl groups perturb silanol O-H stretches, giving rise to the broad positive peak centered around 3400 cm^{-1}. Difference spectra on Ti-Beta-OH-46 do not show further changes to the negative peak areas at 3745 cm^{-1} and 3735 cm^{-1} at relative water pressures of $P/P_0 \geq 0.2$, indicating that the hydroxyl groups are fully perturbed by hydrogen-bonded water by $P/P_0 = 0.1$ (Figure 4.31, Supp. Info.). Therefore, subsequent adsorption of water above this relative pressure occurs via hydrogen-bonding with other water molecules already present within the channels, rather than through additional adsorption at silanol defects. In contrast, the silanol groups on Ti-Beta-F-155 continue to be perturbed gradually across a wider range of water pressures ($P/P_0 = 0.1$–0.75, Figure 4.31, Supp. Info.), indicating that water adsorption continues to occur at silanol defects. These observations are consistent with lower water uptakes from vapor-phase adsorption isotherm experiments, suggesting that water does not fill the micropores of Ti-Beta-F-155 under these conditions. Hence, water adsorbs within Ti-Beta-F at low intraporous densities (0.01-0.16 mol H_2O g^{-1}, Table 4.2) because it predominantly adsorbs at framework Ti sites, but within Ti-Beta-OH with higher intraporous water densities (1.4-4.9 mol H_2O g^{-1}, Table 4.2) because it adsorbs at both framework Ti atoms and silanol defects.

The OH stretching vibrations from adsorbed water molecules are convoluted with the perturbed silanol peak in the 2600–3700 cm^{-1} range, yet differences regarding the structure of adsorbed water in Ti-Beta-OH-46 and Ti-Beta-F-155 are readily apparent. With increasing water partial pressure ($P/P_0 = 0.1$–0.75), the peak maximum in the OH stretching region monotonically shifts from 3375 cm^{-1} to 3190 cm^{-1} on Ti-Beta-OH-46 (Figure 4.2B inset). Shifts in OH stretching frequency to lower wavenumbers reflect greater extents of hydrogen bonding between water molecules [142, 190] suggesting that adsorbed water molecules within Ti-Beta-OH-46 become arranged in extended hydrogen bonding networks that grow with increasing water partial pressure. In addition, this broad peak for adsorbed water can be deconvoluted into two

major components centered in either the ∼3000–3100 cm^{-1} range or the 3630–3665 cm^{-1} range. The latter peak (3630–3665 cm^{-1}) has been assigned to loosely-bound water in one-dimensional chains which are similar in their extent of hydrogen bonding to vapor-phase water located within non-polar carbon nanotubes (¡0.8 nm in diameter) [142] similar in size to Beta micropores. Thus, the continued presence of this peak at higher water partial pressures ($P/ P_0 \geq 0.2$) indicates that some water molecules are occluded within microporous voids and can plausibly be considered vapor-like. The peak ranging from ∼3000–3100 cm^{-1} is shifted to lower wavenumbers than that of OH stretches in bulk ice (3220–3250 cm^{-1}) [191], reflecting contributions of water molecules in extended hydrogen bonding networks. As the water partial pressure increases, this peak becomes more prominent and eventually reflects the hydrogen-bonded structure of the majority of occluded water molecules within the channels of Ti-Beta-OH-46.

The structure of water adsorbed within Ti-Beta-F-155 sharply contrasts that of Ti-Beta-OH-46. First, the water OH stretching peak center remains constant at ∼3400 cm^{-1} in Ti-Beta-F-155 with increasing water partial pressure (Figure 4.2B inset), reflecting weaker contributions from strongly hydrogen bound water stretches in the ∼3000-3100 cm^{-1} range. This provides evidence that adsorbed water molecules in Ti-Beta-F-155 do not significantly increase their extent of hydrogen bonding with increasing water pressure, nor do they form the extended water structures observed in Ti-Beta-OH-46. Indeed, further adsorption of water perturbs additional silanol groups throughout this partial pressure range, evident in increasingly negative peak area for the peak centered at 3735-3745 cm^{-1} and in increasingly positive peak area for the peak centered at ∼3400 cm^{-1} (Figure 4.31, Supp. Info.). A small shoulder present at ∼3100 cm^{-1} in the difference spectra of Ti-Beta-F-155 (Figure 4.2B) increases in area with increasing water partial pressure, however, indicating that some water molecules adsorb via hydrogen bonding in locations with proximal water molecules, but to a much lesser extent than in Ti-Beta-OH-46. The significantly lower water uptakes (Figure 4.30, Supp. Info.) suggest that the lower silanol defect density in Ti-Beta-

F-155 (1.9×10^{-4} mol SiOH g^{-1}, Table 4.2) is insufficient to nucleate the formation of extended hydrogen-bonded water structures within the pores, in contrast to the behavior of water adsorption on Ti-Beta-OH-46 (7.0×10^{-4} mol SiOH g^{-1}, Table 4.2).

From these characterization data in Sections 4.4.1 and 4.4.2, we conclude that the series of samples investigated here contain Ti centers isolated within Beta molecular sieve frameworks over a wide range of Ti content (Si/Ti = 38-297) and residual silanol defect densities ($SiOH/Ti_{LA}$ = 2.0-10, Table 4.2). Water adsorbs preferentially within zeolite Beta micropores at framework Ti atoms, and at surface silanol groups via hydrogen bonding. Methanol adsorption isotherms indicate that Ti-Beta-OH has a significantly higher intrapore silanol defect density than Ti-Beta-F, leading to increased water uptakes and the stabilization of extended hydrogen bonding water structures within their microporous voids. In order to determine the kinetic consequences of these intraporous silanol defects and the extended solvent structures they stabilize, we next interrogate Ti-Beta-F and Ti-Beta-OH samples using aqueous-phase glucose isomerization as a catalytic probe reaction.

4.4.3 Aqueous-Phase Glucose Isomerization Mechanisms and Kinetic Measurements

In this section, we combine insights from experiment and theory to elucidate the underlying phenomena that lead to differences in measured reaction kinetics for Lewis acid-catalyzed glucose isomerization in low-defect and high-defect Ti-Beta zeolites. We use a mechanistic model to identify key differences in glucose isomerization reaction coordinates in terms of free energies of reactive intermediates and transition states that are influenced by intrapore silanol defects and the extended solvent structures they stabilize.

4.4.3.1 Mechanistic Details of Lewis Acid-Catalyzed Glucose Isomerization

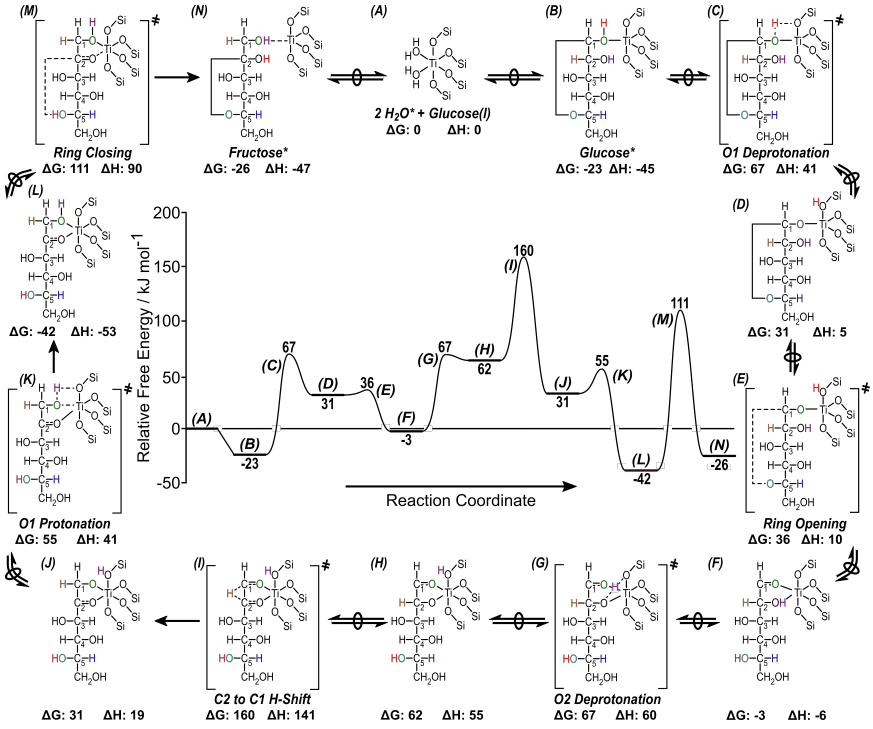

Figure 4.3: Free energy (373 K, 1 bar) reaction coordinate diagram for the formation of fructose from glucose on closed-form Ti Lewis acid sites. Reaction arrows with overlaid circles indicate quasi-equilibrated events or the formation of transition states from relevant precursors. Relative enthalpies are given near inset images.

Figure 4.3 shows the free energy reaction coordinate diagram for glucose-fructose isomerization calculated over a framework coordinated, closed Lewis acidic Ti site at the T6 position in Beta through a mechanism similar to those reported in previous experimental and theoretical studies [34, 161]. Lewis acid-catalyzed glucose isomerization to fructose occurs through quasi-equilibrated adsorption of glucose onto Lewis acid sites through the hemiacetal oxygen (O5), quasi-equilibrated deprotonation of O1 (States B-D, Figure 4.3), followed by protonation of the ring ether oxygen (O5) to facilitate ring opening to form the acyclic, or open-chain, glucose intermediate bound through the carbonyl moiety (States D-F, Figure 4.3) [34]. Subsequent deprotonation of the C2 alcohol to a proximal proton acceptor, such as a nearby framework oxygen, generates a glucose intermediate that can bind to the Lewis acid site in a bidentate fashion (States F-H, Figure 4.3). Glucose deprotonation and ring-opening steps have kinetically-irrelevant barriers, consistent with previous findings [34]. The open-chain glucose intermediate then undergoes a kinetically-relevant 1,2-hydride shift to form a bound acyclic fructose intermediate, an elementary step that has the largest computed free energy barrier in the reaction coordinate (States H-J, Figure 4.3) [34, 65]. Protonation of the fructose C1 alcohol, ring closure, and desorption of fructose from the Lewis acid site closes the catalytic cycle via kinetically-irrelevant steps. The overall free energy barrier to form fructose from desorbed glucose is 160 kJ mol^{-1} (373 K) when using ring-closed glucose in crystalline ice as the reference state for desorbed glucose. The overall free energy barrier from the adsorbed glucose state is 183 kJ mol^{-1} (373 K). This Lewis acid-catalyzed intramolecular 1,2-hydride shift mechanism is dominant over the base-catalyzed enolate mechanism under the conditions studied here, as reported in previously published isotopic tracer studies (see Figure 4.32, Supp. Info., for ^{13}C NMR spectra of monosaccharide products) [51].

Glucose isomerization over Ti-Beta zeolites also forms sorbose, which is a second monosaccharide product formed through a parallel pathway and reaction mechanism analogous to that of fructose formation (free energy reaction coordinate diagram in Figure 4.33, Supp. Info.) [192]. Isomerization to sorbose involves quasi-equilibrated

glucose adsorption, deprotonation of the O1 alcohol moiety, and ring opening to form a bidentate-bound glucose-derived intermediate through O1 and O5 (States B-D, Figure 4.33, Supp. Info.). This is followed by a kinetically-relevant 1,5-hydride shift step (States D-F, Figure 4.33, Supp. Info.), as previously observed by isotopic tracer studies on ^{2}H- and ^{13}C-labeled glucose [192] and confirmed in this work (see Figure 4.32, Supp. Info., for ^{13}C NMR of monosaccharide products). The 1,5-hydride shift transition state that forms sorbose is analogous to the 1,2-hydride shift that forms fructose, in that both involve six-membered ring structures and a C-H bond scissoring mode along the reaction coordinate. The catalytic cycle for sorbose formation is closed via protonation, ring closure, and desorption (States F-H, H-J, and J-A, respectively, Figure 4.33, Supp. Info.). The overall free energy barrier relative to the desorbed glucose state is 154 kJ mol^{-1} (373 K) and suggests that the 1,5-hydride shift is the sole kinetically relevant step, as expected [192]; all other barriers are at least 25 kJ mol^{-1} lower. Free energy barriers for fructose and sorbose formation are similar within the error of DFT, as expected for two parallel reactions with reported initial rates within one order of magnitude [35, 192].

While the exact binding coordination [107], adsorption configurations [161], and site requirements [28, 187] associated with glucose isomerization to fructose and sorbose continue to be studied computationally and experimentally, the kinetic relevance of their respective hydride shift transition states can be experimentally detected through measurement of the H/D kinetic isotope effect (KIE) [34, 35]. KIE values reflect differences in the vibrational frequency and zero-point energy upon isotopic substitution of atoms in bonds that are broken along the reaction coordinate (derivation in Section 4.7.3.2, Supp. Info.). Deuteration of the alpha-carbon in glucose reactants results in measured glucose-fructose isomerization H/D KIE values of 2.1-2.3 ($\pm$ 0.2, 373 K) on both Ti-Beta-F and Ti-Beta-OH samples throughout the range of glucose concentrations studied here (0-50 wt.% glucose). These values are consistent with theoretical H/D KIE values expected for transition state reaction coordinates involving C-H bond scissoring ($\sim$1500 cm^{-1}), consistent with the 1,2-hydride shift

steps confirmed from isotopic tracer studies [50, 51]. Measured KIE values of 2.1 also indicate that intrazeolitic transport artifacts do not corrupt measured rates, which would otherwise result in measurement of the square root of the theoretical KIE value (details in Section 4.7.3.2, Supp. Info.). Therefore, we conclude that the measured glucose-fructose isomerization rates reported here are uncorrupted by transport artifacts and reflect free energy differences between the kinetically-relevant hydride shift transition state and the relevant adsorbed reactive intermediates. Next, we measure glucose isomerization turnover rates on a variety of Ti-Beta-F and Ti-Beta-OH samples and across a wide range of initial glucose concentrations, revealing the presence of different kinetic regimes that correspond to changes in reactive intermediate coverages.

4.4.3.2 Experimental Measurements of Glucose Isomerization Rate Constants on Hydrophobic and Hydrophilic Ti-Beta Zeolites

Initial glucose isomerization rates were collected on all Ti-Beta-F and Ti-Beta-OH samples at low glucose concentrations (1 wt.%, 373 K), which correspond to a first-order kinetic regime in glucose concentration [35]. Apparent first-order glucose isomerization rate constants for fructose and sorbose formation are shown in Figures 4.4A and 4.4B, respectively, as a function of total Ti content for all Ti-Beta samples studied here, and compared to data for Ti-Beta samples reported previously [35] (rate constants plotted as a function of Ti_{LA} per gram in Figure 4.34, Supp. Info.). On average, first-order rate constants are systematically higher (∼6x) on Ti-Beta-F zeolites than on Ti-Beta-OH zeolites across a wide range of Ti content. First-order rate constants vary within ∼3x among all Ti-Beta-F zeolites, and within ∼2x among all Ti-Beta-OH zeolites, which are variations similar to those observed previously among Sn-Beta-F and Sn-Beta-OH zeolites of varying Sn content [26]. Furthermore, rate constants (per Ti) do not depend systematically on Ti content among Ti-Beta-F or Ti-Beta-OH zeolites, consistent with the absence of intracrystalline transport artifacts as expected from measured H/D KIE values of 2.1-2.3 (Section 4.4.3.1).

Next, more detailed kinetic studies are performed on Ti-Beta-F-155 and Ti-Beta-OH-46, which are samples with kinetic behavior representative of the Ti-Beta-F and Ti-Beta-OH series, respectively.

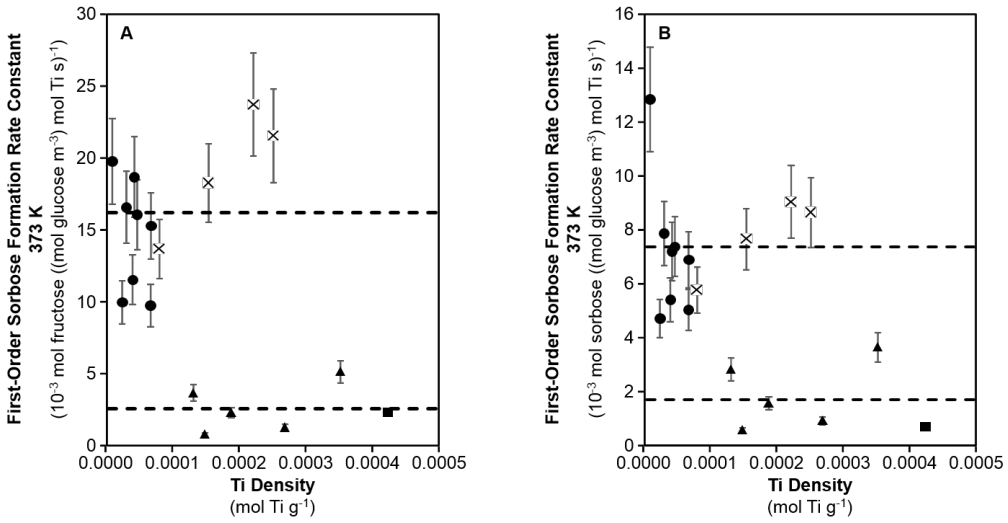

(a) (b)

Figure 4.4: Initial first-order (a) fructose and (b) sorbose formation rates (373 K, pH 4) normalized per total Ti content as a function of Ti/Si ratio, for Ti-Beta-F (circles) and Ti-Beta-OH samples (triangles). Data on Ti-Beta-F (X) and Ti-Beta-OH (squares) samples reported previously in Ref. [35] are plotted for comparison. Dashed lines correspond to average values within the series of Ti-Beta-F and Ti-Beta-OH samples.

Initial glucose isomerization rates were collected across a wide range of glucose concentrations (1-50 wt.%) on both Ti-Beta-F-155 and Ti-Beta-OH-46. Thermodynamic activities for glucose and water are used here to describe rate data at high glucose concentrations due to expected non-ideal solution behavior that affects reaction rates [193]. Non-ideality was accounted for using solution-phase activity coefficients (γ_i) which are unity under ideal conditions and diverge from unity at non-dilute glucose concentrations. Activity coefficients for aqueous glucose solutions (1-52 wt.%) reported at 298 K [194] were adjusted to reaction temperatures using the following equation (details in Section 4.7.3.3, Supp. Info.) [195]:

$$\frac{-\overline{H}_i^E}{RT^2} = \frac{\delta}{\delta T} ln\gamma_i \tag{4.5}$$

Here, $\overline{H}_i^E$ is the excess partial molar enthalpy of species i in solution and is assumed to be constant with temperature, R is the universal gas constant, and T is the absolute temperature in K. Activity coefficients approach unity ($\gamma_i \rightarrow 1$) as temperature increases or glucose concentrations decrease and solutions approach ideal behavior. Thermodynamic activities (a_i) for glucose (a_G) and water (a_W) were calculated using temperature-dependent and concentration-dependent activity coefficients according to the following equation:

$$a_i = \gamma_i \frac{ci}{c^o} \tag{4.6}$$

where c^o is the standard concentration (1 mol m^{-3}).

The dependence of initial fructose and sorbose formation rates (373 K, per Ti_{LA}) on the initial aqueous-phase glucose activity is shown in Figure 4.5 for Ti-Beta-F-155 and Ti-Beta-OH-46. Initial isomerization rates are 3-6x lower on Ti-Beta-OH-46 than on Ti-Beta-F-155 across the full range of a_G values studied, consistent with previously reported rates measured in dilute aqueous glucose solutions (0-1.5 wt.%) [16]. Initial glucose-fructose and glucose-sorbose isomerization rates on both Ti-Beta-F and Ti-Beta-OH zeolites show a first-order kinetic dependence on glucose activity at low a_G values (50-300 mol m^{-3}, ∼1-5 wt.%, Figure 4.5 inset), consistent with previously reported glucose isomerization rates on Ti-Beta [35] and Sn-Beta [26] (isomerization rates shown as a function of glucose concentration in Figure 4.35, Supp. Info.). Glucose-fructose and glucose-sorbose isomerization rates become zero-order in a_G at high a_G values (>2700 mol m^{-3}), which is a kinetic regime that has not been previously reported to our knowledge for sugar isomerization on Lewis acidic zeolites. The onset of the zero-order kinetic regime in formation rates of both fructose and sorbose products, which are formed in parallel reaction pathways, are consistent with

changes in the identities of the most abundant reactive intermediates at Lewis acid active sites and that both products are formed at the same catalytic site.

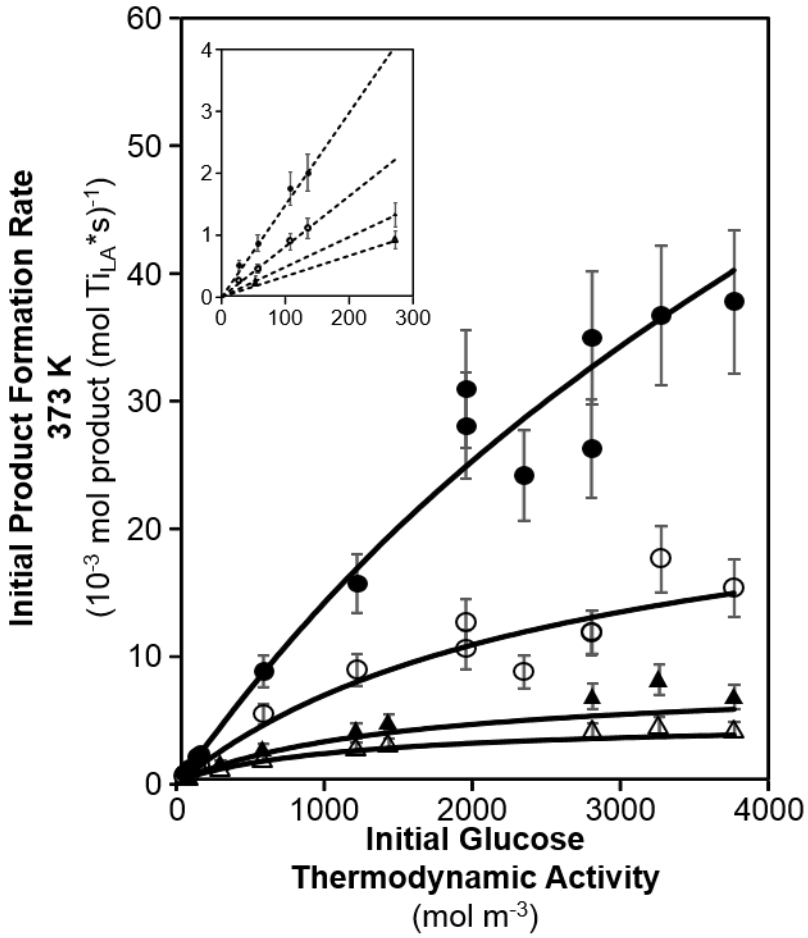

Figure 4.5: Dependence of initial glucose isomerization rates (373 K, pH 4) for fructose (filled) and sorbose (open) formation on Ti-Beta-F-155 (closed circles,open circles) and Ti-Beta-OH-46 (closed triangles, open triangles) as a function of initial glucose thermodynamic activity (corresponding to 1-50 wt% initial glucose concentration). Solid lines represent fits of the experimental data to the rate equation (Eq. 4.9) using activation enthalpies and entropies given in Table 4.4. The inset shows initial glucose isomerization rates at low glucose thermodynamic activities, highlighting the first-order kinetic regime.

Modeling multiple kinetic regimes requires consideration of at least two distinct coverage terms, only one of which is first-order in glucose thermodynamic activity,

and suggests the presence of two distinct MARI species that are dependent on glucose activities. The general form of such a rate equation is:

$$r_{isom} = \frac{k_{first} a_G}{1 + \frac{k_{first}}{k_{zero}} a_G} \tag{4.7}$$

In Eq. 4.7, r_{isom} is the initial glucose isomerization rate, k_{first} and k_{zero} are apparent first-order and zero-order rate constants, and a_G is the initial glucose thermodynamic activity. This rate equation simplifies to first-order and zero-order rate expressions at low and high a_G values, respectively. We next use spectroscopic techniques to characterize the nature of the bound intermediates as a function of glucose concentration in order to assign chemical significance to the first-order and zero-order kinetic regimes that are predicted by the generalized rate expression (Eq. 4.7).

4.4.4 Characterization of Active Site Complexes in First-Order and Zero-Order Kinetic Regimes

4.4.4.1 Characterization of Bound Reactive Intermediates using ATR-IR and Modulation Excitation Spectroscopy (MES)

The competitive adsorption of water solvent, glucose reactants, and glucose isomerization products within microporous voids and at Lewis acidic Ti sites in Ti-Beta-F-155 and Ti-Beta-OH-46 was probed *in situ* with ATR-IR and MES. Figure 4.6A shows spectra corresponding to two independent intermediates extracted by phase sensitive detection (PSD) and multicurve resolution-alternating least squares analysis (MCR-ALS) from experiments with modulated glucose activities within the first-order kinetic regime (0-700 mol m^{-3}, 373 K) (time resolved and phase resolved spectra on Ti-Beta-F-155 shown in Figure 4.36, Supp. Info.). These spectra collected on both Ti-Beta-F-155 and Ti-Beta-OH-46 reflect the two independent reactive intermediates observed from interactions between solid surfaces and fluid phases comprised of modulated glucose and water activities. One intermediate (Figure 4.6A, top) is characterized by water bending (δ(O-H) at 1630 cm^{-1}) and stretching (ν(O-H) around 3400 cm^{-1}) [196] vibrations, and lacks vibrational modes representative of glucose (ν (C-H) at 2900 cm^{-1} [197–199]; concerted vibrations at 900-1500 cm^{-1} [197–200], indicating that this intermediate is not derived from glucose. This species is the MARI and, because it is not glucose-derived, spectra were normalized by the water bending resonance at 1630 cm^{-1} to facilitate comparison between samples in Figure 4.6A. The minor intermediate (Figure 4.6A, bottom) contains spectral features similar to vibrational modes of glucose, and thus was normalized by the most intense glucose resonance ($\sim$1030 cm^{-1}). These features do not show significant differences from those of aqueous-phase glucose flowing over the ZnSe crystal (Figure 4.6A, bottom, dashed line), which suggests that such species are not coordinated to Lewis acidic Ti centers on Ti-Beta-F-155 and Ti-Beta-OH-46 and are likely solution-phase glucose. Together, the two species isolated from MES and sequential PSD and MCR-ALS during glucose concentration modulations at low activities ($\sim$0-700 mol m^{-3}) indicate

that Ti-Beta zeolite surfaces bind a water-derived MARI species and a minor glucose species that is not coordinated to Lewis acid sites, supporting the mechanistic interpretations of first-order rate measurements at low a_G values.

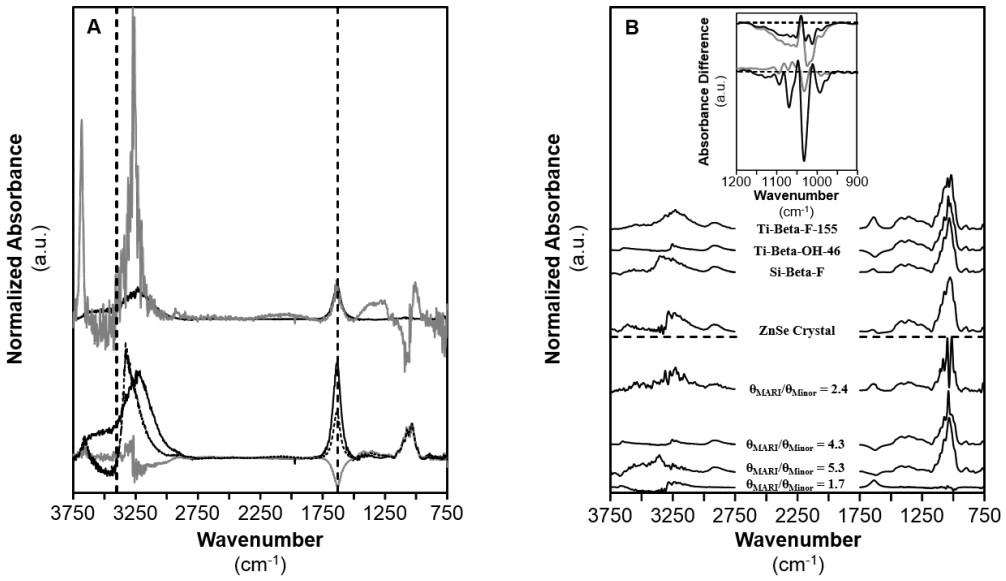

(a) (b)

Figure 4.6: (a) ATR-IR spectra of MARI (top, water derived) and minor (bottom, glucose derived) intermediates on Ti-Beta-F-155 (black) and Ti-Beta-OH-46 (gray) that oscillate with aqueous-phase glucose activity (0-700 mol m^{-3}) at 373 K. Glucose spectra are normalized by the peak at ∼1030 cm^{-1} and water spectra are normalized by the peak at ∼1630 cm^{-1}. Spectra reflecting aqueous-phase glucose (330 mol m^{-3}) flowing over the ZnSe crystal is overlaid on the glucose spectra (dashed). Dashed vertical lines at 1630 and 3400 cm^{-1} indicate water bending and stretching vibrational modes, respectively. (b) ATR-IR spectra of the MARI (bottom four) and minor (top four) species that oscillate with aqueous-phase glucose activity (∼3000-3750 mol glucose m^{-3}, 373 K, normalized by the maximum feature at ∼1030 cm^{-1}) over Ti-Beta-F-155, Ti-Beta-OH-46, Si-Beta-F, and blank ZnSe crystal from top to bottom, respectively. The inset depicts difference spectra between aqueous-phase glucose flowing over the ZnSe crystal and the MARI (black) or minor species (gray) species observed on Ti-Beta-OH-46 (top) and Ti-Beta-F-155 (bottom) spectra from modulating aqueous-phase glucose activity (∼3000-3750 mol glucose m^{-3}) at 373 K after normalization by the peak centered at ∼1030 cm^{-1}; dashed lines (- - -) indicate the baseline. All spectra are obtained during MES experiments and isolated by processing through PSD and MCR-ALS.

Figure 4.6B shows spectra of the MARI species (bottom) and the minor intermediates (top) observed by MES at high glucose activities corresponding to zero-order kinetic regimes (∼3000-3750 mol glucose m^{-3}) on Ti-Beta-F-155, Ti-Beta-OH-46, Si-Beta-F, and the ZnSe crystal. Spectral features between 900 to 1500 cm^{-1} in spectra of both the MARI and minor species reflect concerted ν(C-O), ν(C-C), δ(C-H), and δ(C-O-H) [197–201] vibrations of glucose-derived intermediates. Therefore, MARI and minor intermediates are assumed to be related oxygenate structures with identical molar extinction coefficients, such that their integrated areas correlate with their relative surface coverages with MARI species existing in higher abundances in MES experiments. Relative coverages between MARI and minor species are given in Table 4.3, indicating that MARI species are present at coverages that are 1.7-5.3x greater than the minority species.

Table 4.3: Relative concentrations[a] of MARI and minor species during modulation of liquid-phase glucose concentration (42-50 wt%) at 373 K followed by processing by PSD and MCR-ALS.

Sample	Relative Concentration[a] (θ_{MARI} / $\theta_{\text{Minor species}}$)
Ti-Beta-F-155	2.4
Ti-Beta-OH-46	4.3
Si-Beta-F	5.3
ZnSe Crystal	1.7

[a]Relative concentrations assume the equivalent extinction coefficients for glucose vibrations at approximately 1030 cm^{-1} are between MARI and minor species.

Spectra of isolated species at high glucose activity modulations show relative changes in the quantities of water and glucose present on Ti-Beta-F-155 and Ti-Beta-OH-46 (Figure 4.6B), based on the relative intensities of vibrations from glucose-derived intermediates (ν(C-H) at 2900 cm^{-1} [197–199] and concerted vibrations between 900-1500 cm^{-1}) [197–201] and of the δ(O-H) water vibrations (1630 cm^{-1}) [196]. In hydrophobic Ti-Beta-F-155, the intensity of spectral features attributed to glucose or glucose-derived intermediates (2900 cm^{-1} [197–200]; 900-1500 cm^{-1} [197–201]) and

the intensity of features attributed to water (1630 cm^{-1}) increase concomitantly, indicating that glucose adsorption into hydrophobic Beta pores facilitates co-adsorption of water from its solvation sphere in bulk solution. This observation corroborates previous reports of co-adsorption of water with glucose in both experimental measurements of adsorbed water and glucose content (using TGA-DSC) on Sn-Beta zeolites contacted with aqueous glucose solutions [16] and theoretical Gibbs ensemble Monte Carlo simulations of glucose adsorption from aqueous solutions within hydrophobic Si-Beta zeolites [202]. In contrast, spectra collected on Ti-Beta-OH-46 at identical glucose activities and temperature show that water vibrational modes decrease as glucose vibrational modes increase, suggesting that glucose displaces water molecules previously adsorbed within hydrophilic Beta pores, consistent with the higher gas-phase water uptakes in hydrophilic than hydrophobic materials (Section 4.4.2.2). The differences in relative water and glucose activities present within the hydrophilic and hydrophobic pores indicate that the hydrophobic nature of microporous voids in Beta affect the uptakes of both water and glucose molecules.

At high glucose activities, spectra observed on Ti-Beta-F-155 and Ti-Beta-OH-46 differ from those of the blank ZnSe crystal and Si-Beta-F, indicating that the MARI species on Ti-Beta materials do not reflect solution-phase glucose or physisorbed glucose and instead are glucose-derived intermediates coordinated to Lewis acidic Ti sites within Beta pores. The vibrational features of the MARI observed on Ti-Beta-F-155 at high glucose activities differs significantly from those on Ti-Beta-OH-46 (Figure 4.6B), particularly for ν(C-O), ν(C-C), δ(C-H), and δ(C-O-H) glucose vibrations (900-1200 cm^{-1}) [197–201], suggesting that glucose-derived reactive intermediates are structurally distinct on hydrophobic and hydrophilic Ti-Beta zeolites (additional discussion and DFT evidence on the likely and distinct adsorbate configurations is provided in Section 4.7.4.2, Supp. Info.). The inset of Figure 4.6B shows difference spectra for the two intermediates on each Ti-Beta sample relative to those for aqueous glucose on the ZnSe crystal, which show negative features at $\sim$1030 cm^{-1} that may reflect ring-opened intermediates adsorbed at Ti sites in both Ti-Beta sam-

ples. DFT-calculated intermediates that form fructose and sorbose show the loss of the ∼1030 cm^{-1} vibrational mode upon glucose ring opening (1029 and 1027 cm^{-1}, respectively); however, the ring-opened intermediate that forms sorbose contains a carbonyl group with a resonance at 1737 cm^{-1} (Movie S.2, Supp. Info.) that is not present in any spectra measured on Ti-Beta-F-155 or Ti-Beta-OH-46 (Figure 4.6B). Thus, both the MARI and the minor species on Ti-Beta-F-155 and Ti-Beta-OH-46 likely react to form fructose, which may be expected given the higher selectivity towards fructose over sorbose on both Ti-Beta-F-155 and Ti-Beta-OH-46 at high glucose activities (Figures 4.5 and 4.37, Supp. Info.), yet hydrophobic and hydrophilic pore environments may stabilize different reactive intermediates.

The change in MARI and minor species on both hydrophobic and hydrophilic Ti-Beta samples detected during MES and isolated by PSD and MCR-ALS between low and high glucose activities indicates that the MARI transitions from a water-derived to a glucose-derived intermediate bound to framework Ti atoms, consistent with measured glucose isomerization rates that transition from a first-order to a zero-order kinetic regime with increasing glucose thermodynamic activity (Figure 4.5). Further, the MARI species identified at high a_G values have distinct binding configurations on Ti-Beta-F and Ti-Beta-OH, which depend on the different solvating environments provided by silanol groups and co-adsorbed water structures in hydrophobic and hydrophilic environments. Next, we use *ex situ* XAS to further characterize the structure of the adsorbed species on Ti-Beta observed after exposure to low and high glucose activities.

4.4.4.2 Ti Structural Characterization using XAS

In order to provide corroborating evidence for the predominant reactive intermediates proposed to exist at low and high glucose thermodynamic activity, we use XAS to determine Ti coordination numbers and Ti-O bond lengths in the presence and absence of adsorbed glucose intermediates. Apparent first-order isomerization rates measured at low glucose activities are consistent with dilute glucose coverages. EX-

AFS spectra collected on Ti-Beta-OH-46 (a sample with predominantly Lewis acidic Ti sites (Ti_{LA}/Ti ∼1)) show that Ti sites are octahedrally coordinated at ambient temperature (CN = 6 ± 0.6, Table 4.8 and Figures 4.38-4.40, Supp. Info.) and become tetrahedrally coordinated upon heating to 523 K in flowing helium (CN = 4 ± 0.4), consistent with previous reports on Ti-Beta [106] and the reversible adsorption of water to framework Ti sites upon exposure to ambient conditions. Ti-O bond lengths derived from EXAFS are similar to framework bond distances for dehydrated Lewis acid sites. The loss of two ligands upon heating reflects desorption of two water molecules from each Lewis acidic Ti site. UV-Visible edge energies derived from Tauc plots also increase upon dehydration (523 K) by 0.22 eV on average (Table 4.6 and Figure 4.15, Supp. Info.), indicative of octahedral to tetrahedral coordination changes of Ti sites. Similar findings from EXAFS spectra [52, 71] and UV-Visible edge energies [26] have been reported on Sn-Beta catalysts, in which the shift from octahedral to tetrahedral coordination upon dehydration is corroborated by ^{119}Sn NMR spectra that show the shift from octahedrally coordinated Sn resonances (685-700 ppm) to tetrahedral Sn resonances (425–445 ppm) upon dehydration at 423 K [34, 120]. Thus, we conclude that apparent first-order kinetic regimes measured at low glucose activity correspond to glucose isomerization rates measured on Ti sites covered with two water molecules [34, 120], the most abundant reactive intermediate under these reaction conditions [35].

Ex situ XANES spectra (Figures 4.41 and 4.42, Supp. Info.) at ambient conditions most closely resemble octahedrally coordinated Ti sites (CN = 6, Table 4.8, Supp. Info.) on glucose-adsorbed Ti-Beta-OH-46. After dehydration treatments in flowing helium (523 K, 30 min), Ti sites became pentahedrally coordinated (CN = 5, Table 4.8, Supp. Info.), indicating the loss of one ligand per Ti site. This may reflect a change from bidentate to monodentate binding modes of glucose or desorption of one water molecule if glucose were originally bound in a monodentate fashion. The presence of pentahedrally coordinated Ti sites that persist after dehydration treatments would be consistent either with complete coverage of all Ti sites with a

strongly bound intermediate (e.g., monodentate glucose) or with a mixture of sites in which some remain six-coordinate and populated by a strongly bound bidentate glucose intermediate and others revert to four-coordinate upon desorption of water ligands at 523 K. Although XAS cannot distinguish between these possibilities, the ATR-IR experiments show that Lewis acidic Ti sites in both Ti-Beta-OH-46 and Ti-Beta-F-155 are saturated with bound glucose intermediates at high glucose activities (>3000 mol m^{-3}) that are characteristic of the zero-order kinetic regime observed in Figure 4.5. Therefore, we propose that the octahedrally coordinated Ti sites observed after glucose adsorption reflect monodentate-bound glucose and one water ligand, and that the pentahedrally coordinated Ti sites observed after dehydration results from desorption of the water ligand.

Combining insights from *in situ* ATR-IR, *ex situ* XAS and DFT calculations, we conclude that two different reactive species are dominant at low (∼0-500 mol m^{-3}) and high glucose activities (>3000 mol m^{-3}). The most abundant reactive intermediates are two water molecules bound to Lewis acid centers at low glucose activities and bound glucose intermediates (in two different binding configurations) at high glucose activities. The bound glucose intermediates are distinct for Ti-Beta-F and Ti-Beta-OH, evidenced by shifts in IR peak centers and relative peak areas that are likely caused by the presence of extended solvent structures surrounding the adsorbed glucose.

4.4.5 Enthalpic and Entropic Consequences of Hydrophobic Reaction Pockets for Aqueous-Phase Glucose Isomerization

In this section, experimentally measured activation enthalpies and entropies on Ti-Beta-F and Ti-Beta-OH are compared with DFT-derived free energies to probe the consequences of intrapore silanol defects, and the co-adsorbed water structures they stabilize, on aqueous-phase glucose isomerization catalysis.

4.4.5.1 Experimentally-Determined Activation Enthalpies and Entropies

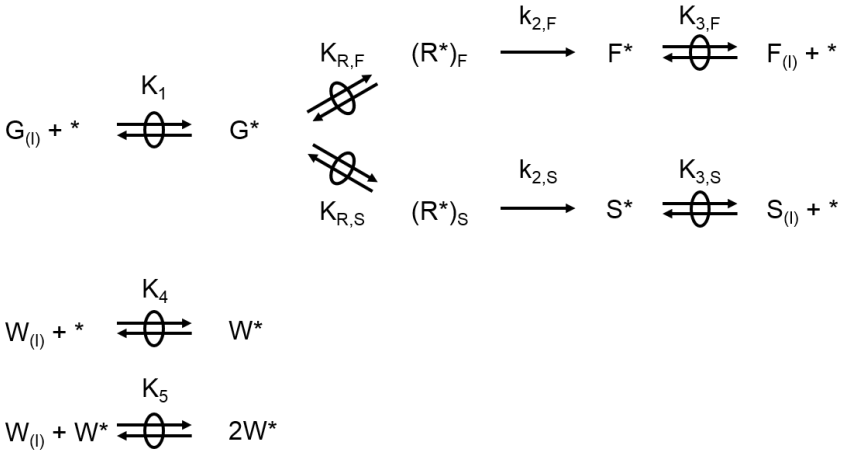

Figure 4.7: Plausible glucose isomerization mechanism for fructose and sorbose formation on Lewis acidic Ti sites

A reaction mechanism is shown in Scheme 1 depicting glucose isomerization pathways to fructose and to sorbose via quasi-equilibrated water adsorption and desorption, glucose adsorption, ring opening, deprotonation, and the kinetically-relevant hydride shift steps, and is adapted from previously published work [35]. Having identified the dominant reactive intermediates at both low and high glucose thermodynamic activities in Section 4.4.4, the following rate equation can be derived from the mechanism in Scheme 4.7 to recover both first-order and zero-order dependences on glucose activity (complete derivation in Section 4.7.5.1, Supp. Info.):

$$r_{isom} = \frac{K_1 K_{R,i} k_{2,i} \frac{a_G}{\gamma_{\ddagger,i}} (1\eta_i)}{\frac{K_4 K_5}{\gamma_{2W*}} a_W^2 + \frac{K_1}{\gamma_{G*}} a_G} \tag{4.8}$$

In Eq. 4.8, i stands for fructose or sorbose, K_1 is the lumped equilibrium constant for adsorbing glucose and forming the glucose-derived MARI at the tetrahedral Ti site, $K_{R,i}$ is the lumped equilibrium constant describing the formation of the structurally distinct intermediates that immediately precede fructose or sorbose formation from the glucose-derived MARI, $k_{2,i}$ is the rate constant for the kinetically-relevant step that forms the hydride shift transition state from the relevant reactive intermediate, and K_4 and K_5 are equilibrium constants relating the sequential adsorption of two water molecules from the liquid phase to the Lewis acid site; all lumped rate and equilibrium constants in Eq. 4.8 are identified in Figure 4.7. Additionally, η_i is the approach to equilibrium term, which is rigorously zero for initial isomerization rates extrapolated to zero conversion. Finally, γ_i is the activity coefficient of species j, where j denotes two bound water molecules (2W*), the bound glucose intermediate identified as MARI at high a_G values (G*), or the hydride shift transition states that form fructose and sorbose (‡,i). This rate equation is the simplest kinetic model that satisfies the requirement of two relevant adsorbed intermediates and accounts for the non-ideality of adsorbed or solution-phase species, which can be reduced to recover first-order and zero-order kinetic regimes at low and high glucose thermodynamic activities. These γ_i values approach unity for ideal solutions and ideal reactive intermediates, in which the ideality of adsorbed intermediates are typically defined as low-coverage and non-interacting species [203]; here, no such co-adsorbate interactions are expected among glucose-derived species and thus γ_i is assumed to be unity for adsorbed species.

Equation 4.8 can be recast in the following form, which was used to regress to initial fructose and sorbose rate data measured on Ti-Beta-F-155 and Ti-Beta-OH-46 as a_G/a_W^2 was varied:

$$r_{isom} = \frac{\frac{K_1}{K_4 K_5} K_{R,i} k_{2,i} \frac{a_G}{a_W^2}}{1 + \frac{K_1}{K_4 K_5} \frac{a_G}{a_W^2}} \tag{4.9}$$

In Eq. 4.9, the apparent zero-order rate constant is defined as:

$$k_{zero,i} = K_{R,i} k_{2,i} \tag{4.10}$$

which describes the formation of the kinetically-relevant hydride shift transition states from the glucose-derived MARI species. Additionally, the competitive adsorption terms for glucose and water can be lumped together into a single apparent equilibrium constant:

$$K_{comp} = \frac{K_1}{K_4 K_5} \tag{4.11}$$

which describes the adsorption of glucose and concomitant displacement of two water molecules from the Ti site. These two values can be combined to define an apparent first-order rate constant:

$$k_{first,i} = k_{zero,i} K_{comp} = \frac{K_1 K_{R,i} k_{2,i}}{K_4 K_5} \tag{4.12}$$

which describes the formation of the kinetically-relevant hydride shift transition state from aqueous-phase glucose and a pair of co-adsorbed waters on the Ti site. Substituting Eqs. 4.10-4.12 into Eq. 4.9 yields the following equation, which follows a Langmuir-Hinshelwood formalism:

$$r_{isom} = \frac{K_{comp} k_{zero,i} \frac{a_G}{a_W^2}}{1 + K_{comp} \frac{a_G}{a_W^2}} \tag{4.13}$$

Figure 4.8 shows initial fructose formation rates on Ti-Beta-F-155 as a function of glucose activity (a_G ~50-4000 mol m^{-3}), water activity (a_W ~40,000-50,000 mol m^{-3}), and temperature (368-383 K), with similar plots of fructose formation rates on Ti-Beta-OH-46 and sorbose formation rates on both Ti-Beta-F-155 and Ti-Beta-

OH-46 available in Figures 4.44-4.46 (Supp. Info.). We note that while water solvent is typically considered to be in excess concentration, water activities vary by ∼20% across the conditions studied here (a_W ∼40,000-50,000 mol m^{-3}) and are accounted for using temperature-dependent activity coefficients and water concentrations following the same procedure used to calculate glucose activities (Section 4.4.3.2). Fructose and sorbose formation rates are plotted as a function of the relevant ratio of glucose and water activities (a_G/a_W^2) in Figures 4.47 and 4.48 (Supp. Info.) at each temperature studied. Formation rates of both products on both Ti-Beta-F-155 and Ti-Beta-OH-46 show the kinetic behavior predicted by Langmuir-Hinshelwood formalisms (Eq. 4.13) with a first-order dependence at low aG values (¡500 mol m^{-3}) and an approximately zero-order dependence at high a_G values (>2700 mol m^{-3}).

Equations 4.10 and 4.11 can be rewritten in terms of apparent entropic and enthalpic contributions using the Eyring equation:

$$k_{zero,i} = \frac{k_B T}{h} e^{\Delta S^{\ddagger}_{zero,i}/R} e^{\Delta H^{\ddagger}_{zero,i}/RT} \tag{4.14}$$

$$K_{comp} = e^{\Delta S_{comp}/R} e^{\Delta H_{comp}/RT} \tag{4.15}$$

Here, k_B is the Boltzmann constant, h is Planck's constant, $\Delta S^{\ddagger}_{zero,i}$ and $\Delta H^{\ddagger}_{zero,i}$ are the apparent activation entropy and enthalpy of the hydride shift transition state referenced to the bound glucose MARI, and ΔS_{comp} and ΔS_{comp} are the apparent reaction entropy and enthalpy changes describing the competitive adsorption of glucose relative to water at the Lewis acid sites. We note that the temperature dependence of any non-unity activity coefficients for adsorbed species and transition state would be convoluted with the temperature dependences of enthalpy terms Eqs. 4.14 and 4.15. Substitution of Eqs. 4.14 and 4.15 into Eq. 4.13 yields:

$$r_{isom} = \frac{k_B T}{h} \frac{e^{\frac{\Delta S^{\ddagger}_{zero,i} + \Delta S_{comp}}{R}} e^{\frac{-(\Delta H^{\ddagger}_{zero,i} + \Delta H_{comp})}{RT}} \frac{a_G}{a_W^2}}{1 + e^{\frac{\Delta S_{comp}}{R}} e^{\frac{\Delta H_{comp}}{RT}} \frac{a_G}{a_W^2}} \tag{4.16}$$

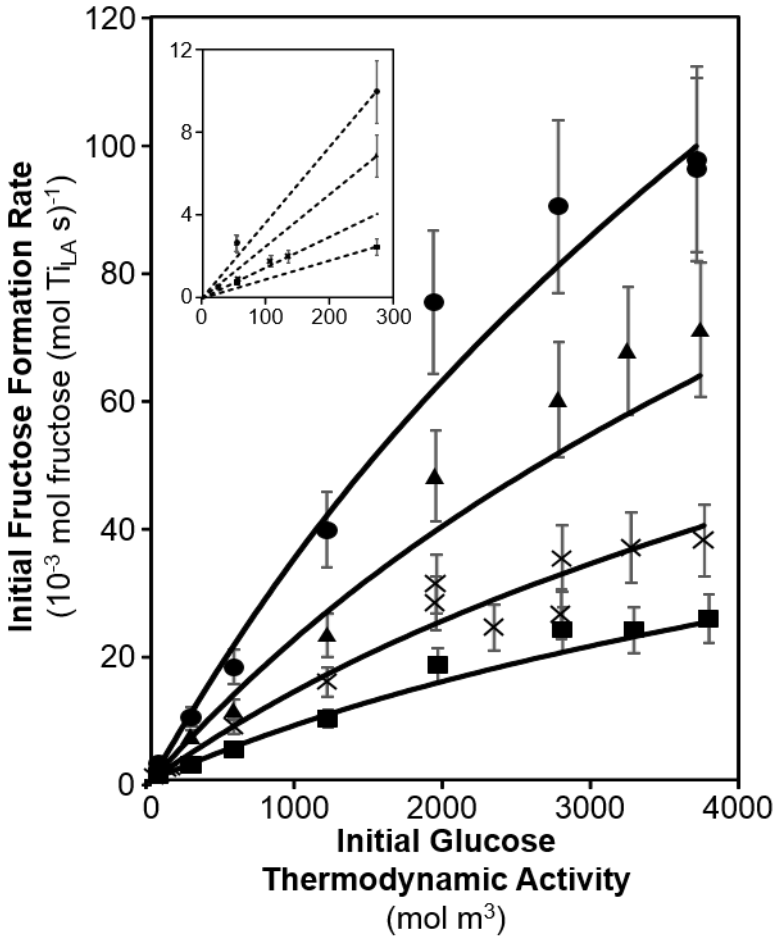

Figure 4.8: Dependence of initial fructose formation rates (pH 3) on Ti-Beta-F-155 on initial glucose thermodynamic activity (corresponding to 1-50 wt% glucose concentration) at 368 (squares), 373 (X), 378 (triangles), and 383 K (circles). Solid lines represent regression of the data to the rate equation (Eq. 4.9) using activation enthalpies and entropies given in Table 4.4. The inset shows initial glucose isomerization rates at low glucose thermodynamic activities, highlighting the first-order kinetic regime.

Table 4.4 lists the apparent activation enthalpies and entropies obtained by regressing Eq. 4.16 to the experimental data for fructose and sorbose formation rates on Ti-Beta-F-155 and Ti-Beta-OH-46 (368-383 K, a_G = 50-4000, a_W = 40,000-50,000 mol m^{-3}, parity plots available in Figures 4.49-4.52, Supp. Info.). Apparent activation enthalpies for glucose-fructose isomerization on Ti-Beta-F-155 are identical (108 kJ mol^{-1}) for both first-order and zero-order rate constants, which measure differences

in enthalpy between the same 1,2-hydride shift transition state and either two bound water molecules or a bound glucose intermediate on the Lewis acid site, respectively. Similarly, apparent activation enthalpies for the parallel glucose-sorbose isomerization reaction on Ti-Beta-F-155 are also identical (121 kJ mol^{-1}) for both first-order and zero-order rate constants. Together, these findings indicate that the competitive adsorption of glucose and two water molecules at Ti sites within low-defect Beta frameworks is isenthalpic and depends weakly on temperature in the range studied. This is consistent with glucose heats of adsorption calculated by theory (108 kJ mol^{-1}) [202] that are approximately twice that of water heats of adsorption ($\sim$50 kJ mol^{-1}) measured by experiment from gravimetric and microcalorimetric studies on Ti-Beta-F [106].

In contrast, apparent activation entropies for both glucose-fructose and glucose-sorbose isomerization on Ti-Beta-F-155 are $\sim$120 J mol^{-1} K^{-1} larger for the first-order rate constant than for the zero-order rate constant. Zero-order activation entropies reflect differences between the relevant hydride shift transition state and the adsorbed glucose state, while first-order activation entropies reflect differences between the same transition state and a precursor state involving two adsorbed water molecules at the Lewis acid site and glucose in aqueous solution. As a result, differences in zero-order and first-order activation entropies reflect differences in the entropy of the precursor states describing adsorbed glucose (with two associated water molecules) or two adsorbed water molecules and aqueous-phase glucose. Therefore, the smaller apparent activation entropies measured in zero-order regimes reflect the losses in entropy upon exchange of two bound water molecules with bound glucose, likely dominated by the entropy losses upon glucose adsorption to active sites from aqueous phases. We note that similar apparent enthalpies and entropies are obtained from the first-order and zero-order rate constants modeled by Eq. 4.16 and from the Eyring equation from single rate measurements in the first-order (a_G = 275 mol m^{-3}) and zero-order ($a_G \sim$ 3500 mol m^{-3}) kinetic regimes, indicating that the data fitting method used here does not significantly change the measured thermodynamic

properties (Table 4.9 and Figures 4.53 and 4.54, Supp. Info.) or the conclusions derived from them.

Apparent activation enthalpies on Ti-Beta-OH-46 are also similar for the first-order and zero-order rate constants for glucose-fructose isomerization (75-86 kJ mol^{-1}, Table 4.4) and for glucose-sorbose isomerization (82-93 kJ mol^{-1}, Table 4.4). These data indicate that competitive adsorption of glucose and water onto Lewis acid sites within hydrophilic void environments also depends weakly on temperature in the range studied. Water adsorption has been reported to be ∼7 kJ mol^{-1} more exothermic within Ti-Beta-OH than Ti-Beta-F from microcalorimetric studies [106], presumably reflecting favorable hydrogen bonding interactions with silanol defects, and similar effects of hydrogen bonding interactions on the adsorption enthalpy of glucose seem reasonable. Indeed, the more exothermic water adsorption enthalpies within hydrophilic channels of Ti-Beta-OH (by ∼7 kJ mol^{-1}) resemble the lower apparent activation energies (by 22-39 kJ mol^{-1}) for glucose-fructose isomerization on Ti-Beta-OH-46 than Ti-Beta-F-155. As in the case for Ti-Beta-F, apparent activation entropies on Ti-Beta-OH-46 are ∼100 J mol^{-1} K^{-1} higher for the apparent first-order rate constant than for the zero-order rate constant for both glucose-fructose and glucose-sorbose isomerization. These findings suggest that the polarity of the channel environment, and the associated co-adsorbed water structures they may stabilize, affect the free energy changes associated with water and glucose competitive adsorption to similar extents. Further, DFT calculations with varying intrapore water (2–10 molecules) show scattered glucose adsorption enthalpies with increasing intraporous water content, but do not show a strong increase or decrease in these values (Figure 4.55A, Supp. Info.), indicating that intraporous water has no systematic impact on glucose adsorption and water displacement (K_{comp}).

The kinetic effects of surrounding hydrophobic reaction pockets can be quantified from the difference in apparent activation enthalpies ($\Delta\Delta H$), entropies ($\Delta\Delta S$), and Gibbs free energies ($\Delta\Delta G$, 373 K) between Ti-Beta-F-155 and Ti-Beta-OH-46 for each parallel reaction (Table 4.4). For both glucose-fructose and glucose-sorbose iso-

merization, both first-order and zero-order apparent activation enthalpies are higher (22-39 kJ mol^{-1}) on Ti-Beta-F-155 than on Ti-Beta-OH-46, which seems reasonable for enthalpic stabilization of isomerization transition states by an additional hydrogen bonding interaction with silanol groups (or co-adsorbed water) present in more defective pore environments. Despite higher apparent activation enthalpies, initial isomerization rates are higher on Ti-Beta-F-155, reflecting greater apparent activation entropy gains ($\sim$85 J mol^{-1} K^{-1} for fructose, $\sim$103 J mol^{-1} K^{-1} for sorbose) in both first-order and zero-order regimes. Similar findings have been observed for first-order glucose isomerization rates on Sn-Beta (373 K, 5 wt.% glucose, per Sn), for which similar apparent activation energies but higher pre-exponential factors are measured on hydrophobic Sn-Beta-F than hydrophilic Sn-Beta-OH [28], although kinetic parameters measured in the first-order regime cannot be separated into individual contributions that affect competitive adsorption and hydride shift transition state formation from the bound glucose MARI species.

For both parallel reactions on Ti-Beta, $\Delta\Delta H$ and $\Delta\Delta S$ values are similar for both the first-order and zero-order rate constants, indicating that the dominant kinetic effect of the hydrophobic reaction pocket is the entropic stabilization of the hydride shift transition state relative to the bound glucose MARI, and not of the bound water or glucose intermediates. For glucose isomerization reaction coordinates, descriptions of the hydride shift transition state include both the transitory glucose-derived complexes bound at Ti sites and the surrounding solvation environment provided by co-adsorbed water molecules and confining lattice atoms. Solvent reorganization to form cavities near hydrophobic surfaces change the hydrogen bonding structure of water and can result in large entropy losses ($\sim$80 J mol^{-1} K^{-1}) [204], and similar entropy losses ($>$70 J mol^{-1} K^{-1}) have been observed as hydrophobic intermediates became more hydrophilic in nature at transition states for the catalytic formation of H_2O_2 on silica-supported Pd clusters [205]. We surmise that the similar ($\sim$85-103 J mol^{-1} K^{-1}) entropy differences measured here for glucose isomerization in Ti-Beta-F and Ti-Beta-OH suggest reorganization of solvating water shells between

the kinetically-relevant precursor and transition states, given that both water and glucose-derived moieties are hydrophilic and able to hydrogen bond with the solvating environment. Further, since the stability of the transition state relative to the bound glucose MARI species affects both first-order and zero-order rate constants, comparison between first-order and zero-order rate constants (Table 4.4) indicates that hydrophobic surrounding environments have a weaker effect on water and glucose competitive adsorption equilibrium constants, and a predominant effect on the stability of kinetically-relevant hydride shift transition states relative to the bound glucose MARI species.

In summary, experimental kinetic measurements indicate that the dominant effect of hydrophobic voids in Ti-Beta-F is the entropic stabilization of the hydride shift transition state relative to bound glucose MARI species ($\Delta\Delta H$ and $\Delta\Delta S$ values for k_{zero}, Table 4.4) and not the competitive adsorption of water and glucose ($\Delta\Delta H$ and $\Delta\Delta S$ values for K_{comp} near zero, Table 4.4). As a result, isomerization turnover rates measured in both first-order and zero-order kinetic regimes (per Ti_{LA}) are higher (by similar factors) when active Ti sites are confined within hydrophobic than hydrophilic voids. Small enthalpic penalties for confining transition states within hydrophobic voids of Ti-Beta-F are compensated by significantly more favorable entropic gains, resulting in higher rate constants than on hydrophilic Ti-Beta-OH. This entropic stabilization of the transition state relative to the adsorbed glucose intermediate is the dominant kinetic effect of confining glucose isomerization reaction coordinates within hydrophobic reaction pockets. In what follows, we assess the effects of hydrophobic and hydrophilic reaction environments on glucose isomerization using DFT calculations that consider the effects of additional water molecules present in reaction environments on glucose isomerization free energy landscapes. These calculations focus primarily on the effects of co-adsorbed water on the stability of the hydride shift transition state, relative to the adsorbed glucose intermediate observed from ATR-IR spectra at high a_G values.

Table 4.4: Apparent enthalpies and entropies for first-order and zero-order rate constants describing fructose and sorbose formation on Ti-Beta-F-155 and Ti-Beta-OH-46.

	ΔH_{app} (kJ mol^{-1})		ΔS_{app} (J mol^{-1} K^{-1})		$\Delta\Delta H_{app}$ (kJ mol^{-1})	$\Delta\Delta S_{app}$ (J mol^{-1} K^{-1})	$\Delta\Delta G_{app}$ (kJ mol^{-1})
rate constant	Ti-Beta-F-155	Ti-Beta-OH-46	Ti-Beta-F-155	Ti-Beta-OH-46	(F-OH)[b]	(F-OH)[b]	(F-OH)[b]
$k_{zero,fructose}$[a]	108 ± 10	86 ± 9	17 ± 26	-56 ± 25	22	73	-5
$k_{first,fructose}$	108	75	133	33	33	100	-4
$k_{zero,sorbose}$[a]	121 ± 7	93 ± 8	46 ± 19	-43 ± 20	28	89	-5
$k_{first,sorbose}$	121	82	162	46	39	116	-4
K_{comp}[a]	0 ± 0.5	-10 ± 0.5	116	89	11	27	1

[a]Errors correspond to 95% confidence intervals from regressions. Errors for first-order rate constants are not given as they reflect combined free energy differences for zero-order and competitive adsorption fits.
[b]Differences in apparent activation enthalpies ($\Delta\Delta H_{app}$), entropies ($\Delta\Delta S_{app}$), and free energies ($\Delta\Delta G_{app}$ at 373 K) are listed as the difference between Ti-Beta-F-155 and Ti-Beta-OH-46.

4.4.5.2 DFT-Derived Activation Enthalpies and Entropies

The kinetic effects of co-adsorbed water on glucose-fructose isomerization were examined by changing the number of intrapore water molecules (2-10) that interact with the transition state for the 1,2-hydride shift step, the adsorbed glucose state, and the desorbed glucose state (the closed Ti site without any organic species present) individually. Additional kinetic effects from proximal silanol groups that may exist in Ti-Beta-OH materials are possible, but cannot be quantified appropriately without more precise definitions of active Ti site structures (e.g., closed, open), which is the subject of ongoing work. Alterations in the nature (e.g., closed, open) of Lewis acidic Sn sites may significantly affect glucose-fructose isomerization activation enthalpies [161], however, the similar activation enthalpies measured experimentally on Ti-Beta-F and Ti-Beta-OH (Table 4.4) do not suggest that such dramatic differences prevail among active Ti site structures in hydrophobic and hydrophilic Ti-Beta zeolites. Therefore, to isolate the kinetic roles of co-adsorbed water molecules on the stability of hydride shift transition states, the active site model was restricted to a closed Ti site without proximal silanol defects.

The positions of water molecules in these studies were determined by first fully solvating three cases: the 1,2-hydride shift transition state, the adsorbed ring-closed glucose state, and the closed Ti site with a proximal, partially-bound water cluster. Water was systematically removed from each position in these clusters to determine the most weakly bound water molecule, which was then used as the basis for each subsequent water removal. For example, starting with 10 water molecules solvating the 1,2-hydride shift transition state, each individual water molecule was removed to create 10 distinct 9-water arrangements, each of which was optimized into its lowest free energy configuration. The 9-water configuration with the lowest free energy was used to generate 9 distinct 8-water arrangements prior to energy minimization, a process that was repeated until no water molecules remained. The arrangement of water molecules at each discrete water density on the 1,2-hydride shift transition

state, the adsorbed glucose state, and the closed Ti site corresponding to the lowest free energy was then used to calculate enthalpy and entropy barriers for the apparent first-order and zero-order rate constants.

The aqueous nature of these reactions prohibits direct assessment of how many water molecules adsorb or desorb over the course of the reaction within hydrophobic and hydrophilic environments. ATR-IR experiments confirm prior reports that glucose adsorption entrains some number of water molecules into hydrophobic channels [16, 202] and indicates that glucose displaces some number of water molecules upon adsorption within hydrophilic channels. Despite these apparent shifts in intrapore water content upon glucose adsorption, K_{comp} values are nearly identical in Ti-Beta-F and Ti-Beta-OH materials, which correspond to the adsorption of glucose and concomitant desorption of two water molecules. Therefore, the difference in reactivity between Ti-Beta-F and Ti-Beta-OH is directly attributable to changes in the zero-order apparent rate constants, which reflect differences in free energy between hydride shift transition states and the adsorbed glucose MARI state. This reaction event likely causes net-zero changes in the amount of co-adsorbed water within either material.

DFT-predicted apparent zero-order activation enthalpies systematically increase from 165 to 276 kJ mol^{-1} and apparent zero-order activation entropies systematically increase from -12 to 49 J mol^{-1} K^{-1} as the co-adsorbed water density increases from 2–10 molecules (Fig. 4.55C, Supp. Info.). Similar increases in apparent activation enthalpies and entropies with increasing intrapore water content were observed for the first-order regime (Fig. S.46B, Supp. Info.). These DFT-predicted trends, however, directly contradict the decrease in experimentally measured activation enthalpies ($\Delta\Delta H_{zero,fructose}$ of 22 kJ mol^{-1}) and large decrease in entropies ($\Delta\Delta S_{zero,fructose}$ of 73 J mol^{-1} K^{-1}) on Ti-Beta-OH-46 compared to Ti-Beta-F-155 (Table 4.4) in the zero-order regime.

The inability to directly quantify the water content within the pores prohibits quantitative comparisons between DFT and experiments. Despite overall trends that

suggest an increase in activation enthalpy with increasing intraporous water density, certain changes in water content produce statistically insignificant changes in activation enthalpies, such as the shift from 2 to 4 intrapore water molecules that results in a slight decrease in the zero-order activation enthalpy from 165 to 155 kJ mol^{-1}, or the shift from 5 to 7 intrapore water molecules that results in a slight increase in the activation enthalpy from 209 to 214 kJ mol^{-1}. The overall results from DFT, however, indicate that large increases in the amount of water that directly solvates glucose-derived species cause an increase in activation enthalpies and entropies, suggesting that such large changes are unlikely between hydrophobic and hydrophilic materials. Further, this suggests that adsorbed glucose species may be sufficiently solvated within Ti-Beta-F because of water molecules entrained upon glucose adsorption and the desorbed waters from the Lewis acid site, and that the increase in intrapore water content at other regions within zeolitic voids has little impact on activation enthalpies.

The significant decrease in activation entropy between Ti-Beta-F and Ti-Beta-OH ($\Delta\Delta S_{zero,fructose}$ of 73 J mol^{-1} K^{-1}) demonstrates that intrapore water must have an impact on these reactions without a concomitant impact on activation enthalpy, which perhaps indicates that these effects are caused by alterations in the *second-layer* solvation shell around glucose-derived intermediates. In other words, glucose adsorption into hydrophobic materials entrains sufficient water molecules to directly solvate itself and the 1,2-hydride shift transition state that forms fructose, yet these materials lack extended water structures otherwise present in defect-laden hydrophilic materials that restrict the mobility of the first solvation shell of glucose. The net result is a decrease in the entropy of the 1,2-hydride shift transition state, reflected in a decrease in both first-order and zero-order activation entropies on Ti-Beta-OH. Although the DFT results and entropy treatments used here do not provide straightforward explanations of the experimental findings, they do appear to capture broader effects of intrapore water that can be used to eliminate some possible hypotheses that would otherwise be difficult to assess without DFT. We note that more accurate modeling of this

solvated reaction coordinate, using *ab initio* molecular dynamics simulations, may be warranted in future efforts that intend to more closely connect with experimental findings.

4.5 Conclusions

The confinement of binding sites within hydrophobic or hydrophilic micropore environments influences turnover rates of aqueous-phase reactions through effects on the competitive adsorption of solvent and reactant molecules at binding sites, and on the structures of solvent clusters and networks within void spaces that influence Gibbs free energies of transition states and kinetically relevant reactive intermediates. These effects were studied here using aqueous-phase glucose isomerization to fructose and sorbose on Ti-Beta samples comprising varying contents (by 10×) of isolated, active Lewis acidic Ti sites that were synthesized directly or modified post-synthetically in order to obtain suites of materials that confined such sites within hydrophobic (Ti-Beta-F) and hydrophilic (Ti-Beta-OH) samples of widely varying residual silanol defect density (by 100×). Hydrophilic Ti-Beta-OH samples adsorbed 20–25× higher amounts of water (P/P_0 = 0–0.2, 293 K) than hydrophobic Ti-Beta-F samples and stabilized water in structures characterized by increased extents of hydrogen-bonded networks than the gas-like molecular structures present within hydrophobic micropores. Initial glucose-fructose and glucose-sorbose isomerization turnover rates (368–383 K, per Ti_{LA}) are first-order at dilute glucose thermodynamic activities (a_G = 50–300 mol m^{-3}) and become zero-order at high glucose thermodynamic activities (a_G = 2700–4000 mol m^{-3}), reflecting a change in the MARI at Ti sites from two bound water ligands to adsorbed glucose-derived intermediates. These changes in the identity of the MARI with increasing glucose thermodynamic activity are consistent with shifts in Ti coordination from XANES spectra and are confirmed by spectral identification of intermediate structures using modulation excitation spectroscopy during ATR-IR experiments.

The measurement of first-order and zero-order kinetic behavior enables decoupling the kinetic effects of glucose and water competitive adsorption at active Ti sites from those of kinetically-relevant isomerization transition state stabilization to assess the effects of hydrophilic and hydrophobic reaction environments on adsorption and

catalytic phenomena independently. Glucose isomerization rates were ∼6× higher (368–383 K, per Ti_{LA}) on Ti-Beta-F than on Ti-Beta-OH in both first-order and zero-order kinetic regimes, reflecting both competitive adsorption constants between two waters and one glucose at Ti sites that are essentially insensitive to the polarity of confining reaction environments, and Gibbs free energy differences of kinetically relevant hydride shift transition states relative to their bound glucose precursors that are significantly lower within hydrophobic environments. Lower zero-order activation enthalpies and entropies measured on Ti-Beta-OH than on Ti-Beta-F reflect the effects of higher co-adsorbed water and silanol defect densities that cause modest enthalpic stabilization by hydrogen bonding, but more severe entropic destabilization, of isomerization transition states. Insights from DFT suggest that glucose is solvated within the hydrophobic micropores characteristic of Ti-Beta-F from water molecules entrained upon sugar adsorption and those desorbed from active Ti sites upon formation of ring-opened sugar intermediates; however, the higher water densities present within hydrophilic environments characteristic of Ti-Beta-OH interact with the hydride shift transition state leading to entropic destabilization.

The experimental and theoretical data presented herein provide evidence that silanol defects and associated co-adsorbed water within the microporous reaction pockets of zeolites mediate entropy-enthalpy compromises that influence Gibbs free energies of kinetically-relevant glucose isomerization transition states. Similar entropy-enthalpy compromises have also been observed within metalloenzyme reaction pockets [132, 206]. For example, freeze-trapping X-ray crystallography studies of D-xylose isomerase have shown the migration of water molecules during protein folding and throughout the glucose-fructose isomerization pathway to assist proton shuttling events involved in glucose ring opening and hydride shift steps [132]. Co-adsorbed water is not expelled from the reaction pocket in D-xylose isomerase and continues to interact with bound intermediates, reminiscent of the entrainment of water molecules with glucose upon adsorption within hydrophobic zeolite pores and the influence of

such co-adsorbed water to mediate entropy-enthalpy compromises in determining intermediate and transition state stability.

These findings indicate that aqueous-phase sugar isomerization turnover rates on hydrophobic and hydrophilic zeolites are sensitive to the presence of co-adsorbed solvent molecules within the reaction environment. As a result, the density and location of intrapore silanol defects in zeolites, which depend on their synthetic and post-synthetic treatment history, are structural features that influence catalytic rates because they determine the amount and structure of co-adsorbed solvent molecules, clusters, and extended networks within reaction environments. The *in situ* and *ex situ* IR characterization techniques described here are particularly useful for quantifying active site and hydrophilic defect densities, and for probing water structures within hydrophobic and hydrophilic confining environments under both gas-phase and liquid-phase conditions. More accurate modeling of co-adsorbed solvent densities within low-defect and high-defect porous structures promise to help establish stronger connections between computational and experimental studies. While the polarity of confining environments around binding sites in zeolites have been recognized to influence turnover rates in aqueous-phase catalysis, including several cases for which rate acceleration within hydrophobic confining environments reflect adsorption phenomena, the findings presented herein document an example of rate acceleration that predominantly reflects the influence of hydrophobic confining environments on transition state stability.

4.6 Acknowledgements

M.J.C., J.W.H., J.C.V.V., J.B., and R.G. gratefully acknowledge financial support provided by the Purdue Process Safety and Assurance Center (P2SAC) and the Ralph W. and Grace M. Showalter Research Trust, and Jacklyn Hall and Alyssa LaRue for assistance with NMR studies. E.C.W and J.T.M. acknowledge support by the National Science Foundation under Cooperative Agreement No. EEC-1647722. Use of the Advanced Photon Source was supported by the U.S. Department of Energy, Office of Basic Energy Sciences, under Contract No. DE-AC02-06CH11357. MR-CAT operations are supported by the Department of Energy and the MRCAT member institutions. M.G., S.K., and D.D.H. acknowledge the Extreme Science and Engineering Discovery Environment (XSEDE) through allocation CTS160041; XSEDE is supported by National Science Foundation grant number ACI-1548562. D.W.F. and M.E.W. acknowledge financial support from the National Science Foundation (CBET-15531377), a National Science Foundation Graduate Research Fellowship Program (DGE-1144245), and the TechnipFMC Educational Fund Fellowship at the University of Illinois, as well as Pranjali Priyadarshini for developing the apparatus and analysis for the MES-PSD experiments.

This chapter was reprinted with permission from the Journal of the American Chemical Society 2018, 140 (43), 14244–14266, were it was originally published.

4.7 Supporting Information

4.7.1 Bulk Structural and Lewis Acid Site Characterization of Ti-Beta Zeolites

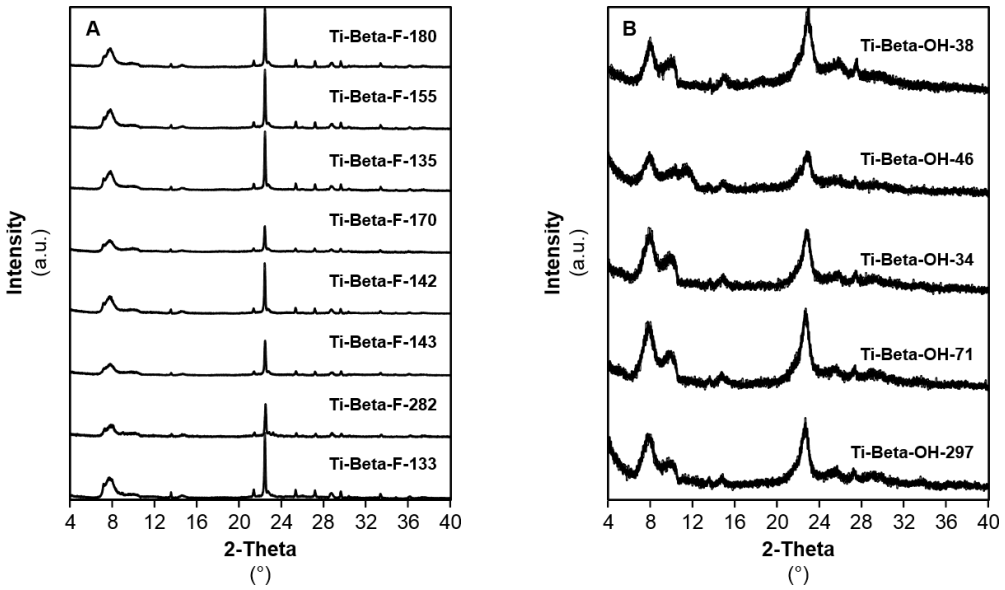

(a) (b)

Figure 4.9: Powder XRD patterns of (a) Ti-Beta-F and (b) Ti-Beta-OH samples studied in this work. Weak signals around 9-10^o reflect an artifact from the sample holders used to collect XRD patterns.

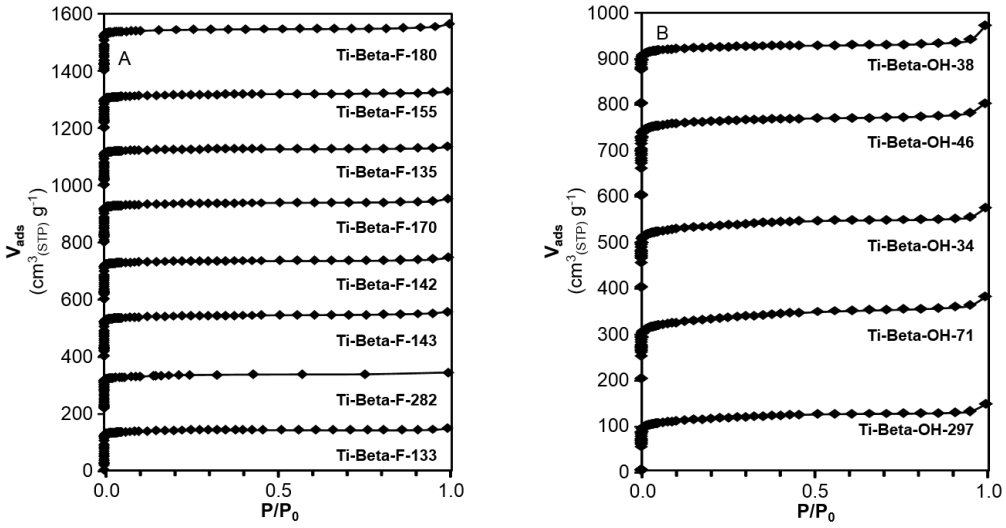

(a) (b)

Figure 4.10: N_2 adsorption isotherms (77 K) of (a) Ti-Beta-F and (b) Ti-Beta-OH samples studied in this work. Isotherms are offset by 200 cm^3 g^{-1} for clarity.

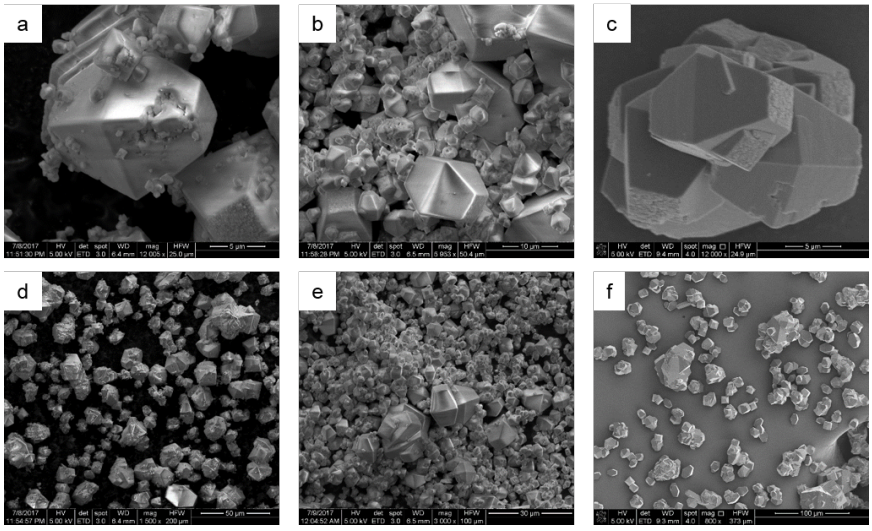

Figure 4.11: SEM images of selected Ti-Beta-F samples: (a) Ti-Beta-F-135, (b) Ti-Beta-F-155, and (c) Ti-Beta-F-180. Bulk sample uniformity is assumed based on images for (d) Ti-Beta-F-135, (e) Ti-Beta-F-155, and (f) Ti-Beta-F-180. Larger crystal aggregates reflect Si-Beta-F seeds used to nucleate the formation of Ti-Beta-F.

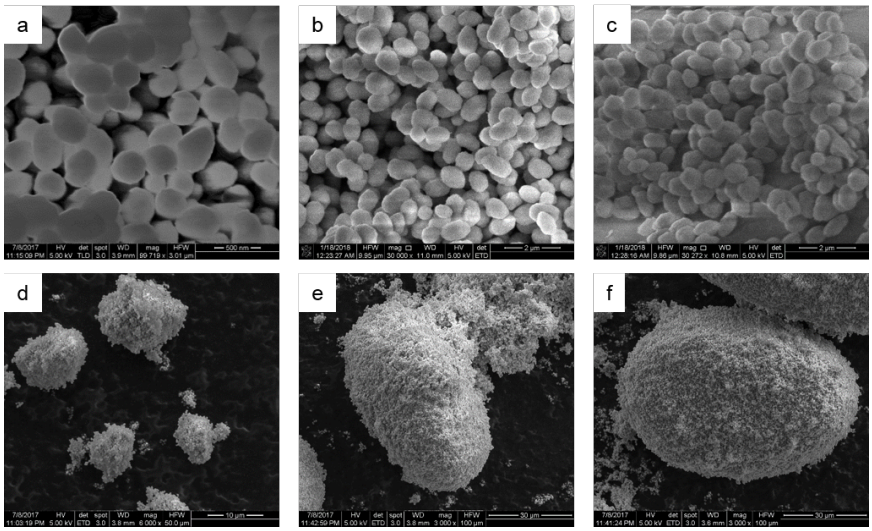

Figure 4.12: SEM images of selected Ti-Beta-OH samples: (a) Ti-Beta-OH-46, (b) Ti-Beta-OH-34, and (c) Ti-Beta-OH-71. Bulk sample uniformity is assumed based on images for (d) Ti-Beta-OH-46, (e) Ti-Beta-OH-34, and (f) Ti-Beta-OH-71 which show larger agglomerates of small crystals.

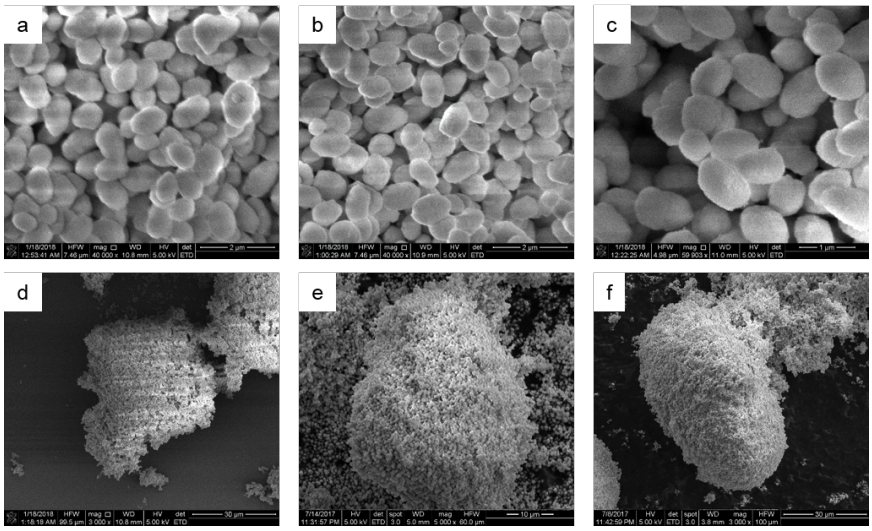

Figure 4.13: SEM images of Ti-Beta-OH-34 at various steps of the synthesis procedure: (a) Al-Beta parent material, (b) after nitric acid treatment for dealumination, and (c) after $TiCl_4$ grafting to form Ti-Beta-OH-34. Bulk sample uniformity is assumed based on images for (d) Al-Beta parent material, (e) after nitric acid treatment for dealumination, and (f) after TiCl4 grafting to form Ti-Beta-OH-34. All show larger agglomerates of small crystals.

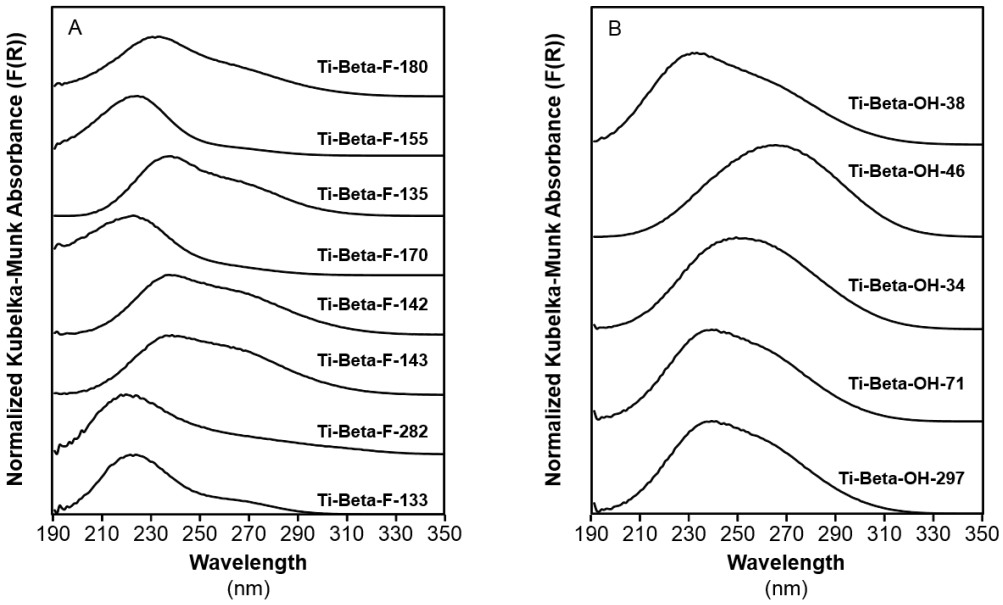

(a) (b)

Figure 4.14: Hydrated UV-Vis spectra of (A) Ti-Beta-F and (B) Ti-Beta-OH samples studied in this work collected prior to dehydration at 523 K.

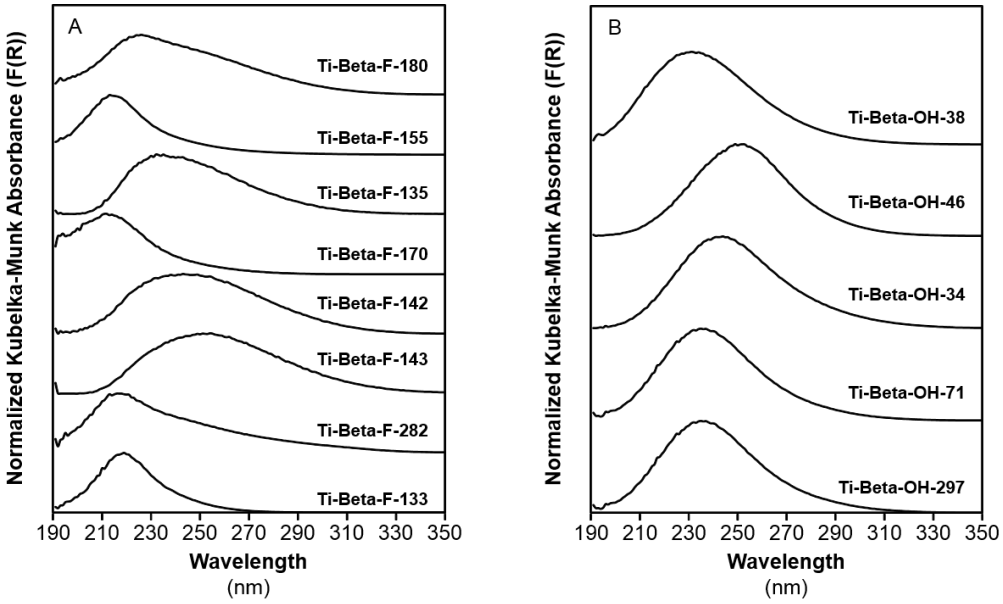

(a) (b)

Figure 4.15: Dehydrated UV-Vis spectra (523 K, 1800 s) of (A) Ti-Beta-F and (B) Ti-Beta-OH samples studied in this work.

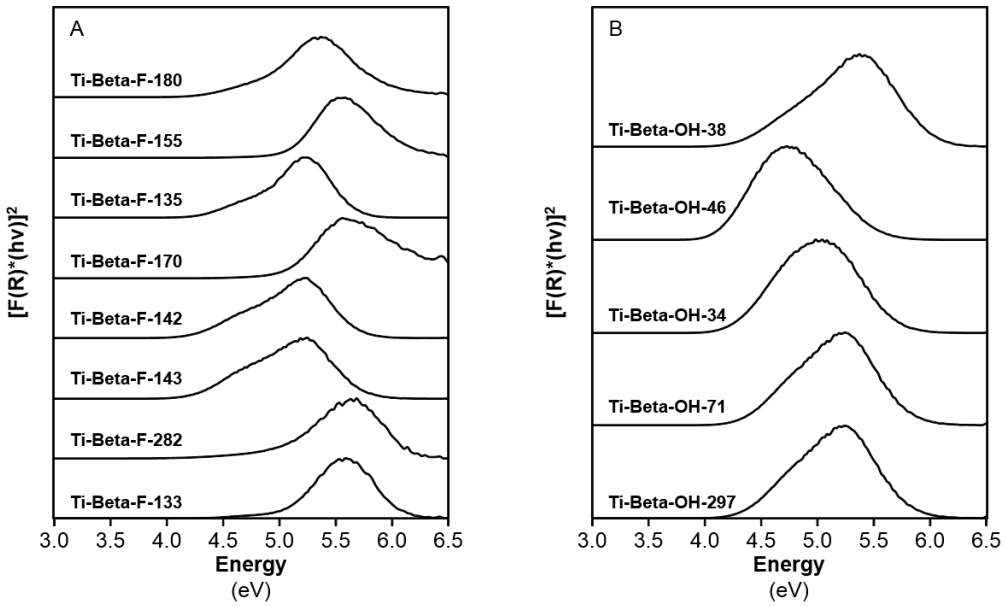

(a) (b)

Figure 4.16: Tauc plots of (A) Ti-Beta-F and (B) Ti-Beta-OH samples studied in this work prior to heating and sample dehydration ("hydrated" samples). Edge energies are summarized in Table 4.5

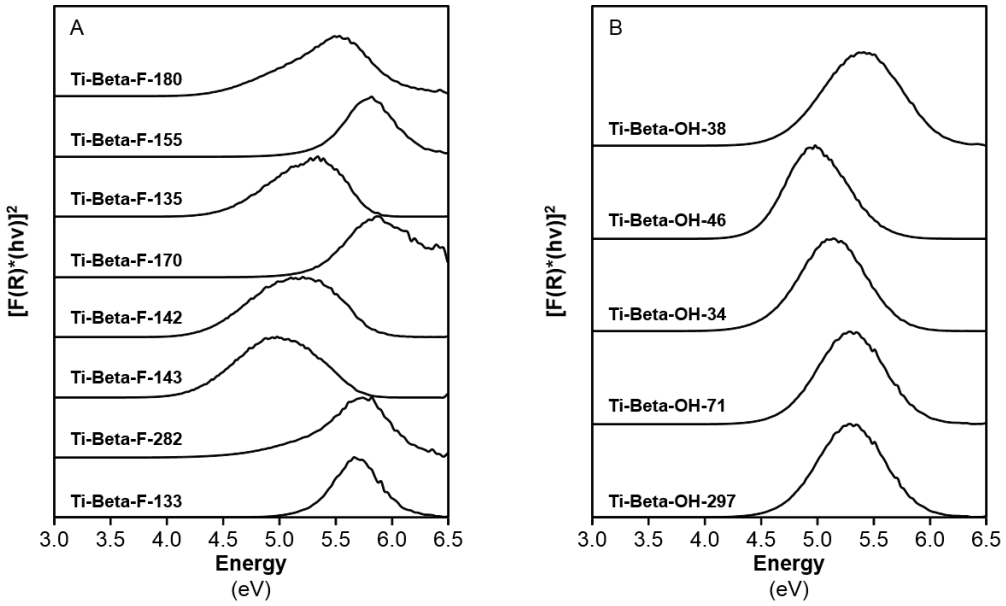

(a) (b)

Figure 4.17: Tauc plots of (A) Ti-Beta-F and (B) Ti-Beta-OH samples studied in this work after treatment in flowing He at 523 K for 1800 s. Edge energies are summarized in Table 4.5

Figures 4.14 and 4.15 above show UV-Vis spectra collected before and after the exposure of Ti-Beta samples to heat treatments (523 K, 1800 s). Band maxima do not shift significantly upon dehydration treatments. Tauc plots corresponding to these spectra are shown in Figures 4.16 and 4.17 and edge energies are x-intercept values measured from extrapolating the first linear regions at low energies of Tauc plots. Dehydration of each sample leads to an increase in the edge energy as shown in Table 4.5. These shifts in edge energy upon dehydration corroborate the changes in Ti coordination number observed in XAS measurements detailed below (Section 4.7.4.3).

Table 4.5: Edge energies of Ti-Beta samples after exposure to ambient conditions, dehydrated, and rehydrated in wet Ar flow. Band maxima correspond to the primary UV-Vis F(R) peaks after dehydration shown in Figure 4.14 above.

Sample	Edge Energies			Band Maximum (nm)
	Ambient (eV)	Dehydrated (eV)	Rehydrated (eV)	
Ti-Beta-F-180	4.4	4.4	4.3	230
Ti-Beta-F-155	5.1	5.3	5.1	216
Ti-Beta-F-135	4.3	4.5	4.3	231
Ti-Beta-F-170	5.1	5.3	5.1	216
Ti-Beta-F-142	4.2	4.3	4.3	246
Ti-Beta-F-143	4.2	4.2	4.2	253
Ti-Beta-F-282	5.0	5.1	5.0	218
Ti-Beta-F-133	5.1	5.3	5.0	219
Ti-Beta-OH-38	4.3	4.7	4.4	234
Ti-Beta-OH-46	4.1	4.4	4.1	253
Ti-Beta-OH-34	4.2	4.5	4.3	246
Ti-Beta-OH-71	4.3	4.7	4.4	235
Ti-Beta-OH-18	4.2	4.5	4.2	235

[a]Dehydration performed in dry flowing He to 523 K and held for 30 min.
[b]Rehydration performed in wet flowing He at ambient temperature.

4.7.1.1 IR Characterization of Titanosilicate Samples using Adsorbed CD3CN

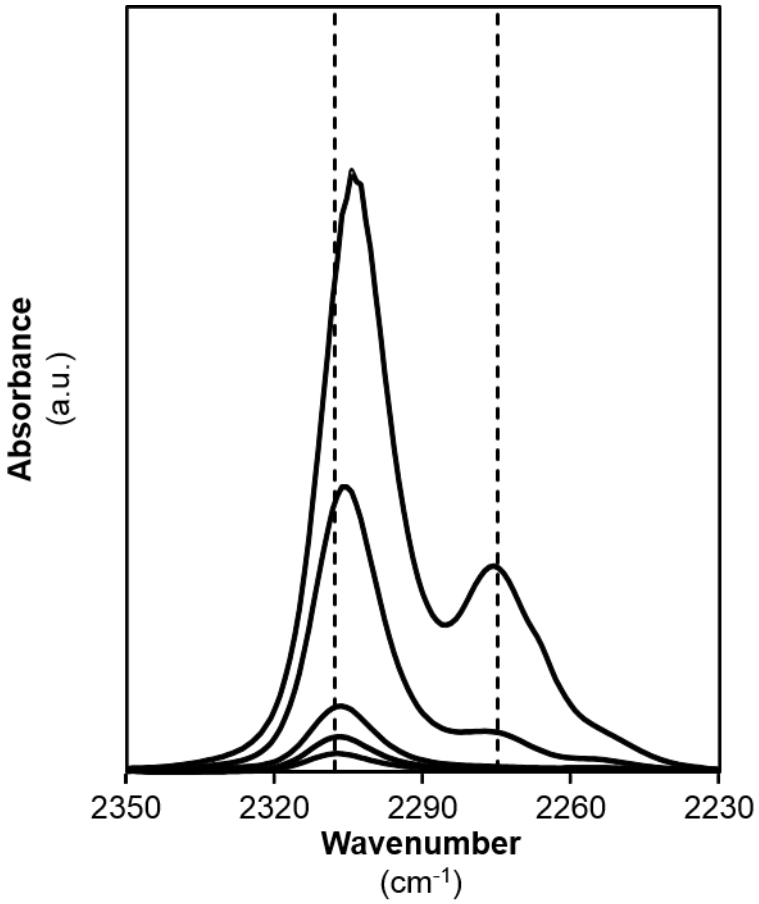

Figure 4.18: IR spectra on Ti-Beta-OH-46 after progressive titration of CD_3CN at 303 K (CD_3CN/Ti = 0.002-2.34). Dashed lines are drawn at 2308 cm^{-1} (CD_3CN bound to Lewis acidic Ti) and 2275 cm^{-1} (CD_3CN hydrogen bound to silanols). Note that the peak center shifts slightly to lower wavenumbers with increasing adsorbed CD_3CN concentrations.

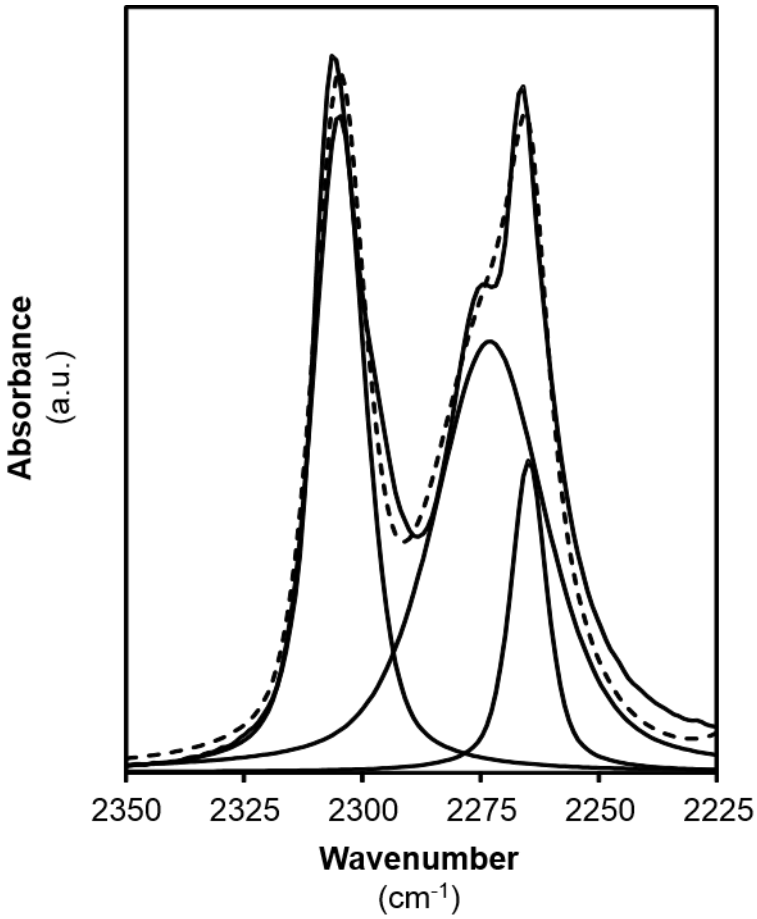

Figure 4.19: CD_3CN-saturated IR spectra for Ti-Beta-F-155. The thickest solid line reflects the measured spectra upon saturation with CD_3CN while thinner lines indicate constitute peaks associated with CD_3CN bound to Lewis acidic Ti sites (2308 cm^{-1}), CD_3CN bound to silanols (2275 cm^{-1}), and gas phase physisorbed CD_3CN (2265 cm^{-1}). The dashed line represents the modeled spectra from combining deconvoluted peaks.

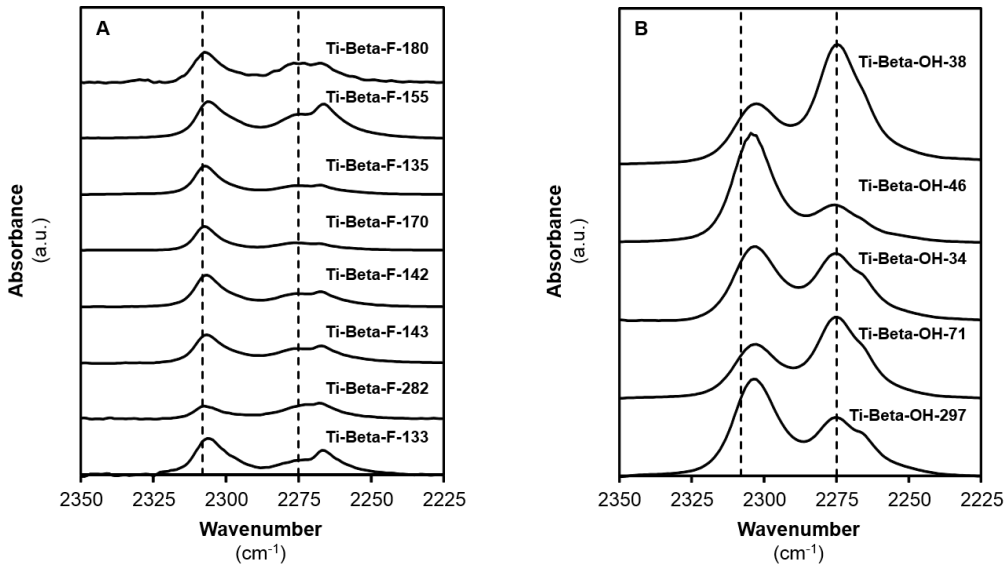

(a) (b)

Figure 4.20: IR spectra collected on (A) CD_3CN-saturated Ti-Beta-F and (B) CD_3CN-saturated Ti-Beta-OH samples studied in this work. Dashed lines are drawn at 2308 cm^{-1} (CD_3CN bound to Lewis acidic Ti) and 2275 cm^{-1} (CD_3CN bound to silanols).

4.7.1.2 IR Characterization of Titanosilicate Samples using Adsorbed Pyridine

Pyridine (Alfa Aesar, >99%) adsorption on self-supporting Ti-Beta wafers was performed following similar procedures to those reported for CD_3CN titration at 423 K under static vacuum conditions including freeze-pump-thaw cycles, pyridine dosing and equilibration, dynamic vacuum exposure to remove residual gaseous titrant upon saturation, and baseline correction, normalization, and subtraction of parent spectra, resulting in IR spectra similar to those shown in Figure 4.21A. Figure 4.21A shows pyridine adsorption spectra with incremental pyridine doses on Ti-Beta-F-135. IR spectra on pyridine saturated Ti-Beta-F-155 is shown in Figure 4.21B which can be deconvoluted to isolate the peak centered at 1605 cm^{-1}.

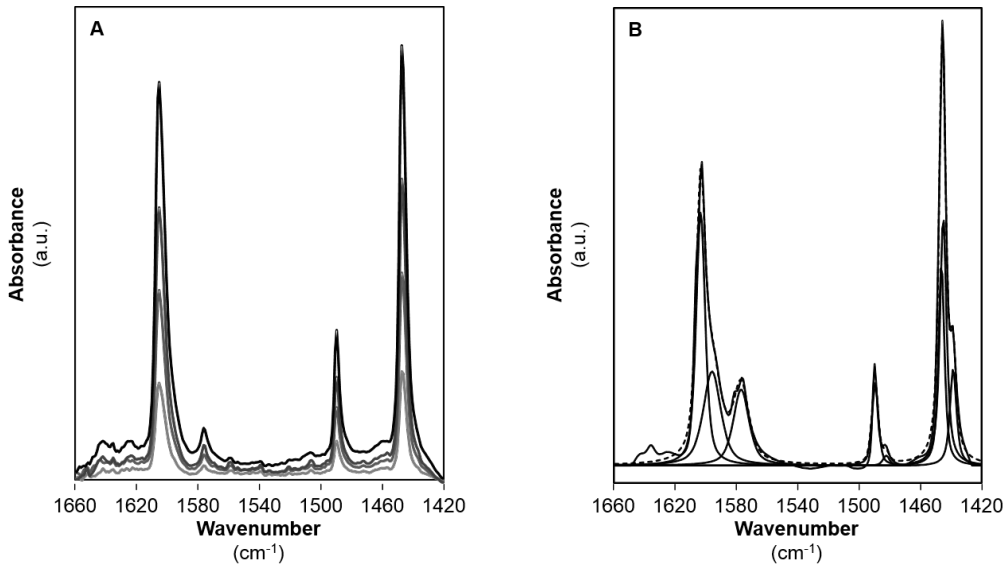

(a) (b)

Figure 4.21: IR spectra measured (a) after the first four doses of pyridine on Ti-Beta-F-135 (0.015-0.058 mol pyridine (mol Ti)$^{-1}$ and (b) after saturation of Ti-Beta-F-135 with pyridine (1.05 mol pyridine (mol Ti)$^{-1}$). The components included in the deconvolution are shown (thin solid lines) with the resulting fit envelope (dotted line) and the measured spectra (thick solid line).

Marginal increases in integrated area of the feature centered at 1605 cm^{-1} correlate linearly with marginal increases in adsorbed pyridine. The linear increase can

be quantified on four distinct Ti-Beta samples which show similar molar extinction coefficients for pyridine adsorption from identical analyses to those of CD_3CN molar extinction coefficient determination in the main text, as seen in Figure 4.22A and Table 4.6. Averaging the linear increases in 1605 cm^{-1} peak area at low pyridine doses (Figure 4.20B) yields a single E(1605 cm^{-1}) value of 1.16 $\pm$ 0.23 cm μ mol^{-1} which can then be used to quantify total Lewis acid density from IR spectra after pyridine saturation on each sample (Table 4.1, Main Text).

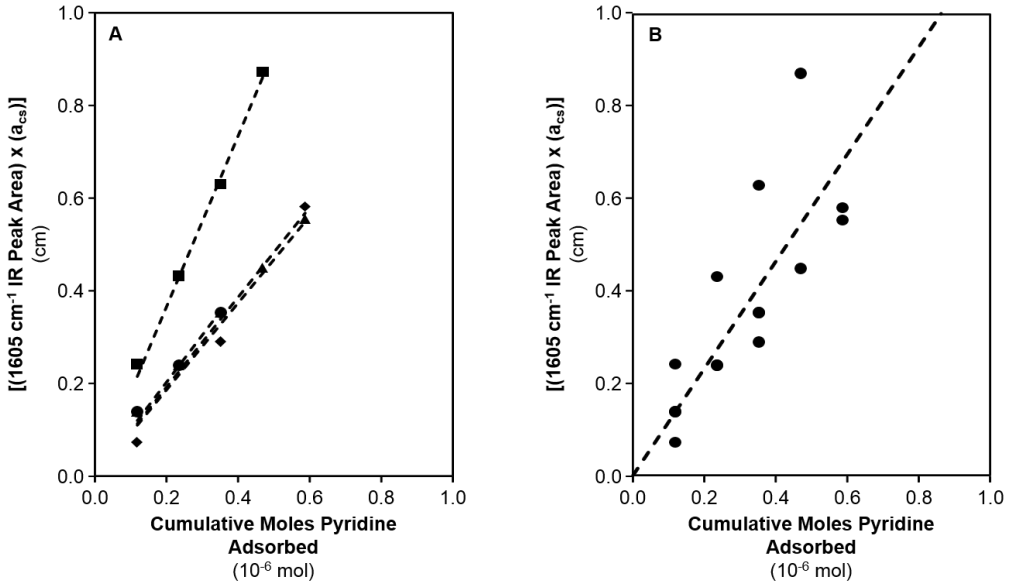

(a) (b)

Figure 4.22: (A) Integrated peak area normalized by wafer cross-sectional areas for the IR feature centered at 1605 cm^{-1} as a function of moles pyridine adsorbed onto Ti-Beta-F-155 (diamonds), Ti-Beta-F-135 (circles), Ti-Beta-F-170 (triangles), and Ti-Beta-OH-46 (squares). Dashed lines indicate best fit lines through the origin for each sample with slopes equal to integrated molar extinction coefficients as listed in Table 4.7 (B) Integrated peak area normalized by wafer cross-sectional areas for the IR feature centered at 1605 cm^{-1} as a function of moles pyridine adsorbed onto Ti-Beta-F-155, Ti-Beta-F-135, Ti-Beta-F-170, and Ti-Beta-OH-46 as a single data set. The dashed line indicates the best fit line through the origin for the combined data set with the slope equal to the average integrated molar extinction coefficient.

Figure 4.23 shows Lewis acid site densities determined from pyridine-saturation infrared experiments plotted against Lewis acid site densities determined from CD_3CN-

Table 4.6: $E(1605\ \mathrm{cm}^{-1})$ values determined for four separate Ti-Beta samples by sequentially dosing pyridine at 423 K.

Sample	$E(1605\ \mathrm{cm}^{-1}$ (cm $\mu\mathrm{mol}^{-1})$
Ti-Beta-F-135	1.84
Ti-Beta-F-170	0.97
Ti-Beta-OH-46	0.93
Ti-Beta-F-155	1.02

saturation infrared experiments from Table 4.2. The two sets of Lewis acid site concentrations linearly correlate with one another, suggesting that they reflect similar site densities.

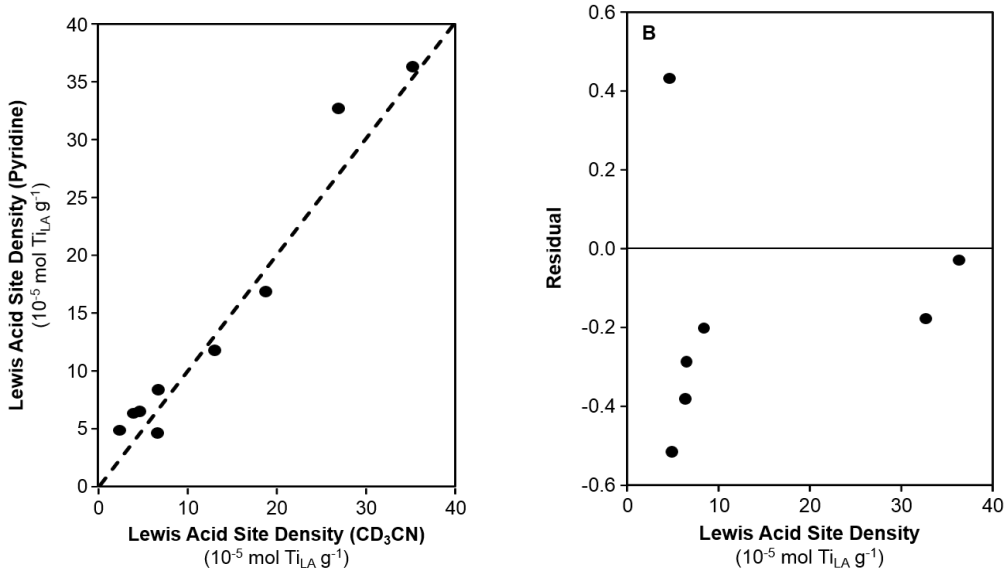

(a) (b)

Figure 4.23: Lewis acid site densities determined from pyridine-saturation IR experiments plotted against Lewis acid site densities determined from CD_3CN-saturation IR experiments. The dashed line is a parity line drawn to guide the eye.

4.7.1.3 Assessing Extracrystalline Surface Areas and Normalized Silanol Densities on Titanosilicate Samples

Ti-Beta-F crystals exhibit square bipyramidal crystal morphology (Figure 4.11). Characteristic lengths were measured along the plane corresponding to the symmetric crystal center and along the terminal planes and the characteristic height was measured as the distance between those two planes. Characteristic length and height measurements were obtained from SEM images of more than 25 individual crystals selected randomly from multiple locations. Surface area and volume measurements were obtained by treating crystals as square frustums sharing a common base along a symmetrical middle plane.

For Ti-Beta-OH samples, the size of the final material is dependent on the size of the Al-Beta parent material which is maintained after dealumination and grafting as shown in Figure 4.13. Ti-Beta-OH crystals are prolate spheres agglomerated together into large clusters (Figure 4.12). Characteristic lengths were determined in both the r and z directions from over 25 individual crystals and averaged to quantify the average surface area and volume per particle.

For materials of consistent zeolite topology, the surface-area-to-volume ratio is an adequate proxy for external surface areas. Surface-area-to-volume ratios per particle were normalized to Ti-Beta-F-155, a representative primary Ti-Beta-F sample studied in this work, assuming a consistent particle density between samples. Table 4.7 lists normalized surface-area-to-volume ratios along with normalized silanol densities quantified using IR spectra from CD3CN titration experiments. A direct correlation between silanol density and external crystal surface area would be expected if all silanols are located only on external crystal surface areas. Silanol densities do not directly scale with surface-area-to-volume ratios, suggesting increased silanol densities present within the microporous environments of Ti-Beta-OH samples.

Table 4.7: Surface-area-to-volume (SA/V) ratios and silanol defect densities for selected Ti-Beta-F and Ti-Beta-OH samples normalized to Ti-Beta-F-155.

Sample	Normalized SA/V	Normalized Silanol Density
Ti-Beta-F-135	0.5	0.45
Ti-Beta-F-155	1.0	1.0
Ti-Beta-F-180	0.5	0.86
Ti-Beta-OH-46	18	3.6
Ti-Beta-OH-34	10	3.5
Ti-Beta-OH-71	10	4.1

4.7.2 Characterization of the Hydrophobic Properties of Ti-Beta Zeolites

4.7.2.1 Vapor-Phase Adsorption Isotherms on Titanosilicate Samples

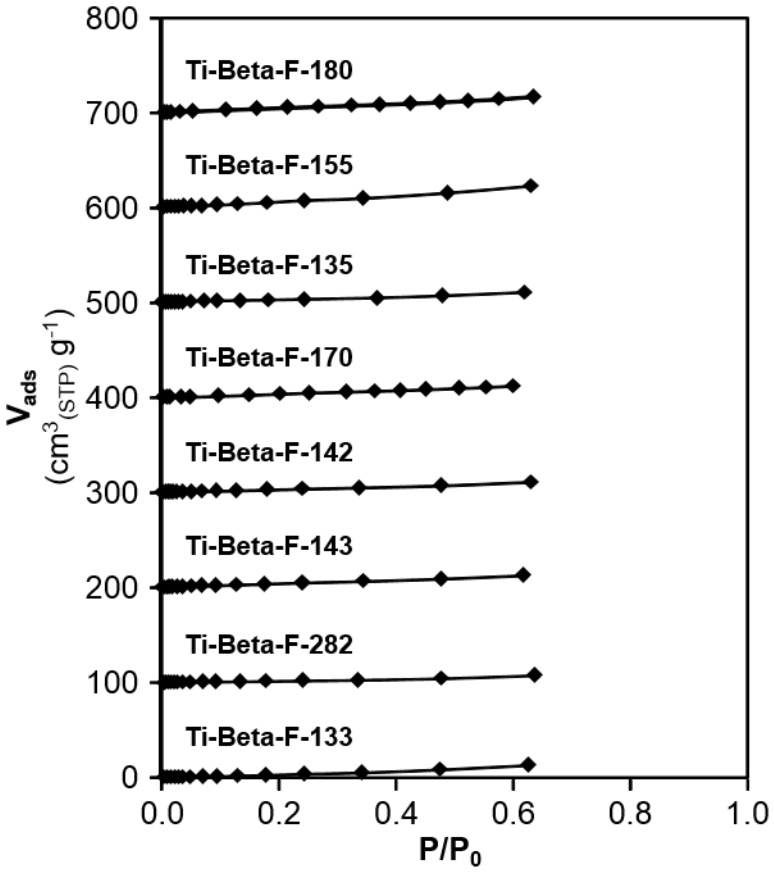

Figure 4.24: Vapor-phase water adsorption isotherms at 293 K on Ti-Beta-F samples studied in this work. Isotherms are offset by 100 cm^3 g^{-1} for clarity.

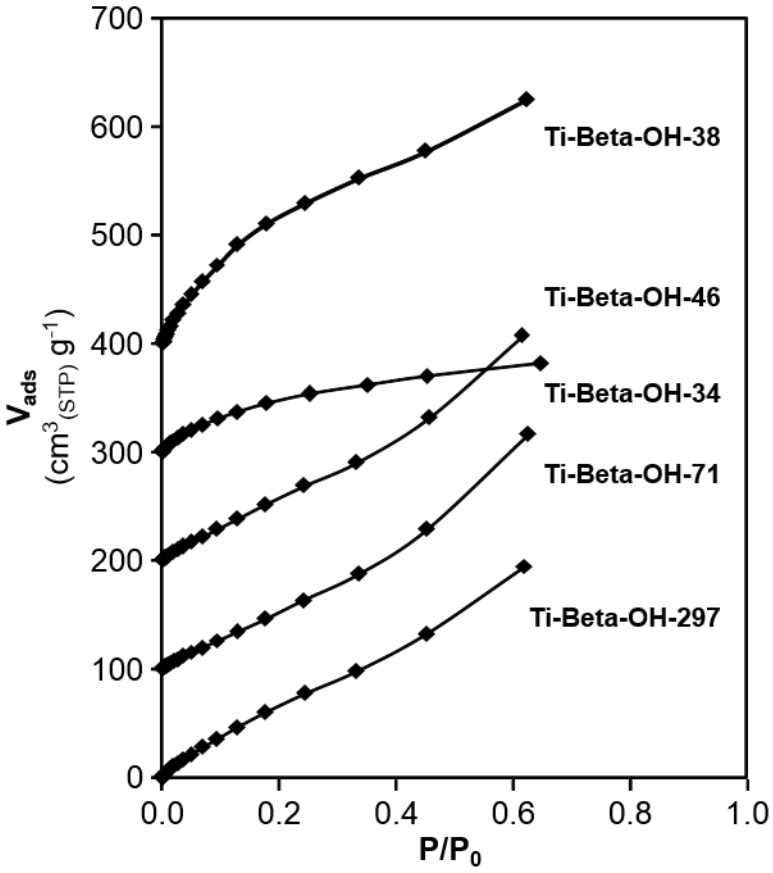

Figure 4.25: Vapor-phase water adsorption isotherms at 293 K on Ti-Beta-OH samples studied in this work. Isotherms are offset by 100 cm^3 g^{-1} for clarity.

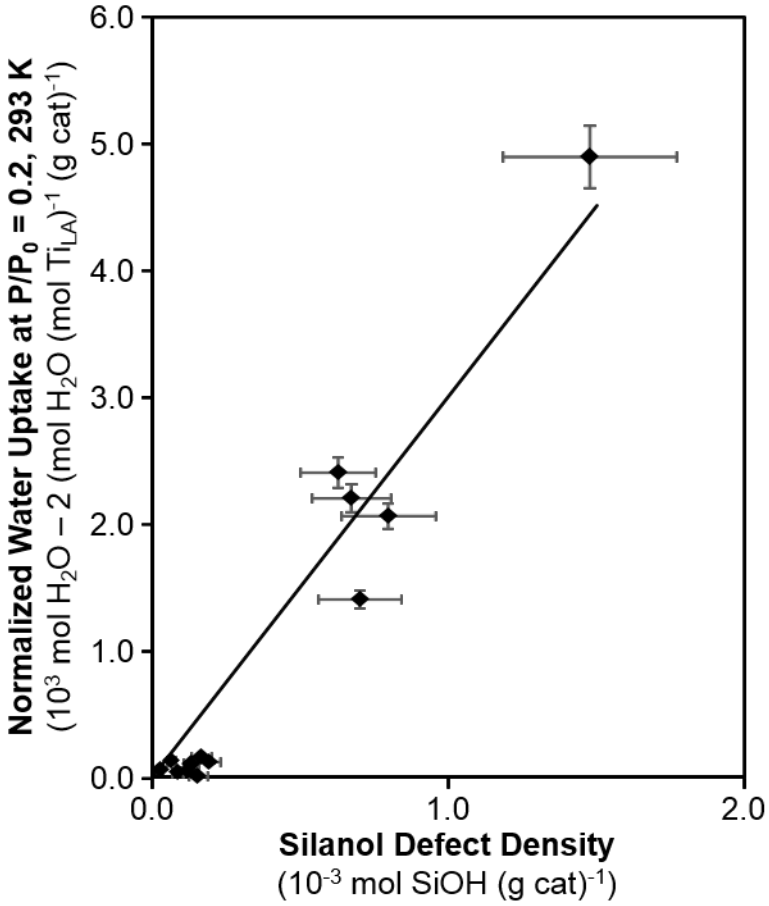

Figure 4.26: Water uptakes at $P/P_0 = 0.2$ (373 K) after subtracting two moles of water molecules per mol Ti Lewis acid site (quantified by CD_3CN IR) as a function of the bulk silanol defect density (quantified by CD_3CN IR). The solid line is a best fit line drawn through the origin to guide the eye.

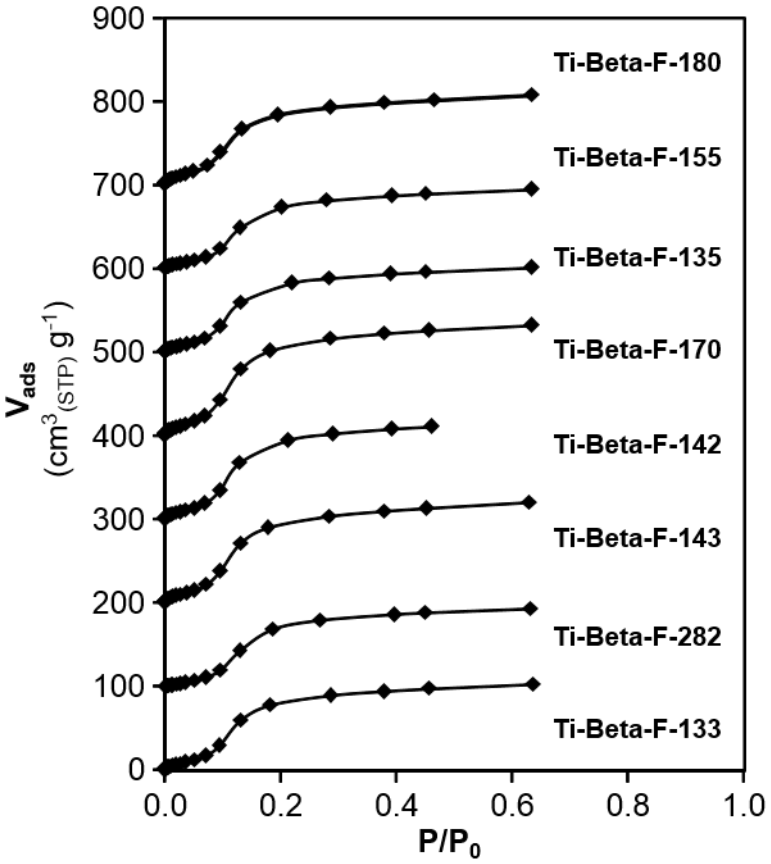

Figure 4.27: Vapor-phase methanol adsorption isotherms at 293 K on Ti-Beta-F samples studied in this work. Isotherms are offset by 100 cm^3 g^{-1} for clarity.

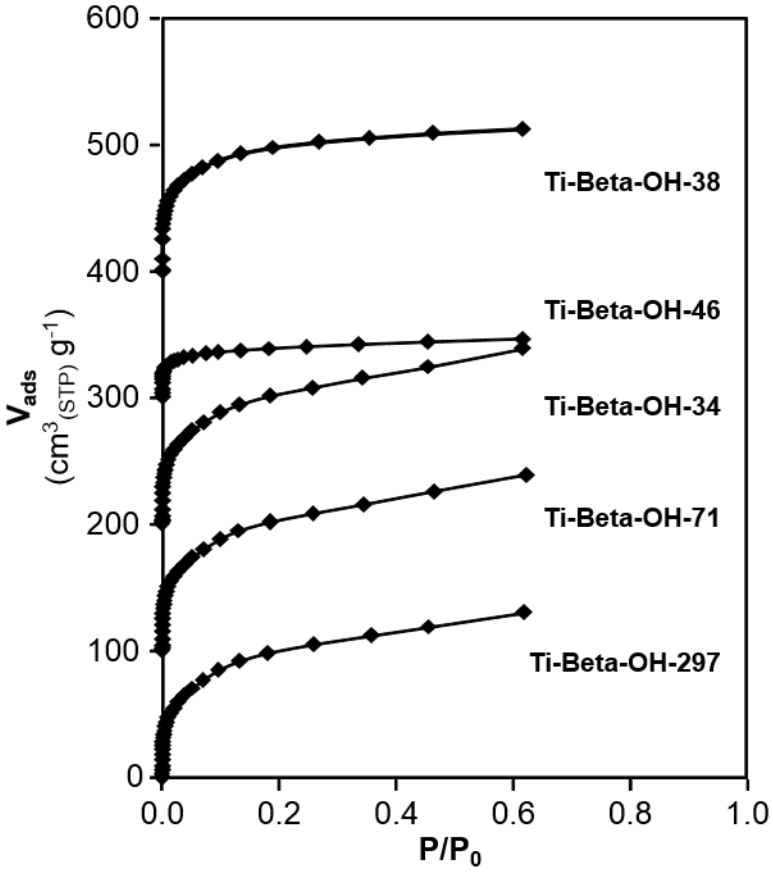

Figure 4.28: Vapor-phase methanol adsorption isotherms at 293 K on Ti-Beta-OH samples studied in this work. Isotherms are offset by 100 cm^3 g^{-1} for clarity.

4.7.2.2 Spectroscopic Characterization of Intraporous Water Structures using Transmission IR

IR spectra of Ti-Beta-F-155 and Ti-Beta-OH-46 with increasing amounts of gas-phase water exposure are shown in Figures 4.29 and 4.31 that correspond to Figures 4.2A and 4.2B in the main text. Peaks centered between 2700-3800 cm^{-1} and 1550-1750 cm^{-1} increase systematically with increasing water partial pressure which can be equated to an adsorbed water density using the adsorption isotherms given in Figure 4.30.

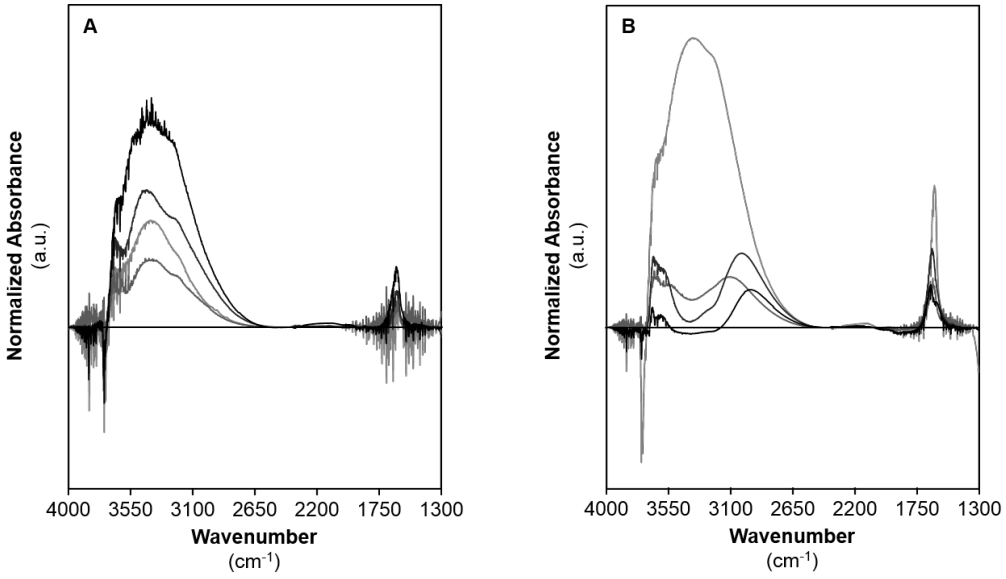

(a) (b)

Figure 4.29: Differential, subtracted, normalized, cell-corrected IR spectra of adsorbed H2O at P/P_0=0.1, 0.2, 0.5, and 0.75 (lightest to darkest, 298 K) on (A) Ti-Beta-F-155 and (B) Ti-Beta-OH-46. Differential spectra are spectral changes between a given P/P_0 value and the previous relative pressure spectra, isolating changes in spectral features due only to increasing water partial pressure.

Figure 4.31 show IR subtraction spectra focusing on the OH stretching region where peaks corresponding to perturbed silanols are observed at 3735 and 3745 cm^{-1}. Spectra collected on Ti-Beta-F-155 observes a continuous increase in perturbed silanol

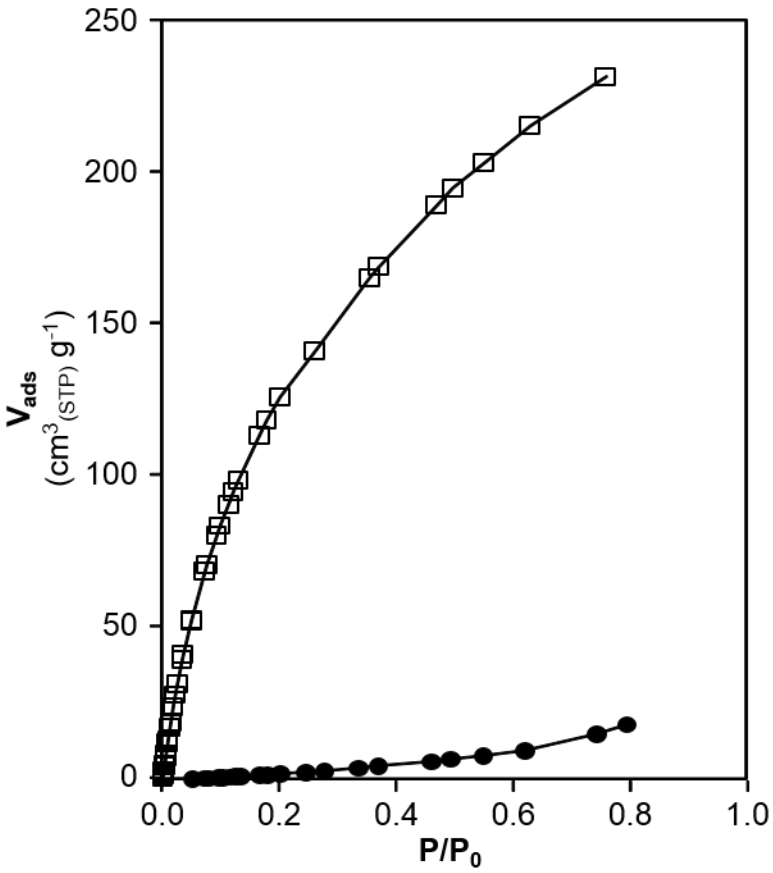

Figure 4.30: Vapor-phase water adsorption isotherms at 298 K on Ti-Beta-F-155 (closed circles) and Ti-Beta-OH-46 (open squares)

peak area while perturbed silanol peaks observed on Ti-Beta-OH-46 are saturated at lower water partial pressures.

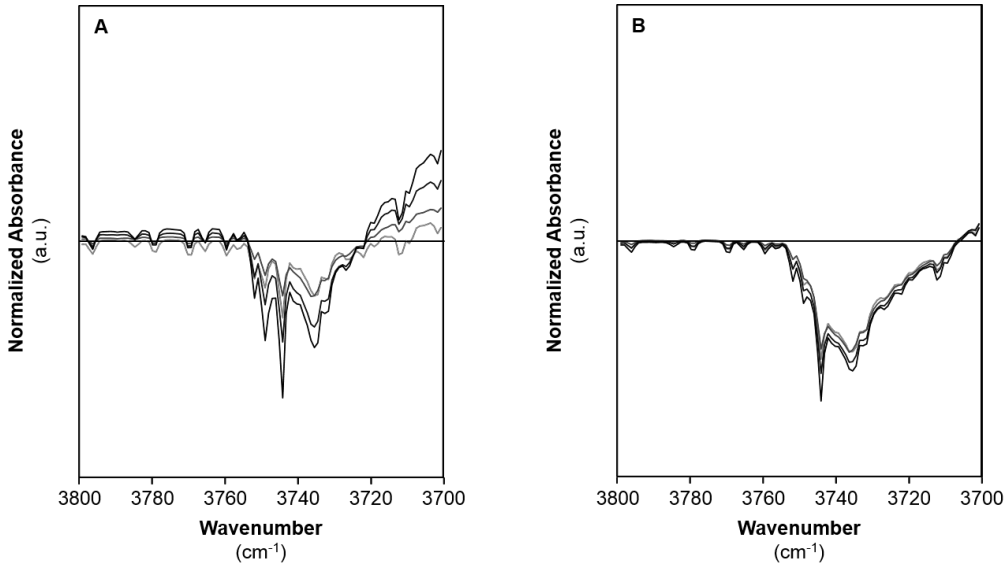

(a) (b)

Figure 4.31: Subtracted IR spectra of the OH stretching region as a function of increased relative pressure of water on (A) Ti-Beta-F-155 and (B) Ti-Beta-OH-46.

4.7.3 Glucose Isomerization Mechanisms and Kinetic Measurements

4.7.3.1 Identification of Fructose and Sorbose Formed via Glucose Isomerization on Ti-Beta Zeolites

Isomerization product identification was performed using solution phase ^{13}C NMR as seen in Figure 4.30 on representative Ti-Beta-F and Ti-Beta-OH samples. Glucose, fructose, and sorbose standards are shown for comparison. The resonances at δ = 61.6 and 67.3 ppm are peaks indicative of sorbose and fructose respectively and used to confirm isomerization products formed on all samples.

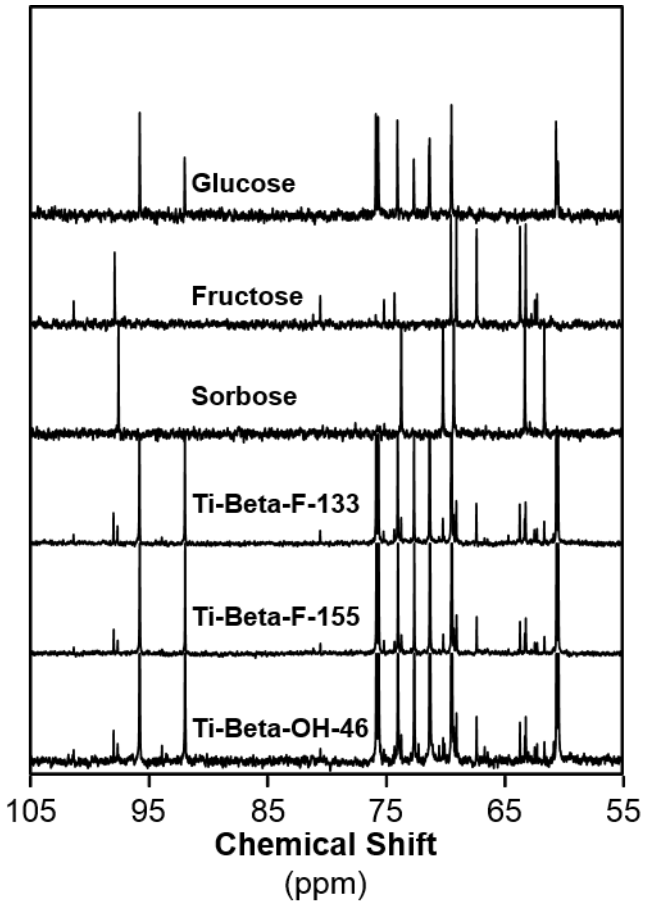

Figure 4.32: Solution phase ^{13}C NMR of monosaccharide solutions after contacting 5 wt% glucose solutions with Ti-Beta-F-133, Ti-Beta-F-155, and Ti-Beta-OH-46. Glucose, fructose and sorbose standards are given for direct comparison.

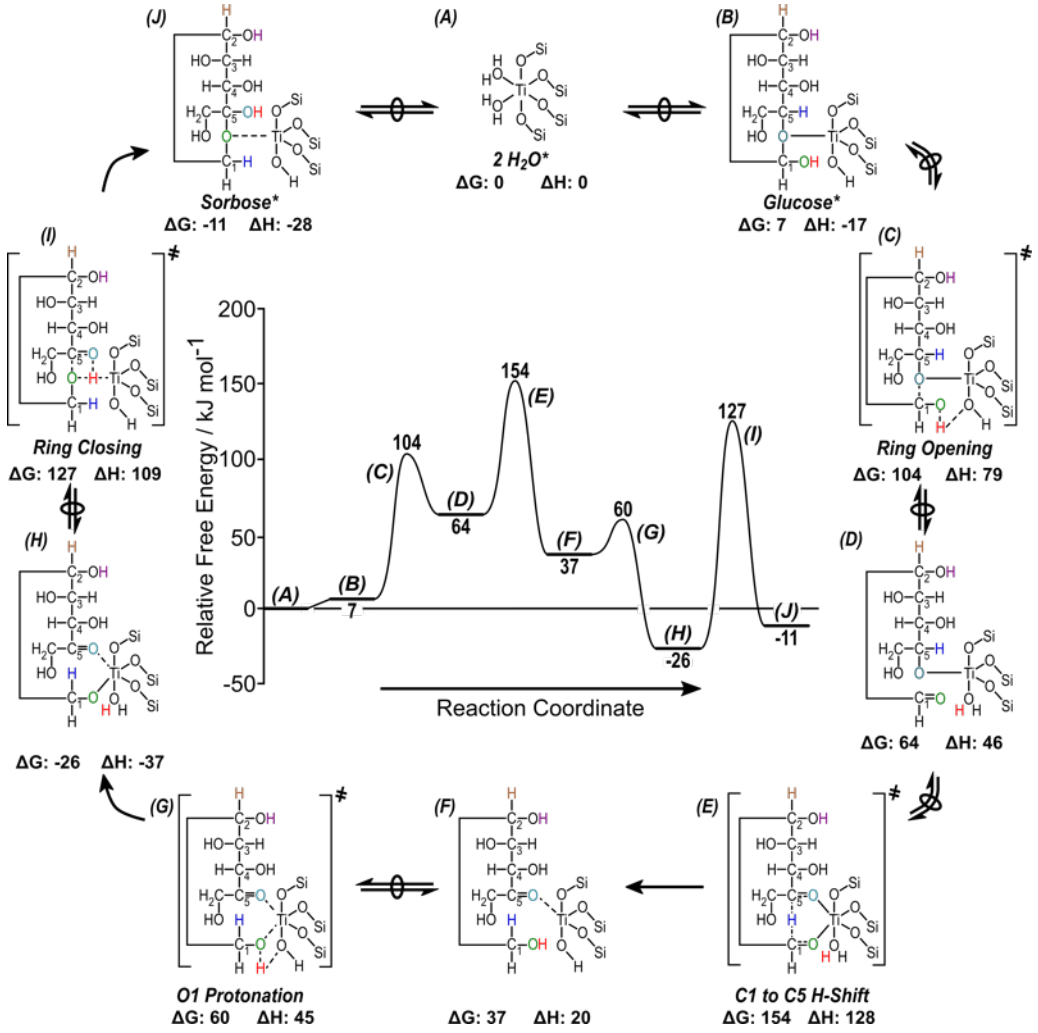

Figure 4.33: Free energy (373 K, 1 bar) reaction coordinate diagram for the formation of sorbose from glucose on closed-form Ti Lewis acid sites. Reaction arrows with overlaid circles indicate quasi-equilibrated events or the formation of transition states from relevant precursors. Relative enthalpies are given near inset images.

4.7.3.2 H/D KIE Derivation as a Function of Temperature for a General Vibrational Frequency using Zero Point Energies

The H/D KIE measures the apparent rate constant ratio resulting from isotopically labeling an atom located in a kinetically relevant bond which is the alpha C-H bond in the case of Lewis acid mediated glucose-to-fructose isomerization. The apparent isomerization rate constant in the first-order regime can be written as a series of coupled rate constants which reflects free energy differences between the hydride shift transition state with two free water molecules and the water dimer surface intermediate with a single free glucose molecule in solution as follows:

$$k_{first_i} = \frac{K_1 k_2}{K_4 K_5} = \frac{k_B T}{h} e^{-((\Delta G^o_{\ddagger} + 2\Delta G^o_W) - (\Delta G^o_{G,i} + \Delta G^o_{2W*}))/RT} \tag{4.17}$$

Taking the ratio of rate constants, defined as the KIE, for glucose-H2 and glucose-D2 and canceling constants yields the following equation, which relates free energy differences between reaction rates with and without isotopic labeling:

$$KIE = \frac{k_{first_H 2}}{k_{first_D 2}} = \frac{e^{-((\Delta G^o_{\ddagger} + 2\Delta G^o_W) - (\Delta G^o_{G,H2} + 2\Delta G^o_{2W*}))/RT}}{e^{-((\Delta G^o_{\ddagger} + 2\Delta G^o_W) - (\Delta G^o_{G,D2} + 2\Delta G^o_{2W*}))/RT}} \tag{4.18}$$

Relevant free energy terms can then be separated between water-dependent and water-independent terms, where water-dependent terms are not affected by isotopically labeling the glucose reactant molecule and thus are irrelevant for observed KIEs:

$$KIE = \frac{e^{-(2\Delta G^o_W + \Delta G^o_{2W*})/RT} e^{-(2\Delta G^o_{\ddagger,H2} - \Delta G^o_{G,H2})/RT}}{e^{-(2\Delta G^o_W + \Delta G^o_{2W*})/RT} e^{-(2\Delta G^o_{\ddagger,D2} - \Delta G^o_{G,D2})/RT}} = \frac{e^{-(2\Delta G^o_{\ddagger,H2} - \Delta G^o_{G,H2})/RT}}{e^{-(2\Delta G^o_{\ddagger,D2} - \Delta G^o_{G,D2})/RT}} \tag{4.19}$$

Similarly, the transition state free energy is not affected by the isotopic label and the associated shift in reduced mass. Therefore, the KIE reflects the free energy difference between the two ground state energies of glucose-D2 and glucose-H2, respectively, which result from differences in zero point energies between C-H and C-D bonds:

$$KIE = e^{(\Delta G^o_{G,H2} - \Delta G^o_{G,D2})/RT} = e^{(ZPE_{H2} - ZPE_{D2})/k_B T} \tag{4.20}$$

Here, ZPE_i is the zero point energy for C-H and C-D bonds and k_B is the Boltzmann constant (1.3806*10^{-23} m^2 kg s^{-2} K^{-1}). Substituting in the definition of the ZPE and accounting for the vibrational frequency shift upon isotopic labeling (ν_D=0.74ν_H), the following is derived to define the following generalized KIE equation:

$$KIE = e^{(\frac{1}{2}ch\nu_H - \frac{1}{2}ch\nu_D} = e^{(0.13ch\nu_H)/k_B T} \tag{4.21}$$

where c is the speed of light in a vacuum (2.998*10^8 m s^{-1}) and h is the Planck constant (6.626*10^{-34} m^2 kg s^{-1}). This equation yields a KIE value of 2.1 at 373 K for a C-H bond scissoring vibration (ν_H=1500 cm^{-1}) and 4.5 at 373 K for a C-H stretching vibration (3000 cm^{-1}) corresponding to the kinetically relevant vibrational mode for the Lewis acid and Lewis base catalyzed transition state, respectively. In the case of severe internal mass transfer limitations, the apparent rate constant ratio is equal to the square root of the intrinsic ratio, yielding lower observed KIE values. In this case, the apparent KIE value for a C-H bond scissoring vibration (intrinsic KIE of 2.1) at 373 K would equal a value of 1.4.

$$(\frac{k_{first_{H2}}}{k_{first_{D2}}})_{app} = \sqrt{\frac{k_{first_{H2}}}{k_{first_{D2}}}} \tag{4.22}$$

The effect of severe internal mass transfer limitations on observed KIEs is independent of the kinetic regime and holds with measured KIE values (2.1-2.3) in both first-order and zero-order regimes.

The apparent lack of mass transfer reflected by experimentally measured KIE values of 2.1 is supported by consistent glucose isomerization rates for fructose and sorbose formation normalized per total Ti content (Figure 4.4, main text) and as a function of Lewis acidic Ti content (Figure 4.34).

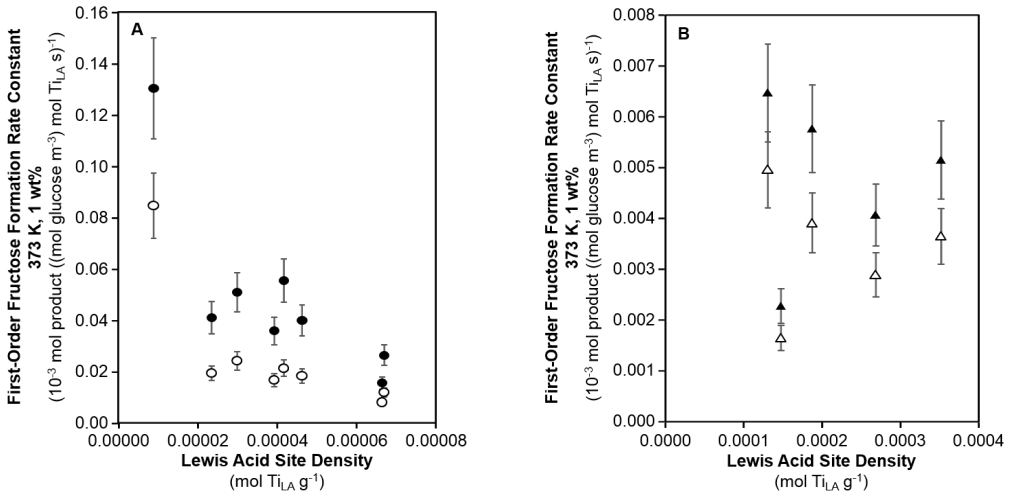

(a) (b)

Figure 4.34: First-order fructose (closed circles, closed triangles) and sorbose (open circles, open triangles) formation rate constants (373 K, pH 4) normalized per total Lewis acidic Ti content (measured from CD_3CN IR) as a function of Lewis acidic Ti density for (A) Ti-Beta-F and (B) Ti-Beta-OH samples.

4.7.3.3 Bulk Solution Glucose and Osmotic Activity Coefficient Quantification

Standard state glucose activity coefficients (298 K), osmotic coefficients, and excess partial molar enthalpies were linearly interpolated from literature values as a function of glucose mole fraction where activity coefficients vary from unity to 1.329 (298 K) at high glucose concentrations approaching the aqueous room temperature solubility of glucose [194]. Interpolated activity coefficients were then adjusted to reaction temperature using the following thermodynamic relationship [195]:

$$\frac{-\overline{H}_i^E}{RT^2} = \frac{\delta}{\delta T} ln\gamma_i \tag{4.23}$$

Here, $\overline{H}_i^E$ is the excess partial molar enthalpy of species i in solution, R is the universal gas constant, T is absolute temperature in K, and $gamma_i$ is the activity coefficient of species i in solution which is a function of temperature and the concentration of species i. Excess partial molar enthalpies are assumed to be independent of temperature across the studied temperature range. Eq. 4.23 can be integrated into:

$$\gamma_i = \gamma_i^o e^{\frac{\overline{H}_i^E}{R}(\frac{1}{T} - \frac{1}{T^o}} \tag{4.24}$$

Here, γ_i and γ_i^o are the activity coefficients of species i at the reaction temperature and standard temperature (298 K) respectively, and T and T^o are the reaction and standard state absolute temperatures respectively. Glucose and osmotic activities at reaction conditions were then calculated from the initial concentrations of glucose and water multiplied by the temperature-adjusted osmotic or activity coefficient as appropriate. We note that all kinetic trends hold constant independent of whether concentrations or thermodynamic activities (using activity coefficients quantified at either 298 K or reaction temperatures, see Figure 4.35 and Section 4.7.5.2 below) are used for glucose and water species. In the main text, temperature-adjusted activities are used as an accurate descriptor in the rate equation models.

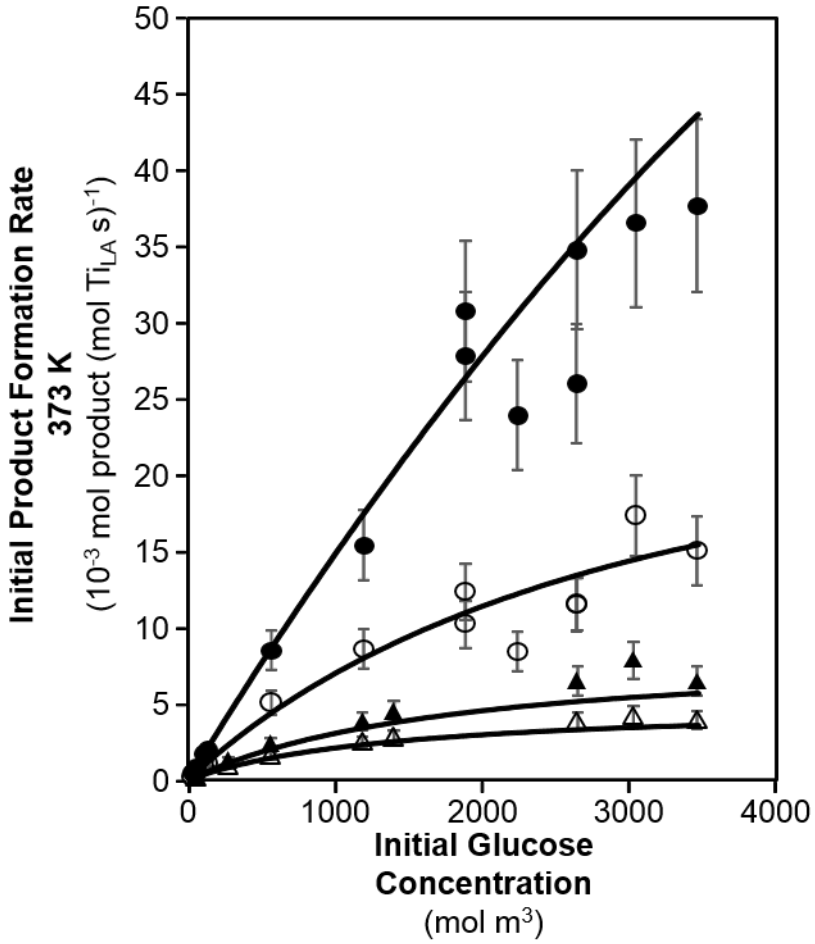

Figure 4.35: Dependence of initial glucose isomerization rates (373 K, pH 4) for fructose (filled) and sorbose (open) formation on Ti-Beta-F-155 (closed circles, open circles) and Ti-Beta-OH-46 (closed triangles, open triangles) as a function of initial glucose concentration (1-50 wt.%). Solid lines represent fits of the experimental data to the rate equation (Eq. 4.9 of the main text) using activation enthalpies and entropies given in Table 4.4.

4.7.4 Characterization and Kinetic Effects of Bound Surface Species in First-Order and Zero-Order Regimes

4.7.4.1 ATR-IR and Modulation Excitation Spectroscopy Quantification for the Identification of Bound Reactive Intermediates using MCR-ALS Data Analysis Techniques

The time-resolved FTIR spectra for each Beta material were collected and processed mathematically prior to analyzing spectral features of individual species. The time-domain raw spectra were first averaged into a single period using:

$$A_{average}(t) = \frac{\tau}{\tau_{total}} \Sigma_{i=0}^{\frac{\tau_{total}}{\tau}} A(t + iT) \tag{4.25}$$

Here A(t+iT) is the absorbance at each time point, $A_{average}$(t) is the absorbance after averaging into a single period, T is the time period of stimulation, and T_{total} is the total time for which the experiment was run; therefore, $\frac{\tau_{total}}{\tau}$ represents the total number of periods measured during a MES experiment. The averaged spectra were then subjected to phase sensitive detection (PSD) using:

$$A_k(\varphi_k^{PSD}) = \frac{2}{T} \int_0^T A_{average}(\vartheta, t) sin(k\omega t + \varphi_k^{PSD}) dt \tag{4.26}$$

Eq. 4.26 was transformed into a Fourier series by Fourier's theorem for a periodic function gives:

$$A(\vartheta, t) = \Sigma_{i=1}^{N} A_{i,o} + \Sigma_{i=1}^{N} \Sigma_{k=1}^{\infty} (A_{i,k}^{0^o}(\vartheta) cos(k\omega t) + A_{i,k}^{90^o}(\vartheta) sin(k\omega t)) \tag{4.27}$$

where $A_{i,o}$ is the dc component, and $A_{i,k}^{0^o}$ and $A_{i,k}^{90^o}$ are the orthogonal components of the vector. Each of the above terms in the integral was converted into a single equation using Simpson's Rule:

$$\int_0^T y(t)dt = \frac{\Delta t}{3}(y_0 + y_1 = 2y_2 + 4y_3 + ... + 2y_{n-2} + 4y_{n-1} + y_n) = \frac{\Delta t}{3} \Sigma_{i=0}^{n} s_i y_i \tag{4.28}$$

where s_i is Simpson's coefficient (where n must be an even number). A detailed mathematical derivation and implications are discussed in detail elsewhere [207]. A self-developed MATLAB code reported previously [181] was used to resample and average the time resolved spectra and then perform the PSD calculations described in Eqs. 4.27 and 4.28 to yield the phase domain spectra. Figures 4.36 show an example of the time resolved and phase resolved spectra for Ti-Beta-F-155.

Phase resolved spectra were then subjected to MCR-ALS to extract independent species, including the surface coverages and spectra. Spectra were truncated to contain wavenumbers 3800-2600 and 1800-700 cm^{-1} and phase angles 1-181o to reduce data set size into MATLAB. Singlular value decomposition suggests only two independent species to fully describe the phase resolved spectra. Two sine wave functions were input for the initial guess of the surface coverages and the spectra were constrained to solve for positive features. The MATLAB program iteratively solved for spectra and surface coverages until the convergence criteria were met and the sum of residuals was less than 10^{-16}. The resulting spectra were smoothed with a Fourier Transform filter, baseline corrected, and normalized to the most intense feature between 1000 and 1150 cm^{-1} using OriginLab's OriginPro 9 software. Initial guesses of three or more species yielded solutions of zero for spectra and surface coverages of all species after two, further indicating that the phase resolved spectra can be completely described by just two independent species.

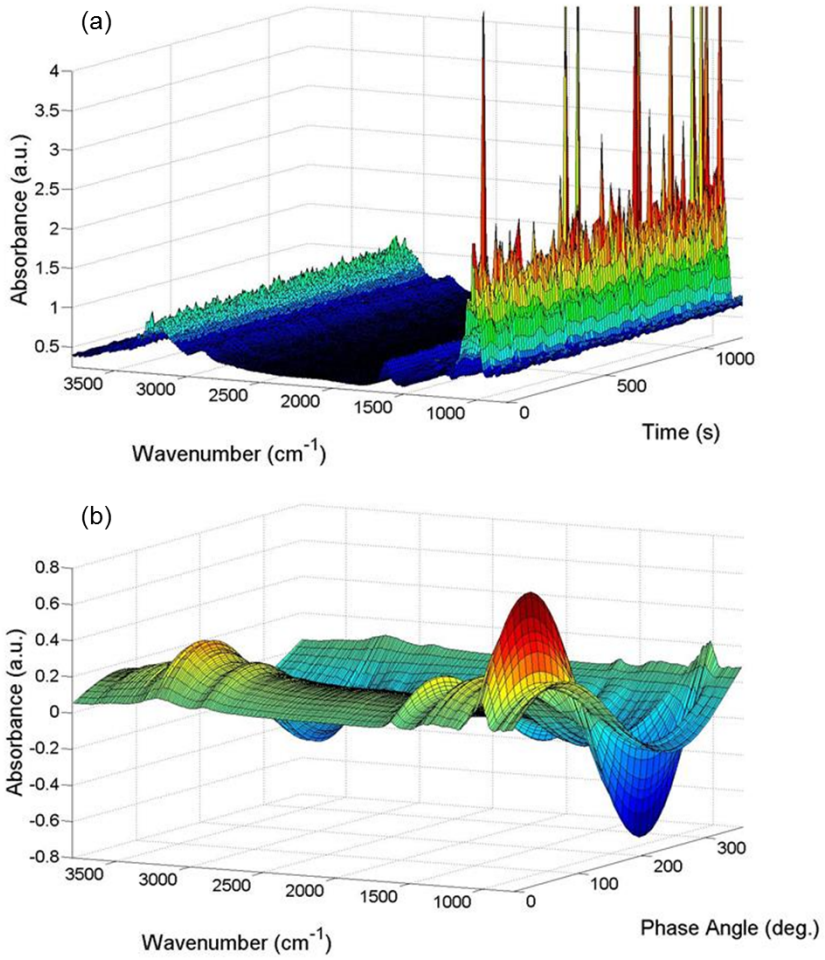

Figure 4.36: a) Time-resolved infrared spectra obtained *in situ* during reactions of glucose and water over Ti-Beta-F-155 while modulating glucose concentrations (42-50 wt%) with a period length of 250 s at 373 K. b) Phase resolved spectra that result from phase sensitive detection of the time resolved spectra in (a). Coloring indicates absorbance intensity.

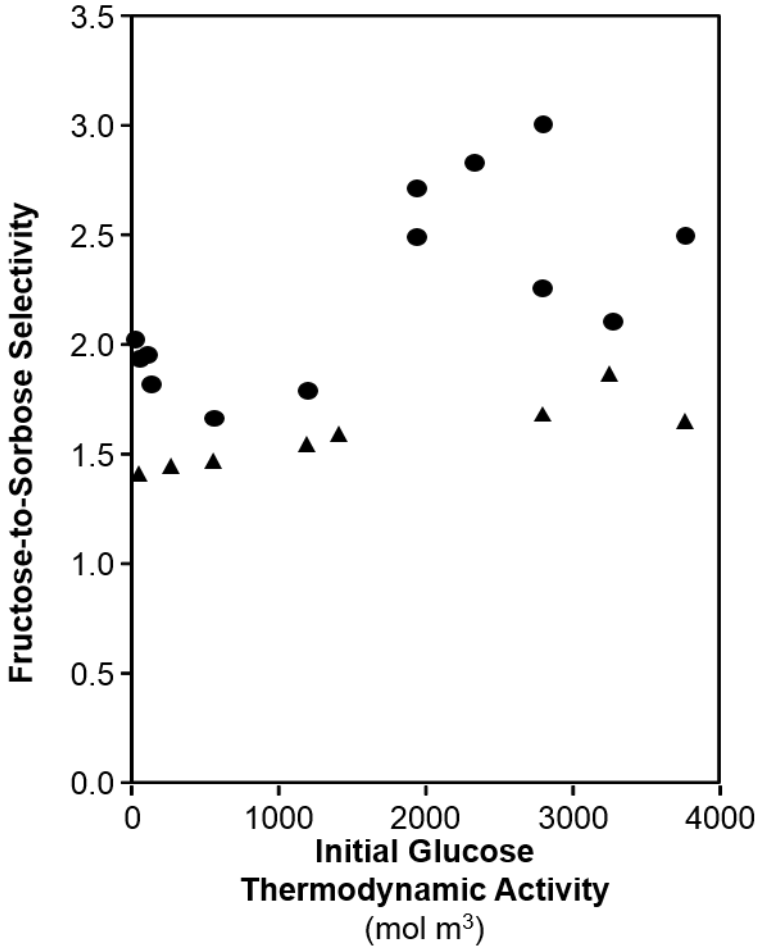

Figure 4.37: Dependence of fructose-to-sorbose selectivity (373 K, pH 4) on Ti-Beta-F-155 (circles) and Ti-Beta-OH-46 (triangles) as a function of initial glucose thermodynamic activity. Relatively constant product selectivities support the identification of the secondary bound glucose species being a bound intermediate which is not directly responsible for sorbose formation as relative coverages of MARI and secondary bound species observed from ATR-IR are affected by changes in initial glucose activity.

4.7.4.2 Comparison of Bound Glucose Intermediates from ATR-IR Spectra and DFT Calculations

Spectra of glucose derived intermediates shown in Figure 4.6B (main text) differ from previous reports of glucose-derived bound to framework Sn atoms in Sn-Beta zeolites from IR spectra; however, the differences are unsurprising given the methods of acquiring each spectra. Previous work characterized glucose derived intermediates measured *ex situ* within dried zeolites. Such experiments revealed a carbonyl feature at 1728 cm^{-1}, a lack of δ(O-H) at 1630 cm^{-1} due to the absence of the solvent, and a different series of features between 1200-1500 cm^{-1} [34]. Intuition and comparisons of the previous results to those in Figure 4.6 show that samples studied *ex situ* (and following dehydrations) do not result in similar charge transfer between intermediates and the Lewis acidic active site and do not reflect hydrogen bonding interactions associated with aqueous solvent. Spectra obtained *in situ* using ATR-IR shown in Figure 4.6B (main text) accurately reflect these consequential interactions and correspond to reactive intermediates that may be catalytically relevant instead of fluid phase reactants or inactive, persistent residues.

The structure of glucose-derived MARI species is characterized by complex vibrational modes particularly between 900 and 1200 cm^{-1}, which previous studies have partially deciphered [200, 208, 209]. Measured spectra of aqueous-phase glucose over the ZnSe crystal also contains a feature at 1024 cm-1 that is attributed to the same $C_1 - O_5 - C_1$ ring breathing mode and is absent in all of the spectra of glucose-derived intermediates over Ti-Beta catalysts (Figure 4.6B, main text). DFT-calculated ring-closed glucose structures bound to Ti sites show a vibrational frequency at 1033 cm^{-1} (Movie S.1, Supp. Info.) that includes $C_1 - O_5 - C_1$ ring breathing modes, which are absent in DFT-calculated ring-opened structures in the gas-phase and within zeolite pores. Thus, glucose observed over the ZnSe crystal exists predominantly in a ring-closed conformation yet the absence of these resonances upon adsorption onto Lewis acidic Ti sites may reflect the presence of ring-opened intermediates.

Further analysis of the bound glucose species can be performed by examining the feature at 1005 cm^{-1} which is present in the spectra reflecting both the MARI and the minor species on Ti-Beta-OH-46, but absent in spectra reflecting the MARI and minor species on Ti-Beta-F-155. DFT-calculated vibrations of reactive intermediates that form fructose show vibrations at 1002 or 1004 cm^{-1} (Movies S.3 and S.4, respectively, Supp. Info.) when silanol groups are located near the Ti active site; however, reactive intermediates that lead to fructose in a defect-free Ti-Beta pore do not show vibrational modes near 1004 cm^{-1}. The correlation between the vibrations near 1004 cm^{-1} in intermediates that lead to fructose and the existence of defect sites (or silanol groups) near the Ti active site suggest the vibrations observed at 1004 cm^{-1}, which result from coordinated ν(C-C) and δ(C-H) modes, must result from interactions with the silanol groups within Beta pores. Differences in these interactions with proximal silanol groups are consistent with the different silanol densities present between the hydrophilic Ti-Beta-OH-46 and hydrophobic Ti-Beta-F-155 samples (Table 4.2, main text). Alternatively, these spectral differences may also reflect interactions with nearby hydroxyl groups formed by *in situ* interconversion of closed (four framework bonds) to open (three framework bonds and one hydroxyl ligand) Ti sites. These hydroxyl groups may hydrogen bond with adsorbed species and cause vibrational modes to appear at 1004 cm^{-1}. These differences between the observed reactive intermediates over Ti-Beta-OH-46 and Ti-Beta-F-155 indicate that hydrophilic and hydrophobic pore environments may stabilize different reactive intermediates that both form fructose, as spectra reflecting both MARI and minor intermediates lack the carbonyl expected in sorbose precursors and may further lead to the measured differences in rates (Figure 4.5, main text).

4.7.4.3 Ti Structural Characterization using XAS and DFT

The Ti-O coordination number of 4 obtained from fitting the EXAFS of the sample after dehydration is consistent with the intense XANES pre-edge peak at 4.9700 keV and the presence of tetrahedral Ti in the zeolite framework. The pre-edge peak in the

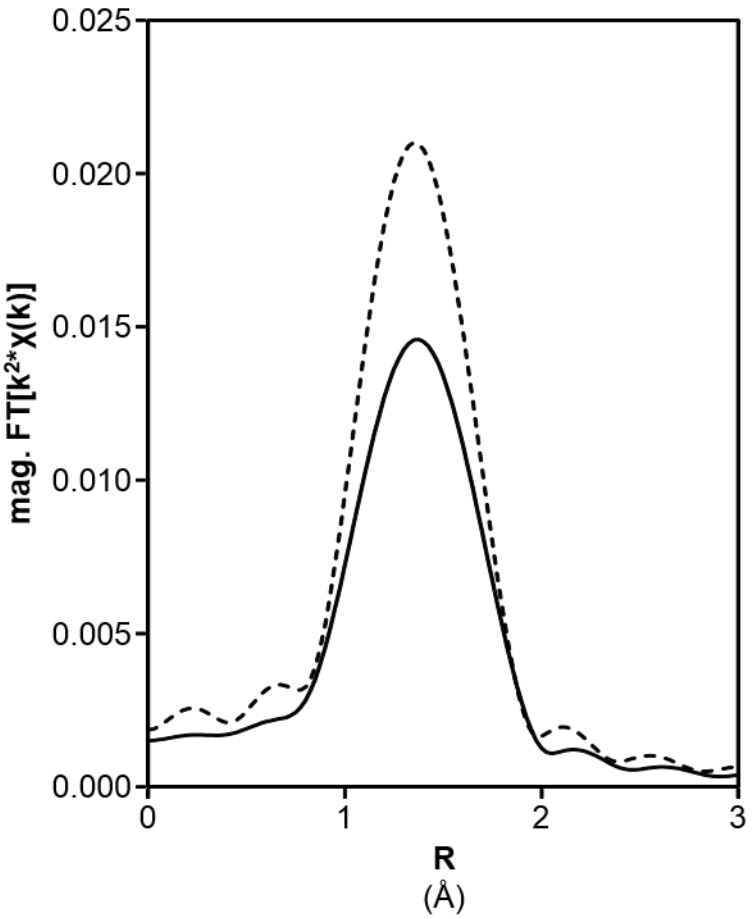

Figure 4.38: Ti K edge XANES of water exchanged Ti-Beta-OH-46 zeolite after dehydration at 523 K in He (solid) and under ambient conditions (dashed). The increase in intensity of the pre-edge peak is consistent with a decrease in coordination number from 6 to 4 upon dehydration.

hydrated sample is less intense and shifted to higher energy (4.9707 keV) than the hydrated sample and is consistent with a Ti coordination number of 6 [209]. However, the magnitude of the Fourier transform of the k^2-weighted EXAFS of the hydrated sample is lower than the dehydrated catalyst. Fitting the EXAFS of the hydrated sample with a single Ti-O path gives a coordination number of 3.8, lower than the value of 6 expected from the XANES, and a bond distance of 1.85 $\AA$. Satisfactory fits of the hydrated and dehydrated spectra were obtained with Debye-Waller factors ($\Delta\ \sigma^{\ 2}$) of 1.0*10^{-3} and -2.0*10^{-3} Å^2, respectively. The higher $\Delta\sigma^2$ indicates a larger

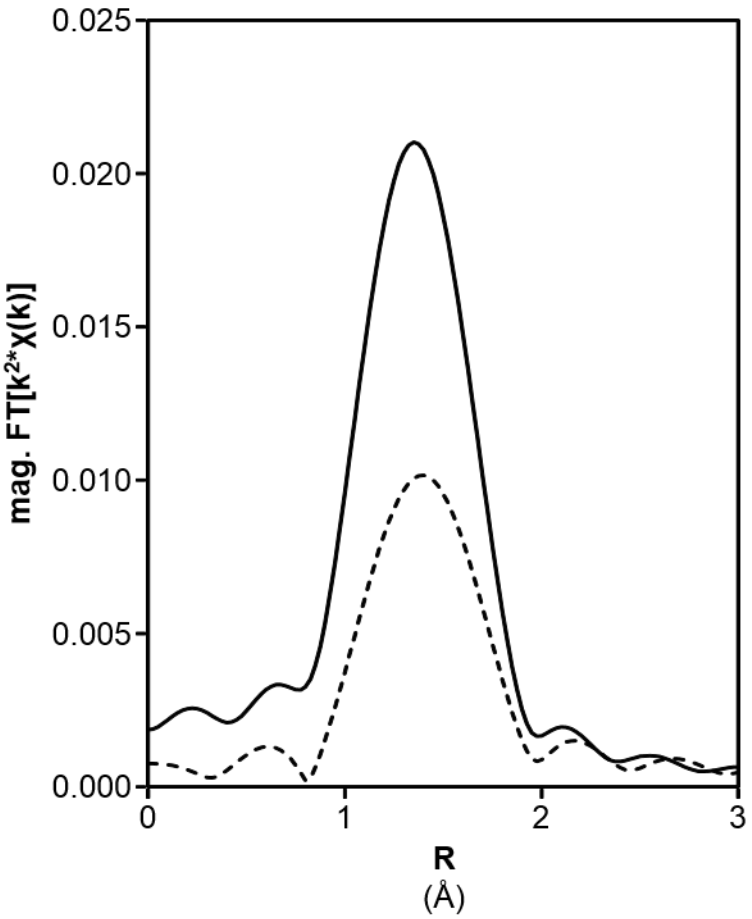

Figure 4.39: Magnitude of the Fourier transform of the k_2-weighted Ti K edge EXAFS of water exchanged Ti-Beta-OH-46 zeolite under ambient conditions (solid) and after dehydration at 523 K in He (dashed).

distributions of Ti-O bond distances under ambient conditions than after dehydration. This suggests that the fitted coordination number of 3.8 is a result of destructive interference between Ti-O scattering paths of different distances (i.e. Ti-$O_{framework}$ and Ti-O_water).

To determine the number and bond distance of the adsorbed water, a ΔEXAFS spectrum was obtained by taking the difference of the k^0-weighted EXAFS of the ambient and dehydrated samples. In obtaining the ΔEXAFS spectrum it was assumed that the four Ti-O framework bonds in the dehydrated sample are unaffected by the adsorption of water. A Ti-O coordination number of 2 and bond distance of

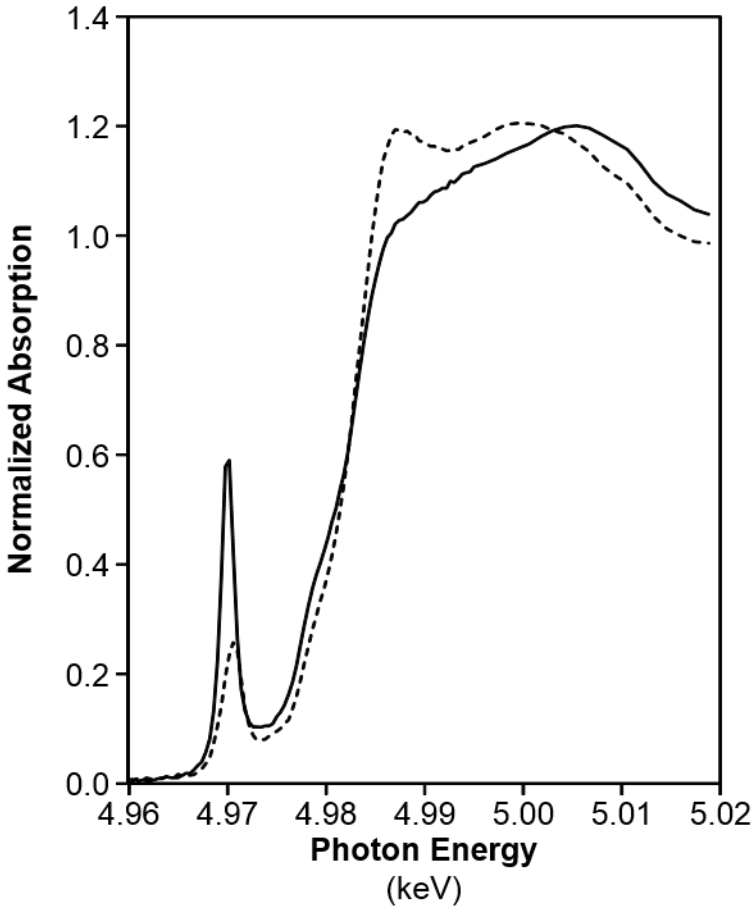

Figure 4.40: Magnitude of the Fourier transform of the k_2-weighted Ti K edge EXAFS of water exchanged Ti-Beta-OH-46 zeolite after dehydration at 523 K in He (solid) and Δ EXAFS of the hydrated and dehydrated water exchanged catalyst (dashed). The Δ EXAFS spectrum was obtained by subtracting the k_0-weighted EXAFS of the sample after dehydration from the k_0-weighted EXAFS of the sample under ambient conditions and is representative of the water adsorbed on Ti under ambient conditions.

1.94 Åwere obtained from fitting the difference spectrum. Therefore, the total Ti-O coordination number of the hydrated sample is 6, consistent with XANES, at an average bond distance of 1.87 Å, consistent with the single scatter fit of the ambient spectrum.

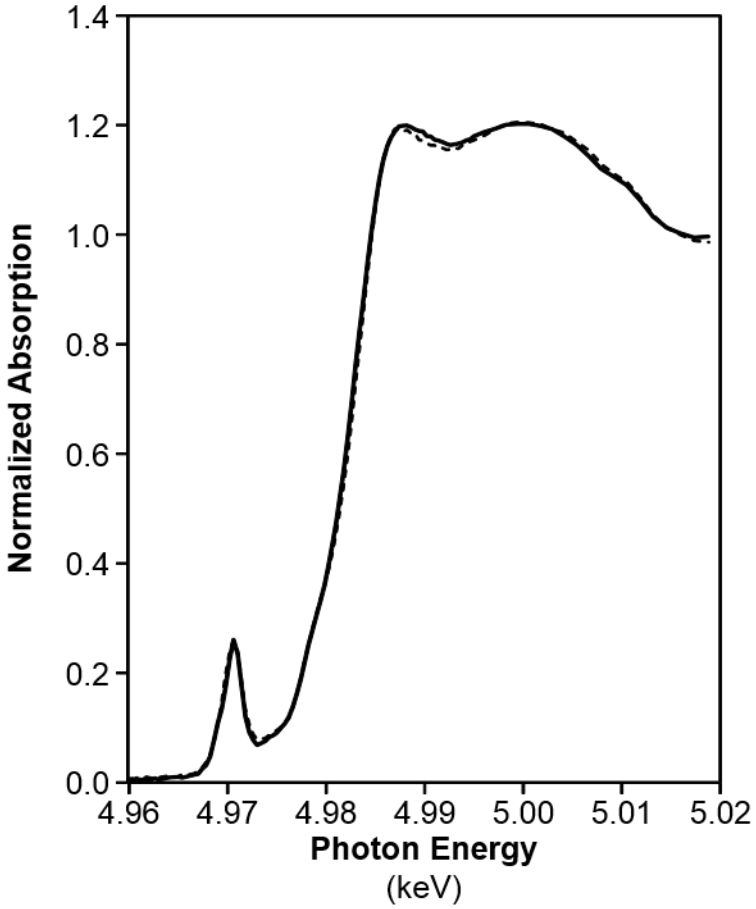

Figure 4.41: Ti K edge XANES of water (dashed) and glucose (solid) exchanged Ti-Beta-OH-46 zeolite under ambient conditions. The spectra are identical within experimental error indicating Ti has equivalent coordination environments in the two samples. The intensity of the pre-edge peak is consistent with a coordination number of 6.

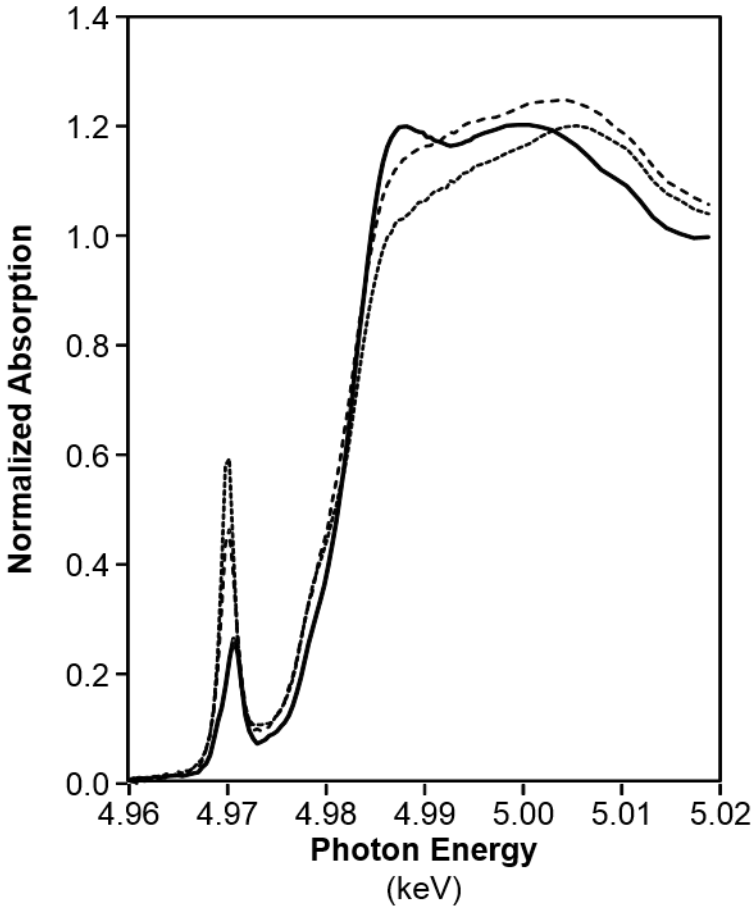

Figure 4.42: Ti K edge XANES of Ti-Beta-OH-46 zeolite: solid – glucose exchanged under ambient conditions, long dashes – glucose exchanged after treatment at 523 K in He, and short dashes – water exchanged after treatment at 523 K in He. The intensity of the pre-edge peak in the glucose exchanged sample after treatment in He at 523 K is consistent with a coordination number of 5 and suggests glucose adsorbed through a single oxygen.

Table 4.8: Ti energies, coordination numbers, and bond distances determined from Ti XAS.

Sample	Pre-edge Energy (keV)	Edge Energy (keV)	Ti-O Coordination Number	Ti-O Bond Distance (Å)	$\Delta\sigma^2$ (10^3 Å^2)	E0 (eV)
Water Exchanged, Dehydrated	4.9700	4.978	4.2	1.83	-2.0	0.3
Water Exchanged, Hydrated (Single scatter fit)	4.9707	4.978	3.8	1.85	1.0	-0.7
ΔEXAFS (ambient – dehydrated)	–	–	2.1	1.94	-3.0	-12
Water Exchanged, Hydrated	–	–	4.2	1.83	-2.0	0.3
(Total, two scatter fit)	–	–	2.1	1.94	-3.0	-12
Glucose Exchanged, Hydrated	4.9707	4.978	6[a]	–	–	–
Glucose Exchanged, Dehydrated	4.9702	4.978	5[a]	–	–	–

[a]Coordination numbers were determined from the intensity of the pre-edge peak of the Ti K edge XANES spectra. Due to poor data quality in the EXAFS region of the absorption spectra reliable fits of these samples could not be obtained.

4.7.5 Thermodynamic Contributions of Hydrophobic Reaction Pockets for Aqueous-Phase Glucose Isomerization

4.7.5.1 Derivation of Mechanism-Based Rate Expressions for Glucose Isomerization Catalyzed by Lewis Acid Sites

A reaction pathway for the parallel formation of fructose and sorbose from glucose is given in Scheme S.1, identical to Scheme 1 from the main text. Here, $G_(l)$, $F_(l)$, and $S_(l)$ stand for glucose, fructose, and sorbose respectively in the liquid phase, * represents a bare Lewis acid site, G* represent the adsorbed glucose intermediate, $(R^*)_F$ and $(R^*)_S$ represent the bound glucose precursors leading to fructose and sorbose respectively, F* and S* represent bound fructose and sorbose respectively, and K_i is the equilibrium coefficient for Step *i*. $k_{2,i}$ is the rate constant for product formation from the kinetically relevant hydride shift transition state for each product. Sequential water (W) adsorption onto a Lewis acid site forms one (W*) and two (2W*) bound water intermediates (Figures 4.43). This scheme and the rate equation derived from it are similar to that reported in Ref. [35].

In Scheme S.1, sequences F and S reflect glucose isomerization to fructose and to sorbose. Net isomerization rates to fructose ($r_{isom,F}$) and sorbose ($r_{isom,S}$) are given by:

$$r_{isom,F} = r_{2,F} - r_{-2,F} \tag{4.29}$$

$$r_{isom,S} = r_{2,S} - r_{-2,S} \tag{4.30}$$

From the law of mass action, reaction rates of elementary steps are proportional to rate constants (k_i) and concentrations of kinetically relevant transition states ($c_{\ddagger,i}$). Therefore, net reaction rates can be written as:

$$r_{isom,F} = k_{2,F} c_{\ddagger,F} - k_{-2,F} c_{F*} \tag{4.31}$$

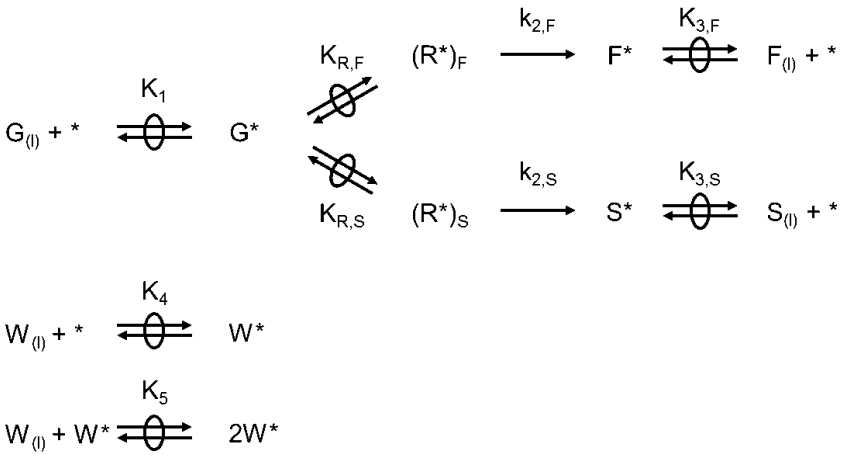

Figure 4.43: Plausible glucose isomerization mechanism for fructose and sorbose formation on Lewis acidic Ti sites. Quasi-equilibrated glucose adsorption (Steps 1a, 1b) forms bound glucose intermediates which form bound fructose (Step 2a) or sorbose (Step 2b) isomers through kinetically relevant hydride shifts. Quasi-equilibrated fructose (Step 3a) and sorbose (Step 3b) desorption phenomena release the product into the liquid phase. Quasi-equilibrated water adsorption onto Lewis acidic active sites (Steps 4 and 5) inhibits isomerization rates at low glucose coverages.

$$r_{isom,S} = k_{2,S} c_{\ddagger,S} - k_{-2,S} c_{S*} \tag{4.32}$$

Concentration terms can be related to the thermodynamic activities through the following relationship which references a standard concentration of 1 mol m^{-3}:

$$a_i = \gamma_i \frac{c_i}{c^o} \tag{4.33}$$

Using the definition of activity in Eq. 4.33, Eqs. 4.31 and 4.32 can then be rewritten as:

$$r_{isom,F} = \frac{k_{2,F}}{\gamma_{\ddagger,F}} a_{\ddagger,F} - \frac{k_{-2,F}}{\gamma_{F*}} a_{F*} \tag{4.34}$$

$$r_{isom,S} = \frac{k_{2,S}}{\gamma_{\ddagger,S}} a_{\ddagger,S} - \frac{k_{-2,S}}{\gamma_{S*}} a_{S*} \tag{4.35}$$

We note that Eqs. 4.34 and 4.35 can rewritten as:

$$r_{isom,F} = \frac{k_{2,F}}{\gamma_{\ddagger,F}} a_{\ddagger,F}(1 - \frac{k_{-2,F} a_{F*} \gamma_{\ddagger,F}}{k_{2,F} a_{\ddagger,F} \gamma_{F*}}) = \frac{k_{2,F}}{\gamma_{\ddagger,F}} a_{\ddagger,F}(1 - \frac{a_{F*} \gamma_{\ddagger,F}}{K_{2,F} a_{\ddagger,F} \gamma_{F*}}) \tag{4.36}$$

$$r_{isom,S} = \frac{k_{2,S}}{\gamma_{\ddagger,S}} a_{\ddagger,S}(1 - \frac{k_{-2,S} a_{S*} \gamma_{\ddagger,S}}{k_{2,S} a_{\ddagger,S} \gamma_{S*}}) = \frac{k_{2,S}}{\gamma_{\ddagger,S}} a_{\ddagger,S}(1 - \frac{a_{S*} \gamma_{\ddagger,S}}{K_{2,S} a_{\ddagger,S} \gamma_{S*}}) \tag{4.37}$$

or:

$$r_{isom,F} = \frac{k_{2,F}}{\gamma_{\ddagger,F}} a_{\ddagger,F}(1 - \eta_F) \tag{4.38}$$

$$r_{isom,S} = \frac{k_{2,S}}{\gamma_{\ddagger,S}} a_{\ddagger,S}(1 - \eta_S) \tag{4.39}$$

Here, η_F and η_S are the approach-to-equilibrium terms for Steps 2F and 2S respectively (Scheme S.1).

The 1,2-hydride shift (or 1,5-hydride shift) step is kinetically relevant for fructose (or sorbose) formation as determined from H/D kinetic isotope effect measurements and isotopic tracer studies [51]. Steps 1F, 1S, 3F, 3S, 4 and 5 are then assumed to be quasi-equilibrated and the following equilibrium expressions are derived to relate thermodynamic activities of reactant and product species:

$$K_1 = \frac{a_{G*}}{a_G a_*} \tag{4.40}$$

$$K_{3,F} = \frac{a_F a_*}{a_{F*}} \tag{4.41}$$

$$K_{3,S} = \frac{a_S a_*}{a_{S*}} \tag{4.42}$$

$$K_4 = \frac{a_{W*}}{a_W a_*} \tag{4.43}$$

$$K_5 = \frac{a_{2W*}}{a_W a_{W*}} \tag{4.44}$$

In addition, the kinetically relevant bound glucose intermediates leading to fructose, $(R^*)_F$, or sorbose, $(R^*)_S$, formation are quasi-equilibrated with the respective hydride shift transition state as follows:

$$K_{R,F} = \frac{a_{\ddagger,F}}{a_G *} \tag{4.45}$$

$$K_{R,S} = \frac{a_{\ddagger,S}}{a_G *} \tag{4.46}$$

Eqs. 4.45 and 4.46 couple together the formation of the kinetically relevant bound glucose intermediate from the adsorbed glucose intermediate with the subsequent formation of the hydride shift transition state into a single equilibrium coefficient, $K_{R,i}$. Solving Eqs. 4.45 and 4.46 for $a_{\ddagger,F}$ and $a_{\ddagger,S}$, isomerization rates can then be expressed as:

$$r_{isom,F} = \frac{k_{2,F}}{\gamma_{\ddagger,F}} K_{R,F} a_{G*} (1 - \eta_F) \tag{4.47}$$

$$r_{isom,S} = \frac{k_{2,S}}{\gamma_{\ddagger,S}} K_{R,S} a_{G*} (1 - \eta_S) \tag{4.48}$$

And further expressed using Eq. 4.40 as:

$$r_{isom,F} = \frac{k_{2,F}}{\gamma_{\ddagger,F}} K_{R,F} K_1 a_G a_* (1 - \eta_F) \tag{4.49}$$

$$r_{isom,S} = \frac{k_{2,S}}{\gamma_{\ddagger,S}} K_{R,S} K_1 a_G a_* (1 - \eta_S) \tag{4.50}$$

Eqs. 4.49 and 4.50 can be rewritten in terms of activity coefficients (γ_i) and concentrations (c_i):

$$r_{isom,F} = \frac{k_{2,F}}{\gamma_{\ddagger,F}} K_{R,F} K_1 \gamma_G \gamma_* c_G c_* (1 - \eta_F) \tag{4.51}$$

$$r_{isom,S} = \frac{k_{2,S}}{\gamma_{\ddagger,S}} K_{R,S} K_1 \gamma_G \gamma_* c_G c_* (1 - \eta_S) \tag{4.52}$$

Total Lewis acid site concentrations ($c_{*,tot}$) are related to the concentrations of unoccupied sites (c_*) and sites with bound monosaccharide or solvent molecules from Scheme S.1 through the following site balance:

$$c_{*,tot} = c_* + c_{G*} + c_{R,F} + c_{R,S} + c_{F*} + c_{S*} + c_{W*} + c_{2W*} \tag{4.53}$$

Eq. 4.53 can be rewritten using Eqs. 4.40-4.46:

$$c_{*,tot} = c_* + \frac{K_1 a_G \gamma_* c_*}{\gamma_{G*}} + \frac{K_1 K_{R,F} a_G \gamma_* c_*}{\gamma_{R,F}} + \frac{K_1 K_{R,S} a_G \gamma_* c_*}{\gamma_{R,S}} + \frac{a_F \gamma_* c_*}{K_{3,F} \gamma_{F*}} + \frac{a_S \gamma_* c_*}{K_{3,S} \gamma_{S*}} + \frac{K_4 a_W \gamma_* c_*}{\gamma_{W*}} + \frac{K_4 K_5 a_W^2 \gamma_* c_*}{\gamma_{2W*}} \tag{4.54}$$

c_* can be factored out of the right-hand side of Eq. 4.54 leading to the following equation:

$$c_{*,tot} = c_* (1 + \frac{K_1 a_G \gamma_*}{\gamma_{G*}} + \frac{K_1 K_{R,F} a_G \gamma_*}{\gamma_{R,F}} + \frac{K_1 K_{R,S} a_G \gamma_*}{\gamma_{R,S}} + \frac{a_F \gamma_*}{K_{3,F} \gamma_{F*}} + \frac{a_S \gamma_*}{K_{3,S} \gamma_{S*}} + \frac{K_4 a_W \gamma_*}{\gamma_{W*}} + \frac{K_4 K_5 a_W^2 \gamma_*}{\gamma_{2W*}} \tag{4.55}$$

Eq. 4.55 can then be rewritten in terms of fractional coverages (θ_i) of each bound adsorbate:

$$c_{*,tot} = c_*(\theta_* + \theta_{G*} + \theta_{R*,F} + \theta_{R*,S} + \theta_{F*} + \theta_{S*} + \theta_{W*} + \theta_{2W*}) \tag{4.56}$$

These fractional coverage terms are located in the isomerization rate expression denominator prior to establishing the most abundant surface intermediates.

From spectroscopic evidence discussed in the main text and both first-order and zero-order kinetic behavior in initial glucose activity, the most abundant surface intermediates are the Lewis acid site with two bound water molecules at dilute glucose concentrations (<1200 mol m^-3) and the Lewis acid site with adsorbed glucose at high glucose concentrations (>2700 mol m^-3). Eq. 4.55 can then be reduced to:

$$c_{*,tot} = c_*(\frac{K_1 a_G \gamma_*}{\gamma_{G*}} + \frac{K_4 K_5 a_W^2 \gamma_*}{\gamma_{2W*}} \tag{4.57}$$

Substitution of Eq. 4.57 into Eqs. 4.51 and 4.52 and yields expressions for isomerization turnover rates per total Lewis acid site in terms of initial glucose thermodynamic activity:

$$\frac{r_{isom,F}}{c_{*,tot}} = \frac{\frac{k_{2,F}}{\gamma_{\ddagger,F}} K_{R,F} K_1 a_G (1 - \eta_F)}{\frac{K_4 K_5 a_W^2}{\gamma_{2W*}} + \frac{K_1 a_G}{\gamma_{G*}}} \tag{4.58}$$

$$\frac{r_{isom,S}}{c_{*,tot}} = \frac{\frac{k_{2,S}}{\gamma_{\ddagger,S}} K_{R,S} K_1 a_G (1 - \eta_S)}{\frac{K_4 K_5 a_W^2}{\gamma_{2W*}} + \frac{K_1 a_G}{\gamma_{G*}}} \tag{4.59}$$

This expression matches the rate equation labeled Eq. 4.8 in the main text and can be rearranged to follow a Langmuir Hinshelwood format which holds for either product:

$$r_i = \frac{\gamma_{G*}}{\gamma_{\ddagger,i}} \frac{\frac{K_1 \gamma_{2W*}}{K_4 K_5 \gamma_{G*}} K_{R,i} k_{2,i} \frac{a_G}{a_W^2} (1 - \eta_i)}{1 + \frac{K_1 \gamma_{2W*}}{K_4 K_5 \gamma_{G*}} \frac{a_G}{a_W^2}} \tag{4.60}$$

Apparent first-order and zero-order rate constants can then be defined as per the main text:

$$k_{app,first,i} = \frac{K_1 K_{R,i} k_{2,i} \gamma_{2W*}}{K_4 K_5 \gamma_{\ddagger,i}} \tag{4.61}$$

$$k_{app,zero,i} = K_{R,i} k_{2,i} \frac{\gamma_{G*}}{\gamma_{\ddagger,i}} \tag{4.62}$$

The equilibrium coefficient corresponding to the competitive adsorption of glucose and water is not dependent on the product formed and can be defined as:

$$K_{app,comp} = \frac{k_{app,first,i}}{k_{app,zero,i}} = \frac{K_1 \gamma_{2W*}}{K_4 K_5 \gamma_{G*}} \tag{4.63}$$

Eq. 4.60 can then be rewritten using Eqs. 4.61-4.63 into:

$$r_i = \frac{k_{app,zero,i} K_{app,comp} \frac{a_G}{a_W^2} (1 - \eta_i)}{1 + K_{app,comp} \frac{a_G}{a_W^2}} \tag{4.64}$$

Rate and equilibrium constants from Eqs. 4.40-4.46 reflect free energy differences between transition states, reactants, and solvent molecules:

$$K_1 = e^{-(\Delta G^o_{G*} - \Delta G^o_G - \Delta G^o_*)/RT} \tag{4.65}$$

$$K_{R,F} = e^{-(\Delta G^o_{R,F} - \Delta G^o_{G*})/RT} \tag{4.66}$$

$$K_{R,S} = e^{-(\Delta G^o_{R,S} - \Delta G^o_{G*})/RT} \tag{4.67}$$

$$k_{2,F} = \frac{k_B T}{h} e^{-(\Delta G^o_{\ddagger,F} - \Delta G^o_{R,F})/RT} \tag{4.68}$$

$$k_{2,S} = \frac{k_B T}{h} e^{-(\Delta G^o_{\ddagger,S} - \Delta G^o_{R,S})/RT} \tag{4.69}$$

$$K_4 = e^{-(\Delta G^o_{W*} - \Delta G^o_W - \Delta G^o_*)/RT} \tag{4.70}$$

$$K_5 = e^{-(\Delta G^o_{2W*} - \Delta G^o_W - \Delta G^o_{W*})/RT} \tag{4.71}$$

Rewriting apparent first-order rate constants, $k_{app,first,F}$ and $k_{app,first,S}$, from Eqs. 4.61 and 4.62 in terms of free energies using Eqs. 4.65-4.71 gives the following expressions:

$$k_{app,first,F} = \frac{K_1 K_{R,F} k_{2,F} \gamma_{2W*}}{K_4 K_5 \gamma_{\ddagger,F}} = \frac{k_B T}{h} e^{-((\Delta G^o_{\ddagger,F} + 2\Delta G^o_W) - (\Delta G^o_G + \Delta G^o_{2W*}))/RT} \tag{4.72}$$

$$k_{app,first,S} = \frac{K_1 K_{R,S} k_{2,S} \gamma_{2W*}}{K_4 K_5 \gamma_{\ddagger,S}} = \frac{k_B T}{h} e^{-((\Delta G^o_{\ddagger,S} + 2\Delta G^o_W) - (\Delta G^o_G + \Delta G^o_{2W*}))/RT} \tag{4.73}$$

These apparent first-order rate constants depend on the free energy of the bound glucose isomerization transition state with two liquid phase solvent molecules relative to two bound water molecules with one liquid phase glucose molecule. Similarly, measured zero-order rate constants depend on the free energy of the hydride shift transition state relative to the adsorbed glucose intermediate:

$$k_{zero,F} = \frac{k_B T}{h} e^{-(\Delta G^o_{\ddagger,F} - \Delta G^o_{G*})/RT} \tag{4.74}$$

$$k_{zero,S} = \frac{k_B T}{h} e^{-(\Delta G^o_{\ddagger,S} - \Delta G^o_{G*})/RT} \tag{4.75}$$

Eqs. 4.72-4.75 therefore reflect the free energy differences reflected in first-order and zero-order rate constants quantified from initial rate measurements at low and high glucose activities.

4.7.5.2 Initial Glucose Isomerization Rates and Enthalpy and Entropy Determination

Figures 4.44-4.46 show the raw data for sorbose formation rates on Ti-Beta-F-155 and both fructose and sorbose formation rates on Ti-Beta-OH-46 which forms the complete set of measured rates on Ti-Beta-F-155 and Ti-Beta-OH-46 when combined with the data presented in Figure 4.8 from the main text.

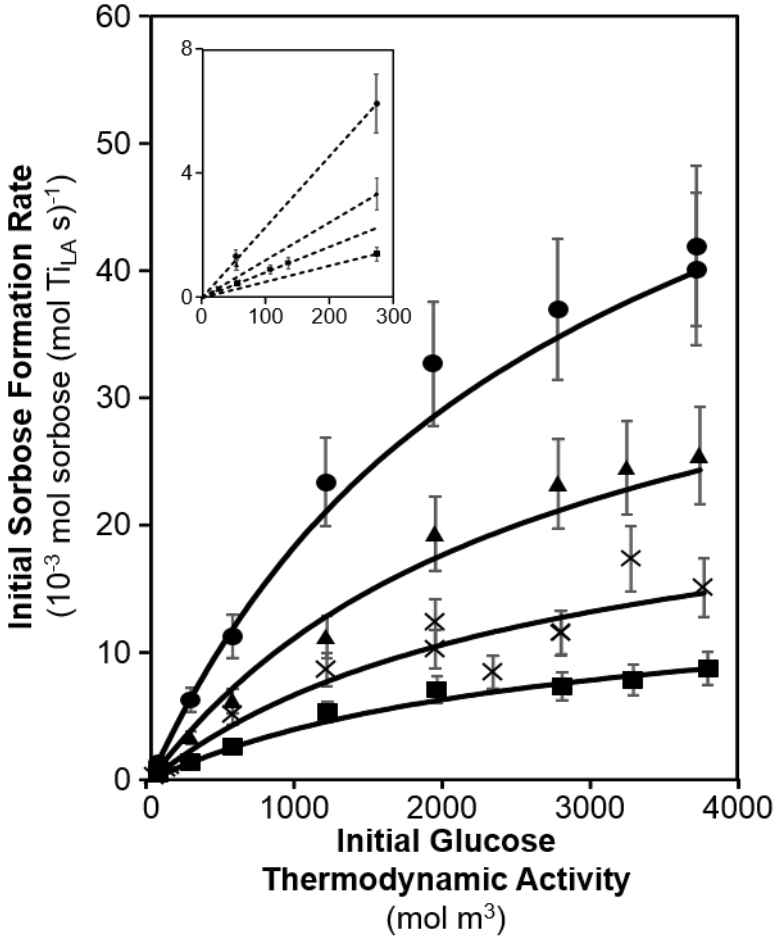

Figure 4.44: Dependence of initial sorbose formation rates (pH 3) on Ti-Beta-F-155 on initial glucose thermodynamic activity (corresponding to 1-50 wt.% initial glucose concentration) at 368 (squares), 373 (cross), 378 (triangles), and 383 K (circles). Solid lines for all data represent modeled regressions of the experimental data to the overall rate equation given in Eq. 4.16 in the main text using activation enthalpies and entropies given in Table 4.4.

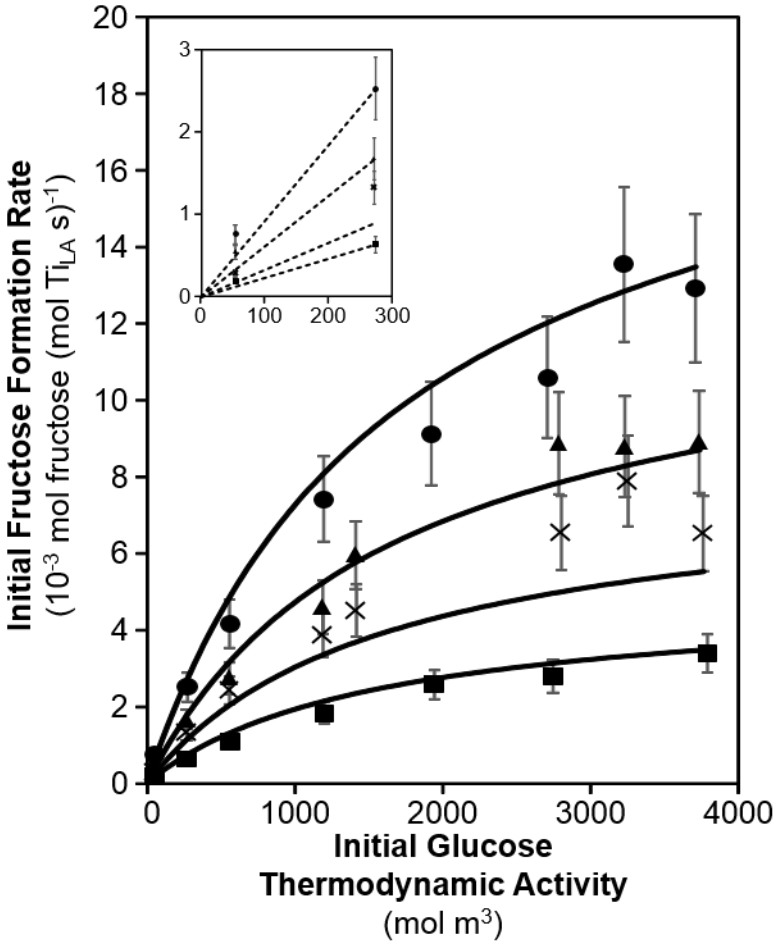

Figure 4.45: Dependence of initial fructose formation rates (pH 3) on Ti-Beta-OH-46 on initial glucose thermodynamic activity (corresponding to 1-50 wt.% initial glucose concentration) at 368 (squares), 373 (cross), 378 (triangles), and 383 K (circles). Solid lines for all data represent modeled regressions of the experimental data to the overall rate equation given in Eq. 4.16 in the main text using activation enthalpies and entropies given in Table 4.4.

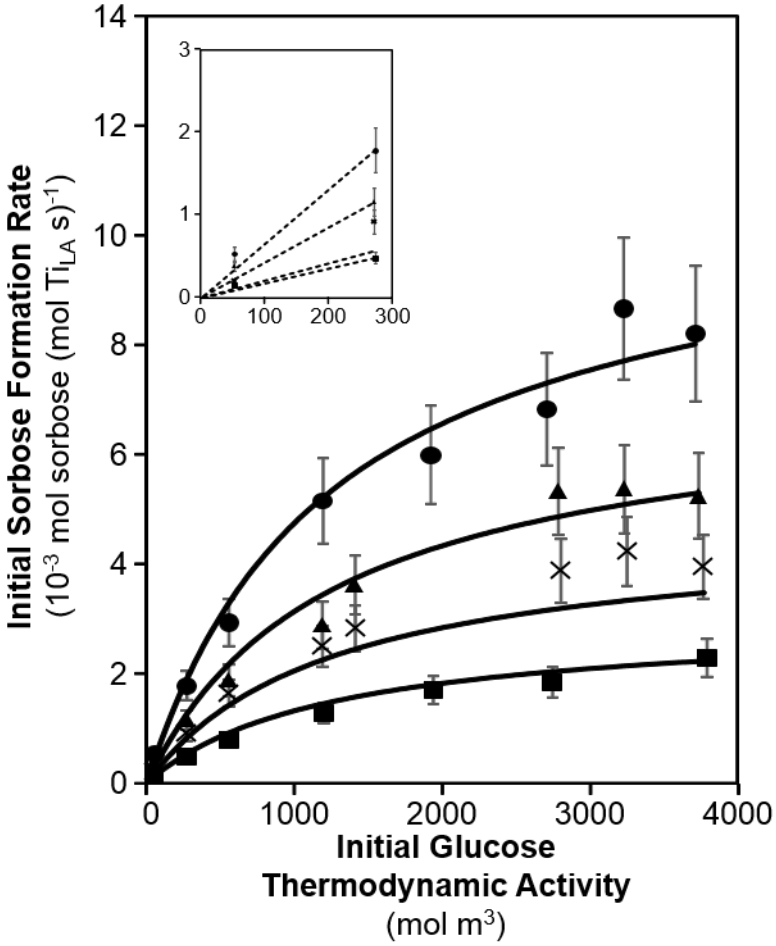

Figure 4.46: Dependence of initial sorbose formation rates (pH 3) on Ti-Beta-OH-46 on initial glucose thermodynamic activity (corresponding to 1-50 wt.% initial glucose concentration) at 368 (squares), 373 (cross), 378 (triangles), and 383 K (circles). Solid lines for all data represent modeled regressions of the experimental data to the overall rate equation given in Eq. 4.16 in the main text using activation enthalpies and entropies given in Table 4.4.

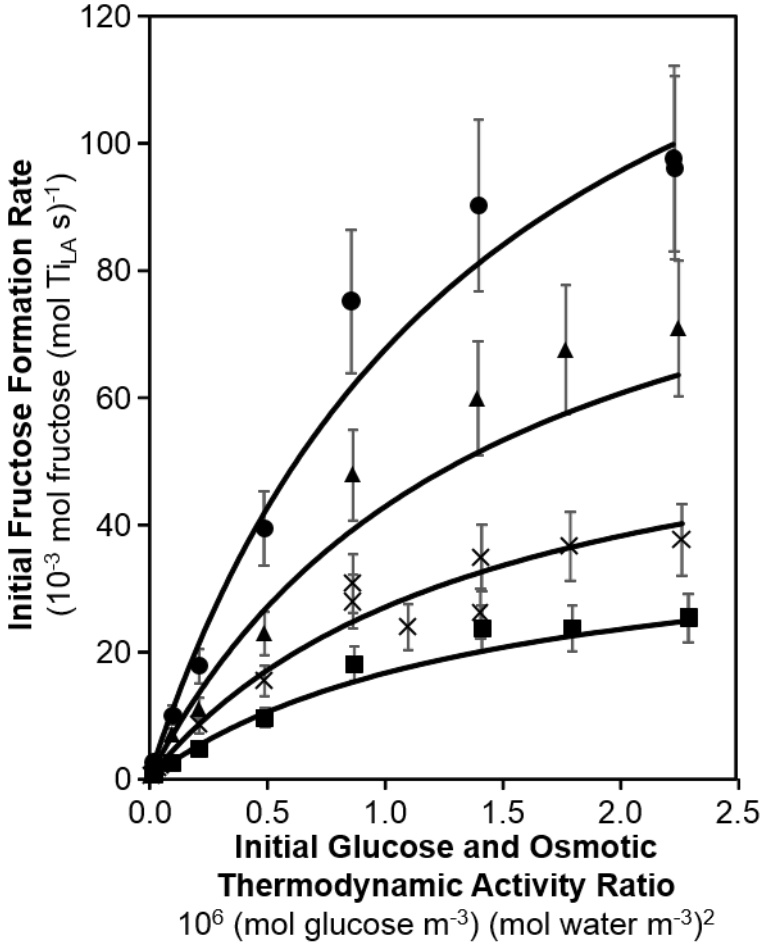

Figure 4.47: Dependence of initial fructose formation rates (pH 3) on Ti-Beta-F-155 on initial glucose and osmotic thermodynamic activity ratio (corresponding to 1-50 wt.% initial glucose concentration) at 368 (squares), 373 (cross), 378 (triangles), and 383 K (circles). Solid lines for all data represent modeled regressions of the experimental data to the overall rate equation given in Eq. 4.16 in the main text using activation enthalpies and entropies given in Table 4.4.

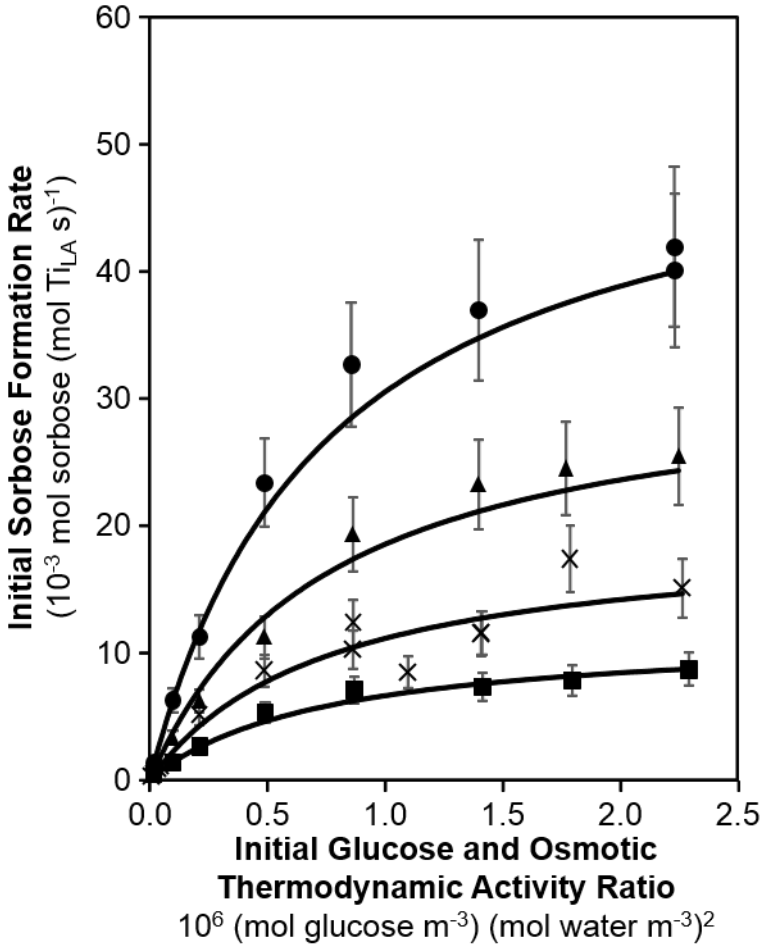

Figure 4.48: Dependence of initial sorbose formation rates (pH 3) on Ti-Beta-F-155 on initial glucose and osmotic thermodynamic activity ratio (corresponding to 1-50 wt.% initial glucose concentration) at 368 (squares), 373 (cross), 378 (triangles), and 383 K (circles). Solid lines for all data represent modeled regressions of the experimental data to the overall rate equation given in Eq. 4.16 in the main text using activation enthalpies and entropies given in Table 4.4.

4.7.5.3 Comparison of Fitted Thermodynamic Properties with Activity Coefficient Sets and for Multiple Fitting Strategies

The modeled behavior derived from the regression of Eq. 4.16 in the main text to the experimental data set leads to the apparent enthalpy and entropy values reported in Table 4.4 when the experimental data points are weighted by experimental rate values. This weighting scheme minimizes the natural tendency for higher measured rates at increased glucose activities and temperature, and therefore higher absolute error differences between the experimental data and the model, to dominate the regression and instill systematic errors in the regressed parameters. Other weighting methods were investigated and did affect regressed activation enthalpies and entropies but led to systematic errors in model regression leading to exaggeration of rate measurements at higher glucose activities and temperatures. The presence of systemic errors derived from regressed parameters were studied by quantifying percent residuals using the following equation:

$$PercentResidual = \frac{(r_{exp} - r_{model})}{r_{exp}} * 100 \tag{4.76}$$

Figures 4.47-4.50 show percent residuals as a function of glucose activity and temperature on both Ti-Beta-F-155 and Ti-Beta-OH-46 for both fructose and sorbose formation from rates given in Figures 4.44-4.46 and Figure 4.8 in the main text. Systematic trends are not observed as a function of initial glucose activity, indicating that the model is not introducing systematic errors derived from the chosen fitting method. We note that negligible differences in fitted apparent enthalpies and entropies are observed when ideality is assumed for all solution-phase species ($\gamma_i \rightarrow 1$) and when activity coefficients are not adjusted for temperature changes. Glucose and water activities are therefore used throughout the main text.

The regressed rates derived from the apparent enthalpies and entropies listed in Table 4.4 of the main text predict zero-order rate constants that are higher than the rates measured at high glucose activities where Lewis acidic Ti sites are covered

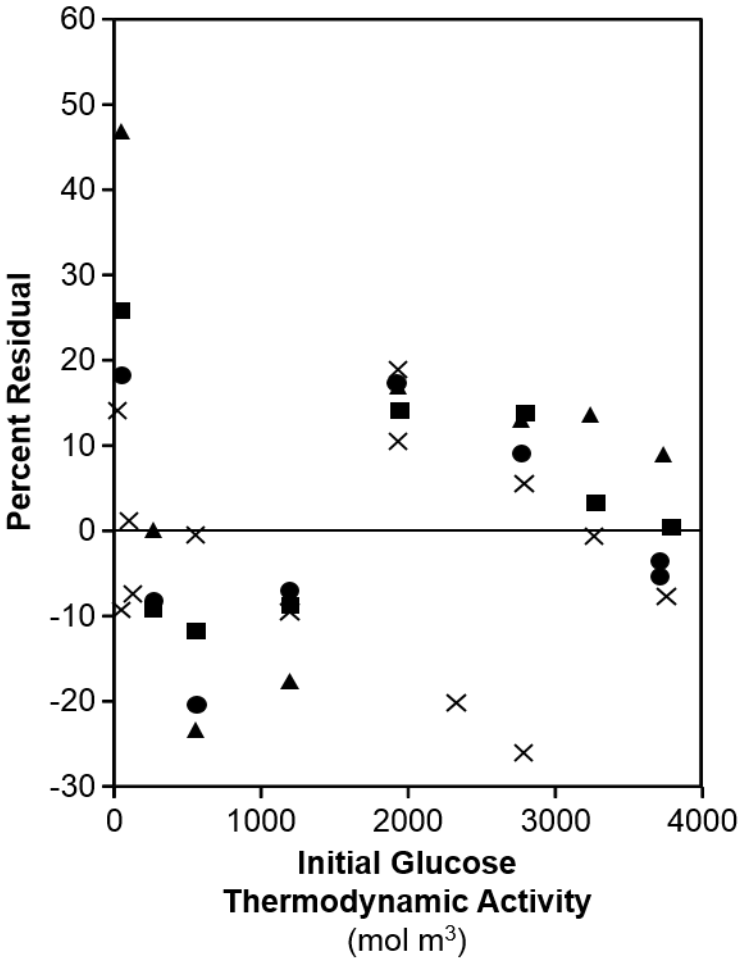

Figure 4.49: Percent residual plot of fructose formation rates on Ti-Beta-F-155 as a function of initial glucose thermodynamic activity (corresponding to 1-50 wt.% initial glucose concentration) at 368 (squares), 373 (cross), 378 (triangles), and 383 K (circles) comparing experimental rate measurements with modeled rate behavior from Eq. 4.16 from the main text. Percent residuals were obtained from Eq. 4.72.

with bound glucose MARIs as seen from ATR-IR spectra. These differences result from measured isomerization rates that are not precisely zero-order at high glucose activities at all temperatures as shown in Figures 4.52, but are less significant for measured first-order rate constants (Figure 4.51). First-order and zero-order rate constants can then be estimated from single rate measurements at low (a_G = 275 mol m^{-3}) and high (a_G = 3500 mol m^{-3}) glucose activities, respectively. Apparent

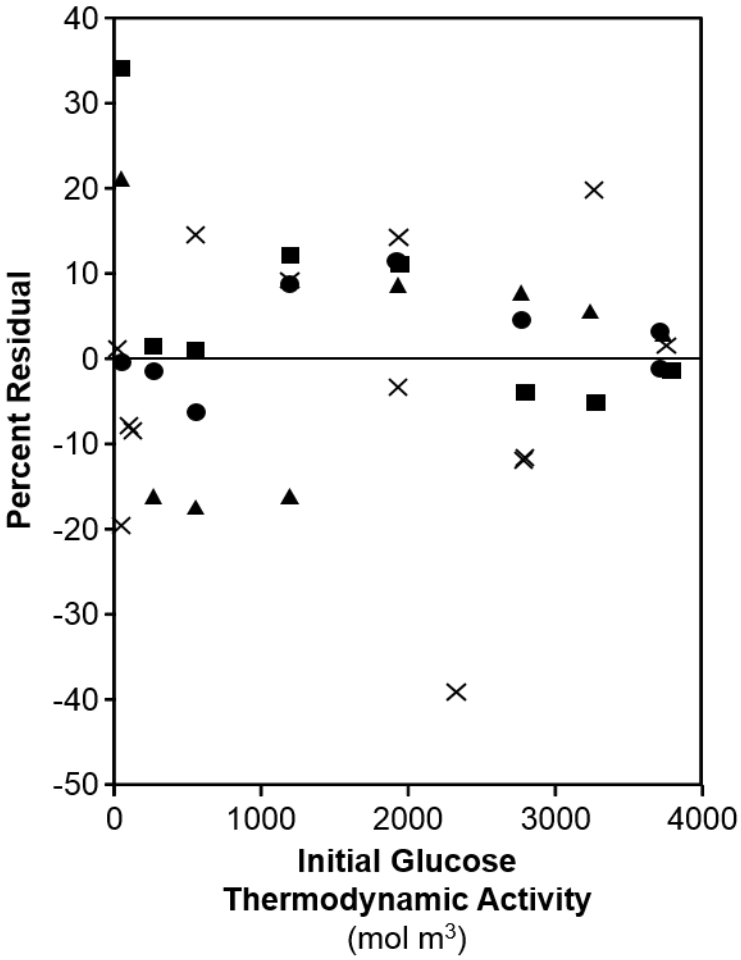

Figure 4.50: Percent residual plot of sorbose formation rates on Ti-Beta-F-155 as a function of initial glucose thermodynamic activity (corresponding to 1-50 wt.% initial glucose concentration) at 368 (squares), 373 (cross), 378 (triangles), and 383 K (circles) comparing experimental rate measurements with modeled rate behavior from Eq. 4.16 from the main text. Percent residuals were obtained from Eq. 4.72.

activation enthalpies and entropies listed in Table 4.9 were determined from these measured rates at consistent glucose activities.

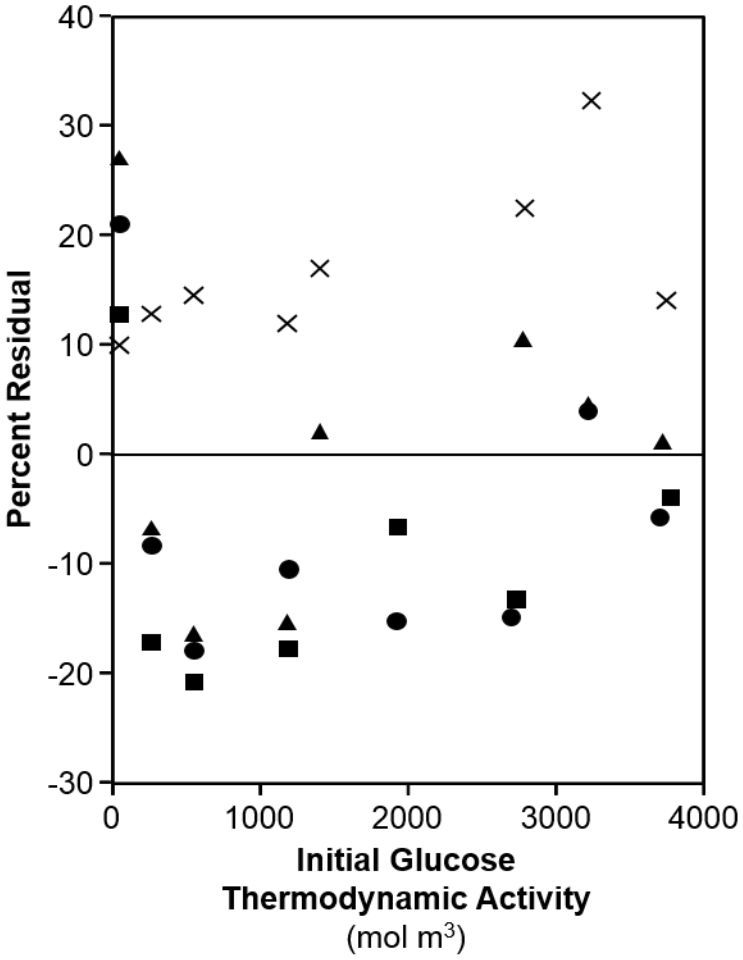

Figure 4.51: Percent residual plot of fructose formation rates on Ti-Beta-OH-46 as a function of initial glucose thermodynamic activity (corresponding to 1-50 wt.% initial glucose concentration) at 368 (squares), 373 (cross), 378 (triangles), and 383 K (circles) comparing experimental rate measurements with modeled rate behavior from Eq. 4.16 from the main text. Percent residuals were obtained from Eq. 4.72.

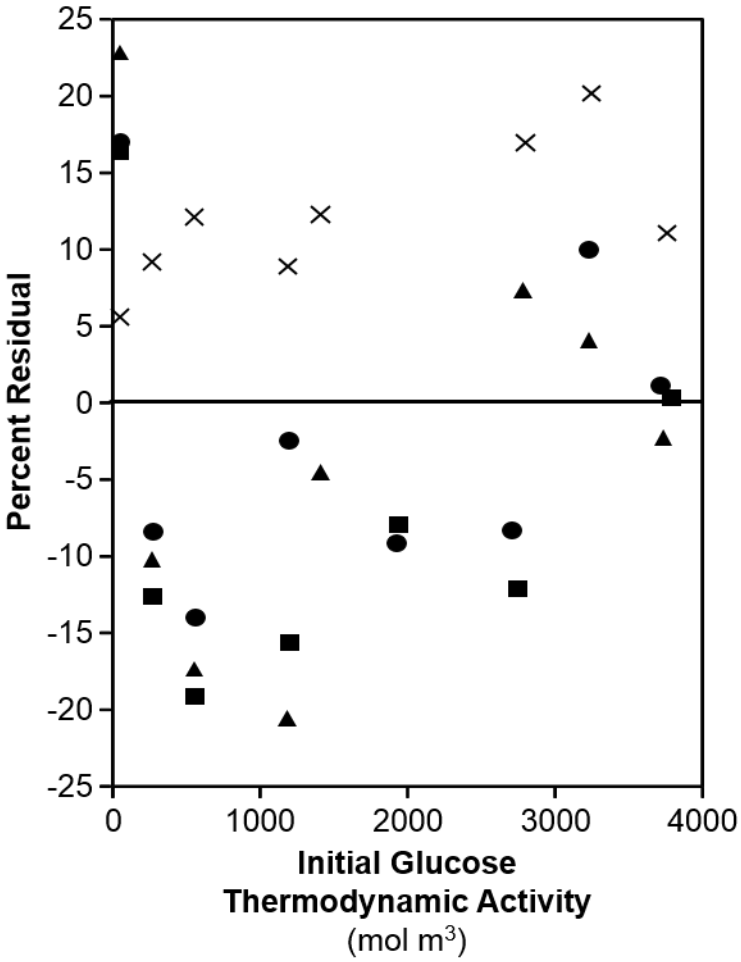

Figure 4.52: Percent residual plot of sorbose formation rates on Ti-Beta-OH-46 as a function of initial glucose thermodynamic activity (corresponding to 1-50 wt.% initial glucose concentration) at 368 (squares), 373 (cross), 378 (triangles), and 383 K (circles) comparing experimental rate measurements with modeled rate behavior from Eq. 4.16 from the main text. Percent residuals were obtained from Eq. 4.72.

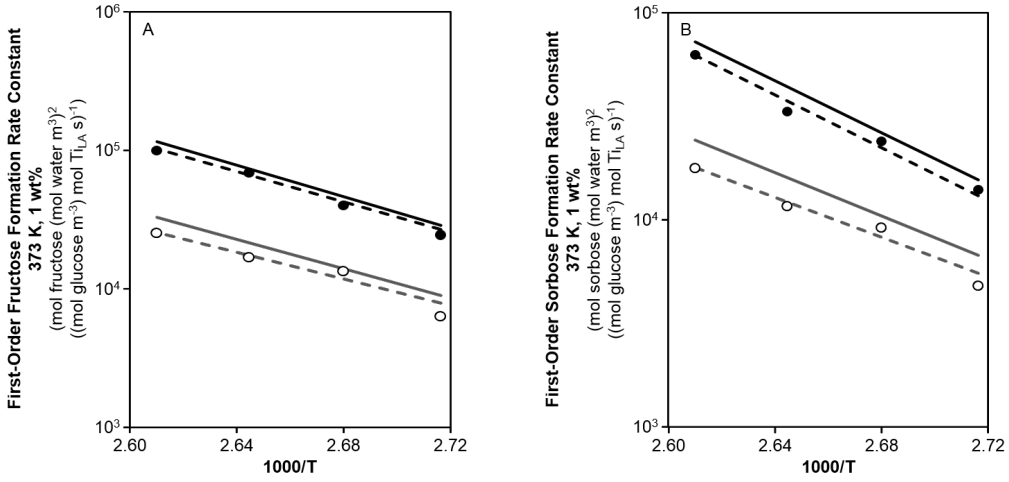

(a) (b)

Figure 4.53: Arrhenius plot for apparent first-order fructose (A) and sorbose (B) formation rate constants (368-383 K, 5 wt.%) on Ti-Beta-F-155 (closed circles) and Ti-Beta-OH-46 (open circles). Solid lines represent the results of the regression of Eq. 4.16 and dashed lines represent regressions using rate measurements at 5 wt.% on Ti-Beta-F-155 (black) and Ti-Beta-OH-46 (gray). Both regression lines follow the Eyring equation with activation enthalpies and entropies given in Table 4.4 of the main text and Table 4.9, respectively.

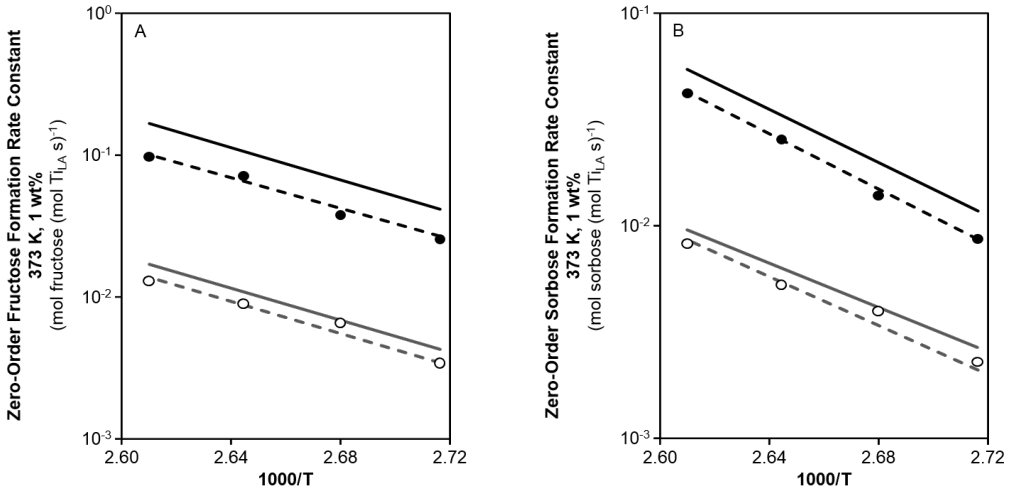

(a) (b)

Figure 4.54: Arrhenius plot for apparent zero-order fructose (A) and sorbose (B) formation rate constants (368-383 K, 50 wt.%) on Ti-Beta-F-155 (closed circles) and Ti-Beta-OH-46 (open circles). Solid lines represent the results of the regression of Eq. 4.16 and dashed lines represent regressions using rate measurements at 50 wt.% on Ti-Beta-F-155 (black) and Ti-Beta-OH-46 (gray). Both regressions follow the Eyring equation with activation enthalpies and entropies given in Table 4.4 of the main text and Table 4.9, respectively.

Table 4.9: Apparent enthalpies and entropies for first-order and zero-order rate constants describing fructose and sorbose formation on Ti-Beta-F-155 and Ti-Beta-OH-46 derived from single rate measurements at 5 and 50 wt.% corresponding to first-order and zero-order rates. Differences in apparent activation enthalpies ($\Delta\Delta$ H_{app}) and entropies ($\Delta\Delta$ S_{app}) are listed as the difference between Ti-Beta-F-155 and Ti-Beta-OH-46.

	ΔH_{app} (kJ mol^{-1})		ΔS_{app} (J mol^{-1} K^{-1})		$\Delta\Delta H_{app}$ (kJ mol^{-1})	$\Delta\Delta S_{app}$ (J mol^{-1} K^{-1})
Rate constant	Ti-Beta-F-155	Ti-Beta-OH-46	Ti-Beta-F-155	Ti-Beta-OH-46	(F-OH)[b]	(F-OH)[b]
$k_{zero,fructose}$	100	105	4	0	-5	4
$k_{first,fructose}$	102	89	124	78	13	46
$K_{comp,fructose}$	-2	16	-120	-78	18	42
$k_{zero,sorbose}$	122	106	53	0	16	53
$k_{first,sorbose}$	119	89	163	76	30	87
$K_{comp,sorbose}$	3	17	-90	-76	14	34

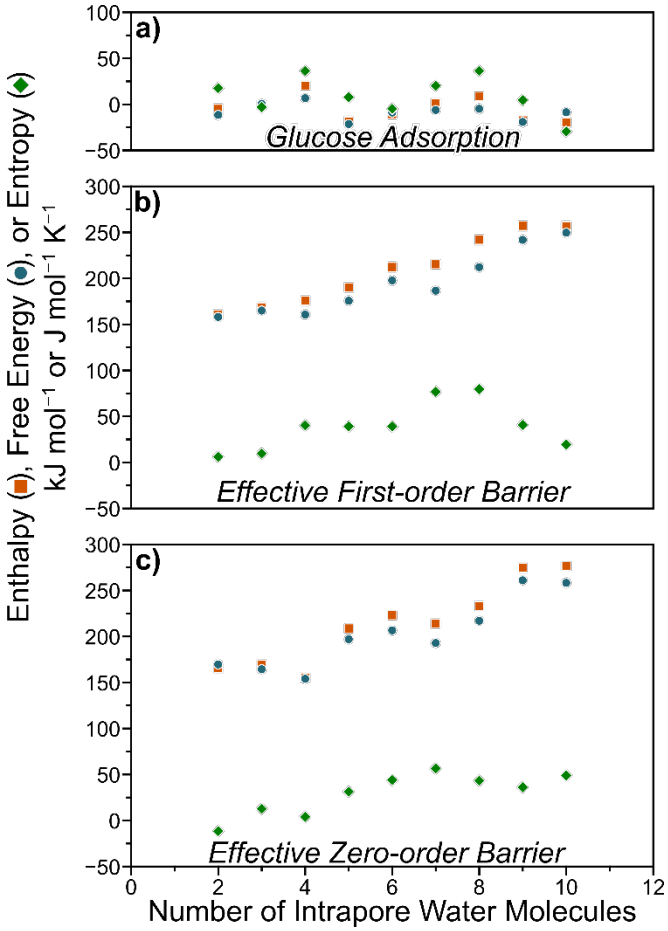

Figure 4.55: DFT-calculated glucose adsorption energies (a) and effective first-order (b) and zero-order (c) energy barriers for glucose-fructose isomerization. Enthalpies (squares) and free energies (circles) are shown in kJ mol^1 and entropies (diamonds) in J mol^1 K^1 (373 K). The intrapore water molecule density was assumed to remain constant during glucose adsorption and reaction for first-order analyses yet water molecules were allowed to reorient into lowest energy configurations in all cases.

5. QUANTIFICATION OF INTRAPOROUS HYDROPHILIC BINDING SITES IN LEWIS ACID ZEOLITES AND CONSEQUENCES FOR SUGAR ISOMERIZATION CATALYSIS

5.1 Abstract

Lewis acid sites catalyze aqueous-phase glucose-fructose isomerization at different turnover rates (per open Sn, 373 K) when located within zeolitic micropores containing silanol defects present in high (hydrophilic) and low (hydrophobic) densities, because hydrophilic binding sites stabilize extended networks of water molecules that entropically destabilize isomerization transition states. Sn-Beta zeolites with varying density of hydrophilic binding sites were prepared by grafting stannic chloride to different extents into different dealuminated Beta supports, which were synthesized from parent Al-Beta to contain varying initial aluminum content (Si/Al = 19–180, 0.4–3.2 Al (unit cell)$^{-1}$) and residual defect sites depending on the mineralizing agent used (e.g., fluoride or hydroxide). Intrapore packing densities of methanol were assessed from single-component adsorption isotherms (293 K) by comparing the total methanol uptake at the point of micropore filling to that of nitrogen (77 K). Intrapore methanol packing densities decreased systematically from 0.98 to 0.07 among Sn-Beta zeolites with increasing density of silanol (SiOH) groups, quantified by H/D isotopic exchange with D_2 in temperature-programmed surface reactions (500–873 K). The density of intraporous SiOH groups is quantifiable from IR spectra (2275 cm^{-1}) of Sn-Beta samples saturated with deuterated acetonitrile (CD_3CN, 303 K), because van der Waals interactions with zeolitic walls leads to preferential CD_3CN adsorption at SiOH groups at intrapore locations over such groups located at extracrystalline surfaces. IR spectra collected at low partial pressures of methanol ($P/P_0 < 0.2$, 303 K) provide evidence that methanol molecules arrange in isolated

clusters within microporous voids of Sn-Beta with low silanol densities ($<$ 1 silanol (unit cell)$^{-1}$), but form extended hydrogen-bonded networks within those containing high silanol densities ($>$ 1 silanol (unit cell)$^{-1}$). As a result, Sn-Beta zeolites prepared post-synthetically from dealuminated Beta supports that initially contained a lower density of framework vacancy defects (parent Si/Al $>$ 100, $<$ 0.6 Al (unit cell)$^{-1}$) showed aqueous-phase first-order glucose isomerization rate constants (per open Sn, 373 K) that were 4x higher than those measured on Sn-Beta prepared with higher initial density of vacancy defects (parent Si/Al $<$ 100, $>$ 0.6 Al (unit cell)$^{-1}$). These findings enable developing strategies for post-synthetic preparations of hydrophobic Lewis acid zeolites and methods to quantify their intraporous hydrophilic binding site density, and provide links between their intraporous defect sites and turnover rates of sugar isomerization catalysis in aqueous media.

5.2 Introduction

Microporous zeolites and molecular sieves are crystalline oxide structures comprised of tetrahedrally-coordinated silicon atoms, which can be isomorphously substituted with tetravalent metal heteroatoms (e.g., Sn^{4+}, Ti^{4+}) to generate isolated framework Lewis acid sites [5]. These Lewis acid centers can be located within hydrophobic micropores of zeolites as in the case of Sn-Beta, which can be prepared via hydrothermal crystallization using cationic tetraethylammonium (TEA^+) structure directing agents and fluoride anions (413 K, >20 days) that selectively form nonpolar siloxane bridges and minimize formation of anionic siloxy defects as otherwise occurs in hydroxide media [5, 11, 12]. Post-synthetic incorporation of Sn heteroatoms through grafting of stannic chloride precursors into dealuminated Beta supports via vapor-phase deposition [17], solid-state ion exchange [18–20], or liquid-phase grafting [22–24], however, provide routes to locate framework Sn sites in microporous cavities that also contain silanol groups, often present as residual framework vacancy defects because of incomplete reactions with Sn precursors.

The structure and stability of extended networks of polar molecules around framework Lewis acid sites depends on the density of silanol groups and their proximity within zeolitic frameworks [16, 116, 117]. Differences in the density of silanol groups within Lewis acid zeolites of varied treatment history are detected by differences in water uptakes in single-component water adsorption isotherms (293 K) at a relative pressure of 0.2 [16, 41], a value that represents the micropore filling of hydrophobic micropores with cyclohexane [83]. This water uptake, however, represents an integral measurement of adsorption onto silanol groups located within microporous voids, at external crystallite surfaces, and onto metal heteroatoms and other hydrophilic binding sites [26]. In contrast, methanol preferentially adsorbs (293 K) within microporous voids until the point of pore condensation, followed by adsorption at external crystallite surfaces [126–128, 210]. Terminal silanol groups and silanol nests are observed in the OH stretching region of infrared (IR) spectra of dehydrated samples

with peaks centered at 3740 cm^{-1} [103] and 3500-3600 cm^{-1} [24], respectively. IR spectra of deuterated acetonitrile (CD_3CN, 303 K) adsorbed onto solid acids show a perturbed $\nu(C{\equiv}N)$ peak at 2275 cm^{-1} reflecting nitrile hydrogen bonding with silanol groups [26, 80, 81]. Lastly, resonances at 1.8 and 2.0 ppm in ^1H NMR of dehydrated zeolites have been attributed to the presence of external and intraporous silanol groups, respectively [45]. The sensitivity of turnover rates in Lewis acid zeolites to variations in their micropore polarity motivates the development of methods to quantify intraporous hydrophilic binding sites.

Here, we evaluate the influence of the synthesis conditions on the micropore polarity of post-synthetically prepared Sn-Beta samples. Sn-Beta prepared via liquid-phase grafting in dichloromethane reflux (333 K) using dealuminated Beta supports of varied treatment history allowed preparing zeolites with varied densities of silanol groups. The framework polarity of Sn-Beta zeolites was assessed by the ability of methanol to pack at densities expected of liquid phases, evaluated by comparing its volumetric adsorption at the point of micropore filling (293 K) compared to that of nitrogen (77 K), which decreased systematically among samples with increasing defect density. Differences in structures of polar molecules stabilized within the pores of Sn-Beta zeolites were observed in the OH stretching region (∼3000-3800 cm^{-1}) of IR spectra after exposure to varying methanol pressures (P/P_0 = 0.02–0.20, 303 K), in which Sn-Beta-PS-F showed the presence of local clusters of methanol molecules that increase in size with increasing methanol partial pressures, while Sn-Beta-PS-OH showed evidence of forming extended networks of hydrogen-bonded methanol molecules under these conditions. The total number of hydrophilic binding sites was quantified through isotopic H/D exchange with D_2, while the number of intraporous silanol groups was quantified from IR spectra of Sn-Beta saturated with CD_3CN (2275 cm^{-1}, 303 K). The Sn-Beta-PS-F sample allowed incorporating Sn within micropores containing dilute silanol defects (< 1 (unit cell)$^{-1}$) insufficient to stabilize extended water networks during aqueous-phase glucose-to-fructose isomerization catalysis (373 K), resulting in 4x higher first-order rate constants than those measured on Sn-Beta-

PS-OH of higher silanol density (1.4–3.8 silanol (unit cell)$^{-1}$). These results link the post-synthetic preparation of solid Lewis acid zeolites to the density of hydrophilic binding sites relevant to forming solvent structures around kinetically-relevant transition states, which dictate aqueous-phase glucose-fructose isomerization rate constants (373 K).

5.3 Experimental Methods

5.3.1 Catalyst synthesis

Al-Beta zeolites were synthesized in hydroxide media with different Si/Al ratios by adapting the procedure reported by Chang et al. [12]. Tetraethylammonium hydroxide (TEAOH, Sigma Aldrich, 35%) and Ludox HS-30 colloidal silica (Sigma Aldrich, 30%) were added to a perfluoroalkoxy alkane container (PFA, Savillex Corp.) that was covered and stirred for 1 h at ambient conditions. Subsequently, sodium hydroxide (NaOH, Avantor, 98%) and deionized water (18.2 MΩ) were stirred until completely dissolved, followed by the addition of aluminum isopropoxide (Sigma Aldrich, 98%) to the synthesis gel. The resulting gel was stirred for 24 h at ambient conditions in the closed PFA container. The target H_2O/SiO_2 ratio was obtained by complete evaporation of ethanol and partial evaporation of water. The final gel composition was 1 SiO_2: x Al_2O_3: 13.24 H_2O: 0.18 TEAOH: 0.014 Na_2O (where x was 0.0165, 0.01, and 0.005 for target solid Si/Al ratios of 30, 50, and 100, respectively). The gel was placed into a 45 cm^3 Teflon-lined stainless steel autoclave and heated to 413 K for 7 days under static conditions. The recovered solids were washed thoroughly with water and acetone, isolated by centrifugation, and dried overnight at 373 K. Afterward, the solids were treated at 853 K (0.0167 K s^{-1}) for 10 h in air (Ultra Zero Grade, Indiana Oxygen, 1.67 cm^3 s^{-1} (g zeolite)$^{-1}$) in a muffle furnace (Nabertherm P300).

Al-Beta zeolites were also synthesized in fluoride media with different Si/Al ratios. Following a similar procedure, TEAOH was mixed with tetraorthosilicate (TEOS, Sigma Aldrich, >98 wt.%) and stirred for 1 h in a closed PFA container. Then, deionized water and aluminum isopropoxide were added and the resulting synthesis gel was stirred for 24 h in the covered PFA container. After reaching the desired H_2O/SiO_2 ratio by evaporation of ethanol and water, hydrofluoric acid (HF, Sigma Aldrich, 48 wt.%) was added to the synthesis gel and stirred manually with a Teflon spatula for ∼300 s. Dealuminated Beta zeolites (initial Si/Al = 54) were used as

seeds for this synthesis (4 wt.% of SiO_2). The final gel molar ratio was 1 SiO_2: 0.02 Al_2O_3: 7.52 H_2O: 0.54 TEAOH: 0.54 HF. As in the case of Al-Beta-OH syntheses, the gel was placed into a 45 cm^3 Teflon-lined stainless steel autoclave and heated to 413 K for 7 days under static conditions. The recovered solids were washed thoroughly with water and acetone, isolated by centrifugation, and dried overnight at 373 K. Afterward, the solids were treated at 853 K (0.0167 K s^{-1}) for 10 h in air (1.67 cm^3 s^{-1} (g zeolite)$^{-1}$) in a muffle furnace.

Dealumination treatments of Al-Beta zeolites were performed using nitric acid. In a typical dealumination procedure, 25 cm^3 of concentrated nitric acid (HNO_3, Avantor, 69%) were added to 1 g of Al-Beta and stirred in a covered PFA jar for 16 h at 353 K. The recovered solids were washed thoroughly with water until neutral pH was observed in the supernatant, isolated by centrifugation, and dried overnight at 373 K. Dealuminated Beta zeolites were used for liquid-phase grafting of tin precursors in dichloromethane reflux (333 K). In a typical post-synthetic procedure, dealuminated Beta zeolites were placed into a three-neck round-bottom flask (500 cm^3) with a septum stopper (white rubber, Ace Glass) on one of the openings, connected to a Schlenk line, and dried overnight at 423 K under vacuum conditions ($\sim$0.005 kPa, Oerlikon Trivac 140002E2). Separately, dichloromethane (Sigma Aldrich, 99.8%) was dried using molecular sieves (W. R. Grace, Type 3A, Grade 562, 4-8 mesh) for 72 h in inert atmosphere (Argon, Indiana Oxygen, 99.999%) prior to grafting procedures. Dichloromethane was added to the round-bottom flask through moisture-free cannula transfer, followed by tin (IV) chloride ($SnCl_4$, Sigma Aldrich, 1 M in dichloromethane) addition (0.001–0.040 mol Sn (g zeolite)$^{-1}$) with 1 or 10 cm^3 syringes (Becton, Dickinson, and Company) with attached precision needles (Becton, Dickinson, and Company). The resulting solution was heated to 333 K for 7 h under reflux conditions in argon. After reflux procedures were completed, solids were recovered by centrifugation, washed thoroughly with $\sim$120 cm^3 (g zeolite)$^{-1}$ of methanol (Sigma Aldrich, 99.9%), and dried overnight at 373 K. The recovered solids were treated at 473 K

(0.05 K s^{-1}) for 6 h and 823 K (0.05 K s^{-1}) for 6 h in air (1.67 cm^3 s^{-1} (g zeolite)$^{-1}$) in a muffle furnace.

Samples are represented as M-Beta-X-Y-Z, where M corresponds to the metal heteroatom in the framework, X represents whether the samples were prepared hydrothermally (HT) or post-synthetically (PS), Y represents the mineralizing agent of the parent Al-Beta (e.g., OH for hydroxide media and F for fluoride media), and Z represents the Si/M molar ratio.

5.3.2 Catalyst Characterization

Powder X-ray diffraction (XRD) patterns were collected in the range 4–40° of 2θ (scan rate of 0.0044° s^{-1} and a step size of 0.02°) using a Rigaku Smartlab X-ray diffractometer with a Cu κ α X-ray source (1.76 kW) and an ASC-6 automated sample changer (Section 5.7.1, Supporting Information).

Vapor-phase N_2 (77 K) and CH_3OH (293 K) adsorption isotherms were collected with a Micromeritics ASAP2020 instrument. Typically, ∼0.04 g of zeolite sample, sieved to retain particles between 180–250 μm in diameter, were degassed by heating under vacuum (<0.0007 kPa) to 393 K for 2 h and 623 K for 8 h prior to adsorption measurements. The micropore volume was determined from semi-log derivative analysis of the isotherm ($\delta(V_{ads}/g)/\delta(\log(P/P_0)$ vs. $\log(P/P_0)$), where the first maximum represents the micropore filling transition and the subsequent minimum represents the end of micropore filling (Section 5.7.2, Supporting Information).

Atomic absorption spectroscopy (AAS) was performed with a Perkin Elmer AAnalyst 300 to determine bulk elemental compositions. The instrument was calibrated prior to measurements with standards for each metal (Alfa Aesar, TraceCERT, ±4ppm). Samples (∼0.02 g) were dissolved overnight in 2 g of HF (48 wt.%, Alfa Aesar) and diluted with ∼50 g of deionized water. The measured values of absorbance were collected at 284.0 nm and 396.2 nm in an acetylene/nitrous oxide flame for Al and Sn, respectively. The Si/M ratios were calculated using the unit cell formula for the Beta framework topology. The fraction of vacancies grafted (Sn/vacancy) were calculated

from the molar ratio of Sn in the final material to the Al present initially in the Al-Beta sample, which assumes that every Al atom was removed from the framework and formed a vacancy available for grafting.

Diffuse reflectance UV-Vis spectra were collected using a Varian Cary 5000 spectrometer with an *in situ* Harrick Praying Mantis cell. Spectra were collected at after dehydration treatments in flowing helium (4.17 cm^3 s^{-1} (g zeolite)$^{-1}$) at 523 K ($\sim$0.5 K s^{-1}) for 0.5 h [26]. All spectra were corrected with poly(tetrafluoroethylene) (PTFE, 1 μm, Sigma Aldrich) as the 100% reflectance standard at all conditions (ambient and dehydrated) and converted to absorption spectra using the Kubelka-Munk function (F(R)) (Section 5.7.3, Supporting Information).

Quantification of the silanol groups in Sn-Beta samples was performed by H/D isotopic exchange experiments carried out in an Autochem II 2920 Chemisorption analyzer equipped with an SRS RGA 200. Typically, $\sim$0.050 g of Sn-Beta were treated in air (0.83 cm^3 s^{-1}) at 823 K (0.083 K s^{-1}) for 2 h, then cooled down to 303 K, and maintained at 303 K in flowing argon (0.83 cm^3 s^{-1}) for 0.5 h. Afterward, samples were exposed to gas-phase D2 (5% in argon, 99.999%, UHP, Matheson Tri-gas,, 0.83 cm^3 s^{-1}) and heated to 873 K (0.167 K s^{-1}) for 0.5 h. The evolution of HD molecules, monitored through the RGA m/z = 3 signal, was quantified to calculate the density of silanol groups and is collected for Sn-Beta-PS samples in Figs. 5.17–5.19 (Supporting Information). The response factor of HD will be estimated as the geometric average of response factors of the H_2 and D_2 [211].

Infrared (IR) spectra were collected using a Nicolet 4700 spectrometer with a Hg-Cd-Te (MCT, maintained at 77 K by liquid N_2) detector by averaging 64 scans at 2 cm^{-1} resolution from 4000 to 400 cm^{-1} and were taken relative to an empty cell background reference collected under dynamic vacuum (rotary vane rough pump, Alcatel 2008A, <0.01 kPa) at 303 K. Self-supporting wafers of zeolite samples (0.02–0.04 g cm^{-2}) were sealed within a custom-built quartz IR cell with CaF_2 windows [163], which was inserted into a mineral-insulated resistive heating coil (ARi Industries) encased in an alumina silicate ceramic chamber (Purdue Research Machining Services).

The quartz IR cell was connected to a custom glass vacuum manifold that was used for sample pretreatment and exposure to controlled amounts of CD_3CN (Sigma-Aldrich, 99.96% D-atom). Prior to measurement of spectra at 303 K, wafers were treated in flowing dry air (6.66 cm^3 s^{-1} (g zeolite)$^{-1}$) purified by an FTIR purge gas generator (Parker Balston, <1 ppm CO_2, 200 K H_2O dew point) to 723 K (0.083 K s^{-1}) for 1 h, and then held under dynamic vacuum (rotary vane rough pump, Alcatel 2008A, <0.01 kPa) at 723 K for 1 h before cooling under dynamic vacuum to 303 K. After sufficient dosing to saturate the samples until equilibrium with a residual gas phase pressure of CD_3CN (0.07–0.67 kPa), samples were exposed to dynamic vacuum (at 303 K) in order to remove gas-phase and weakly-bound species, which occurred when the pressure was recorded as 0.0 kPa. IR spectra reported here were baseline-corrected and normalized to combination and overtone modes of zeolite Si-O-Si stretches (1750–2100 cm^{-1}). Integrated molar extinction coefficients (E) for CD_3CN bound to open (2316 cm^{-1}) and closed (2308 cm^{-1}) Sn sites, small domains of tin oxide (2287 cm^{-1}, hydrogen-bound to Si-OH sites (2275 cm^{-1}), and physisorbed or gas phase CD_3CN (2265 cm^{-1}) on Sn-Beta determined in Harris et al. [26] were used to quantify the density of each species.

5.3.3 Kinetic studies of glucose isomerization

Glucose isomerization (373 K) studies were performed in batch reactors with 1% (w/w) glucose (Sigma Aldrich, ≥99.5%) solutions in water (18.2 MΩ), controlled to a pH of 4 (Mettler Toledo Seven Compact pH Ion S220 probe) by addition of hydrochloric acid (Macron, 37%) and then filtered with 0.2 μm PTFE filters (VWR). In a typical experiment, ∼0.01 g of catalyst were added to 10 cm^3 glass batch reactors (VWR) and sealed with crimp tops (PTFE/silicone septum, Agilent). The reactor containing the catalyst was heated to 373 K for 600 s. In a separate 2 cm^3 vial, the reactant solution was heated to 373 K for 600 s. The reaction was started by injecting the preheated reactant solution through the silicone septum in the crimp top into the reactor containing the preheated catalyst. The reactor remained at 373 K with

stirring at 750 RPM in an oil bath for reaction times chosen to maintain differential conditions (<5% conversion). Afterward, the reactors were quenched in an ice bath and the product solutions were filtered through 0.2 μm PTFE filters. Products were analyzed using high-performance liquid chromatography (HPLC, Agilent 1260 with a Hi-Plex Ca column) with an evaporative light scattering detector (Agilent 1260 Infinity ELSD). An aqueous mannitol (1% (w/w), Sigma Aldrich, ≥99.8%) solution was used as an internal standard for product quantification. Isotopic tracer studies were performed with 1% (w/w) glucose-D_2 (Cambridge Isotope Laboratories, 2-D, 98%) solutions in pH-controlled water (pH = 4) to obtain the kinetic isotope effects (Section 5.7.6, Supporting Information).

5.4 Results and Discussion

5.4.1 Preparation of solid Lewis acids with varying density of hydrophilic binding sites

All samples are referred to as M-Beta-X-Y-Z, where M is the metal heteroatom in the framework, X corresponds to the synthesis procedure (e.g., HT for hydrothermal and PS for post-synthetic), Y is the mineralizing agent used to prepare the parent aluminosilicate or stannosilicate (e.g., OH for hydroxide media and F for fluoride media), and Z is the Si/M ratio in the crystalline solid as measured by AAS. Sn-Beta-PS-Y-Z samples were prepared by liquid-phase grafting of stannic chloride into dealuminated Beta supports in dichloromethane reflux (333 K) [25], which involves the selective reaction between the chlorine ligands of $SnCl_4$ and the OH groups in the silanol nest defects formed after dealumination. XRD patterns of the parent Al-Beta samples, dealuminated Beta supports, and Sn-Beta-PS-Y-Z samples after high temperature oxidative treatment show diffraction peaks at 6–8∘ and 22.5∘ characteristic of the Beta topology (Figs. 5.8–5.11, Supporting Information). Micropore volumes were determined by analyzing the semi-log derivative of N_2 adsorption isotherms (77 K) and were 0.20–0.23 $cm^3\ g^{-1}$ for all samples studied, consistent with the Beta topology (Table 5.2, Supporting Information). These diffraction patterns and micropore volume measurements are consistent with the intended topological structure and microporous cavities of Beta molecular sieves.

Solid Lewis acids with varied amounts of hydrophilic binding sites were prepared via post-synthetic grafting of Sn precursors into dealuminated Beta supports of varied treatment history. Within the same dealuminated Beta support, increasing the starting concentration of tin tetrachloride in dichloromethane allows for higher incorporation of framework Sn heteroatoms under reflux conditions (333 K) [22, 25] with concomitant decreases in the residual density of vacancy defects. The density of residual silanol groups in Sn-Beta prepared by this route, however, is also influenced by the mineralizing agent used to prepare the parent Al-Beta sample. Synthesis of Al-Beta in hydroxide media promotes formation of anionic framework siloxy defects

(OSi^-) to compensate the cationic charge of the structure-directing agent (SDA) and become silanol groups after high temperature oxidative treatment, but not in fluoride media because occlusion of F^- to compensate cationic SDAs results in selective formation of framework siloxane connectivities [16, 116, 117]. Thus, Al-Beta was also prepared in fluoride media to decrease the density of residual silanol groups. We next develop methods to quantify the number of silanol groups and assess their location within zeolitic environments.

5.4.2 Evaluation of micropore polarity using alcohol probe molecules

Methanol adsorption isotherms (303 K) are used to qualitatively and semi- quantitatively probe the micropore polarity of solid Lewis acids of varied synthetic and treatment history. Single-component adsorption isotherms of water are more difficult to interpret than those of alcohols [16, 83] because water adsorbs non-selectively at binding sites within intracrystalline and extracrystalline locations. In contrast, alcohols adsorb selectively at binding sites within microporous voids until the point of pore filling and before adsorption occurs at extracrystalline silanol groups [125–128]. Methanol adsorption isotherms (303 K) collected on a suite of Sn-Beta are compiled in Fig. 5.1 (isotherms on all samples in Fig. 5.10, Supporting Information). Methanol adsorption onto Sn-Beta-HT-F samples occurs by a type V isotherm, characteristic of alcohol adsorption within hydrophobic micropores, where condensation within pores is driven by strong adsorbate-adsorbate interactions. Methanol adsorption on Sn-Beta-PS-OH samples, in contrast, occurs by a type I isotherm, wherein condensation within pores is driven by strong adsorbate-adsorbent interactions reflecting methanol hydrogen bonding with silanol groups. Sn-Beta-PS-F catalysts show type I adsorption isotherms when the parent Al-Beta sample initially contained high Al densities (Si/Al < 100, > 0.6 Al (unit cell)$^{-1}$), yet show a type V isotherm when the parent Al-Beta sample initially contained dilute Al content (Si/Al > 100, < 0.6 Al (unit cell)$^{-1}$). These results indicate that the initial density of vacancy defects, which depends on the mineralizing agent used to synthesize the parent Al-Beta material and its Al den-

sity, influences the density of hydrophilic binding sites in the final Sn-Beta sample. These results also suggest that the post-synthetic preparation of Sn-Beta with hydrophobic micropores requires methods to minimize the total number of intraporous hydrophilic binding sites, which includes silanol groups and Sn heteroatoms.

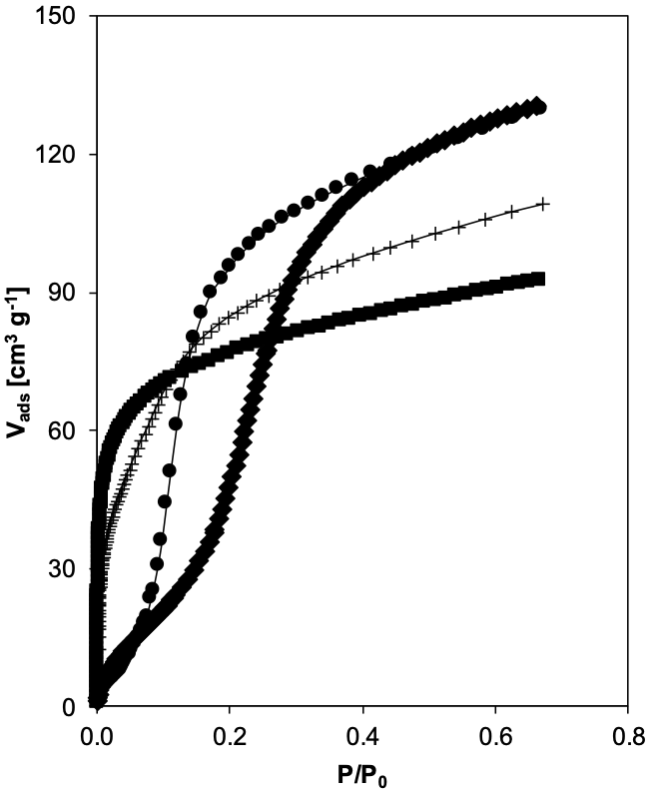

Figure 5.1: Methanol adsorption isotherms (293 K) of Sn-Beta-HT-F-220 (circles), Sn-Beta-PS-OH-80 (squares), Sn-Beta-PS-F-50 (plus), and Sn-Beta-PS-F-284 (diamonds).

The ability of methanol molecules to survey intraporous zeolitic environments before adsorption onto the external crystallite surface allows for the evaluation of its packing capacity within microporous cavities of different polarity. The methanol packing density (MPD) can be estimated using the following equation:

$$MPD = \frac{V_{ads,cH_3OH}\rho_{liq,CH_3OH}}{V_{ads,N_2}\rho_{liq,N_2}} \tag{5.1}$$

where V_{ads} terms reflect the volume of gas adsorbed at the point of micropore filling, and ρ values are the liquid densities of methanol and nitrogen. The effective packing density of methanol within microporous voids represents the volume of methanol adsorbed (in $cm^3\ g^{-1}$) with respect to the volume of nitrogen adsorbed (in $cm^3\ g^{-1}$) after micropore filling, assuming that nitrogen can pack at its liquid density within the micropores. This functional definition resembles that used to evaluate the microporous packing density of n-hexane and toluene within CIT-1 to evaluate micropore accessibility [212], whereas here the microporous packing density probes the capacity of methanol to pack within microporous cavities compared to the capacity of nitrogen to do so as a bulk liquid (maximum value of 1).

Methanol packing densities of Sn-Beta-PS-OH grafted within the same dealuminated Beta support increase with the fraction of vacancies grafted, as estimated from the elemental composition of the parent Al-Beta and assuming that every Al removed from the framework results in a vacancy defect (four silanol groups) that is available for Sn grafting (Table 5.1). Sn-Beta-PS-F-284, prepared from a lower starting vacancy defect density (starting Si/Al $>$ 100, $<$ 0.6 Al (unit cell)$^{-1}$), has a higher methanol packing density ($>$ 0.90) than Sn-Beta-PS-OH samples ($<$ 0.65). Differences in methanol packing density suggest that methanol interactions with pore surfaces influence the structure of adsorbed methanol complexes within Sn-Beta-PS-OH, but not Sn-Beta-PS-F, and decreases its density relative to liquid-phase methanol. These differences in packing density suggest that methanol molecules arrange differently within the pores of Sn-Beta-PS-OH and Sn-Beta-PSF-284 molecular sieves, as we explore next in the context of IR spectra collected in flowing methanol (303 K).

Table 5.1: Density of hydrophilic binding sites quantified via H/D isotopic exchange and IR spectra of samples saturated with CD_3CN (303 K), along with the methanol packing densities within solid Lewis acid zeolites.

Samples	Parent Si/Al	Fraction of Vacancies Grafted$_a$	Methanol Packing Density[b]	Total Silanol Density[c]	Intrapore Silanol Density[d]	Intrapore Silanol Density[e]
Sn-Beta-PS-OH-95	19	0.20	0.33	9.65	9.78	3.82
Sn-Beta-PS-OH-46	19	0.41	0.42	8.66	5.06	2.01
Sn-Beta-PS-OH-41	19	0.46	0.49	9.17	3.85	1.53
Sn-Beta-PS-OH-30	19	0.64	0.65	7.23	3.64	1.42
Sn-Beta-PS-OH-80	29	0.36	0.07	9.87	9.09	3.56
Sn-Beta-PS-OH-40	29	0.73	0.56	–	7.93	3.16
Sn-Beta-PS-OH-32	29	0.90	0.32	–	3.80	1.53
Sn-Beta-PS-OH-84	54	0.64	0.23	9.11	7.37	2.88
Sn-Beta-PS-OH-47	54	1.15	0.30	7.38	10.56	4.18
Sn-Beta-PS-F-50	45	0.90	0.85	–	3.57	1.41
Sn-Beta-PS-F-284	180	0.63	0.98	4.64	1.10	0.42

[a]Estimated by the molar ratio of Si/Al and Si/Sn (Sn/Al) from AAS.
[b] Defined by eq. 5.1.
[c] Units are $/10^{-4}$ mol g^{-1}. Quantified via H/D isotopic exchange during D_2 temperature-programmed surface reaction (500-873 K).
[d] Units are $/10^{-4}$ mol g^{-1}. Quantified by the IR peak at 2275 cm^{-1} in CD_3CN IR spectra (303 K) formation rate.
[e] Units are mol silanol (unit cell)$^{-1}$. Quantified by the IR peak at 2275 cm^{-1} in CD_3CN IR spectra (303 K) of saturated samples.

5.4.3 IR spectra of Sn-Beta in flowing CH_3OH

IR spectra in flowing methanol (303 K) were collected on a representative hydrophilic Sn-Beta sample (Sn-Beta-PS-OH-80, MPD = 0.07) in Figure 5.2a and on a representative hydrophobic Sn-Beta sample (Sn-Beta-PS-F-284, MPD = 0.98) in Figure 5.2b at various methanol partial pressures representing sections of methanol adsorption isotherms prior to micropore filling (P/P_0 = 0.018, 0.05, and 0.20). IR spectra collected after high temperature dehydration treatments in flowing helium (823 K, 2 h), show peaks for terminal silanol groups at 3740 cm^{-1} and perturbed silanol groups within vacancy defects at ∼3500–3600 cm^{-1} (Fig. 5.2) [24, 213]. The IR peak at 3740 cm^{-1} decreases with a concomitant increase in a broad peak at ∼3100–3500 cm^{-1} with increasing methanol partial pressures on both materials. The rapid decrease of the silanol peak (3740 cm^{-1}) in Sn-Beta-PS-OH-80 compared to that in Sn-Beta-PS-F-284 (even at P/P_0 = 0.02) reflects stronger interactions of methanol with Sn-Beta-PS-OH-80 whose micropores contain higher densities of silanol groups (Fig. 5.2), evident in their ∼14x difference in MPD values. Silanol groups (3740 cm^{-1}) in Sn-Beta-PS-F-284, however, were not saturated with methanol until P/P_0 = 0.05 (Fig. 5.2b), after which subsequent adsorption is driven by hydrogen bonding interactions among methanol molecules. Altogether, terminal silanol groups (3740 cm^{-1}) and vacancy defects (∼3500–3600 cm^{-1}) within zeolitic walls participate in hydrogen bonding networks with with methanol molecules (303 K) until they reach saturation coverages at conditions that depend on the density and proximity of such silanol groups.

Evaluation of the broad IR peak located at 3100–3500 cm^{-1} (Fig. 5.3) and the position of this peak maximum (Fig. 5.4) for Sn-Beta-PS-OH-80 and Sn-Beta-PS-F-284 after exposure to varying pressures of methanol (P/P_0 = 0.02–0.20) provides additional insights about the arrangement of methanol clusters within high-defect and low-defect zeolitic frameworks. The peak maximum for Sn-Beta-PS-F-84 shifts from 3330 to 3180 cm^{-1} with increasing methanol partial pressures (P/P_0 = 0.02–0.20 (Fig.

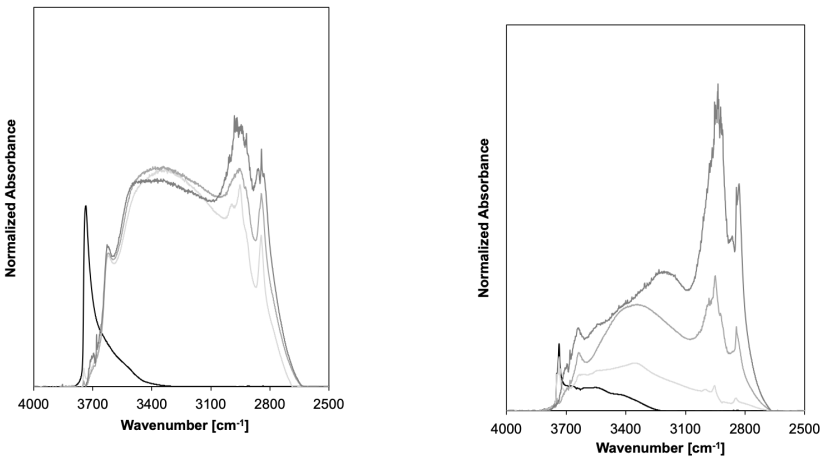

(a) (b)

Figure 5.2: IR spectra of Sn-Beta-PS-OH-OH-80 (a) and Sn-Beta-PS-F-284 (b) collected after high temperature oxidative treatments (823 K, black) and in flowing methanol (303 K) at $P/P_0 = 0.02$, 0.05, and 0.20 (increasing shade of gray).

5.4), reflecting the formation of methanol clusters that increase in size with increasing partial pressures [214,215]. This IR peak shift also suggests a change in the proximity of methanol molecules transitioning from liquid-like (3337 cm^{-1}) clusters at $P/P_0 =$ 0.02–0.05 to a configuration that resembles that of an extended solid (3187 cm^{-1}) at $P/P_0 = 0.20$ [216]. The peak maximum for Sn-Beta-PS-OH-80 (Fig. 5.4), however, does not vary as a function of methanol partial pressure. A broad peak centered at $\sim$3290 cm^{-1} at all methanol partial pressures suggests methanol clusters are present in extended networks formed through hydrogen bonding interactions [214–216], similar to water networks formed within dealuminated Beta supports in flowing water (293 K) [31, 38, 217].

IR spectra of Sn-Beta-PS-OH-80 and Sn-Beta-PS-F-284 in flowing methanol (303 K) suggest that the size of methanol clusters increases around hydrophilic binding sites present in both samples. In Sn-Beta-PS-F-284, the cluster size increases because methanol molecules are nucleated locally around silanol groups without the formation of extended networks through hydrogen bonding [214, 215], as previously predicted

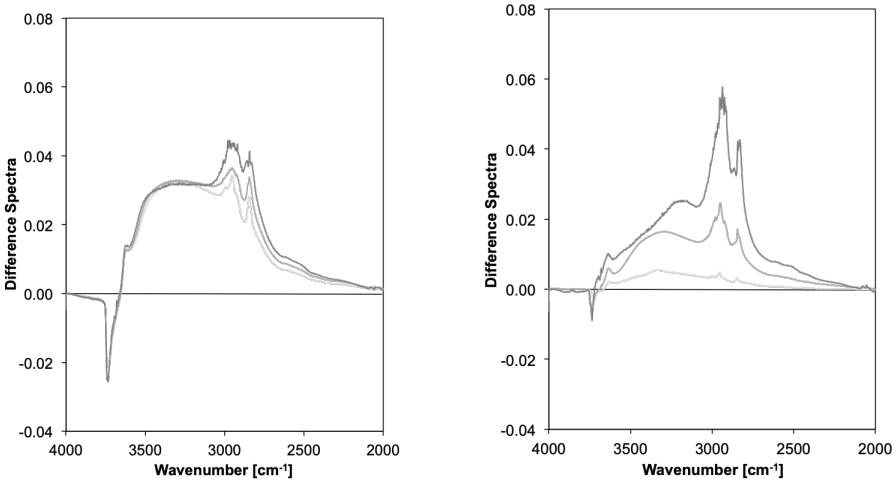

Figure 5.3: Difference spectra of Sn-Beta-PS-OH-80 (a) and Sn-Beta-PS-F-284 (b) after subtraction of the contributions from the dehydrated spectrum.

by ab-initio molecular dynamics simulations of isolated silanol groups in Sn-Beta in the presence of water [217]. The high density of hydrophilic binding sites in Sn-Beta-PS-OH-80, however, facilitates the formation of methanol clusters that are in close proximity and can form extended hydrogen-bonded networks, as observed by the broad OH stretching band at all the conditions studied here (Figs. 5.3-5.4). Developing quantitative relationships between the polar complexes formed within micropores of Sn-Beta and their treatment history, however, requires the quantification of silanol groups in Lewis acid zeolites. We next use H/D isotopic exchange and IR spectra of samples after exposure to CD_3CN (303 K) to quantify silanol groups.

5.4.4 Quantification of silanol groups in Lewis acid zeolites via H/D isotopic exchanges

Hydrogen atoms are located within terminal silanol groups, vacancy defects, and Brønsted acid sites present in zeolitic surfaces. The number of each site type in zeolitic materials can be probed through isotopic exchange with D_2 [211]. Transfer of protium species from Brønsted acid sites to bridging deuterated molecules results in the for-

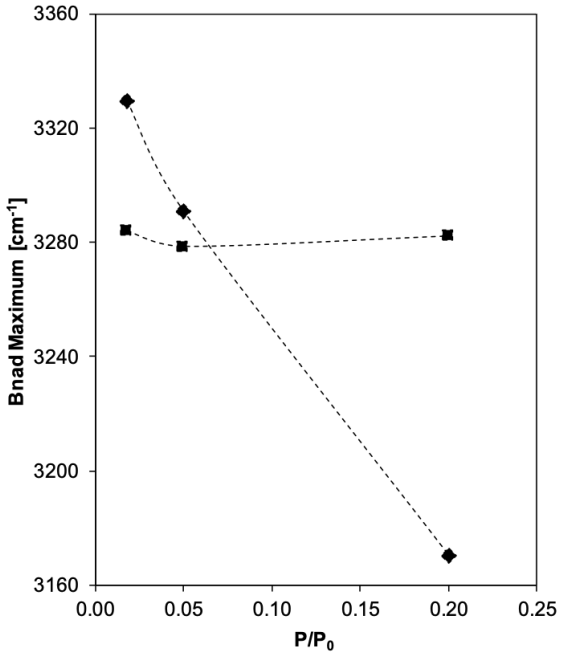

Figure 5.4: Band maxima of the OH stretching vibration of Sn-Beta-PS-OH-80 (squares) and Sn-Beta-PS-F-284 (diamonds) as a function of the methanol partial pressure.

mation of HD molecules in processes that take place at elevated temperatures (> 750 K) [218, 219]. Silanol groups also interact with gas-phase D_2 to exchange its hydrogen atom and produce HD molecules at lower temperatures (< 750 K) [220]. Prior to grafting procedures, framework Al heteroatoms, and their associated Brønsted acid sites, are removed from the framework during dealumination procedures (residual Si/Al > 1500, < 0.04 Al (unit cell)$^{-1}$) and become undetectable by IR spectroscopy [25]. HD formation over Sn-Beta zeolite prepared post-synthetically would thus only be associated with silanol groups (Section 5.7.5, Supporting Information).

The density of OH groups in Sn-Beta molecular sieves was quantified via H/D isotopic exchange with D2 and their values are compiled in Table 5.1. The number of OH groups (per g) decreases (9.78x10^{-4} to 3.64x10^{-4} mol g^{-1}) with increasing fractions of vacancies grafted (0.20 to 0.64), estimated from the molar ratio of Sn incorporated in Sn-Beta to the initial Al content in the parent Al-Beta material (Table 5.1). These

findings are consistent with the incorporation of framework metal heteroatoms into dealuminated supports upon consumption of silanol groups, as monitored previously by Q_3 site resonances in ^{29}Si NMR spectra [24] and the IR peak at 3500–3600 cm^{-1} associated with OH stretching vibrations of silanol defects [24, 27].

Comparing Sn-Beta-PS-OH samples prepared from the same dealuminated Beta support show that methanol packing densities (0.33 to 0.65) increase systematically as the density of OH groups quantified through H/D isotopic exchanges decreases (9.78x10^{-4} to 3.64x10^{-4} mol g^{-1}, Fig. 5.5). Figure 5.5 shows the density of OH groups for Sn-Beta samples as a function of the methanol packing density. The consumption of silanol groups upon Sn grafting decreases the density of OH groups that are available as binding sites for polar molecules, allowing methanol molecules to pack in structures that more closely resemble those in bulk liquid phases. OH groups quantified via HD exchanges correspond to silanol groups located both within microporous regions and at external crystallite surfaces, however, only those located within micropores influence the stability of co-adsorbed water structures that determine turnover rates in sugar isomerization catalysis, motivating the development of methods to selectively quantify OH groups within microporous voids.

5.4.5 Quantification of silanol groups via IR spectroscopy in Lewis acid zeolites with CD_3CN

Sn heteroatoms and silanol groups in Sn-zeolites are often detected via adsorption of probe molecules during acquisition of vibrational spectra, because perturbation of vibrational modes in probe molecules are sensitive to the properties of the binding site. CD_3CN, for instance, adsorbs within Sn-Beta to discern among Sn heteroatoms with an open (2316 cm$^{-1)}$ and closed (2308 cm^{-1}) configuration, small tin oxide domains (2287 cm^{-1}), and silanol groups (2275 cm^{-1}) [26, 30, 50, 221]. At saturation coverages (303 K), IR spectra collected on Sn-Beta can be deconvoluted into its component peaks, which can be quantified using molar extinction coefficients reported

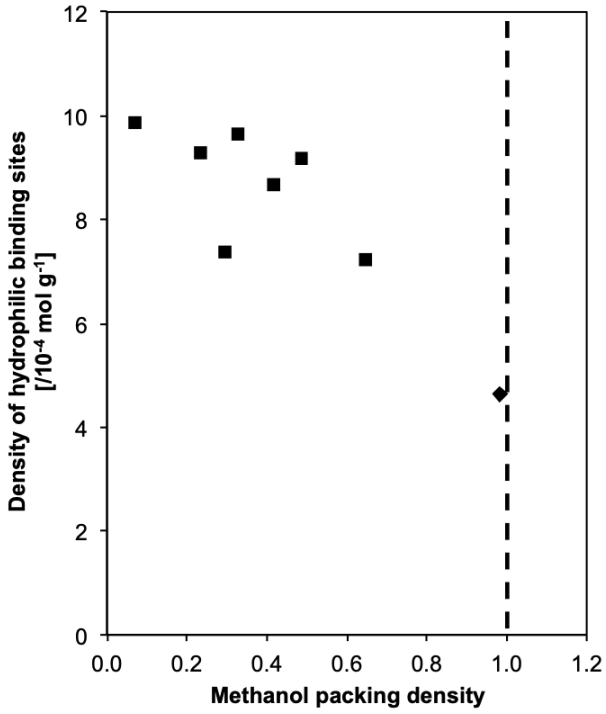

Figure 5.5: Methanol packing density (293 K) with respect to the density of hydrophilic binding sites quantified through H/D isotopic exchanges of Sn-Beta-PS-OH (squares) and Sn-Beta-PS-F-284 (diamonds). Dashed line represents the value associated with Sn-Beta-HT-F.

elsewhere16 to determine the density of Lewis acidic Sn heteroatoms and silanol groups.

The density of silanol groups (2275 cm^{-1}) was probed by quantification of IR spectra at saturation coverages of Sn-Beta with CD_3CN (303 K), and their values are compiled with respect to those obtained from H/D exchange in Figure 5.6 [26]. Comparisons of the OH groups quantified via H/D exchange and deconvolution of IR spectra after saturation of Sn-Beta with CD_3CN (303 K) shows a deviation from parity (Fig. 5.6), wherein OH groups quantified via H/D are systematically higher than expected if both methods surveyed the same pool of OH groups. CD_3CN titrates open Sn sites (2316 cm^{-1}), closed Sn sites (2308 cm^{-1}), and tin oxide in small domains (2287 cm^{-1}) concomitantly until saturation occurs, followed by adsorption

onto silanol groups (2275 cm^{-1}) [26]. IR peaks associated to adsorption onto silanol groups (2275 cm^{-1}), however, continue to increase in intensity after gas-phase CD_3CN species (2265 cm^{-1}) are detected and at conditions of higher dosing coverages than used to quantified spectra (0.0 kPa of gas-phase). These IR experiments performed at substoichiometric coverages of CD_3CN (303 K) suggest that CD_3CN interacts with multiple types of silanol groups (i.e., terminal silanol groups and silanol nests), some of which are preferentially titrated at 303 K [26]. Van der Waals interactions between adsorbates and the zeolitic walls causes preferential adsorption at silanol groups confined within microporous voids than those at extracrystalline locations. As a result, we surmise that CD_3CN preferentially titrates only a subset of silanol groups, which reside within the micropores of Sn-Beta, at conditions corresponding to saturation coverages. This hypothesis in in agreement with the overestimation of the silanol groups quantified via H/D isotopic exchange, as this technique quantifies the total number of silanol groups present within pores and at external surfaces.

Taken together, we have developed methods to quantify the density of hydrophilic binding sites, resulting in differences in the framework polarity (quantified via methanol packing density) among Sn-Beta samples of varied treatment history. Preparation of Sn-Beta-PS with high starting vacancy defects (starting Si/Al < 100, > 0.6 Al (unit cell)$^{-1}$) results in micropores that pack methanol (< 0.65) in extended, hydrogen-bonded networks because of their high density of intraporous silanol groups (> 1.41 silanol (unit cell)$^{-1}$). The micropore voids of Sn-Beta-PS with lower starting density of vacancy defects (starting Si/Al > 100, < 0.6 Al (unit cell)$^{-1}$), on the other hand, allows methanol to pack in structures similar to those of liquid methanol (> 0.90) because of its decreased density in internal silanol groups (< 1.41 silanol (unit cell)$^{-1}$). The ability of the microporous environments of Sn-Beta-PS-OH and Sn-Beta-PS-F to form different structures of polar molecules results in reaction environments influence turnover rates in aqueous-phase catalysis, as we probe next using glucose isomerization.

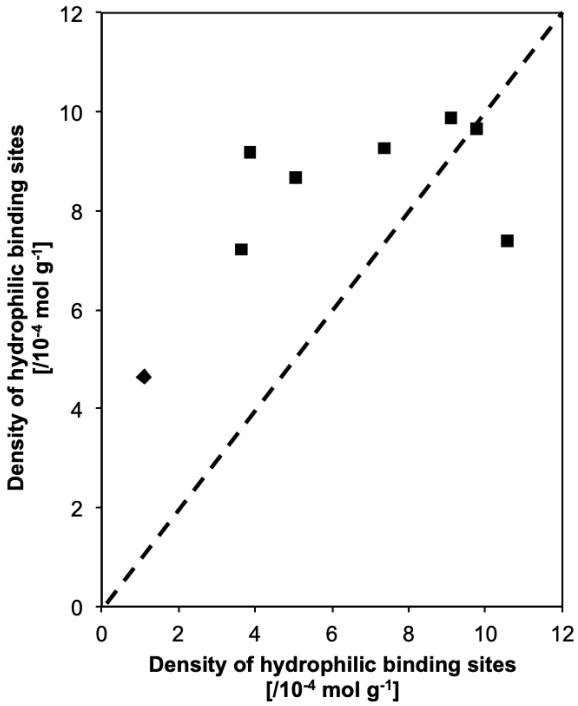

Figure 5.6: Density of hydrophilic binding sites quantified through H/D isotopic exchanges (y-axis) and by deconvolution of the 2275 cm^{-1} contribution in IR spectra after saturation with CD_3CN (303 K, x-axis) of Sn-Beta-PS-OH samples (squares) and Sn-Beta-PS-F-284 (diamonds). Dashed line represents parity.

5.4.6 Influence of intrapore silanol density on sugar isomerization catalysis

The influence of framework polarity on liquid-phase sugar isomerization catalysis was investigated using aqueous-phase glucose-fructose isomerization as a probe reaction. Glucose isomerization takes place via quasi-equilibrated desorption of two water molecules from open Sn sites, adsorption and ring-opening of glucose molecules, kinetically-relevant 1,2-hydride shift transition state, and quasi-equilibrated ring-closing and desorption of fructose molecules to regenerate open Sn sites [32, 34, 51]. In a kinetic regime characterized by a first-order dependence of turnover rates on the initial glucose thermodynamic activity, first-order rate constants reflect Gibbs free energy differences between two water molecules adsorbed onto open Sn sites,

which is the most abundant surface intermediate at dilute glucose concentrations (<10% (w/w) glucose in water), and the kinetically-relevant 1,2-hydride shift transition state [26, 35, 38, 51]. Figure 5.7 shows first-order isomerization rate constants (373 K) normalized rigorously by the number of active sites (open Sn sites, quantified by CD_3CN IR) [26, 32, 50] and uncorrupted by intracrystalline transport phenomena assessed from glucose-H_2/glucose-D_2 kinetic isotope effect values of 2.1 (Section 5.7.6, Supporting Information).

The polarity of the environment that confines open Sn sites within Sn-Beta was systematically modified through the incorporation of varied amounts of Sn heteroatoms within the same dealuminated Beta support (mol Sn (mol vacancy)$^{-1}$ = 0.15–1.15) [25]. Sn-Beta-PS-OH samples, however, show first-order isomerization rate constants (per open Sn, 373 K) that are invariant (within 2x) with increasing Sn density (Fig. 5.7) [22, 25, 120]. In addition, hydrothermally-synthesized Sn-Beta (Sn-Beta-HT-F) show isomerization rate constants (per open Sn, 373 K) that are 15x higher than Sn-Beta-PS-OH catalysts (Fig. 5.7). These first-order isomerization rate constants (per open Sn, 373 K) suggest that the post-synthetic preparation of Sn-Beta samples with glucose isomerization turnover rates comparable to Sn-Beta-HT-F would require further decreases in the density of intraporous silanol groups.

Reducing the density of silanol groups in Sn-Beta-HT-F samples, however, does not necessarily lead to differences in isomerization rate constants (per open Sn, 373 K) among Sn-Beta-PS-OH and Sn-Beta-HT-F samples, as shown by measured first-order rate constants of Sn-Beta-PS-F-50 that were similar to those measured on Sn-Beta-PS-OH (Fig. 5.7). The density of intrapore silanol groups (per unit cell, Table 5.1) in Sn-Beta-PS-F-50 suggests that there is at least one (∼1.40) silanol group available for the formation of clusters of polar molecules within each unit cell. Previously reported ab-initio molecular dynamics simulations of water structure and phase behavior at vacancy defects and Sn heteroatoms in Beta zeolites indicate that water molecules arrange in isolated clusters around Sn heteroatoms, but form delocalized networks of hydrogen bonded water when around silanol nests [217]. The lower isomerization rate

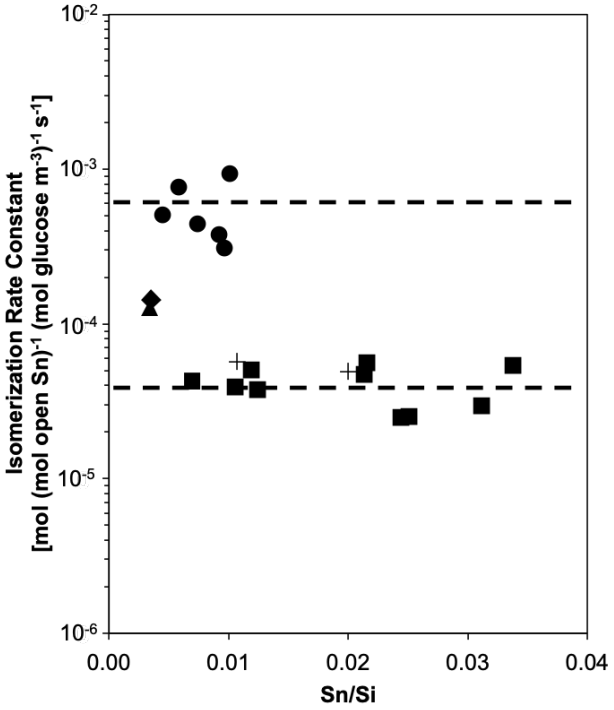

Figure 5.7: Isomerization rate constants (per open Sn, 373 K) of Sn-Beta-HT-F (circles) [26], Sn-Beta-PS-OH (squares) [25], Sn-Beta-PS-F with starting Si/Al = 50 (plus), Sn-Beta-PS-F with starting Si/Al = 180 (diamond), and Sn-Beta-PS-F with a starting Si/Al = 110 (triangle). Dashed lines represent the average isomerization rate constants (per open Sn, 373 K) of Sn-Beta-HT-F and Sn-Beta-PS-OH.

constants (per open Sn, 373 K) measured on Sn-Beta-PS-F-50 than on Sn-Beta-HT-F (0.3 Sn (unit cell)$^{-1}$, 0.3 silanol (unit cell)$^{-1}$) likely reflects interactions between water complexes formed around Sn heteroatoms (1.3 Sn (unit cell)$^{-1}$) and silanol groups (1.4 silanol (unit cell)$^{-1}$) to stabilize extended networks of water molecules within the pores of Sn-Beta-PS-F-50 during aqueous-phase catalysis.

The influence of silanol groups and Sn heteroatoms when present in high Sn densities ($>$ 0.6 Sn (unit cell)$^{-1}$) on the ability of micropores to stabilize extended networks of polar molecules was evaluated by post-synthetically grafting dealuminated Beta supports with a lower starting density of vacancy defects (starting Si/Al = 180, 0.35 Al (unit cell)$^{-1}$). In contrast to other post-synthetically prepared Sn-Beta samples,

Sn-Beta-PS-F-284 has an isomerization rate constant (per open Sn, 373 K) that is ∼4x higher than those measured on Sn-Beta-PS-OH (Fig. 5.7). The preparation of Sn-Beta-PS-F-294, a second sample from a different starting Al-Beta-HT-F (starting Si/Al = 110, 0.6 Al (unit cell)$^{-1}$), also resulted in isomerization rate constants that were 4x higher than other Sn-Beta-PS-OH samples (Fig. 5.7). These kinetic data suggest that the density of hydrophilic binding sites in Sn-Beta-PS-F-284 (Table 5.1) is lower than the threshold limit to form extended networks of water molecules within the micropores during catalysis, which would have resulted in a lower isomerization rate constant (per open Sn, 373 K).

The density of intrapore hydrophilic binding sites dictates the arrangement and proximity of polar molecules within the micropores of Sn-Beta molecular sieves. The high density of intraporous silanol groups (> 1 silanol (unit cell)$^{-1}$) and Sn heteroatoms (> 0.6 Sn (unit cell)$^{-1}$) within Sn-Beta-PS-OH facilitates the formation of extended networks of polar molecules (at $P/P_0 < 0.2$, section 3.4) that lead to low packing densities (<0.65, Table 5.1). Lower hydrophilic binding sites within Sn-Beta-PS-F-284 (< 1 silanol (unit cell)$^{-1}$, 0.2 Sn (unit cell)$^{-1}$), however, leads to nucleation of local clusters of polar molecules (section 3.4) and higher methanol packing densities (0.98, Table 5.1). Isomerization rate constants (per open Sn, 373 K), as a result, are 4x higher on Sn-Beta-PS-F-284 than on Sn-Beta-PS-OH. As in the case of glucose-fructose isomerization (per Ti, 373 K) over Ti-Beta zeolites [38], these differences in first-order rate constants (per open Sn, 373 K) can be attributed to an entropic penalty in forming hydride shift transition states caused by reorganization of the extended, hydrogen-bonded networks of water molecules present in microporous voids of Sn-Beta-PS-OH, but not Sn-Beta-PS-F-284. Altogether, these spectral and kinetic differences indicate that the density of hydrophilic binding sites around open Sn sites influences the structures of polar molecules and in turn sugar isomerization catalysis in polar solvents.

5.5 Conclusions

Synthetic protocols were developed in this study to interrogate and quantify hydrophilic binding sites within microporous environments of solid Lewis acids that catalyze glucose isomerization in aqueous media. Sn-Beta molecular sieves of varied framework polarity were prepared by variations in the synthesis conditions of the parent Al-Beta zeolite that underwent subsequent dealumination, and the grafting procedures used to insert Sn heteroatoms within framework vacancy defects. Within the same dealuminated Beta support, varied amounts of Sn heteroatoms were grafted to systematically decrease the amount of residual vacancy defects and silanol groups. The density of silanol groups was also modified by changes in the mineralizing agent and starting Al content of the parent Al-Beta sample.

The framework polarity of Sn-Beta samples was quantified from methanol packing densities, H/D isotopic exchange during temperature-programmed surface reaction (500–873 K), and IR spectra after saturation with CD_3CN (303 K). Low methanol packing densities (< 0.65) on Sn-Beta-PS-OH samples reflected the formation of extended networks of hydrogen-bonded methanol within highly-defective pore environments, while high methanol packing densities (> 0.90) observed for Sn-Beta-PS-F-284 reflected the ability of its micropores to allow methanol to pack in densities similar to that of its bulk liquid phase. These differences in micropore polarity were corroborated with the number of silanol groups quantified via H/D exchange that were higher for Sn-Beta-PS-OH (> 2.9 silanol (unit cell)$^{-1}$-1) than for Sn-Beta-PS-F-284 (< 2.9 (unit cell)$^{-1}$). Van der Waals interactions between the zeolitic walls and CD_3CN (303 K) allowed for selective quantification of silanol groups located within microporous voids rather than at extracrystalline surfaces, and lower numbers of silanol groups compared to those quantified by H/D exchange.

First-order glucose-fructose isomerization rate constants (per open Sn, 373 K) of Sn-Beta-PS-OH are invariant with Sn content (Si/Sn = 30–95, 0.7–2.1 Sn (unit cell)$^{-1}$) and residual silanol groups (3.57–10.56x10^{-4} mol g^{-1}, 1.4–4.2 silanol (unit

cell)$^{-1}$), and are 15x lower than those measured on Sn-Beta-HT-F (0.3 Sn (unit cell)$^{-1}$, 0.3 silanol (unit cell)$^{-1}$). The preparation of Sn-Beta-PS-F-284 from a lower starting density of vacancy defects (starting Si/Al $>$ 100, $<$ 0.6 Al (unit cell)$^{-1}$) showed isomerization rate constants (per open Sn, 373 K) that were $\sim$4x higher than those measured on Sn-Beta-PS-OH. The low density of intraporous silanol groups ($<$ 3x10^{-4} mol g^{-1}, 0.4 silanol (unit cell)$^{-1}$) suggest that more than one silanol per unit cell is required to stabilize extended networks of water molecules that, in turn, lead to entropic penalties in forming hydride shift transition states that decrease isomerization rate constants (373 K) [38]. The density of intrapore hydrophilic binding sites affects the structure and packing density of polar molecules within confined voids that contain active sites, and thus influence turnover rates in liquid media.

5.6 Acknowledgements

We acknowledge the financial support provided by the Purdue Process Safety and Assurance Center (P2SAC).

5.7 Supporting Information

5.7.1 X-ray diffractograms patters of Sn-Beta zeolites and parent Al-Beta

Samples are referred to as M-Beta-X-Y-Z, where M is the metal heteroatom in the framework, X corresponds to the synthesis procedure performed (e.g., HT for hydrothermal crystallization and PS for post-synthetic modification), Y represents the mineralizing agent of the starting aluminosilicate or stannosilicate (e.g., OH for hydroxide media and F for fluoride media), and Z is the Si/M ratio in the crystalline solid as measured by atomic absorption spectroscopy (AAS). XRD patterns in Figs. 5.8-5.10 were reported originally in Vega-Vila et al. [25] and are compiled here for reference, and for other Sn-Beta zeolites in Fig. 5.11. XRD patterns collected on Sn-Beta samples of varied treatment history, together with their parent Al-Beta and their dealuminated Beta supports, show distinctive diffraction peaks at 6-8◦ and 22.5◦, as expected for the Beta topology. Broad diffraction peaks observed on zeolites prepared from starting Al-Beta-HT-OH samples, but not Al-Beta-HT-F samples, are consistent with small primary crystallite sizes (∼500 nm), observed by scanning electron microscopy (SEM) images reported elsewhere [25], and the presence of highly defective zeolitic frameworks when parent Al-Beta were synthesized in hydroxide media compared to those prepared in fluoride media (Fig. 5.11).

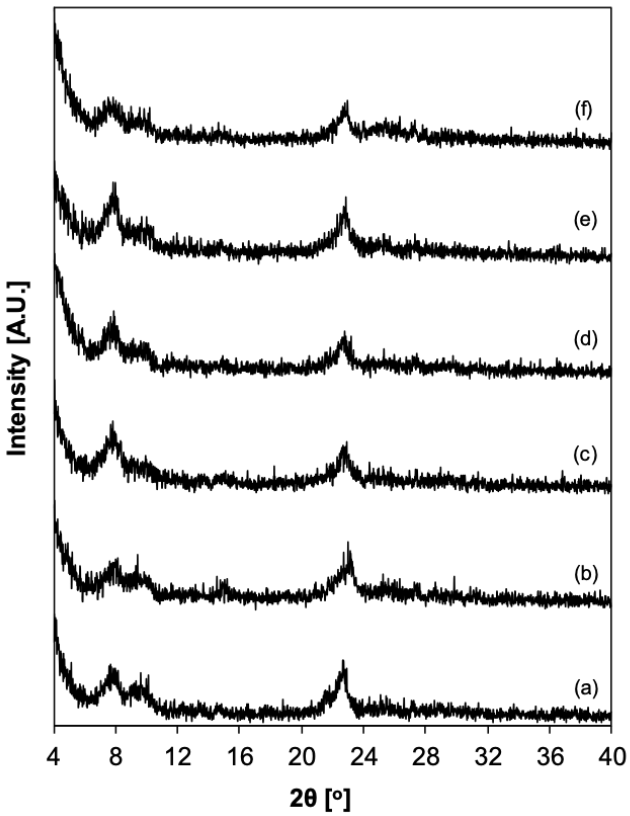

Figure 5.8: Powder XRD patterns of (a) Al-Beta-HT-OH-19, (b) dealuminated Beta from Al-Beta-HT-OH-19, (c) Sn-Beta-PS-OH-95, (d) Sn-Beta-PS-OH-46, (e) Sn-Beta-PS-OH-41, and (f) Sn-Beta-PS-OH-30.

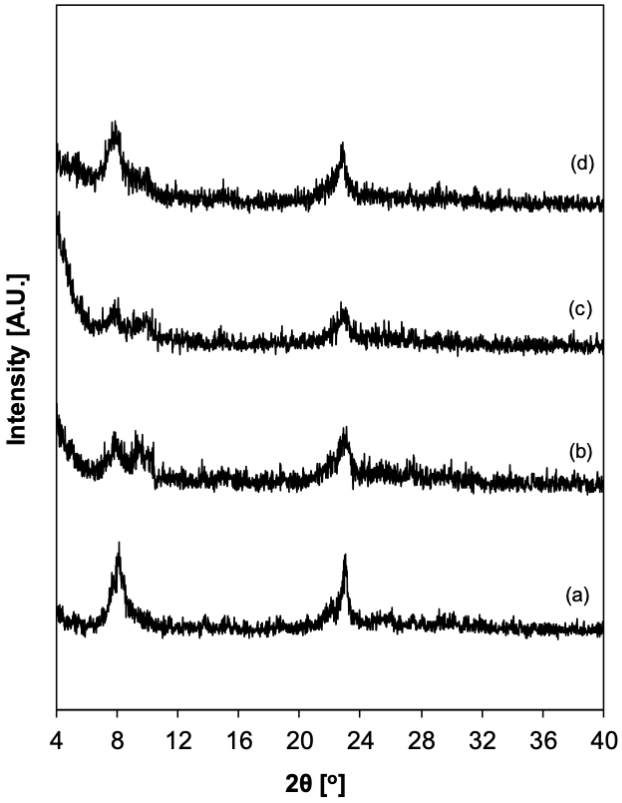

Figure 5.9: Powder XRD patterns of (a) Al-Beta-HT-OH-29, (b) Sn-Beta-PS-OH-32, (c) Sn-Beta-PS-OH-40, and (d) Sn-Beta-PS-OH-80.

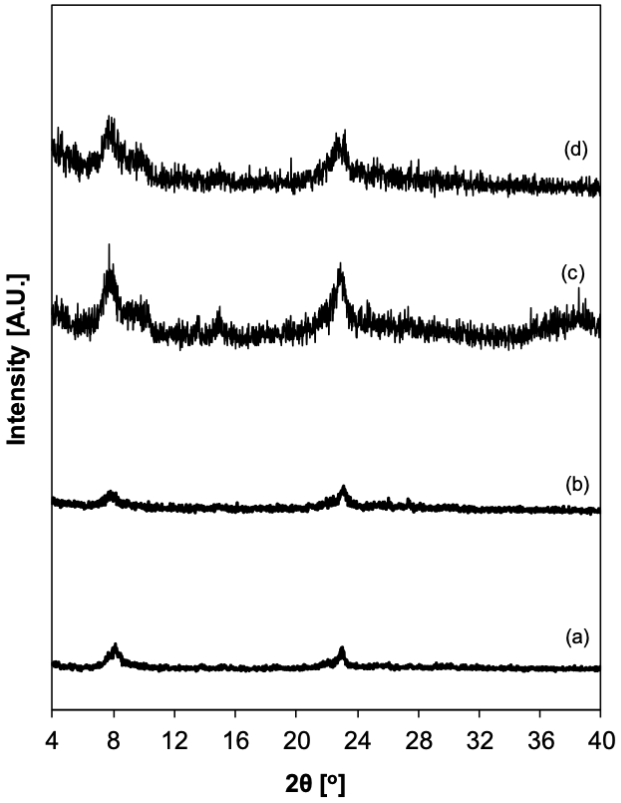

Figure 5.10: Powder XRD patterns of (a) Al-Beta-HT-OH-54, (b) dealuminated Beta from Al-Beta-HT-OH-54, (c) Sn-Beta-PS-OH-47, and (d) Sn-Beta-PS-OH-84.

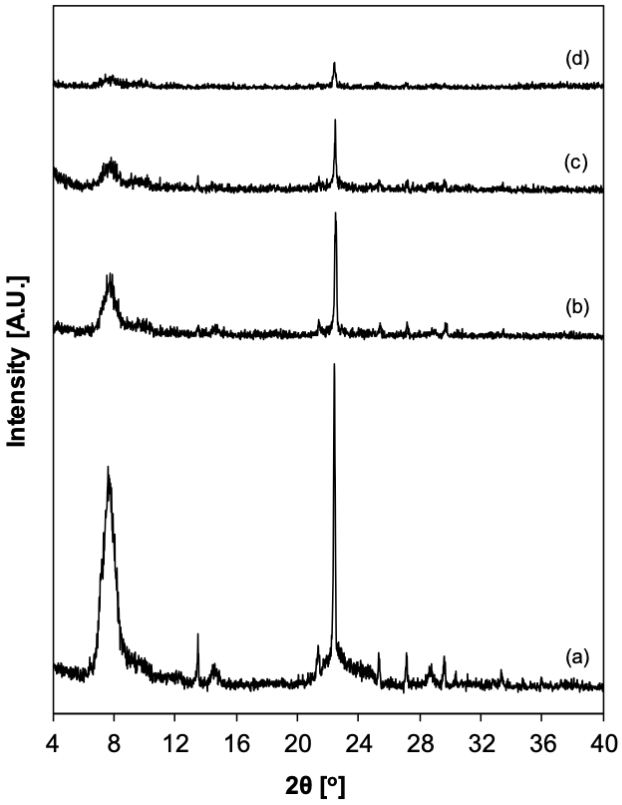

Figure 5.11: Powder XRD patterns of (a) Al-Beta-HT-F-45, (b) dealuminated Beta from Al-Beta-HT-F-45, (c) Sn-Beta-PS-F-93, and (d) Sn-Beta-PS-F-50.

5.7.2 Micropore volumes and physicochemical properties of zeolite samples

Elemental compositions and micropore volumes of zeolite samples are summarized in Table 5.2. Micropore volumes were determined by analyzing the semi-log derivative of the isotherm ($\delta(V_{ads}/g)/\delta(\log(P/P_0)$ vs. $\log(P/P_0)$), where the first maximum of the function represents the micropore filling transition and the subsequent minimum corresponds to the end of micropore filling. V_{pore} values ranged from 0.19-0.22 cm^3 (per g) on all samples, consistent with the Beta topology.

5.7.3 Diffuse reflectance UV-Vis spectra of stannosilicate samples

Diffuse reflectance UV-Visible (DRUV) spectra were measured on Sn-Beta-PS-F samples, and Sn-Beta-PS-OH samples previously reported in Vega-Vila et al. [25], and compiled in Figure 5.9. Spectra were collected at after treatment at 523 K for 0.5 h in flowing He (4.17 cm^3 s^{-1} (g zeolite)$^{-1}$) to discern tetrahedrally-coordinated Sn heteroatoms (band center < 220 nm) from small tin oxide domains (band center > 230 nm).2 Spectra and edge energies for Sn-Beta-HT-F-220 were first published in Harris et al. [26] Edge energies of Sn-Beta-PS (Table 5.3) were calculated by extrapolating linear regressions from the low energy absorbance in Tauc plots.

Table 5.2: Density of hydrophilic binding sites quantified via H/D isotopic exchange and IR spectra of samples saturated with CD_3CN (303 K), along with the methanol packing densities within solid Lewis acid zeolites.

Sample	Initial Si/Al[a, b]	Si/Sn[a, b]	V_{pore} [cm^3 g^{-1}][c]
Al-Beta-OH-19	19	–	0.22
Dealuminated Beta	>1500	–	–
Sn-Beta-OH-95	19	95	0.22
Sn-Beta-OH-46	19	46	0.19
Sn-Beta-OH-41	19	41	0.19
Sn-Beta-OH-30	19	30	0.16
Al-Beta-OH-29	29	–	0.24
Dealuminated Beta	>1500	–	–
Sn-Beta-OH-80	29	80	0.22
Sn-Beta-OH-40	29	40	0.19
Sn-Beta-OH-32	29	32	0.19
Al-Beta-OH-54	54	–	0.22
Dealuminated Beta	>1500	–	–
Sn-Beta-OH-84	54	84	0.20
Sn-Beta-OH-47	54	47	0.21
Al-Beta-OH-22	22	–	0.22
Dealuminated Beta	>1500	–	–
Sn-Beta-OH-144	22	144	0.23
Al-Beta-F-45	45	–	0.22
Dealuminated Beta	>1500	–	0.23
Sn-Beta-F-93	45	93	0.22
Sn-Beta-F-50	45	50	0.22

[a]Measured by AAS.
[b] Error are ±15%.
[c] Calculated from semi-log derivative of the N_2 isotherm.

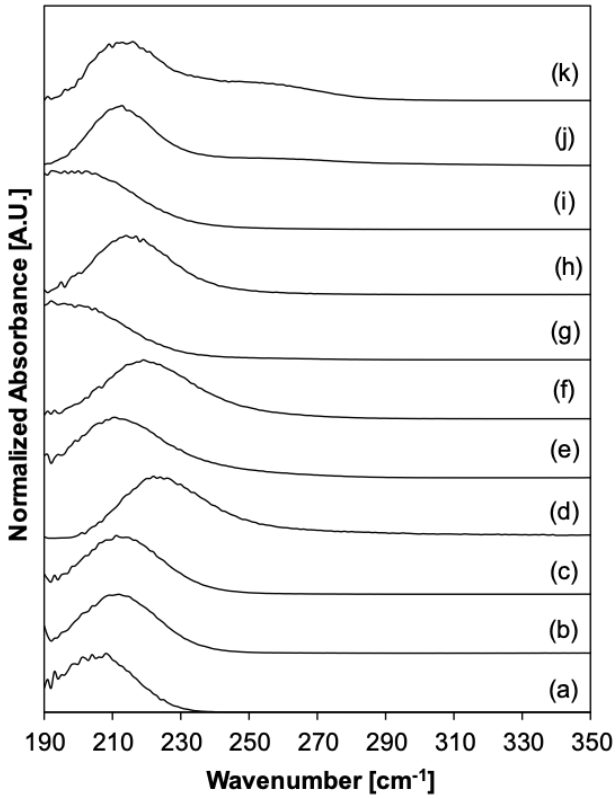

Figure 5.12: DRUV spectra of (a) Sn-Beta-PS-OH-95, (b) Sn-Beta-PS-OH-46, (c) Sn-Beta-PS-OH-41, (d) Sn-Beta-PS-OH-30, (e) Sn-Beta-PS-OH-32, (f) Sn-Beta-PS-OH-40, (g) Sn-Beta-PS-OH-80, (h) Sn-Beta-PS-OH-47, (i) Sn-Beta-PS-OH-84, (j) Sn-Beta-PS-F-93, and (k) Sn-Beta-PS-F-50 after dehydration treatments (523 K, 0.5 h).

Table 5.3: Density of hydrophilic binding sites quantified via H/D isotopic exchangeand IR spectra of samples saturated with CD_3CN (303 K), along with the methanolpacking densities within solid Lewis acid zeolites.

Sample	Band Center Maximum [nm][a]	Edge Energy[a]
Sn-Beta-OH-95	208	5.60
Sn-Beta-OH-46	212	5.42
Sn-Beta-OH-41	211	5.40
Sn-Beta-OH-30	222	5.06
Sn-Beta-OH-32	211	5.32
Sn-Beta-OH-40	219	5.15
Sn-Beta-OH-80	192	5.61
Sn-Beta-OH-47	214	5.32
Sn-Beta-OH-84	200	5.54
Sn-Beta-OH-144	193	5.60
Sn-Beta-F-93	213	4.35 (5.45)[b]
Sn-Beta-F-50	216	4.47 (5.37)[b]

[a]Originally reported in [25]

[b]Value in parenthesis represents the x-intercept of a distinct linear regime at a higher energy.

5.7.4 Assessment of the hydrophobicity of Sn-Beta with vapor-phase adsorption of CH_3OH at 293 K

CH_3OH adsorption isotherms (293 K) were collected for the Sn-Beta samples prepared-post-synthetically and one representative sample prepared hydrothermally in fluoride media [26] to evaluate the hydrophobic character of these zeolites. Type I isotherms were observed for Sn-Beta-PS-OH samples, as well as Sn-Beta-PS-F-50, representing micropore condensation driven by strong adsorbate-adsorbent interactions. Type V isotherms, however, were observed for Sn-Beta-PS-F-284 and Sn-Beta-HT-F-220, where condensation within the pores is driven by strong adsorbate-adsorbate interactions.

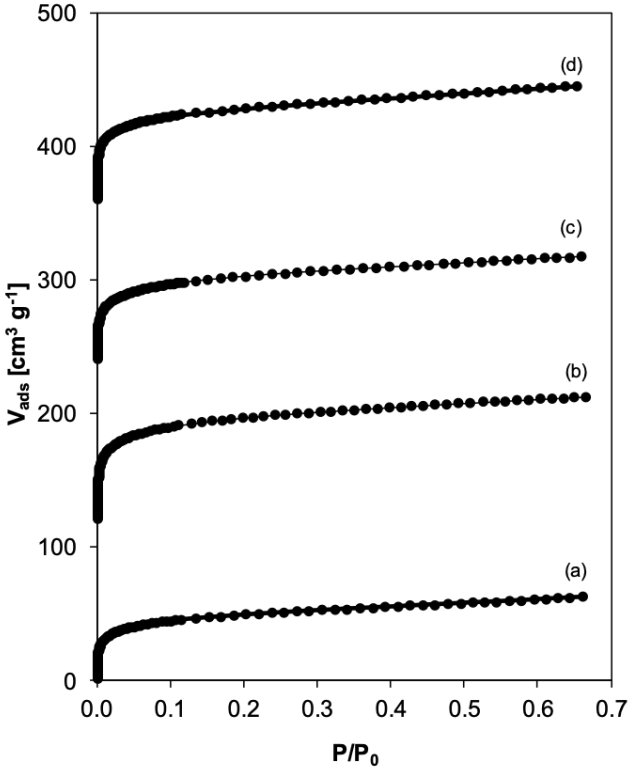

Figure 5.13: CH_3OH adsorption isotherms (293 K) of (a) Sn-Beta-PS-OH-95, (b) Sn-Beta-PS-OH-46, (c) Sn-Beta-PS-OH-41, and (d) Sn-Beta-PS-OH-30. Isotherms are offset by 120 cm^3 g^{-1} for clarity.

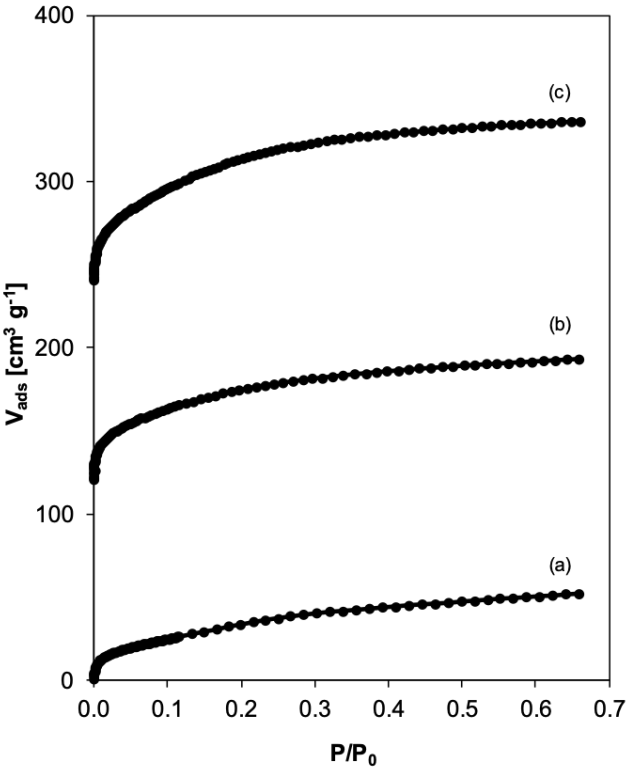

Figure 5.14: CH_3OH adsorption isotherms (293 K) of (a) Sn-Beta-PS-OH-32, (b) Sn-Beta-PS-OH-40, and (c) Sn-Beta-PS-OH-80. Isotherms are offset by 120 cm^3 g^{-1} for clarity.

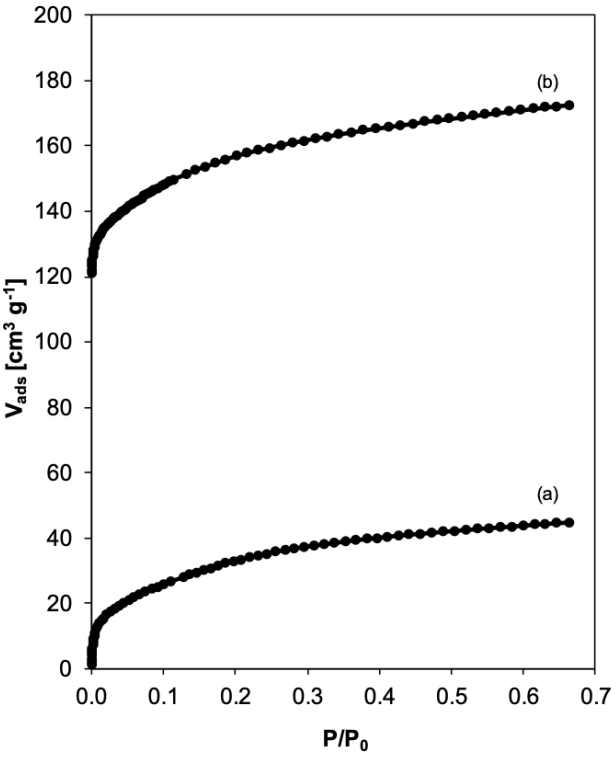

Figure 5.15: CH_3OH adsorption isotherms (293 K) of (a) Sn-Beta-PS-OH-47 and (b) Sn-Beta-PS-OH-84. Isotherms are offset by 120 cm^3 g^{-1} for clarity.

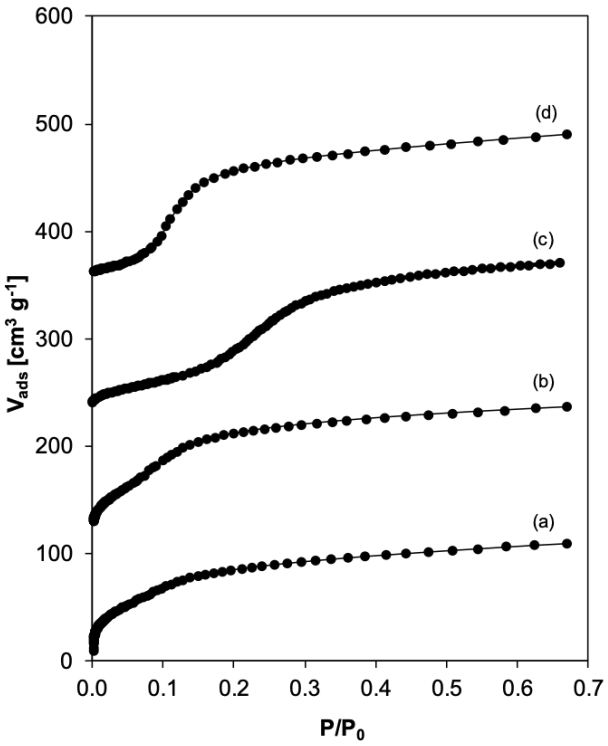

Figure 5.16: CH_3OH adsorption isotherms (293 K) of (a) Sn-Beta-PS-F-93, and (b) Sn-Beta-PS-F-50, (c) Sn-Beta-PS-F-284, and (d) Sn-Beta-HT-F-220. Isotherms are offset by 120 cm^3 g^{-1} for clarity.

5.7.5 Isotopic H/D exchange experiments on stannosilicates

Isotopic H/D exchange of surface OH groups of stannosilicates was performed by flowing 5% D_2 in a temperature programmed surface reaction (TPSR) to 873 K (0.167 K s^{-1}). In a typical TPSR experiment, Sn-Beta samples were treated in dry air (10 cm^3 s^{-1} g^{-1}) at 823 K for 2 h, cooled in flowing Ar (10 cm^3 s^{-1} g^{-1}), held at 303 K in flowing Ar for 0.5 h, and heated to 873 K (0.167 K s^{-1}). Signals were continuously recorded for m/z of 2 (H_2), 3 (HD), 4 (D_2), 20 (Ar^{2+}), and 40 (Ar^+). Sequential exchange of OH groups with HD to form H_2 was not detected, as H_2 was not evolved during TPSR experiments. HD formation rates (mol g^{-1} s^{-1}) were calculated from m/z = 3 signals and response factors estimated as the geometric average of the H_2 and D_2 response factors. HD formation rates for Sn-Beta samples prepared post-synthetically are collected in Figures 5.17–5.19.

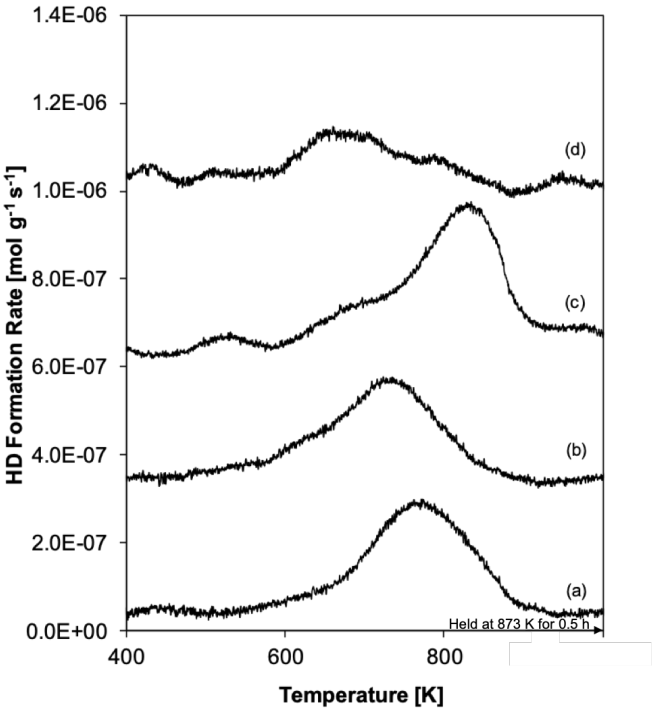

Figure 5.17: HD formation rate of (a) Sn-Beta-PS-OH-46, (b) Sn-Beta-PS-OH-41, (c) Sn-Beta-PS-OH-95, and (d) Sn-Beta-PS-OH-30. Formation rates are offset between samples for clarity.

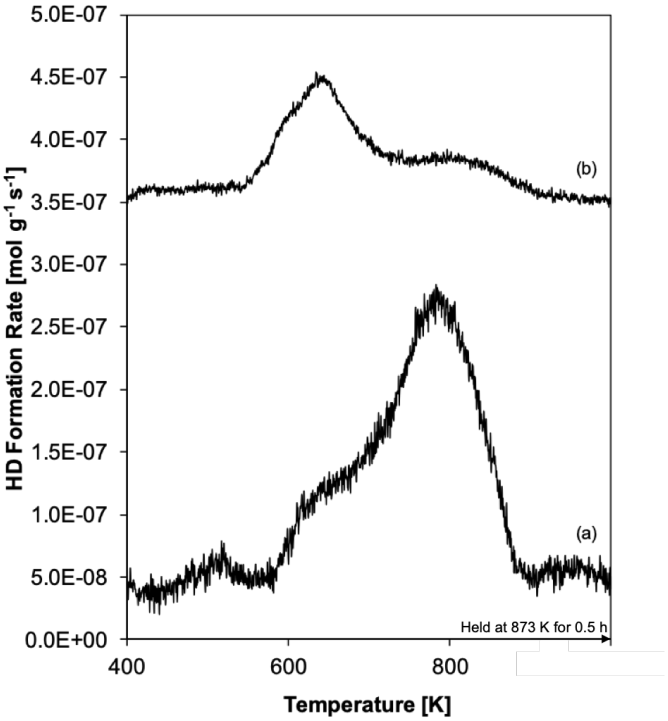

Figure 5.18: HD formation rate of (a) Sn-Beta-PS-OH-80 and (b) Sn-Beta-PS-F-284. Formation rates are offset between samples for clarity.

5.7.6 Assessment of intraparticle mass transfer limitations

Turnover rates (per open Sn, 373 K) of glucose-fructose isomerization show a first-order dependence on the initial glucose concentration at low values (<10% (w/w) in water), consistent with rates limited by kinetically relevant hydride shift steps [16, 26, 35]. Rates corrupted by intrazeolitic glucose transport, however, would also cause a first-order dependence on initial glucose concentration. First-order rate constants (373 K) measured with deuterated glucose reactants at their α-carbonyl position (glucose-D_2) should result in a kinetic isotope effect ($k_{isom.,unlabeled}/k_{isom.,labeled}$ or k_H/k_D) equal to ∼2.1 when measured rates are limited by 1,2-hydride shift (C-H scissoring vibrational frequency of ∼1500 cm^{-1}) [34], and result in to ∼1.4 if rates are instead restricted by intracrystalline mass transfer [35]. Glucose-H_2/glucose-D_2

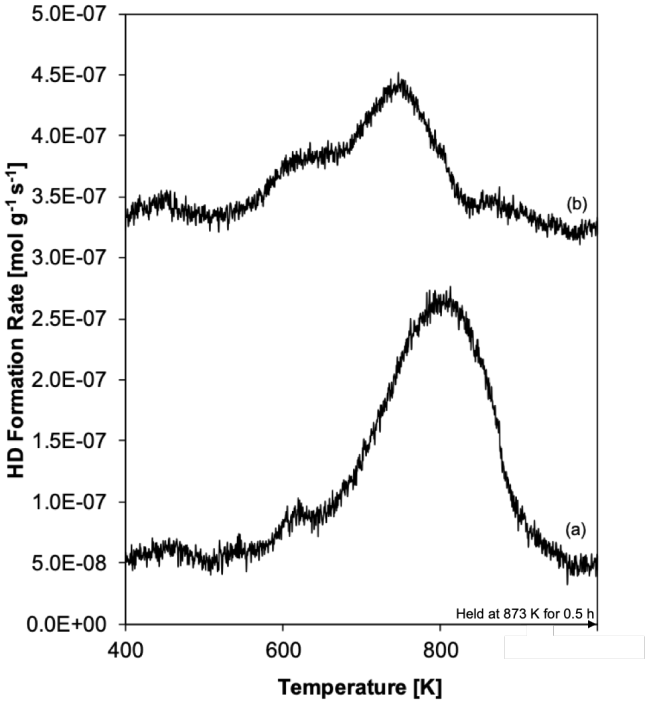

Figure 5.19: HD formation rate of (a) Sn-Beta-PS-OH-84 and (b) Sn-Beta-PS-OH-47. Formation rates are offset between samples for clarity.

KIE experiments performed on the Sn-Beta-OH sample with the highest measured isomerization rate constant (per total Sn, 373 K), which is the sample most likely to be limited by intracrystalline mass transport limitations, resulted in measurement of a k_H/k_D of ∼2.1 [25]. Thus, initial rates reported on all of the samples studied here are limited by rates of 1,2-hydride shift steps.

6. TIGHTER CONFINEMENT INCREASES SELECTIVITY OF D-GLUCOSE ISOMERIZATION TOWARDS L-SORBOSE IN TI-ZEOLITES

6.1 Abstract

Aqueous-phase isomerization of D-glucose to D-fructose and L-sorbose are catalyzed in parallel by Lewis acidic Ti sites in zeolite frameworks. Glucose isomerization turnover rates (per Ti, 373 K) are negligible when Ti sites are confined within mesoporous voids of silicates (Ti-MCM-41, TiO_2-SiO_2) and increase to high values when Ti sites are confined within twelve-membered ring (12-MR) micropores (Ti-Beta). Turnover rates decrease to lower values (by ∼20x) with further decreases in micropore size as Ti sites are confined within 10-MR pores (Ti-MFI, Ti-CON) because of transport restrictions, and reach undetectable values within the 8-MR pores of Ti-CHA as intrapore reactant diffusion is prevented altogether. Remarkably, the selectivity toward L-sorbose over D-fructose increases systematically as spatial constraints around Ti sites become tighter, and are >10 on Ti-MFI, reflecting the marked influence of confinement around Ti active sites on the selectivity between parallel stereoselective isomerization pathways of D-glucose.

6.2 Introduction

Catalytic routes to produce renewable chemicals from lignocellulosic biomass sources often involve strategies that convert sugar derivatives (e.g., glucose) via isomerization pathways using heterogenous Lewis acid catalysts [34, 222, 223]. The incorporation of tetravalent metal heteroatoms within silica-based zeolite frameworks provides access to a suite of catalysts that enable isolating Lewis acid sites of different identity and coordination [30–32, 51, 58] within secondary confining environments [38, 159], which provide two orthogonal design criteria to influence catalytic rates and selectivities. Confinement of active sites within microporous environments can prevent intrapore diffusion of large reactants (reactant shape selectivity) [224], influence product selectivity through relative diffusion rates of products of varying size (product shape selectivity) [225, 226] or through selective formation of specific transition states based on size restrictions (transition state selectivity) [227]. Confinement within microporous voids can also influence selectivity via the stabilization by van der Waals forces of certain transition states among parallel pathways [228]. Here, we report the influence of confining environment size on relative rates of reactions that form different stereoisomers of D-glucose, which demonstrates how confining microporous voids of Lewis acid zeolites can be tailored to selectively form certain products in biomass upgrading reactions.

Aqueous-phase isomerization of D-glucose to D-fructose on Lewis acidic Ti-Beta zeolites involves reaction mechanisms analogous to those on metalloenzyme catalysts (e.g., D-xylose isomerase) [34, 132], which proceed via kinetically-relevant 1,2-hydride shift as confirmed by isotopic tracer studies [51]. In a parallel pathway, D-glucose also produces L-sorbose on Ti-Beta zeolites, through an analogous 1,5-hydride shift transition state (Fig. 6.1) [35, 192]. In contrast to fructose, metalloenzymes are not known to produce sorbose from glucose [192], and other metallosilicates or Lewis acid zeolites (e.g., Sn-Beta) have not been reported to form sorbose in significant quantities [26, 32, 50]. Sorbose can be formed via Lewis base-catalyzed Lobry de

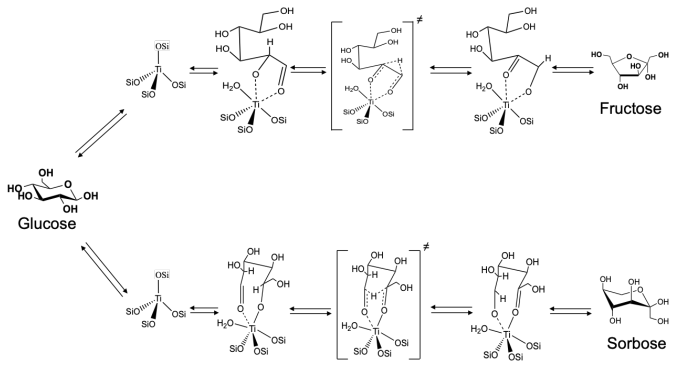

Figure 6.1: Reaction scheme for fructose and sorbose formation over tetrahedrally-coordinated Ti sites.

Bruyn-Alberta van Ekenstein rearrangements [229], but only as side-products in a mixture of undesirable products. Current synthetic pathways for converting glucose to sorbose follow a two-step process to reduce glucose to sorbitol via hydrogenation over Ni-based catalysts, followed by the selective oxidation of sorbitol to sorbose over D-sorbitol dehydrogenase [230], which in turn undergoes Pt-catalyzed oxidation into ascorbic acid, a vitamin C precursor [231]. Thus, zeolites containing isolated Ti active sites appear to be a unique class of heterogeneous materials capable of directly isomerizing D-glucose into L-sorbose, and here we investigate the effects of confinement on selectivity toward L-sorbose over D-fructose.

6.3 Experimental Methods

6.3.1 Synthesis of titanosilicates with varying pore sizes

Ti-Beta zeolites containing tetravalent metal heteroatoms were made via both hydrothermal synthesis procedures [106]. Hydrothermal Ti-Beta zeolites with fluoride mineralizing agents were synthesized using gel molar ratios of 1 TEOS / X TEOTi / 0.55 TEAOH / 7.5 H_2O / 0.55 HF where X = 0.008–0.013. In a typical Ti-Beta synthesis, 21.77 g of tetraethylammonium hydroxide (TEAOH, 35%, Sigma Aldrich) was diluted in 12.72 g deionized water in a perfluoroalkoxy alkane (PFA) jar that was covered and stirred at ambient temperature for 0.25 h. 20.00 g of tetraethylorthosilicate (TEOS, 98%, Sigma Aldrich) were then added and stirred for 0.75 h prior to the addition of ∼0.2 g of tetraethyl orthotitanate (TEOTi, 99.99%, Alfa Aesar). The jar was then sealed to stir for 12 h. The resulting solution was then exposed to air to evaporate ethanol and excess water to achieve the desired molar ratios. 2.16 g of hydrofluoric acid (HF, 48%, Alfa Aesar) were added to the resulting gel prior to the addition of 0.28 g of Si-Beta seeds. The resulting gel was loaded into a 45 cm^{-3} Teflon liner inside of a stainless steel autoclave (Parr Instruments) and placed into a forced convection oven (Yamato DKN-402C) at 413 K for 21 days while rotating (60 rpm). Recovered solids were washed with ∼150 cm3 of deionized water per gram, isolated by centrifugation, and dried for 16 h at 373 K in air. Organic occluded within the solids were removed through 10 h of high temperature oxidative treatment in flowing dry air (1.67 $cm^3\ s^{-1}\ g_{cat}{}^{-1}$, 99.999% UHP, Indiana Oxygen) at 823 K (0.0167 K s^{-1}).

Ti-MFI (TS-1) was hydrothermally-synthesized using gel molar ratios of 1 SiO_2 / 0.076 TEOTi / 1 NH_4F / 0.25 TPABr / 31.56 H_2O. In a typical synthesis, ammonium fluoride (NH4F, 98%, Sigma Aldrich) and tetrapropylammonium bromide (TPABr, 98%, Sigma Aldrich) were diluted in 31.46 g of deionized water and stirred for 0.25 h in a covered PFA jar. 3 g of fumed silica (Cab-o-sil SiO2, 99.9%, Cabot) were added to the synthesis gel and stirred for 0.75 h prior to the addition of 0.076 g of TEOTi. The resulting gel was covered and stirred overnight before evaporating

evolved ethanol and excess water to achieve the desired molar ratios. The resulting gel was loaded into a 45 cm^{-3} Teflon liner in a stainless steel autoclave and heated to 413 K for 14 days while rotating at 60 rpm. Recovered solids were washed with ∼150 cm^3 of deionized water per gram, isolated by centrifugation, and dried for 16 h at 373 K in air. Organic occluded within the solids were removed through 10 h of high temperature oxidative treatment in flowing dry air (1.67 cm^3 s^{-1} $g_{cat}{}^{-1}$, 99.999% UHP, Indiana Oxygen) at 823 K (0.0167 K s^{-1}).

Nanosheet Ti-MFI (Ti-MFI-NS) zeolites are single-unit-cell thick titanium-containing zeolites synthesized through the use of a $[C_{18}H_{37}\text{-}N^+(CH_3)_2\text{-}C_6H_{12}\text{-}N^+(CH_3)_2\text{-}C_6H_{13}]OH_2$ surfactant, denoted $C_{18-6-6}OH_2$ and synthesized in house following the procedure reported by Choi et al. [232]. The final gel molar ratios are 1 SiO_2 / 0.07 $C_{18-6-6}OH_2$ / 0.01 TBOT / 60 H_2O. 25.19 g of 0.13 M aqueous $C_{18-6-6}OH_2$ solution were diluted in 30.16 g of deionized H_2O in a covered PFA jar and stirred for 0.2 h prior to the addition of 10 g of TEOS followed by 0.5 h of stirring. Later, 0.16 g of tetrabutyl orthotitanate (TBOT, >99.99%, Alfa Aesar) were added to the synthesis gel and the resulting solution was stirred overnight in the covered PFA jar. The resulting gel was exposed to air to allow for excess water and evolved ethanol and butanol evaporation to achieve target molar ratios. The gel was loaded into a 45 cm^{-3} Teflon liner and stainless steel autoclave prior to heating to 413 K for 10 days while rotating at 60 rpm. Recovered solids were washed with ∼150 cm^3 of deionized water per gram, isolated by centrifugation, and dried for 16 h at 373 K in air. Organic occluded within the solids were removed through 10 h of high temperature oxidative treatment in flowing dry air (1.67 cm^3 s^{-1} $g_{cat}{}^{-1}$, 99.999% UHP, Indiana Oxygen) at 823 K (0.0167 K s^{-1}).

Ti-CON catalysts were prepared via post-synthetic grafting procedures of titanium precursors into deboronated CON. B-CON was synthesized using 1,4-bis(1-cyclohexyl-1,4-pyrrolidin-1-yl)butane (BCPB) as the structure directing agent and a final gel molar ratio of 1 SiO_2 / 2 NaOH / 0.1 BCPB / 0.0055 $Na_2B_4O_7$ / 45.6 H_2O. In a typical synthesis, 3.62 g of aqueous BCPB (9.9%) were diluted in 7.39 g of deionized water and 0.72 g of 1 M NaOH (99.99%, Avantor) in a PFA liner and

stirred for 0.08 h. Afterwards, 0.036 g of sodium tetraborate decahydrate ($Na_2B_4O_7$, 99.99%, Sigma Aldrich) were added and stirred for 0.08 h prior to the addition of 0.54 g of fumed silica (Cab-o-sil SiO_2, 99.9%, Cabot). The resulting gel was stirred in a covered PFA jar for 1 h before loading into a 23 cm^{-3} Teflon liner and encased in a stainless steel autoclave. The synthesis gel was heated to 433 K for 7 days rotating at 60 rpm. Recovered solids were thoroughly washed in water and acetone, isolated by centrifugation, dried overnight at 373 K, and treated at 823 K in oxygen for 10 h. B-CON zeolites were treated at 353 K in 25 cm^3 of concentrated nitric acid per gram of zeolite for 16 h to remove boron heteroatoms from the framework. Deboronated solids were washed with copious amounts of water ($\sim$200 cm^3 (g zeolite)$^{-1}$), isolated via centrifugation, and dried overnight at 373 K.

Deboronated CON (De-B-CON) was subjected to post-synthetic grafting procedures to incorporate titanium heteroatoms into the framework. Typically, $\sim$0.5 g of zeolite were loaded into a three-neck, 500 cm^{-3} round-bottom flask with a septum stopper on one opening. The flask was attached to a Schlenk line and De-B-CON precursors were dried overnight (423 K) under vacuum ($\sim$0.005 kPa). In a separate flask, dichloromethane was dried over molecular sieves (Type 3A, Grade 562, 4-8 mesh, W.R. Grace) in an inert atmosphere (Ar, Indiana Oxygen, 99.999%) for 72 h. $\sim$0.5 cm3 of 1 M titanium tetrachloride in dichloromethane ($TiCl_4$, 99.99%, Sigma Aldrich) were transferred to a pear-shaped flask and dried dichloromethane were transferred to the round-bottom flask via moisture-free cannula transfer. The resulting solution were heated to 383 K for 7 h under reflux conditions in an argon atmosphere. The resulting solids were recovered via centrifugation, washed with $\sim$120 cm^3 of methanol (99.99%, Sigma Aldrich) per gram of zeolite, and dried overnight at 373 K. Solids were treated in flowing air (1.67 cm^3 s^{-1} $g_{cat}{}^{-1}$, 99.999% UHP, Indiana Oxygen) to 473 K (0.05 K s^{-1}) for 6 h and then heated further to 823 K (0.05 K s^{-1}) for an additional 6 h.

Ti-CHA was synthesized hydrothermally by adapting the synthesis procedure reported previously [233, 234]. Briefly, 40 g of ethanol (200 proof, Koptec) and 25 g of

TEOS were added to a PFA jar and stirred for 300 s at ambient conditions. Next, a solution containing 0.601 g of TEOTi dissolved in 10 g of ethanol was added dropwise to the solution containing ethanol and TEOS and stirred for 300 s at ambient conditions. Afterward, 0.577 g of hydrogen peroxide (H_2O_2, 30 wt.%, Alfa Aesar) were added and stirred for 900 s. Next, 42.329 g of an aqueous N,N,N-trimethyl-1-adamantylammonium hydroxide solution (TMAdaOH, 25 wt.%, Sachem) were added dropwise, where the solution gelatinized after the addition of 15–20 g of TMAdaOH and required the addition of 49.920 g of deionized water and manual stirring with a Teflon spatula until the solution was uniform. The rest of the TMAdaOH was added immediately after and the solution was covered and stirred for 24 h at ambient conditions. Ethanol and excess water were evaporated from the obtained solution to reach the desired H_2O/SiO_2 molar ratio of 3. The resulting powder was rehydrated with 80 g of water, stirred for 24 h, and dehydrated again to obtain the desired H_2O/SiO_2 molar ratio of 3. Finally, 2.69 g of HF were added dropwise to the synthesis powder and stirred manually for 300 s. Residual HF was allowed to evaporate for 900 s. The final molar ratio of the gel solution was 1 SiO_2/0.014 TiO_2/0.43 TMAdaOH/0.38 HF/3 H_2O. The gel was loaded into a 45 cm^{-3} Teflon liner and stainless steel autoclave prior to heating to 423 K for 2 days while rotating at 40 rpm. Recovered solids were washed thoroughly with water and acetone, isolated by centrifugation, and dried for 16 h at 373 K in air. Organic occluded within the solids were removed through 10 h of high temperature oxidative treatment in flowing dry air (1.67 $cm^3\ s^{-1}\ g_{cat}{}^{-1}$, 99.999% UHP, Indiana Oxygen) at 823 K (0.0167 K s^{-1}).

6.3.2 Characterization of materials

Bulk crystal topologies of synthesized materials were determined from powder X-ray diffraction (XRD) patterns collected on a Rigaku SmartLab X-ray diffractometer using a Cu $\kappa\alpha$ source (1.76 kW) measured from 4-40° (2θ, 0.00417° s^{-1}). Micropore volumes were calculated from N_2 adsorption isotherms (77 K) collected on a Micromeritics ASAP 2020 Surface Area and Porosity Analyzer via linear extrapolation

from the beginning of the mesopore filling regime (∼0.05–0.30 P/P_0). All micropore volumes align with known micropore volumes of each desired zeolite topology.

Bulk titanium concentrations were determined via atomic absorption spectroscopy (AAS, PerkinElmer AAnalyst 300 Atomic Absorption Spectrometer). Typically, ∼0.2 g of solid were dissolved in ∼2 g of hydrofluoric acid (48 wt.%), left overnight, then diluted with ∼50 g of deionized water. Absorbances were measured in a reducing acetylene and nitrous oxide flame at 399.9 nm and compared to calibration curves from titanium solutions of known composition.

Nitrogen (N_2, 77 K), and argon (Ar, 87 K) adsorption isotherms were collected using a Micromeritics ASAP2020 Surface Area and Porosity Analyzer on ∼0.03 g of sample pelleted and sieved to maintain uniform particle diameters between 180 and 250 μm. Samples were degassed prior to analysis by heating to 393 K (0.0167 K $s^{-}1$) under vacuum (<0.005 Torr) for 2 h then heating to 623 K (0.0167 K $s^{-}1$) under vacuum for 8 h. Micropore volumes were calculated from the semi-log derivative analysis of N_2 (or Ar) adsorption isotherms ($\delta(V_{ads}/g)/\delta(\log(P/P_0)$ vs. $\log(P/P_0)$).

6.3.3 Glucose isomerization kinetic studies

Kinetic measurements were carried out in 10 cm^{-3} thick-walled batch reactors (VWR) with 0.01–0.1 g of sample and 5 wt.% aqueous-phase D-glucose (Sigma-Aldrich, >99.5%) solutions. Distilled water (18.2 MΩ) was pH-controlled (pH=3) with hydrochloric acid (HCl, Macron, 37 wt.%) and mixed with D-glucose to the desired weight percent. Solutions were filtered through 0.2 μm PTFE filters (VWR) and loaded into 2 cm^{-3} glass vials capped with a PTFE/silicone septum (Waters) until full. Batch reactors were loaded with a stir bar and ∼0.01–0.1 g of catalyst and sealed with a crimp top (PTFE/silicone septum, Agilent). Reactant solution vials and reactors were separately heated (373 K) for 600 s atop a digital stirred hotplate (IKA RCT basic) prior to injecting ∼1 cm^3 of preheated reactant solution into the capped reactors. Reactors were maintained at temperature (373 K, autogenous pres-

sure, 750 rpm) for various time intervals (1800–21600 s) prior to quenching in an ice bath to stop the reaction.

Product solutions were filtered (0.2 μm PTFE filters), diluted to 1 wt.% with deionized water, and mixed with an internal quantification standard of a 1 wt.% aqueous D-mannitol (Sigma Aldrich, >98 wt.%) solution. Product separation and quantification were performed using a high performance liquid chromatograph (Agilent 1260) equipped with a Hi-Plex Ca column (7.7 x 300 mm, 8 μm particle size, 0.01 cm^3 s^{-1} aqueous mobile phase, 353 K) and inline evaporative light scattering detector (Agilent 1290). Quantification was performed using separate calibration curves for individual sugar species. All reported rates and selectivities correspond to conversions of less than 5% and match initial rate measurements from transient kinetic measurements.

Isotopic labeling studies to identify isomerization products were performed by reacting 1 cm^3 of a 5 wt.% aqueous D-glucose-D_2 (Cambridge Isotope Laboratories, 98% 2-D) solution and 0.01–0.04 g of catalytic solids (373 K, 1800–21600 s) prior to quenching, filtering product solutions, and separating as described above. Product solutions were prepared by freezing in liquid N2 (77 K) and removing water via freeze-drying on a Labconco FreeZone lyophilizer (<0.01 Torr, 36 h). Dried sugars were then dissolved in 0.06 cm^3 of D_2O (Cambridge Isotope Laboratories, 99.9%) and loaded into NMR tubes (Wilmad LabGlass, 5 mm thin wall, 7 in., 500 MHz) for NMR analysis. ^{13}C NMR spectra were collected at ambient temperature on a Bruker ARX500 spectrometer equipped with a 5 mm QNP probe by averaging 256–1500 scans acquired at ∼0.3 scans per second.

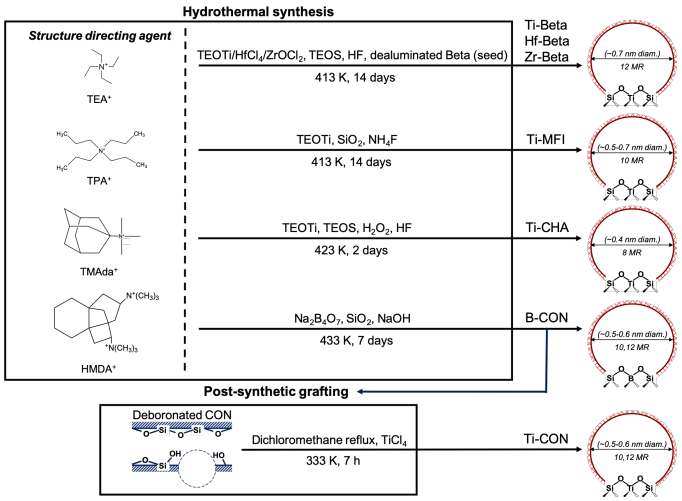

Figure 6.2: Hydrothermal and post-synthetic strategies for the preparation of titanosilicates with varied pore diameters and confining environments.

6.4 Results and Discussion

Zeotypes with Lewis acidic Ti sites were synthesized (Fig. 6.2) with a range of confining void sizes (6- to 14-MR) in order to probe the influence of confining void size on the stability of hydride shift transition states in sugar isomerization pathways. XRD patterns and micropore volumes (Table 6.2, Supporting Information) calculated from N_2 (77 K) and Ar (87 K) adsorption isotherms of Ti-Beta, Ti-MCM-41, Ti-CON, Ti-MFI, Ti-MFI-NS (nanosheet morphology) [232], and Ti-CHA are consistent with values expected for these topologies (Figs. 6.5-6.8, Supporting Information). Diffuse reflectance UV-Vis (DRUV) spectra of dehydrated samples (523 K) show absorption bands with maxima located <220 nm and edge energies that are >4.2 eV (Fig. 6.9, Table 6.7.1.4, Supporting Information). Concomitantly, Lewis acidic Ti centers (per Ti) were quantified from IR spectra after saturation with pyridine (423 K) and CD_3CN (303 K), which values varied around unity for all the samples reported here (Fig. 6.10, Table 6.7.1.4, Supporting Information). These results indicate that tetrahedrally-coordinated Ti centers are incorporated within the pores of zeotype frameworks of varying confining environments.

Initial glucose isomerization rates to fructose and sorbose (per Ti, 373 K) are measured among Ti-silicates of varying micropore size (∼4–15 nm in diameter) to interrogate the site requirements that preferentially stabilize transition states for sorbose formation. Proposed mechanisms for aqueous-phase D-glucose isomerization (373 K) to D-fructose and L-sorbose over Ti sites in zeolites involve quasi-equilibrated desorption of two water molecules from Lewis acidic Ti sites, followed by glucose adsorption and ring opening, kinetically-relevant 1,2 hydride shift transition state (for fructose formation) or 1,5 hydride shift transition state (for sorbose formation), and ring closing and desorption of the respective product [35, 192]. Glucose isomerization rates (373 K) are measured under dilute glucose thermodynamic activities (<2000 mol m^{-3}, < 10 wt.%) corresponding to kinetic regimes that are first-order in initial glucose activity, in which rate constants reflect differences in the Gibbs free energy between water-covered Ti sites and the kinetically-relevant hydride shift transition state [35, 38]. Lewis-acid catalyzed glucose isomerization rates (373 K), measured at low pH to suppress background reactions from base-mediated pathways over oxide domains [50], were undetectable on amorphous titanosilicates (TiO_2-SiO_2, Table 6.1) [35, 192]. This suggests that van der Waals stabilization of hydride shift transition states, relative to two water molecules bound at isolated Ti active sites, within confining microporous voids is required for appreciable catalytic turnover in aqueous media at 373 K.

Initial glucose-fructose and glucose-sorbose isomerization rates (373 K, 5 wt.% glucose) on titanosilicate catalysts of varying pore size are reported in Table 6.1. Isomerization rates (per Ti, 373 K) are negligible when Ti sites are embedded within the larger mesoporous cavities (>1.5 nm diam.) of Ti-MCM-41 (Table 6.1). Similar to glucose isomerization (373 K) experiments performed over amorphous TiO_2-SiO_2, these results suggest that the mesoporous voids of Ti-MCM-41 (14-MR) lack sufficient confinement and solvation of transition states required for detectable isomerization turnovers at the conditions studied.

Initial glucose isomerization rates (per Ti, 373 K), by contrast, are readily measured in aqueous media on Ti-Beta (12-MR) zeolites under these conditions. Turnover rates for glucose-fructose isomerization are invariant among samples with varying Ti content (Si/Ti = 133–282, Table 6.4, Supporting Information), with kinetic isotope effects of 2.1 measured when glucose reactants are deuterated at the α-carbonyl position [38] that indicate turnover rates are not limited by intrazeolite glucose transport to active sites [35]. On Ti-Beta, glucose-sorbose isomerization rates (per Ti, 373 K) are lower (by ∼2.5x) than glucose-fructose isomerization rates (Table 6.1). The ability of Ti-Beta to isomerize D-glucose to both D-fructose and L-sorbose suggests that confining environments characteristic of 12-MR micropores (∼0.7 nm diam.) are able to stabilize 1,2- and 1,5- hydride shift transition states, respectively, to similar extents.

The influence of 12-MR confining environments on glucose isomerization rates and selectivities was next probed using Ti-CON molecular sieves, which consist of a three-dimensional pore system with intersecting 10-MR (∼0.5–0.6 nm diam.) and 12-MR (0.7 nm diam.). Glucose isomerizes (373 K) on Ti-CON to form fructose and sorbose, but at rates (per Ti) that are 10x lower than those on Ti-Beta (Table 6.1). Differences in rates (per Ti) could arise from variations in the number of Ti sites that are tetrahedrally-coordinated within each sample, or because of restrictions on glucose (∼0.7 nm diam.) transport through the 10-MR micropores present in CON. Interestingly, sorbose formation rates (per Ti, 373 K) are >2x higher than fructose formation rates on Ti-CON (Table 6.1), suggesting that either local differences in the confining 12-MR structures of CON and Beta, or the tighter confinement provided by the 10-MR structures in CON lead to preferential sorbose formation.

The influence of confining 10-MR voids on glucose isomerization rates and selectivities was further investigated on Ti-MFI zeolites, which consist of 10-MR straight and sinusoidal channels (∼0.5 nm diam.) and their larger intersections (∼0.7 nm diam.). Glucose isomerization formed undetectable amounts of fructose on Ti-MFI, but detectable amounts of sorbose at rates (per Ti, 373 K) that are >20x lower than glucose

isomerization rates measured on Ti-Beta (Table 6.1). These measurements indicate that confinement within 10-MR selectively destabilizes reaction coordinates involving 1,2-hydride shift transition states that form fructose over those involving 1,5-hydride shift transition states that form sorbose, while the lower rates on Ti-MFI than on Ti-Beta likely reflect limitations in intrazeolitic glucose transport to framework Ti sites within 10-MR voids. Thus, we synthesized a Ti-MFI sample with nanosheet morphology (Ti-MFI-NS) following previously reported methods [232, 235], in an attempt to decrease diffusion pathlengths and alleviate potential transport restrictions of glucose to active Ti sites within 10-MR voids. An XRD pattern of this sample is consistent with the MFI structure (Fig 6.6, Supporting Information), and the N_2 adsorption-desorption isotherm (Figure 6.8, Supporting Information) shows hysteresis behavior consistent with mesoporous voids likely present within intercrystalline spaces between adjacent nanosheets. Rates of glucose-sorbose isomerization (per Ti, 373 K) are ∼1.3x higher on Ti-MFI-NS than on Ti-MFI (Table 6.1), while rates of glucose-fructose formation become detectable and similar (within 4x) to glucose-sorbose rates (Table 6.1). From these comparisons, we surmise that glucose-fructose isomerization does not occur within 10-MR microporous voids or at external surfaces of Ti-MFI-NS nanosheets, but rather at Ti sites located within its mesoporous regions. Further decreases in confining pore sizes to the 8-MR of Ti-CHA (∼0.4 nm diam. windows) resulted in undetectable glucose isomerization rates (373 K, Table 6.1), as expected from prevention altogether of glucose diffusion and adsorption within microporous voids containing Ti active sites. Taken together, these results indicate that framework Ti sites confined within 10-MR and 12-MR voids catalyze glucose isomerization to fructose and sorbose at higher rates than analogous sites within smaller or larger voids, but do so with different selectivity toward sorbose.

The selectivity of glucose isomerization (373 K) toward sorbose, defined as the initial sorbose-to-fructose formation rate ratio, varies among molecular sieves containing 10-MR and 12-MR (Table 6.1). These selectivities are calculated from initial rates measured in kinetic regimes that are first-order in glucose thermodynamic activity,

and thus reflect the relative stability of hydride shift transition states associated with forming each product (details in Section 6.7.3, Supporting Information). Ti-Beta only contains 12-MR voids and show sorbose selectivities of 0.4 (Fig. 6.3), in agreement with previously reported studies [38, 192]. Ti-CON contains both 12-MR and 10-MR voids, and show sorbose selectivities that are 5x higher than Ti-Beta. Interestingly, Ti-MFI contains 10-MR voids and forms sorbose exclusively, with order-of-magnitude higher selectivities (>10) than any larger-pore 12-MR titanosilicate analogs studied (Fig. 6.3). These results are corroborated by the higher sorbose selectivity measured on a single unit cell-thick Ti-MFI-NS sample (3.4), indicating the preferential formation of sorbose over fructose at Ti sites confined within 10-MR voids.

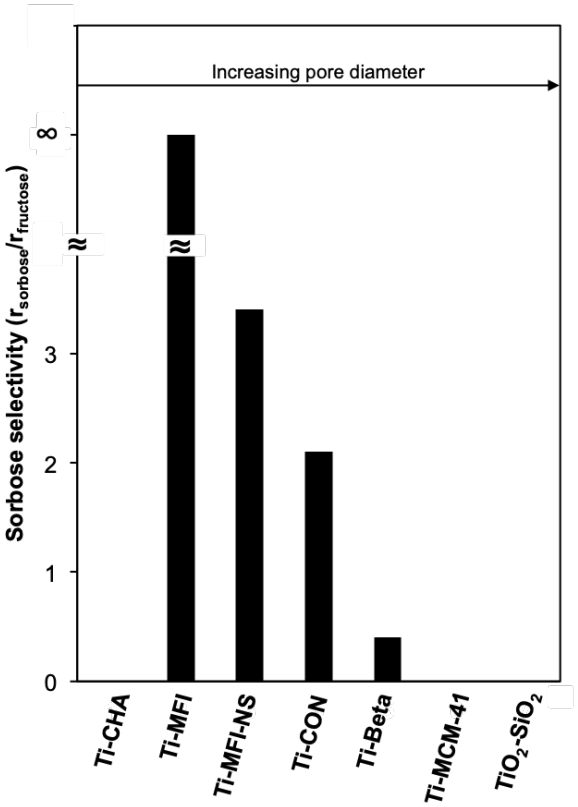

Figure 6.3: Sorbose selectivity, over fructose, of Ti-containing zeotype materials of varied pore diameter and confining environment.

Selective aqueous-phase isomerization of glucose to fructose or sorbose are influenced by the confining environment around the tetrahedrally-coordinated Ti sites. Fructose and sorbose formation require the adsorption of glucose molecules through the O5 position, ring-opening through a deprotonation step to form a carbonyl group at the C1 position and co-adsorbed water at Ti sites, and re-coordination of the carbonyl group with Ti sites (steps 1-3, Fig. 6.4) [34]. For the pathway that forms fructose, proton transfer from the co-adsorbed water onto O5, desorption and re-adsorption through the O2 position, and deprotonation to coordinate O1 to the Ti sites (steps 4-6, Fig. 6.4) are required prior to forming the kinetically-relevant 1,2-hydride shift transition state (step 7, Fig. 6.4). For the pathway that forms sorbose, however, the intermediate formed after step 3 can directly form the kinetically-relevant 1,5-hydride shift transition state (step 9, Fig. 6.4). By comparing these two reaction coordinates after their branching point (step 3, Fig. 6.4), it seems plausible that the preferential formation of sorbose within 10-MR than within 12-MR voids reflects destabilization of the re-protonation, desorption and re-adsorption, and de-protonations steps en route to fructose (steps 4-6, Fig. 6.4) within more spatially constrained 10-MR voids. We surmise that once ring-opened intermediates are formed at active Ti sites, the subsequent barriers in steps that involve 1,5-hydride shift and ring-closing and desorption to make sorbose products are not further penalized by the spatial constraints of 10-MR voids, or at least are not as severely penalized by them as the barriers involved in the reaction coordinate to form fructose.

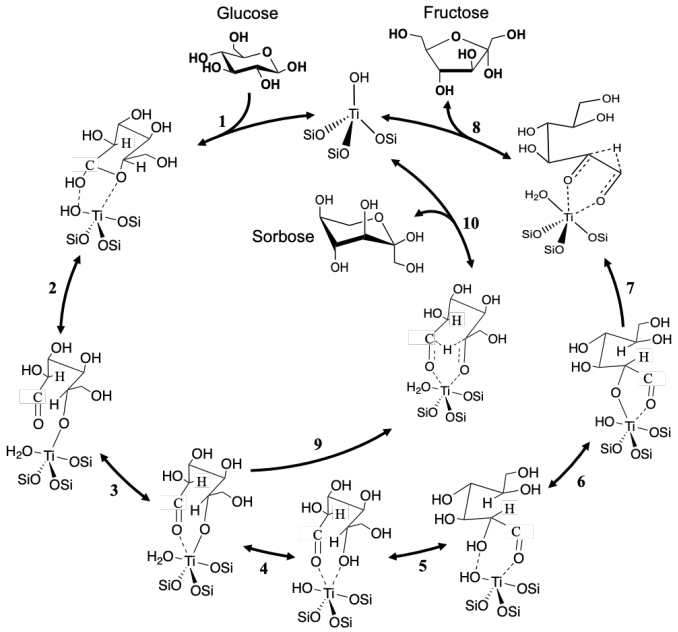

Figure 6.4: Plausible sequence of elementary steps for the catalytic turnover of glucose isomerization to fructose and sorbose over Ti-containing zeotypes.

Table 6.1: Fructose and sorbose reaction rates (per Ti) and selectivities at 373 K for Ti-containing zeotype materials.

Catalyst	Fructose formation[a]	Sorbose formation[a]	Selectivity[b]
Ti-CHA	n.d.[c]	n.d.[c]	–
Ti-Beta	$1.03\text{x}10^{-3}$	$0.40\text{x}10^{-3}$	0.4
Ti-CON	$1.69\text{x}10^{-4}$	$3.65\text{x}10^{-4}$	2.2
Ti-MFI	n.d.[c]	$5.33\text{x}10^{-5}$	>10
Ti-MFI-NS	$2.16\text{x}10^{-5}$	$7.27\text{x}10^{-5}$	3.4
Ti-MCM-41	n.d.[c]	n.d.[c]	–
TiO_2-SiO_2	n.d.[c]	n.d.[c]	–

[a]Units are [mol product (mol Ti)$^{-1}$ s^{-1}]. Catalyst loading per volume of 5 wt.% glucose solution (mg catalyst (mL solution)$^{-1}$ was 100 for TiO_2-SiO_2, Ti-MCM-41, Ti-MFI, Ti-MFI-NS and Ti-CHA, 50 for Ti-CON, and 10 for Ti-Beta.
[b]Selectivities are calculated as the ratio of initial sorbose formation rate to initial fructose formation rate.
[c]n.d. = not detected (<0.3% conversion).

6.5 Conclusions

Altogether, these kinetic data indicate that Lewis acid sites confined within microporous environments that approach the size of glucose (∼0.7 nm kinetic diam.) can selectively stabilize reaction coordinates involving 1,5-hydride shift transition states that form sorbose, over those involving 1,2-hydride shift transition states that form fructose. The combination of Lewis acid active sites (Ti) and tightly confining secondary environments (10-MR) around glucose reactants to enable selective stereoselective isomerization toward one product over other competing ones. This provides an example of a general catalyst design strategy to regulate reaction selectivity by positioning active sites within tightly confining environments that approach the size of reactants.

6.6 Acknowledgements

We acknowledge the financial support provided by the Purdue Process Safety and Assurance Center (P2SAC).

6.7 Supporting Information

6.7.1 Characterization of titanosilicate catalysts

6.7.1.1 Powder XRD patterns

All samples are denoted as Ti-IZA-X, where IZA stands for the IZA code of each zeolite topology and X represents the Si/Ti molar ratio. XRD patterns were collected on Ti-Beta zeolites with varied Ti content (Fig. 6.5) and on titanosilicates of varied pore sizes (Fig. 6.6). Predominant diffraction peaks are characteristic of each of the intended topologies.

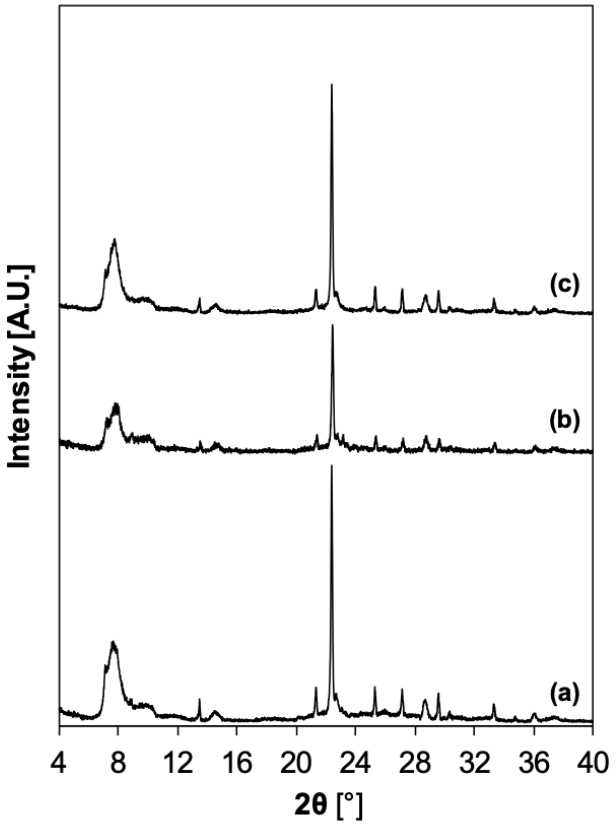

Figure 6.5: Powder XRD patterns of (a) Ti-Beta-133, (b) Ti-Beta-282, and (c) Ti-Beta-155.

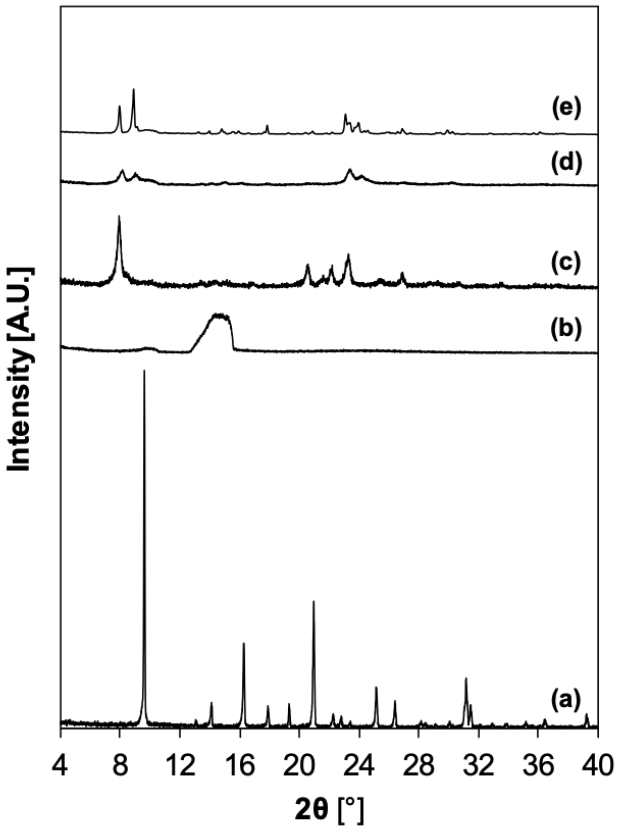

Figure 6.6: Powder XRD patterns of (a) Ti-CHA, (b) Ti-MCM-41, (C) Ti-CON, (d) Ti-MFI-NS, (e) Ti-MFI.

6.7.1.2 Gas adsorption to determine micropore volumes

Single-component isotherms were collected on titanosilicates in order to calculate the micropore volumes, collected in Table 6.2 and are characteristic of the intended topology.

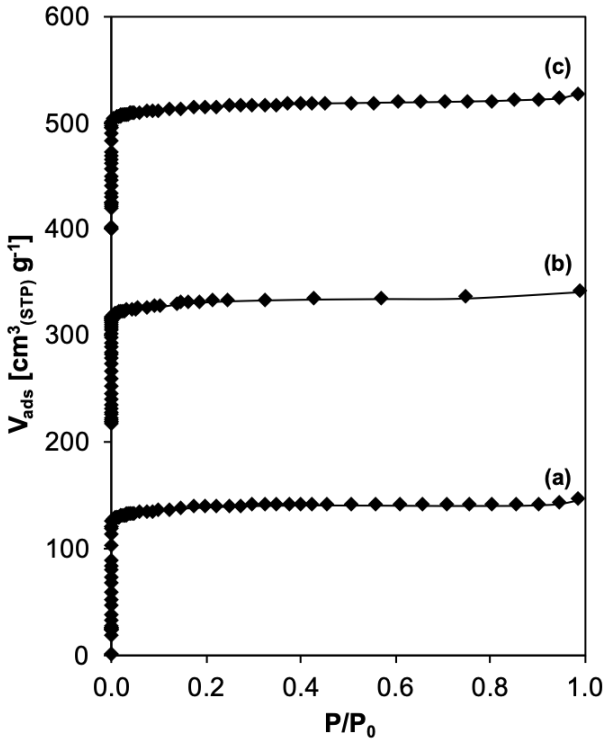

Figure 6.7: N_2 adsorption isotherms (77 K) of (a) Ti-Beta-133, (b) Ti-Beta-282, and (c) Ti-Beta-155. Isotherms are offset by 200 cm^3 g^{-1} for clarity.

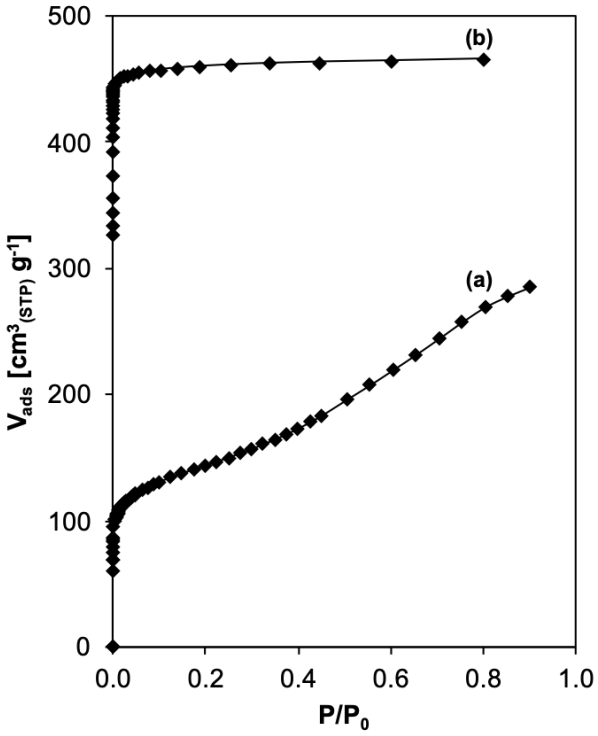

Figure 6.8: N_2 adsorption isotherms (77 K) of (a) Ti-MFI-NS and Ar adsorption isotherm (87 K) of (b) Ti-CHA. Isotherms are offset by 300 cm^3 g^{-1} for clarity.

Table 6.2: Physicochemical properties and topological details of titanosilicates of varied metal content and pore size.

Catalyst	V_{pore} [cm^3 g^{-1}][a]	Si/Ti[b]	Primary MicroporeRing Size
Ti-Beta-282	0.20	282	12
Ti-Beta-155	0.20	155	12
Ti-Beta-133	0.21	133	12
Ti-CON-109	–	109	12, 10
Ti-MFI-305	–	305	10
Ti-MFI-NS-69	0.18	69	10
Ti-CHA	0.19	–	8
TI-MCM-41	–	–	>20

[a]Calculated from semi-log derivative plot of nitrogen or argon (only for Ti-CHA) adsorption isotherms.
[b](b) Measured using atomic adsorption spectroscopy (AAS).

6.7.1.3 DR-UV-Visible spectra to determine Ti coordination

UV-Vis spectra of dehydrated samples (523 K, 0.5 h) were used as a characterization of the titanium heteroatom coordination. Here, the band maxima (<220 nm), together with edge energies calculated from Tauc plots (>4.1 eV), suggest that some titanium heteroatoms have a tetrahedral coordination, as expected upon incorporation to zeolitic frameworks [236].

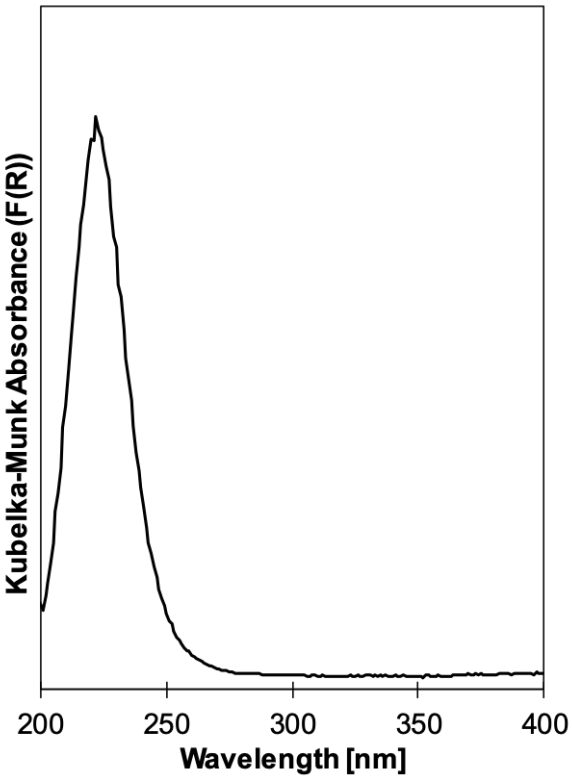

Figure 6.9: Dehydrated DRUV spectra of Ti-MFI-NS.

6.7.1.4 CD_3CN IR spectra to determine Ti coordination

The number of Lewis acidic titanium sites were quantified using infrared spectroscopy after adsorption of Lewis bases. Here, CD_3CN was dosed onto Ti-containing samples at 303 K until saturation. Deconvolution of bands associated to Lewis acid sites (2308 cm^{-1}) were quantified using molar extinction coefficients and procedures reported elsewhere [38].

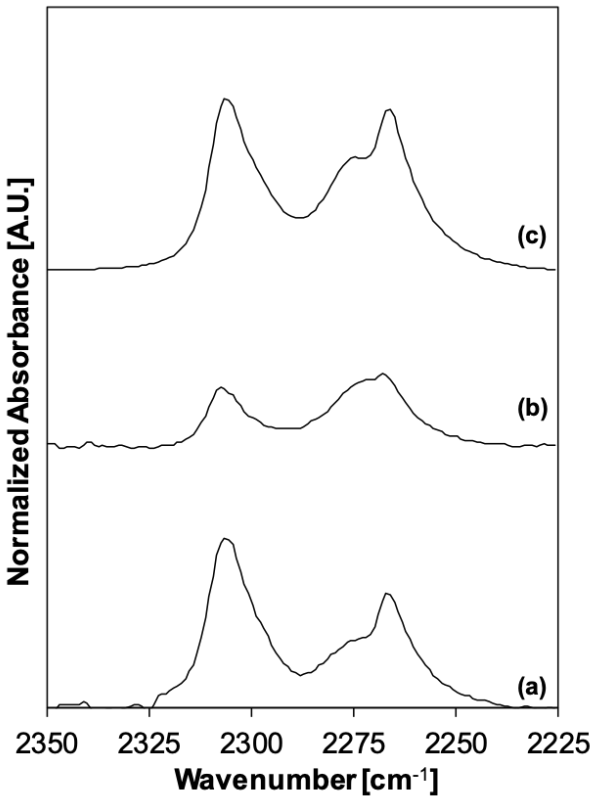

Figure 6.10: IR spectra collected at saturation coverages of CD_3CN (303 K) on (a) Ti-Beta-133, (b) Ti-Beta-282, and (c) Ti-Beta-155.

6.7.2 Liquid NMR analysis for detection of products

Reaction products were separated and collected after reactions were carried out in order to further investigate the identity of the products. The identity of the collected mixture of products were further interrogated with ^{13}C NMR, where fructose has characteristic resonances centered at 67.3 and 97.6 ppm, whereas sorbose has characteristic resonances at 61.6 and 70.2 ppm (Figs. 6.11-6.12) [192]. Ti-Beta (Fig. 6.12), Ti-CON, and Ti-MFI-NS molecular sieves have resonances for fructose and sorbose, while Ti-MFI only has resonances characteristic of sorbose (Fig. 6.11), as expected from the kinetic results discussed in the main text.

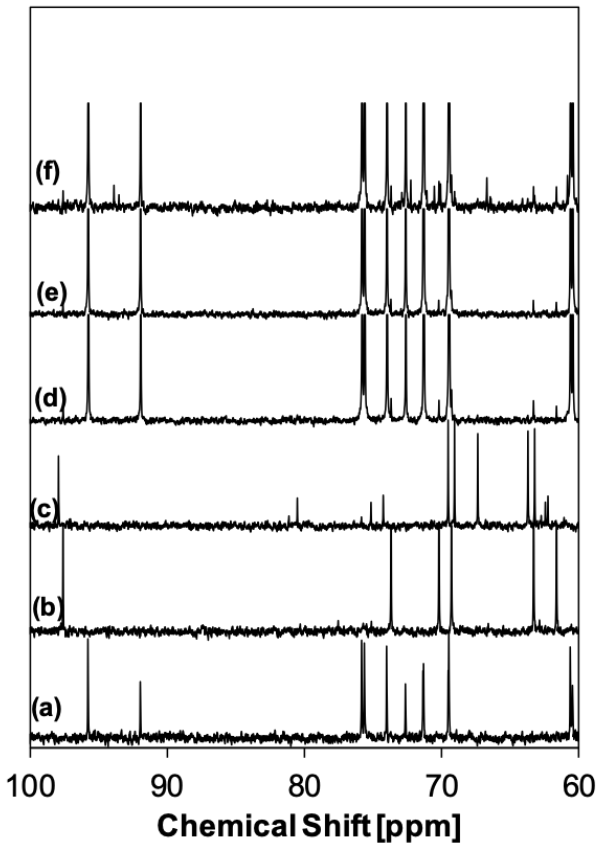

Figure 6.11: ^{13}C NMR spectra of (a) glucose, (b) fructose, and (c) sorbose standards, together with product solutions of reactions performed over (d) Ti-CON, (e) Ti-MFI-NS, and (f) Ti-MFI.

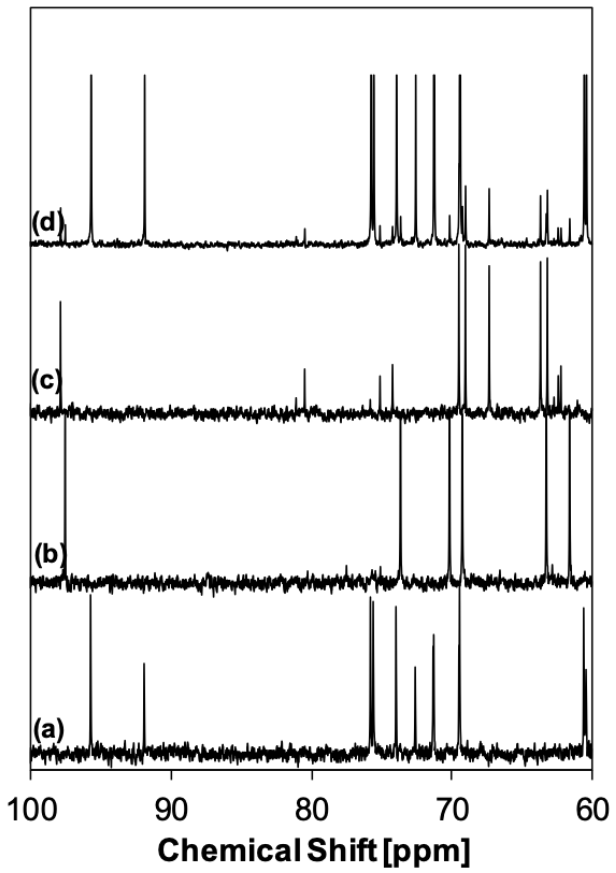

Figure 6.12: ^{13}C NMR spectra of (a) glucose, (b) fructose, and (c) sorbose standards, together with product solutions of reactions performed over (d) Ti-Beta.

6.7.3 Kinetic details of fructose and sorbose formation over titanosilicates

6.7.3.1 Mechanistic interpretation of sorbose selectivity

Aqueous-phase glucose reactants (G) undergo quasi-equilibrated adsorption onto Lewis acidic Ti sites to form ring-opened intermediates (G), followed by kinetically-relevant 1,2- or 1-5-hydride shift transition state for fructose and formation and 1,5-hydride shift transition state for sorbose formation, and finally quasi-equilibrated ring closing and desorption of the product (F for fructose and S for sorbose) [34]. Considering that two water molecules are the most abundant surface intermediate (2W), and that glucose-fructose and glucose-sorbose rates are measured in a conversion regime of negligible approach to equilibrium values ($\eta << 1$):

$$\frac{r_{fructose}}{[L]} = \frac{\gamma_{2W*}\gamma_G\gamma_*}{{\gamma_W}^2{C_W}^2\gamma_*}\frac{k_2K_1}{K_4K_5}C_G \tag{6.1}$$

$$\frac{r_{sorbose}}{[L]} = \frac{\gamma_{2W*}\gamma_G\gamma_*}{{\gamma_W}^2{C_W}^2\gamma_*}\frac{k_7K_1}{K_4K_5}C_G \tag{6.2}$$

Here, γ_j are activity coefficients for species j, C_W is the water concentration, C_G is the glucose concentration, K_j is the equilibrium coefficient for a given step, and k_2 and k_7 are the isomerization rate constants for the kinetically-relevant 1,2- and 1,5-hydride shift steps for fructose and sorbose formations, respectively. Furthermore, the selectivity towards sorbose, which is defined as the $r_{sorbose}/r_{fructose}$, equals:

$$\frac{r_{sorbose}}{r_{fructose}} = \frac{k_7}{k_2} \tag{6.3}$$

6.7.3.2 Fructose and sorbose formation rate of Ti-Beta molecular sieves

Rates of sorbose and fructose formation (per Ti, 373 K) over Ti-Beta zeolites of varied Ti content are adapted in Table 6.4 from Cordon et al. [38], where they were originally reported.

Table 6.4: Fructose and sorbose reaction rates (per Ti) and selectivities at 373 K for Ti-Beta molecular sieves of varied Ti content.

Catalyst	Fructose formation[a]	Sorbose formation[a]	Selectivity[b]
Ti-Beta-282	1.09×10^{-3}	0.71×10^{-3}	0.6
Ti-Beta-155	0.54×10^{-3}	0.28×10^{-3}	0.5
Ti-Beta-133	1.03×10^{-3}	0.40×10^{-3}	0.4

[a]Units are [mol product (mol Ti)$^{-1}$ s^{-1}]. Catalyst loading per volume of 1 wt.% glucose solution was 10 for Ti-Beta.
[b]Selectivities reflect the ratio of initial sorbose formation rate to initial fructose formation rate.

REFERENCES

[1] J. C. van der Waal, K. Q. Tan, and H. vanBekkum. Zeolite titanium Beta: A selective and water resistant catalyst in Meerwein-Ponndorf-Verley-Oppenauer reactions. *Catalysis Letters*, 41(1-2):63–67, 1996.

[2] J. C. van der Waal, P. J. Kunkeler, K. Tan, and H. van Bekkum. Zeolite titanium Beta - a selective catalyst for the gas-phase Meerwein-Ponndorf-Verley, and Oppenauer reactions. *Journal of Catalysis*, 173(1):74–83, 1998.

[3] H. Y. Luo, D. F. Consoli, W. R. Gunther, and Y. Román-Leshkov. Investigation of the reaction kinetics of isolated Lewis acid sites in Beta zeolites for the Meerwein-Ponndorf-Verley reduction of methyl levulinate to γ-valerolactone. *Journal of Catalysis*, 320:198–207, 2014.

[4] M. Boronat, A. Corma, and M. Renz. Mechanism of the Meerwein-Ponndorf-Verley-Oppenauer (MPVO) redox equilibrium on Sn- and Zr-Beta zeolite catalysts. *Journal of Physical Chemistry B*, 110(42):21168–21174, 2006.

[5] A. Corma, L. T. Nemeth, M. Renz, and S. Valencia. Sn-zeolite Beta as a heterogeneous chemoselective catalyst for Baeyer-Villiger oxidations. *Nature*, 412(6845):423–425, 2001.

[6] A. Corma and H. Garcia. Lewis acids as catalysts in oxidation reactions: From homogeneous to heterogeneous systems. *Chemical Reviews*, 102(10):3837–3892, 2002.

[7] H. Y. Luo, J. D. Lewis, and Y. Roman-Leshkov. Lewis acid zeolites for biomass conversion: Perspectives and challenges on reactivity, synthesis, and stability. *Annual Review of Chemical and Biomolecular Engineering, Vol 7*, 7:663–692, 2016.

[8] H. Y. Luo, L. Bui, W. R. Gunther, E. Min, and Y. Román-Leshkov. Synthesis and catalytic activity of Sn-MFI nanosheets for the Baeyer-Villiger oxidation of cyclic ketones. *ACS Catalysis*, 2(12):2695–2699, 2012.

[9] P. Y. Dapsens, C. Mondelli, and J. Perez-Ramirez. Design of Lewis-acid centres in zeolitic matrices for the conversion of renewables. *Chemical Society Reviews*, 44(20):7025–7043, 2015.

[10] P. Ferrini, J. Dijkmans, R. De Clercq, S. Van de Vyver, M. Dusselier, P. A. Jacobs, and B. F. Sels. Lewis acid catalysis on single site Sn centers incorporated into silica hosts. *Coordination Chemistry Reviews*, 343:220–255, 2017.

[11] S. V. Valencia and A. Corma. Three-dimensional framework of silica, germania, and tin oxide: selective oxidation catalysts. U.S. Pat. No. 5968473 A, 1999.

[12] C. C. Chang, Z. P. Wang, P. Dornath, H. J. Cho, and W. Fan. Rapid synthesis of Sn-Beta for the isomerization of cellulosic sugars. *RSC Advances*, 2(28):10475–10477, 2012.

[13] Z. H. Kang, X. F. Zhang, H. O. Liu, J. S. Qiu, W. Han, and K. L. Yeung. Factors affecting the formation of Sn-Beta zeolites by steam-assisted conversion method. *Materials Chemistry and Physics*, 141(1):519–529, 2013.

[14] Z. H. Kang, X. F. Zhang, H. O. Liu, J. S. Qiu, and K. L. Yeung. A rapid synthesis route for Sn-Beta zeolites by steam-assisted conversion and their catalytic performance in Baeyer-Villiger oxidation. *Chemical Engineering Journal*, 218:425–432, 2013.

[15] C. C. Chang, H. J. Cho, Z. P. Wang, X. T. Wang, and W. Fan. Fluoride-free synthesis of a Sn-BEA catalyst by dry gel conversion. *Green Chemistry*, 17(5):2943–2951, 2015.

[16] R. Gounder and M. E. Davis. Beyond shape selective catalysis with zeolites: Hydrophobic void spaces in zeolites enable catalysis in liquid water. *AICHE Journal*, 59(9):3349–3358, 2013.

[17] P. Li, G. Q. Liu, H. H. Wu, Y. M. Liu, J. G. Jiang, and P. Wu. Postsynthesis and selective oxidation properties of nanosized Sn-Beta zeolite. *Journal of Physical Chemistry C*, 115(9):3663–3670, 2011.

[18] C. Hammond, S. Conrad, and I. Hermans. Simple and scalable preparation of highly active Lewis acidic Sn-Beta. *Angewandte Chemie-International Edition*, 51(47):11736–11739, 2012.

[19] C. Hammond, D. Padovan, A. Al-Nayili, P. P. Wells, E. K. Gibson, and N. Dimitratos. Identification of active and spectator Sn sites in Sn-Beta following solid-state stannation, and consequences for Lewis acid catalysis. *Chemcatchem*, 7(20):3322–3331, 2015.

[20] P. Wolf, C. Hammond, S. Conrad, and I. Hermans. Post-synthetic preparation of Sn-, Ti- and Zr-Beta: a facile route to water tolerant, highly active Lewis acidic zeolites. *Dalton Transactions*, 43(11):4514–4519, 2014.

[21] B. Tang, W. L. Dai, G. J. Wu, N. J. Guan, L. D. Li, and M. Hunger. Improved postsynthesis strategy to Sn-Beta zeolites as Lewis acid catalysts for the ring-opening hydration of epoxides. *ACS Catalysis*, 4(8):2801–2810, 2014.

[22] J. Dijkmans, J. Demol, K. Houthoofd, S. Huang, Y. Pontikes, and B. Sels. Post-synthesis Sn-β: An exploration of synthesis parameters and catalysis. *Journal of Catalysis*, 330:545–557, 2015.

[23] J. Dijkmans, D. Gabriels, M. Dusselier, F. de Clippel, P. Vanelderen, K. Houthoofd, A. Malfliet, Y. Pontikes, and B. F. Sels. Productive sugar isomerization with highly active Sn in dealuminated Beta zeolites. *Green Chemistry*, 15(10):2777–2785, 2013.

[24] W. N. P. van der Graaff, G. N. Li, B. Mezari, E. A. Pidko, and E. J. M. Hensen. Synthesis of Sn-Beta with exclusive and high framework Sn content. *Chemcatchem*, 7(7):1152–1160, 2015.

[25] J. C. Vega-Vila, J. W. Harris, and R. Gounder. Controlled insertion of tin atoms into zeolite framework vacancies and consequences for glucose isomerization catalysis. *Journal of Catalysis*, 344:108–120, 2016.

[26] J. W. Harris, M. J. Cordon, J. R. Di Iorio, J. C. Vega-Vila, F. H. Ribeiro, and R. Gounder. Titration and quantification of open and closed Lewis acid sites in Sn-Beta zeolites that catalyze glucose isomerization. *Journal of Catalysis*, 335:141–154, 2016.

[27] D. T. Bregante, A. M. Johnson, A. Y. Patel, E. Z. Ayla, M. J. Cordon, B. C. Bukowski, J. Greeley, R. Gounder, and D. W. Flaherty. Cooperative effects between hydrophilic pores and solvents: Catalytic consequences of hydrogen bonding on alkene epoxidation in zeolites. *Journal of the American Chemical Society*, 141(18):7302–7319, 2019.

[28] P. Wolf, M. Valla, F. Nunez-Zarur, A. Comas-Vives, A. J. Rossini, C. Firth, H. Kallas, A. Lesage, L. Emsley, C. Coperet, and I. Hermans. Correlating synthetic methods, morphology, atomic-level structure, and catalytic activity of Sn-Beta catalysts. *ACS Catalysis*, 6(7):4047–4063, 2016.

[29] S. Tolborg, A. Katerinopoulou, D. D. Falcone, I. Sadaba, C. M. Osmundsen, R. J. Davis, E. Taarning, P. Fristrup, and M. S. Holm. Incorporation of tin affects crystallization, morphology, and crystal composition of Sn-Beta. *Journal of Materials Chemistry A*, 2(47):20252–20262, 2014.

[30] M. Boronat, P. Concepcion, A. Corma, M. Renz, and S. Valencia. Determination of the catalytically active oxidation Lewis acid sites in Sn-Beta zeolites, and their optimisation by the combination of theoretical and experimental studies. *Journal of Catalysis*, 234(1):111–118, 2005.

[31] J. S. Bates, B. C. Bukowski, J. W. Harris, J. Greeley, and R. Gounder. Distinct catalytic reactivity of Sn substituted in framework locations and at defect grain boundaries in Sn-zeolites. *ACS Catalysis*, 9(7):6146–6168, 2019.

[32] R. Bermejo-Deval, M. Orazov, R. Gounder, S. J. Hwang, and M. E. Davis. Active sites in Sn-Beta for glucose isomerization to fructose and epimerization to mannose. *ACS Catalysis*, 4(7):2288–2297, 2014.

[33] C. M. Osmundsen, M. S. Holm, S. Dahl, and E. Taarning. Tin-containing silicates: structure-activity relations. *Proceedings of the Royal Society a-Mathematical Physical and Engineering Sciences*, 468(2143):2000–2016, 2012.

[34] R. Bermejo-Deval, R. S. Assary, E. Nikolla, M. Moliner, Y. Román-Leshkov, S. J. Hwang, A. Palsdottir, D. Silverman, R. F. Lobo, L. A. Curtiss, and M. E. Davis. Metalloenzyme-like catalyzed isomerizations of sugars by Lewis acid zeolites. *Proceedings of the National Academy of Sciences of the United States of America*, 109(25):9727–9732, 2012.

[35] R. Gounder and M. E. Davis. Monosaccharide and disaccharide isomerization over Lewis acid sites in hydrophobic and hydrophilic molecular sieves. *Journal of Catalysis*, 308:176–188, 2013.

[36] C. X. A. da Silva, V. L. C. Goncalves, and C. J. A. Mota. Water-tolerant zeolite catalyst for the acetalisation of glycerol. *Green Chemistry*, 11(1):38–41, 2009.

[37] M. Moliner, Y. Román-Leshkov, and M. E. Davis. Tin-containing zeolites are highly active catalysts for the isomerization of glucose in water. *Proceedings of the National Academy of Sciences of the United States of America*, 107(14):6164–6168, 2010.

[38] M. J. Cordon, J. W. Harris, J. C. Vega-Vila, J. S. Bates, S. Kaur, M. Gupta, M. E. Witzke, E. C. Wegener, J. T. Miller, D. W. Flaherty, D. D. Hibbitts, and R. Gounder. Dominant role of entropy in stabilizing sugar isomerization transition states within hydrophobic zeolite pores. *Journal of the American Chemical Society*, 140(43):14244–14266, 2018.

[39] N. Hoeven, G. Mali, M. Mertens, and P. Cool. Design of Ti-Beta zeolites with high Ti loading and tuning of their hydrophobic/hydrophilic character. *Microporous and Mesoporous Materials*, 288, 2019.

[40] K. Hadjiivanov, E. Ivanova, R. Kefirov, J. Janas, A. Plesniar, S. Dzwigaj, and M. Che. Adsorption properties of Fe-containing dealuminated BEA zeolites as revealed by FTIR spectroscopy. *Microporous and Mesoporous Materials*, 131(1-3):1–12, 2010.

[41] S. Conrad, P. Wolf, P. Muller, H. Orsted, and I. Hermans. Influence of hydrophilicity on the Sn-Beta-catalyzed Baeyer-Villiger oxidation of cyclohexanone with aqueous hydrogen peroxide. *Chemcatchem*, 9(1):175–182, 2017.

[42] M. B. Sayed, R. A. Kydd, and R. P. Cooney. A fourier-transform infrared spectral study of H-ZSM-5 surface sites and reactivity sequences in methanol conversion. *Journal of Catalysis*, 88(1):137–149, 1984.

[43] S. Prodinger, M. A. Derewinski, A. Vjunov, S. D. Burton, I. Arslan, and J. A. Lercher. Improving stability of zeolites in aqueous phase via selective removal of structural defects. *Journal of the American Chemical Society*, 138(13):4408–4415, 2016.

[44] S. Prodinger, H. Shi, S. Eckstein, J. Z. Hu, M. V. Olarte, D. M. Camaioni, M. A. Derewinski, and J. A. Lercher. Stability of zeolites in aqueous phase reactions. *Chemistry of Materials*, 29(17):7255–7262, 2017.

[45] X. C. Zhu, N. Kosinov, J. P. Hofmann, B. Mezari, Q. Y. Qian, R. Rohling, B. M. Weckhuysen, J. Ruiz-Martinez, and E. J. M. Hensen. Fluoride-assisted synthesis of bimodal microporous ssz-13 zeolite. *Chemical Communications*, 52(15):3227–3230, 2016.

[46] M. Hunger, J. Karger, H. Pfeifer, J. Caro, B. Zibrowius, M. Bulow, and R. Mostowicz. Investigation of internal silanol groups as structural defects in ZSM-5-type zeolites. *Journal of the Chemical Society-Faraday Transactions I*, 83:3459–, 1987.

[47] J. B. Nagy, Z. Gabelica, and E. G. Derouane. A cross-polarization magic-angle-spinning ^{29}Si-NMR identification of the silanol group resonance in ZSM-5 zeolites. *Chemistry Letters*, (7):1105–1108, 1982.

[48] G. Boxhoorn, Agtg Kortbeek, G. R. Hays, and N. C. M. Alma. A high-resolution solid-state ^{29}Si NMR-study of ZSM-5 type zeolites. *Zeolites*, 4(1):15–21, 1984.

[49] E. E. Mallon, M. Y. Jeon, M. Navarro, A. Bhan, and M. Tsapatsis. Probing the relationship between silicalite-1 defects and polyol adsorption properties. *Langmuir*, 29(22):6546–6555, 2013.

[50] R. Bermejo-Deval, R. Gounder, and M. E. Davis. Framework and extraframework tin sites in zeolite Beta react glucose differently. *ACS Catalysis*, 2(12):2705–2713, 2012.

[51] Y. Román-Leshkov, M. Moliner, J. A. Labinger, and M. E. Davis. Mechanism of glucose isomerization using a solid Lewis acid catalyst in water. *Angewandte Chemie-International Edition*, 49(47):8954–8957, 2010.

[52] J. Dijkmans, M. Dusselier, W. Janssens, M. Trekels, A. Vantomme, E. Breynaert, C. Kirschhock, and B. F. Sels. An inner-/outer-sphere stabilized Sn active site in Beta-zeolite: Spectroscopic evidence and kinetic consequences. *ACS Catalysis*, 6(1):31–46, 2016.

[53] B. Notari. Titanium silicalites. *Catalysis Today*, 18(2):163 – 172, 1993.

[54] R. Gounder. Hydrophobic microporous and mesoporous oxides as Brønsted and Lewis acid catalysts for biomass conversion in liquid water. *Catalysis Science Technology*, 4(9):2877–2886, 2014.

[55] Y. Roman-Leshkov and M. E. Davis. Activation of carbonyl-containing molecules with solid Lewis acids in aqueous media. *ACS Catalysis*, 1(11):1566–1580, 2011.

[56] S. Caratzoulas, M. E. Davis, R. J. Gorte, R. Gounder, R. F. Lobo, V. Nikolakis, S. I. Sandler, M. A. Snyder, M. Tsapatsis, and D. G. Vlachos. Challenges of and insights into acid-catalyzed transformations of sugars. *Journal of Physical Chemistry C*, 118(40):22815–22833, 2014.

[57] M. Moliner. State of the art of Lewis acid-containing zeolites: lessons from fine chemistry to new biomass transformation processes. *Dalton Transactions*, 43(11):4197–4208, 2014.

[58] J. D. Lewis, S. Van de Vyver, A. J. Crisci, W. R. Gunther, V. K. Michaelis, R. G. Griffin, and Y. Román-Leshkov. A continuous flow strategy for the coupled transfer hydrogenation and etherification of 5-(hydroxymethyl)furfural using Lewis acid zeolites. *ChemSusChem*, 7(8):2255–2265, 2014.

[59] S. Bordiga, F. Bonino, A. Damin, and C. Lamberti. Reactivity of ti(iv) species hosted in ts-1 towards h2o2-h2o solutions investigated by ab initio cluster and periodic approaches combined with experimental xanes and exafs data: a review and new highlights. *Physical Chemistry Chemical Physics*, 9(35):4854–4878, 2007.

[60] P. Y. Dapsens, C. Mondelli, J. Jagielski, R. Hauert, and J. Perez-Ramirez. Hierarchical Sn-MFI zeolites prepared by facile top-down methods for sugar isomerisation. *Catalysis Science Technology*, 4(8):2302–2311, 2014.

[61] M. Moliner-Marin, Y. Román-Leshkov, M. E. Davis, and E. Nikolla. Isomerization of sugars. U.S. Pat. No. 8729256 B2, 2014.

[62] Y. O. Xiao, S. J. Hwang, D. Xie, T. Rea, S. I. Zones, and A. Katz. Heteroatom-substituted delaminated zeolites as solid Lewis acid catalysts. *ACS Catalysis*, 5(5):3108–3119, 2015.

[63] B. S. Kulkarni, S. Krishnamurty, and S. Pal. Probing Lewis acidity and reactivity of Sn- and Ti-Beta zeolite using industrially important moieties: A periodic density functional study. *Journal of Molecular Catalysis a-Chemical*, 329(1-2):36–43, 2010.

[64] N. Rai, S. Caratzoulas, and D. G. Vlachos. Role of silanol group in Sn-Beta zeolite for glucose isomerization and epimerization reactions. *ACS Catalysis*, 3(10):2294–2298, 2013.

[65] Y. P. Li, M. Head-Gordon, and A. T. Bell. Analysis of the reaction mechanism and catalytic activity of metal-substituted Beta zeolite for the isomerization of glucose to fructose. *ACS Catalysis*, 4(5):1537–1545, 2014.

[66] L. Li, C. Stroobants, K. F. Lin, P. A. Jacobs, B. F. Sels, and P. P. Pescarmona. Selective conversion of trioses to lactates over Lewis acid heterogeneous catalysts. *Green Chemistry*, 13(5):1175–1181, 2011.

[67] E. E. Platero, M. P. Mentruit, C. O. Arean, and A. Zecchina. FTIR studies on the acidity of sulfated zirconia prepared by thermolysis of zirconium sulfate. *Journal of Catalysis*, 162(2):268–276, 1996.

[68] G. T. Palomino, J. J. C. Pascual, M. R. Delgado, J. B. Parra, and C. O. Arean. FT-IR studies on the acidity of gallium-substituted mesoporous MCM-41 silica. *Materials Chemistry and Physics*, 85(1):145–150, 2004.

[69] M. R. Basila, K. H. Rhee, and T. R. Kantner. Nature of acidic sites on silica-alumina . characterization by infrared spectroscopic studies of trimethylamine + pyridine chemisorption. *Journal of Physical Chemistry*, 68(11):3197–3207, 1964.

[70] H. J. Cho, P. Dornath, and W. Fan. Synthesis of hierarchical Sn-MFI as Lewis acid catalysts for isomerization of cellulosic sugars. *ACS Catalysis*, 4(6):2029–2037, 2014.

[71] S. R. Bare, S. D. Kelly, W. Sinkler, J. J. Low, F. S. Modica, S. Valencia, A. Corma, and L. T. Nemeth. Uniform catalytic site in Sn-Beta-zeolite determined using X-ray absorption fine structure. *Journal of the American Chemical Society*, 127(37):12924–12932, 2005.

[72] P. Y. Dapsens, C. Mondelli, B. T. Kusema, R. Verel, and J. Perez-Ramirez. A continuous process for glyoxal valorisation using tailored Lewis-acid zeolite catalysts. *Green Chemistry*, 16(3):1176–1186, 2014.

[73] L. Li, X. Collard, A. Bertrand, B. F. Sels, P. P. Pescarmona, and C. Aprile. Extra-small porous Sn-silicate nanoparticles as catalysts for the synthesis of lactates. *Journal of Catalysis*, 314:56–65, 2014.

[74] J. Dijkmans, M. Dusselier, D. Gabriels, K. Houthoofd, P. C. M. M. Magusin, S. G. Huang, Y. Pontikes, M. Trekels, A. Vantomme, L. Giebeler, S. Oswald, and B. F. Sels. Cooperative catalysis for multistep biomass conversion with Sn/Al Beta zeolite. *ACS Catalysis*, 5(2):928–940, 2015.

[75] V. L. Sushkevich, A. Vimont, A. Travert, and I. I. Ivanova. Spectroscopic evidence for open and closed Lewis acid sites in Zr-BEA zeolites. *Journal of Physical Chemistry C*, 119(31):17633–17639, 2015.

[76] C. L. Angell and M. V. Howell. Infrared spectroscopic investigation of zeolites and adsorbed molecules .4. acetonitrile. *Journal of Physical Chemistry*, 73(8):2551–, 1969.

[77] P. Venkateswarlu. The rotation-vibration spectrum of methyl cyanide in the region 1.6-mu-20-mu. *Journal of Chemical Physics*, 19(3):293–298, 1951.

[78] Sounak Roy, Kevin Bakhmutsky, Eyas Mahmoud, Raul F. Lobo, and Raymond J. Gorte. Probing Lewis acid sites in Sn-Beta zeolite. *ACS Catalysis*, 3(4):573–580, 2013.

[79] J. Barthel and R. Deser. FTIR study of ion solvation and ion-pair formation in alkaline and alkaline-earth metal salt-solutions in acetonitrile. *Journal of Solution Chemistry*, 23(10):1133–1146, 1994.

[80] J. Penzien, A. Abraham, J. A. van Bokhoven, A. Jentys, T. E. Muller, C. Sievers, and J. A. Lercher. Generation and characterization of well-defined Zn^{2+} Lewis acid sites in ion exchanged zeolite BEA. *Journal of Physical Chemistry B*, 108(13):4116–4126, 2004.

[81] B. Wichterlova, Z. Tvaruzkova, Z. Sobalik, and P. Sarv. Determination and properties of acid sites in H-ferrierite - a comparison of ferrierite and MFI structures. *Microporous and Mesoporous Materials*, 24(4-6):223–233, 1998.

[82] R. van Grieken, C. Martos, M. Sanchez-Sanchez, D. P. Serrano, J. A. Melero, J. Iglesias, and A. G. Cubero. Synthesis of Sn-silicalite from hydrothermal conversion of SiO_2-SnO_2 xerogels. *Microporous and Mesoporous Materials*, 119(1-3):176–185, 2009.

[83] N. Y. Chen. Hydrophobic properties of zeolites. *Journal of Physical Chemistry*, 80(1):60–64, 1976.

[84] C. A. Emeis. Determination of integrated molar extinction coefficients for infrared-absorption bands of pyridine adsorbed on solid acid catalysts. *Journal of Catalysis*, 141(2):347–354, 1993.

[85] M. Behrens and R. Schlˆgl. *X-ray diffraction and small angle X-ray scattering*, page 653. Wiley, Weinheim, Germany, 2012.

[86] N. K. Mal and A. V. Ramaswamy. Hydroxylation of phenol over Sn-silicalite-1 molecular sieve: Solvent effects. *Journal of Molecular Catalysis a-Chemical*, 105(3):149–158, 1996.

[87] M. Bhagwat, P. Shah, and V. Ramaswamy. Synthesis of nanocrystalline SnO_2 powder by amorphous citrate route. *Materials Letters*, 57(9-10):1604–1611, 2003.

[88] N. Chiodini, A. Paleari, D. Di Martino, and G. Spinolo. SnO_2 nanocrystals in SiO_2: A wide-band-gap quantum-dot system. *Applied Physics Letters*, 81(9):1702–1704, 2002.

[89] F. Gu, S. F. Wang, C. F. Song, M. K. Lu, Y. X. Qi, G. J. Zhou, D. Xu, and D. R. Yuan. Synthesis and luminescence properties of SnO_2 nanoparticles. *Chemical Physics Letters*, 372(3-4):451–454, 2003.

[90] G. S. Pang, S. G. Chen, Y. Koltypin, A. Zaban, S. H. Feng, and A. Gedanken. Controlling the particle size of calcined SnO_2 nanocrystals. *Nano Letters*, 1(12):723–726, 2001.

[91] E. P. Parry. An infrared study of pyridine adsorbed on acidic solids characterization of surface acidity. *Journal of Catalysis*, 2(5):371–379, 1963.

[92] E. Selli and L. Forni. Comparison between the surface acidity of solid catalysts determined by tpd and FTIR analysis of pre-adsorbed pyridine. *Microporous and Mesoporous Materials*, 31(1-2):129–140, 1999.

[93] N. S. Nesterenko, F. Thibault-Starzyk, V. Montouilliout, V. V. Yushchenko, C. Fernandez, J. P. Gilson, F. Fajula, and II Ivanova. The use of the consecutive adsorption of pyridine bases and carbon monoxide in the IR spectroscopic study of the accessibility of acid sites in microporous/mesoporous materials. *Kinetics and Catalysis*, 47(1):40–48, 2006.

[94] A. I. Biaglow, D. J. Parrillo, and R. J. Gorte. Characterization of h,na-y using amine desorption. *Journal of Catalysis*, 144(1):193–201, 1993.

[95] W. E. Farneth and R. J. Gorte. Methods for characterizing zeolite acidity. *Chemical Reviews*, 95(3):615–635, 1995.

[96] O. Kresnawahjuesa, R. Heussner, C. C. Lee, G. Kuehl, and R. J. Gorte. An examination of acid sites in h-lta zeolites. *Applied Catalysis a-General*, 199(1):53–60, 2000.

[97] D. J. Parrillo, A. T. Adamo, G. T. Kokotailo, and R. J. Gorte. Amine adsorption in H-ZSM-5. *Applied Catalysis*, 67(1):107–118, 1990.

[98] G. L. Woolery, G. H. Kuehl, H. C. Timken, A. W. Chester, and J. C. Vartuli. On the nature of framework Brønsted and Lewis acid sites in ZSM-5. *Zeolites*, 19(4):288–296, 1997.

[99] J. R. Di Iorio, S. A. Bates, A. A. Verma, W. N. Delgass, F. H. Ribeiro, J. T. Miller, and R. Gounder. The dynamic nature of bronsted acid sites in cu-zeolites during nox selective catalytic reduction: Quantification by gas-phase ammonia titration. *Topics in Catalysis*, 58(7-9):424–434, 2015.

[100] S. A. Bates, W. N. Delgass, F. H. Ribeiro, J. T. Miller, and R. Gounder. Methods for nh3 titration of bronsted acid sites in cu-zeolites that catalyze the selective catalytic reduction of nox with nh3. *Journal of Catalysis*, 312:26–36, 2014.

[101] S. J. Hwang, R. Gounder, Y. Bhawe, M. Orazov, R. Bermejo-Deval, and M. E. Davis. Solid-state NMR characterization of Sn-Beta zeolites that catalyze glucose isomerization and epimerization. *Topics in Catalysis*, 58(7-9):435–440, 2015.

[102] S. Conrad, R. Verel, C. Hammond, P. Wolf, F. Goltl, and I. Hermans. Silica-grafted Sn-IV catalysts in hydrogen-transfer reactions. *Chemcatchem*, 7(20):3270–3278, 2015.

[103] N. Y. Topsøe, K. Pedersen, and E. G. Derouane. Infrared and temperature-programmed desorption study of the acidic properties of ZSM-5-type zeolites. *Journal of Catalysis*, 70(1):41–52, 1981.

[104] T. D. Courtney, C. C. Chang, R. J. Gorte, R. F. Lobo, W. Fan, and V. Nikolakis. Effect of water treatment on Sn-BEA zeolite: Origin of 960 cm^{-1} FTIR peak. *Microporous and Mesoporous Materials*, 210:69–76, 2015.

[105] N. Rajabbeigi, A. I. Torres, C. M. Lew, B. Elyassi, L. M. Ren, Z. P. Wang, H. J. Cho, W. Fan, P. Daoutidis, and M. Tsapatsis. On the kinetics of the isomerization of glucose to fructose using Sn-Beta. *Chemical Engineering Science*, 116:235–242, 2014.

[106] T. Blasco, M. A. Camblor, A. Corma, P. Esteve, J. M. Guil, A. Martinez, J. A. Perdigon-Melon, and S. Valencia. Direct synthesis and characterization of hydrophobic aluminum-free Ti-Beta zeolite. *Journal of Physical Chemistry B*, 102(1):75–88, 1998.

[107] J. R. Christianson, S. Caratzoulas, and D. G. Vlachos. Computational insight into the effect of Sn-Beta Na exchange and solvent on glucose isomerization and epimerization. *ACS Catalysis*, 5(9):5256–5263, 2015.

[108] W. S. Borghard, P. T. Reischman, and E. W. Sheppard. Argon sorption in ZSM-5. *Journal of Catalysis*, 139(1):19–23, 1993.

[109] W. S. Borghard, E. W. Sheppard, and H. J. Schoennagel. An automated, high-precision unit for low-pressure physisorption. *Review of Scientific Instruments*, 62(11):2801–2809, 1991.

[110] J. Tauc, R. Grigorovici, and A. Vancu. Optical properties and electronic structure of amorphous germanium. *Physica Status Solidi*, 15(2):627–+, 1966.

[111] J. Tauc. Optical properties and electronic structure of amorphous ge and si. *Materials Research Bulletin*, 3(1):37 – 46, 1968.

[112] E.A. Davis and N.F. Mott. Conduction in non-crystalline systems v. conductivity, optical absorption and photoconductivity in amorphous semiconductors. *The Philosophical Magazine: A Journal of Theoretical Experimental and Applied Physics*, 22(179):0903–0922.

[113] J. Datka, A. M. Turek, J. M. Jehng, and I. E. Wachs. Acidic properties of supported niobium oxide catalysts - an infrared-spectroscopy investigation. *Journal of Catalysis*, 135(1):186–199, 1992.

[114] T. R. Hughes and H.M. White. A study of the surface structure of decationized y zeolite by quantitative infrared spectroscopy. *The Journal of Physical Chemistry*, 71(7):2192–2201, 1967.

[115] M. S. Holm, S. Saravanamurugan, and E. Taarning. Conversion of sugars to lactic acid derivatives using heterogeneous zeotype catalysts. *Science*, 328(5978):602–605, 2010.

[116] H. Koller, R. F. Lobo, S. L. Burkett, and M. E. Davis. Siohosi hydrogen bonds in as-synthesized high-silica zeolites. *Journal of Physical Chemistry*, 99(33):12588–12596, 1995.

[117] A. Corma and M. E. Davis. Issues in the synthesis of crystalline molecular sieves: Towards the crystallization of low framework-density structures. *ChemPhysChem*, 5(3):304–313, 2004.

[118] Stephen K. Brand, Tyler R. Josephson, Jay A. Labinger, Stavros Caratzoulas, Dionisios G. Vlachos, and Mark E. Davis. Methyl-ligated tin silsesquioxane catalyzed reactions of glucose. *Journal of Catalysis*, 341:62–71, 2016.

[119] S. K. Brand, J. A. Labinger, and M. E. Davis. Tin silsesquioxanes as models for the "open" site in tin-containing zeolite Beta. *Chemcatchem*, 8(1):121–124, 2016.

[120] P. Wolf, M. Valla, A. J. Rossini, A. Comas-Vives, F. Nunez-Zarur, B. Malaman, A. Lesage, L. Emsley, C. Coperet, and I. Hermans. NMR signatures of the active sites in Sn-Beta zeolite. *Angewandte Chemie-International Edition*, 53(38):10179–10183, 2014.

[121] A. Zecchina, S. Bordiga, G. Spoto, L. Marchese, G. Petrini, G. Leofanti, and M. Padovan. Silicalite characterization .2. IR spectroscopy of the interaction of Co with internal and external hydroxyl-groups. *Journal of Physical Chemistry*, 96(12):4991–4997, 1992.

[122] M. T. Aronson, R. J. Gorte, and W. E. Farneth. An infrared-spectroscopy study of simple alcohols adsorbed on H-ZSM-5. *Journal of Catalysis*, 105(2):455–468, 1987.

[123] Jacques C. Védrine, Aline Auroux, Vera Bolis, Pierre Dejaifve, Claude Naccache, Piotr Wierzchowski, Eric G. Derouane, Janos B. Nagy, Jean-Pierre Gilson, Jan H. C. van Hooff, Jan P. van den Berg, and Jillus Wolthuizen. Infrared, microcalorimetric, and electron spin resonance investigations of the acidic properties of the H-ZSM-5 zeolite. *Journal of Catalysis*, 59(2):248–262, 1979.

[124] A. Zecchina, S. Bordiga, G. Spoto, D. Scarano, G. Petrini, G. Leofanti, M. Padovan, and C. O. Arean. Low-temperature fourier-transform infrared investigation of the interaction of co with nanosized zsm5 and silicalite. *Journal of the Chemical Society-Faraday Transactions*, 88(19):2959–2969, 1992.

[125] E. M. Flanigen, J. M. Bennett, R. W. Grose, J. P. Cohen, R. L. Patton, R. M. Kirchner, and J. V. Smith. Silicalite, a new hydrophobic crystalline silica molecular-sieve. *Nature*, 271(5645):512–516, 1978.

[126] J. L. Guth, H. Kessler, J. M. Higel, J. M. Lamblin, J. Patarin, A. Seive, J. M. Chezeau, and R. Wey. Zeolite synthesis in the presence of fluoride ions - a comparison with conventional synthesis methods. *ACS Symposium Series*, 398:176–195, 1989.

[127] I. Halasz, S. Kim, and B. Marcus. Uncommon adsorption isotherm of methanol on a hydrophobic y-zeolite. *Journal of Physical Chemistry B*, 105(44):10788–10796, 2001.

[128] K. Zhang, R. P. Lively, J. D. Noel, M. E. Dose, B. A. McCool, R. R. Chance, and W. J. Koros. Adsorption of water and ethanol in MFI-type zeolites. *Langmuir*, 28(23):8664–8673, 2012.

[129] J. M. Berg, J. L. Tymoczko, and L. Stryer. *Biochemistry*. W. H. Freeman, New York, fifth edition, 2002.

[130] P. W. Snyder, M. R. Lockett, D. T. Moustakas, and G. M. Whitesides. Is it the shape of the cavity, or the shape of the water in the cavity? *European Physical Journal-Special Topics*, 223(5):853–891, 2014.

[131] R. U. Lemieux. How water provides the impetus for molecular recognition in aqueous solution. *Accounts of Chemical Research*, 29(8):373–380, 1996.

[132] A. Y. Kovalevsky, L. Hanson, S. Z. Fisher, M. Mustyakimov, S. A. Mason, V. T. Forsyth, M. P. Blakeley, D. A. Keen, T. Wagner, H. L. Carrell, A. K. Katz, J. P. Glusker, and P. Langan. Metal ion roles and the movement of hydrogen during reaction catalyzed by d-xylose isomerase: A joint x-ray and neutron diffraction study. *Structure*, 18(6):688–699, 2010.

[133] T. S. G. Olsson, J. E. Ladbury, W. R. Pitt, and M. A. Williams. Extent of enthalpy-entropy compensation in protein-ligand interactions. *Protein Science*, 20(9):1607–1618, 2011.

[134] W. Kauzmann. Some factors in the interpretation of protein denaturation. *Advances in Protein Chemistry*, 14:1–63, 1959.

[135] B. Breiten, M. R. Lockett, W. Sherman, S. Fujita, M. Al-Sayah, H. Lange, C. M. Bowers, A. Heroux, G. Krilov, and G. M. Whitesides. Water networks contribute to enthalpy/entropy compensation in protein-ligand binding. *Journal of the American Chemical Society*, 135(41):15579–15584, 2013.

[136] A. M. Schrader, J. I. Monroe, R. Sheil, H. A. Dobbs, T. J. Keller, Y. X. Li, S. Jain, M. S. Shell, J. N. Israelachvili, and S. G. Han. Surface chemical heterogeneity modulates silica surface hydration. *Proceedings of the National Academy of Sciences of the United States of America*, 115(12):2890–2895, 2018.

[137] T. Ohba. Size-dependent water structures in carbon nanotubes. *Angewandte Chemie-International Edition*, 53(31):8032–8036, 2014.

[138] N. Giovambattista, P. G. Debenedetti, and P. J. Rossky. Hydration behavior under confinement by nanoscale surfaces with patterned hydrophobicity and hydrophilicity. *Journal of Physical Chemistry C*, 111(3):1323–1332, 2007.

[139] S. Chakraborty, H. Kumar, C. Dasgupta, and P. K. Maiti. Confined water: Structure, dynamics, and thermodynamics. *Accounts of Chemical Research*, 50(9):2139–2146, 2017.

[140] M. Majumder, N. Chopra, R. Andrews, and B. J. Hinds. Nanoscale hydrodynamics - enhanced flow in carbon nanotubes. *Nature*, 438(7064):44–44, 2005.

[141] J. K. Holt, H. G. Park, Y. M. Wang, M. Stadermann, A. B. Artyukhin, C. P. Grigoropoulos, A. Noy, and O. Bakajin. Fast mass transport through sub-2-nanometer carbon nanotubes. *Science*, 312(5776):1034–1037, 2006.

[142] S. D. Bernardina, E. Paineau, J. B. Brubach, P. Judeinstein, S. Rouziere, P. Launois, and P. Roy. Water in carbon nanotubes: The peculiar hydrogen bond network revealed by infrared spectroscopy. *Journal of the American Chemical Society*, 138(33):10437–10443, 2016.

[143] M. A. Mellmer, C. Sener, J. M. R. Gallo, J. S. Luterbacher, D. M. Alonso, and J. A. Dumesic. Solvent effects in acid-catalyzed biomass conversion reactions. *Angewandte Chemie-International Edition*, 53(44):11872–11875, 2014.

[144] Y. S. Liu, A. Vjunov, H. Shi, S. Eckstein, D. M. Camaioni, D. H. Mei, E. Barath, and J. A. Lercher. Enhancing the catalytic activity of hydronium ions through constrained environments. *Nature Communications*, 8, 2017.

[145] D. F. Shantz, C. Fild, H. Koller, and R. F. Lobo. Guest-host interactions in as-made al-zsm-12: Implications for the synthesis of zeolite catalysts. *Journal of Physical Chemistry B*, 103(49):10858–10865, 1999.

[146] D. F. Shantz, Jsad Gunne, H. Koller, and R. F. Lobo. Multiple-quantum ^{1}H MAS NMR studies of defect sites in as-made all-silica ZSM-12 zeolite. *Journal of the American Chemical Society*, 122(28):6659–6663, 2000.

[147] S. A. Axon and J. Klinowski. Synthesis and characterization of defect-free crystals of MFI-type zeolites. *Applied Catalysis a-General*, 81(1):27–34, 1992.

[148] J. M. Chezeau, L. Delmotte, J. L. Guth, and M. Soulard. High-resolution solid-state ^{29}Si and ^{13}C NMR on highly siliceous MFI-type zeolites synthesized in nonalkaline fluoride medium. *Zeolites*, 9(1):78–80, 1989.

[149] L. Zhang, K. Z. Chen, B. H. Chen, J. L. White, and D. E. Resasco. Factors that determine zeolite stability in hot liquid water. *Journal of the American Chemical Society*, 137(36):11810–11819, 2015.

[150] E. Bourgeat-Lami, F. Fajula, D. Anglerot, and T. D. Courieres. Single-step dealumination of zeolite-Beta precursors for the preparation of hydrophobic adsorbents. *Microporous Materials*, 1(4):237–245, 1993.

[151] R. Deruiter, A. P. M. Kentgens, J. Grootendorst, J. C. Jansen, and H. Vanbekkum. Calcination and deboronation of B-MFI single-crystals. *Zeolites*, 13(2):128–138, 1993.

[152] D. H. Mei and J. A. Lercher. Mechanistic insights into aqueous phase propanol dehydration in H-ZSM-5 zeolite. *AICHE Journal*, 63(1):172–184, 2017.

[153] C. B. Khouw and M. E. Davis. Catalytic activity of titanium silicates synthesized in the presence of alkali-metal and alkaline-earth ions. *Journal of Catalysis*, 151(1):77–86, 1995.

[154] N. A. Grosso-Giordano, C. Schroeder, A. Olkrut, A. Solovyoy, C. Schottle, W. Chasse, N. Marinkoyic, H. Koller, S. I. Zones, and A. Katz. Outer-sphere control of catalysis on surfaces: A comparative study of ti(iv) single-sites grafted on amorphous versus crystalline silicates for alkene epoxidation. *Journal of the American Chemical Society*, 140(15):4956–4960, 2018.

[155] P. A. Zapata, J. Faria, M. P. Ruiz, R. E. Jentoft, and D. E. Resasco. Hydrophobic zeolites for biofuel upgrading reactions at the liquid-liquid interface in water/oil emulsions. *Journal of the American Chemical Society*, 134(20):8570–8578, 2012.

[156] P. A. Zapata, Y. Huang, M. A. Gonzalez-Borja, and D. E. Resasco. Silylated hydrophobic zeolites with enhanced tolerance to hot liquid water. *Journal of Catalysis*, 308:82–97, 2013.

[157] H. Zhao, T. Yokoi, J. N. Kondo, and T. Tatsumi. Hydrophobicity enhancement of ti-mww catalyst and its improvement in oxidation activity. *Applied Catalysis a-General*, 503:156–164, 2015.

[158] B. C. Bukowski, J. S. Bates, R. Gounder, and J. Greeley. First principles, microkinetic, and experimental analysis of Lewis acid site speciation during ethanol dehydration on Sn-Beta zeolites. *Journal of Catalysis*, 365:261–276, 2018.

[159] J. S. Bates and R. Gounder. Influence of confining environment polarity on ethanol dehydration catalysis by Lewis acid zeolites. *Journal of Catalysis*, 365:213–226, 2018.

[160] W. N. P. van der Graaff, C. H. L. Tempelman, G. Li, B. Mezari, N. Kosinov, E. A. Pidko, and E. J. M. Hensen. Competitive adsorption of substrate and solvent in Sn-Beta zeolite during sugar isomerization. *ChemSusChem*, 9(22):3145–3149, 2016.

[161] G. Yang, E. A. Pidko, and E. J. M. Hensen. The mechanism of glucose isomerization to fructose over Sn-BEA zeolite: A periodic density functional theory study. *Chemsuschem*, 6(9):1688–1696, 2013.

[162] S. H. Mushrif, J. J. Varghese, and C. B. Krishnamurthy. Solvation dynamics and energetics of intramolecular hydride transfer reactions in biomass conversion. *Physical Chemistry Chemical Physics*, 17(7):4961–4969, 2015.

[163] V. J. Cybulskis, J. W. Harris, Y. Zvinevich, F. H. Ribeiro, and R. Gounder. A transmission infrared cell design for temperature-controlled adsorption and reactivity studies on heterogeneous catalysts. *Review of Scientific Instruments*, 87(10), 2016.

[164] G. Kresse and J. Furthmuller. Efficient iterative schemes for ab initio total-energy calculations using a plane-wave basis set. *Physical Review B*, 54(16):11169–11186, 1996.

[165] G. Kresse and J. Furthmuller. Efficiency of ab-initio total energy calculations for metals and semiconductors using a plane-wave basis set. *Computational Materials Science*, 6(1):15–50, 1996.

[166] G. Kresse and J. Hafner. Abinitio molecular-dynamics for liquid-metals. *Physical Review B*, 47(1):558–561, 1993.

[167] P. E. Blochl. Projector augmented-wave method. *Physical Review B*, 50(24):17953–17979, 1994.

[168] G. Kresse and D. Joubert. From ultrasoft pseudopotentials to the projector augmented-wave method. *Physical Review B*, 59(3):1758–1775, 1999.

[169] J. P. Perdew, K. Burke, and M. Ernzerhof. Generalized gradient approximation made simple. *Physical Review Letters*, 77(18):3865–3868, 1996.

[170] Y. K. Zhang and W. T. Yang. Comment on "generalized gradient approximation made simple". *Physical Review Letters*, 80(4):890–890, 1998.

[171] B. Hammer, L. B. Hansen, and J. K. Norskov. Improved adsorption energetics within density-functional theory using revised perdew-burke-ernzerhof functionals. *Physical Review B*, 59(11):7413–7421, 1999.

[172] S. Grimme, S. Ehrlich, and L. Goerigk. Effect of the damping function in dispersion corrected density functional theory. *Journal of Computational Chemistry*, 32(7):1456–1465, 2011.

[173] S. Grimme, J. Antony, S. Ehrlich, and H. Krieg. A consistent and accurate ab initio parametrization of density functional dispersion correction (dft-d) for the 94 elements h-pu. *Journal of Chemical Physics*, 132(15), 2010.

[174] H. J. Monkhorst and J. D. Pack. Special points for brillouin-zone integrations. *Physical Review B*, 13(12):5188–5192, 1976.

[175] H. Jónsson, G. Mills, and K. W. Jacobsen. Nudged elastic band method for finding minimum energy paths of transitions. pages 385–404.

[176] G. Henkelman and H. Jonsson. Improved tangent estimate in the nudged elastic band method for finding minimum energy paths and saddle points. *Journal of Chemical Physics*, 113(22):9978–9985, 2000.

[177] G. Henkelman and H. Jonsson. A dimer method for finding saddle points on high dimensional potential surfaces using only first derivatives. *Journal of Chemical Physics*, 111(15):7010–7022, 1999.

[178] C. Baerlocher and L. B. McCusker. Database of zeolite structures; http://www.iza-structure.org/databases/ (accessed 2018).

[179] J. M. Newsam, M. M. J. Treacy, W. T. Koetsier, and C. B. Degruyter. Structural characterization of zeolite-Beta. *Proceedings of the Royal Society of London Series a-Mathematical Physical and Engineering Sciences*, 420(1859):375–, 1988.

[180] A. Urakawa, T. Burgi, and A. Baiker. Sensitivity enhancement and dynamic behavior analysis by modulation excitation spectroscopy: Principle and application in heterogeneous catalysis. *Chemical Engineering Science*, 63(20):4902–4909, 2008.

[181] D. T. Bregante, P. Priyadarshini, and D. W. Flaherty. Kinetic and spectroscopic evidence for reaction pathways and intermediates for olefin epoxidation on nb in *BEA. *Journal of Catalysis*, 348:75–89, 2017.

[182] T. Ressler. Winxas: a program for x-ray absorption spectroscopy data analysis under ms-windows. *Journal of Synchrotron Radiation*, 5:118–122, 1998.

[183] M. A. Camblor, A. Corma, and S. Valencia. Characterization of nanocrystalline zeolite Beta. *Microporous and Mesoporous Materials*, 25(1-3):59–74, 1998.

[184] N. E. Thornburg, A. B. Thompson, and J. M. Notestein. Periodic trends in highly dispersed groups iv and v supported metal oxide catalysts for alkene epoxidation with h2o2. *ACS Catalysis*, 5(9):5077–5088, 2015.

[185] F. Bonino, A. Damin, S. Bordiga, C. Lamberti, and A. Zecchina. Interaction of cd3cn and pyridine with the ti(iv) centers of ts-1 catalysts: a spectroscopic and computational study. *Langmuir*, 19(6):2155–2161, 2003.

[186] V. Eroshenko, R. C. Regis, M. Soulard, and J. Patarin. The heterogeneous systems 'water-hydrophobic zeolites': new molecular springs. *Comptes Rendus Physique*, 3(1):111–119, 2002.

[187] M. E. Dose, K. Zhang, J. A. Thompson, J. Leisen, R. R. Chance, W. J. Koros, B. A. McCool, and R. P. Lively. Effect of crystal size on framework defects and water uptake in fluoride mediated silicalite-1. *Chemistry of Materials*, 26(15):4368–4376, 2014.

[188] P. A. Thiel and T. E. Madey. The interaction of water with solid-surfaces - fundamental-aspects. *Surface Science Reports*, 7(6-8):211–385, 1987.

[189] J. A. Lercher and A. Jentys. *Infrared and Raman Spectroscopy for Characterizing Zeolites*, volume 168, pages 435 – 476. Elsevier Science, Amsterdam, 2007.

[190] C. P. Lawrence and J. L. Skinner. Vibrational spectroscopy of HOD in liquid D_2O. iii. spectral diffusion, and hydrogen-bonding and rotational dynamics. *Journal of Chemical Physics*, 118(1):264–272, 2003.

[191] D. Eisenberg and W. Kauzmann. *The Structure and Properties of Water*. Oxford Classic Texts in the Physical Sciences. Oxford, 2005.

[192] R. Gounder and M. E. Davis. Titanium-Beta zeolites catalyze the stereospecific isomerization of d-glucose to l-sorbose via intramolecular c5-c1 hydride shift. *ACS Catalysis*, 3(7):1469–1476, 2013.

[193] R. J. Madon and E. Iglesia. Catalytic reaction rates in thermodynamically non-ideal systems. *Journal of Molecular Catalysis a-Chemical*, 163(1-2):189–204, 2000.

[194] K. Miyajima, M. Sawada, and M. Nakagaki. Studies on aqueous-solutions of saccharides .1. activity-coefficients of monosaccharides in aqueous-solutions at 25-degrees-c. *Bulletin of the Chemical Society of Japan*, 56(6):1620–1623, 1983.

[195] M. Koretsky. *Engineering and Chemical Thermodynamics*. John Wiley Sons, Inc., Hoboken, NJ, 2004.

[196] Coblentz Society. *Evaluated Infrared Reference Spectra*. National Institute of Standards and Technology, Gaithersburg, MD, 2018.

[197] M. Hineno. Infrared spectra and normal vibration of -d-glucopyranose. *Carbohydrate Research*, 56(2):219 – 227, 1977.

[198] J. J. Cael, J. L. Koenig, and Blackwel.J. Infrared and Raman-spectroscopy of carbohydrates .4. identification of configuration-sensitive and conformation-sensitive modes for D-glucose by normal coordinate analysis. *Carbohydrate Research*, 32(1):79–91, 1974.

[199] H. A. Wells and R. H. Atalla. An investigation of the vibrational-spectra of glucose, galactose and mannose. *Journal of Molecular Structure*, 224:385–424, 1990.

[200] M. Mathlouthi and D. V. Luu. Laser-raman spectra of d-glucose and sucrose in aqueous-solution. *Carbohydrate Research*, 81(2):203–212, 1980.

[201] M. Ibrahim, M. Alaam, H. El-Haes, A. F. Jalbout, and A d. Leon. Analysis of the structure and vibrational spectra of glucose and fructose. *Eclética Química*, 31:15–21, 2006.

[202] P. Bai, J. I. Siepmann, and M. W. Deem. Adsorption of glucose into zeolite Beta from aqueous solution. *AICHE Journal*, 59(9):3523–3529, 2013.

[203] J. W. Liu, D. Hibbitts, and E. Iglesia. Dense co adlayers as enablers of co hydrogenation turnovers on ru surfaces. *Journal of the American Chemical Society*, 139(34):11789–11802, 2017.

[204] D. Chandler. Interfaces and the driving force of hydrophobic assembly. *Nature*, 437(7059):640–647, 2005.

[205] N. M. Wilson and D. W. Flaherty. Mechanism for the direct synthesis of h2o2 on pd clusters: Heterolytic reaction pathways at the liquid-solid interface. *Journal of the American Chemical Society*, 138(2):574–586, 2016.

[206] T. H. Kim, P. Mehrabi, Z. Ren, A. Sljoka, C. Ing, A. Bezginov, L. B. Ye, R. Pomes, R. S. Prosser, and E. F. Pai. The role of dimer asymmetry and protomer dynamics in enzyme catalysis. *Science*, 355(6322), 2017.

[207] D. Baurecht and U. P. Fringeli. Quantitative modulated excitation fourier transform infrared spectroscopy. *Review of Scientific Instruments*, 72(10):3782–3792, 2001.

[208] P. D. Vasko, J. Blackwell, and J. L. Koenig. Infrared and raman spectroscopy of carbohydrates .2. normal coordinate analysis of alpha-d-glucose. *Carbohydrate Research*, 23(3):407–+, 1972.

[209] F. Farges, G. E. Brown, and J. J. Rehr. Coordination chemistry of ti(iv) in silicate glasses and melts .1. xafs study of titanium coordination in oxide model compounds. *Geochimica Et Cosmochimica Acta*, 60(16):3023–3038, 1996.

[210] R. M. Dessau. Selective sorption properties of zeolites. *ACS Symposium Series*, 135:123–135, 1980.

[211] C. D. Baertsch, S. L. Soled, and E. Iglesia. Isotopic and chemical titration of acid sites in tungsten oxide domains supported on zirconia. *Journal of Physical Chemistry B*, 105(7):1320–1330, 2001.

[212] J. M. Guil, R. Guil-Lopez, J. A. Perdigon-Melon, and A. Corma. Determining the topology of zeolites by adsorption microcalorimetry of organic molecules. *Microporous and Mesoporous Materials*, 22(1-3):269–279, 1998.

[213] Herman van Bekkum, Edith M. Flanigen, and J. C. Jansen. *Introduction to zeolite science and practice*. Studies in surface science and catalysis. Elsevier, Amsterdam ; New York, 1991.

[214] Udo Buck and Friedrich Huisken. Infrared spectroscopy of size-selected water and methanol clusters. *Chemical Reviews*, 100(11):3863–3890, 2000.

[215] Matthias Van Thiel, Edwin D. Becker, and George C. Pimentel. Infrared studies of hydrogen bonding of methanol by the matrix isolation technique. *The Journal of Chemical Physics*, 27(1):95–99, 1957.

[216] M. Falk and E. Whalley. Infrared spectra of methanol and deuterated methanols in gas, liquid, and solid phases. *The Journal of Chemical Physics*, 34(5):1554–1568, 1961.

[217] B. C. Bukowski, J. S. Bates, R. Gounder, and J. Greeley. Defect-mediated ordering of condensed water structures in microporous zeolites. *Angewandte Chemie-International Edition*.

[218] A. A. Gabrienko, S. S. Arzumanov, A. V. Toktarev, I. G. Danilova, D. Freude, and A. G. Stepanov. H/D exchange of molecular hydrogen with Brønsted acid sites of Zn- and Ga-modified zeolite BEA. *Physical Chemistry Chemical Physics*, 12(19):5149–5155, 2010.

[219] J. A. Biscardi, G. D. Meitzner, and E. Iglesia. Structure and density of active Zn species in Zn/H-ZSM-5 propane aromatization catalysts. *Journal of Catalysis*, 179(1):192–202, 1998.

[220] K. Chakarova, N. Drenchev, M. Mihaylov, P. Nikolov, and K. Hadjiivanov. OH/OD isotopic shift factors of isolated and H-bonded surface silanol groups. *Journal of Physical Chemistry C*, 117(10):5242–5248, 2013.

[221] V. L. Sushkevich, II Ivanova, and A. V. Yakimov. Revisiting acidity of Sn-BEA catalysts by combined application of FTIR spectroscopy of different probe molecules. *Journal of Physical Chemistry C*, 121(21):11437–11447, 2017.

[222] M. E. Davis. Heterogeneous catalysis for the conversion of sugars into polymers. *Topics in Catalysis*, 58(7-9):405–409, 2015.

[223] M. Dusselier, P. Van Wouwe, A. Dewaele, P. A. Jacobs, and B. F. Sels. Shape-selective zeolite catalysis for bioplastics production. *Science*, 349(6243):78–80, 2015.

[224] S. M. Csicsery. Shape-selective catalysis in zeolites. *Zeolites*, 4(3):202–213, 1984.

[225] L. B. Young, S. A. Butter, and W. W. Kaeding. Shape selective reactions with zeolite catalysts .3. selectivity in xylene isomerization, toluene methanol alkylation, and toluene disproportionation over ZSM-5 zeolite catalysts. *Journal of Catalysis*, 76(2):418–432, 1982.

[226] D. Seddon. Selectivity for para-xylene in the isomerization of xylenes catalyzed by zeolites with 10-ring windows. *Journal of Catalysis*, 98(1):1–6, 1986.

[227] T. F. Degnan. The implications of the fundamentals of shape selectivity for the development of catalysts for the petroleum and petrochemical industries. *Journal of Catalysis*, 216(1-2):32–46, 2003.

[228] R. Gounder and E. Iglesia. The catalytic diversity of zeolites: confinement and solvation effects within voids of molecular dimensions. *Chemical Communications*, 49(34):3491–3509, 2013.

[229] S. J. Angyal. The lobry de bruyn-alberda van ekenstein transformation and related reactions. *Glyoscience: Epimerisation, Isomerisation and Rearrangement Reactions of Carbohydrates*, 215:1–14, 2001.

[230] K. Matsushita, H. Toyama, and O. Adachi. Respiratory chains and bioenergetics of acetic-acid bacteria. *Advances in Microbial Physiology, Vol 36*, 36:247–301, 1994.

[231] C. Bronnimann, Z. Bodnar, P. Hug, T. Mallat, and A. Baiker. Direct oxidation of l-sorbose to 2-keto-l-gulonic acid with molecular-oxygen on platinum-based and pallaium-based catalysts. *Journal of Catalysis*, 150(1):199–211, 1994.

[232] M. Choi, K. Na, J. Kim, Y. Sakamoto, O. Terasaki, and R. Ryoo. Stable single-unit-cell nanosheets of zeolite MFI as active and long-lived catalysts. *Nature*, 461(7261):246–U120, 2009.

[233] E. A. Eilertsen, S. Bordiga, C. Lamberti, A. Damin, F. Bonino, B. Arstad, S. Svelle, U. Olsbye, and K. P. Lillerud. Synthesis of titanium chabazite: A new shape selective oxidation catalyst with small pore openings and application in the production of methyl formate from methanol. *Chemcatchem*, 3(12):1869–1871, 2011.

[234] J. W. Harris, W. C. Liao, J. R. Di Iorio, A. M. Henry, T. C. Ong, A. Comas-Vives, C. Coperet, and R. Gounder. Molecular structure and confining environment of Sn sites in single-site chabazite zeolites. *Chemistry of Materials*, 29(20):8824–8837, 2017.

[235] K. Na, C. Jo, J. Kun, W. S. Ahn, and R. Ryoo. MFI titanosilicate nanosheets with single-unit-cell thickness as an oxidation catalyst using peroxides. *ACS Catalysis*, 1(8):901–907, 2011.

[236] T. R. Eaton, A. M. Boston, A. B. Thompson, K. A. Gray, and J. M. Notestein. Counting active sites on titanium oxide-silica catalysts for hydrogen peroxide activation through in situ poisoning with phenylphosphonic acid. *Chemcatchem*, 6(11):3215–3222, 2014.

VITA

Juan Carlos Vega-Vila was born in Humacao, but grew up with an older sister in Las Piedras, Puerto Rico. Besides Juan Carlos' passion for science and mathematics from a young age, he also grew up playing volleyball, singing, and dancing. He went to the "Colegio Nuestra Señora del Perpetuo Socorro" until ninth grade, where he graduated from middle school. Juan Carlos graduated from high school in two years from the "Centro Residencial de Oportunidades Educativas de Mayagüez (C.R.O.E.M.)," a boarding school specialized in science and mathematics education, in 2009. Juan Carlos obtained a Bachelor's Degree in Chemical Engineering from the University of Puerto Rico-Mayagüez Campus (UPRM), where he had honors registration throughout his time there as part of the top 5% GPAs in the chemical engineering graduating class. During his time at UPRM, he performed research under the advise of Prof. Nelson Cardona-Martínez on catalyst design for biomass applications. Juan Carlos proceeded to become a doctoral student at Purdue University, as the recipient of the Frederick N. Andrews Fellowship, to focus on the preparation of Lewis acid zeolites with tailored active and defect site structures and the catalytic consequences of such structures on aqueous-phase sugar isomerization catalysis. His scientific contributions led to various technical articles, as well as several oral and poster presentations in national and local conferences, some of which resulted in presentation awards.